Tampere University

SHINYA ABE

Exercise and Proximal Femur Bone Strength to Reduce Fall-Induced Hip Fracture

Tampere University Dissertations 908

Tampere University Dissertations 908

SHINYA ABE

Exercise and Proximal Femur Bone Strength to Reduce Fall-Induced Hip Fracture

ACADEMIC DISSERTATION
To be presented, with the permission of
the Faculty of Engineering and Natural Sciences
of Tampere University,
for public discussion in the auditorium RG202
of the Rakennustalo, Korkeakoulunkatu 5, Tampere,
on 15 December 2023, at 12 o'clock.

ACADEMIC DISSERTATION
Tampere University, Faculty of Engineering and Natural Sciences
Finland

Responsible supervisor and Custos
Professor
Reijo Kouhia
Tampere University
Finland

Supervisor
Research Director, Adjunct Professor
Harri Sievänen
The UKK Institute for Health Promotion Research
Finland

Pre-examiners
Professor
Joyce H. Keyak
University of California, Irvine
United States of America

Academy Research Fellow
Timo Rantalainen
University of Jyväskylä
Finland

Opponent
Professor Emeritus
Jukka Jurvelin
University of Eastern Finland
Finland

The originality of this thesis has been checked using the Turnitin OriginalityCheck service.

Cover design: Roihu Inc.

ISBN 978-952-03-3165-8 (print)
ISBN 978-952-03-3166-5 (pdf)
ISSN 2489-9860 (print)
ISSN 2490-0028 (pdf)
http://urn.fi/URN:ISBN:978-952-03-3166-5

HIILINEUTRAALI PAINOTUOTE
ClimateCalc CC-000025/FI
PunaMusta Printing

Carbon dioxide emissions from printing Tampere University dissertations have been compensated.

PunaMusta Oy – Yliopistopaino
Joensuu 2023

ACKNOWLEDGEMENTS

Throughout my doctoral research journey, I have been fortunate to receive a great deal of support and assistance from various individuals and resources. I would certainly not have reached this far with any of them missing.

I would like to express my deepest appreciation to Research Director, Adjunct Professor Harri Sievänen ScD and Professor Reijo Kouhia PhD for their invaluable guidance, unwavering support, and patience. Dr. Sievänen has supervised my research during both master's and doctoral degrees. I deeply appreciate his detailed feedback on my academic writing and his expert guidance on various aspects of bone research. I am profoundly thankful to Prof. Kouhia for his skilled mentorship on the technical aspects of my research. Furthermore, I am sincerely grateful to both for providing various opportunities that allowed me to expand my knowledge and improve my skills. I am also thankful to coauthors, Professor Jari Hyttinen PhD, Senior Researcher Nathaniel Narra PhD, and Professor Riku Nikander PhD for their invaluable assistance and substantial contributions to my research.

Importantly, this endeavor would not have been possible without the financial support from the following funding bodies: Tampere University's (former Tampere University of Technology's) Graduate School and Industrial Research Fund, the Pirkanmaa Regional Fund from the Finnish Cultural Foundation, and the Päivikki and Sakari Sohlberg Foundation. I extend my sincere thanks to the Steering Committee and Education Specialist Anna Nykänen from Doctoral Programme in Engineering Sciences in the Faculty of Engineering and Natural Sciences for their guidance. I'd also like to acknowledge my colleagues from Structural Engineering Research Group for their supports and fruitful discussions.

Words cannot express my gratitude to Professor Randall Jensen PhD and Professor Phillip Watts PhD for their endless support and inspirations. They are my supervisors during my bachelor's studies in USA who introduced me to the world of research and the joy in science.

Last but not least, I would like to extend my sincere thanks to my family and friends for their valuable advice and support, and especially my partner – Nelli for her endless support and keeping my spirits and motivation high.

ABSTRACT

Bone mass and structure, constituting its strength, adapt to prevalent mechanical environment. Physical activity and exercise provide natural ways to apply the mechanical loading to bone. Finding effective osteogenic exercise types to improve proximal femur bone strength is of great importance to reduce hip fracture incidence and consequent substantial socioeconomic burden. Importantly, almost all hip fractures are caused by falls. Therefore, the primary objective of the present doctoral research was to find such effective exercise types by exploring the effect of long-term specific exercise loading on proximal femur bone strength in the fall situation using a finite element (FE) method. The secondary objective was to analyze 3D morphological adaptation of proximal femur cortical bone to the specific exercise loading. The results from this secondary objective were anticipated to help understanding the findings pertinent to the primary objective.

To achieve these objectives, proximal femur MRI data were obtained from 91 young adult female athletes (aged 24.7 $\pm$ 6.1 years, > 8 years competing career) and 20 nonathletic but physically active controls (aged 23.7 $\pm$ 3.8 years). The athletes were classified into five distinct exercise loading groups based on the typical loading patterns of their sports: high-impact (H-I: triple- and high-jumpers), odd-impact (O-I: soccer/football and squash players), high-magnitude (H-M: powerlifters), repetitive-impact (R-I: endurance runners), and repetitive non-impact (R-NI: swimmers). Based on their MRI data, proximal femur FE models were first created in a single fall configuration (direction) to compare 1) cortical stresses in eight anatomical octants of femoral neck cross-sections in the proximal, middle, and distal femoral neck regions and 2) fracture behavior (load, location, and mode) between each exercise loading and control groups. The athletic bones are adapted to the long-term specific exercise loading characterized by not only the loading magnitude, rate, and frequency but also direction. Given this, the study was extended to simulate the FE models in multiple fall directions to examine whether potentially identified higher proximal femur bone strength to reduce fall-induced hip fracture risk, attributed to the long-term specific exercise loading, depends on the direction of the fall onto the greater trochanter or hip. For the secondary objective, a new computational anatomy method called Ricci-flow conformal mapping (RCM) was implemented to obtain 3D

distribution of the cortical thickness within the proximal femur and to perform its spatial between-group statistical comparisons.

Key results from the present research demonstrated that young adult females with the exercise loading history of high ground impacts (H-I), ground impacts from unusual/odd directions (O-I), or a great number of repetitive ground impacts (R-I) had 10-22%, 12-16%, and 14-23% lower fall-induced cortical stress at the fracture-prone superolateral femoral neck and 11-17%, 10-11%, and 22-28% higher fracture loads (higher proximal femur bone strength) in the fall situations compared to the controls, respectively. These results indicate that the long-term H-I, O-I, and R-I exercise loadings may reduce the fall-induced hip fracture risk. Furthermore, the present results showed that the higher proximal femur bone strength to reduce hip fracture risk in athletes engaged in the high-impact or repetitive-impact sports are robust and independent of the direction of fall. In contrast, the higher strength attributed to the odd-impact exercise loading appears more modest and specific to the fall direction. The analysis of the minimum fall strength spanning the multiple fall directions also supported the higher proximal femur bone strength in the athletes engaged in these impact exercises. In concordance with the literature, the present results also confirmed in these young adult females that 1) the fall-induced hip fracture most likely initiates from the superolateral femoral neck's cortical bone, particularly at its posterior aspect (superoposterior cortex) in the distal femoral neck region, and 2) the most dangerous fracture-causing fall direction is the one where the impact is imposed to the posterolateral aspect of the greater trochanter.

It would be ideal if impact exercise loading could induce beneficial cortical bone adaptation in the fracture-prone posterior aspect of superolateral femoral neck cortex. However, such apparently beneficial cortical adaptation was not observed in any of the impact or nonimpact exercise loading types examined in the present research based on the supplementary RCM-based 3D morphological analyses of proximal femur cortical bone. This analysis importantly showed that the higher proximal femur bone strengths to reduce fall-induced hip fracture risk in athletes engaged in the high- or odd-impact exercise types are likely due to thicker cortical layers in other femoral neck regions including the inferior, posterior, and/or superior-to-superoanterior regions. Interestingly, the higher proximal femur strength in the athletes with the repetitive-impact exercise loading was not supported by such cortical adaptation. This suggests that other structural/geometrical adaptation contributes to their higher strength. This calls for further studies to elucidate the source of the higher proximal femur bone strength in this type of athletes.

In contrast to the impact exercise loading histories, the exercise loading history of the high-magnitude (e.g., powerlifting) or repetitive, non-impact (e.g., swimming) was not associated with higher proximal femur bone strength to reduce fall-induced hip fracture risk. This most likely reflects the lack of any beneficial structural adaptations of cortical bone around the femoral neck in the athletes with these exercise loading histories. Considering the loading characteristics of the exercise types examined in the present doctoral research, the moderate-to-high loading magnitude alone appears insufficient but needs to be generated at the high loading rate and/or frequency to induce the beneficial adaptation in the proximal femur cortical bone. Therefore, in addition to aforementioned three impact exercise loading types, other exercise or sport types satisfying this condition may also be effective to increase or maintain the proximal femur bone strength to reduce fall-induced hip fracture risk.

As a clinical prospect, the present findings highlight the importance of impact exercise in combating fall-induced hip fracture. Compared to the high-impact loading exercises (e.g., triple/long and high jumping exercise), the odd-impact [ball or invasion games (e.g., football/soccer, tennis)] and/or repetitive-impact loading exercises (e.g., endurance running, jogging, and perhaps vigorous walking) likely provide a safer and more feasible choice for the populations covering the sedentary adults to old people. This is due to the relatively more moderate ground impact involved in the odd- and repetitive-impact loading exercises than in the high-impact exercises. For young, physically active, and/or fit people, the above-mentioned or similar jumping exercises and any other exercise types consisting of the high ground impact (e.g., volleyball, basketball, gymnastics) can also be incorporated into their habitual exercise routines. Lastly, the present results were observed in the young adult females who had engaged in sport-specific training from their childhood/adolescence to early adulthood. Therefore, this calls for the prospective and/or retrospective observational studies to investigate whether the higher proximal femur bone strength to reduce fall-induced hip fracture risk obtained from the long-term specific impact exercise loading during these early phases of life can sustain into the later stages, especially after age of 65 years when the hip fracture is generally more common.

CONTENTS

List of Figures

List of Tables

ABBREVIATIONS

2D	two-dimensional
3D	three-dimensional
aBMD	areal bone mineral density
AUC	area under the curve
BMC	bone mineral content
BMI	body mass index
BW	body weight
CBM	cortical bone mapping
CSA	cross-sectional area
CSMI	cross-sectional moment of inertia
CT	computed tomography
DA	degree of anisotropy
DOF	degrees of freedom
DXA	dual-energy X-ray absorptiometry
FE	finite element
GR	gradient risk
GRF	ground reaction force
H-I	high-impact
H-M	high-magnitude
HR	high resolution
HSA	hip structural/strength analysis
LM	lean body mass
MFS	minimum fall strength
MRI	magnetic resonance imaging
μCT	micro-computed tomography
O-I	odd-impact
pQCT	peripheral quantitative computed tomography
QCT	quantitative computed tomography
RCM	Ricci-flow based conformal mapping
RCT	randomized controlled trial

R-I	repetitive-impact
RMSE	root mean square error
R-NI	repetitive, non-impact
ROC	receiver operating characteristic analysis
ROI	region of interest
SD	standard deviation
SEE	standard error of estimate
SPM	statistical parametric mapping
TBM	tensor-based morphometry
VBM	voxel-based morphometry
vBMD	volumetric bone mineral density
Z	section modulus

ORIGINAL PUBLICATIONS

Publication I S. Abe, N. Narra, R. Nikander, J. Hyttinen, R. Kouhia, H. Sievänen, Exercise loading history and femoral neck strength in a sideways fall: A three-dimensional finite element modeling study, Bone 92 (2016) 9-17, https://doi.org/10.1016/j.bone.2016.07.021

Publication II S. Abe, N. Narra, R. Nikander, J. Hyttinen, R. Kouhia, H. Sievänen, Impact loading history modulates hip fracture load and location: A finite element simulation study of the proximal femur in female athletes, J. Biomech. 76 (2018) 136-143, https://doi.org/10.1016/j.jbiomech.2018.05.037

Publication III S. Abe, R. Kouhia, R. Nikander, N. Narra, J. Hyttinen, H. Sievänen, Effect of fall direction on the lower hip fracture risk in athletes with different loading histories: A finite element modeling study in multiple sideways fall configurations, Bone 158 (2022) 116351, https://doi.org/10.1016/j.bone.2022.116351

Publication IV N. Narra, S. Abe, V. Dimitrov, R. Nikander, R. Kouhia, H. Sievänen, J. Hyttinen, Ricci-flow based conformal mapping of the proximal femur to identify exercise loading effects, Scientific Reports 8 (2018) 4823, https://doi.org/10.1038/s41598-018-23248-y

AUTHOR'S CONTRIBUTION

Publication I	Study design. Medical image processing – manual segmentation of proximal femur MRI data of all 111 study participants, and the subsequent conversion of the segmented data into the FE software (ANSYS)-compatible 3D proximal femur models (volume meshes). Finite element (FE) modeling - creation of 111 proximal femur FE models in a single sideways fall configuration in ANSYS. Post-FE analyses – octant cortical stress analyses with MATLAB and the statistical analyses with SPSS. Manuscript drafting including figures and tables, and the subsequent editing/revising.
Publication II	Study design. FE modeling - creation of 111 proximal femur FE models in a single fall configuration in ANSYS. Post-FE analyses – an implementation of failure criterion to calculate the fracture load, mode, and location based on FE-derived nodal strain data with MATLAB, and the subsequent statistical analyses. Manuscript drafting including figures and tables, and the subsequent editing/revising.
Publication III	Study design. FE modeling – creation of 111 proximal femur models in 12 different fall configurations (a total of 1332 FE models) in ANSYS. Post-FE analyses – estimation of fall direction-wise fracture loads and the minimum fall strengths, and the subsequent statistical analyses. Manuscript drafting including figures and table, and the subsequent editing/revising.
Publication IV	Study design. Processing and preparation of the FE results (strain and surface mesh) for the Ricci-flow based conformal mapping (RCM)-based 3D morphological (cortical thickness) and strain analyses. Collection of data for the inter-operator sensitivity analysis for the identification of anatomical features. Interpretation of the study results. Editing the manuscript. Contribution to the revision during the review.

1 INTRODUCTION

Bone mass and structure constitute the bone strength [1] and adapt to habitual mechanical environment [2,3]. Exercise and physical activity offer natural modes of the mechanical loading to the bone and greatly contribute to bone strength by promoting bone formation in growth [4–6] and maintaining the skeletal strength or slowing down age-dependent bone loss with aging [4,7–9]. Nevertheless, not all exercises are equally osteogenic and the effectiveness may differ from one anatomical site to another [10–13]. In general, based on animal experimental studies, the effective loading types are dynamic [14,15] consisting of sufficiently high-magnitude strains [16–18] generated at high strain rate [19–21] or frequencies [22–24]. Discovering the effective osteogenic exercises for the hip bone, the proximal femur, is important because of the rapidly increasing socioeconomic burden caused by hip fracture.

Hip fracture is a major public healthcare problem resulting in high rates of morbidity, disability, and even mortality in the older adults [25,26]. It is twice more common in females than in males [27,28]. Within one year after the fracture, only a half of the hip fracture patients regain their pre-fracture mobility and even up to 30% of the patients die due to the fracture and their comorbidities [26,29–32]. Globally, the annual number of hip fractures and consequent financial costs are estimated to reach 6.3 million fractures [33] and $132 billion, respectively, by 2050 due to aging population worldwide [34]. With advancing age, the amount of vigorous physical activity declines, and the physical activity primarily consists of less intensive walking [35]. Walking is the predominant form of human locomotion and induces an asymmetric loading in the femoral neck: higher compressive and smaller tensile loads at its inferomedial and superolateral aspects, respectively [36,37]. Due to this, the femoral neck typically has a thicker inferomedial and thinner superolateral cortical walls [38,39]. The age-related reduction in the skeletal loading may progress this thinning of the superolateral cortex. In fact, it has been observed in adult females that the cortical thickness at the posterior aspect of the superolateral region decreases fivefold from 1.63 mm at age of 25 years to 0.33 mm at age of 85 years whereas its counterpart, the thickness of inferior femoral neck cortex, remains almost

unchanged [40]. Accordingly, Mayhew and his colleagues (2005) suggested that this site-specific cortical thinning significantly contributes to the hip fragility [38].

The problem due to such fragility comes to the surface when the person falls, and the fall-induced ground impact is imposed to the posterolateral or lateral aspect of the greater trochanter or hip. In such a fall, the loading mechanism is reversed, causing unusually high compressive loading at the fracture-prone thin superolateral cortex [37,41–44]. The peak magnitude of this fall-induced compressive loading can be up to 4 times greater than the loading during the walking [36,42]. Accordingly, numerous studies consistently confirmed that the femoral neck is at the greatest risk in the fall situation and the fracture most likely initiates from this thin superolateral cortex due to the unusually high compressive loading [37,41–50]. As a matter of fact, it has been reported that over 90% of the hip fractures are caused by the fall [51–53]. Therefore, if a specific type of exercise can deliver the osteogenic loading to the proximal femur (particularly to the femoral neck and its superolateral region) to increase or maintain its strength, the hip fracture risk may be reduced.

Comparing athletes' bones with bones from nonathletic persons has a potential to find such osteogenic targeted exercise through examination of the long-term adaptation of bones to specific exercise loading. Such studies based on dual-energy X-ray absorptiometry (DXA) reported that proximal femora of young adult female athletes with a history of high-impact (e.g., jumping exercises, producing high ground reaction forces at the take-off) and/or odd-impact exercise (e.g., experiencing ground impact from unusual directions, typical in ball games like tennis, squash, and football) had greater areal bone mineral density (aBMD), bone mineral content (BMC), cross-sectional area (CSA), and section modulus (Z) in the femoral neck than those of nonathletic female controls [54–59]. Next, Nikander et al. (2009) reported that, based on magnetic resonance imaging (MRI), distribution of cortical bone around the femoral neck cross-section varied among athletes with different sport backgrounds. For example, compared to nonathletic controls, the proximal femora with the high-impact loading history had significantly ~60% thicker cortical bone at the inferior quadrant of the femoral neck. Also, those with the high- and odd-impact loading histories had significantly ~20% thicker cortexes at the anterior and posterior quadrants. [60] It should be noted that this posterior quadrant partially includes the vulnerable fracture-prone superolateral region. However, to the best of author's knowledge, there have been very few studies which investigated whether these apparent beneficial adaptations of proximal femur bone to specific exercise loading histories translate into a higher proximal femur bone strength to reduce fall-induced hip fracture risk [61–63]. The proximal femur bone strength in the fall

situation is best evaluated by measuring or estimating a fracture load that is equal to the minimum applied load to cause the fracture. *In vitro* and/or *in vivo* estimations of such loads can be realized through an experimental mechanical testing of cadaveric bones and a finite element (FE) method [45,46,50,64,65]. Importantly, it was found that FE-derived fracture load (proximal femur bone strength) can predict the hip fracture risk more accurately than a traditional aBMD-based risk assessment or more comprehensive risk assessment tool such as FRAX [66,67].

Given above, it is yet unclear whether the long-term specific exercise loading can result in the higher proximal femur bone strength to reduce fall-induced hip fracture risk though inducing beneficial adaptations within the proximal femur. Thus, the primary research question in the present doctoral research was whether the proximal femur adapted to the long-term specific exercise loading has the higher bone strength to reduce the hip fracture risk in the fall situation. Furthermore, the results from the above-mentioned previous studies of athletic and nonathletic proximal femur bones were limited to two-dimensional (2D) planar analyses of femoral neck cross-section. Hence, an additional question was how the specific exercise-induced adaptations of proximal femur bone contribute to the higher bone strength three-dimensionally. Particularly, it is of interest whether any specific exercise type can induce three-dimensional (3D) beneficial adaptations to the fracture-prone superolateral femoral neck cortical bone considering the mechanism of the fall-induced hip fracture. Addressing these questions has a potential to identify the effective osteogenic exercise types to increase or maintain the proximal femur bone strength. The results are anticipated to facilitate devising effective exercises to increase the strength, which would be of utility in practical preventive actions against the hip fractures. This could translate into reduced number of the hip fractures and associated costs to society, and into better quality of life and independent living of old people because of improved neuromuscular performance and balance, besides improved hip bone strength. These research questions are addressed in the present doctoral research with following two objectives.

The primary objective of the present doctoral research was to scrutinize the effect of long-term specific exercise loading on the proximal femur bone strength in the fall (onto the greater trochanter) configuration using the FE method. The secondary objective was to investigate the 3D morphological adaptation of proximal femur cortical bone to different exercise loading history using a new computational anatomy method, called Ricci-flow based conformal mapping (RCM). Additionally, the fall-induced strain distribution at the proximal femur surface was analyzed three-dimensionally using the same method. It was anticipated that the results from this

secondary objective would help understand the higher proximal femur bone strength induced by the specific exercise loading (a potential finding in the primary objective) in addition to previous 2D-based results.

These objectives were addressed through a total of four publications: **Publications I, II, and III** for the primary objective; and **Publication IV** for the secondary objective. In the **Publication I**, the proximal femur FE models were created in a single fall configuration/direction (a fall onto the greater trochanter) based on the same proximal femur MRI data used in one of aforementioned studies by Nikander et al. (2009) [60], consisting of 91 young adult female athletes representing five distinct exercise loading histories and 20 nonathletic but physically active female controls. Based on the FE models, the fall-induced stress distributions within femoral neck were compared between each of five exercise loading groups and the control group through the octant-wise stress analyses on the femoral neck's cross-section in three longitudinal sub-sections (proximal, middle, and distal sites/regions) along the femoral neck. However, these stress analyses alone are insufficient to infer the proximal femur bone strength in fracture-causing fall situations. Therefore, in the **Publication II**, the fracture load was estimated for each proximal femur based on the same FE models with a principal strain failure criterion. It was evaluated whether the proximal femur bone strength in fall situation in the specific exercise loading group was different from the nonathletic control group. Furthermore, the effect of the long-term distinct exercise loading on the fracture location was examined in this publication. In these **Publications I and II**, the FE analyses were limited only to the single fall configuration (a single direction of fall onto the greater trochanter). The athletic bones are adapted to the long-term specific exercise loadings characterized by not only the loading magnitude, rate, and frequency but also direction. Given this, in the **Publication III**, the study was extended to simulate FE models in the multiple fall configurations (a total of 12 directions per each proximal femur) to examine whether the specific exercise-induced gains in the proximal femur bone strength persist regardless of the direction of fall onto the greater trochanter or whether they depend on the direction. Moreover, because a fall is an unpredictable event, it is difficult to forecast its direction and the weakest fall direction is likely specific to each femur. Considering these, a minimum fall strength (MFS) among the multiple fall directions was also calculated for each proximal femur and its between-group differences were analyzed accordingly. In the **Publication IV**, the RCM method was implemented to analyze the 3D distributions of 1) the cortical thickness across the proximal femur and 2) FE-derived surface strains in the fall situation. Subsequently, their spatial between-

group differences were analyzed statistically with statistical parametric mapping (SPM).

Lastly, it is noted that aforementioned fracture-causing fall type where the ground impact is imposed to the posterolateral or lateral aspect of the greater trochanter or hip is often referred to as "sideways fall" in literature including **Publications I-IV** with an assumption that the fall to the side results in the ground impact onto the (posterolateral or lateral aspect of) greater trochanter. However, this is not necessarily true since fallers often avoid the fall onto the greater trochanter by rotating their trunk during the fall descent as a natural protective response [68–70]. Therefore, "a fall onto the (posterolateral or lateral aspect of) greater trochanter" or similar phrases will be used henceforth throughout this doctoral dissertation instead of "sideways fall".

2 LITERATURE REVIEW

This section provides a literature review for the potential readers to gain sufficient information to understand the contents of the present doctoral research. It consists of following topics: 1) **Bone** - covering its basic anatomy and physiology, proximal femur anatomy, bone biomechanics, and functional adaptation of bone; 2) **Medical Imaging** – including Dual-energy X-ray absorptiometry (DXA), quantitative computed tomography (QCT), magnetic resonance imaging (MRI), their basic principles and limitations, and respective measurable bone properties; 3) **Exercise on Proximal Femur** – describing the effects of various exercises on proximal femur bone at different stages in life; 4) **Hip Fracture** – covering its definition, treatment, epidemiology and socioeconomic impact, cause and mechanics, risk factors, and risk assessment tools; 5) **Fall** in relation to the hip fracture – discussing the estimation of fall-induced impact force and factors influencing the force including the direction of fall onto the greater trochanter or hip; 6) **Proximal Femur Finite Element Modeling** – covering the principle of FE modeling, history of early development of the proximal femur FE models, model specifications (homogeneous vs. inhomogeneous material property assignment, linear vs. nonlinear modeling, quasi-static vs. dynamic simulation, and iso- vs. anisotropic material properties), fracture load estimation with different failure criteria, boundary conditions, directions of fall onto the greater trochanter, and the applications; and lastly 7) **Computational Anatomy** – including brief description on its principle and different methods such as cortical bone mapping (CBM), voxel-based morphometry (VBM), and tensor-based morphometry (TBM), and their applications.

2.1 Bone

2.1.1 Basic Anatomy and Physiology

Bone is a living organ consisting of bone tissue, cartilage, dense connective tissues, epithelium, adipose tissue, and nervous tissue. It constitutes the skeletal system together with other connective tissues such as ligaments, tendons, and cartilage. [71,72] The adult human skeleton has a total of 206 bones comprising 74 bones of the axial skeleton, 126 bones of the appendicular skeleton, and 6 auditory ossicles [71,73]. The skeleton is among the largest human organs contributing up to approximately 15% of total body weight [74,75].

Bone provides two major functions: mechanical and homeostatic functions. The former includes providing the structural framework for the body, protection for the vital internal organs, and assistance in movement by acting as a lever system to transfer forces. On the other hand, the latter includes maintenance of minerals (especially, calcium and phosphorus), secretion of endocrine products, and providing a home for red and yellow bone marrow. The red marrow produces red and white blood cells, and platelets while the yellow marrow stores triglycerides. [71,73,74,76–78]

Based on the shape, a majority of bones falls into five categories: long (e.g., humerus and femur), short (e.g., wrist bone), flat (e.g., cranial bones), irregular (e.g., vertebra), and sesamoid bones (e.g., patella) [71,73]. Accordingly, its mechanical function varies depending on the shape. For example, the function of the long bone is to serve as a stiff lever arm to transmit force (e.g., generated by muscle) over joints while the function of the flat bone is mainly to protect internal organs. [72] Despite its "static and inert" stereotypical image that the bone does not change once formed, it is rather a dynamic organ continuously renewing itself through processes called remodeling [76,79,80].

For the sake of readability of the following sections, some of the basic anatomical features of long bones such as the femur are introduced here first (**Figure 1**). Long bones consist of three major sections: the diaphysis, metaphysis, and epiphysis. The diaphysis is its central section formed by long hollow cylindrically shaped dense cortical (or compact) bone and its internal cavity is called the medullary cavity, where yellow bone marrow stored. The epiphyses are the proximal and distal ends of the bone, and their articulating surfaces are covered by hyaline cartilage. The metaphyses are located between the diaphysis and epiphysis. These metaphyses and epiphyseal

sections are formed by the internal spongy, trabecular bone, in the outer cortical bone layer. [72,73,81] Epiphyseal and metaphyseal trabecular porous structure is typically filled with red bone marrow (only in the proximal side after age of 5-10 years old) [82]. Except for the articulating surface of the epiphyses, the outer and inner surfaces of the bone are covered by membranous layers called periosteum and endosteum, respectively (**Figure 1**). [72,73,81] It is noted that these layers play significant roles in both bone metabolism and fracture healing [81].

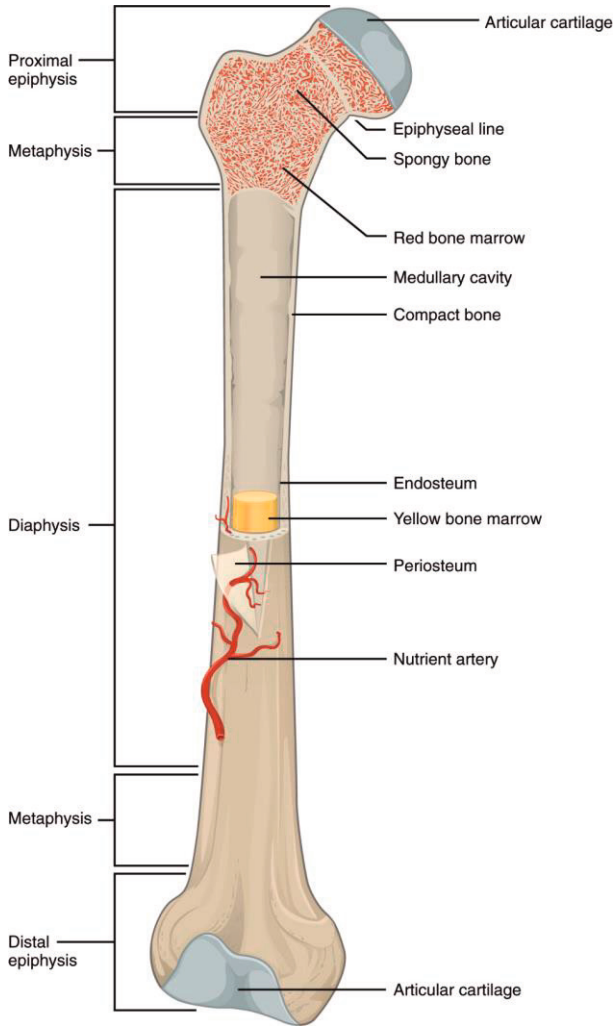

Figure 1. Anatomy of long bone - Femur. (Modified from Betts et al. (2013) [83] under CC BY 4.0 license). Note: The location of the epiphyseal line is moved to near femoral head compared to the original figure. Access for free at https://openstax.org/books/anatomy-and-physiology/pages/1-introduction

An anatomical focus in the present doctoral research is the proximal femur. Therefore, its key anatomical features and hip joint are briefly introduced here. The femur is the strong and longest bone among the human bones [84]. The proximal femur is its proximal end covering from the top of the femoral head to the region 5-cm below the lesser trochanter in the subtrochanteric region of the femoral shaft (**Figure 2**) [85,86]. It consists of the proximal epiphysis, metaphysis, and upper part of the diaphysis. To withstand repetitive loads induced by daily activities such as walking, jogging, and running, the cortical and trabecular bone in the proximal femur take on different mechanical roles. The dense cortical bone is especially thicker in the inferior femoral neck and entire femoral shaft, enabling the proximal femur to carry large external loads whereas the reinforcing internal "spongy" trabecular bone is responsible for absorbing the energy, for example, from walking and running and of a fall. [84]

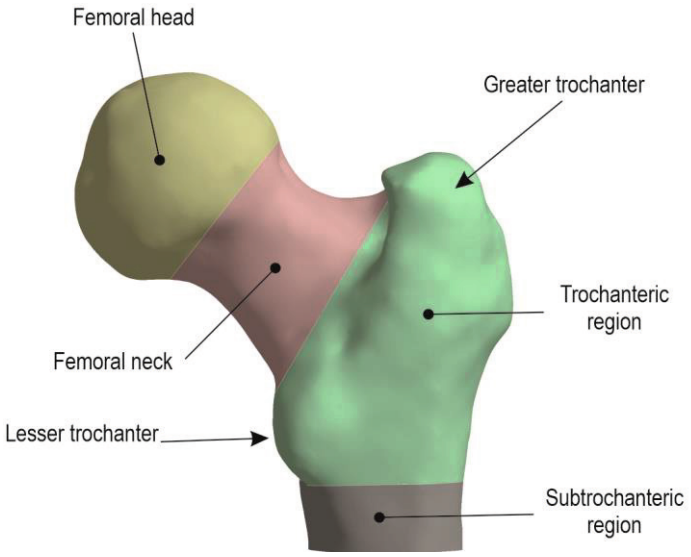

Figure 2. Proximal femur. (posterior view).

The proximal femur is characterized by four major anatomical features: the femoral head, femoral neck, and lesser and greater trochanters (**Figure 2**). The spherical-shaped femoral head is covered by hyaline cartilage except for the medial non-articular cavity called the fovea capitis. The femoral neck is a cylindrical-structured bone (with approximately elliptical cross-section) connecting the femoral head to the upper part of femoral shaft. The greater and lesser trochanters are bony protuberances located proximal to the upper part of the femoral shaft, and distal to

the femoral neck, providing attachment sites for several muscles. The greater trochanter covers the area from the superolateral end of femoral neck to the lateral aspect of the proximal femoral shaft. It also has a deep depression at its posterior part called the trochanteric fossa. In contrast, the lesser trochanter is smaller and is located at the medial aspect of proximal femoral shaft, just distal to the inferomedial end of the femoral neck. [84,87]

Together with pelvic bones and a large cup-shaped socket called acetabulum, the femoral head forms the hip joint. It is a large synovial multiaxial ball-and-socket type joint. Its deep acetabulum and surrounding labrum allow following movements in several planes while restricting femoral head translation: flexion and extension in the sagittal plane; abduction and adduction in the coronal/frontal plane; internal and external rotation in the transverse plane; and circumduction. Its main functions are supporting the body weight and enabling locomotion. [84,87,88]

2.1.1.1 Hierarchical Structure

In this section, the hierarchical structure of bone (**Figure 3**) is described in ascending order from 1) molecular (< 200-300 nm) to nanoscale (200-300 nm to 1 μm), 2) microscale (1 to 10 μm), to 3) meso- (10 to 500 μm) to macroscale (tissue-level, > 1 mm) [89].

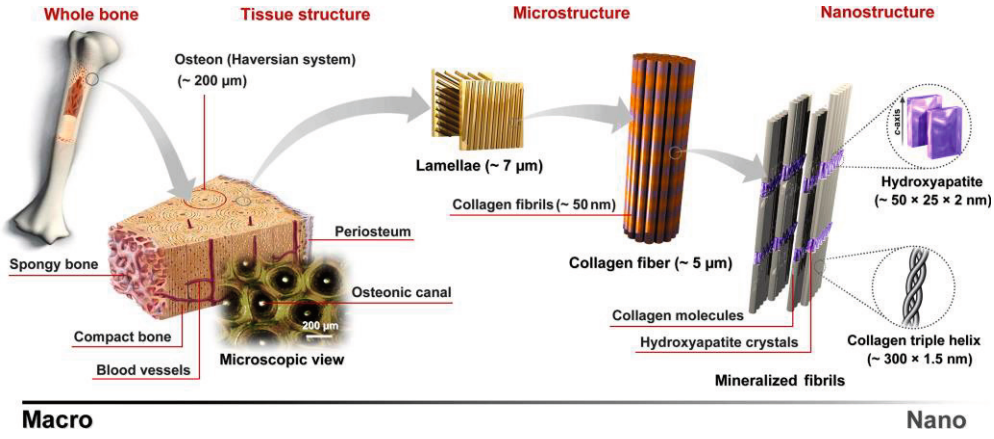

Figure 3. Hierarchical structure of bone. Nanostructure to whole bone levels are shown. (Reprinted, with permission, from Sadat-Shojai et al. (2013) [90] © 2013 Acta Materialia Inc. Published by Elsevier Ltd.)

2.1.1.1.1 Molecular (< 200-300 nm) to Nanoscale levels (200-300 nm to 1 um)

At the molecular level, the bone is a heterogeneous material composed of inorganic mineral crystals, an extracellular organic matrix, water, living cells, and blood vessels. The proportions of the mineral crystals, organic matrix, and water are approximately 60%, 30%, and 8-10% by weight, and 40%, 25%, and 35% by volume, respectively. [76,81,91,92] The inorganic mineral crystal is made of a hydroxyapatite $[Ca_{10}(PO_4)_6(OH)_2]$, a combination of calcium phosphate $[Ca_3(PO_4)_2]$ with calcium hydroxide $[Ca(OH)_2]$ [71]. The hydroxyapatite crystals exist in the small plate-shaped form (20-50 nm long, 15 nm wide, and 2-5 nm thick) in bone (**Figure 3)** [76,81,91,92].

The organic matrix contains mostly type I collagen (~90 % by weight), non-collagenous proteins (~5%), and lipids (~2%) [76,91]. The type I collagen molecule is a unique triple helical molecule built from three polypeptide chains, each of which is comprised of approximately 1000 amino acids. These chains create a 300 nm-long very rigid linear molecule. By being aligned parallelly with other type I collagen molecules, they form a collagen fibril. Consequently, the collagen fibrils are bundled together to form the collagen fiber (**Figure 3**). There exist gaps or holes within the collagen fibril where the non-collagenous proteins and mineral deposits occupy. The type I collagen has several important roles: providing elasticity and structural support in the matrix, promoting initial mineral deposition, and binding other macromolecules. [81,91,93,94] Once the mineral crystals congregate on the collagen fibril bundles in the extracellular matrix, their crystallization occurs; hence the tissue hardens. While the crystallization of the bone mineral takes responsibility for the hardness of the tissue, the collagen fibers provide the flexibility. The crystallization process is known as calcification and is initiated by one of bone cells, osteoblast. [71]

2.1.1.1.2 Microscale level (1 to 10 μm)

The mineralized collagen fibrils (~0.1-3 μm in diameter/each fibril) form a next structuring unit at microscopic level: woven bone or lamella (~2-9 μm in thickness) [81,93,94]. In the woven bone, these mineralized fibrils are placed in a disorganized fashion while they are arranged parallelly to each other in a thin sheet in the lamella. Then, the lamellae are layered in a twisted plywood-like arrangement to form lamellar bone (**Figure 3**). [81] The woven bone is typically viewed as a primary or immature bone since they are present in embryonic and fetal development, and in some metaphyseal domains of the growing bones. In the adult skeletons, they can also be found at insertions of the ligament and tendon, in abnormal bone tissues due to

pathological conditions (e.g., osteogenic tumor, Paget's disease), or in a callus of the fractured bone during its healing process, which will be replaced by the lamellar bone eventually. [73,81,95]

The mechanical stimuli can induce the rapid deposition of the woven bone. Then, these woven bones and pre-existing lamellar tissues are transformed into the lamellar bone as the entire skeleton grows. Given this, the lamellar bone is considered a mature bone. In the human skeleton, the lamellar bones start growing around age of one month and comprise the most of bones by the age of four years. Due to the organized layering arrangement, the lamellar bone has the greater strength than the woven bone. [73,81,95]

2.1.1.1.3 Meso- (10 to 500 μm) to Macroscale levels (> 1 mm)

Both woven and lamellar bones contain small ellipsoidal cavities called lacunae (5 μm minor diameter; 7-8 μm major diameter) which are occupied by one of the bone cells, osteocytes. The lacunae are placed along the interfaces between the lamellae (**Figure 4**). Approximately 25,000 lacunae are found in every cubic millimeter in bone tissue and its number decreases with aging. [79,81,96] The lamellar bone normally forms a smaller cylindrical structure called an osteon or Haversian system (170-250 μm in diameter and 1-3 mm in length) in the cortical bone (**Figure 3** and **Figure 4**). There are 10-30 concentric rings of lamellae in each osteon, surrounding central cavity, Haversian canal (60-90 μm in diameter), where blood vessels and nerves go through. [81,93] These osteons and Haversian canals are usually aligned with the longitudinal axis of the diaphysis of the long bone while another type of the canals, Volkmann canals, establish the transverse connection for the blood vessels and nerves between the medullary cavity, Haversian canals, and periosteum [81]. The longitudinal arrangement of osteons enables the shaft of a long bone to resist bending [71,80].

At the scale of 1-10 mm, the bone can be categorized into two types: cortical or trabecular bone (**Figure 4**). They are also known as compact or dense bone, and spongy or cancellous bone, respectively. As the skeleton reaches its maturity, the cortical bone is made of mainly osteons and small amounts of circumferential and interstitial lamellae (**Figure 4**). The functions of the cortical bone are to provide rigid protection and structural support, and to resist against the mechanical loading due to body weight and movements. In contrast, the trabecular bone is formed by rod- and plate-shaped trabeculae (50 μm to 300 μm in thickness) consisting of mostly lamellar bone. [71,81,97] The lamellae are arranged parallelly to these trabeculae [95]. Various combinations of these trabeculae form a highly porous 3D lattice structure

with their irregular interconnected pore spaces filled by bone marrow (**Figure 4**). The major difference between these two bone types is their porosity. The cortical bone has 5-20% of porosity mainly due to Haversian and Volkmann canals. In contrast, the trabecular bone has higher porosity varying substantially (30 – 90%) depending on anatomical sites: for example, 40% in femoral neck and 95% in the elderly spine. [81,97]

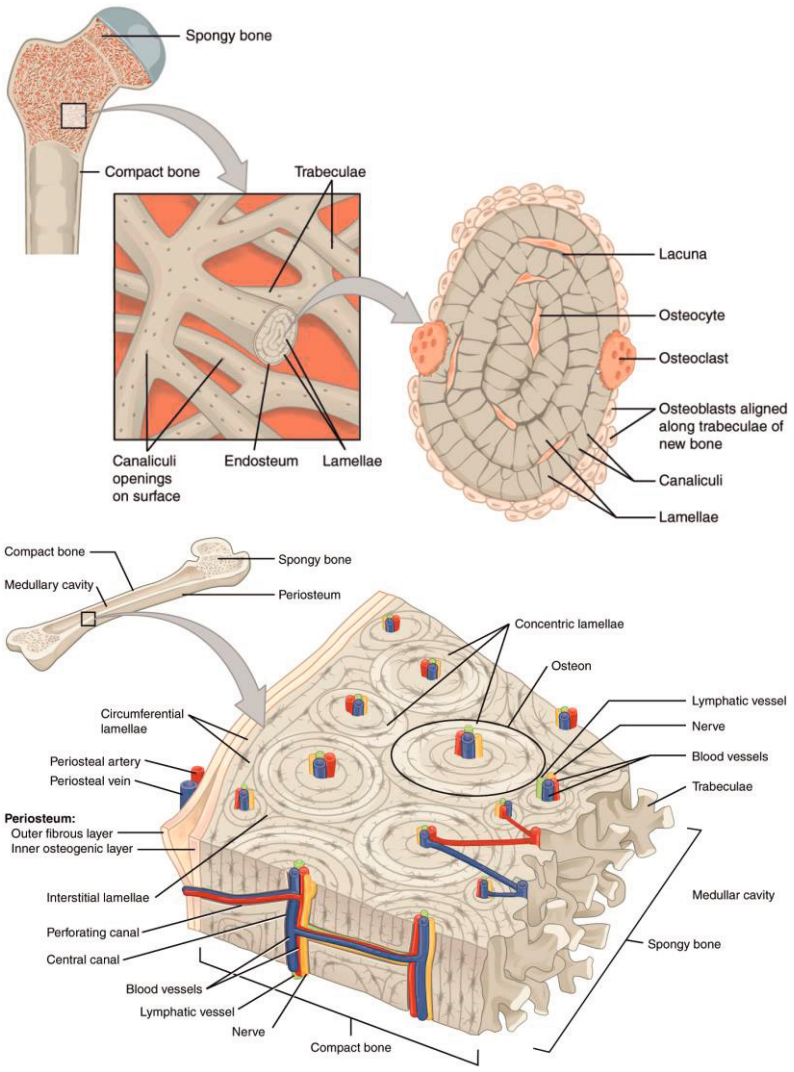

Figure 4. Anatomy of cortical and trabecular bones. (Modified from Betts et al. (2013) [83], CC BY 4.0 license). Note: The location of the epiphyseal line is moved to near femoral head compared to the original figure. Access for free at https://openstax.org/books/anatomy-and-physiology/pages/1-introduction

2.1.2 Bone Biomechanics

This section explains basic bone biomechanics covering the following topics: 1) loading types, stress, and strain, 2) the density- and time-dependent mechanical properties of bone, 3) anisotropic mechanical properties of bone, and 4) asymmetric strengths of bone.

2.1.2.1 Loading Types, Stress, and Strain

Types of the mechanical loading the bone experiences can be categorized into five different types or their combinations: compression, tension, shear, bending, and torsional loadings (**Figure 5**) [1]. Regardless of the types, the structure can experience either normal and/or shear stresses [98].

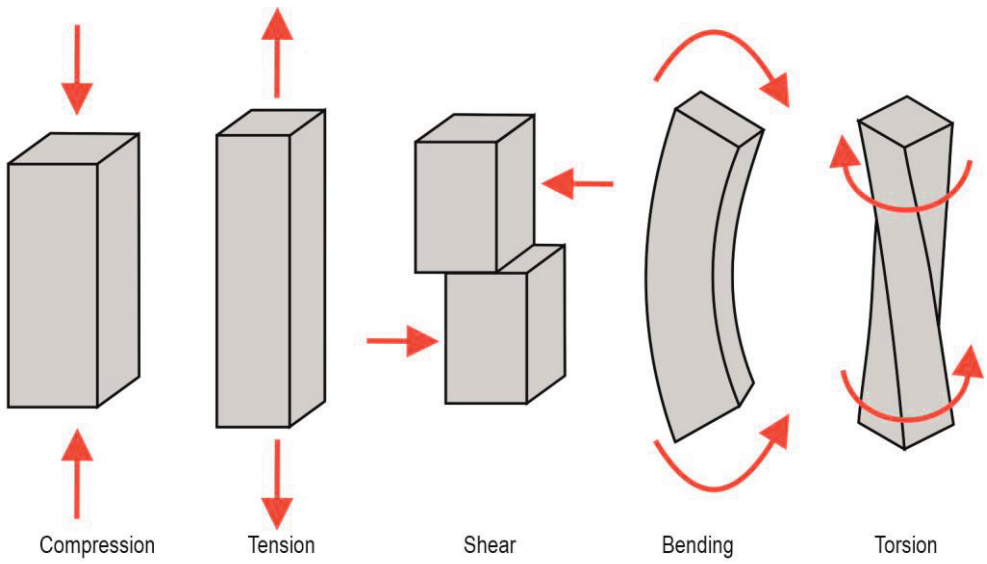

Figure 5. Mechanical loading types in bone.

Stress is defined as the applied force divided by the area where the force was applied to, expressed in a unit of newtons per square meter (N/m^2) or pascals (Pa). It is considered as a normal stress (σ) if the direction of the applied force is perpendicular to the area (normal direction) over which the force acts. In contrast, if the direction is parallel to the area (shear direction), it is considered as shear stress (τ). Strain is the deformation of the structure due to the loading and defined as the

change in the length divided by the original length. It is unitless and commonly expressed as microstrain ($\mu\varepsilon$) or as a percentage (%) in the bone research. Similar to the stress, the strains in the normal and shear directions are referred to as normal strain (ε) and shear strain (γ), respectively. These aspects are summarized in **Figure 6**. The ratio of the normal stress to the normal strain (due to tension or compression) is referred to as Young's modulus (or elastic modulus, denoted as E, in a unit of MPa or GPa) whereas the ratio in the shear loading is called shear modulus (G, in a unit of MPa or GPa), described as follows, respectively: [1,72,98]

$$E = \sigma/\varepsilon \tag{1}$$

$$G = \tau/\gamma \tag{2}$$

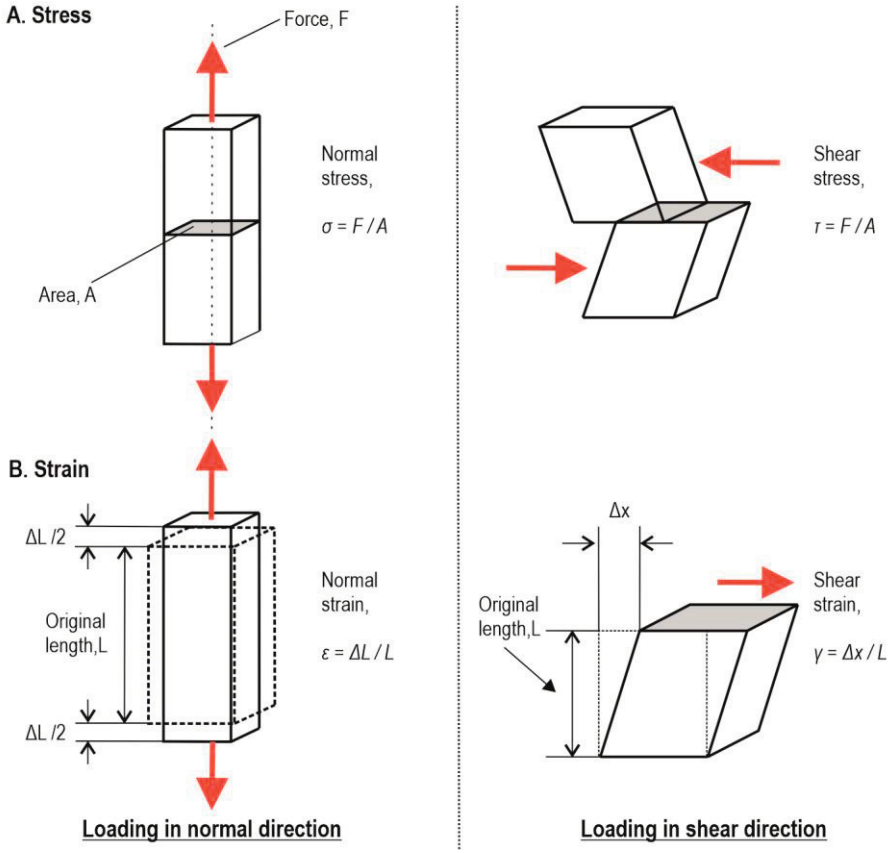

Figure 6. Stress and strain in normal and shear directions. Note: ΔL and Δx denote the changes in the lengths in the normal and shear directions, respectively.

The mechanical properties of bone such as the Young's modulus and strength can be measured through the experimental mechanical testing. For example, a uniaxial loading is applied to the bone tissue to obtain the compressive and/or tensile properties. By converting the magnitude of applied force and measured deformation to respective stress and strain, the stress-strain curve (**Figure 7**) can be obtained. [1,98]

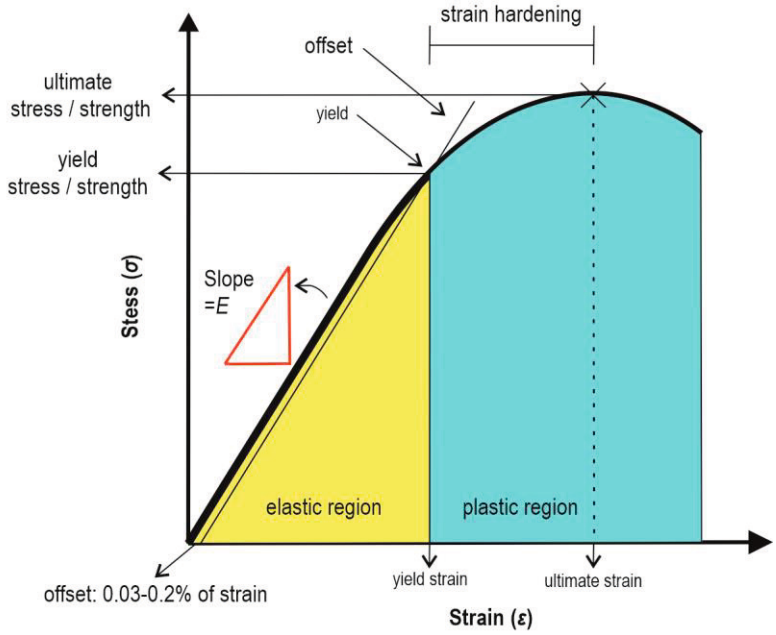

Figure 7. Stress-strain curve. This is rather an ideal stress-strain curve and is drawn to explain the mechanical behavior of material in general. Bone (at organ level, e.g., proximal femur) does not necessarily exhibit this ideal curve. It typically shows the brittle fracture characterized by little or no post-yield behavior.

The stress-strain curve (**Figure 7**) describes some of the important mechanical properties of bone or the material of interest in general. The linear slope of the curve in the elastic region represents the Young's modulus [1,98]. The stress-strain relationship in this region can be expressed by the following equation:

$$\sigma = E\varepsilon \tag{3}$$

where σ is stress (in Pa), ε is strain (unitless), and E is the Young's modulus. It is noted that this **equation (3)** is just a reformulation of the earlier **equation (1)**. This equation is also known as Hooke's law and the materials including bone, whose elastic region can be modeled by this law, are referred to as the linear elastic material.

The linear elastic material can recover its original state without any permanent deformation once the loading is removed. The stress-strain relations like the Hooke's law describing the state of stress in a given material with respect to the strain state are known as constitutive relations or equations. [99,100]

The elastic region is defined as the area under the curve until the yield point, which also corresponds to the elastic strain energy stored during the loading. The yield point can be defined as the point where a line originated at 0.03-0.2% offset strain, parallel to the linear slope of the stress-strain curve, coincides with the stress-strain curve (**Figure 7**). It is a transitional threshold where the linear elastic mechanical behavior becomes nonlinear. Beyond this point, the further loading induces permanent damages (e.g., microcracks in bone structure) resulting in a decrease in the material resilience. It is the material capacity to store the elastic strain energy during loading and recover the original state during unloading without the permanent deformation. The permanent deformation and the area under the curve beyond the yield point are also known as plastic deformation and plastic region, respectively (**Figure 7**). As the strain increases, the stress reaches its local maximum, called the ultimate stress. [1,98] Beyond the yield point, bone tissue becomes harder as mineralized collagen fibers begin to connect emerging microcracks [101]. In general, the nonlinear mechanical behavior between the yield and ultimate points is referred to as strain hardening. These yield and ultimate stresses/strains are also referred to as the yield and ultimate strengths, respectively. These mechanical properties are the intrinsic (material) properties of bone, meaning that they are independent of size and shape of bone (extrinsic properties). [1,98]

The stress-strain curve for bone tissue or any material in general usually includes until little after the ultimate stress if the loading range is limited to the small strain. However, if the compressive loading is continued for the larger strain, the bone tissues (particularly trabecular bone) exhibit softening and densification behaviors (**Figure 8**). Once the ultimate strength is reached, the stiffness decreases as the strain increases due to the collapse of the (trabecular) pores. This phenomenon is referred to as strain softening. Once the strain level reaches around 15%, the curve starts flattening. Then, suddenly around 20-50% of strain level, the stiffness starts increasing drastically due to the pore closures. This is called densification since the pore closure presses the collection of fractured trabeculae to be dense. [43,102,103]

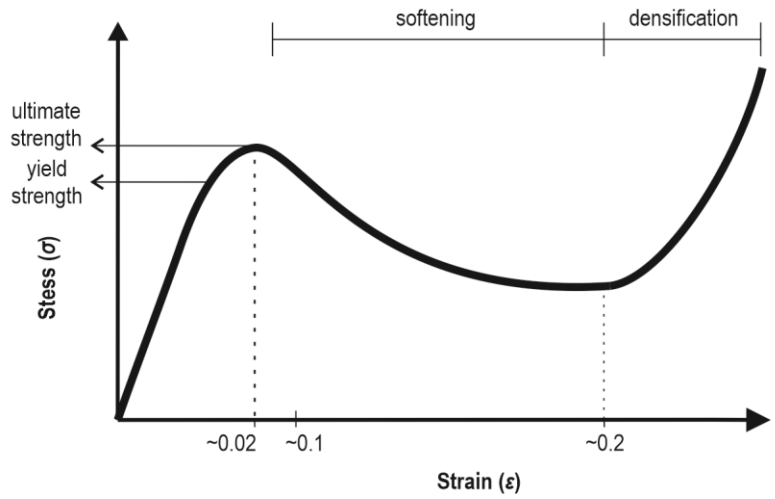

Figure 8. Stress-strain curve for the large compressive strain - softening and densification of bone. (Redrawn based on Helgason et al. (2014) [43]).

Lastly, it is important to note that the structure may fail before the yield point due to a sudden change in its shape under compressive loading. This type of the failure is due to geometric instability and referred to as buckling. It is common in thin-walled structure including bone. [100] For example, femoral neck or diaphysis can fail due to the buckling under compression if their cortical wall is thin enough [38,104].

2.1.2.2 Density-Dependent Mechanical Properties of Bone

Bone (particularly trabecular bone) is a two-phased material comprising a mineralized bone tissue (solid phase, forming a highly porous 3D lattice structure), and interstitial fluid and bone marrow (fluid phase, filling the interconnected pores). As described earlier, while the trabecular porosity varies from 30 to 90% depending on anatomical sites, the cortical porosity varies ~5–20% mainly due to Haversian and Volkmann canals. Besides, the trabecular porosity varies within a same bone due to its heterogeneous spatial distribution. Accordingly, the bone (apparent) density characterized by this porosity varies not only from one bone to another (e.g., tibia vs. femur), but also within a single anatomic site (e.g., within proximal femur). Importantly, this site-specific bone density is strongly related to mechanical properties of bone such as elastic modulus and strength. [81,97,105–107] Due to the

greater apparent density, the cortical bone typically has the higher elastic modulus and greater strength than the trabecular bone [1,97,108].

The trabecular elastic modulus and strength can vary by a factor of a few hundred within a same bone due to aforementioned substantial variation in the porosity and consequent density [106,109–111]. Also, the softening and densification phenomena (**Figure 8**) are affected by the density [43]. Because of the density-dependent variation in the mechanical properties, the bone (particularly trabecular bone) is considered the density-dependent inhomogeneous material. In contrast, the material is referred to as a homogeneous material if its mechanical properties are independent of the density and do not vary from one location to another within the same structure. [112]

The relationships between the density and mechanical properties can be expressed mathematically, especially using power law [105,109,113]. For the last few decades, numerous experimental studies reported various mathematical relations at different anatomic sites. Several reviews summarized them [108,113–115] and some selected equations are presented in **Table 1**.

The discussion on the mechanical properties of bone has been so far limited to at the tissue- or apparent-level (characteristic dimension of the test specimen: on the order of ~1 cm). However, it is important to note that the cortical and trabecular mechanical properties are comparable at the microstructural level (< 200 μm). Using the acoustic microscopy (resolution: 20-60 μm) and nanoindentation (resolution: 1-5 μm), several investigators reported that, at the microstructural level, the elastic modulus of the trabeculae was ~11-18 GPa whereas the cortical elastic moduli were 16-23 GPa for osteon and 18-26 GPa for interstitial lamellae. [116–118] This suggests that the substantial differences in the cortical and trabecular mechanical properties at the tissue- and apparent-level originate from the spatial distribution of bone tissue (the dense organization of osteons vs. porous trabecular network). Lastly, it is noted that the strain (loading) rate also affects the density-dependent mechanical properties [115]. This aspect will be discussed in the next section.

Table 1. Empirical relationships between bone density and mechanical properties of human cortical and trabecular bones

Study	Equation	ρ_{app} or ρ_{ash} (g/cm^3)	Anatomical location	R^2
Cortical bone				
Lotz et al. (1991) [119]	$E = -13.43 + 14.261\rho_{app}$	ρ_{app}: 1.20-1.85*	Proximal femur (metaphysis)	0.67
Öhman et al. (2011) [120]	$E = 12.9\rho_{ash}^{2.0}$†	ρ_{ash}: 0.6-1.3	Femoral and Tibial diaphysis	0.86
Lotz et al. 1991) [119], Wirtz et al. (2000) [108]	$\sigma_{ult} = 72.4\rho_{app}^{1.88}$†	ρ_{app}: 1.5-2.0	Femur	N.A.
Trabecular bone				
Morgan et al. (2003) [105]	$E = 4.730\rho_{app}^{1.56}$	ρ_{app}: 0.11-0.35	Vertebrae	0.73
Wirtz et al. (2000) [108]	$E = 1.904\rho_{app}^{1.64}$†	ρ_{app}: 0.1-0.7	Femur	N.A.
Kaneko et al. (2004) [121]	$E = 10.88\rho_{ash}^{1.61}$	ρ_{ash}: 0.10-0.33	Distal femur	0.78
Morgan et al. (2003) [105]	$E = 6.850\rho_{app}^{1.49}$	ρ_{app}: 0.26-0.75	Femoral neck	0.85
Morgan et al. (2003) [105]	$E = 15.010\rho_{app}^{2.18}$	ρ_{app}: 0.14-0.28	Greater trochanter	0.82
Morgan & Keaveny (2001) [109]	$\sigma_y = 37.1\rho_{app}^{1.74}$	ρ_{app}: 0.18	Vertebrae	0.80
Morgan & Keaveny (2001) [109]	$\sigma_y = 38.5\rho_{app}^{1.48}$	ρ_{app}: 0.58	Femoral neck	0.62
Pooled (cortical + trabecular bones)				
Keller (1994) [122]	$E = 10.5\rho_{ash}^{2.29}$	ρ_{ash}: 0.092-1.22	Human femur	0.85

Note: N.A. = not available, E = elastic modulus (in GPa), σ_y = compressive yield strength (in MPa), and σ_{ult} = compressive ultimate strength (in MPa), R^2 = determination coefficient, ρ_{app} = apparent density (hydrated tissue mass/total specimen volume), ρ_{ash} = ash density (ash mass/total specimen volume).

* estimated based on the graphs in the review by Helgason et al. (2008) [113]

† The elastic modulus in the axial direction is presented here. The transverse elastic modulus can be found in the original study [108]

2.1.2.3 Time-Dependent Mechanical Properties of Bone

Both cortical and trabecular bones are time-dependent viscoelastic materials characterized by the following properties: creep - under a constant stress loading, the deformation (strain) continues increasing with time; stress relaxation - under a constant deformation (strain) loading, the stress decreases with time; hysteresis - under cyclic loading, the unloading curve differs from the loading curve, causing a mechanical energy dissipation; and strain-rate dependency - the mechanical behavior depends on the strain rate (**Figure 9**) [98,123–127]. Furthermore, the strain-rate dependent variation in the yield strength is sometimes referred to as viscoplasticity [128]. The viscoelasticity of bone originates from a multiscale hierarchical solid structure including pores [e.g., inter-trabecular (< 1mm) and vascular pores (~20 μm)], and fluid phase (marrow, fat, blood vessels, and other bone fluids) filling these pores. [98,129,130].

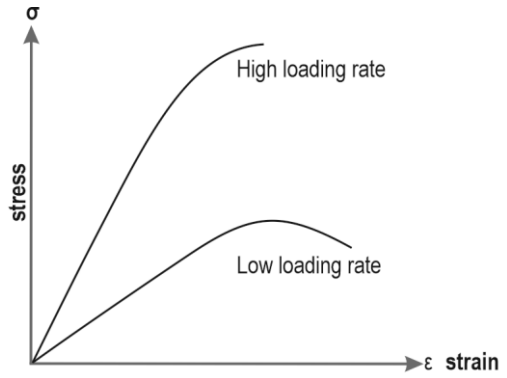

Figure 9. Strain rate-dependent mechanical properties. (Redrawn, with permission, from Johnson et al. (2010) [128] © 2010 Acta Materialia Inc. Published by Elsevier Ltd.)

Due to the strain rate-dependency, the mechanical properties of both cortical and trabecular bone tissues vary depending on the strain rate [97,128,131,132]. Carter and Hayes (1977) conducted compression tests of human and bovine trabecular bones, and observed that a compressive strength and elastic modulus rise as the strain rate is increased from 0.001 s^{-1} to 10 s^{-1} [97]. Combining with results on the cortical bones from others [133–135], they concluded that the relationships between the strain rate and these mechanical properties are similar in both cortical and trabecular bone types and can be expressed mathematically by the power law: the ultimate compressive strength and elastic modulus are approximately proportional to the strain rate to the power of 0.06 [97]. Together with the density-dependency,

they derived the following strain rate- ($\dot{\varepsilon}$) dependent constitutive equations for the ultimate strength (S) and compressive elastic modulus (E):

$$S = S_{ref}\ \dot{\varepsilon}^{0.06}\left(\frac{\rho}{\rho_{ref}}\right)^2 \tag{4}$$

$$E = E_{ref}\ \dot{\varepsilon}^{0.06}\left(\frac{\rho}{\rho_{ref}}\right)^3 \tag{5}$$

where S_{ref}, E_{ref}, and ρ_{ref} are the reference ultimate compressive strength, elastic modulus, and apparent density of compact bone tested at a strain rate of 1.0 s^{-1}, respectively. For example, using the reference values of S_{ref} = 221 MPa, E_{ref} = 22.1 GPa, and ρ_{ref} = 1.8 g/cm^3 (an apparent density for the cortical bone), these equations are further simplified into:

$$S = 68\ \dot{\varepsilon}^{0.06}\rho^2 \tag{4-2}$$

$$E = 3790\ \dot{\varepsilon}^{0.06}\rho^3 \tag{5-2}$$

Importantly, these relations were limited only to the lower strain rate ranges (0.001 s^{-1} to 10 s^{-1}). [97] However, later on, other investigators confirmed the strain-rate dependency of bone's mechanical properties also at the higher rates such as at the intermediate (1 s^{-1} to 200 s^{-1}), high (up to 600 s^{-1}), and very high strain rates (up to 1300 s^{-1}) based on the mechanical testing of the human and bovine trabecular bones [136–139].

The fluid phase of bone tissue such as marrow in the trabecular pores, and bone fluid in the vascular canals (Haversian and Volkmann canals) and lacuna-canalicular network of the cortical bone tissue may have a strain rate-dependent hydraulic stiffening/strengthening effect on the mechanical properties such as the elastic modulus and strengths [97,129,130,140–144]. However, this stiffening effect may be limited to at the tissue level (the largest dimension of the tested specimen was < 20 mm), and there has been a long debate for a past few decades whether the effect is present at the organ level [145–148]. For example, Ochoa et al. (1991 and 1997) confirmed the presence of such effect due to the pore fluid pressure in their *ex vivo* and *in vivo* dynamic cyclic loading tests of intact canine femoral heads [149,150] whereas Haider et al. (2013) observed that the degree of the effect was marginal in a recent organ-level FE modeling study of the human proximal femur [151]. This discrepancy calls for the further investigation to confirm or reject the presence of the hydraulic stiffening effect at the organ level.

2.1.2.4 Isotropy vs. Anisotropy

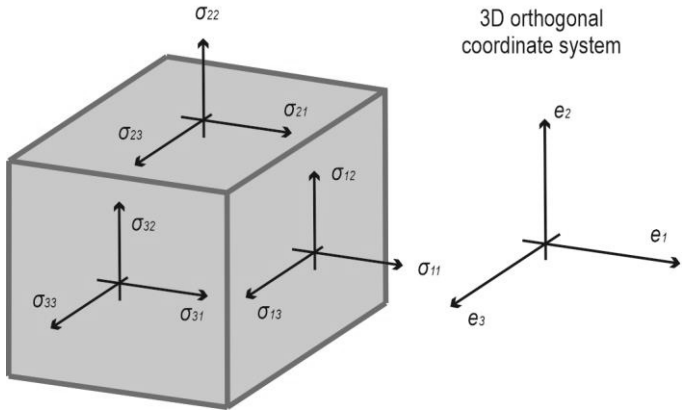

Figure 10. Cauchy stress tensor.

The stress state can be described in the 3D orthogonal coordinate system expressed by basis vectors (e_1, e_2, and e_3) where each normal stress (σ_{11}, σ_{22}, and σ_{33}) is imposed on a face perpendicular to each coordinate axis (**Figure 10**). Other stress components represent respective shear stresses. These nine stress components expressed in a tensor form are known as Cauchy stress tensor. If a Cartesian coordinate system is used as the orthogonal coordinate system (e.g., e_1 = *x*-axis, e_2 = *y*-axis, and e_3 = *z*-axis), each stress component can be described using normal and shear stress symbols (σ and τ). The Cauchy stress tensor, and its matrix forms in the arbitrary orthogonal coordinate system [the leftmost matrix in the **equation (6)**] and in the Cartesian coordinate system [the rightmost matrix in the **equation (6)**] are shown below:

$$\boldsymbol{\sigma} = \sigma_{ij} = \begin{bmatrix} \sigma_{11} & \sigma_{12} & \sigma_{13} \\ \sigma_{21} & \sigma_{22} & \sigma_{23} \\ \sigma_{31} & \sigma_{32} & \sigma_{33} \end{bmatrix} = \begin{bmatrix} \sigma_{xx} & \tau_{xy} & \tau_{xz} \\ \tau_{yx} & \sigma_{yy} & \tau_{yz} \\ \tau_{zx} & \tau_{zy} & \sigma_{zz} \end{bmatrix} \quad (6)$$

where *i, j* = 1, 2, 3 (or = *x, y, z*). Importantly, according to the principle of conservation of angular momentum, the followings are true: $\sigma_{12} = \sigma_{21}$, $\sigma_{13} = \sigma_{31}$, and $\sigma_{23} = \sigma_{32}$. This shows that the Cauchy stress tensor has only six stress components which can be expressed in Voigt notation:

$$\boldsymbol{\sigma} = \sigma_{ij} = [\sigma_{11}\ \sigma_{22}\ \sigma_{33}\ \sigma_{23}\ \sigma_{13}\ \sigma_{12}]^T = [\sigma_{xx}\ \sigma_{yy}\ \sigma_{zz}\ \tau_{yz}\ \tau_{xz}\ \tau_{xy}]^T \quad (7)$$

where superscript *T* is a transpose operator. [99,100,152]

The material is considered an anisotropic material if its material (mechanical) properties depend on the direction of loading. In contrast, the mechanical properties of the isotropic material are independent of the loading direction. [99,100] Both cortical and trabecular bones are anisotropic materials because of their complex multi-level hierarchical structure, mineralized collagen fibril alignment, directions of the bone tissues (lamellae, osteon, and trabeculae), the interaction of two main bone constitutes (mineral and protein components), and the complex porous trabecular microarchitecture. [89,106,108,153–166] It is noted that the trabecular anisotropy varies depending on the anatomical sites [103,167]. For the anisotropic material, the constitutive equation describing the stress-strain relationship during the elastic deformation can be described in the following tensor form with the indexes:

$$\sigma_{ij} = C_{ijkl}\varepsilon_{kl} \tag{8}$$

where Einstein's summation rule is applied and C_{ijkl} is a fourth order elastic stiffness tensor (*i, j, k, l* = 1, 2, 3). Although this tensor has a total of 81 elements (elastic/stiffness constants), the number of the independent elements is only 21 due to the symmetry of this tensor. Consequently, this anisotropic constitutive relation can be expressed in the matrix form as follows, using Voigt notation:

$$\begin{bmatrix}\sigma_{11}\\ \sigma_{22}\\ \sigma_{33}\\ \sigma_{23}\\ \sigma_{13}\\ \sigma_{12}\end{bmatrix} = \begin{bmatrix}c_{11} & c_{12} & c_{13} & c_{14} & c_{15} & c_{16}\\ c_{12} & c_{22} & c_{23} & c_{24} & c_{25} & c_{26}\\ c_{13} & c_{23} & c_{33} & c_{34} & c_{35} & c_{36}\\ c_{14} & c_{24} & c_{34} & c_{44} & c_{45} & c_{46}\\ c_{15} & c_{25} & c_{35} & c_{45} & c_{55} & c_{56}\\ c_{16} & c_{26} & c_{36} & c_{46} & c_{56} & c_{66}\end{bmatrix}\begin{bmatrix}\varepsilon_{11}\\ \varepsilon_{22}\\ \varepsilon_{33}\\ 2\varepsilon_{23}\\ 2\varepsilon_{13}\\ 2\varepsilon_{12}\end{bmatrix} \tag{9}$$

where c_{ij} is the elastic/stiffness constant. [166,168–170]

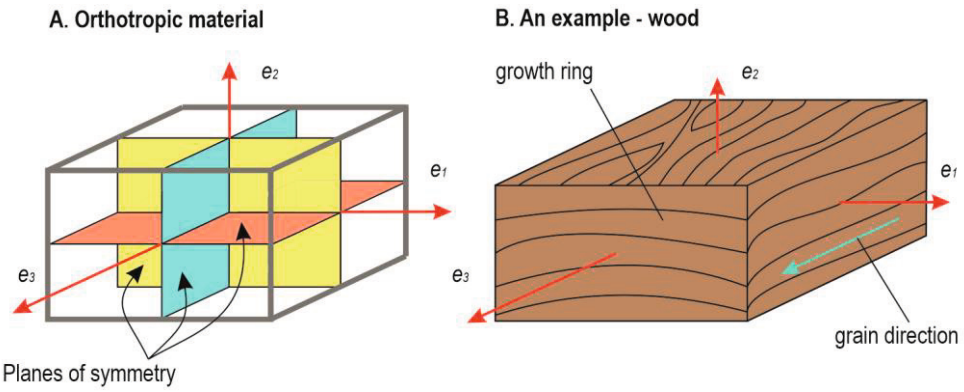

Figure 11. Orthotropic material. (A) An orthotropic material is shown with three mutually perpendicular planes of mirror symmetry. (B) an example – wood.

Anisotropy of the material/mechanical properties can be simplified into orthotropy by assuming the structure possesses orthotropic symmetry which is described by three mutually perpendicular planes of mirror symmetry (**Figure 11**). Such orthotropic material has its mechanical properties varying along three orthogonal axes, each of which is perpendicular to the plane. An example of the orthotropic materials is a wood where one of the orthogonal directions (e_3) is parallel to the grain direction while other orthogonal directions (e_2 and e_1) are perpendicular and tangent to the growth ring, respectively. The bone tissue is often modeled as the orthotropic material due to its satisfactory accuracy representing its mechanical behavior. This leads to the simplification of the anisotropic constitutive relation [**equation (9)**] and the orthotropic elastic constitutive relation can be expressed as follows:

$$\begin{bmatrix}\sigma_{11}\\ \sigma_{22}\\ \sigma_{33}\\ \sigma_{23}\\ \sigma_{13}\\ \sigma_{12}\end{bmatrix} = \begin{bmatrix}c_{11} & c_{12} & c_{13} & 0 & 0 & 0\\ c_{12} & c_{22} & c_{23} & 0 & 0 & 0\\ c_{13} & c_{23} & c_{33} & 0 & 0 & 0\\ 0 & 0 & 0 & c_{44} & 0 & 0\\ 0 & 0 & 0 & 0 & c_{55} & 0\\ 0 & 0 & 0 & 0 & 0 & c_{66}\end{bmatrix}\begin{bmatrix}\varepsilon_{11}\\ \varepsilon_{22}\\ \varepsilon_{33}\\ 2\varepsilon_{23}\\ 2\varepsilon_{13}\\ 2\varepsilon_{12}\end{bmatrix} \quad (10)$$

where the number of the elastic constants (c_{ij}) is reduced to nine. These nine constants in the **equation (10)** can be expressed using only three Young's moduli (E_1, E_2, and E_3), three shear moduli (G_{12}, G_{23}, and G_{31}), and six Poisson's ratios ($\nu_{23}, \nu_{32}, \nu_{13}, \nu_{31}, \nu_{12}$, and ν_{21}) as shown below in the **equation (11)**:

$$\begin{bmatrix} \varepsilon_{11} \\ \varepsilon_{22} \\ \varepsilon_{33} \\ 2\varepsilon_{23} \\ 2\varepsilon_{13} \\ 2\varepsilon_{12} \end{bmatrix} = \begin{bmatrix} \frac{1}{E_1} & \frac{-\nu_{21}}{E_2} & \frac{-\nu_{31}}{E_3} & 0 & 0 & 0 \\ \frac{-\nu_{12}}{E_1} & \frac{1}{E_2} & \frac{-\nu_{32}}{E_3} & 0 & 0 & 0 \\ \frac{-\nu_{13}}{E_1} & \frac{-\nu_{23}}{E_2} & \frac{1}{E_3} & 0 & 0 & 0 \\ 0 & 0 & 0 & \frac{1}{G_{23}} & 0 & 0 \\ 0 & 0 & 0 & 0 & \frac{1}{G_{31}} & 0 \\ 0 & 0 & 0 & 0 & 0 & \frac{1}{G_{12}} \end{bmatrix} \begin{bmatrix} \sigma_{11} \\ \sigma_{22} \\ \sigma_{33} \\ \sigma_{23} \\ \sigma_{13} \\ \sigma_{12} \end{bmatrix} \tag{11}$$

where the inverse relation ($\boldsymbol{\varepsilon = C^{-1}\sigma}$) is presented for the sake of simplicity. [72,98,166,170] Finally, in case of the isotropic material, the followings are true for the elastic constants:

$$E_1 = E_2 = E_3 = E,\ \nu_{12} = \nu_{21} = \nu_{31} = \nu_{32} = \nu_{13} = \nu_{23} = \nu,$$

$$G_{23} = G_{31} = G_{12} = \frac{E}{2(1+\nu)} \tag{12}$$

Using these, the isotropic elastic stress-strain relation is finally expressed as: [98]

$$\begin{bmatrix} \varepsilon_{11} \\ \varepsilon_{22} \\ \varepsilon_{33} \\ 2\varepsilon_{23} \\ 2\varepsilon_{13} \\ 2\varepsilon_{12} \end{bmatrix} = \begin{bmatrix} \frac{1}{E} & -\frac{\nu}{E} & -\frac{\nu}{E} & 0 & 0 & 0 \\ -\frac{\nu}{E} & \frac{1}{E} & -\frac{\nu}{E} & 0 & 0 & 0 \\ -\frac{\nu}{E} & -\frac{\nu}{E} & \frac{1}{E} & 0 & 0 & 0 \\ 0 & 0 & 0 & \frac{1}{G} & 0 & 0 \\ 0 & 0 & 0 & 0 & \frac{1}{G} & 0 \\ 0 & 0 & 0 & 0 & 0 & \frac{1}{G} \end{bmatrix} \begin{bmatrix} \sigma_{11} \\ \sigma_{22} \\ \sigma_{33} \\ \sigma_{23} \\ \sigma_{13} \\ \sigma_{12} \end{bmatrix} \tag{13}$$

To demonstrate the anisotropic mechanical properties of bone, some of the mechanical properties of both human femoral cortical and trabecular bones in the longitudinal (parallel to the diaphyseal axis) and transverse directions are presented in **Table 2**. The anisotropic mechanical properties can be seen by observing the mechanical properties such as the elastic modulus and strengths (e.g., compressive yield stress) are higher in the longitudinal than in the transverse direction. [1,72,106]

Table 2. Anisotropic mechanical properties of human femoral cortical and trabecular bones

Direction	Properties	Cortical*	Trabecular †
Longitudinal	Elastic modulus (GPa)	15.6−19.1[a-f]	1.1−1.5[g,h]
	Shear modulus (GPa)	4.7[f]	
	Compressive yield stress (MPa)	111-148[d,e]	7.3[h]
	Compressive yield strain (%)	0.91[e]-0.98[d,e]	
	Compressive ultimate stress (MPa)	154−209[b-d]	
	Tensile ultimate stress (MPa)	93−140[b-d]	
Transverse	Elastic modulus (GPa)	5.7-11,5[b,e,f]	~0.5-1.0[g,h]
	Shear modulus (GPa)	3.3[f]	
	Compressive yield stress (MPa)	42-44[e]	4.7[h]
	Compressive yield strain (%)	0.83−0.84[e]	
	Compressive ultimate stress (MPa)	63-133[b,e]	
	Tensile ultimate stress (MPa)	51[b]	

*The characteristic dimension of mechanically tested specimens was on the order of 1 cm [171–175].

† To show the anisotropy in the trabecular bone, only values in the similar magnitude from studies which measured the mechanical properties both in the longitudinal and transverse directions are presented.

Studies: [a] obtained from Reilly et al. (1974) [171]; [b] obtained from Reilly & Burstein (1975) [176]; [c] obtained from Burstein et al. (1976) [177]; [d] obtained from Mirzaali et al. (2016) [172]; [e] obtained from Dong et al. (2012) [173]; [f] obtained from Dong et al. (2004) [174]; [g] estimated from Ciarelli et al. (1991) [110] based on an assumption of the apparent density of 0.62 for femoral neck trabecular bone from Bayraktar et al. (2004) [178]; and [h] estimated by μFE models from Yu et al. (2021) [179].

2.1.2.5 Asymmetric Strength of Bone

Yield and ultimate strengths are the important material properties governing the failure of structure. Importantly, both cortical and trabecular bones have the asymmetric strength (**Figure 12**) such that their strengths are typically higher in compression than in tension. This asymmetry in the yield strength plays an important role in failure criteria, defining the fracture load in the proximal femur FE analysis. Several studies reported this asymmetric strength of bone and some of selected values are presented in **Table 3**. [171,176,178,180]. To show the asymmetric strengths, the values in the longitudinal direction from **Table 2** are reused in **Table 3** for the cortical bone. In contrast, only values from another experimental study [178] which conducted both tensile and compressive tests are presented for the trabecular bone. The discrepancy in the magnitude of the trabecular values between **Table 2** and **Table 3** is mainly due to the great dependency of trabecular mechanical properties on the bone density, and differences in the tested specimens and testing environment between studies.

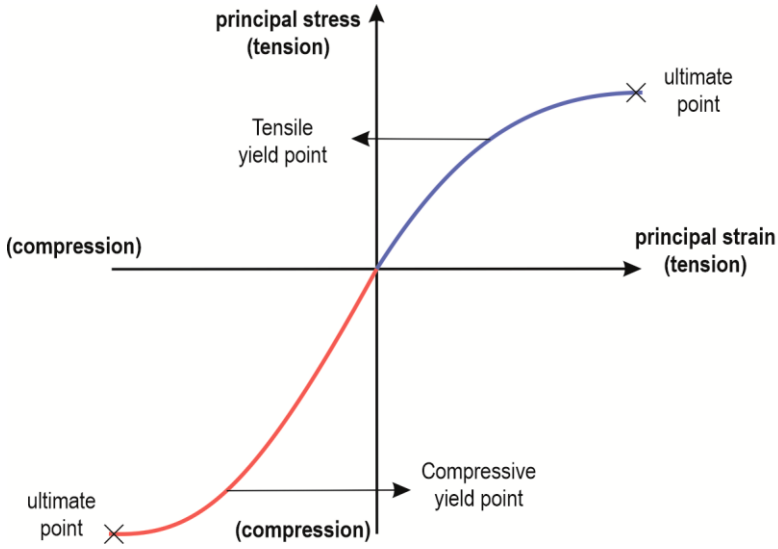

Figure 12. Asymmetric strengths of bone. This figure shows the stress-strain curve from the uniaxial tensile and compressive loading. The curve is only for demonstration purpose and not scaled. (Redrawn, with permission, from Niebur et al. (2000) [181] @ 2000 Elsevier Science Ltd.)

Table 3. Asymmetric strength of human femoral cortical and trabecular bones

Strength	Mode	Cortical*†	Trabecular*†
Yield stress (MPa)	compressive	111-148[a, b]	135[c]
	tensile	85-108[b, c]	85[c]
Yield strain (%)	compressive	0.91-0.98[a,b]	1.04[c]
	tensile	0.67-0.73[b, c]	0.62[c]
Ultimate stress (MPa)	compressive	154-209[b, d, e]	N.A.
	tensile	93-140[b, d, e]	N.A.
Ultimate strain (%)	compressive	1.3[b]	N.A.
	tensile	1.9[b]	N.A.

Note: N.A. = not available.

***** The characteristic dimension of the tested bone specimens was on the order of 1 cm.

† Cortical and trabecular bones were extracted from femoral mid-diaphysis and proximal femur, respectively.

Studies: [a] from Dong et al. (2012) [173]; [b] from Mirzaali et al. (2016) [172]; [c] from Bayraktar et al. (2004) [178]; [d] from Reilly & Burstein (1975) [176]; and [e] from Burstein et al. (1976) [177].

2.1.3 Functional Adaptation of Bone

Bone is a mechanosensitive tissue adapting its mass, structure, and material properties to habitual mechanical loading environment [2,3,14–16,19,20,182–187]. This concept was first introduced by Georg Hermann von Meyer in 1867 [188] and Wilhelm Roux in 1881 [189]. Based on Meyer's observation regarding to the proximal femur, later in 1892, Julius Wolff proposed that the structure of trabecular bone in the proximal femur was aligned to the stress trajectories (principal directions) of externally applied load [190]. Generally, his theory is widely known as Wolff's law. [3,182,183,190] However, today, it is known that the mechanical loading affects not only the trabecular bone but also cortical bone. Besides, this adaptive response has been observed in other skeletal sites such as vertebrae, tibia, and calcaneus. [3,191,192] The original Wolff's law contains misconceptions and has been criticized by others [3,182,183]. Therefore, the general idea of the Wolff's law that "the bone adapts to the prevalent mechanical loading" is commonly known as functional adaptation of bone to this day [3,191]. This section describes the relevant topics in the bone's functional adaptation to the present doctoral research including 1) bone cell types, 2) two important bone's metabolic processes such as modeling and remodeling, 3) underlying effective mechanical loading properties to induce the adaptation, 4) effects of disuse and overuse, 5) age-dependent changes in the functional adaptation, 6) an importance of cortical thickening during growth, and 7) mechanotransduction (cellular and molecular mechanism behind the functional adaptation).

2.1.3.1 Bone Cells

There are four bone cells such as osteoblast, bone lining cell, osteocyte, and osteoclast. Each of them has unique roles in the bone metabolism. The osteoblasts are new bone forming cells laying along the bone surface, constituting for 4-6% of the total bone cells, and originated from pluripotent mesenchymal stem cells. They are present in the extracellular matrix of the bone marrow and periosteum and regulate its mineralization. There are two main processes involved in the formation of new bone by osteoblasts: secretion of osteoid (unmineralized organic phase consisting of type I collagen, non-collagenous proteins, and other proteins) in the bone matrix and its subsequent mineralization. The osteoblast changes its shape from cuboidal in its active state to flat in its inactive state. The latter is also known as a bone lining cell. [79,95,192]

The bone lining cells are the inactive flat-shaped osteoblasts covering the bone surface (quiescent state) where neither bone formation nor resorption takes place. Although their functions are not completely understood, it is known that they prevent the interaction between bone matrix and osteoclasts if the bone resorption should not occur. Some of their cytoplasmic processes are extended into canaliculi to communicate with neighboring osteocytes via gap junctions. [79] A recent study showed that the quiescent bone lining cells can be reactivated back to the osteoblasts and are the major source of the osteoblasts in the adulthood [193].

The osteocytes are the most common bone cells representing 90-95% of the total bone cells in the adult skeleton and can live up to 25 years. They are present in the lacunae between the mineralized bone matrices and have different shapes depending on the type of bone: a round and elongated shapes in the trabecular and cortical bones, respectively. They originate in the pluripotent mesenchymal stem cells via the osteoblast differentiation. At the end of the bone formation cycle, some of osteoblasts remain in the bone matrix and are differentiated into osteocytes by reducing their cell organelles. Each osteocyte has up to 50 cytoplastic processes which come out of the lacuna space through small tunnels called canaliculi. [79,95] These lacuna spaces and canaliculi form a porous network, called lacunocanalicular network [194]. Through this network, the osteocytes communicate with each other, the bone lining cells, and osteoblasts through their cytoplastic processes and the interstitial fluid flow. Consequently, this network enables the osteocyte to operate as the mechanosensors to detect mechanical loads, facilitating bone's functional adaptation. Furthermore, the apoptosis of the osteocyte triggers the bone resorption by the osteoclast. Due to these, the osteocytes are considered as the orchestrators of the functional adaptation by modulating the activities of both osteoblasts and osteoclasts. [79,95]

The osteoclasts are bone-resorbing cells, which are derived from the hematopoietic stem cell descent. Once activated, an osteoclast can resorb fully mineralized bone up to 200,000 μm^3/day, for which ~100-200 days are needed for the generations of osteoblasts to build. The osteoclasts are more common in the inner layer of bone (endosteum). In the resorption process, they release powerful lysosomal enzymes and acids to dissolve organic and mineral crystals of the bone matrix. [71,79,95]

2.1.3.2 Modeling and Remodeling

The bone's functional adaptation is carried out through two metabolic processes of bone called modeling and remodeling [191,192]. The modeling is responsible for the skeletal growth and the adaptations of bone shape and mass to the mechanical loading. It takes place predominantly during the skeletal growth and its amount normally starts declining to a trivial level once the skeletal maturity is achieved. [192,195] The modeling occurs on the (sub)periosteal, endosteal (endocortical), and trabecular surfaces and consists of either/both of following cellular activities: the activation of osteoblast followed by bone formation (A-F, formation modeling) and/or the activation of osteoclasts followed by bone resorption (A-R, resorption modeling) [192,195,196]. These activities happen independently of each other at the different locations or in a coordinated approach (e.g., modeling drift) [195]. To optimize the structure of bone corresponding to changes in the mechanical environment, the formation and resorption activities are regulated. For example, an increased level of mechanical loads through physical activities and/or by an increase in the body weight can induce more bone formation over resorption, resulting in the bone gain. [192,195,196] Once the new bone tissue is formed, it is maintained by the bone lining cells and osteocytes [192,195].

In the modeling, shaping the bone depending on the mechanical loading is referred to as modeling drift (**Figure 13**). The modeling drift is a coordinated selective response of the bone formation or resorption occurring on the different or even same bone surfaces. It does not simply form a uniform shape of the bone (e.g., circular cross-section) but can form the irregular shape (e.g., oval- or random-shaped cross-section) depending on the mechanical loading. [192,195]

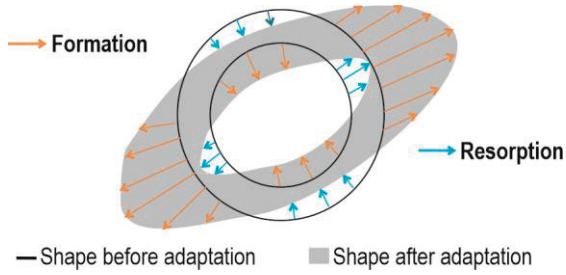

Figure 13. Modeling drift. (Redrawn based on Allen & Burr (2014) [197]).

The remodeling is in charge of a renewal of bone including the adaptation, maintenance, and repairment of the damaged bone tissue [192,195,196]. Unlike the modeling, the remodeling occurs continuously throughout all stages of life. In

addition to the subperiosteal, endosteal, and trabecular surfaces, it can also occur in the intracortical envelop (Haversian canal). [192,195] In the remodeling, the osteoblasts and osteoclasts form a functional unit called basic multicellular unit (BMU) to perform coupled activities on the same surface in the following specific order: an activation, the resorption of bone, and then formation (A-R-F) [2,192,195,198,199]. In the intracortical envelop, the BMUs move along its longitudinal axis to preserve its 3D structure. The leading osteoclasts excavate the tunnel by the resorption, creating the characteristic "cutting cone" shape at its front. This tunnel is subsequently refilled by centripetal deposit of new layers of osteons by the osteoblasts. On the trabecular and endocortical surfaces, the BMUs resorb and replace pancake-shaped packets of bone. [192,200]

The net amount of bone after each remodeling cycle is called bone balance. The positive bone balance suggests that the bone formation dominates over the resorption resulting in the increases in the bone mass while the negative balance suggests vice versa. [192,201] Mechanical loading induces the formation over resorption which can lead to the positive bone balance while a condition like osteoporosis promotes resorption over formation leading to the negative balance [192,195,202]. In the healthy individuals, the normal bone balance is slightly negative after each remodeling cycle. This means that the amount of bone resorbed is not completely refilled by the formation. With aging, this contributes to bone loss and thinning. In adulthood, the remodeling is influenced by age, genetics, and modifiable factors such as nutrition, hormonal status, physical activity level, diseases, and their medication. [195] Importantly, a menopause (around age 50 years) also induces more resorption due to the loss of ovarian estrogen production, which had previously minimized the osteoclastic resorption during pre-menopausal phase. This causes the further acceleration of bone loss. [195,203] Similar but less dramatic bone loss also takes place about 10 years later in male. The increased resorption due to aging or diseases also lead to the trabecularization of the intracortical and endocortical bone. This results in the increase in the cortical porosity, the enlargement of endocortical diameter, and finally the fragility of bone. [195]

2.1.3.3 Effective mechanical loading properties

The bone's functional adaptation suggests only the general concept that the bone adapts to changes in the mechanical environment, but an important question remains: "What kinds of mechanical loadings are effective to induce the osteogenic adaptation?" In 1987, Harold Frost proposed his theory regarding this question, known as mechanostat theory. He suggested that the adaptive modeling and remodeling responses have its own windows defined by upper and lower strain thresholds known as minimum effective strain (MES) (**Figure 14**). [2,198]

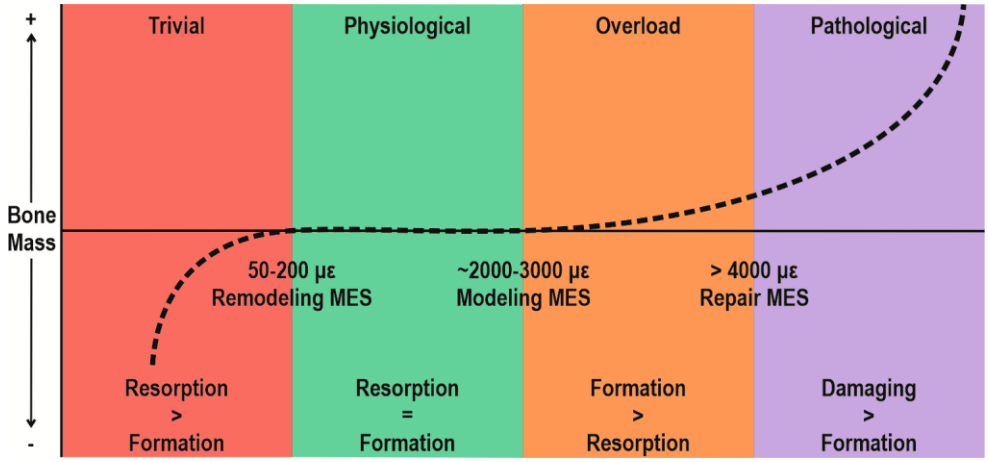

Figure 14. Frost's mechanostat theory. (Redrawn, with permissions, from Forwood & Turner (1995) [204] © 1995 Published by Elsevier Inc., and Burr (1992) [205] © 1992 by the Center for Human Growth and Development, The University of Michigan).

According to this theory, there are four windows, each of which has the distinctive adaptive modeling or remodeling response. If the strain magnitude of the local mechanical signals is between the remodeling MES (50 – 200 με) and the modeling MES (~2000-3000 με), the normal physiological (or homeostatic) response is expected so that the equal amount of the remodeling formation and resorption occurs, leading to the maintenance of bone mass. When the strain magnitude falls below the remodeling MES (trivial or disuse), more remodeling resorption is induced over the formation, causing the bone loss. In contrast, if it falls in the window between the modeling MES and repair MES (> 4000 με), it is considered as overloading inducing more modeling formation over the resorption, resulting in the (lamellar) bone gain. Lastly, when it exceeds this repair MES, it is considered pathological overloading in which the strain magnitude is large enough to damage

the bone tissue and the damaged lamellar bone is replaced by the woven bones. Frost's mechanostat theory is strict in its distinction between remodeling and modeling in each window. However, this is not entirely true. For example, today, it is known that the remodeling can occur in overloading and pathological overloading windows besides modeling. [2,182,198,204,206,207] This strain magnitude-dependent adaptive response of bone has been confirmed in several previous animal experimental studies where the external mechanical loadings were applied to ulna bone of e.g., turkeys or rats with various strain magnitudes [16,17,186,208].

Frost's mechanostat theory is obviously simplified and the bone functional adaptation is also influenced by other mechanical loading properties. Based on the numerous animal experimental studies conducted over the past few decades, it was found that the effective osteogenic mechanical loading is a dynamic against the static loading type and should be produced at high strain rate and/or frequencies. Furthermore, the adaptive response is associated with the loading duration and resting periods between the loading cycles or sessions. [182,191,192,209–211] The following sections summarize these aspects.

2.1.3.3.1 Dynamic loading

Around 50 years ago, Hert, Lisková, and their colleagues (1969, 1971, and 1972) were the first to report that the dynamic loading (intermittent or cycling loading) is a necessary characteristic of the mechanical loading to induce new bone formation rather than static loading (constant loading magnitude) through series of their animal experiments [212–215]. Later, Lanyon and Rubin (1984) also confirmed this in their study of avian ulnae. After 8-weeks follow-up, they observed that dynamically loaded bones had a significant increase in their bone mass primarily due to new bone deposition on periosteal surface while no changes occurred in the statically loaded bones. [15] In fact, the static loading has no beneficial effect or even an adverse effect suppressing normal periosteal appositional growth [216]. Identifying the dynamic loading as the effective loading type suggests that impact exercise such as a jumping has the potential to cause the beneficial osteogenic adaptation. Umemura et al. (1997) confirmed this by observing that the rats which performed jumping exercise 5 days a week for 8 weeks had the significantly greater bone mass in their tibiae and femora than the control rats [217].

2.1.3.3.2 Strain rate and frequency

The osteogenic response to the mechanical loading was found proportional to the strain rate based on the several animal experiments. In these studies, the dynamic loadings with various strain rates (e.g., low, medium, and high) were applied to bones while the peak strain magnitude, frequency, and loading duration were kept the same. [19–21,218] Similar to the strain rate, there is the dose-response relationship between the loading frequency and osteogenic adaptation of bone [22,24,219]. However, to promote the osteogenesis, the frequency needs to be at least 0.5 Hz [219]. Moreover, above the frequency of 10 Hz, the degree of adaptative response plateaus and no further osteogenic adaptation can be achieved [23]. Importantly, the minimum strain threshold (magnitude) to induce the bone formation can be lowered if the frequency is increased. Hsieh et al. (2001) examined the effect of various combination of loading magnitudes and frequencies on the new bone formation and observed that the minimum strain threshold can be decreased from 1820 με to 650 με as the loading frequency increased from 1Hz to 10 Hz. [24]

Importantly, these dynamic loading properties (the strain magnitude, rate, and frequency) are interrelated so that the strain rate ($\dot{\varepsilon}$, in unit of s^{-1}) is linearly proportional to strain magnitude (ε, unitless) and frequency (f, in unit of s^{-1}) as shown below:

$$\dot{\varepsilon} = \varepsilon f \tag{14}$$

Given this, Turner (1998) proposed that the dynamic loading stimulus inducing the adaptive response of bone can be expressed mathematically as follows:

$$Strain\ stimulus = k\epsilon f \tag{15}$$

where k is a proportional constant, ϵ is a peak-to-peak strain magnitude, and f is the loading frequency. [209] Combing this concept with the experimental results, Turner and his colleagues (1994, 1995, and 1998) demonstrated that the bone formation rate is highly and linearly correlated to this strain stimulus. Importantly, this suggests that the osteogenic response is determined by a combination of magnitude and frequency of the applied strain, which is equivalent to strain rate alone as described in the **equation (14)** above. [21,209,219]

2.1.3.3.3 Duration and resting interval

Extending the duration of loading does not lead to further osteogenic adaptation of bone. The mechanosensitivity of bone and osteogenic response start declining after the certain duration. This phenomenon was observed in the animal experiments conducted by Rubin and Lanyon (1984) and Umemura et al. (1997) where the increases in bone mass due to the skeletal loading began leveling off after approximately 40 cycles per day (jumping exercise). [187,211,217]

Fortunately, it was found possible to restore the mechanosensitivity by inserting resting periods between loading sessions and/or between cycles. Based on the animal experiments, a 4 – 8 hours of inter-session [220] and/or a 7 – 14 seconds of inter-cycle resting periods [220,221] are sufficient to re-sensitize the bone tissue to the mechanical loading and can lead to the significantly greater bone formation than the shorter resting periods. With 8 hours of resting, the mechanosensitivity can be fully recovered [220]. Furthermore, Robling and his colleagues (2000, 2002) found that, despite the same total loading volume (with respect to the loading magnitude and frequency), the osteogenic effect is greater if the loading was applied in multiple sessions (e.g., 90 cycles x 4 sessions) rather than in a single session (e.g., 360 cycles x 1 session) [222–224]. To summarize, the dynamic loading should be applied to bone in the multiple sessions, rather than in a single session, with sufficient inter-session (4-8 hours) and inter-cycle (≥ 7 seconds) resting periods to maximize the osteogenic adaption of bone.

2.1.3.3.4 Accommodation

Bone cells acclimate to the predominant habitual mechanical loading types. Once this occurs, further osteogenic adaptation cannot be expected by the same already-familiarized mechanical loading type. In other words, the initial or unfamiliar mechanical stimulus has the greater osteogenic effect. [225,226] This phenomenon is referred to as accommodation of bone [192,209]. Importantly, this accommodation can be prevented by inserting a "time off" (e.g., a 5-weeks unloading period) between the long-term loading periods (e.g., 15 weeks). This "time off" can improve the mechanosensitivity and result in the greater bone formation than without it [226].

2.1.3.4 Disuse and Overuse

Disuse and substantial overuse of bone cause negative consequences. In case of the disuse, the bone resorption dominates the formation leading to a rapid bone loss. For example, this is common in astronauts who returned from the long-term micro-gravitational space environment. [191,192] Importantly, the predominant location and mechanism of the bone loss differ depending on the stage of life. Based on the experiments of growing and mature dogs, the disuse decreases the bone formation at the periosteal surface in the growth phase while it increases the resorption at the endosteal and trabecular surfaces in the adulthood. [227,228]. The disuse in the adulthood also leads to the substantial increase in the intracortical porosity [228]. These deteriorations obviously contribute to the reduced bone strength [227,228].

In the physiological loading condition, the loading-induced microdamage (e.g., microcracks) in the bone is repaired through the resorption followed by the bone formation. However, in case of the overuse (e.g., due to substantially high repetitions and/or long loading duration), the rate of damaging exceeds that of repairing, leading to the accumulation of damaged bone tissues. This results in reduced bone strength and stiffness. Eventually, the microcracks merge each other leading into a fatigue-induced fracture, also known as stress fracture. [191,192] This overuse bone injuries are common in runners and ballet dancers [229,230].

2.1.3.5 Age-Dependent Changes in Functional Adaptation

Bone's adaptive response to the mechanical loading changes with aging. Once skeletal maturity is reached after age of 18 to 25 years, its mechanosensitivity and osteogenic potential start declining. Besides, the main role of loading-induced bone adaptation shifts from adding new bone mass during the growth to maintenance of the existing bone in the adulthood. [3,231,232] Furthermore, the decrease in estrogen production due to menopause (or amenorrhea) does not only accelerate the age-related bone loss but also reduces the sensitivity to the mechanical loading [203,233–235]. Nonetheless, the additional mechanical loading through physical activities in the adulthood is not totally meaningless in terms of strengthening the bone. Despite the age-related declines, the exercise loading can still cause small but cumulatively significant benefits in bone mass and structure if the adequate amount of the mechanical loading is applied with the optimal frequency. Although this cumulative benefit is greater in the young adult, it can still be obtained even in the older adults. [3,231,232] For example, Kerr et al. (1996) reported that even postmenopausal

females (mean age: 58 years) could increase their bone mineral density at several skeletal sites including hip by small amount but significantly (~2%) after a 1 year progressive resistance training program [10]. It is noteworthy that such a small increase can still improve bone strength considerably [222,236]

Not only does the mechanosensitivity decline with aging, but also the primary responsive surface to the mechanical loading changes. Similar to the disuse-induced bone loss, the location of loading-induced new bone formation shifts from the periosteal surface before and during early puberty to the endosteal surface after the puberty. The former results in the expansion of outer circumference of the bone (periosteal expansion) while the latter leads to mainly the maintenance of the inner circumference (endocortical/-steal width). [3,237–239] Besides, this surface shift is sex-dependent and begins earlier in female than in male. While the exercise-induced periosteal apposition still takes place in male during or late in puberty, the shift to the endosteal surface already begins in female [237–240]. This is likely because an increase in estrogen production during the puberty inhibits the periosteal bone formation but stimulates the endosteal apposition [203,239,241–243]. Accordingly, a window of opportunity [the period during growth when the bone is most responsive to the (exercise-induced) mechanical loading] is likely shorter in female than in male [237–239].

Furthermore, the surface response to the mechanical loading appears site-specific even within a same bone. The relative contribution of the periosteal and endosteal bone apposition to the greater cortical area due to the mechanical loading varies from proximal to distal, anterior to posterior, and/or medial to lateral site, at least in humerus. [238,244,245] This is likely because the loading condition varies from the proximal to distal side of the humerus [244]. To summarize, the bone functional adaptation is not only age- and maturity-dependent (depending on the onset of puberty or menopause) but also surface-, site-, and sex-specific [12,240].

2.1.3.6 Importance of Cortical Thickening during Growth

From an engineering perspective, increasing the cortical thickness is an important aspect with respect to strengthening the bone against the bending. A tube-shaped bone including the femoral neck is subjected to the bending loading, where the resultant deflection (δ) can be expressed as follows:

$$\delta = \frac{ML^2}{8EI} \tag{16}$$

where M is the (applied) bending moment, L is the length of bone, E is the elastic modulus, and I is the second moment of area. The fracture occurs when deflection exceeds the bone's ability to bend elastically. Thus, bending strength of the bone can be increased by minimizing this deflection (δ). For given M and L, this can be achieved by increasing E and/or I. Now, this I for the tube-shaped bone can be expressed as:

$$I = \frac{\pi}{4}(r_o^4 - r_i^4) \tag{17}$$

where r_o and r_i are the outer and inner radii of the cross-section of bone, respectively (**Figure 15**). Thus, the I can be increased by increasing r_o (periosteal expansion) and/or decreasing r_i (endosteal contraction). [191]

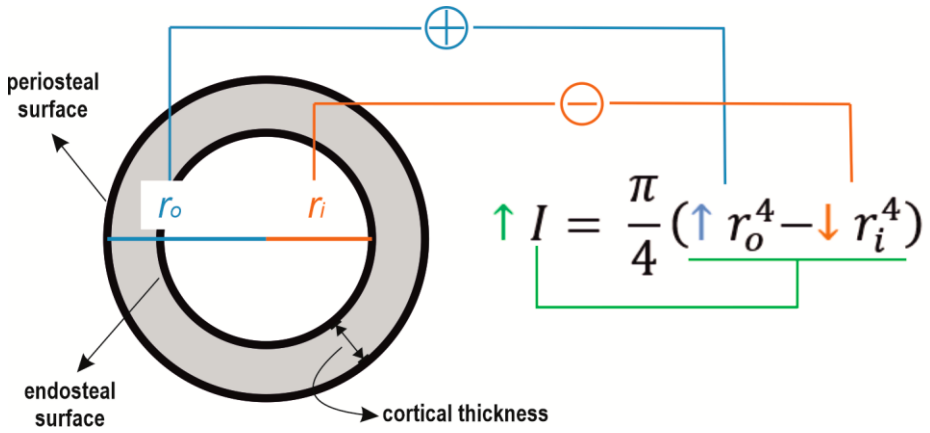

Figure 15. Cortical thickness and the second moment of area. This figure shows the outer (r_o) and inner radii (r_i) of the tube-shaped bone, the second moment of area (I), and a schematic presentation of the potential contribution of the periosteal expansion ($\uparrow r_o$) and endosteal contraction ($\downarrow r_i$) into I.

As mentioned earlier, the cortical thickening by the mechanical loading-induced periosteal expansion ($\uparrow r_o$) (in addition to the normal age-dependent expansion) takes place mainly until the puberty. This highlights the importance of engaging in exercise during the skeletal growth to maximize I and consequently to minimize δ. Such decrease in δ may help reducing hip fracture risk. [191]

2.1.3.7 Mechanotransduction

Cellular and molecular mechanisms how applied mechanical stimuli are converted into biochemical signals to trigger the anabolic or catabolic adaptation of bone are called mechanotransduction of bone [77,210,246]. Mechanotransduction in the bone tissues involves numerous cellular functions including gene expression, protein synthesis, and cell proliferation and differentiation [247]. It can be divided into four stages: 1) mechanocoupling – the transduction of applied mechanical load to a local mechanical signal; 2) mechanoreception and biochemical coupling – sensing the local mechanical stimuli and converting them to biochemical signals within cell membrane and cytoskeleton; 3) cell-to-cell signaling – the communication from one cell to others (e.g., a sensor cell to effector cells); and 4) the effector response – activation of either bone formation or resorption [210]. Since the details of each stage are beyond the scope of this dissertation, the readers are referred to the reviews for the further details [77,196,207,210,246–253]. The relevant information to the present research is briefly discussed here.

The most important player in the mechanotransduction is the osteocyte which does not only take a major mechanosensory role, but also orchestrate both osteoblastic formation and osteoclastic resorption through various signaling pathways [247]. Utilizing the cytoplasmic processes in the widespread lacunocanalicular network, the osteocytes communicate with each other and other neighboring cells (e.g., osteoblasts, bone lining cell, endothelial cells) through gap junctions [77,194,247,248,250,251]. The mechanical loading causes deformation of bone tissue that creates the hydrostatic pressure gradient inside of the bone tissue. This results in the extracellular fluid flow across the osteocytes in the lacunocanalicular network which induces shear stress on the osteocyte due to fluid's viscosity. It is believed that its cellular membrane can sense these shear stress and hydrostatic pressure. [210,246,247,249,250,252] The loading magnitude of this fluid flow is proportional to the loading rate. This explains why the dynamic loading was found more effective than the static loading to induce the osteogenic adaptation in the animal experimental studies as mentioned earlier. [216,249] Furthermore, it was

found that the fluid drag force can stretch the cell membrane up to loading frequency of 10Hz [249,254,255]. This is also highly consistent with the observation from another aforementioned animal experimental study which demonstrated that the osteogenic adaptation can be induced up to this frequency of strain loading [23].

Lastly, the bone resorption is also possibly regulated by the strain-dependent osteocyte apoptosis. The osteocyte apoptosis is reduced under physiological/normal strain range while it is increased in abnormal strain ranges typical in disuse or fatigue/overloading. In the overloading, the osteocyte apoptosis takes place where microdamage occurs and the osteocyte apoptosis may send signals to osteoclasts to remove the damaged bones. However, it is noted that the mechanism of osteocyte apoptosis-regulated bone resorption is not fully elucidated. [246,251,253,256]

2.2 Medical Imaging

Effects of exercise-induced mechanical loading on human proximal femur bone will be discussed in the next section. Such effects can be examined by evaluating bone properties such as bone mass, mineral density, and structure. These properties can be measured using non-invasive medical imaging methods. For the sake of the readability, basic principles and major limitations of three medical imaging methods such as dual-energy X-ray absorptiometry (DXA), quantitative computed tomography (QCT), and magnetic resonance imaging (MRI) are briefly discussed in this section.

2.2.1 Dual-energy X-ray Absorptiometry (DXA)

Dual-energy X-ray absorptiometry (DXA) is a medical imaging method to measure areal bone mineral density (aBMD, in g/cm^2) using two X-ray beams with different photon energy levels. The aBMD can be calculated by utilizing the dependencies of the magnitude of the radiation attenuation (attenuation coefficient) on the energy level and on two tissue types: 1) bone tissue (including bone material and red/yellow marrows), and 2) soft tissue (including fat and lean tissues). [257,258] Importantly, in DXA, it is assumed that the scanned region of interest (ROI) consists of only two components (soft and bone tissues) and fat tissues are homogeneously distributed within these tissues [259]. Principally, DXA can be used for any skeletal site; however, the lumbar spine, proximal femur (hip), forearm, and total body have been the most measured sites for the clinical use. In case of the proximal femur, aBMD can be determined for the following (sub)regions: femoral neck, trochanter, Ward's triangle, and total hip. Furthermore, bone mineral content (BMC, in gram) can be determined by multiplying aBMD by the measured area. Also, DXA can be used to measure body composition such as total/regional body fat and lean body masses/percentages by obtaining the attenuation coefficients of the fat and lean tissues separately. There are several limitations in the DXA-based aBMD measurement. First, DXA analysis is limited to 2D plane. For spine and hip, the posteroanterior scan (on the frontal plane) is typically analyzed. Next, it does not distinguish well between cortical and trabecular bones. [257,258] Furthermore, above-mentioned two assumptions (two-components concept and homogeneous distribution of fat tissue) lead to the inaccuracy of aBMD measurement [compared to the true value (e.g., the value based on cadaver)]. In fact, the scanned ROI typically consists of at least four components

(bone material and marrows in the bone tissue, and fat and lean tissues in the soft tissue), and the fat tissues (including marrows) are inhomogeneously distributed within the soft and bone tissue types. Besides, the higher hydrogen content in the fat than in the lean tissue also contributes to this measurement inaccuracy. The reported accuracy error can be up to 20-50% [257–260]. An improper positioning of patient's body (e.g., femoral neck not parallel to the scanning table) can also contribute to this error. [257,258]

A noteworthy DXA-derived invention is a program called hip structural/strength analysis (HSA) which estimates cross-sectional structural properties of proximal femur. Utilizing the X-ray absorption curve along the axis (e.g., femoral neck axis), cross-sectional area (CSA, in a unit of mm^2, an index to resist the axial force) and cross-sectional moment of inertia (CSMI, in a unit of mm^4, an index to resist the bending in a cross-section) can be estimated. [261–263] HSA can be used for the narrowest point of femoral neck, femoral shaft, and the trochanteric region. Furthermore, it can also provide the following properties: subperiosteal (outer) and endosteal (inner) diameters, section modulus (Z, in a unit of mm^3, another strength index against bending), cortical thickness, buckling ratio (an index of propensity for compression-induced cortical buckling), femoral neck shaft angle, hip axis length (a length from the pelvic brim to the greater trochanter along the femoral neck axis), and femoral neck axis length (a hip axis length without the pelvic brim). [264–268] It is noted that since these properties are estimated based on the 2D plane, their precision is sensitive to aforementioned positioning issue [261].

2.2.2 Quantitative Computed Tomography (QCT)

Computed tomography (CT) is another medical imaging method to acquire 3D detailed image on the internal organs using a rotating X-ray tube. By measuring the radiation attenuation by different tissues, it generates the stack of cross-sectional images (slices) which form 3D volume images of ROI. [269] Quantitative computed tomography (QCT) is a method to measure the bone mineral density based on the CT scans. The CT scans contains CT numbers, also known as Hounsfield Units (HU), describing the degree of the X-ray attenuation relative to water (0 HU) at each image location (pixel or voxel). Based on the appropriate calibration phantom (describing the bone mineral densities for different HU units) included in the scan, the HUs can be converted into the bone mineral density values. In contrast to 2D-based DXA, QCT can measure volumetric bone mineral density (vBMD, in a unit

of g/cm^3), and cortical and trabecular vBMDs separately. The type of CT scanner can be either whole body or peripheral scanner (pQCT). The former is used to scan, for example, the lumber spine and proximal femur whereas the latter is for more distal skeletons such as radius, tibia, and humerus. The pQCT is not only smaller, more mobile, and cheaper than the whole body CT, but also some machines can acquire high resolution (HR) images to capture trabecular structure (HR-pQCT). [270] In addition to vBMD and BMC of cortical and/or trabecular bone, the following structural variables can be determined by (p)QCT: cross-sectional properties (CSA, CSMI, and Z), femoral neck axis length, femoral neck shaft angle, subperiosteal and endosteal diameters, cortical thickness, and cortical and/or trabecular volume [11,271–278].

One of the disadvantages of QCT is the higher radiation dose compared to DXA. In case of hip scan, the radiation dose is several orders of magnitude higher in QCT (effective dose, 2.5-3.0 mSv) than DXA (0.009-0.022 mSv) [270,279]. On the other hand, due to the smaller scanning volume, the dose in pQCT (0.01 mSv) is much smaller than QCT and comparable to DXA. [280,281] Furthermore, when a CT-voxel contains more than one tissue type (e.g., cortical bone + fat tissue), the attenuation of radiation in this voxel represents a mean value. This leads to a problem known as partial volume effect resulting in a measurement inaccuracy of the bone structure and vBMD. [270]

2.2.3 Magnetic Resonance Imaging (MRI)

Magnetic resonance imaging (MRI) is another method to obtain 3D detailed image on the internal organs using strong magnetic fields and radiofrequency pulses. By applying the strong magnetic field, protons in the human body (e.g., a proton in the hydrogen atom, the most abundant atom in biological tissues) aligned parallelly to the longitudinal direction of the applied magnetic field. An additional radiofrequency excitation pulse can rotate these aligned protons by 90 degrees so that they lie on the transverse plane, perpendicular to the longitudinal direction (transverse magnetization). The radiofrequency coils in the MRI scanner can detect this magnetization to generate grayscale images of the ROI. The MRI scanner type primarily varies depending on the magnetic field strength [expressed in a unit of Tesla (T)]. The most widely used ones are 1.5-T and 3.0-T MRI systems. Owing to the higher field strength, the 3.0-T system has the improved signal-to-noise ratio resulting in the higher image resolution than the 1.5-T system. [282,283] In contrast

to DXA and (Q)CT, one of the advantages of MRI is an absence of the radiation exposure, and thus it is a more appropriate method for fertile population [283,284]. MRI is typically more suitable to image the soft tissue (since it's reflected brighter) over the hard tissues such as bones, tendons, and ligaments [282]. However, MRI has also been found a precise and reasonably accurate method to assess the cortical bone geometry [284,285]. With standard 1.5-T MRI system, Sievänen et al. (2007) reported an *in vivo* precision of ~1% in evaluating the periosteal and endosteal boundaries of femoral neck's cortical bone [284]. In case of the femoral neck, for example, the following structural variables can be determined by the extracted cortical bone geometry: cross-sectional properties (CSA, CSMI, Z), periosteal and endosteal circumferences, and cortical thickness [284,286,287] However, there are several technical difficulties involved in the extraction of the cortical bone geometry. First, the presences of the tendon and ligament attachments at the periosteal surface and bone marrow near the endosteal surface can lead to the erroneous detection of the periosteal and endosteal boundaries. Also, the gradual transition from trabecular to cortical bone near the endosteal surface can induce the partial volume effect. [284,285,288] Moreover, the different resonance frequencies between water and fat tissues can result in the spatial misregistration of these molecules, known as chemical shift artifact, leading to the inaccurate image presentation of the tissues [283,285,288].

2.3 Exercise on Proximal Femur

Physical activity and exercise are natural modes of the mechanical loading to bones. They greatly contribute to the bone strength by facilitating the bone formation in growth and maintaining the bone mass or slowing down age-related bone loss in the adulthood [4,5,7–9]. The beneficial effects of various exercises on bone properties, measured by DXA, (p)QCT, and/or MRI, have been reported for several anatomical sites in both observational (cross-sectional or longitudinal design) [11,55,56,58,60,273,274,277,289–296] and randomized/nonrandomized controlled trial [(R)CT] studies [297–307]. However, not all exercise types are equally osteogenic and the effectiveness varies depending on anatomical sites [10,11,58,289,297,308]. Therefore, to be in line with the focus of the present doctoral research, this section reviews the effect of various exercise types exclusively on proximal femur.

Due to the dependency of bone functional adaptation on age or maturity (puberty and menopause) [3,203,235,239], the present section is divided into two periods in life: 1) the 1st period including childhood (~3-11 years of age) [309], adolescent (~10 ≤ age ≤ 19) [310], and young adulthood (~until late 20s) [311], and 2) adulthood as the 2nd period (after the late 20s) including middle-aged and old males, and pre- and postmenopausal females. Also, based on the study type, the 1st period is further divided into 1) observational studies and 2) randomized/nonrandomized controlled trials [(R)CT].

Henceforward, based on exercise classification scheme defined by Nikander et al. (2005 and 2006), exercise/sport types are categorized into following five types based on the typical loading patterns of the sports if applicable: 1) high-impact loading (abbreviated as H-I) consisting of high ground reaction force (GRF[1]) and loading rate, common in the jumping exercise (e.g., volleyball, triple and high jumps); 2) odd-impact loading (O-I) consisting of ground impact from unusual directions and rapid acceleration and deceleration, common in ball games (e.g., soccer/football, tennis, and squash); 3) high-magnitude loading (H-M) characterized by very high muscle force production in coordinated movements, common in weight- and powerlifting; 4) repetitive-impact (R-I) loading consisting of a large number of the repetitive ground impact, common in endurance sports such as long-distance running and orienteering; 5) and lastly repetitive, non-impact loading (R-NI) which is also endurance sports but without ground impact such as swimming and cycling [11,57].

2.3.1 Childhood, Adolescent, and Young Adulthood

2.3.1.1 Observational Studies

Exploring differences of bones between athletes and nonathletes provide a unique opportunity to identify the potentially effective exercises to induce beneficial adaptations in the proximal femur. With this respect, numerous observational studies have been conducted in which the proximal femora of athletic participants with a history of specific exercise loading were compared with their nonathletic counterparts.

Several cross-sectional and prospective longitudinal studies of male and female athletes reported that a long term 5-to-10-year H-I exercise loading (gymnastics, triple-, high-jumping, volleyball, or hurdling) from the childhood/adolescent to young adulthood resulted in the significantly higher femoral neck aBMD (19-31%) and proximal femur, femoral neck, and trochanteric BMCs (13-23%) compared to their age-matched controls [57,58,60,273,312,313]. Similarly, a 6-to-11-year O-I exercise loading (squash, badminton, soccer, ice hockey, speed-skating, or step aerobics) from the childhood/adolescent to young adulthood induced the significantly higher femoral neck and trochanteric aBMD (9-29%) and BMC (13-22%) [56,57,60,313,314]. Moreover, > 12-year slalom and/or freestyle mogul skiing exercises, which consist of moderate-to-high impact (H-I) and multidirectional impact (O-I) loading, from childhood to young adulthood was also associated with the significantly 15-20% higher femoral neck aBMD [275,315].

On the other hand, inconsistent results have been reported on the effects of H-M and R-I exercise loadings on the proximal femur. Several cross-sectional studies reported that a 3-to-8-year H-M exercise loading (weightlifting or powerlifting) from late adolescent to young adulthood did not result in the higher femoral neck aBMD in the female athletes (aged 25-28 years) than the sedentary controls [55,60]. Similarly, a > 11-year R-I exercise loading (middle-distance running or orienteering) from childhood/adolescent to young adulthood did not lead to the higher femoral neck aBMD and BMC in both male and female athletes except for the BMC (~8%) in the adolescent female middle-distance runners [55,60,316]. In contrast, Nikander et al. (2005) reported the beneficial adaptation at femoral neck in young female H-M (weightlifters, mean age: 24 years with 3.3 years of training) and R-I athletes (orienteers and cross-country skiers, aged 21-24 years with 11-13 years of training): significantly 16% and 14% higher femoral neck aBMDs than the controls, respectively [57].

Importantly, the exercise-induced benefits reflected in the structure and bone strength indexes at the femoral neck have also been observed in some exercise types based on the DXA-based HSA in above-mentioned and other studies. The H-I athletes had the significantly greater benefits at a narrow part of femoral neck compared to their controls: CSA (+13-21%), Z (+9-21%), cortical thickness (+15%), endosteal diameter (-8-15%), and buckling ratio (-20%) [57,58,273,312]. Similarly, the O-I exercise loading also resulted in the significantly higher CSA (15-27%) and Z (16-26%), and lower buckling ratio (% difference not available) [57,317]. The world-class competitive young male slalom and mogul skiers also had 20-24% and 25-34% higher CSA and Z than the controls, respectively [275]. The CSAs in the H-M and R-I female athletes were also 11-13% higher than their controls. However, unlike H-I or O-I exercise, the bending strength (Z) in the H-M and R-I female athletes were not different from the controls [57]. Lastly, in contrast to aforementioned exercise types, a 6-11 year R-NI exercise loading (cycling or swimming) from the childhood/adolescent to young adulthood did not induce any beneficial adaptations in female (with respect to aBMD, CSA, Z, and buckling ratio at femoral neck) [55,57,60,317].

These observational studies compared the between-group differences in the bone properties. The issue inherent to this study design is a selection bias which may lead to under-/overestimation of the true exposure-outcome relationship [318]. Instead, this type of the systematic error can be minimized by implementing a within-subject comparison where, for example, the dominant-to-nondominant arm/leg differences are examined. However, to perform this, athletic study participants need to be exposed to asymmetric loading where only one side (e.g., dominant arm) is exposed to greater and/or unique mechanical loading compared to the other side (nondominant arm). Due to this, except for a few studies below, the application of within-subject study design has been mainly limited to the examination of upper extremities in the racket (e.g., tennis and squash) and throwing sports (e.g., baseball and softball), where the asymmetric loading is evident [237,238,244,245,319–324].

Recently, Fuchs et al. (2019) conducted a within-subject and between-group cross-sectional study of young adult male baseball pitchers, jumpers, young female softball pitchers (mean age: 27.5, 21.1, and 20.6 years with mean competing careers of 21.4, 6.3, and 13.2 years, respectively), and their age-matched controls. The significant dominant-to-nondominant leg side differences in the proximal femur, femoral neck, and trochanteric aBMD (4-7%) and BMC (4-10%) were observed in both baseball and softball pitchers. These differences were also significantly higher than the controls (except for femoral neck BMC of the baseball pitchers). In contrast,

the side differences in the jumpers were not only smaller compared to the pitchers' (e.g., proximal femur aBMD, 1.6%; and femoral neck and trochanteric BMC, ~4%), but were also not different from the controls. Based on the DXA-based HSA, there was no side difference in the structural variables such as CSA, CSMI, Z, and cortical thickness at the narrow femoral neck region in the baseball pitchers and jumpers except for the CSA (2-3%) in the pitchers. In contrast, the side differences of these structural variables (~7-13%) in the female softball pitchers were not only significant but also significantly higher than all other groups except for the cortical thickness compared to the baseball pitchers. Important observation in this study was that the dominant (landing) leg-favored beneficial adaptation due to the asymmetric loading was more evident in baseball/softball pitchers, especially in the female softball pitchers. In contrast, such side differences were not clear in the jumping athletes. This is somewhat contradictory since the impact-generating jumping exercise has been well reported as the effective osteogenic loading. However, this result is likely attributed to the following aspects: 1) later introduction of jumping-specific training (mean starting age for the competition: 14 years of age in the jumpers vs. 8-9 years of age, prior to adolescent growth spurt, in the baseball and softball pitchers), 2) shorter years of competing (mean 6.3 years in jumpers vs. 13-21 years in the baseball and softball pitchers), and 3) the jumping athletes may have been exposed to less asymmetric and more symmetric (bilateral) loadings such as sprinting as a part of practice than other groups. [325] In fact, the significant side difference was reported in other H-I exercise types. Wu et al. (1998) reported the significant ~5-10% side differences in the aBMD at femoral neck, greater trochanter, and Ward's triangle in young female rhythmic gymnasts (mean age: 19 years with 7 years of the gymnastic training) [326].

So far, the above-mentioned observations were limited to DXA-based 2D planar analyses of the proximal femur. Therefore, either or both (p)QCT and/or MRI measurement is needed to explore the 3D exercise-induced adaptations (reflected in the structural variables, cortical thickness, or vBMD) in the proximal femur. However, it is noteworthy that the use of pQCT in the observational studies has been limited to more distal skeletal sites than the proximal femur, such as distal femur and tibia [11,273–275,277,293]. Its use on the proximal femur would be impractical due to the small device size and too low X-ray intensity to capture the hip region with sufficient image quality [327,328]. Besides, the radiation exposure for a nondiagnostic application is considered unethical especially for the young fertile people.

A particularly important study in this respect was an MRI-based cross-sectional study by Nikander et al. (2009) where 91 young female athletes (mean age: 24.7 years with > 8 years competitive career) and their 20 female controls (mean age: 23.7 years) were recruited to investigate the long-term specific exercise-induced structural adaptation in the femoral neck. These athletic participants were divided into following five exercise loading groups based on the typical loading patterns of their sports: H-I (9 triple- and 10 high-jumpers, mean age: 22.3 years), O-I (9 soccer and 10 squash players, mean age: 25.3 years), H-M (17 powerlifters, mean age: 27.5 years), R-I (18 endurance runners, mean age: 28.9 years), and R-NI (18 swimmers, mean age: 19.7 years). Particularly important findings were that H-I and O-I groups had regionally thicker cortical wall at their femoral necks compared to the controls. The H-I group had the significantly thicker cortical bone at inferior (~60%), anterior (~20%), and posterior (~20%) quadrant of the femoral neck while their superior cortex was non-significantly ~10% thicker. The O-I group had consistently 15-20% thicker cortical bone around the femoral neck although only the anterior and posterior quadrants had statistically significant results. In contrast, none of other exercise loading groups had the regional cortical thickening at their femoral necks. It is important to note that, even though the whole proximal femur was scanned in this MRI study, only a part of femoral neck at the insertion of articulation capsule (2 MRI slices, ~2 mm thickness) was used for their analyses. Therefore, it is reasonable to say that the actual 3D analysis of the exercise-induced structural adaptation was not performed in this study either. [60] It is noted that the same proximal femur MRI data obtained in this study by Nikander et al. (2009) were utilized in the present doctoral research to create their 3D FE models and to investigate the 3D adaptation of proximal femur cortical bone to specific exercise loading.

To summarize, the weight-bearing H-I and O-I exercise from the childhood/adolescent to young adulthood resulted in the beneficial adaptation in the proximal femur, reflected not only in bone mass and density but also in the femoral neck structure and strength indexes. The beneficial adaptation induced by these impact and other impact exercises such as ballet dancing and basketball have also been confirmed by several systematic reviews and meta-analyses of the observational studies [59,329–333]. Although H-M and R-I loadings also led to the increased proximal femur bone mass and density, the magnitude of the benefits was smaller than above-mentioned two impact exercise loading types. Lastly, R-NI exercise appeared to have no beneficial effect on proximal femur bone properties regardless of age, and this was also confirmed by the systematic reviews and meta-analyses [59,334–336]. Nevertheless, these results were based on the 2D analyses of proximal

femur cross-sections. Therefore, further observational studies are needed to investigate the 3D adaptation of proximal femur to specific exercise loadings.

2.3.1.2 Randomized/Nonrandomized Controlled Trials

The effect of different exercise types, particularly impact exercise such as jumping and plyometrics, on the proximal femur has been investigated not only through the observational studies, but also randomized/nonrandomized control trials [(R)CTs] of the exercise interventions. Due to the dependency of the bone's functional adaptation on pubertal maturity status [3,203,235,239], these exercise-(R)CTs often studied the population at the specific pubertal stage, to find the ideal window of opportunity. This section briefly discusses the results of the exercise-(R)CTs mainly based on their systematic reviews and meta-analyses.

Hind and Burrows (2007) published a systematic review of the exercise-(R)CTs with the duration of 6.5-24 months in the childhood and adolescents (aged 8-17 years; 9, 8, and 5 trials in prepubertal, early pubertal, and pubertal stages, respectively). Over 6-month regular weight-bearing exercise interventions, most of which consisted of moderate-to-high H-I and/or O-I exercise (e.g., various jumping including multidirectional jumps generating ground impacts with GRFs of 3.5-8.8 times BW, plyometrics, gymnastics, ball games, dancing, and step aerobics), resulted in the increases in bone mineral accrual in proximal femur (reflected in BMC and aBMD for total hip, femoral neck or inter/trochanteric area): 0.9-3.9% in prepubertal; 1.4-6.2% in early pubertal; and 0.4-1.9% in pubertal stages. Not only the magnitude of beneficial adaptation was the highest in the early pubertal stage, but also the number of the trials observed the positive results declined toward pubertal stage: 5 out of 7, 7 out of 7, and 2 out of 4 trials in prepubertal, early pubertal, and pubertal stages respectively. In contrast, H-M or resistance training alone appeared less osteogenic especially in the pubertal females. [337]

Similarly, two more recent meta-analyses of the exercise-(R)CTs by Specker et al. (2015) and Ishikawa et al. (2013) observed the significant exercise-induced bone gain in the proximal femora in the childhood and adolescents. Importantly, Ishikawa et al. (2013) also reported that the plyometrics (e.g., jumping, hopping, and skipping) is more effective osteogenic exercise type for the femoral neck than the general resistance training. However, conflicting to Hind and Burrows (2007), Specker et al. (2015) reported that the exercise-induced benefit was limited to the pre-pubertal period, not in the early pubertal period. On the other hand, Ishikawa et al. (2013) reported that the early- and pubertal periods are more ideal time for femoral neck to

achieve exercise-induced bone gain. This discrepancy calls for further studies although it may be attributed to differences in study design between these meta-analyses. For example, Hind and Burrows (2007) and Ishikawa et al. (2013) included the (R)CTs which were longer than 6 months while Specker et al. (2015) included the (R)CT of as short as the 3-month intervention. Furthermore, Malmö Prospective Pediatric Osteoporosis Prevention (POP) studies [338–340] were also included in Specker et al. (2015). In these POP studies, same physical education (PE) exercise programs were assigned into both intervention and control groups except its duration was longer in the intervention group (200 min/week vs. 60 mins/week, respectively). Thus, the effect of exercise duration on bone properties was examined instead of the effect of specific exercise. Furthermore, only female population was analyzed by Ishikawa et al. (2013). Despite the discrepancy, these meta-analyses and systematic reviews suggest the importance of the weight-bearing exercises, particularly impact-generating jumping exercises, in terms of maximizing bone gain and the window of opportunity likely lies around the early pubertal stage. [337,341,342]

2.3.2 Adulthood

The results from the observational studies and (R)CTs in the young population helps finding and designing the effective osteogenic exercise programs since the exercise-induced bone adaption is more evident during growth than later in life [343]. However, its efficacy and feasibility need to be evaluated for the older generations. In this respect, the numerous (R)CTs of various exercise interventions were also conducted in the middle-aged/old males and pre-/peri-/postmenopausal females.

The beneficial effects of the moderate-to-high impact (H-I and/or O-I) exercise loadings (multidirectional jumping exercises generating ground impacts with GRF ranging ~2 to 6 times BW) has been reported in premenopausal females aged 18-45 years based on the 6-18-month RCTs [299,305,344]. For example, Bailey and Brooke-Wavell (2010) reported that a 6-month unilateral multidirectional hopping (GRF: 2.5-3 times BW) induced substantial increases in the following DXA-based proximal femur properties in the exercised legs of the premenopausal females compared to their control legs: femoral neck aBMD (1.7% vs. -0.6%, respectively) and BMC (1.2% vs. -0.3%), and superior femoral neck aBMD (2.2% vs -0.9%) and BMC (1.8% vs. -0.6%) [344]. This moderate H-I and O-I hopping exercise has also been found beneficial in the old males aged 65-80 although the effect was smaller

[345,346]. Allison et al. (2013) reported that a 12-month unilateral multidirectional hopping exercise resulted in the following significantly higher femoral neck properties in the exercised legs of the old males compared to their control legs: aBMD (0.7% vs. -0.9%, respectively), BMC (0.9% vs. -0.4%), CSA (1.2% vs. -1.2%), and Z (2.3% vs. 0.7%) [345]. Importantly, this hopping exercise also led to the substantial regional bone gain (> 6% gain in QCT-based cortical mass surface density) at inferoanterior and superoposterior aspect of the femoral neck [346]. Since the age-related cortical thinning at the latter aspect is known to contribute to the hip fracture risk considerably, such regional bone gain may mitigate this risk [37,38]. Therefore, these results suggest that the moderate H-I and O-I exercise can induce the beneficial adaptations in the femoral neck regardless of age. Furthermore, the beneficial effect of moderate R-I exercise has also been observed in perimenopausal females. Heinonen et al. (1998) reported in their 18-month RCT that endurance training consisting of walking, stair climbing, ergometer cycling, and jogging can contribute to maintain the femoral neck aBMD in perimenopausal females (aged 52-53 years) while their age-matched controls had the declining trend [298].

The effective exercise types for the proximal femur appear to vary depending on age based on numerous meta-analyses which reviewed total of over 50 (R)CTs [347–356]. In the premenopausal females (aged 18-50 years), the moderate H-I or O-I exercise alone (e.g., various jumping including multidirectional hopping/jumping, and skipping) and the combined H-I or O-I exercise program with the H-M exercise (high intensity resistance training) were found effective to significantly increase femoral neck and trochanteric aBMD [352,354]. Although the beneficial effect was smaller, these combined impact exercises and the moderate R-I (jogging combined with walking and stair climbing) may also be effective in the postmenopausal females to increase femoral neck aBMD [348,351,355,356]. The H-M exercise alone was found ineffective in any ages [349,350,353,356]. Importantly, the feasibility of the impact exercise to the older population with respect to safety should be well considered. Some impact exercises may not be suitable for the frail old population due to risk for musculoskeletal injuries. However, it is noteworthy that very low number of the injuries, if any, were reported in the previous exercise interventions involving multidirectional hopping as long as participants' exercise were supervised and its intensity and volume were gradually increased [345,357].

Lastly, there have been fewer RCTs conducted which examined the effect of exercise on proximal femur in male regardless of age compared to females [12,358–362]. Based on two meta-analyses by Kelley et al. (2013) and Hamilton et al. (2022), the 6-18 month ground reaction and joint reaction force exercises (incl. jogging,

resistance training, and/or moderate-impact weight-bearing exercise such as jumping, hopping, stepping, and football) have small-to-moderate and statistically significant beneficial effects on increasing femoral neck aBMD in the middle-aged and old males (aged 41-80 years) [363,364]. However, based on other recent systematic review and meta-analyses, the osteogenic effect of exercise on the proximal femur and effective exercise types should remain inconclusive in the middled-aged and old males (aged 36-79 years) due to limited statistical power (insufficient data available) [358,360,365]. Thus, this calls for further RCTs.

2.4 Hip Fracture

2.4.1 What is Hip Fracture?

Hip fracture is a fracture of proximal femur bone (**Figure 16**). Depending on its location, the fracture type is first defined as either intracapsular or extracapsular fracture. The former includes femoral head and neck fractures while the latter includes intertrochanteric and subtrochanteric fractures. [366–368] The femoral neck fracture can be further categorized into subcapital, mid/transcervical, or basicervical fracture [366]. The femoral neck and intertrochanteric fractures comprise the majority of hip fractures and occur with similar prevalence rate [369–372]. Compared to other types of hip fractures, the femoral head fracture occurs less frequently and is typically caused by car accidents [373,374].

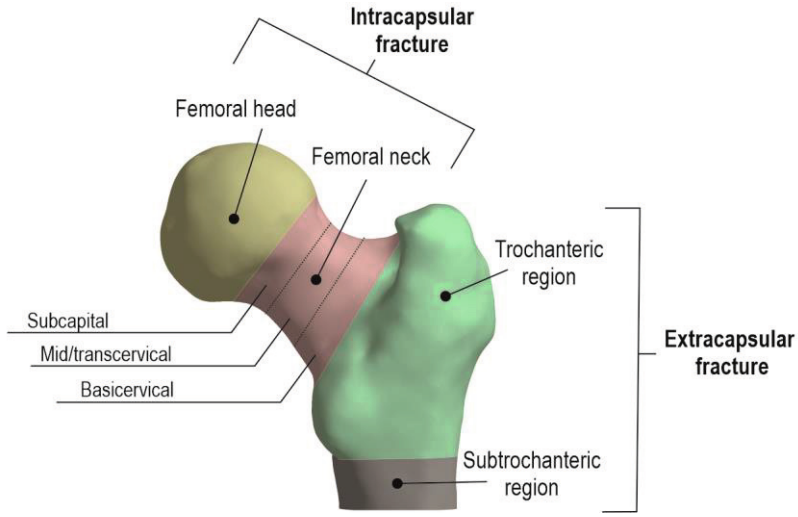

Figure 16. Hip fracture and its types.

The majority of acute hip fractures are treated surgically unless the patients have the high risk for intraoperative death and severe postoperative complications. Today, non-surgical conservative treatment is rarely chosen due to poor outcome (permanent disability) and prolonged hospitalization unless the fracture stays with only small crack in the femoral neck and the patient does not have severe osteoporosis. [366–368,375,376] The acute hip fracture patients are at risk for cardiovascular, pulmonary, thrombotic, infectious, and bleeding complications,

which can ultimately result in death [366,368]. Therefore, the short time (6 to 48 hours) from the incident to the surgery is desired for the better postoperative outcomes (e.g., the earlier mobilization, faster functional recovery, and lower mortality) [366,368,375]. Depending on the fracture location and stage (the degree of displacement, separation, and/or stability), either internal fixation or arthroplasty is selected as the surgical option [366,368,374,375].

2.4.2 Epidemiology and Socioeconomic Impact

Hip fracture is a major public health care problem leading to high rates of morbidity, disability, and even mortality in the older adults [25]. Approximately 90% of hip fractures occur in the old adults aged > 65 years [377] and its incidence reaches the peak around age of 75-80 years [28,378]. Compared to male, hip fracture is twice more common in female [27,28]. This is because of the higher likelihood of fall in female than in male [379–382] and the reduced estrogen level due to the menopause which accelerates the age-related bone loss [195,383].

Globally, the annual number of hip fractures was increased from 1.3 million in 1990 to 1.6 million in 2000 and is predicted to reach 6.3 million by 2050 due to aging population worldwide [27,28,33]. The number of > 65 years old people worldwide is expected to grow over 1 billion by 2050 just by considering those in Europe and Asia (133 and 894 million people, respectively) [29]. Accordingly, the global financial burden due to the hip fracture is predicted to increase from $34.8 billion in 1990 to $131.5 billion by 2050 [34]. Long-term hospitalization, rehabilitation, and placement in nursing home are the major contributors to this tremendous cost [26,384].

Quality of life significantly declines in the hip fracture patients due to their long-term inability to walk. Only half of the hip fracture patients regain their pre-fracture mobility and up to one third of the patients become permanently disabled, likely resulting in residing in the nursing home. Furthermore, up to ~20−30% of the hip fracture patients die within first year after the fracture [26,29–32,384]. This high mortality rate is partially due to comorbidity. Compared to the general population, the hip fracture patients typically have more underlying medical conditions prior to the fracture. Likelihood of dying from these comorbid illnesses is likely increased by the hip fracture incident. However, it is still estimated that about one fourth of hip fracture patients' deaths is causally related to the fracture itself. [30,31,378,385]

2.4.3 Causes and Mechanism

Hip fracture can be caused by various traumatic conditions. For example, femoral head fractures typically result from a high-energy trauma due to the car accident where the dashboard strikes the knee, delivering the high impact to the hip joint [373,374,386]. Also, the hip fracture can even occur under physiological loadings such as standing, walking, jogging, and stair ambulation with/without abnormal sudden overloading (stumbling or mis-stepping) [387,388]. This type of hip fracture is referred to as spontaneous fracture, typically leading to the femoral neck fractures [389]. It is particularly common in the frail elderly and is associated with the low bone density (severe osteoporosis) and degradation of neuromotor control [387,388,390]. In other words, their proximal femora are already so fragile that they can fracture even under such normal loading conditions. Yet, these hip fractures are rare, accounted for ~5-10% of all hip fractures [388,390,391].

In fact, over 90% of the hip fractures are caused by fall [51–53]. This high incidence is attributed to site-specific thinning of femoral neck cortex with aging and fall-induced unusual loading mechanism. Femoral neck cortex is thicker at the inferomedial than superolateral side (**Figure 17**) due to the asymmetric loading caused by the predominant form of human locomotion such as walking, which imposes the higher compressive and smaller tensile loadings at respective cortexes (**Figure 18**) [36–39].

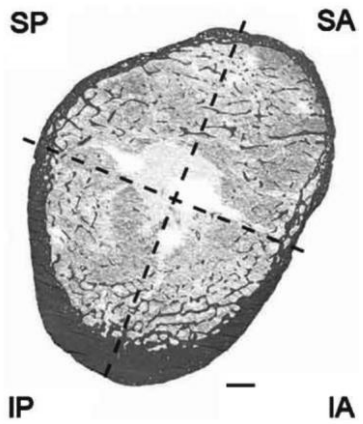

Figure 17. Asymmetric femoral neck structure. This figure demonstrates the thinner and thicker cortical layers at the superolateral [including the superoanterior (SA) and superoposterior (SP) quadrants] and inferomedial aspects [including the inferoanterior (IA) and inferoposterior (IP) quadrants], respectively. (Adapted, with permission, from Poole et al. (2010) [40] © 2010 American Society for Bone and Mineral Research).

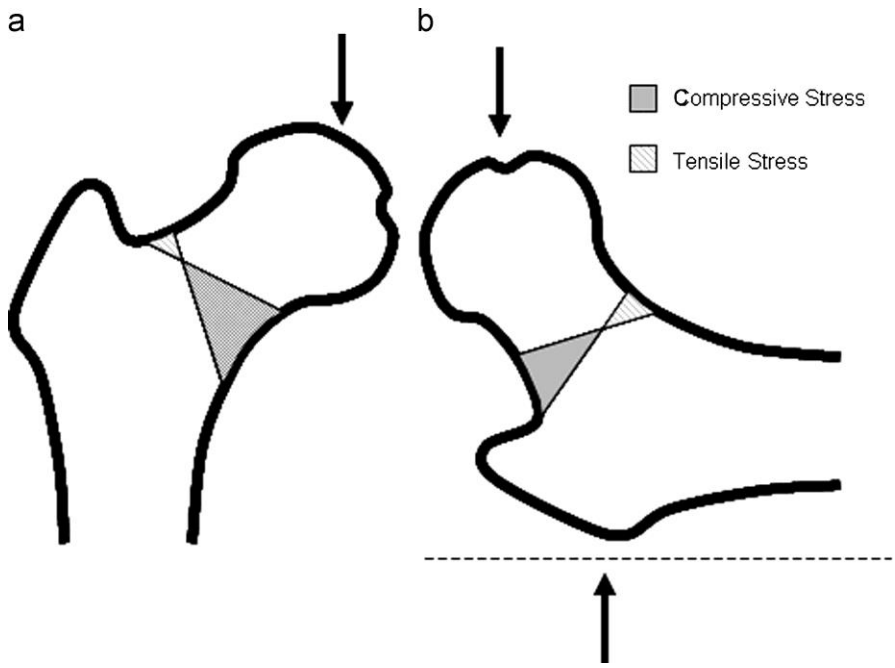

Figure 18. Loading mechanisms in stance and fall. The high compressive and small tensile stresses were induced at the inferomedial and superolateral cortical bones of the femoral neck, respectively, during the standing and walking (a); and at the superolateral and inferomedial sides, respectively, during the fall (b). Arrows indicate the (impact) force applied to the proximal femur. (Reprinted, with permission, from de Bakker et al. (2009) [37] © 2009 Elsevier Ltd.)

With advancing age, the amount of vigorous physical activity decreases, and the physical activity primarily comprises less intensive walking [35]. Consequently, the femoral neck is mainly exposed to the asymmetric loading by walking and reduction in the skeletal loading may accentuate the thinning of the superolateral cortex. In fact, it was reported that the mean cortical thickness of superoposterior quadrant (**Figure 17**) decreases fivefold from 1.63 mm at age of 25 years to 0.33 mm at age of 85 years while that of the inferoanterior quadrant changes only marginally from 3.9 to 3.3 mm during the same period [40]. Mayhew and his colleagues (2005) suggested that this superolateral cortical thinning contributes significantly to hip fragility and this cortical region is particularly vulnerable in a fall situation where the ground impact is imposed onto the posterolateral or lateral aspect of the greater trochanter or hip. [38]. To support this, Johannesdottir et al. (2011) reported that the superior cortical thickness is a stronger hip fracture predictor than the inferior cortical thickness [392].

When one falls onto the greater trochanter, the loading mechanism is reversed (**Figure 18**), resulting in the unusually high compressive loading at this fracture-prone thin superolateral cortex due to the high impact force imposed onto the posterolateral or lateral aspect of the greater trochanter [37,41–44,49]. The peak magnitude of this fall-induced compressive strain and stress can reach up to ~1.5-2.0 and 4 times greater than those at the inferomedial cortex in the physiological loadings (stance or walking), respectively [36,42]. Accordingly, both cadaveric experimental and FE modeling studies consistently confirmed that the femoral neck is at the greatest risk in the fall (onto the greater trochanter) situation and the fracture mostly initiates from the superolateral cortex due to this unusually high compressive loading [37,41–50]. It is noted that, compared to the impact on the lateral aspect of the greater trochanter, the impact on the posterolateral aspect causes a much greater degree of torsion (twisting) about the axis of femoral shaft. This likely increases the compressive loading at the superolateral cortex, which contributes to the fracture further.

The important fracture mechanism, two-steps failure, has been reported through several destructive mechanical testing of cadaveric femora in the fall (onto the greater trochanter) configuration [37,42–44,393]. This failure mechanism is described here using the results from a recent experimental study by Grassi et al. (2020) where the full-field deformations on the (infero)medical and (supero)lateral aspects of the femoral neck were reported (**Figure 19**) [44]. In the 1st step, the local failure (yielding) initiates from approximately 50% of the peak force due to the compressive strain exceeding its yield strength of -10400 με [178] (shown as the appearance of a small blue area in the leftmost image of the lateral side of proximal femur, **Figure 19**). This local compressive failure continues expanding (characterized by an expansion of this blue area in the 2nd leftmost image of the lateral side, **Figure 19**). This indicates the failure (crack) initiation [e.g., an increase in or coalesce of the (micro)cracks] likely takes place before the peak force. This eventually results in the (macro)failure (crack, crush, or collapse) of the superolateral femoral neck cortex (more specifically, posterolateral aspect of femoral neck, near trochanteric fossa). This superolateral cortical failure corresponds to the peak force of the force-displacement curve and is reflected by the larger area exceeding the yield limit (almost completely blue area in the 2nd rightmost image of the lateral side, **Figure 19**). It is noteworthy that the tensile strain at the inferomedial cortex did not even reach its yield limit (7300 με) [178] until the failure of the superolateral cortex at the peak force. [44] In the 2nd step, if the energy from the fall was sufficiently high to drive the crack across half the femoral neck width, a section modulus (Z) (a measure for

the bending resistance) of the unfractured cortical cross-section of the femoral neck would be substantially decreased. This is because Z depends on the square of the femoral neck width. [37,38] Then, the tensile loading in the inferior femoral neck becomes high enough to initiate another crack at the inferior femoral neck cortex or inferomedial intertrochanteric cortex, ultimately resulting in the complete fracture, corresponding to a sudden drop of the force-displacement curve (**Figure 19**). [37,42–44,393]

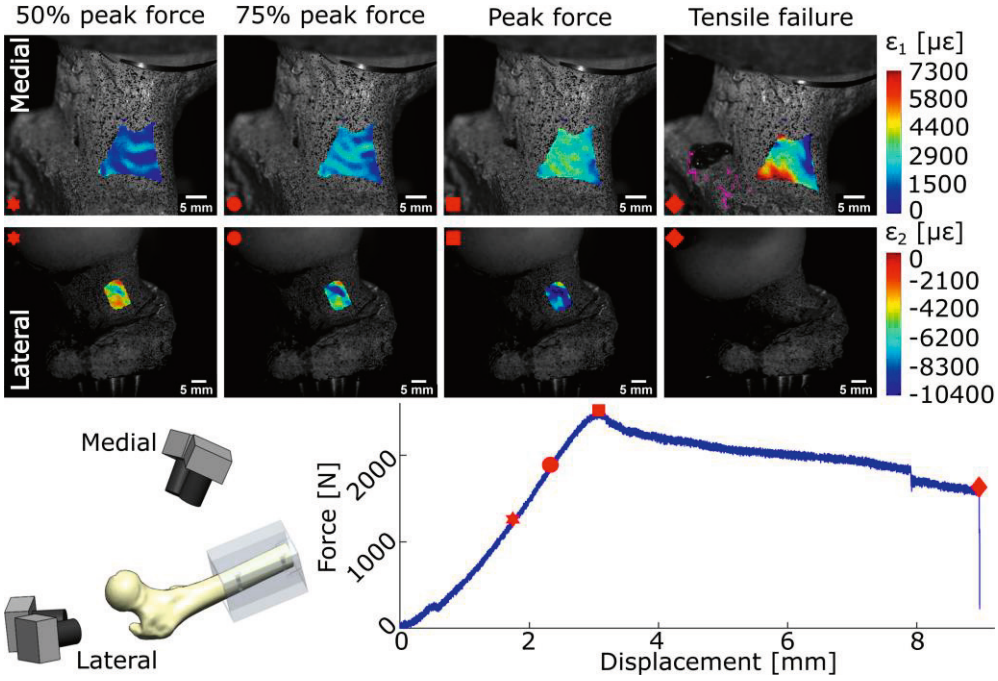

Figure 19. Two-steps failure mechanism of fall-induced hip fracture. This figure shows the maximum (tensile) and minimum (compressive) principal strain fields on the (infero)medial and (supero)lateral aspects of femoral neck, respectively, and a force-displacement curve during the mechanical testing of a cadaveric femur where strain fields were captured using two high-speed cameras and digital image correlation method. Red hexagon, circle, square, and diamond symbols correspond to four different stages of the mechanical test: 1) at 50% of the peak force, 2) at 75% of the peak force, 3) at the peak force, and 4) at complete failure, respectively. (Reprinted, with permission, from Grassi et al. (2020) [44] © 2020 Elsevier Ltd.)

Another important observation from the experimental studies was that the majority of proximal femora tested both in the fall and the normal physiological loading conditions (e.g., single-leg stance) experienced a brittle fracture at least for the 1st failure characterized by a linear elastic behavior up to the failure with little or

no plastic deformation. Moreover, the interval between the 1st and 2nd failures was very short (a few milliseconds) under the loading rates which are assumed to be close to the ones in the physiological falls (~2-100 mm/s). [37,42,44,394,395]

Two different failure modes are suspected to cause the 1st failure at the superolateral cortex due to the compression: 1) material yield failure or 2) structural failure due to local buckling. In the former mode, the magnitude of compressive loading exceeds the (yield) strength of the material, resulting in the failure of the cortex. In contrast, in the latter mode, the superolateral cortex thinning may cause the structural instability of the cortical shell. This can lead to the local bucking before the yield limit under the compression. The buckling is a common failure mechanism for the thin-walled structure. [37,38] In fact, a buckling ratio at the superolateral cortex was found significantly ~35% higher in the old males (aged >70 years) with hip fractures cases than their age-matched controls without the fractures [396]. If trabecular bone was present under the superolateral cortex, it could reinforce this thin cortical wall to prevent the buckling. However, several studies reported that the significant age-related reduction in the superolateral trabecular bone (~40% decrease over five decades), contributing to the cortical structural instability. [104,397,398] Moreover, Milovanovic et al. (2012) observed that significant microstructural deterioration of superolateral trabecular bone in postmenopausal females with hip fractures compared to age-matched controls. The microstructural trabecular deterioration was characterized by the lower trabecular volume and connectivity, more rod like trabecular structure, higher trabecular separation, and thinned trabeculae. [399] Therefore, the trabecular reinforcement may not be expected with aging.

Another noteworthy aspect is that a femoral neck diameter slowly expands with aging due to subperiosteal apposition and endosteal resorption of bone, and the diameter is positively associated with history of lifetime physical activity [39,400–402]. This expansion adapting to the physical activity level is a "smart" regulatory system of bone to maintain the bending resistance (Z) by gradually increasing the diameter to compensate for the age-related gradual bone loss [38,39,401,403]. The superolateral cortical thinning also shifts a center-of-mass inferiorly from a geometric center by 59% in females from at age of 20 years to 90 years (**Figure 20**). This inferior shift together with the superolateral cortical thinning increases the buckling ratio [calculated as a ratio of buckling radius to cortical thickness] significantly by 151% (9 to 23) during the same age period [39]. This further supports above-mentioned buckling theory for the fracture initiation. **Figure 20** conceptually summarizes these age-related changes in the cortical structure of femoral neck.

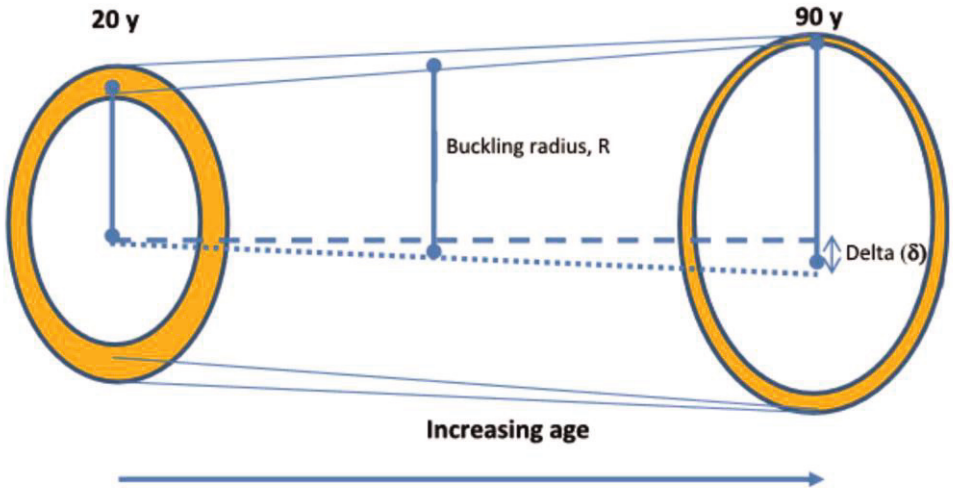

Figure 20. Age-dependent changes in femoral neck's cortical bone structure. This figure is a conceptual diagram illustrating the change in the femoral neck's cortical structure during 70 years from age of 20 years (left) to 90 years (right). As the superior cortical thickness decreases, the buckling radius (R) and Delta (δ) increases, resulting in the increase in the buckling ratio. (Reprinted, with permission, from Khoo et al. (2019) [39] © 2018 The International Society for Clinical Densitometry. Published by Elsevier Inc.)

Importantly, some of above-mentioned aspects have been clinically confirmed in a recent study by Tang et al. (2018) where the microcracks in femoral neck's cortical bone retrieved from intracapsular hip fracture patients were examined. They found strong evidence confirming 1) fracture initiation at the superior cortex characterized by the significantly higher microcrack density in the superior cortex than in the inferior cortex, and 2) the failure mode at the superior cortex was due to compressive material yielding or buckling judged by microcrack patterns. [404]

Lastly, it is noted that the fall-induced femoral neck fractures are mainly discussed so far in this section in association with the structural deficit or deterioration of the superolateral femoral neck. Compared to the femoral neck fractures, it has been found that the (inter)trochanteric fractures are associated more with total hip, femoral neck, and especially trochanteric aBMD [405–409] and older age (= elderly with low aBMD) [371,372,410]. It has been speculated that the energy available from the fall-induced impact may get dissipated by fracturing trochanteric region if the trochanteric bone mineral density is sufficiently low. Otherwise, the energy is likely transmitted to the femoral neck region where the structure may play a more important role to resist the fall-induced loading. [372]

2.4.4 Risk Factors

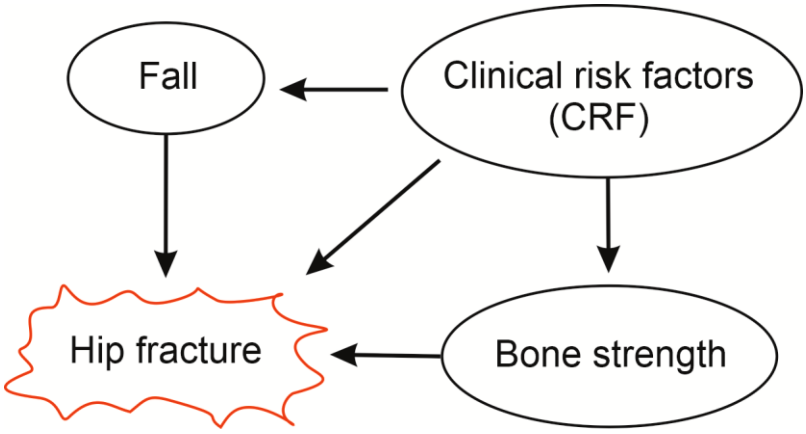

Figure 21. Hip fracture and three risk factor categories. (Redrawn, with permission, from Wehren and Magaziner (2003) [379] © 2003, Current Science Inc.)

Risk factors for hip fracture are summarized in **Table 4** and can be categorized into: 1) those contributing through lowering bone strength, 2) those through increasing the likelihood of fall, and 3) clinical risk factors (CRF) contributing to the hip fracture directly or indirectly through the former two categories (**Figure 21**) [379,411]. In the following sections, some of the important risk factors in each category are briefly discussed. To increase the readability in this section, two different types of risk measures such as the relative and absolute risks are first explained here. The relative risk compares the risk between two groups and is often expressed as the gradient risk (GR) in the context of hip fracture risk: X-fold increase in the fracture risk for each SD decrease in e.g., aBMD. In contrast, the absolute risk shows the likelihood of hip fracture happening over a specific time-period. [411]

Table 4. Categorized hip fracture risk factors

Risk factors for the lower proximal femur bone strength	Risk factors for the higher likelihood of fall	CRFs
Low (a)BMD	Functional impairments	Age
Bone structure/geometry	Muscle weakness	Weight
High bone turnover (remodeling state)	Vision impairments	Height
	Neuromuscular disorder	Genetics
Accumulation of microdamage	Lower limb dysfunction	Female sex
Degree of bone mineralization	Cognitive impairment	Race (Asian or Caucasian)
	Proprioception impairment	Poor nutrition
	Physical inactivity	Low calcium intake
	Delirium	Vitamin D deficiency/insufficiency
	Previous stroke	Cigarette smoking
	Parkinson's disease	High alcohol consumption
	Barbiturate (sedative) use	Prior fracture
	Antidepressants use	Parental history of hip fracture
	Height of fall	Rheumatoid arthritis
	Improper protective response	Socioeconomic status
	Imbalance by alcohol consumption	Medication
	Footwear (bad fitting)	Glucocorticoids
	Poor lightening	Benzodiazepines
	Floor conditions	Psychotropic drugs
	Uneven surface	Anticonvulsants
	Hard surface	
	Slippery condition	

This table was created based on [25,51,379,411–418]

2.4.4.1 Risk Factors For the Lower Proximal Femur Bone Strength

A low aBMD or osteoporosis (defined by aBMD T-score < -2.5 SD) is likely the most known risk factor in this category. It has been found that the low aBMD, particularly at femoral neck, is strongly associated with the hip fracture risk. [411,412,419] Every 1 SD decline of the femoral neck aBMD can increase the age-adjusted relative risk by 2.6. In other words, a person with the femoral neck aBMD T-score of -3 SD would have 2.6^3 (= 17.6) higher relative hip fracture risk than a person with the T-score of 0 SD. [411,420,421] The absolute hip fracture risk increases with age up to ~70 years old but reaches plateaus afterward. This is because the risk for death surpasses the hip fracture risk. [411] The factors that determine the bone strength include not only bone density but also bone structure/geometry, bone turnover state, microdamage accumulation, and degree of mineralization

(**Table 4**) [379,405]. The structural or geometric variables of proximal femur were found important factors influencing the hip fracture risk. For example, a decrease in cortical thickness at the femoral neck, a wider trochanteric region [422], and the longer hip axis length [423] were found to increase the hip fracture risk significantly.

Importantly, an ability of aBMD predicting hip fractures declines noticeably with aging: the relative risk for each SD reduction in the femoral neck aBMD decreases from ~4 at age of 50 years old to < 2 at the age of 85 years old [419]. Age and other risk factors, especially those contributing to a fall, become more important risk factors [381,413,416,419].

2.4.4.2 Risk Factors For Fall

A fall is a stronger predictor for the hip fracture than the femoral neck aBMD. Compared to 2.6 times increase in the fracture risk due to a 1 SD reduction in the femoral neck aBMD [411,420], the fall increases the risk by 3-5 folds [424]. In particular, if the fall-induced impact is applied around the greater trochanter, the risk is increased even by ~30 times [68]. The risk of fall increases drastically with aging, especially starting from menopause, mainly due to balance and functional impairment, and disability [25,381,425]. With aging, muscles weaken, and reflex response becomes slower. The muscle weakness is associated with the decline of muscle mass, strength, and power. The skeletal muscle weights ~45% of body weight at age of 21-30 years old; however, reduces up to only ~27% after age of 70 years old. Besides, the thigh muscle strength decreases by 40% over the adult life span. [25,381,426] Importantly, females fall approximately 1.5-1.8 times more likely than males, which also explains why the hip fracture is more common in female than in male [379–382]. Approximately one third of healthy individuals aged > 65 years and more than a half of those aged > 80 years living in long-term care facilities fall at least once a year although only 1% of them result in the hip fracture [381,425,427,428].

2.4.4.3 Clinical Risk Factors

In this category, age is the most important risk factor, independent of comorbid conditions and aBMD. While the hip fracture risk from 50 to 90 years old is increased by 30-folds, age-dependent decline in aBMD is responsible for only the 4-folds

increased risk. This indicates that age is approximately 7 times more important risk factor than aBMD. [411,429–432]

Next, current cigarette smoking and heavy alcohol consumption can increase the risk. The current cigarette smoking after menopause, around age 50, is associated with 2% decline in femoral neck aBMD in each decade in addition to the normal age-related bone loss and can increase a lifetime hip fracture risk by 50% [433]. Overall, it is estimated ~13% of all hip fractures in female are related to the smoking [434]. While the light alcohol consumption (0.01–12.5 g of ethanol per day, equivalent to 1 – 1.5 units/day) is associated with the lower hip fracture risk and increased hip aBMD, the heavy consumption (≥ 50 g of ethanol per day) is associated with the higher risk and the decreased hip aBMD [435–437]. Besides, the likelihood of fall is increased under the heavy influence of alcohol [435]. Prior and current use of glucocorticoids is associated with the reduced aBMD including at the femoral neck and is known as a frequent cause of the secondary osteoporosis. It leads to the increase in the relative hip fracture risk from 2.1- to 4.4-folds depending on age in the dose-response fashion. [411,438,439] These factors contribute to the higher hip fracture risk by decreasing bone formation and/or increasing bone resorption [434–436,440–444]. A family history of hip fracture, especially the maternal history, and a prior fracture are independent risk factors of aBMD and can double the hip fracture risk [411,412]. Furthermore, Vitamin D deficiency can cause malabsorption of calcium, hasten age-dependent bone loss, and consequently increase hip fracture risk [445].

Evaluating the effect of body weight and height on the hip fracture risk is not straightforward. The heavier and taller individuals have the lower risk due to: 1) the greater bone mass and higher bone density to support their larger body size, and/or 2) the greater protective effect by the thicker fat tissue around the hip absorbing the fall-induced impact [51,446]. However, the heavier body weight and/or taller height also increase the fracture risk by increasing available initial potential energy in the fall [51,446,447]. Therefore, it is more ideal to assess them together. Accordingly, the body mass index (BMI) estimated from both body weight and height was mainly investigated with respect to the hip fracture risk [411]. A meta-analysis of 60,000 males and females showed that the low BMI is associated with a significant increase in the hip fracture risk while the high BMI serves as more protective. Compared with a BMI of 25 kg/m^2, a BMI of 20 kg/m^2 increases relative risk by two-folds while a BMI of 30 kg/m^2 decreases the hip fracture risk by 17%. This association of the BMI with hip fracture risk highly depends on aBMD. [448]. That is because the low body weight or BMI is highly associated with the low aBMD [449].

2.4.5 Risk Assessment Tools

Hip fracture risk assessment had primarily relied on the aBMD measurement and diagnosis for the aBMD-defined osteoporosis (aBMD T score < -2.5 SD) despite the involvement of other risk factors until the beginning of the first decade in the 21st century [450–452]. This was because various noninvasive bone density measurement techniques (e.g., DXA) were available and previously there was a tacit assumption that individuals with aBMD-defined osteoporosis would be same as those who sustain hip fracture. However, this was found not necessarily true throughout previous researches. [381,414,421,453] The aBMD-based fracture risk assessment has major drawbacks such as the age-dependent decline in its hip fracture predicting ability and its low sensitivity (true positive rate) [413,421,450,452,454]. This low sensitivity means that the majority of fractures happen to the individuals who do not have osteoporosis. In fact, only less than 30% of the individuals with the hip fractures had the aBMD-defined osteoporosis. [381,455] Furthermore, the most common aBMD measurement technology such as DXA has a measurement inaccuracy, leading to the over- or underestimation of the aBMD by 20-50% [259,260]. This means that the individuals with aBMD T score of -1.5 SD may have a true value between 0 and -3.0 SD ranging from normal to osteoporosis [424]. These drawbacks and discovery of other risk factors led to develop more comprehensive fracture assessment tools such as FRAX, the Garvan Institute Fracture Risk Calculator (Garvan), and QFracture.

In 2008, WHO Collaborating Centre for Metabolic Bone Diseases released a new fracture risk assessment tool called FRAX. It estimates individualized 10-year probability of hip and major osteoporotic fracture (hip, spine, distal forearm, and proximal humerus) using age, sex, BMI and seven dichotomous aBMD-independent CRFs with or without femoral neck aBMD. [431,450,452,454] Seven CRFs are: 1) prior fragility fracture, 2) parental hip fracture, 3) smoking, 4) systemic glucocorticoid use, 5) excess alcohol intake, 6) rheumatoid arthritis, and 7) cause of secondary osteoporosis [413,450]. Compared to the aBMD-based fracture risk assessment or by CRFs alone, FRAX resulted in the higher fracture discriminating performance with an improved sensitivity [413,456]. In the receiver operating characteristic (ROC) analyses, areas of under curves (AUC, a measure for the discriminating capability) of 0.83, 0.79, and 0.80 were reported for FRAX with femoral neck aBMD, without femoral neck aBMD (CRFs alone), and femoral neck aBMD alone, respectively, based on Canadian Manitoba cohorts comprising 36,730 females (mean age: 65.7 years) and 2873 males (mean age: 68.2 years) [456]. Similarly,

respective GRs for the hip fracture (the higher it is, the higher sensitivity is) were reported to be 3.5, 2.0, and 3.1 at the age of 60 years, respectively [413].

Despite its superior performance, several limitation has been identified in FRAX: dichotomous (yes or no) evaluation of CRFs (not by dose-response manner); exclusions of lumber spine aBMD and parental histories of non-hip osteoporotic fractures; and importantly, an exclusion of the risk factors related to the fall [421,450,452,457]. Furthermore, similar to the aBMD-based risk assessment, the hip fracture predicting performance of FRAX declines with aging. This further indicates other risk factors such as those related to fall play a more important role with aging. [381,413]

In contrast to FRAX, Garvan [458] and QFracture [459] assessment tools can include the history of prior fall in their 5- or 10- year fracture probability estimation in addition to age, sex, and other CRFs with/without the femoral neck aBMD. Despite the inclusion, no difference in the fracture discriminating performance has been reported between FRAX and Garvan [460,461] while the QFracture showed a slight improvement compared to FRAX [459]. It is noted that an important factor, age-dependent mortality, is not incorporated in Garvan. Accordingly, Garvan-based fracture probability continue rising with aging whereas the FRAX-based probability starts declining around age 80-85 years due to the age-dependent mortality. [421]

2.4.6 Sectional Summary

Hip fracture, a fall as its major cause, risk factor categories, risk assessment tools, and their interactions are schematically summarized in **Figure 22**. From the biomechanical perspective, the hip fracture risk can be indicated by a ratio of an applied load to proximal femur bone strength. The former is the magnitude of the fall-induced peak impact force whereas the latter is the minimum applied load at which the proximal femur fractures, also referred to as fracture load. By this definition, the hip fracture is predicted when the ratio is ≥ 1. [446,462] An important observation here is that the indicated risk is increased as the applied load is increased, the fracture load (= proximal femur bone strength) is decreased, or their combination. Alternatively, the risk can be indicated by the hip fracture load alone. In other word, the lower the fracture load is, the higher the indicated hip fracture risk is. In fact, it has been found that (FE-derived) fracture load (proximal femur bone strength) can predict the hip fracture risk more accurately than other traditional methods such as aBMD-based risk assessment or FRAX [66,67]. This fracture load

(= proximal femur bone strength) is not only determined by bone properties such as its density and structure [12,446,463–465], but also influenced by the loading conditions (e.g., direction of fall onto the greater trochanter or hip) [446]. Therefore, compared to the currently available risk assessment tools, a more comprehensive assessment can be realized by measuring or estimating the fracture load. The fall-induced fracture load and impact force can be measured experimentally or estimated by the mathematical models or simulation (FE modeling). These will be discussed in detail in upcoming sections.

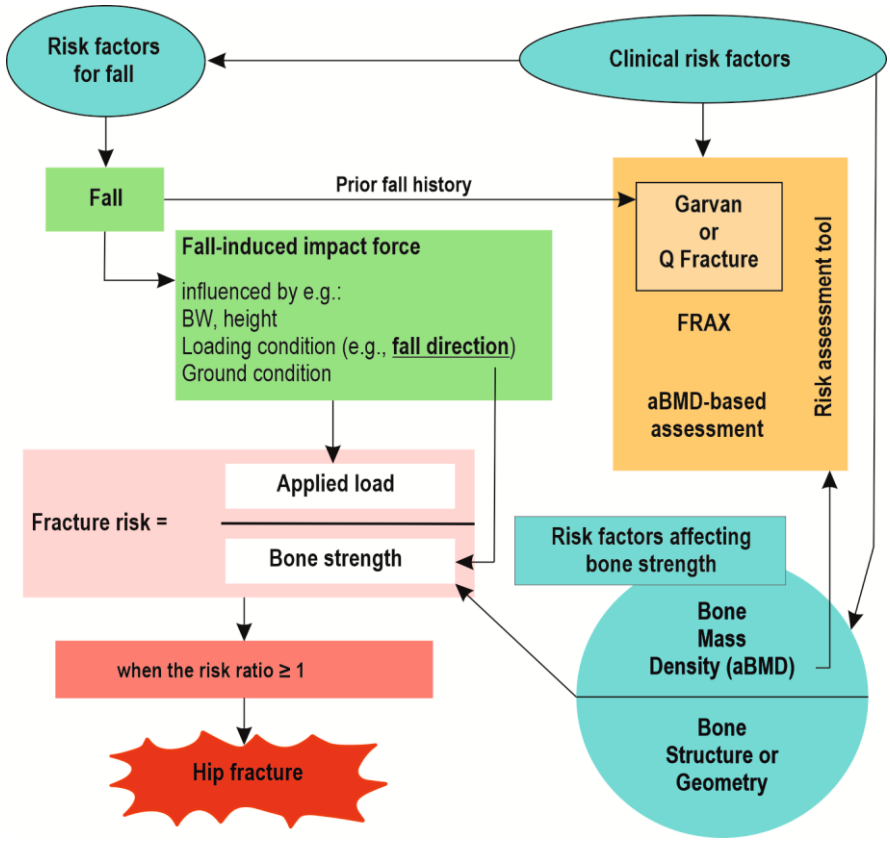

Figure 22. Overall schematic of hip fracture risk, risk factors, risk assessment tools, and their interactions. (Redrawn and adapted, with permission, from Luo (2016) [446] © 2015, International Osteoporosis Foundation and National Osteoporosis Foundation. Compared to the original figure, risk assessment tool and the variation of proximal femur bone strength depending on fall direction are added).

2.5 Fall

2.5.1 Fall-Induced Impact Force

The *in vivo* fall-induced peak impact forces of ~1650-3750 N (imposed on the surface of hip) have been reported from experimental studies where the participants performed the actual falls to a padded or unpadded force platform on the ground [466–470]. However, due to safety concerns, the majority of these studies measured the peak impact forces in the fall from kneeling height instead of from standing height with a few exceptions. Nankaku et al. (2005) measured the forces from the standing height and reported the peak impact force of 2250-3250 N [467]. However, to minimize the risk of potential injuries, the thickness of the padding was considerably greater (13 cm) [467] than in other studies (< 4 cm-thick) [466,468–470]. Similarly, van der Zijden et al. (2012) reported the impact force of ~3750 N from the standing height to the padded surface. However, the participants were experienced judo athletes. They performed the falls with a martial arts' fall technique consisting of a lateral rolling on the ground and a hand/arm slapping the ground at or right after the impact. [470] This technique was found to decrease the impact force by up to 30% [466,468–470]. Given these, these reported *in vivo* impact forces are likely lower than the actual impact force in the real-life scenario, where a person falls from the standing height to the unprotected hard surface on the ground.

The difficulty to measure the realistic peak impact force values via the *in vivo* studies led to the development of the mathematical models to estimate the impact force. In the 1990s, the kinematics and dynamics of the fall to the side were studied through experimental studies where human participants performed either the actual fall to the thick mattress or a fall-mimicking pelvis release experiment (**Figure 23**) by van den Kroonenberg et al. (1996) and Robinovitch et al. (1991), respectively [471,472].

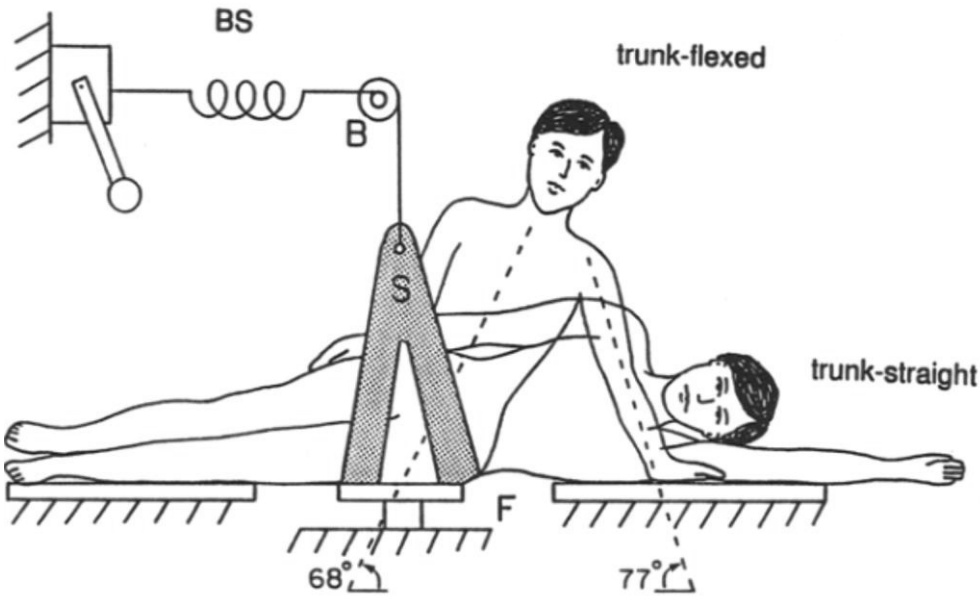

Figure 23. Pelvis release experiment. Two trunk position are shown: trunk-flexed and trunk-straight position. (Reprinted, with permission, from Robinovitch et al. (1997) [473] © 1997, Biomedical Engineering Society.)

Utilizing information from these experiments, van den Kroonenberg et al. (1995) developed several dynamic models and derived the following mathematical approximation of the peak impact force [474]. Considering the oscillatory response of the body at the ground impact, the peak impact force (F_{peak}) was first described as:

$$F_{peak} = Mg\left(\frac{V}{g}\sqrt{\frac{K}{M}}\sin(\omega t) - \cos(\omega t) + 1\right) \tag{18}$$

where V is the impact velocity (m/s), g is the gravitational constant (9.81 m/s^2), K is the effective pelvic stiffness constant [e.g., 71 kN/m from Robinovitch et al. (1991)[472]], M is the effective mass (kg), ω is the angular frequency (degree/s), and t is time (s). According to van den Kroonenberg et al. (1995), by neglecting "+1" and assuming $\omega t \approx 90°$, the above **equation (18)** can be further simplified to:

$$F_{peak} = V\sqrt{KM} \tag{19}$$

where the impact velocity can be expressed as:

$$V = \sqrt{2gh_{cg}} \approx 4.43\sqrt{h_{cg}} \quad (20)$$

where h_{cg} is the height of the center of gravity of the body (4.43 is in a unit of $\frac{\sqrt{m}}{s}$). Finally, F_{peak} becomes:

$$F_{peak} = \sqrt{2gh_{cg}KM} \quad (21)$$

where the effective mass *M* can be now estimated as $7/20$ × total body mass (kg). [471,472,474] As seen in the **equation (19)**, the impact force magnitude can be determined by the following three major contributors: the impact velocity (*V*), effective pelvic mass (*M*), and effective pelvic stiffness (*K*) [472]. The effective pelvis mass represents the mass of pelvis and connecting structures that contribute to the impact force while the effective pelvic stiffness presents the spring stiffness due to the soft tissue around the hip, pelvis, and connecting structures. Furthermore, these three variables can be influenced by the following factors: age, sex, body height and weight, other body anthropometry (e.g., body segment length), knee and trunk configurations at the impact (e.g., trunk-flexed position, **Figure 23**), movements during the descent, soft tissue thickness around hip, landing surface, muscle state (relaxed vs. tensed), and/or gait velocity (falls from standing vs. during walking) [462].

The velocity in the **equation (20)**, $V = \sqrt{2gh_{cg}}$ was derived based on a simple point-mass model by van den Kroonenberg et al. (1995) where a whole body was considered as the point mass. Alternatively, a smaller velocity estimate $V = 2.72\sqrt{h}$ [where h is body height (m) and 2.72 is in a unit of $\frac{\sqrt{m}}{s}$] can be used. This velocity estimate was derived based on their two-link model where the upper and lower body segments were considered the individual segment. [474] The height of the center of gravity (h_{cg}) can be assumed, for example, as 0.51 × height (m) [475]. In addition to above-mentioned effective pelvic stiffness value (*K* = 71 kN/m) [472], various stiffness values were estimated (**Table 5**) by several mathematical models based on the kinetic and kinematic data obtained from the pelvis release experiments (the impact velocity up to 1.0 m/s) (**Figure 23**). As shown in **Table 5**, there is a considerable discrepancy in the magnitude of *K* between the earliest study by Robinovitch et al. (1991) (60-110 kN/m) [472] and others (20-60 kN/m) [473,476,477]. The reasons are not known nor speculated by these investigators; however, it can be hypothesized that it is likely due to 1) differences in the study participants, 2) the height of release/drop, 3) different mathematical models for the estimation of the pelvic stiffness, and 4) differences in the measurement techniques.

Table 5. Effective pelvic stiffness from the pelvis release experiment with impact velocity (0.1-1.0 m/s)

Study	Subject characteristics*	Trunk position	Muscle state	Effective pelvic stiffness, *K*
Robinovitch et al. (1991) [472]	7 females (26 years, 62 kg)	straight	relaxed	71 kN/m
	7 males (28 years, 77kg)	straight	relaxed	90 kN/m
	female + male pooled	straight	relaxed	58 kN/m
			active	108kN/m
Robinovitch et al. (1997) [473]	5 females (33 years, 60kg)	straight	relaxed	30 kN/m
			active	37 kN/m
		flexed**	relaxed	58 kN/m
	5 males (21 years, 76kg)	straight	relaxed	50 kN/m
			active	33 kN/m
		flexed**	relaxed	50 kN/m
Laing & Robinovitch, (2010) [476]	14 females (23 years, 56 kg)	straight	relaxed	21-32 kN/m
Martel et al. (2018) [477]	7 males (23 years, 77 kg)	straight	relaxed	~45-57kN/m
			active	~45-55kN/m
	8 females (21 years, 62 kg)	straight	relaxed	~32-41kN/m
			active	~40-51kN/m

Note: The impact velocity of 0.1-1.0 m/s induces the impact force ranging from 0 N to ~1500 N.

*Means of age and BW are presented.

**The trunk was tilted to the ground by 68°

The effective pelvic stiffnesses of 20-110 kN/m (**Table 5**) were reported based on the pelvis release experiments from the low height (up to 5 cm) (**Figure 23**), which produced the impact velocity of 0.1-1.0 m/s and the peak impact force up to ~1500 N [472,473,476,477]. These pelvic stiffness values are likely underestimated since this test setup does not reflect the realistic fall situation with respect to the impact velocity and force. For example, the impact velocity in a fall from the standing height is on average 3 m/s or higher [478,479]. Considering the fall is a truly dynamic event, Fleps and his colleagues recently confirmed this underestimation issue by examining the effective pelvic stiffness at the higher impact velocity (3 m/s) and corresponding higher impact force range (from 300 N to the peak force, e.g., ~7600 N) based on an inverted pendulum impact testing of cadaveric femur (a drop from the standing height) with hip soft tissue surrogate and its dynamic FE model. They found that the effective pelvic stiffness can increase up to ~200-360 kN/m on

average as the impact velocity and impact force increase to ~3 m/s and ~7600 N, respectively. [480–482]

Next, the peak impact force of 4260 N was estimated for the 95th percentile of females based on the two-links model by van den Kroonenberg et al. (1995) with the effective pelvic stiffness of 71 kN/m by Robinovitch et al. (1991) [472,474]. Furthermore, a recent review on the fall-induced peak impact force by Nasiri Sarvi and Luo (2017) estimated a median peak impact force of 5200 N (for an average individual, data based on males and females pooled) based on both *in vivo* experimental and model-based estimated values [462]. These estimated peak impact force values are apparently greater than aforementioned *in vivo* impact force of ~1650-3750 N [466–470].

Lastly, the magnitude of the fall-induced impact force imposed on the hip surface discussed so far is not necessarily same as the one imposed to the proximal femur bone or the greater trochanter. This is because the soft tissues around the hip can attenuate the impact force to some extent. [462,483] Robinovitch et al. (1995) reported that every 1 mm thickness of trochanteric soft tissue can absorb ~71 N of the impact force based on the pendulum impact testing with surrogate human pelvis (proximal femur and trochanteric tissues) [483]. Utilizing this soft tissue attenuating effect with the **equation (21)**, Bouxsein et al. (2007) demonstrated that the hip impact forces were reduced on average by 50% (from 5641 N to 2772 N) and by 61% (from 5795 N to 2258 N) in hip fracture cases and controls of postmenopausal females, respectively (mean age: 74 years for both cohorts, thickness of the soft tissue: 40 mm and 50mm, respectively). Accordingly, this study showed that the thinner trochanteric soft tissues is associated with the higher hip fracture risk in the postmenopausal females. [475]

2.5.2 Fall Directions

The effect of fall direction on the hip fracture has been studied via experimental and/or FE modeling studies. Nankaku et al. (2005) reported in their *in vivo* study where the participants performed the falls to the thick padded mattress that the peak impact force in the posterior direction (backward fall) (3250 N) was significantly ($p < 0.05$) greater than those in the posterolateral or lateral directions (2500 N and 2250 N, respectively). However, unlike in the posterolateral or lateral falls, none of the participants in the posterior fall hit the posterolateral or lateral aspect of the leg or the greater trochanters. [467] As discussed earlier, the fall-induced hip fracture is

mainly due to the impact applied to the posterolateral or lateral aspect of the greater trochanter [37,41–44,49]. Besides, compared to the posterolateral and lateral aspects, the posterior aspect of the hip side can attenuate the impact force more due to its thicker soft tissue layer. Thus, the impact force reaching the proximal femur bone is likely smaller in the posterior fall than in the other directions. Moreover, the impact velocity in the posterolateral fall was also found the greatest among three directions. Therefore, they concluded that the posterolateral fall is the most dangerous fall, likely causing the hip fracture. [467] Not only the impact force varies depending on the direction of fall or impact, but also the fracture load (= proximal femur bone strength). For example, Pinilla et al. (1996) reported that the fracture load was the lowest in a fall onto the posterolateral aspect of the greater trochanter compared to the falls on the more lateral aspect in their experimental study of cadaveric proximal femora. This also supported that the posterolateral fall or fall onto the posterolateral aspect of the greater trochanter is the most dangerous fall situation. [48] The effect of direction of fall onto the greater trochanter (or fall-induced ground impact) on the fracture load from both experimental and/or FE modeling studies will be further discussed in the upcoming section (2.6.6). From an engineering perspective, compared to the fall-induced impact on the lateral aspect of the greater trochanter, the impact on the posterolateral aspect induces a much greater degree of torsion (twisting) about the axis of femoral shaft which increases the compressive loading at the fracture-prone superolateral cortex.

These results suggesting the posterolateral fall or fall onto the posterolateral aspect of the greater trochanter is the most dangerous fall situation has also been confirmed clinically by Yang et al. (2020) in their recent cohort study of video-captured falls (> 2300 falls) of over 600 elderly persons (mean age: 83 years) in long-term care facilities. They found that the majority of the fall-induced hip fractures occurred when the impact was imposed on the posterolateral aspect (77%, 23 out of 30 cases), followed by on the lateral (13%, 4 cases), the anterior (7%, 2 cases), and the posterior aspect (3%, 1 case) of the pelvis. [69] It is important to note that a fall initially directed in the posterolateral or lateral direction does not necessarily result in the ground impact onto the posterolateral or lateral aspect of the greater trochanter or pelvis if the faller manages to rotate his/her trunk during the fall descent. In fact, Robinovitch et al. (2003) confirmed that the trunk rotation is one of protective strategies to avoid the impact to the posterolateral or lateral aspect of pelvis (or the greater trochanter) in an *in vivo* study where young females (mean age: 23 years) managed to perform forward or backward rotation during the fall descent [68]. In line with this, Yang et al. (2016) also reported in another recent study of

video-captured falls (520 falls) of 160 elderly persons (aged > ~80 years) that up to 35% of the initial posterolateral/lateral fallers managed to rotate forward or backward to avoid the impact to the posterolateral or lateral aspect of pelvis (or the greater trochanter) [70]. Notably, these two video-capturing studies of falls also showed that the hip fracture risk in the initial forward fall is as high as the initial posterolateral/lateral fall since the forward fallers tend to rotate backward as a natural response, resulting in the ground impact onto the greater trochanter [69,70]. To summarize, the posterolateral fall, more precisely the fall resulting in the ground impact to the posterolateral aspect of the greater trochanter, appeared the most dangerous situation unless such impact is prevented by the trunk rotation during the descent.

2.6 Proximal Femur Finite Element Modeling

The fracture load (= proximal femur bone strength) can be measured experimentally (*in vitro*) through the mechanical testing of cadaveric femur, but obviously not *in vivo*. Finite element (FE) modeling appears a better and attractive alternative due to its abilities not only to predict the *in vivo* fracture load but to assess the hip fracture risk comprehensively by including bone properties such as its density and geometry/structure, and the loading condition in the fall (e.g., direction). Although DXA-based and QCT-based a/vBMDs can also predict the fracture load, it has been reported that the FE model can predict it 5-20% more accurately [484,485]. Given these, for last two decades, numerous research has been conducted to develop a subject-specific proximal femur FE model which can be used clinically to assess the *in vivo* hip fracture risk more accurately than other existing methods. In fact, it was found that the fracture loads predicted by the developed FE models can discriminate the hip fracture cases out of non-cases more accurately (AUC of 0.77-0.88) than the aBMD- and FRAX-based risk assessments (AUC of 0.73-0.79 and 0.69, respectively) [66,67]. In this section, the following relevant topics regarding the proximal femur FE model will be discussed: 1) principle of the FE method, 2) history of early development of the proximal femur FE model, 3) FE model specification (material properties, model linearity, failure criteria, boundary conditions, direction of fall onto the greater trochanter, and simulation types), and 4) applications. In the end, comparisons of the predictive accuracy (R^2) for the fall-induced fracture load among different FE models are presented as the sectional summary.

2.6.1 Principle of Finite Element Method

The FE method is a powerful numerical simulation technique to solve partial differential equations (PDE) arising from the mathematical modeling of various physical phenomena. It is an attractive alternative especially when, due to geometric and material complexities, such phenomena cannot be investigated via experiments, or analytical solutions cannot be obtained for the necessary mathematical models. In the FE method, the approximate solution is found by the Ritz-Galerkin approach, e.g., projecting the solution of the original PDE into a finite dimensional function space. A resulting algebraic equation system, either linear or nonlinear depending on the PDE, will be solved. The FE method was developed to solve the real-world problem consisting of complicated physics, geometry, and/or boundary conditions.

In the mechanical engineering, the FE method allows non-destructive assessment of the material or structure to examine their mechanical behavior under the certain loading configurations. [486] This is very advantageous in the hip fracture research or in assessment of the individual fracture risk. With an accurate measurement of bone geometry via the medical imaging and a proper understanding of its material properties, the FE models enables us to estimate the mechanical behavior of proximal femur bone (e.g., the hip fracture load) in a traumatic loading condition such as the fall (onto the greater trochanter) situation, *in vivo* (a bone still inside of a living human) instead of *in vitro* (cadaveric bone).

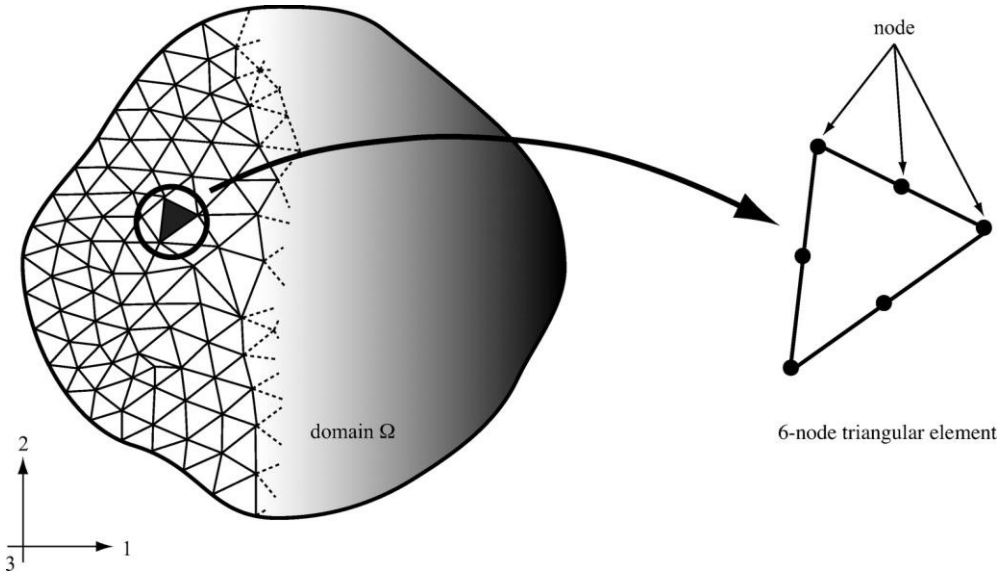

Figure 24. Discretization – FE meshing. (left) A 2D original domain (Ω) is represented by the discretized/meshed domain which is constructed by a collection of triangular elements. (right) A single 6-node (triangular) finite element. (Reprinted, with permission, from Bobet et al. (2009) [487] © 2009 ASCE).

In the FE method, a given domain or geometry (such as the proximal femur bone) is discretized into a collection of subdomains called finite elements which are made of nodes and edges (which connect nodes) (**Figure 24**). This discretization process is called meshing. In each FE element, the unknown field variables to be solved (e.g., displacements in solid mechanics problems) are often interpolated by low order polynomials, usually linear or quadratic. The unknown discrete parameters, degrees-of-freedom (DOF), are usually located at the elemental nodes. In structural analysis of the solid material, the DOF defines the number of directions to which each node is allowed to move (displacement by translation and/or rotation). The

material behavior of each element is governed by constitutive relations (e.g., linear elasticity). Contributions of all individual elemental stiffness matrices (where the constitutive relations are included) and force vectors are put together into global assembled system, representing the equilibrium equations of a whole domain:

$$Ku = f \tag{22}$$

where K is a stiffness matrix, and u and f are displacement and force vectors, respectively. The size of the stiffness matrix and these vectors depends on the number of elements and nodes in each element, and the number of DOF in each node. Finally, this global system is solved for given boundary conditions to obtain the approximated solution such as nodal displacements, based on which stress and strain of ROI can be estimated. [486]

To create the proximal femur FE model, there are basically three required components: 1) geometry, 2) material (mechanical) properties, and 3) boundary conditions. First, the proximal femur geometry can be acquired by medical imaging techniques such as DXA, QCT, or MRI. The acquired geometry is subsequently segmented to create its 3D model. Second, the material properties of bone need to be assigned into the segmented 3D bone structure by specifying the followings: 1) homogeneous or density-dependent inhomogeneous material properties, 2) linear or nonlinear material behavior, and 3) isotropic or anisotropic material properties. Furthermore, to define the fracture load, an appropriate failure criterion needs to be chosen. Also, the simulation type varies either quasi-static or dynamic simulation. Lastly, the boundary condition needs to be specified to simulate the desired loading configuration such as the fall (onto the greater trochanter) situation.

2.6.2 History of Early Development of Proximal Femur FE Model

The very first and pioneering FE model of proximal femur, to the best of author's knowledge, was introduced by Keyak and her colleagues through a series of three publications in 1990, 1992, and 1993 [488–490]. In these studies, they developed an automatic method generating a subject-specific 3D proximal femur FE model from CT scan data [488], reported that the element (edge) size should be ≤ 3 mm [489], and validated their FE method with mechanical testing by comparing FE-derived strain at different locations within a single proximal femur with experimentally measured values (R^2 = 0.59) [490]. In this FE model, the proximal femur was modeled as the density-dependent inhomogeneous, isotropic, linear elastic material

[488]. However, in these studies, only a single-leg stance loading condition was simulated. Besides, the fracture load was not estimated. [488–490] The fall (onto the greater trochanter) condition was first simulated by Lotz et al. (1991) in their FE modeling studies [491,492]. It is noted that, in all of above-mentioned studies here, only one proximal femur was modeled in each loading condition; therefore, statistically meaningful comparison between experimental and FE-derived results were not performed [488–492].

Given these, from the late 1990s to the early 2000s, Keyak and her colleagues extended their earlier linear FE models to examine if their method can accurately predict hip fracture load, location, and types in both stance and fall (onto the greater trochanter) configurations (**Figure 25**) [64,493]. To estimate the fracture load of each femur, a factor of safety (FOS) was calculated for each FE element:

$$FOS = \frac{element\ strength\ (converted\ from\ HU\ unit)}{element\ von\ Mises\ stress\ (derived\ by\ FE\ model)} \quad (23)$$

where the elemental strength was derived based on empirical density-strength relationship by Keller et al. (1994) and Keyak et al. (1994) [122,494].

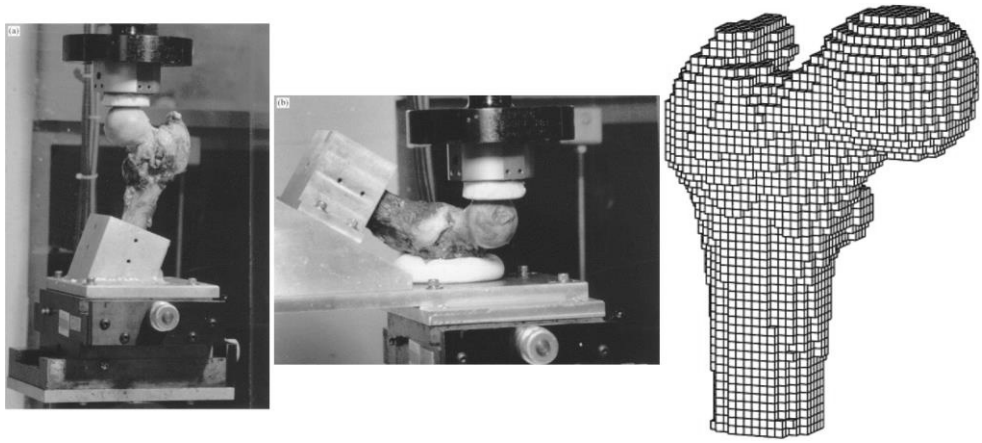

Figure 25. Mechanical testing of a proximal femur in stance and fall configurations (more precisely, the fall onto the posterolateral aspect of the greater trochanter) and the proximal femur FE model by Keyak et al. (1998). This figure shows the mechanical testing in the single-leg stance (left) and the fall (middle) configurations, and FE-meshed proximal femur with cubic elements (meshed with a voxel-based meshing method) (right). (Adapted, with permission, from Keyak et al. (1998) [64] © 1998 Elsevier Science Ltd.)

When a FOS of specific element is < 1, the failure of the element is indicated. The FE-predicted fracture load was defined as the load at which 15 contiguous non-surface elements had their FOSs < 1. This method was intended to predict the

fracture load at the onset of fracture. For each proximal femur, it was required to solve the FE model only for once with an arbitrary magnitude of a force (e.g., 1000 N) applied to the femoral head in each loading configuration. This was because, by taking advantage of the linear FE model, the FE-predicted fracture load was estimated by scaling the result of a single FE solution until the 15 contiguous elements had their FOSs < 1. Based on the results from the FE models of cadaveric proximal femora of 18 old people (mean age: 70.3 years, ranging 52-92 years), their FE methods can predict experimentally measured fracture loads slightly more accurately than QCT-based densitometry data: R^2 were 0.76 and 0.90 in the stance and fall configurations, respectively, by their FE models whereas the R^2 by the density-based prediction were 0.61 and 0.83, respectively. [64] Furthermore, their method can predict the fracture location and type (cervical/femoral neck or trochanteric type) with the accuracies of ~70% and 80%, respectively [493].

The last noteworthy study from the early development was the one by Lengsfeld et al. (1998) where they compared a geometry-based with voxel-based meshing methods in the FE models. In the former meshing, the element surfaces follow along the surface contours, realizing the smooth surface in the FE models (**Figure 26**). On the other hand, in the voxel-based meshing, they are oriented parallel to the three-orthogonal axes of CT scanner's coordinate system, resulting in the unsmooth surface (**Figure 25**). Their results demonstrated that both meshing methods produced very similar strain results; R^2 compared to experimentally measured strain were 0.84 and 0.85 in the geometry- and voxel-based meshing methods, respectively. [495] However, Helgason et al. (2008) reported in their recent review that the geometry-based meshing is better in predicting the strains and stresses than the voxel-based method: average R^2s based on several studies were 0.83 and 0.72, in the geometry- and voxel-based methods, respectively. The inferior performance of the voxel-based FE models is likely because their inability to capture superficial (surface) stress and strain field. [496]

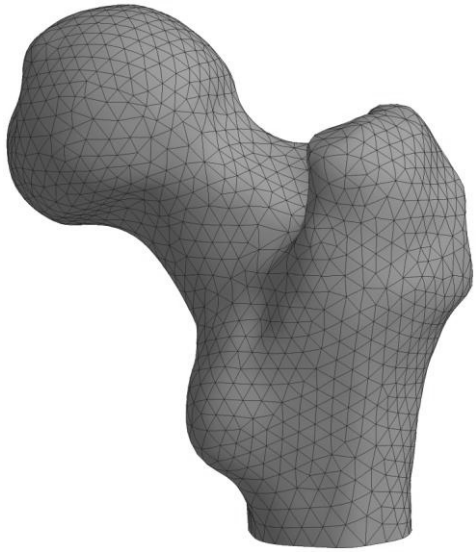

Figure 26. Proximal FE model meshed with a geometry-based meshing method. An example is shown.

2.6.3 Homogeneous vs. Inhomogeneous Material Property Assignment

The material (mechanical) properties such as the elastic modulus and strength can be assigned into the 3D proximal femur bone structure either homogeneously or inhomogeneously. In the homogeneous method, fixed values of these properties are assigned into the entire compartments of cortical and trabecular bones, separately. These values can be obtained from the literature, where the mechanical testing was performed to acquire the mechanical properties of the cortical and trabecular bones. For example, the elastic moduli of 15-20 GPa and 590-2000 MPa have been assigned into the entire cortical and trabecular bone compartments, respectively, in some of the previous proximal femur FE modeling studies [112,495,497–500]. This homogeneous material property assigning method is also referred to as the two-material modeling method [112]. This method is an alternative when the density-based inhomogeneous material property information based on CT scan data (HU unit) is not available due to, for example, the use of MRI data.

The two-material or homogeneous method is unrealistic and may reduce the accuracy of FE model despite its easy implementation. This is because the material (mechanical) properties of bone vary from one anatomic site to another, even within the same bone, due to heterogeneous distribution of the apparent bone density

[97,105–107]. Therefore, the inhomogeneous material property assignment or mapping has been used in the most of previous QCT-based FE modeling studies [43,45,50,64,65,67,112,395,488,501–513]. This inhomogeneous method can be realized by utilizing the empirical mathematical relations between 1) the HU unit and apparent density, and 2) the density and material (mechanical) properties of bone such as the elastic modulus and strength. Because of the step-by-step and thorough development, the inhomogeneous method is briefly explained using the one established by Schileo, Taddei, and their colleagues from Instituti Ortopedici Rizzoli in Bologna, Italy as an example [514–517].

First, the CT scan data (HU unit) is converted into the CT-density (the radiological density) based on the calibration phantom such as European Spine Phantom (ESP) by Kalender (1992) as follows:

$$\rho_{QCT} = 0.007764HU - 0.056148 \tag{24}$$

where ρ_{QCT} is the CT density (in g/cm^3) [514,518]. It is noted that the linear HU-ρ_{QCT} relation varies depending on the CT machines and calibration phantom used in each study (typically based on dipotassium phosphate, K_2HPO_4, or calcium hydroxyapatite, HA) [113,519]. Next, the CT-density (ρ_{QCT}) is converted to the apparent density (ρ_{app}, the wet weight divided by bulk bone specimen volume, in g/cm^3) via the ash density (ρ_{ash}, burned bone ash weight divided by bulk specimen volume, in g/cm^3) using the following equations:

$$\rho_{ash} = 0.877\rho_{QCT} + 0.079 \tag{25-1}$$

$$\rho_{app} = 0.6\rho_{ash} \tag{25-2}.$$

These linear ρ_{ash}-ρ_{QCT} and ρ_{app}-ρ_{ash} relations were experimentally obtained in a study by Schileo et al. (2008), where excellent linear correlations were reported for each of these relations (cortical and trabecular bones pooled); R^2 of 0.997 and 0.992, respectively. [514] Lastly, the elastic modulus is computed using the empirical density-modulus relationship by Morgan et al. (2003) based on human femoral neck specimen as follows:

$$E = 6.85\rho_{app}^{1.49} \tag{26}$$

where E is the elastic modulus (in GPa) [105]. Schileo et al. (2007) found that the accuracy of predicting experimental strains by FE models with this **equation (26)** is higher than the FE models with other commonly used empirical density-modulus

equations by Carter & Hayes (1977) ($E = 3.790\rho_{app}^{3}$) [97] or by Keller (1994) ($E = 10.5\rho_{ash}^{2.29}$) [122]: R^2 of 0.91, 0.55, and 0.63, respectively [105,516]. Other empirical density-modulus/strength relations, which can be used instead of the **equation (26)**, are summarized earlier (**Table 1**) or can be found in (review) studies by Wirtz et al. (2000) [108], Helgason et al. (2008, 2016) [113,114], and Fleps et al. (2020) [115].

Next, the computed elastic modulus needs to be assigned into each FE element. In the voxel-based meshing, this process is simple. Each cubic finite element is constructed by utilizing the preexisting CT voxels and grid axis. Then, the HU units of the CT voxels inside of each element are averaged and subsequently converted into the element-specific modulus using the empirical relationships [e.g., the **equations (24-26)**]. [515,517,520] The inhomogeneous mapping process becomes more complicated in the geometry-based meshing especially when unstructured finite element mesh is generated where the boundary between the trabecular and cortical bones is not distinct. In such a case, a more sophisticated approach is necessary. To address issue, Zannoni, Taddei, Schileo, and their colleagues (1999, 2004, 2007, 2020) developed an automatic inhomogeneous material property mapping algorithm (from the CT data to FE model) and released a free software called Bonemat (available at http://www.bonemat.org/). This software outputs the FE mesh which is compatible with the commercial FE software such as Abaqus or ANSYS. The output FE mesh contains the element-specific inhomogeneous material property mapping information. [515,517,520,521] Two latest versions (Bonemat – V3 and V4) are briefly explained here. First, Bonemat V3 converts the 3D scalar HU field into an elastic modulus continuum field using e.g., the **equations from (24) to (26)**. Next, the numerical integration of the modulus over the element's volume is performed to compute the element-specific modulus value. Bonemat allows the user to define the precision (also referred to as gap) of the elastic modulus value assigned to each element. For example, with the gap of 50 MPa, if one element has the modulus of 50 MPa, the next lower or higher moduli other elements can have are 50MPa or 100 MPa, respectively. This means that the number of FE elements is not necessarily equal to the number of material models unless a very small gap value is used (e.g., 0.01 MPa). For example, in a study by Taddei et al. (2007), the proximal femur FE model constructed by ~76,000 FE elements was characterized by 388 different material models with gap of ~50 MPa using Bonemat V3 [517]. This is computationally advantageous since decreasing the number of material models likely reduces the computational cost and improves performance of the FE software. An example of the inhomogeneous material property mapping in

proximal femur FE model using Bonemat V3 (geometry-based meshing) is shown in **Figure 27** below.

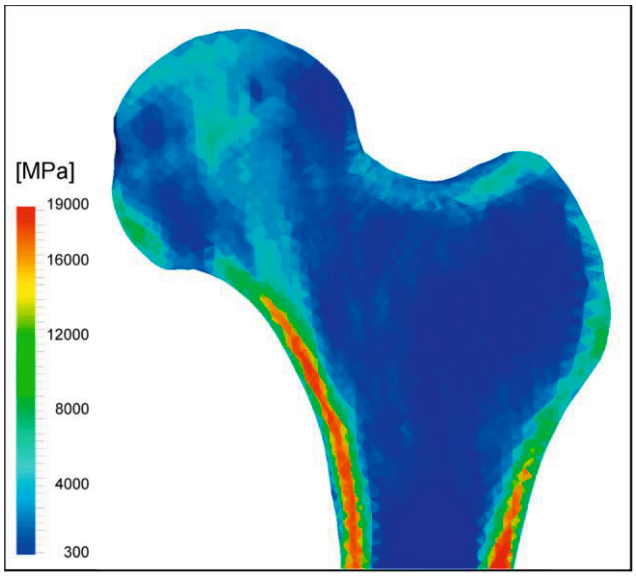

Figure 27. Inhomogeneous material property (elastic modulus) mapping with Bonemat. The view is coronal cross-section of proximal femur. (Adapted, with permission, from Taddei et al. (2014) [522] © 2014 Elsevier Ltd.)

Until the latest version (Bonemat V4), the computation of the element-specific material properties was performed without distinguishing the trabecular and cortical bone types. In Bonemat V4, cortical thickness and cortical bone density calculated from one of computational anatomy technique called Cortical Bone Mapping (CBM, the detail will be described in an upcoming section 2.7) are used to compute the material properties for each cortical FE element through similar numerical integration from Bonemat V3. Schileo et al. (2020) reported that the accuracy of predicting the experimental strains in the stance and fall (onto the greater trochanter) configurations (pooled) is higher in V4-based than in V3-based FE model: the error estimates (SEE and RMSE) were approximately 25-30% lower in the V4-based than the V3-based FE models. [521]

Lastly, despite the homogeneous material property assigning method being less realistic than the inhomogeneous method, a question remains; to what extent is the inhomogeneous method superior to the homogeneous method in predicting the mechanical behavior of proximal femur? Taddei et al. (2006) partially addressed this and found that the accuracy of the homogeneous proximal femur FE model in

predicting the experimental stress was only slightly lower (R^2 = 0.89) than the inhomogeneous model (R^2 = 0.91) [112]. Nevertheless, the caution is needed here. The high accuracy in predicting stress does not necessarily guarantee similar accuracy in predicting strain. Stress state will often be correct to satisfy the static equilibrium condition. However, even if the stress value is accurate, the strain value may still be predicted inaccurately with inaccurate estimate of the elastic modulus which depends on the inhomogeneous distribution of the bone mineral density. This issue likely becomes more evident at the boundary between the cortical and trabecular bones such as the endocortical surface. Even if the stress in the trabecular bone adjacent to the cortical bone would be correct, the strain would significantly depend on the value of the elastic modulus of the cortical bone. Furthermore, in this study, only the physiological loading conditions (e.g., single leg stance) were simulated using a single femur [112]. Therefore, additional studies are necessary to validate the use of homogeneous material properties in predicting the (experimental) strain and fracture load based on the stress- and strain-based failure criteria in the fall (onto the greater trochanter) configuration with a larger sample size.

2.6.4 Model Linearity and Failure Criteria

The definition of experimentally measured fracture load (= proximal femur bone strength) is typically the peak force (= the ultimate load) in the force-displacement or force-time curve during the mechanical testing. In contrast, the one predicted by the FE model varies from one study to another: either same as the experimentally measured fracture load (the ultimate load) or the load at the onset of fracture (referred to as the fracture onset load henceforth in the present doctoral dissertation) (**Figure 28**). [43,45,50,64,65,395,503,510,513,523–526]

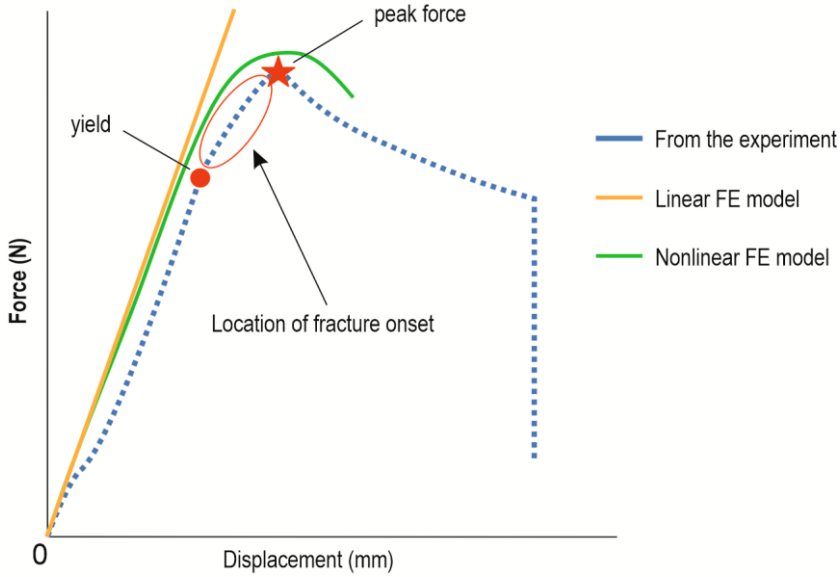

Figure 28. Conceptual presentation of force-displacement curves by linear and nonlinear FE models with the experimental force-displacement curve.

Compared to the ultimate fracture load, the location of the fracture onset load in the force-displacement curve is obscure. Based on the yield criteria and the definitions of the fracture onset load implemented in the previous FE modeling studies, the fracture onset load is assumed to be located between the peak force and yield point (**Figure 28**). [50,64,523] In case of the fall, this seems reasonable assumption because the crack initiation (or the onset of fracture) due to the local failure (yielding or buckling by compression) at the superolateral femoral cortex takes place before the peak force where the 1st macro-failure (crush or collapse) at the superolateral cortex takes place [the 1st failure in the two-step failure as described earlier] [44]. Besides, based on the destructive testing, the proximal femur does not

only typically behave linearly up to this 1st failure [42,394,504], but also go through the brittle fracture at least for this 1st failure characterized by little or no plastic deformation [37,42,44,394,395]. These imply that modeling linear elastic mechanical behavior of proximal femur (= linear FE model) may be sufficient to estimate the fracture load, particularly for the fracture onset load. However, theoretically speaking, the nonlinear FE model is inevitably more suitable to estimate the ultimate fracture load because of its ability to capture post-yield nonlinear plastic behavior. Regardless of the type, the fracture load needs to be determined with an appropriate yield and failure criteria. In this section, the model linearity and various yield and failure criteria are discussed with respect to predicting the (experimentally measured) fracture load.

In one of the first proximal femur FE models by Keyak et al. (1998) (linear FE model), the fracture load was predicted as the load at the onset of fracture at which 15 contiguous non-surface elements reached the yield point defined by von Mises yield criterion [also known as the distortion energy (DE) or von Mises Hencky theory]. This linear FE model resulted in a high correlation (predictive accuracy) between experimentally measured and FE-predicted fracture loads in the stance and fall (onto the greater trochanter) configuration (R^2 of 0.75 and 0.90, respectively). [64] However, the von Mises yield criterion used in this model was originally developed for ductile materials such as steel. Besides, the asymmetric (yield) strength of bone [178] was not considered in this model. Therefore, using the same linear FE model, they compared the performance of the following 9 different stress- and strain-based yield criteria in predicting the fracture loads in both stance and fall configurations: Hoffman, Coulomb-Mohr, modified Mohr, DE, maximum principal stress, and maximum shear stress (also known as Tresca theory) as the stress-based criteria; strain-based Hoffman analog, maximum principal strain, and maximum shear strain as the strain-based criteria. It is noted that the Coulomb-Mohr, modified Mohr, maximum principal stress/strain, and Hoffman criteria were more appropriate for the brittle materials like rock, concrete, and bone tissue than the others. Moreover, these criteria also consider the asymmetry strength of bone. They reported that the DE and maximum shear stress criteria are the most robust ones to predict the experimentally measured fracture load although they are more for the ductile material and do not consider the asymmetric strength. [527].

Using the DE yield criterion, Keyak (2001) subsequently developed their nonlinear FE models, where element-wise (material-point-level) nonlinear material behavior of bone tissue was first modeled as the elasto-perfectly-plasto-strain softening material (**Figure 29**). In this material-point-level constitutive law, the yield and ultimate strengths of each element were assumed to coincide. At the whole bone

level, the FE-derived ultimate fracture load was defined as the peak total femoral head reaction force in the force-displacement curve (**Figure 29**). [523]

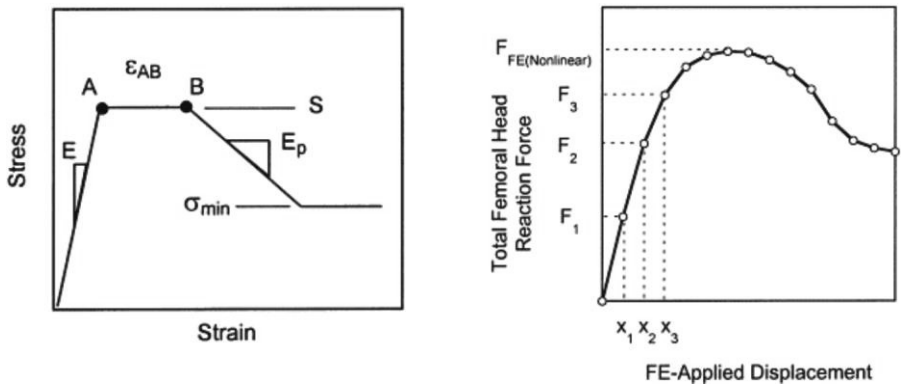

Figure 29. Nonlinear FE model by Keyak (2001). An elasto-perfectly-plasto-strain softening material model (left, material-point-level) where *E, S,* ϵ_{AB}, E_p, and σ_{min} are the elemental elastic modulus, strength, plastic strain, plastic modulus, and minimum stress (defining the indefinite perfectly plastic phase), respectively. Further information can be found in a study by Keyak (2001) [523]. FE-derived force displacement curve (right). The displacement was increased incrementally, and the total femoral head reaction force was calculated by summing the reaction forces from nodes over the femoral head at each displacement increment. (Adapted, with permission, from Keyak (2001) [523] © 2001 IPEM. Published by Elsevier Ltd.)

It was demonstrated that this nonlinear FE model can predict the fracture load more accurately than their earlier linear model: R^2 compared to the experimentally measured fracture loads were 0.93 and 0.77 by the nonlinear and linear FE models, respectively. However, the application of this nonlinear model was first limited to only the stance loading configuration. [523] Therefore, this nonlinear FE model was applied to the fall configuration with a modification of the post-yield material behavior. The modified nonlinear model resulted in a good but slightly lower accuracy of predicting the experimentally measured fracture load in the fall configuration (R^2 = 0.81) [524,528] than their earlier linear model (R^2 of 0.90) [64].

Other researchers have also developed the nonlinear proximal femur FE models by modeling bone tissue as bi-linear or step-wise linear elasto-plastic, or elasto-damage material with different yield and failure criteria [45,46,65,501,502,511,525,529]. For example, in the model developed by Bessho et al. (2007, 2009), the yielding of each cortical and trabecular element was determined to take place when its Drucker-Prager stress exceeds the respective elemental compressive yield stress. Then, the post-yield modulus (5% of pre-yield elastic

modulus) was assigned to the yielded element. Subsequently, the tensile and compressive failure of each element was determined by the maximum principal stress and minimum principal strain thresholds (-10,000 με), respectively. The asymmetry in compressive-tensile strength was taken into account by setting the ultimate tensile stress (the threshold for the maximum principal stress) as 0.8 times the compressive yield stress. The ultimate fracture load was defined as the load at which at least one surface cortical shell element experienced its failure. This method also resulted in a high correlation (R^2 = 0.96) between FE-predicted and experimentally measured fracture loads. However, their model validation was again limited to only the stance configuration. [46,502] Thus, Koivumäki et al. (2012) validated the same method, except for lowering the minimum principal strain threshold for the compressive failure to -7300 με, in the fall configuration and also achieved the high correlation (R^2 = 0.87) between the FE-predicted and experimentally measured ultimate fracture loads [65]. In these studies, the Drucker-Prager yield stress criterion was implemented instead of the von Mises stress (DE) criterion because the former criterion is more suitable for the brittle materials [46,65,502,530]. It is noted that the Newton-Raphson method (an iterative method to solve nonlinear algebraic equations) was used to perform the nonlinear FE analysis in these studies.

Furthermore, Dragomir-Daescu et al. (2011) also achieved a high correlation (R^2 = 0.86) between the FE-predicted and the experimentally measured ultimate fracture loads by adopting von Mises yield strain criterion in their nonlinear FE model [45]. By replacing this criterion with maximum principal strain or stress criterion, Liebl et al. (2015) found that the maximum principal strain criterion leads to less overestimation (by ~5%) of the experimentally measured ultimate fracture load than the maximum principal stress criterion (by ~15%) [511].

As described so far, both stress- and strain-based criteria were used to define the yield and failure of the bone tissue at the material point-level. Thus, a question arises: is the bone fracture controlled dominantly by stress or strain, or by both? Recent experimental evidence from basic bone biomechanics research strongly suggest that the yield, fracture initiation, crack developments, and failure of bone tissue are rather strain-driven than stress-driven [531–533]. Above-mentioned result by Liebl et al. (2015) is in line with this. The mechanical properties of bone are typically anisotropic and density dependent as described earlier. However, the yield strength in strain is an important exception since it is rather isotropic and independent of the bone density [178,534–540]. Furthermore, based on previous experimental studies, strains of human proximal femora increase highly linearly up to failure (for the 1st failure)

in both stance and fall (onto the greater trochanter) configurations [42,394,504]. Importantly, Schileo et al. (2007) and Grassi et al. (2012) demonstrated that linear FE models can accurately predict the experimentally measured strains in both loading configurations ($R^2 = 0.91$) [504,516]. Considering these, Schileo et al. (2008, 2014) implemented the maximum principal strain criterion in their linear FE model and achieved high correlations between FE-predicted fracture onset loads and experimentally measured fracture loads, for the fall and pooled (stance + fall) configurations ($R^2 = 0.81$, and 0.89, respectively). Importantly, they also included the asymmetry of compressive-tensile yield strength (compressive and tensile yield strain limits are -1.04% and 0.73%, respectively) in their model based on an experimental study by Bayraktar et al. (2004) [178]. [50,395] Moreover, this FE method correctly recognized the failure mode and location of the onset of fracture: compressive and tensile failures at the superolateral femoral neck in the fall (onto the greater trochanter) and stance configurations, respectively. However, it should be noted that the sample size in each loading configuration was small (= 7) in this study. [50] Thus, this calls for the further study to confirm these high R^2 values in the fall configuration with larger sample size.

Schileo and his colleagues (2008) also compared the performance of predicting the fracture load using this maximum principal strain criterion with two other stress-based criteria such as von Mises stress (DE) and maximum principal stress criteria. Compared to the strain-based criterion, not only the fracture onset loads predicted by stress-based criteria are likely more underestimated (**Figure 30**), but also the predicted fracture locations are twice farther to the experimentally observed locations. [395] This result is discordant with the one by Keyak et al. (2000) where the von Mises stress (DE) criterion was found one of the most robust yield criteria to predict the fracture onset load over the maximum principal strain criterion [527]. However, the accuracy of predicting the experimentally measured strain was lower in the linear FE models by Keyak et al. ($R^2 = 0.59$) [490] compared to the one by Schileo and his colleagues ($R^2 = 0.91$) [50,504]. This lower accuracy likely prevented from a correct evaluation of the strain-based criteria in the study by Keyak et al. (2000) [527]. Besides, the methods to define the fracture onset load differed between these linear models. In Schileo's linear FE model, nodal strains were first averaged with its neighboring nodal strains within a circle of 3 mm radius and then the fracture onset load was defined as the load at which one cortical surface element fails [50]. In contrast, the fracture onset load was defined as the load at which at least 15 contiguous non-surface elements fail in Keyak's model [64]. This methodological difference also likely contributed to above-mentioned discordance. To summarize

and avoid the confusion, compared to the maximum principal strain criterion, the use of the stress-based criteria [the maximum principal and von Mises (DE) stress criteria] appeared to likely underestimate the fracture onset load [395] and overestimate the ultimate fracture load [511].

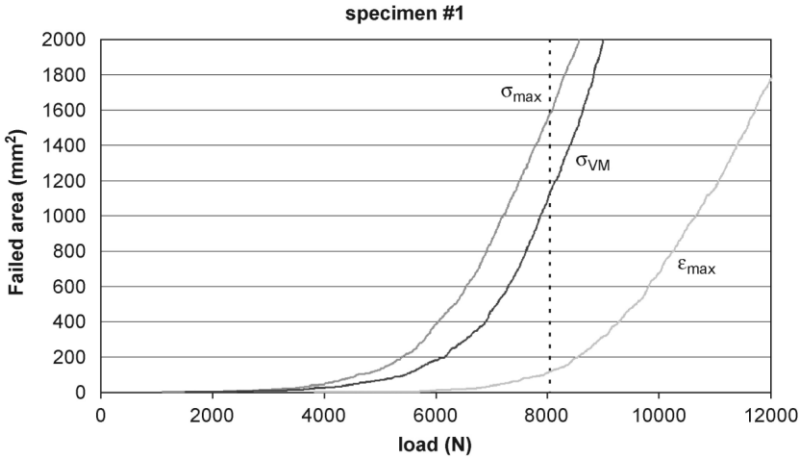

Figure 30. Comparison of stress-based and strain-based failure criteria. This figure presents failed area-load curves by three different failure criteria: maximum principal stress (σ_{max}), von Mises (DE) stress (σ_{VM}), and the maximum principal strain (ε_{max}) criteria. It demonstrates that stress-based criteria underestimate the fracture (onset) load compared to the maximum principal strain criterion. For example, if the fracture load was defined as the load at which 1000 mm^2 of finite elements fail, then the fracture loads would be estimated to ~7000N, ~7800N, and ~10800N for the σ_{max}, σ_{VM}, and ε_{max} criteria, respectively. (Adapted, with permission, from Schileo et al. (2008) [395] © 2007 Elsevier Ltd.)

As mentioned earlier, theoretically speaking, the nonlinear FE models are more suitable than the linear FE model to predict the ultimate fracture load due to its ability to model the post-yield nonlinear plastic behavior. Accordingly, above-mentioned numerous investigators confirmed that the nonlinear FE models can accurately predict the ultimate fracture loads (R^2 = 0.80-0.96 and 0.78-0.87 for the stance and fall configuration, respectively) [45,65,502,523–525,529]. Despite this, Mirzaei et al. (2014) and Nishiyama et al. (2013) demonstrated that the linear FE model can also predict the ultimate fracture load accurately for both configurations using the yield criteria based on the strain energy density (R^2 = 0.86 and 0.81 for the stance and fall, respectively) [503,510]. Again, this is likely because the proximal femur typically experiences the brittle fracture and behaves linearly elastic up to the 1st failure.

An advantage of the linear FE method compared to the nonlinear method is its smaller computation cost [< a few minutes vs. up to 10 hours or more (depending on the element size), respectively] [45,50,395,502,503,510,523,541]. Therefore, the linear FE method with the yield criteria (e.g., the maximum principal strain criterion) may be more suitable in the clinical research where a large number of proximal femur FE models need to be created. It is noted that this linear FE method with the maximum principal strain criterion has also been used in the hip fracture research not only by Schileo et al. but also by a few other researchers such as Haider et al. (2013) [151] and Verhulp et al. (2008) [41].

It should be noted that the fracture onset load could have been defined as the yield load in this section. However, strictly speaking, the fracture onset load is likely slightly greater than the yield load based on the definition of each fracture load type implemented in the FE modeling studies by different investigators. For example, in addition to the ultimate fracture load, Bessho et al. (2007) also estimated the yield load as the load at which only one element exceeds the elemental yield limit utilizing the linear elastic response within their nonlinear FE model [502]. In contrast, as described earlier, the fracture onset load was defined as the load at which 15 contiguous non-surface elements exceeds the yield point in the linear FE models by Keyak et al. (1998) [64]. Due to this definition, the onset load is most likely greater than the yield load. Although the onset load was defined as the load when only one surface element exceeds the yield limit in the FE model by Schileo et al. (2014), smoothing the surface nodal strains with its neighboring values had a similar overestimating effect to the one above by Keyak et al. (1998). In fact, although the number of FE modeling studies which reported the yield load is very limited, the yield load of ~3600N was reported by Bessho et al. (2007) from people aged (mean) 64.8 years (30-90 years) in the stance configuration [502], which was slightly smaller than, for example, the fracture onset load of ~4500N reported by Keyak et al. (1998) from similar aged people (mean age: 70.3 years, ranging 52-92 years) [64]. Given this, the author of the present doctoral dissertation contemplated that it is more appropriate to distinguish the fracture onset load from the yield load.

Lastly, it is noteworthy that the most advanced, to author's knowledge, nonlinear FE models introduced by Helgason, Ariza, and their colleagues (2014, 2015). In their model, the bone tissue was modeled as a piecewise linear plasticity material including not only the strain-rate dependent material properties but also post-yield softening and densification phenomena in the large strain (**Figure 8**). [43,526] In their more recent model (2018), not only the asymmetric strength of bone was included, but also their material model was replaced by a rate-sensitive crushable foam plasticity

model [513]. These modifications resulted in an improvement in the correlation between the FE-predicted and experimentally measured ultimate fracture loads from no correlation ($p > 0.05$) in their initial model [526] to R^2 of 0.56 in the recent model (2018) [513]. However, this still calls for the further improvement since R^2 of 0.56 is still the lowest compared to aforementioned R^2 values reported by others. Another notable feature of these studies was that their FE models were simulated dynamically by considering the fall is a dynamic event; however, this aspect will be further discussed in an upcoming section 2.6.7.

2.6.5 Boundary Conditions

Boundary conditions (BC) in the FE models are loading and constraining conditions applied to certain parts of the geometry to simulate the desired loading configurations such as experimental stance and fall (onto the greater trochanter) configurations (**Figure 31**). For the fall configuration, the loading (force) and constraining BCs are typically applied at the femoral head and the lateral aspect of greater trochanter, respectively, or vice versa directly or indirectly through polymethyl methacrylate (PMMA) protecting caps. When the force BC was applied to the femoral head directly or via its protecting PMMA cap at a chosen loading angle (direction of fall-induced impact), surface nodes of the lateral side of greater trochanter or its PMMA cap were constrained in the direction of the loading (force). The distal end of the proximal femur is either fully constrained directly or partially constrained by a hinge-type BC via a connecting aluminum pot. In the latter case, nodes at the distal face of this aluminum pot are allowed to rotate freely in the quasi-frontal plane while all other degrees of freedom were constrained. The BCs for the stance configuration are similar to those in the fall configuration except for the different loading direction and no constraining BC at the lateral aspect of the greater trochanter. [43,45,46,50,64,65,502–504,511]

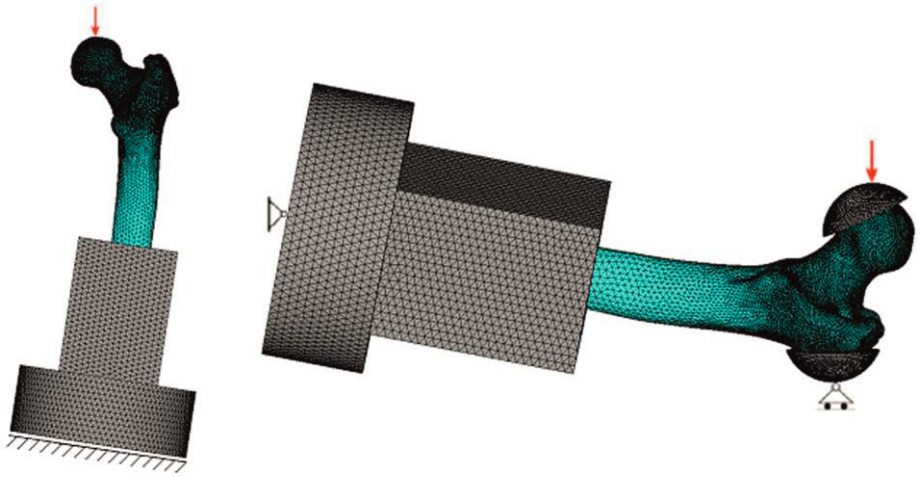

Figure 31. Boundary conditions for simulations of experimental single-leg stance and fall (onto the greater trochanter) configurations. (Left) Single leg stance configuration. (Right) Fall configuration. (Adapted, with permission, from Schileo et al. (2014) [50] © 2014 Elsevier Ltd.)

The effects of the following variations in the BCs on FE results have been explored previously: 1) locations of loading and constraining BCs, 2) direct or indirect application of the BCs, and 3) different constraining BC types (e.g., full or partial constraining, and linear or nonlinear contact BCs) [151,505,542]. Haider et al. (2013) found that the location of the load application and constraining BC types (full constraining or partial constraining allowing translation and/or rotation in one or all directions) had little effect on strain distribution pattern and consequent prediction of fracture location and pattern. However, compared to applying the load to the femoral head, the load application to the greater trochanter decreased peak strain magnitude by 22% and accordingly increased predicted fracture load by 18%. [151] Although an impact force is applied to around the lateral aspect of greater trochanter in a real fall (onto the greater trochanter) situation, it is unclear why it has usually been applied to the femoral head in the majority of previous FE modeling studies. To author's knowledge, this may be because the loading was first applied to the femoral head in the most referred experimental study for the fall configuration by Courtney (1994, 1995) [543,544]. Essentially, the force on the femoral head represents the force of the pelvis on it. The location where the impact force is applied, whether it is on the femoral head or the greater trochanter, affects the position of the greater trochanter relative to the constrained distal shaft. When the impact force is applied to the femoral head while constraining the greater trochanter, they mimic the situation where the motion of femoral head relative to the greater trochanter and ground is likely and primarily responsible for inducing the fracture instead of the motion of the greater trochanter relative to the constrained leg. In most real fall situations, it is reasonable to assume that the former motion is likely greater than the latter, unless the person falls on a slippery, icy, or irregular surface that may lead to the greater motion of the greater trochanter. Therefore, the application of the force to the femoral head may still provide a more accurate mechanical representation of the event. Nonetheless, this calls for further investigation.

Furthermore, compared to applying a partial constraining BC to the cross-sectional surface of the mid-to-distal diaphysis, it was found that an application of full constraining BC at the cross-sectional surface right below the lesser trochanter altered the strain profile and increased the predicted fracture load by up to ~26% in the fall (onto the greater trochanter) configuration. Application of the constraining BC at the mid-to-distal diaphysis is assumed to represent the movement of knee joint, to some extent, at the ground impact due to the fall. Thus, application of full constraint right below the lessor trochanter neglects this and seems to over-constrain the model. [505]

Next, compared to the linear contact BC, the nonlinear contact BC can allow larger movements (slide and rotate) and/or friction at contact surfaces (e.g., between the lateral aspect of the greater trochanter and ground, and between the PMMA caps and proximal femur surfaces) [505,542]. Rossman et al. (2015) reported that the linear contact BC can over-constrain the model, potentially leading to overestimation of the fracture load [542]. Besides Altai et al. (2019) demonstrated that hip fracture discrimination performance is slightly higher with the nonlinear contact BC (AUC = 0.82) than with the linear contact BC (AUC = 0.80); however, this slightly higher performance may not counterbalance its higher computational cost (a few minutes vs. a few hours for solving FE models with linear and nonlinear contact BCs, respectively) [505]. These results highlight the importance of applying appropriate BCs, reflecting not only experimental setups but also a realistic fall (onto the greater trochanter) configuration. However, the consensus using the same BCs across the FE studies has not yet been reached in the bone research community, and thus this calls for further investigation in this regard.

2.6.6 Directions of Fall onto the Greater Trochanter / Fall-Induced Impact

The effect of fall direction on the impact force was discussed earlier. In this section, the effect of direction of fall onto the greater trochanter or fall-induced ground impact on the fracture load is discussed based on both experimental and FE modeling studies. The direction is defined by two angles: the hip adduction angle (*a*, an angle between the femoral shaft and ground) and internal rotation angle of hip (β) (**Figure 32**). It is noted that each direction is presented by a *a*-β pair henceforth in the present doctoral dissertation (e.g., 10°–15°: $a = 10°$ and $\beta = 15°$). As the *a* and β angles increase, the fall-induced impact force is applied to a more superior and a more posterolateral aspect of the greater trochanter, respectively. When the $\beta = 0°$, the impact force is applied to a more lateral aspect. If the $\beta < 0°$, the impact is imposed to a more anterior aspect. [42,46–48,65–67,503–505,519,528,545–548] **Table 6** summarizes the directions examined by various experimental and/or FE modeling studies where multiple fall configurations were examined to investigate the effect of the direction of fall onto the greater trochanter on the fracture load.

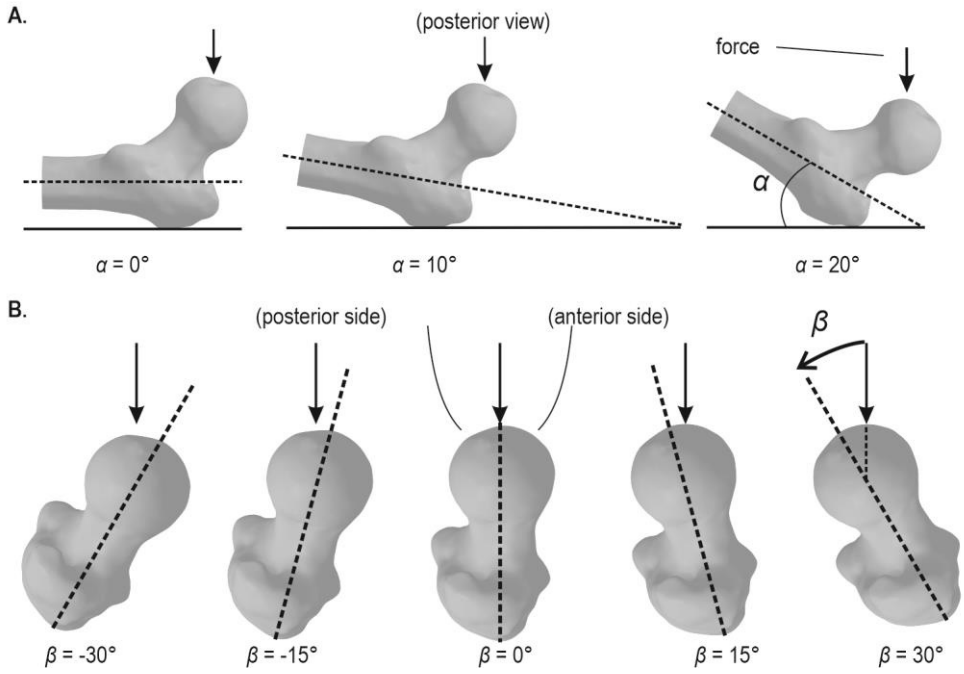

Figure 32. Different fall configurations defined by two angles, α and β. (A) The hip adduction angle (α) is defined as the angle between the femoral shaft and ground. (B) The β angle is the internal rotation angle of hip.

Table 6. Directions of fall-induced impact on the greater trochanter examined in experimental and/or FE modeling studies

Internal rotation angle, β° \ Hip adduction angle between the femoral shaft and ground, α°	-30°	0°	10°	15°	20°	30°
-30°	[46]	[505]	[503,505,546, 547]		[505]	[505]
-20°		[505]	[505]		[505]	[505]
-15°			[503,546,547]			
-10°		[505]	[505]		[505]	[505]
0°		[42,66,67,504 ,505,519]	[42,47,48,65, 503– 505,546,547]	[66,67,519,52 8]	[42,504,505]	[42,46,66,67, 504,505,519]
5°			[548]		[548]	[548]
10°		[505]	[505]		[505]	[505]
15°		[42,66,67,504 ,519]	[42,47,48,65– 67,503,504,5 19,546–548]	[66,67,519]	[42,504,548]	[42,46,66,67, 504,519,548]
20°		[505]	[505]		[505]	[505]
25°			[548]		[548]	[548]
30°		[42,66,67,504 ,505,519]	[42,47,48,65, 503– 505,546,547]	[66,67,519]	[42,504,505]	[42,66,67,504 ,505,519]
35°			[548]	[528]	[548]	[548]
45°			[47,503,546– 548]		[548]	[46,548]
65°				[528]		

Note 1: Only studies, where the multiple fall configurations were examined, are included.

Note 2: [42] – Zani et al. (2015); [46] – Bessho et al. (2009); [47] - Ford et al. (1996); [48] – Pinilla et al. (1996); [65] – Koivumäki et al.(2012); [66] - Falcinelli et al. (2014); [67] – Qasim et al. (2016); [503] - Nishiyama et al. (2013); [504] – Grassi et al. (2012); [505] - Altai et al. (2019); [519] – Taddei et al. (2016); [528] – Keyak et al. (2013); [546] - Wakao et al. (2009); [547] – Nishiyama et al. (2014); [548] - Keyak et al. (2001).

Previous studies of the multiple fall configurations revealed the followings: 1) fracture loads vary depending on the directions of the fall onto the greater trochanter [46,48,66,505,548]; 2) strain distribution pattern depends on the direction [42,504]; and 3) the multiple fall simulation is essential to examine the ability of FE-derived fracture load (= proximal femur bone strength) to predict the actual hip fracture incidents in clinical applications [46,66,67,505,545,547]. A particularly important finding was that proximal femur bone strength (fracture load) decreased by 12-38% as either or both of fall angles increased from 0° to 30° [46–48,66,505,548]. This finding indicates that hip fracture risk increases if the fall impact is applied to a more superior aspect (reflected by an increase in the *a* angle) and/or a more posterolateral

aspect (reflected by an increase in the β angle) than the lateral aspect of greater trochanter (e.g., 0°–0° direction). This is essentially in line with a recent cohort study of video-captured falls of over 600 elderly persons, which demonstrated that 77% (23 out of 30 fractures) of the fall-induced hip fractures took place when the impact was imposed on the posterolateral aspect of the pelvis whereas the impact on the lateral aspect caused only 13% of them [69]. Compared to the impact on the lateral aspect, the impact on the posterolateral aspect causes a much greater degree of torsion (twisting) about the axis of femoral shaft. This likely increases the compressive loading at the superolateral aspect of femoral neck, which explains why the proximal femur failed at the lower loads when the loading was applied to the posterolateral aspect in the above-mentioned studies.

Lastly, it is noted that the 10°–15° direction is the most adopted fall (onto the greater trochanter) configuration in the experimental and/or FE modeling studies not only where multiple fall configurations were examined (**Table 6**), but also where a single fall configuration was investigated [37,41–43,45,50,65,151,501,513,526,542]. However, it is still unclear why this fall configuration has been investigated the most. This fall configuration was introduced as the typical body position at the impact by Courtney et al. (1994) in their experimental study without the evidence [543]. Despite this, according to Grassi et al. (2020) [44], this fall configuration may date back to a study by Backman in 1957 where no physiological reasons to use this configuration were provided, either [549]. To be consistent with this and to author's knowledge, there is no evidence in the literature suggesting this configuration is the most typical and/or the most dangerous fall configuration. Recent FE modeling studies of the multiple fall configurations gave an important insight into this. It was found that the minimum fall strength (the lowest fracture load) among the multiple fall configurations (directions) can classify the hip fracture cases slightly more accurately than the fracture load in a single fall configuration (e.g., the fracture load in the 10°–15° fall direction) (AUC, 0.79-0.88 vs. 0.77, respectively) [66,67]. This highlights the importance of simulating multiple fall configurations (directions) instead of just a single fall configuration such as the 10°–15° direction.

2.6.7 Quasi-static vs. Dynamic Simulation

In the mechanical testing or FE models of the cadaveric proximal femora, a loading type can vary either quasi-static or dynamic type depending on the loading rate. In quasi-static loading, the load is applied so slowly that the deformation of the structure also takes place very slowly (= low strain rate). For example, the strain rate of $< 0.1\ s^{-1}$ is considered the quasi-static loading in the bone [137]. Consequently, the inertia force is very small and can be neglected. [550] In contrast, the loading rate is higher in the dynamic loading so that the inertial force should be considered [551]. Experimental studies reported that physiological loading conditions such as walking and running induce the strain rate ranging approximately from $0.005\ s^{-1}$ to $0.08\ s^{-1}$ in human bone [131,552–554]. Thus, this indicates that the quasi-static loading is likely still appropriate for such loading conditions. On the other hand, a fall is a truly dynamic event and the impact velocity in the fall from the standing height is on average 3 m/s or higher [478,479]. Accordingly, Jazinizadeh et al. (2020) reported that the fall-induced strain rate can reach up to $38\ s^{-1}$ at the femoral neck based on the dynamic impact experiment of cadaveric proximal femora [555]. Besides, the bone is strain rate-dependent viscoelastic and viscoplastic material such that the mechanical properties such as the elastic modulus and strength increases as the strain rate increases [97,128,131,132].

Considering above, it would be more appropriate to apply the dynamic loading in the mechanical testing or FE models of the proximal femora in the fall configuration. However, most of the FE models in the fall configuration discussed so far was simulated quasi-statically. Also, the *in vitro* mechanical testing of cadaveric femora for the validation of these FE models were performed under the quasi-static loading with the controlled constant displacement rate of 0.008-50 mm/s or controlled strain rate of $0.005\ s^{-1}$ or $0.05\ s^{-1}$. [42,46,50,64,65,493,502–504,511] It is noted that these strain rates ($0.005\ s^{-1}$ or $0.05\ s^{-1}$) result in the displacement rate of 1.7-5.5 mm/s or 17.5-32.5 mm/s, respectively [42,50,504]. This choice of the quasi-static loading is likely to avoid above-mentioned complexities associated with the dynamic event. Nonetheless, in addition to the strain rate-dependent viscoelasticity and viscoplasticity and inertial effect, these quasi-static FE modeling and corresponding mechanical testing also disregard other dynamic aspects such as, for example, shock wave propagation and a potential strain rate-dependent hydraulic stiffening effect due to the bone fluid in the pores. [128,141,151,507,513]

To realize more realistic simulation of the fall event, Helgason and his colleagues (2014, 2015, 2018, and 2019) developed the dynamic FE models in the fall (onto the

pelvis or greater trochanter) configuration based on the inverted pendulum impact testing of cadaveric femora with hip soft tissue surrogate and the biofidelic drop tower testing without the soft tissue surrogate [43,480,481,506,513,526,556,557]. Their dynamic FE models based on the drop tower testing with the impact velocity of 3 m/s also showed the high strain rate over 100 s^{-1} in the femoral neck and greater trochanter [513]. Given the strain rate-dependent mechanical properties of bone, this result also indicates the importance of the dynamic simulation of proximal femur in the fall event. However, the accuracy of predicting the experimental peak force (= ultimate fracture load) by these dynamic FE models was lower ($R^2 < 0.57$) [513,526] than those (R^2 = 0.78-0.9) from the quasi-static FE models [45,50,64,65,503,524,525,529]. A comparable R^2 of 0.85 was reported from the other dynamic FE models based on the pendulum impact testing with the hip soft tissue surrogate; however, in these models, the fall impact forces on the lateral surface of hip were estimated instead of the fracture loads of proximal femur bone [482]. Moreover, the performance of classifying the actual hip fracture cases by these dynamic FE model even with the hip soft tissue surrogate remained slightly lower (AUC = 0.72) than by the quasi-static FE models (AUC = 0.77-0.88) [66,67,557]. It is noted that it is not clear how much the strain rate-dependent viscoelasticity and viscoplasticity, and hydraulic stiffening effect can affect the fracture load. In fact, although previous experimental studies indicated that fracture loads tend to increase as the loading rate increases, conflicting results has been reported on whether the fall-induced fracture loads are statistically different ($p < 0.05$) between the quasi-static and dynamic loadings. [393,543,555,558] This may partially explain the results above why the R^2s and AUCs by the dynamic FE models are lower or comparable to those by the quasi-static models. Nonetheless, this calls for the further studies to clarify the effect of loading rate on the fall-induced fracture load. Furthermore, the quasi-static FE model was also found capable to accurately predict the fracture loads that were measured by the dynamic impact drop tower testing (R^2 = 0.84) [507]. Given these, the quasi-static FE modeling may still be considered adequate in terms of predicting the fall-induced fracture loads. Besides, it should be noted that the dynamic FE simulation is certainly more computationally demanding compared to the quasi-static simulation. For example, simulating 40 milliseconds of the fall-induced impact event required 17-30 hours in the FE models created by Fleps et al. (2018, 2019) [482,506].

The strain rate-dependent mechanical properties of bone were incorporated in aforementioned dynamic FE models by Helgason and his colleagues [43,506,513,526,556,557]. It is noteworthy that, despite its drawback, at least the

strain-rate viscoelasticity can be implemented in the quasi-static FE models [50,151] by scaling FE results with a following correction factor:

$$Scaling\ factor = \frac{\dot{\varepsilon}_{act}}{\dot{\varepsilon}_{ref}} \quad (27)$$

where $\dot{\varepsilon}_{ref}$ is the reference strain rate whereas $\dot{\varepsilon}_{act}$ is the actual strain rate that was used in the (non)destructive testing of the cadaveric femora for the validation of the FE model. The reference strain rate can be found in an experimental study from which the density-modulus/strength relationship is adopted in each FE study. For example, in the FE modeling study by Schileo et al. (2014), the density-modulus relationship was adopted from the experimental study by Morgan et al. (2003) [105] where strain rate of 0.005 s^{-1} ($\dot{\varepsilon}_{ref}$) was used in the mechanical testing of bone. [50]

2.6.8 Isotropic vs. Anisotropic Material Behavior

In the FE model, the material can be modeled as either an isotropic or anisotropic (orthotropic) material. It is modeled as the anisotropic material if its material (mechanical) properties depend on the direction of loading. In contrast, it is modeled as the isotropic if the properties are independent of the direction. [99,100] As described earlier, both cortical and trabecular bones are the anisotropic materials due to, in short, their complex multi-level hierarchical porous structures and orientations of mineralized collagen fibrils, lamellae, osteons, and trabeculae [89,106,156,158,159].

A proximal femur anisotropic FE model can be realized as a more simplified orthotropic model where the material (mechanical) properties of bone are implemented as a function of the orthotropic loading directions. However, to date, the bone tissue has been modeled as the isotropic material in nearly all proximal femur FE modeling studies. This is because insufficient data on anisotropic (orthotropic) material properties of bone, particularly for cortical bone, are available from experimental studies to realize the anisotropic FE model. [108,115] Nonetheless, a few investigators attempted to develop the anisotropic FE model of proximal femur and some examples are presented here [559–564].

Prior to the following explanation, concepts of degree of anisotropy (DA), directionality, and fabric tensor are briefly explained first for the sake of readability. To realize the anisotropic (orthotropic) material properties of bone, high-resolution (HR) 3D medical imaging [e.g., a micro-computed tomography (μCT), (p)QCT, and MRI] are typically required to capture the microscale spatial configuration of trabeculae (trabecular architecture). On the scanned cross-sectional images, a

method such as, for example, the mean intercept length (MIL) analysis is typically applied so that the trabecular directionality is considered as an ellipsoid. Its largest principal axis describes the directionality (principal or axial direction) of the bone and the ratio between the lengths of its major and minor axes characterizes the DA. This DA basically describes the ratio of the material stiffnesses between the orthogonal planes. These anisotropic information can be quantified in an orthotropic stiffness tensor (also known as a fabric tensor) where its eigenvectors and the ratio of its eigenvalues define the directionality and DA, respectively. [98,106,561,565] Although the fabric tensor with MIL analysis is the most known method for this purpose, the DA and directionality can also be defined by other methods. However, the details of the MIL and other methods are beyond the scope of this dissertation. The readers are referred to a book by Cowin (2001)[98] for the further details.

Based on HR-pQCT (resolution = 80 μm), Enns-Bray et al. (2014) developed their anisotropic FE model where the mechanical anisotropy of bone tissue was mapped to FE elements by quantifying local anisotropy using a direct mechanics method (different from the one with the fabric tensor and MIL analysis) proposed by van Rietbergen et al. (1996) [166,560]. This method successfully characterized the DA of bone tissue and directionality of all the major stress lines within trabecular network and harversian alignment of cortical bone. Such directionality was at last interpolated into the orthotropic material properties of FE models. However, the performance of this anisotropic FE model to capture the experimental mechanical behavior (e.g., stiffness) of proximal femur loaded in the fall (onto the greater trochanter) configuration was not improved compared to the isotropic model (R^2 of 0.79 and 0.78, respectively). [560]

Subsequently, Enns-Bray et al. (2016) modified their model by obtaining morphological anisotropy described by a second-order fabric tensor through the MIL analysis based on the HR-pQCT (resolution of 82 μm). Using the resulting eigenvectors and eigenvalues, the orthotropic stiffness tensor was constructed for each FE element. The directionality (of the primary eigenvector) derived by this anisotropic FE model had a good agreement with orientation of the trabecular microstructure observable in the HR-pQCT (**Figure 33**). [561] A similar good visual agreement was also reported in their earlier model in 2014 [560]. However, again, the accuracy of this anisotropic FE model to predict experimentally measured whole bone stiffness and surface strain at the femoral neck surface in the fall configuration was not different from the isotropic model: for the stiffness, R^2 of 0.69-0.72 and

0.69-0.72, respectively; for the strain, R^2 of 0.87-0.89 and 0.90-0.91, respectively [561].

Similarly, with the fabric tensor derived from the MIL analysis, Luisier, Panyasantisuk and their colleagues (2014 and 2018) developed their anisotropic FE models based on both HR-pQCT (resolution = 82 μm) and QCT scans (resolution = 0.33 mm). However, the accuracy of predicting the experimental ultimate fracture load in the fall configuration by both QCT- and HR-pQCT-based anisotropic FE models were not any higher (R^2= 0.85-0.86) than those by their isotropic models (R^2 = 0.84-0.87) [562,563].

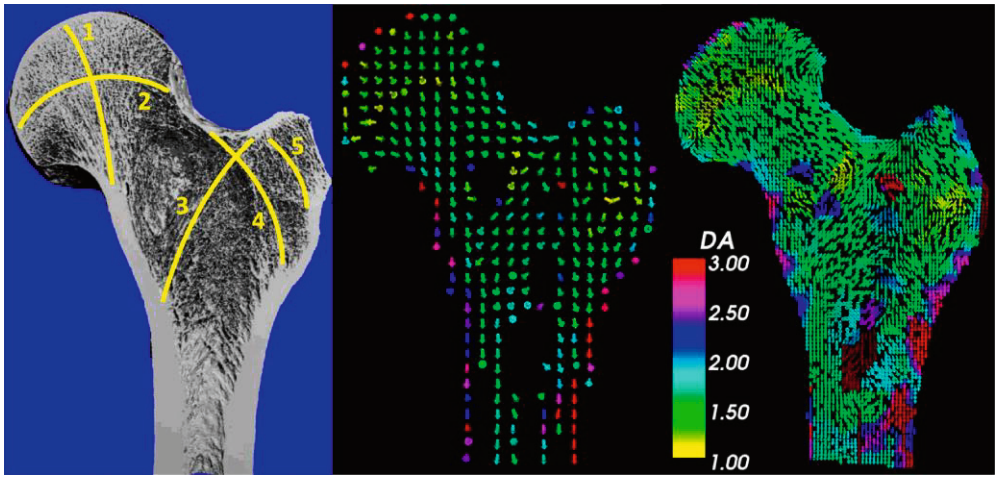

Figure 33. Anisotropic FE model by Enns-Bray et al. (2016). Comparison and a good agreement between orientation of trabecular micro-network in the segmented HR-pQCT scan (left) and directionality (of the primary eigenvectors) in the anisotropic map (middle), and FE elements (right) with DA. Segmented HR-pQCT scan (left) and each yellow line representing characteristic stress line within proximal femur: 1) the primary compression, 2) primary tension, 3) secondary tension, 4) secondary compression, and 5) greater trochanteric lines. (Reprinted, with permission, from Enns-Bray et al. (2016) [561] © 2016 IPEM. Published by Elsevier Ltd.)

In summary, based on these results, the addition of anisotropic material properties of bone did not improve the accuracy of predicting the experimental mechanical behavior of proximal femur including the fracture load in the fall (onto the greater trochanter) configuration compared to the isotropic model. Panyasantisuk et al. (2018) hypothesized that this was because the loading pattern in the fall configuration does not match with the orientation of trabecular alignment unlike in the standing or walking. Thus, the directionality of bone tissue is less sensitive to the loading pattern in the fall. [562] Besides, the anisotropic FE models

typically require the high resolution medical imaging (e.g., HR-pQCT) and accordingly the high computational cost due to a large number of the FE elements (e.g., ~3 hours due to 10 million FE elements) [560]. Therefore, its clinical use is likely not practical. Nonetheless, these call for further studies to improve the proximal femur anisotropic FE model to capture the mechanical behavior of the proximal femur more accurately in the fall configuration.

2.6.9 Applications

The developed proximal femur FE models have been used to investigate various aspects of the hip fracture, and some of the applications are briefly discussed here. First, the age- and sex-dependent declines in the proximal femur bone strengths have been confirmed by several FE modeling studies [528,566–569]. For example, by investigating the proximal femur bone strengths (= ultimate fracture loads) of an age-stratified cohort of 362 males and 317 females (age ranged from 21 to 89 years) in the fall configuration, Keaveny et al. (2009) demonstrated that the decline in the FE-predicted proximal femur bone strengths from age 30 to 85 years was larger in female (55%, from ~4900 N to ~2200 N) than in male (39%, from ~5200 N to ~3200 N). Likewise, the increase in the annual decline from age 45 to 85 years was higher in female (1.3% to 2.8% declines) than in male (1.1% to 1.7%). Furthermore, it was observed that the notable decline in the proximal femur bone strength began in the mid-40s in female whereas it started a decade later in male. [567] Similarly, Keyak et al. (2020) reported that the larger decline in the proximal femur bone strength (= fracture onset load) in the fall configuration from age 30 to 90 years in female (~65-70%, from ~1900 N to ~600 N) than in male (~45%, from ~2000 N to ~1100 N) based on the same cohort [568]. These results confirmed not only the age-dependent decline in the proximal femur bone strength, but the rate of its loss is higher in females. Together with the approximately twice higher likelihood of fall in female than in male [379–382], this also explains why more females experience the hip fractures than males.

Next, the FE models can predict experimental fracture load more accurately than DXA- or QCT-derived a/vBMD-based predictions (R^2 of 0.77-0.80, 0.55-0.69, and 0.65-0.72, respectively) [484,485,570,571]. Besides, the classification performance of hip fracture cases out of non-cases (AUC) was higher by FE models than by proximal femur, femoral neck, or trochanteric aBMDs, especially when multiple fall configurations (directions) were simulated (AUC = 0.77-0.88 vs. 0.73-0.79 by FE

models and aBMD, respectively) [66,67]. These suggest the high potential of the FE models for its clinical use. Furthermore, the fracture initiation at superolateral cortex of femoral neck due to substantially thin cortex and unusually high compressive loading in the fall (onto the greater trochanter) configuration was well reproduced by numerous FE modeling studies [41,43,45–47,50,64,505,521,548,572].

Importantly, the beneficial effect of (long-term) specific exercise loading on proximal femur bone has also been explored but in a few FE modeling studies [61–63]. Warden, Fuchs, and their colleagues (2020, 2021) reported that, compared to non-dominant leg, the long-term (> 6 years) impact loading induced from baseball or softball pitching resulted in 13% and 11% higher FE-predicted proximal femur bone strength (the fracture onset load) for the fall (onto the greater trochanter) configuration in the dominant leg in young adult males (aged 18-30 years) and females (aged 18-25 years), respectively [62,63].

Also, the effects of glucocorticoid and anti-osteoporosis drugs [such as Denosumab, parathyroid hormone (PTH), and alendronate] on proximal femur bone strength in the fall configuration have been studied with the FE models [573–575]. For example, Lian et al. (2005) reported that a >1 year glucocorticoid treatment in postmenopausal females aged over 50 years has a detrimental effect on the FE-predicted bone strength (= ultimate fracture load, reduced by 16 %) [573]. In contrast, a 36-month (once every 6 months) Denosumab treatment in osteoporotic individuals (aBMD T-score < -2.5, aged between 60 and 90 years) increased the FE-predicted bone strength (= ultimate fracture load) by 8-9 % compared to their baseline values [574,575]. Furthermore, Keaveny et al. (2008) showed that a 2-year treatment of PTH, alendronate, or their combination can slightly improve the FE-predicted bone strength (= ultimate fracture load) by 4-8 % compared to baseline in the postmenopausal osteoporotic females (aged 55-85 years) [576].

Lastly, the negative effect of micro- or nongravitational environment from the long-term spaceflights [e.g., missions in the International Space Station (ISS)] on the proximal femur bone strength and the effect of in-flight exercise program on prevention of the decline in bone strength have also been explored with the FE models by Keyak and her colleagues [577–579]. They investigated pre- and post-spaceflight proximal femur bone strength (= fracture onset load) of 10 male and 1 female ISS astronauts (aged 40-55 years, flight durations ranged from 4.3 to 6.5 months). Regardless of exercises the astronauts performed to maintain their bone strength [2h/day, 4 days/week including treadmill running at 0.6G, cycling, squat, and some resistance exercises using the interim Resistive Exercise Device (iRED, the maximum loading capability up to 1334 N)], the FE-predicted proximal femur

bone strength in the fall configuration declined by 2.0% (0.6% to 3.9%) per each month during the spaceflight. Such decline was substantially greater than their monthly decline in the proximal femur aBMD (1.2% decline on average, ranged 0.4% to 1.8%). An average reduction in the proximal femur bone strength after 4.3 to 6.5 months spaceflight was ~12%. Such reduction is certainly considerable and is even equivalent to 27% of the lifetime loss. [577] Thankfully, in-spaceflight exercises were found to mitigate such substantial reduction of the proximal femur bone strength and apparently the magnitude of loading appeared a key factor. Sibonga et al. (2019) found that the ~6-month in-spaceflight exercise using the Advanced Resistive Exercise Device (ARED, the maximum loading capability up to 2669 N) resulted in significantly less decline in the FE-predicted proximal femur bone strength (= ultimate fracture load) in the fall configuration (by ~4% decline compared to the pre-flight strength) than using iRED (by ~10% decline) [579].

2.6.10 Sectional Summary – Prediction of Fracture Load by Different Proximal Femur FE Models

The FE modeling studies which reported both experimentally measured and FE-predicted fracture loads in the fall configuration, and their correlations (R^2) as the accuracy of the FE models predicting the experimental loads are summarized in **Table 7**. The FE model specifications such as its linearity (linear or nonlinear), an/isotropic and in/homogeneous material property assignment, and simulation types (quasi-static or dynamic) are also listed. Based on this table, several points are noteworthy.

First, the FE-predicted mean fracture onset loads ranged from ~1700 N to 3100 N in the fall configuration in people aged 52-92 years old [50,64]. These values appeared slightly lower than the FE-predicted ultimate fracture loads (~2000-3900 N) in the similar aged people (46-100 years old) [45,65,503,513,524–526,529,563]. This is in line with the assumption mentioned earlier that the FE-predicted fracture onset load is likely smaller than the ultimate fracture load (the peak force).

Next, theoretically speaking, an anisotropic and/or dynamic FE modeling of the proximal femur in the fall configuration is undoubtedly more realistic simulation. However, despite its higher computational cost, the accuracy of predicting the experimental fracture loads by the anisotropic or dynamic FE models (R^2: ≤ 0.86 and ≤ 0.85, respectively) [482,513,526,562,563] were not different from those by the isotropic or quasi-static FE models (**Table 7**). Besides, the good accuracy (above-mentioned R^2 of 0.85) reported by the dynamic model by Fleps et al. (2019) was for predicting the experimentally measured fall-induced impact force (imposed on the lateral surface of the hip) instead of the fracture load (the load applied on the proximal femur surface) [482]. In contrast, the accuracy of predicting the fracture load was reported no greater than R^2 of 0.56 by the dynamic FE models by Ariza et al. (2015) and Enns-Bray et al. (2018) [513,526].

Furthermore, the accuracies (R^2) of the nonlinear FE models to predict the experimental fracture loads appeared comparable to those by the linear models despite, again, its higher computational cost. The R^2 of 0.81-0.90 are reported by the linear FE models (for predicting both fracture onset and ultimate loads) [50,64,503] whereas R^2 of 0.78-0.87 were reported by the nonlinear FE models (**Table 7**) (NOTE: R^2 from only the isotropic and quasi-static FE models are compared here) [45,65,524,525,529]. Importantly, the fracture onset loads were predicted quite accurately by the linear FE models (R^2 of 0.81-0.90) [50,64].

Lastly, the homogeneous material property assignment (two-material model) was not used in any of those FE modeling studies which compared the FE-predicted fracture loads with the experimental values (**Table 7**). As mentioned earlier, Taddei et al. (2006) reported that the accuracy of predicting the experimentally measured stresses by the homogeneous FE model is only slightly lower than the inhomogeneous model (R^2: 0.89 and 0.91, respectively). However, again, the accuracies of predicting the experimentally measured strains and fracture loads were not measured in this FE modeling study. Besides, only the physiological loading conditions (e.g., single leg stance) were simulated using a single cadaveric femur. [112] Therefore, additional studies are necessary to validate the use of homogeneous material properties in the proximal femur FE models in predicting the (experimental) strain and fracture load based on the stress- and strain-based failure criteria in the fall (onto the greater trochanter) configuration with a larger sample size. To summarize, the density-based inhomogeneous isotropic, linear, or nonlinear quasi-static proximal femur FE models appear the adequate choice to predict the fall-induced hip fracture loads to this day.

Table 7. Comparisons of different proximal femur FE model types

Study	N femur	Age Mean (range)	Lin or NoL	Homo- or Inhomo	Iso or Ani	QS or DY	Fall direction (α-β)	Experimental Fracture load (kN)	FE-predicted Fracture load (kN)	R^2	SEE (kN) or RMSE (%)
Keyak et al. (1998) [64]	18	70.3 (52-92)	Lin	Inhomo	Iso	QS	20°-35°[a]	2.34±1.29[b]	OL: 1.65±0.74[b]	0.90[c]	1.23 kN
Keyak & Lang (2012) [524]	S.A.	S.A.	NoL	Inhomo	Iso	QS	25°-35°[a]	2.34±1.32[b]	UL: 2.86±0.77[b]	0.81[d]	N.A
Dragomir-Daescu et al. (2011) [45]	9	60.0 (51-69)	NoL	Inhomo	Iso	QS	10°-15°	4.07±1.77	UL: 3.42±1.21	0.86	N.A
Koivumäki et al. (2012) [65]	40	80.5 (55-100)	NoL	Inhomo	Iso	QS	10°-15°	3.46±1.02[b]	UL: 3.47±1.08[b]	0.87	0.39 kN
Dall'Ara et al. (2013) [525]	36	76.0 (46-96)	NoL	Inhomo	Iso	QS	30°-20°[e]	3.12±1.14	UL: 2.64±1.18[b]	0.85	0.44 kN
Roberts et al. (2009) [529]	76	74.2 (55-98)	NoL	Inhomo	Iso	QS	10°-15°[f]	3.57±1.82	UL: 3.91±1.95[b,g]	0.78	N.A
Schileo et al. (2014) [50]	14	76.6 (62-84)	Lin	Inhomo	Iso	QS	10°-15°	2.89±1.21[h]	OL: 3.10±1.03[h]	0.81[h]	0.57 kN[h]
Nishiyama et al. (2013) [503]	20	76.7 (55-95)	Lin	Inhomo	Iso	QS	10°-15°	2.65±0.81[b]	UL: 1.96±0.62[b]	0.81	0.28 kN
Ariza et al. (2015) [526]	15	76.0 (50-96)	NoL	Inhomo	Iso	DY[i]	10°-15°	2.49±0.68[b]	UL: 2.21±0.55[b]	No R^2 (p = 0.8)	23%
Enns-Bray et al. (2018) [513]	S.A.	S.A.	NoL	Inhomo	Iso	DY[i]	10°-15°	2.66±0.67[b]	UL: 2.76±0.83[b]	0.56	15%
Fleps et al. (2019) [482]	11	77.1 (54-94)	NoL	Inhomo	Iso	DY[j]	α = ~15° β = N.A.[k]	Peak impact force: 5.45±1.31[b,l]	Peak impact force: 5.6±1.1[b,l]	R^2 = 0.85	10.7%

Luisier et al. (2014) [563]	72	76.0 (46-96)	NoL	Inhomo	Iso Ani	QS	30°-20°[e]	3.09±1.14[b] 3.07±1.16[b]	UL: 3.24±1.56[b] UL: 3.47±1.72[b]	0.84 0.86	0.43 kN[m] 0.45 kN[m]
Panyasantisuk et al. (2018) [562]	S.A.	S.A.	NoL	Inhomo	Iso Ani	QS	30°-20°[e]	N.A	N.A.	Iso: 0.87 Ani: 0.85-0.86	0.41 kN 0.42-0.44kN

Note 1: N.A. = not available, S.A. = same as above.

Note 2: This table summarizes proximal femur FE modeling studies which reported both experimentally measured and FE-predicted fracture loads in the fall (onto the greater trochanter) configuration with the coefficient of determination (R^2). Following FE model features are included: linear (Lin) vs. nonlinear (NoL); homogeneous (Homo) vs. inhomogeneous (Inhomo); isotropic (Iso) vs. anisotropic (Ani); and quasi-static (QS) vs. dynamic (DY). The experimental fracture load was typically defined as the maximum/peak load (ultimate fracture load, abbreviated as UL) in the force-displacement curve. In contrast, the FE-predicted fracture load type varies from either 1) the fracture onset load (OL), or 2) UL (the peak load or specified otherwise). The R^2 was based on the linear regression analysis (specified otherwise) and error estimates such as standard error of estimate (SEE) or root-mean-square deviation (RMSE) are also presented.

[a] this information was provided by the author, professor Keyak.

[b] estimated based on the graph

[c] by nonlinear regression

[d] The R^2 of 0.81 was obtained from their test set (N = 9).

[e] The internal rotation angle (β) of femoral neck was not clearly specified, but assumed to be 20° based on the description.

[f] this fall-induced impact direction was assumed based on their another study by Orwoll et al. (2009) [501].

[g] the UL was assumed as the load at 4% of displacement of femoral head with respect to the greater trochanter based on their other study [501].

[h] calculated based on values reported.

[i] Dynamic FE models based on drop tower impact testing without hip soft tissue surrogate.

[j] Dynamic FE models based on inverted pendulum impact test with hip soft tissue surrogate.

[k] An α angle (in °) was assumed to be ~15° and set by the pelvic rotation of the inverted pendulum testing in the coronal plane. A β angle was not specified.

[l] the maximum impact force imposed onto the lateral surface of the hip (not on the greater trochanter) during the impact test.

[m] Since SEE was originally reported in %, SEE in kN was estimated.

2.7 Computational Anatomy

In the previous sections, the age-dependent changes in the femoral neck in relation to the fall-induced hip fracture risk (particularly on femoral neck fracture) and the effect of various exercises on the proximal femur bone were discussed. For example, regarding the former aspect, substantial superolateral cortical thinning with aging due to the asymmetric loading from the predominant daily physical activity such as walking was found associated with the fall-induced hip fracture [35,37–40,392,396]. Such cortical thinning leads to the failure of the superolateral femoral neck due to the compressive yielding or buckling in the fall (onto the greater trochanter) configuration [37,38,396]. Besides, the supporting trabecular bone structure under the superolateral cortex also deteriorates with aging, contributing further to the fragility of the proximal femur [104,399]. With respect to the latter aspect, numerous observational studies of athletes and nonathletic controls showed that the long-term weight-bearing H-I and/or O-I loadings from the childhood/adolescent to young adulthood can induce the beneficial osteogenic adaptation within proximal femur reflected in aBMD, BMC, and structural variables in the femoral neck (e.g., CSA, Z, and buckling ratio) [56–58,60,273,275,312–315,317]. Importantly, young adult female athletes with the history of these impact exercise loadings had the thicker cortex at the fracture-prone superolateral cortex compared to the controls to some extent [60], suggesting the potential of these impact exercise loading types to prevent the hip fractures. Moreover, the osteogenic effect of these impact loadings within the proximal femur have also been confirmed at least for aBMD and BMC by (R)CTs regardless of age [299,305,344,351,352,354–356,364]. However, these observations and nearly all studies discussed so far (in Section 2 - Literature Review) were limited to either the 2D planar analyses of cross-sectional images or 3D analyses of up to a few millimeter-thick image volume (e.g., mid-femoral neck volume) based on DXA, QCT, and/or MRI except for a few exceptions [61–63,345]. Therefore, more comprehensive 3D analyses on whole structure of proximal femur/femoral neck and spatial distribution of bone within its structure were not explored, to author's knowledge, at least until year ~2010.

To address this issue, for the last two decades, a set of image-analyzing algorithms called computational anatomy (originally developed for brain imaging analysis) has been adopted into bone research. This method models anatomical structures of bone from each individual (acquired from the medical image scans) as 3D curves, feature maps, surfaces, and volume to aim to merge them across the study participants in a standardized space. This enables to perform 3D spatial statistical analyses on bone's

structure and distribution of bone. Consequently, 3D visual examination of, for example, the followings becomes possible: the effect of anti-osteoporotic drug or exercise on the bone health; and the effect of structural defect within proximal femur on its strength between the hip fracture patients and healthy individuals. [580,581] The typical procedures in the computational anatomy are briefly explained first.

First, anatomic feature variables (e.g., cortical thickness and vBMD) are calculated at every location across the selected bone (e.g., proximal femur) of each individual based on the medical image scans. Then, the individual bone scans with these computed features are registered into a standardized space by spatial normalization so that same anatomic locations (e.g., a tip of the greater trochanter) are corresponded each other between different individuals' bones and subsequently spatial comparison of these anatomic features becomes possible between the individuals/groups. This spatial normalization is typically achieved through following three steps: 1) creating or choosing the standardized space, 2) performing the affine transformation to correct for size, translation, and rotation of the individual scans so that they are rearranged to fit the standardized space, and 3) adjusting the remaining anatomical variabilities by nonlinear registration of the individual rearranged scans. Typically, the last two steps are performed together. Next, 3D statistical feature maps are created for the registered anatomic feature variables in the standardized space via a method like statistical parametric mapping (SPM) or Student's t test statistical maps (T-maps). These methods result in the spatial presentation of regional statistical differences of the featured variables, mapped with either *p*-values or t-values. This allows the visual detection of the region where statistically significant differences in the selected anatomic feature variables (e.g., cortical thickness and vBMD) are present, for example, between groups (hip fracture patients vs. healthy individuals) in the cross-sectional study or between baseline and follow-up in the longitudinal study. To study the proximal femur anatomy, several computational anatomy methods have been developed based on the (Q)CT scans: for example, cortical bone mapping (CBM), voxel-based morphometry (VBM), and tensor-based morphometry (TBM). [580,581] The following sections will briefly explain each of these methods and their applications in the hip fracture research. To be in line with the topic of the present doctoral research, their applications in investigating the effect of exercise on the proximal femur will be discussed in the end.

2.7.1 Cortical Bone Mapping (CBM)

Cortical bone mapping (CBM) enables the measurement of the following variables: cortical thickness (in mm), cortical mass surface density (in mg/cm^2, the cortical mass per unit cortical surface area), cortical vBMD (in mg/cm^3, the cortical mass per unit cortical volume), and endocortical (or endosteal) trabecular vBMD (in mg/cm^3, the average volumetric trabecular bone density close to the endocortical surface). In CBM, the segmentation of the obtained (Q)CT images of each study participant is first performed to create a triangulated surface mesh consisting of 5,000-15,000 vertices, which are distributed uniformly over the surface of proximal femur. Next, the measurement of the CBM data (above-mentioned four variables) is performed at each of these vertices based on the CT data. The triangulated surface mesh with this CBM data of each proximal femur is registered into a canonical femoral surface (a standardized space in CBM) prior to the SPM. This canonical femoral surface represents an averaged proximal femoral surface constructed based on hundreds of femora. [582–585] The further details on the CBM method can be found in the studies by Treece et al. (2010, 2012, and 2015) [583–585].

Using CBM on clinical CT scans, Poole, Treece, and their colleagues (2012, 2015, 2017) compared the proximal femur structure and spatial distribution of bone between hip fracture cases (femoral neck and trochanteric fractures) and non-cases in the old population aged over 65 years [582,586,587]. They reported that the old people with femoral neck and trochanteric hip fractures had substantially thinner cortical walls (up to 20-30%) at femoral neck and trochanteric regions, respectively, compared to their age-matched controls. A particularly important finding was that there was a thumbnail-sized patch of focal osteoporosis (significantly up to 20-30% less cortical thickness compared to controls, $p < 0.05$) at the fracture-prone superior femoral neck cortex (especially at the head-neck junction) in the femoral neck fracture cases (**Figure 34**, showing only female data). [582,586].

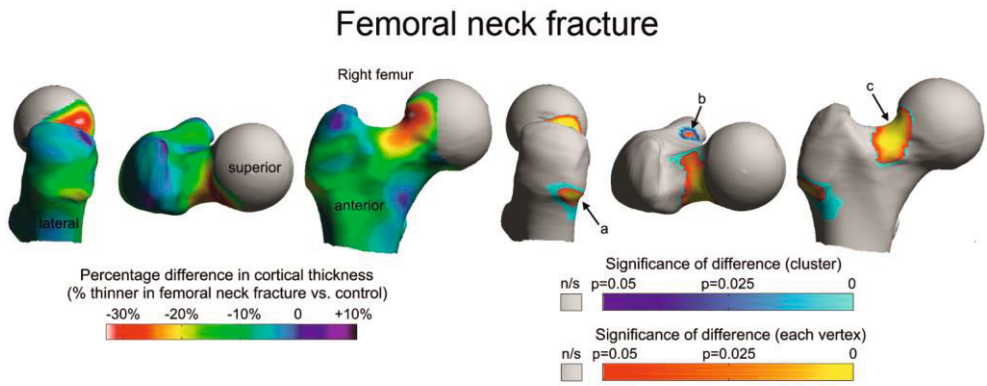

Figure 34. CBM example 1 – Comparison of 3D cortical thickness distribution between females with femoral neck fracture and age-matched controls. (Left) A feature map showing the between-group mean % difference in the cortical thickness. (Right) Another map showing statistically significant ($p < 0.05$) between-group difference in the cortical thickness. (Adapted under CC BY 4.0 license from Poole et al. (2012) [586] © 2012 Poole et al.)

Furthermore, the cortical mass surface density was reported to be ~15-20% lower in this region in the femoral neck fracture cases of both sexes [582,587]. This patch of the lower cortical mass surface density extends around inferior femoral neck, and toward the anterior part of trochanter, especially in the female cases (A in **Figure 35**). The female trochanteric fracture cases had significantly >15% lower focal cortical deficit (cortical mass surface density) similar to femoral neck fracture cases but covering wider area of the superior femoral neck, and lateral trochanter (C in **Figure 35**). [587] Also, compared to the age-matched controls, endocortical trabecular vBMD was significantly >20-30% lower at the superolateral femoral neck, distal inferoposterior femoral neck, and some anterior aspect and inferoposterior aspect of the greater trochanter in the femoral neck fracture cases of both sexes [B in **Figure 35** (showing only female data)] and throughout almost whole proximal femur except for the medial aspect of femoral head in trochanteric fracture cases [D in **Figure 35** (showing only female data)] [582,587]. Importantly, compared to DXA-based aBMD, the CBM variables (cortical mass surface density and endocortical trabecular vBMD) improved hip fracture discriminating ability (AUC in ROC) as follows: from 0.76 to 0.82 and 0.71 to 0.77 for the femoral neck and trochanteric fractures in the old males (aged > 65 years), respectively [582]; from 0.77 to 0.84 and from 0.74 to 0.82 in the old females (aged > ~65-70 years), respectively [587]. This suggests the high potential of CBM for its clinical use.

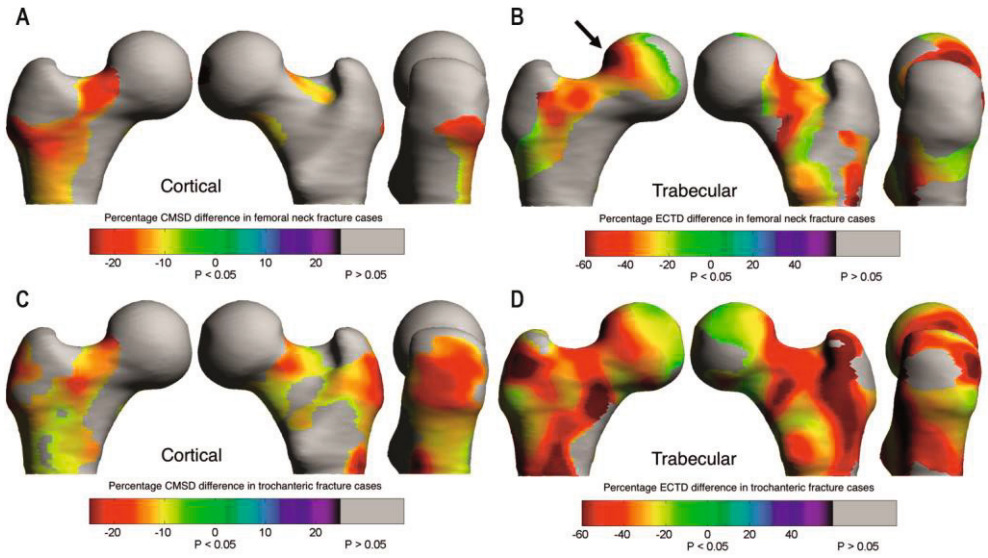

Figure 35. CBM example 2 – Comparisons of 3D distributions of 1) cortical mass surface density and 2) endocortical trabecular vBMD between female femoral neck/trochanteric fracture cases and controls. Cortical mass surface density (abbreviated as CMSD) map (A) and endocortical trabecular vBMD (abbreviated as ECTD) map (B) between the femoral neck fracture cases and controls. CMSD map (C) and ECTD map (D) between the trochanteric fracture cases and controls. The % and statistically significant ($p < 0.05$) between-group differences of these variables are presented. In this figure, statistically nonsignificant ($p > 0.05$) differences compared to the controls are displayed gray. (Adapted under CC BY 4.0 license from Poole et al. (2017) [587] © 2016 The Authors. Published by Elsevier Inc.)

2.7.2 Voxel-based Morphometry (VBM)

Voxel-based morphometry (VBM) enables mapping of 3D spatial distribution of vBMD. Hounsfield units (HU) of obtained CT scans were first converted to QCT density (equivalent K_2HPO_4 density or concentration of calcium hydroxyapatite) based on the calibration phantoms. Subsequently, the QCT density values are converted into vBMD. Next, 3D representations of proximal femur bone shape are obtained by the segmentation of proximal femur contours prior to its registration into a minimum deformation template (MDT, a standardized space in VBM) by spatial normalization. This MDT characterizes the average size and shape of proximal femora from a selected study cohort and is created by multiresolution affine and nonlinear transformation. To ensure the continuity of the spatial distribution of vBMD across proximal femur, spatially normalized and calibrated images were smoothed by a filtering method like an isotropic gaussian kernel. Similar

to SPM in CBM, statistical differences in the spatial distribution of vBMD between groups were analyzed by creating Student's t test statistical maps (T-maps) with a general linear model approach. [397,588]

Using VBM, Carballido-Gamio et al. (2013) demonstrated the effect of aging on the spatial distribution of bone within the proximal femur. The spatial vBMD difference between young (aged < 45 years, mean 34.1 years), middle-age (aged < 59 years, mean 51.9 years), and older American females (aged ≥ 60 years, mean 72.5 years) and its T-map are presented in **Figure 36**. They demonstrate the 3D age-dependent rapid bone loss in the superior cortex, medial aspect of the femoral head, and trabecular bone in the femoral neck and trochanteric regions. In contrast, the vBMD in the load-bearing inferior femoral neck was largely preserved with aging. This was coincided with regions where FE-derived high vonMises stresses (**Figure 36**) were observed in the single-leg stance configuration. This suggests that walking as the predominant daily mechanical loading led to the preservation of bone at the load-bearing inferior femoral neck. [397]

Furthermore, they compared the spatial vBMD distribution between older Icelandic females with hip fractures and their age-matched controls without hip fractures (aged > 67 years, mean 79 years). In proximal femora of the female hip fracture patients compared to those of the female controls, there were large areas of the significantly lower vBMD in the fracture-prone superior and load-bearing inferior femoral neck cortex, and in the trabecular bone in the intertrochanteric region (**Figure 37**). Importantly, their FE simulation demonstrated that these superior femoral neck and intertrochanteric regions coincide with where the higher von Mises stresses and lower (more compressive) minimum principal (compressive) strains were observed in the fall (onto the greater trochanter) configuration (**Figure 37**). This suggests that these deficits likely contribute to the hip fracture. [397]

Lastly, using VBM and surface SPM (which maps cortical features such as the cortical thickness, cortical vBMD, and endocortical trabecular vBMD, similar to CBM) [589], Yu, Carballido-Gamio, and their colleagues (2017) investigated the differences in the spatial vBMD distribution and cortical features between old Chinese females with femoral neck fractures (mean age: 71 years) and trochanteric fractures (mean age: 76 years). Compared to the femoral neck fracture cases, those with trochanteric fractures had the significantly lower vBMD (incl. cortical and endocortical vBMD) in the greater trochanter. In contrast, the femoral neck fracture cases had significantly thinner superior femoral cortex compared to the trochanteric cases. [590] Importantly, these 3D-based results are closely in line with the previous 2D-based studies which suggested that, in the fall, the femoral neck fractures are

likely due to the structural deficits (thin cortical wall) at the superolateral femoral neck [37–40] whereas the trochanteric fractures are most likely attributed to the low trochanteric aBMD [372,405–409].

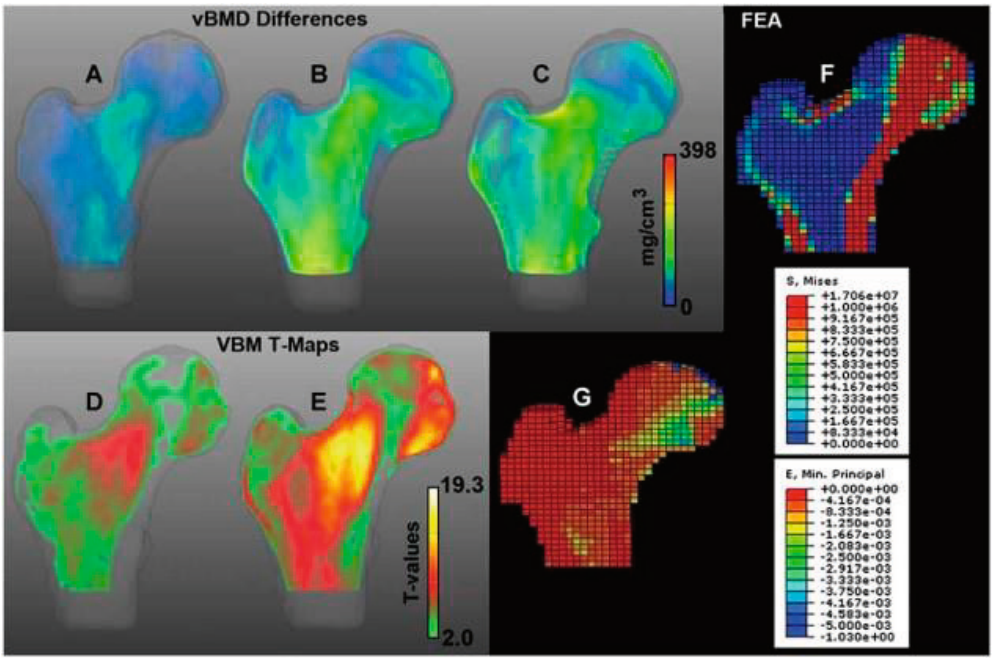

Figure 36. VBM example 1 – The effect of age on 1) spatial distribution of vBMD and 2) FE-derived stress and strain distributions in a single leg stance configuration. 3D feature map displaying spatial vBMD difference between young and middle-age American females (A); between young and older American females (B); and between young and older Icelandic control females without hip fractures (C). VBM-vBMD T-maps at the mid-coronal cross-section between young and middle-age American females (D); and between young and older American females (E). In these maps, the voxels were displayed transparently if no vBMD differences were found. Positive difference and T values mean the higher vBMD in the younger females compared to the older females. FE-derived von-Mises stress (F) and minimum principal (compressive) strain (G) distributions at the mid-coronal cross-section in a control female in a single-leg stance configuration, respectively. (Reprinted, with permission, from Carballido-Gamio et al. (2013) [397] © 2013 American Society for Bone and Mineral Research).

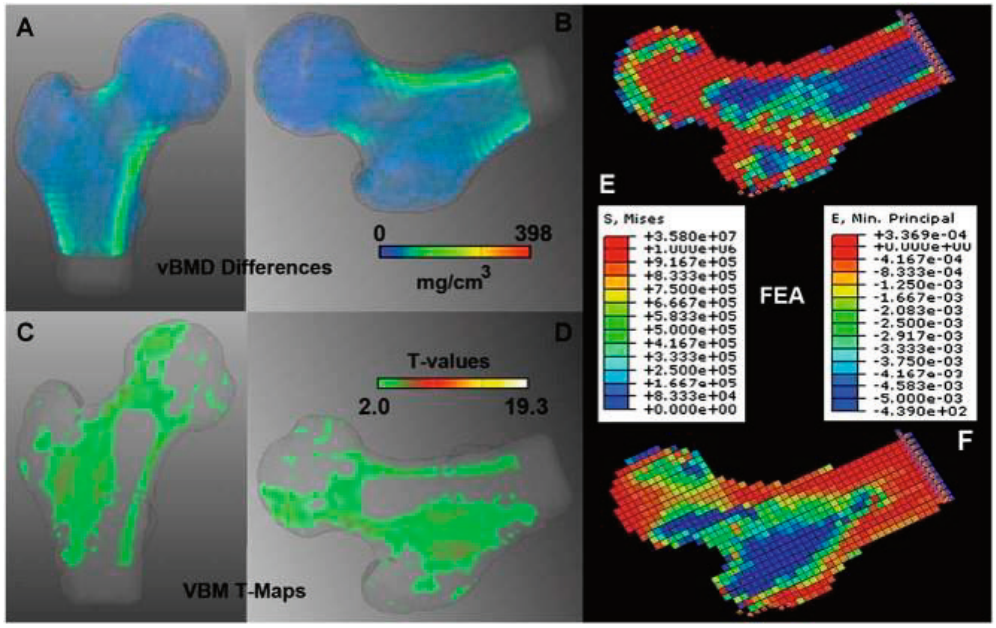

Figure 37. VBM example 2 – Differences in 1) spatial distribution of vBMD and 2) FE-derived stress and strain distributions between the old Icelandic females with and without hip fractures. 3D feature map displaying the spatial vBMD difference between older Icelandic female fracture cases and controls (A); and the rotated version of A (B). VBM-derived vBMD T-map at the mid-coronal cross-section between older Icelandic female fracture cases and controls (C); and the rotated version of C (D). In these maps, the voxels were displayed transparently if no vBMD differences were found. Positive difference and T values mean the higher vBMD in the controls compared to the hip fracture cases. FE-derived von-Mises stresses (E) and minimum principal (compressive) strain (F) at the mid-coronal cross-section in a female with the hip fracture in a fall configuration, respectively. (Reprinted, with permission, from Carballido-Gamio et al. (2013) [397] © 2013 American Society for Bone and Mineral Research).

2.7.3 Tensor-based Morphometry (TBM)

Tensor-based morphometry (TBM) is a deformation-based shape analyzing technique using (Q)CT images, which can quantify local shape difference compared to the average-sized and -shaped proximal femur. TBM is similar to VBM by including the following similar procedures: image segmentation to create the 3D representation of the proximal femur, registration of segmented images to a standardized space (MDT, the average-sized and -shaped proximal femur representing a selected cohort) by spatial normalization, smoothing the normalized images by the filter method (e.g., an isotropic gaussian kernel method), and T-maps

using a general linear model. Unlike VBM, a displacement vector for each voxel during the nonlinear transformation in the spatial normalization is computed, describing the local anatomic variability. This results in dense maps of the displacement vectors known as deformation fields. TBM analyzes these deformation fields to construct 3D feature maps depicting the shape in the form of local volume changes. The Jacobian matrix (J) of the deformation is calculated for each voxel by taking spatial derivatives of the nonlinear deformation. Based on the determinant of the Jacobian matrix [det(J)], the local volume change around each voxel is evaluated [if det(J) = 1, no local volume change; if det(J) < 1, local volume contraction; if det(J) > 1, local volume expansion]. [398,591]

Using TBM, Carballido-Gamio et al. (2013) investigated whether internal structural changes of the proximal femur are associated with aging and hip fractures, similar to their aforementioned study with VBM [397]. Compared to the young American females (aged < 45 years, mean 34.1 years), a particularly important observation was that proximal femora of the older American females (aged ≥ 60 years, mean 72.5 years) had statistically significant 1) expansion of the central aspect of the trabecular bone compartment in the femoral neck and 2) contraction of the superior femoral neck cortical bone (**Figure 38**). These local changes were also observed in the old Icelandic females with hip fractures (aged > 67 years, mean 79 years) compared to their age-matched controls, confirming their association with the hip fracture (**Figure 38**). The combination of these local volume changes results in the superior cortical thinning. [398] This cortical thinning and its association with hip fracture are consistent with previous findings of not only 2D analyses of femoral neck cross-section by Mayhew et al. (2005) and Poole et al. (2010), but also CBM-based 3D analyses by Poole et al. (2012) and Treece et al. (2015) [38,40,582,586]. Furthermore, distinct from the age-related structural changes, Carballido-Gamio et al. (2013) observed that there was a focal contraction of superior femoral neck cortex and focal expansion of the trabecular bone compartment in the superior femoral neck in hip fracture cases, compared to the controls [398]. The location of these focal changes was closely in line with that of aforementioned thumbnail-sized patch of focal osteoporosis (20-30% thinner cortical wall, **Figure 34**) observed at the superior femoral neck cortex, particularly at the head-neck junction, identified by Poole, Treece, and their colleagues in their CBM studies [582,586]

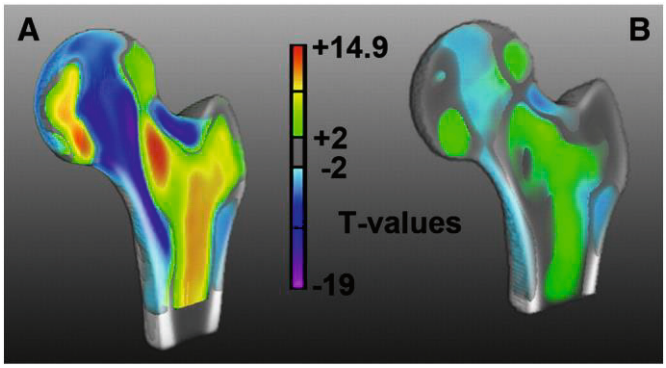

Figure 38. TBM example – 3D morphometric changes within proximal femur associated with aging and hip fracture. Internal views of the anterior half of the proximal femur are presented. (A) Local volume changes (expressed in T-value) associated with ~30-40 years of aging. (B) Local volume changes associated with hip fractures. Colors corresponding to the positive T-values mean the local volume expansion while those corresponding to the negative T-values indicate the local volume contraction. (Reprinted, with permission, from Carballido-Gamio et al. (2013) [398] © 2013 Elsevier Inc.)

With VBM, TBM, and surface SPM, Marques, Carballido-Gamio, and their colleagues (2018) reported the effect of sex on the spatial vBMD distribution, and cortical structure in the old Icelandic people (aged 66-92 years). Particularly important observation was, compared to the male hip fracture cases, the female fracture cases had the following statistically significant lower values: 1) vBMD in the superior femoral neck, and intertrochanteric region; 2) cortical vBMD in anterior and posterior femoral neck and almost whole trochanteric region, 3) endocortical trabecular vBMD in the superior femoral neck and almost whole trochanteric region. This study showed the sex-difference in 3D bone structure and spatial distribution of bone in hip fracture cases and confirmed the importance of analyzing male and female fracture cases separately in the evaluation of hip fracture risk. [592] In addition to the approximately twice higher likelihood of fall [379–382] and the larger age-dependent decline in the FE-predicted proximal femur bone strength in the fall configuration in female [567,568], the above-mentioned results further explains why the hip fracture is more common in female than in male

2.7.4 Application – Effect of Exercise on Proximal Femur

With the computational anatomy methods described so far, the effects of exercise on proximal femur have been investigated. Using CBM, Allison et al. (2015)

observed in a 12-month RCT that daily unilateral multidirectional hopping exercises significantly ($p < 0.05$) increased cortical mass surface density and endocortical trabecular vBMD in the proximal femur including the fracture-prone superolateral femoral neck (**Figure 39**): 6% increase in the cortical mass surface density at the superoposterior femoral neck and 10% increase in endocortical trabecular vBMD in the superior femoral neck in old males (aged 65-80 years) compared to their baseline values [346].

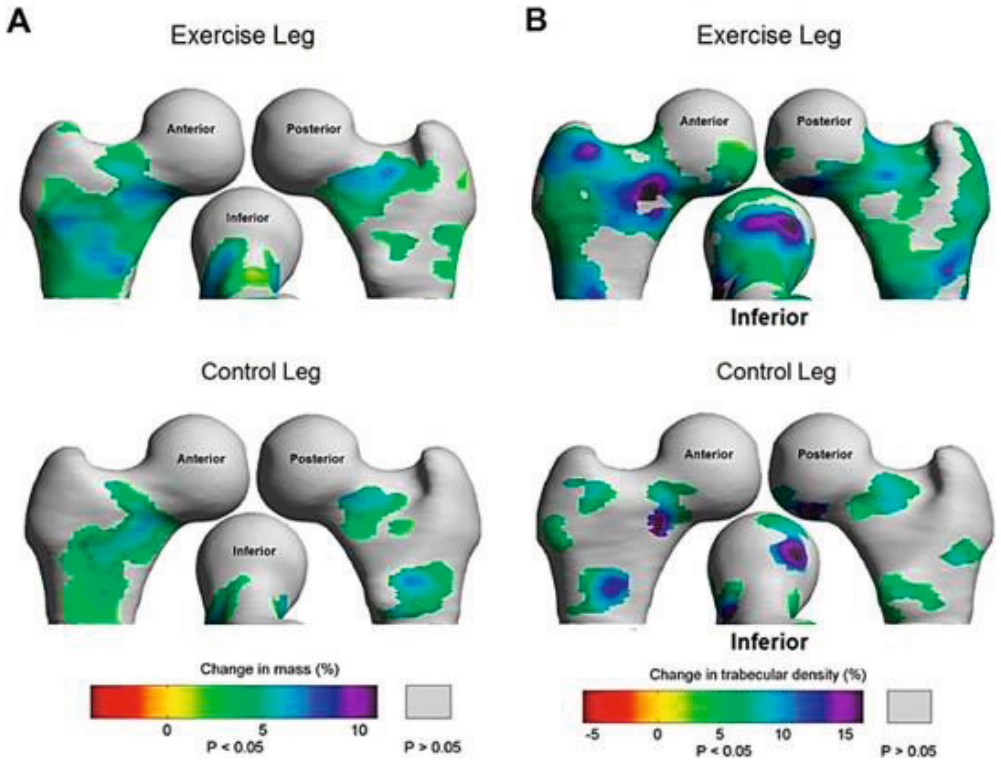

Figure 39. Application of CBM - The effect of 12-month daily unilateral multidirectional hopping exercise on the cortical mass surface density and endocortical trabecular vBMD within proximal femur. This figure shows the % differences in the cortical mass surface density (A) and endocortical trabecular vBMD (B) between at the baseline and follow-ups, respectively. (Reprinted, with permission, from Allison et al. (2015) [346] © 2015 American Society for Bone and Mineral Research).

Similarly, using VBM, Lang et al. (2014) reported that a 16-week squats and deadlifts exercises intervention (4 sets per session, three times a week) significantly ($p < 0.05$) increased cortical vBMD on average by 12% in the anterior and posterior regions of femoral head and neck in male and female subjects (mean age: 36.1 years,

ranging 25-55 years), compared to their baseline values. However, based on their FE simulation of these proximal femur, it was demonstrated that that these beneficial adaptations did not translate into the higher proximal femur bone strength in the fall (onto the greater trochanter) configuration. Nonetheless, the effect of these exercise on the fall-induced hip fracture risk should remain inconclusive because of the short study duration (14 weeks). [61]

Using VBM and CBM, Warden et al. (2020) and Fuchs et al. (2021) investigated the dominant-to-nondominant leg difference in 3D spatial distribution of vBMD and cortical structure in proximal femora of young male baseball pitchers (mean age: 26.8 years, mean 18.1 years of playing), male long/high jumpers (mean age: 21.1 years, mean 6.3 years of playing), and female softball pitchers (mean age: 20.4 years, mean 13.6 years of playing) to explore the effect of asymmetric exercise loading on the proximal femur [**Figure 40** (only female pitchers' cases shown)]. In the asymmetric exercise loadings, the dominant leg (e.g., the take-off leg in the jumping or the contralateral side of a throwing arm of the baseball or softball pitchers) experiences more impact-generating loading than the non-dominant leg. Although beneficial spatial adaptations in terms of vBMD and CBM-variables (cortical thickness, cortical vBMD, and endocortical trabecular vBMD) were observed in some parts of femoral head, inferior femoral neck, intertrochanteric, and/or greater trochanteric regions, there were no such apparent benefits at the fracture-prone superior femoral neck except for a few small patches of some higher values. Interestingly, the female pitchers even had a small area of the lower cortical vBMD, cortical thickness, and endocortical trabecular vBMD at the proximal-to-middle superoposterior femoral neck in the dominant side compared to the nondominant side (**Figure 40**). Nonetheless, these beneficial adaptations likely explain, at least partially, why both male and female pitchers had the higher proximal femur bone strengths in the fall (onto the greater trochanter) configuration in their dominant proximal femora compared to the non-dominant side. While the male pitchers had the 13% higher ($p < 0.05$) FE-predicted fracture onset load, the female pitchers had ~11% and 5% higher fracture onset and ultimate fracture loads, respectively. In contrast, there was no such dominant-to-nondominant difference in the proximal femur bone strength in the male jumpers. The jumpers might have been exposed to more symmetric loading (e.g., during training). Besides, their duration of the asymmetric exercise loading (mean: 6 years) was at least twice shorter than those in the pitchers (~14-18 years). Therefore, it can be speculated that these may explain why the male jumper did not have the dominant-to-nondominant difference in their proximal femur bone strength. [62,63]

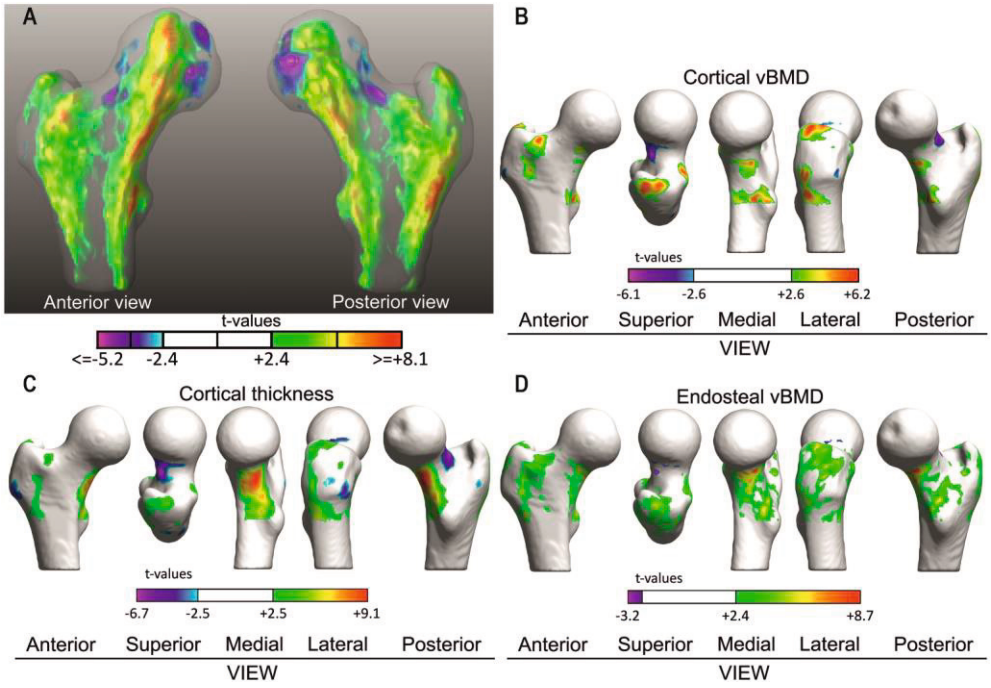

Figure 40. Application of VBM and CBM – The dominant-to-nondominant leg differences in the spatial distribution of VBM-derived vBMD, CBM-derived cortical thickness, and cortical and endocortical trabecular vBMDs within proximal femur in the female softball pitchers. (A) VBM-derived vBMD T-map. (B) Cortical vBMD T-map. (C) Cortical thickness T-map. (D) Endosteal vBMD T-map. The statistically significant side differences are shown as T-maps where positive and negative t-values correspond to significantly higher and lower values in the dominant side than the nondominant side, respectively. (Adapted, with permission, from Fuchs et al. (2021) [63] © 2021 Elsevier Inc.)

To summarize, with the computational anatomy methods, the RCT and observational studies confirmed 1) the beneficial 3D adaptations induced by some weight-bearing impact loading exercises within the proximal femur including the fracture-prone superolateral femoral neck, and 2) the higher proximal femur bone strengths in athletes with the impact loading histories. Thus, the exercise-induced beneficial spatial adaptations can likely translate into the reduction of hip fracture. Nonetheless, more research is certainly needed to investigate whether 1) other types of exercise can induce the beneficial spatial adaptation and 2) they can contribute to the higher proximal femur bone strength in the fracture-causing fall situation.

2.8 Summary of Literature Review

Bone provides the structural framework for the body and enables the movements by acting as the lever arms for the muscle while resisting the mechanical loads [73,76,77]. Its mechanical properties depend on not only its heterogeneous density distribution [97,105–107,109,113,132] but also strain rate [97,98,128,131,132,141]. The bone is also an anisotropic material so that its mechanical properties vary depending on the direction of loading [89,106,108,158,159]. Furthermore, it is a mechanosensitive tissue adapting its mass, structure, and material properties to habitual mechanical loading environment [2,3]. Not all mechanical loading types are equally osteogenic, and the effectiveness may differ from one anatomical site to another [10–13]. In general, based on the animal experimental studies, the effective osteogenic mechanical loadings are the dynamic types [14,15] consisting of sufficiently high strain (loading) magnitude [16–18] generated at high strain rate [19–21] or frequencies [22–24].

Effects of the various exercise-induced mechanical loading on human proximal femur bone properties such as bone mineral mass and density, and structural variables have been investigated in the numerous observational and (R)CT studies using non-invasive medical imaging such as DXA, QCT, and MRI. The weight-bearing moderate-to-high vertical (H-I) and/or multidirectional (O-I) ground impact-generating exercise loadings (common in e.g., jumping/hopping, plyometrics, ball games, gymnastics, dancing) during childhood to young adulthood were found particularly effective to induce beneficial adaptations in the proximal femur reflected in aBMD, BMC, and femoral neck structure. [12,59,329–333,337,341,342] In contrast, the repetitive ground impact (R-I, e.g., endurance running) and high-magnitude exercise loadings (H-M, e.g., weight- and powerlifting or high-intensity resistance trainings) were found less effective whereas the non-ground-impact, repetitive exercise loading (R-NI, e.g., swimming) was found ineffective during these periods [12,334–337]. Although the beneficial effect of these impact exercise loadings is smaller, these impact exercise loadings alone or the combined impact exercises with the H-M exercises were found effective to maintain the bone mass or induce the small cumulative gains after young adulthood [348,352,354–356]. In addition, the moderate R-I exercise loading (jogging combined with walking and stair climbing) was found likely effective [351] while the H-M exercise alone was found ineffective in the adulthood [349,350,353,356]. A particularly important finding in regard to the effect of specific exercise was that young adult female athletes with the history of these H-I and O-I exercise loading had the regionally thicker cortical bone

at the superolateral femoral neck to some extent [60], which is prone to fracture in the fall [37,44]. This suggests the potential of these impact exercise types to reduce the hip fracture incidents. However, there have been very few studies [61–63] which investigated whether these beneficial adaptations in proximal femur bone to specific exercise loading histories translate into reduced hip fracture risk.

Hip fracture is the major public health problem [25] and common in people aged > 65 years [377], especially in female [27,28]. Importantly, over 90% of the hip fractures are caused by the fall [51–53] where the high impact force is applied to the posterolateral or lateral aspect of hip (greater trochanter). A mean fall-induced impact force of ~4200-5200 N has been estimated for an average individual based on the impact velocity, and pelvic stiffness and mass [462,474]. This high hip fracture incidence is due to the fall-induced unusual loading mechanism [37,44] and thinning of fracture-prone superolateral femoral neck cortex with aging, particularly at its posterior aspect [38,40]. Various factors are associated with the hip fracture risk [379,411]. The risk had been previously evaluated mainly by femoral neck aBMD alone or the assessment tools like FRAX which considers clinical risk factors with/without femoral neck aBMD [450–452]. However, it has been found that (FE-derived) fracture load (proximal femur bone strength) can predict fall-induced hip fracture risk more accurately than these aBMD-based assessment or FRAX [66,67]. Therefore, the risk should also be evaluated by estimating the fracture load (= proximal femur bone strength that is equal to the minimum applied load to cause the fracture) since it enables the more comprehensive assessment by considering not only factors affecting the bone strength but also fall loading conditions [446].

The estimation of *in vivo* fall-induced hip fracture load can be realized by the FE modeling. Importantly, it was found that the FE-derived fracture load can predict the hip fracture risk more accurately than aBMD- and FRAX-based risk assessment [66,67]. Due to this, over the past last few decades, numerous research has been conducted to develop the accurate proximal femur FE models. The model linearity can vary either linear or nonlinear model depending on the desired fracture load types: fracture onset/yield load or ultimate fracture load, respectively. It was found that density-based inhomogeneous isotropic, linear, or nonlinear quasi-static FE models can predict the fracture load similarly or more accurately compared to the more realistic anisotropic or dynamic FE models, respectively. [45,50,64,65,482,503,513,524–526,529,562,563]

The fall-induced fracture load and impact force vary depending on the direction of fall onto the greater trochanter or hip [46,48,66,467,505,548]. A fall is an unpredictable event. Thus, it is difficult to predict its direction and the weakest fall

direction is likely specific to each femur. Accordingly, several proximal femur FE modeling studies demonstrated the importance of simulating the multiple fall configurations (directions) with respect to assessing the hip fracture risk with the fracture load [66,67].

Lastly, nearly all hip fracture studies and those investigated the effect of various exercise loading on the proximal femur bone at least until year ~2010 were limited to either the 2D planar analyses of cross-sectional images or 3D analyses of up to a few millimeter-thick image volume (e.g., mid-femoral neck volume) based on DXA, QCT, and/or MRI. This issue was recently overcome by utilizing the computational anatomy methods such as CBM, VBM, and TBM in the bone research [580,581] which enables 3D analyses of bone. However, there has been very few studies [61–63,346] which performed 3D analyses of proximal femur bone adaptation to specific exercise loading histories using the computational anatomy methods.

3 PURPOSE OF STUDY

The purpose of the present doctoral research was to investigate whether the beneficial structural adaptations in proximal femur cortical bone in response to long-term specific exercise loading from childhood to young adulthood translate into higher proximal femur bone strength to reduce hip fracture risk in a fall. The results were anticipated to help identify effective exercise types to prevent the fall-induced hip fractures. Utilizing proximal femur medical image data from young athletic females with distinct long-term exercise loading histories and their nonathletic control counterparts, this was first addressed by creating individual 3D proximal femur FE models in a single fall configuration (direction) and performing following subsequent analyses:

- **Publication I**. Regional cortical stress analysis in the femoral neck was performed where octant-wise cortical stress on the femoral neck cross-section in proximal, middle, and distal femoral neck regions were compared between each of the exercise loading groups and the control group.
- **Publication II**. Hip fracture load was estimated for each proximal femur and subsequently its between-group comparison was performed. Additionally, the location and mode of fracture were analyzed.

The athletic bones are adapted to the long-term specific exercise loadings characterized by not only the loading magnitude, rate, and frequency but also direction. Moreover, because a fall is an unpredictable event, it is difficult to forecast its direction and the weakest fall direction is likely specific to each femur. To address these aspects, the study was extended by performing:

- **Publication III**. Individual proximal femur FE models were simulated in the multiple fall configurations (a total of 12 directions per each proximal femur) to examine whether the specific exercise-induced higher proximal femur bone strength (fracture load) depends on the direction of fall onto the greater trochanter. Concerning the latter aspect above, a minimum fall strength among the multiple fall directions was also obtained for each proximal femur. Consequently, their between-group comparisons were performed.

Long-term specific exercise-induced beneficial structural adaptation in the femoral neck cortical bone was observed in the same study participants in the previous research. However, the analyses were limited to 2D planar analyses of femoral neck cross-section. Therefore, it was of great interest to obtain information on 3D morphological adaptation of proximal femur cortical bone to the specific exercise loading. Such information may help understand the high proximal femur bone strength due to the specific exercise loading histories (the potential findings from the **Publications I-III** above). This was addressed by performing:

- **Publication IV**. A new computational anatomy method, Ricci-flow conformal mapping (RCM), was implemented to obtain 3D distribution of the cortical thickness and fall-induced principal strains within each proximal femur. Their spatial between-group comparisons were subsequently performed.

4 MATERIALS AND METHODS

To achieve the objectives of the present doctoral research, the proximal femur MRI data of young adult female competitive athletes with five distinct exercise loading histories and their nonathletic (non-competitive) female controls were obtained from a previous study by Nikander et al. (2009) [60]. Based on this data set, the followings were performed: the FE modeling of individual proximal femur in the fall (onto the greater trochanter) configuration(s) (for **Publications I-III**) and RCM-based 3D spatial analyses of proximal femur (for **Publication IV**). Subsequently, the obtained features of interest from these processes were compared between each of the exercise loading groups and the control group through statistical analyses. The workflow of the present doctoral research is briefly summarized in **Figure 41**.

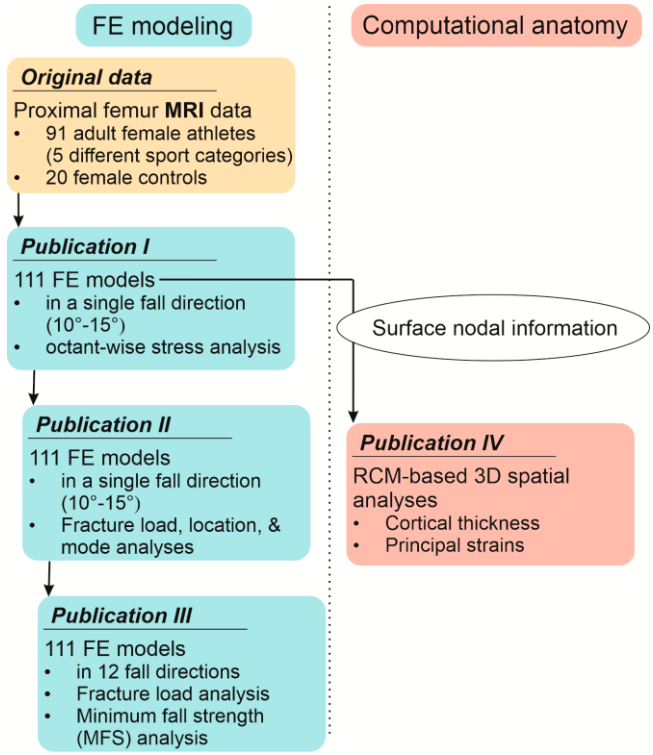

Figure 41. Workflow from the original MRI data to Publications I-IV.

4.1 Study Participants

Ninety-one young adult female athletes (aged 24.7 ± 6.1 years), competing different sports actively at national or international level, were recruited from national sports associations and local athletic clubs whereas 20 nonathletic female control participants (23.7 ± 3.8 years) were recruited mostly from local medical and nursing schools. It is noted that these control participants were habitually active by engaging in recreational exercise 2-3 times a week but had never participated in any sports at the competitive level. In accordance with exercise categorization scheme by Nikander et al. (2005, 2006) [11,57], the athletes were classified into five distinct exercise loading groups based on the characteristic loading patterns of their sports: high-impact (H-I) (nine triple- and ten high-jumpers); odd-impact (O-I) (nine soccer and ten squash players); high-magnitude (H-M) (17 powerlifters); repetitive impact (R-I) (18 endurance runners); and the repetitive, non-impact group (R-NI) (18 swimmers). The study protocol was approved by the Ethics Committee of the Pirkanmaa Hospital District, and written informed consent was acquired from each participant prior to data collection. [60]

Body height and weight (BW) of the participants were obtained in light indoor clothing without shoes with standard methods while the body fat-% and lean body mass (LM) were measured with DXA (GE Lunar Prodigy Advance, Madison, WI, USA). Also, their training history (competing years, and weekly sport-specific training hours and training sessions) during at least the five preceding years were collected through the questionnaires. [60]

4.2 MRI Scanning Procedure

A 1.5-T MRI system (Avanto Syngo MR B15, Siemens, Erlangen, Germany) was used to scan a hip region of each participant's dominant side, covering the proximal femur from the top of the femoral head to the subtrochanteric levels of the femoral diaphysis. The imaging sequence was a standardized axial T1-weighted gradient echo volumetric interpolated breath-hold (VIBE)-examination with the following settings: FOV 35 × 26 cm, TR 15.3 ms, TE 3.32 ms, in-plane resolution (pixel size) 0.9 mm × 0.9 mm, slice thickness 1 mm without gaps, echo train length = 1, flip angle = 10°, matrix 384 × 288. The sagittal, axial, and coronal images of the hip region were scanned with two half-Fourier acquisition single-shot turbo spin-echo localization series. The reconstructed imaging plane was adjusted so that the cross-sectional

plane of the femoral neck was perpendicular to the femoral neck axis. [60] Most previous studies of proximal femur FE models have been created based on QCT scans [43,45,50,64,65,151,482,501–503,510,511,513,525,562,563]. However, the MRI scan was used in the present research because exposing fertile young adult females to ionizing radiation from QCT for non-diagnostic purposes would have been ethically unacceptable.

4.3 FE Model Construction

4.3.1 Segmentation of Proximal Femur MRI Data

Based on the scanned MRI data, the 3D proximal femur geometry was extracted and converted into a FE software-compatible file format. First, the proximal femur MRI scans of all participants were manually segmented. This was performed by delineating the periosteal and endocortical boundaries of the cortical bone using a touch panel (Wacom Tablet Cintiq 12WX, Wacom Technology Corp., Vancouver, WA, USA) with a medical image processing software called ITK-SNAP (www.itksnap.org) [593]. The *in vivo* precision of delineating these boundaries in the femoral neck has been reported ~1% [284]. In addition, in the **Publication III**, it was demonstrated that the effect of segmentation error on the estimated fracture load (RMS-CV, 2.3%; mean CV, 0.9%) was marginal in terms of examining the expectedly much higher between-group differences in the fracture load. The magnitude of these errors were also comparable to those reported in the literature [589,594,595]. (The estimation of fracture load will be explained shortly). Next, the segmented bone geometries were converted into a volume mesh with its surface smoothed by a Taubin method [596], followed by the generation of 3D solid bodies in SolidWorks (SolidWorks Corp., Waltham, MA, USA). This smoothing method was adopted due to its known performance in minimizing the shrinkage of the geometry during the smoothing. Finally, the created 3D proximal femur solid bodies were imported into ANSYS (ANSYS Inc., Houston, PA, USA) for FE meshing and analysis. Further details on the processes above can be found in the **Publication I**. The resulting proximal femur geometry consisted of an individually segmented outer cortical bone layer, enfolding the inner trabecular bone volume within the endocortical bone boundary.

4.3.2 Simulated Directions of Fall onto the Greater Trochanter

To simulate the fall configuration(s), the direction of fall onto the greater trochanter (direction of fall-induced impact) was defined by two angles: a hip adduction angle (a, an angle between the femoral shaft and the ground) and an internal rotation angle (β, a rotation about the femoral shaft) (**Figure 42**). It is noted, again, that each direction is denoted by a a-β pair throughout this doctoral dissertation (e.g., 10°–15°: a = 10° and β = 15°). As the a and β angles increase, the fall-induced impact force is applied to a more superior and a more posterolateral aspect of the greater trochanter, respectively. When the β = 0°, the impact force is applied to a more lateral aspect. In the **Publications I and II**, the most frequently examined direction (10°-15°) [37,41–43,45,50,65,151,501,513,526,542,543] was used. In the **Publication III**, a total of 12 different fall configurations were simulated by increasing the a and β angles in steps of 10° and 15°, respectively (**Figure 42**). These 12 fall configurations covered the wide ranges of directions of fall onto the greater trochanter examined by the most of multiple fall experimental and FE modeling studies [42,46–48,65–67,503–505,519,528,545–548] (**Table 6**).

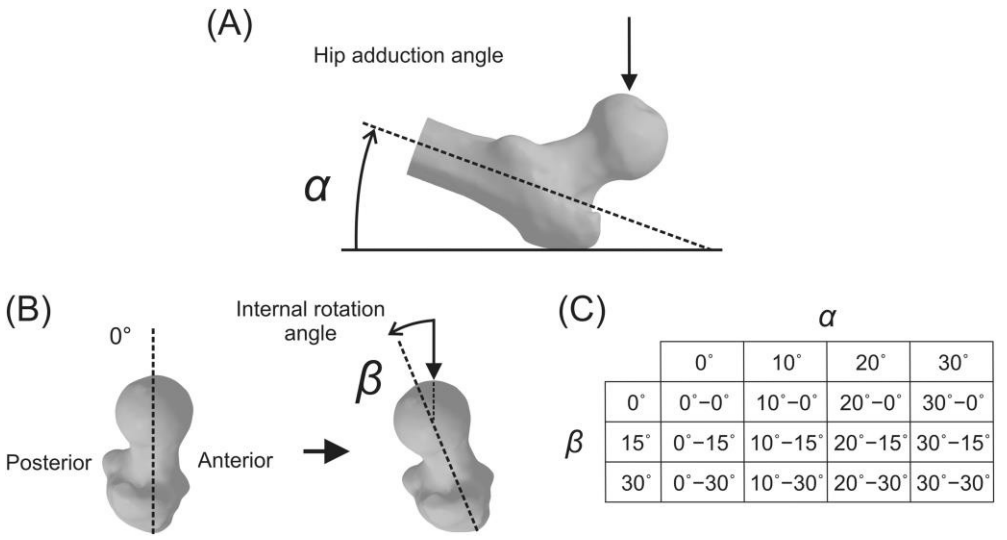

β \ α	0°	10°	20°	30°
0°	0°–0°	10°–0°	20°–0°	30°–0°
15°	0°–15°	10°–15°	20°–15°	30°–15°
30°	0°–30°	10°–30°	20°–30°	30°–30°

Figure 42. Fall configurations in the present proximal femur FE model. Each direction of fall onto the greater trochanter was defined by (A) the hip adduction angle (α) and (B) the internal rotation angle (β) of femoral neck. A total of 12 different directions of the fall (C) were simulated for each proximal femur in the Publication III whereas a single direction (10°-15°) was used in the Publications I and II. (Reprinted under CC BY 4.0 license from Publication III © 2022 The Authors).

4.3.3 FE Model Specifications and Boundary Conditions

The cortical and trabecular bone tissues of the proximal femur were modeled as homogeneous isotropic, linear elastic materials. Young's moduli of 17 GPa [497,498,500] and 1500 MPa [497,498] were assigned to entire cortical and trabecular bone compartments, respectively. Poisson's ratio was assumed to be 0.33 [497,498,500]. Since comparable cortical moduli of ~15-20 GPa have been found for the adult femora (aged 22-61 years) [120], the present choice of 17 GPa was deemed adequate. Concerning the trabecular modulus, Sylvester and Kramer (2018) [597] reported that the organ-level modulus for the whole trabecular compartment within the proximal femur likely lies between 500 MPa and 1500 MPa based on a comparison of their recent homogeneous proximal femur FE models with the experimental data by Cristofolini et al. (2010) [598]. Given that the present study participants were young female athletes and physically active controls, the adoption of 1500 MPa was considered reasonable in the present research. To simulate the fall configuration(s), similar BCs from the previously validated FE studies [43,50] were adopted in the present research (**Publications I-III**) (**Figure 43**).

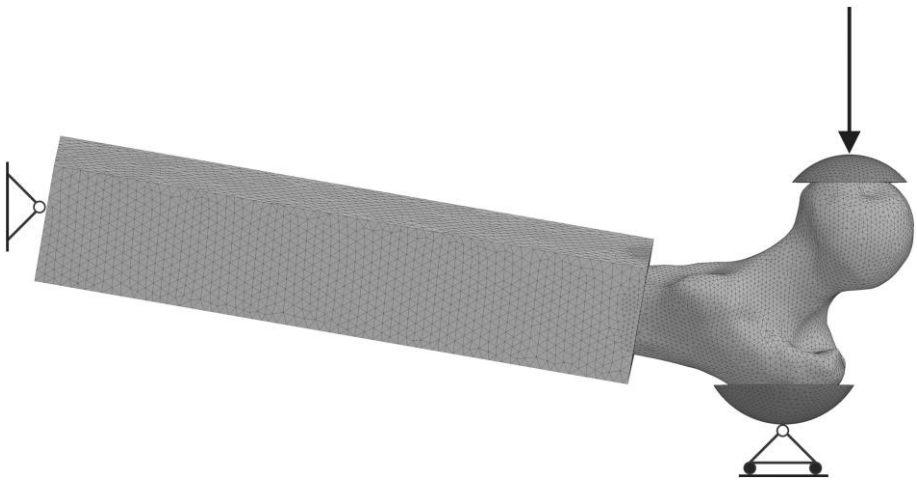

Figure 43. Boundary conditions to simulate the fall. The BCs were applied through the protecting PMMA caps and a 200 mm long aluminum pot with Young's moduli of 2 GPa and 70 GPa, respectively. The loading force was applied to the entire upper face of the femoral head PMMA cap at the desired fall angle whereas the restraining BC was applied to the trochanteric PMMA cap such that the movement in the direction of the force was prohibited. The distal end of the aluminum pot was restrained with the hinge-type BC. This restraining BC allows the free rotation in the quasi-frontal plane while all other degrees of freedom were restrained. [50] Further details on the BCs are found in the Publication I. (Reprinted under CC BY 4.0 license from Publication III © 2022 The Authors).

It is noted that, as a consequence of adopting the homogeneous material property assignment, the present doctoral research exclusively assesses the influence of the cortical structure/geometry on the hip fracture behavior while the potential influence of inhomogeneous trabecular bone distribution was not examined. The structural deficit and deterioration of superolateral femoral cortex are associated with femoral neck fracture [37–40,44] whereas the low bone mineral density (particularly trochanteric aBMD) was found as the stronger predictor for trochanteric fracture [372,405–409]. Given this, the use of the homogeneous assignment may have resulted in focusing more on the femoral neck fracture than the trochanteric fractures.

All materials were meshed with a 10-noded tetrahedral finite element. In the **Publications I and II**, a 1 mm element size was used to mesh the whole proximal femur geometry, the boundaries between the distal aluminum pot, two PMMA caps, and the proximal femur. This element size was considered to produce satisfactorily accurate FE-derived (von Mises) stress results based on the mesh convergence analysis: the error estimating the stress was 2.4% with the 1 mm mesh. However, to realize total of 1332 FE models (111 individual proximal femur bones × 12 fall configurations) in the **Publication III**, it was necessary to decrease the computational cost. Thus, it was explored whether a larger element size could be used to evaluate the hip fracture load and its between-group difference. Based on another mesh convergence analysis, the error estimating the fracture load and the relative between-group difference were consistently below 3% (2.9% and 1.5 %, respectively) for the 2 mm element-sized FE models. Therefore, the 2 mm element size deemed satisfactory and adopted in the **Publication III**. The element size for the aluminum distal pot was kept 4 mm for the **Publications I-III**. The details on each of above-mentioned convergence analyses are found in the **Publications I and III**, respectively.

4.3.4 Magnitude of Applied Load

In **Publication I**, the subject (participant)-specific peak impact force was applied to the proximal femur to examine the stress distribution within the proximal femur in the fall configuration. This subject-specific peak impact force (F_{peak} in N) was estimated using the **equation (21)**:

$$F_{peak} = \sqrt{2gh_{cg}KM} \tag{21}$$

where g is the gravitational constant (9.81 m/s^2), h_{cg} is the height of center of gravity (assumed to be 0.51 × body height in m), K is the stiffness constant (71 kN/m), and M is the effective mass [$7/20$ × total body mass (kg)] [471,472,474,475]. In contrast, in the **Publications II and III**, the arbitrary magnitude of the impact force (100N) was applied. This was because the fracture loads could be estimated by taking an advantage of the linearity of FE models.

4.4 Post-FE Analyses

4.4.1 Octant-Wise Cortical Stress Analysis (Publication I)

Based on the impact force applied, the nodal von Mises stresses in the femoral neck's cortical bone were computed from each FE model. Subsequently, these stress results were utilized to perform octant-wise cortical stress analyses (**Figure 44**) in MATLAB (MathWorks, Inc., Natick, MA, USA). First, the whole femoral neck cortical volume was split into three longitudinal sub-volume sites (regions) along the femoral neck axis: proximal, middle, and distal sites. These three sites were then divided into equal 45° octant regions, each of which represents a distinct anatomic orientation of the respective cross-section of the femoral neck: inferior (I), inferoanterior (IA), anterior (A) superoanterior (SA), superior (S), superoposterior (SP), posterior (P), and inferoposterior (IP) octants. Femoral neck axis was utilized as a center for the octant-division instead of the geometric centroid, but otherwise this octant-division was carried out similar to previous studies [38,60,104,599]. Finally, for each participant, the mean nodal von Mises stress was calculated for each octant (referred to as octant cortical stress henceforth) in all three sites [a total of 24 octant cortical stress values per participant (8 octant cortical stresses × 3 sub-volume sites)].

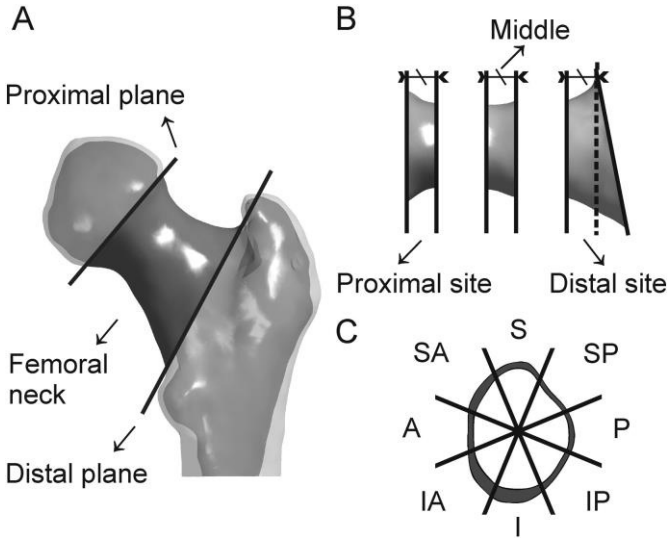

Figure 44. Octant-division of femoral neck cross-section in three longitudinal sub-volume sites. Details of these procedures can be found in the Publication I. (Reprinted from Publication I © 2016 Elsevier Inc.)

4.4.2 Fracture Load and Mode (Publications II and III)

Contrary to the use of von Mises stress in the **Publication I**, a method using a simple maximum principal strain yield criterion, proposed by Schileo et al. (2008, 2014) [50,395], was adopted in the **Publications II and III** to compute the fracture load for each proximal femur. This choice was made by considering the followings: the bone fracture is strain-driven [531–533]; and the asymmetric yield strength of bone [178].

First, nodal strains together with their coordinates were obtained from the outer surface of each proximal femur FE model. Subsequently, each nodal strain was averaged with its neighboring nodal strains within a 3 mm radius to minimize local effects and to ensure the hypothesis of continuum media. Based on this averaged nodal strain tensor, the principal strains were then calculated for each node. It is noted that the maximum and minimum principal strains describe the tensile and compressive strains, respectively. The fracture load was defined as a load when a maximum or minimum principal strain of one surface node exceeds the tensile yield limit (0.73%) or the compressive yield limit (-1.04%), respectively [178]. By taking advantage of the present linear FE model, this was performed by increasing the magnitude of the applied load until this condition was met. [50,395] It is noted that the present method estimates the load at the onset of fracture (fracture onset load) similar to the previous studies [41,50,64]. The use of the linear FE model was considered appropriate for the estimation of the fracture onset load since the strains of human proximal femur increases highly linearly up to failure (for the 1st failure at the superolateral femoral neck cortex in the two-steps failure as mentioned earlier) [42,394,504] and the proximal femur typically experiences the brittle fracture at least for the 1st failure characterized by little or no plastic deformation [37,42,44,394,395]. Furthermore, the fracture mode (compression or tension) was determined for each femur in the **Publication II**. Estimations of the fracture load, location (described shortly), and mode were carried out in MATLAB

In the **Publication II**, the fracture load was estimated only in a single fall configuration (10°-15° direction) for each femur. In contrast, in the **Publication III**, the fracture loads in the 12 different directions (**Figure 42**) were computed for each femur to evaluate the effect of the direction of fall onto the greater trochanter on the fracture load and whether the specific exercise-induced higher proximal femur bone strength (higher fracture load) depended on the direction. Furthermore, a minimum fall strength (MFS) [66,67,505], the lowest fracture load among the 12 directions, was computed for each proximal femur in the **Publication III**.

4.4.3 Fracture Location (Publication II)

It is of interest to determine if the fracture location varies depending on the exercise loading history. Thus, based on the surface nodal coordinates used for the fracture load estimation, the location was estimated for each proximal femur in the **Publication II**. Cross-sectional and axial fracture locations were estimated as a polar angle (in °) and a relative axial location (in %), respectively (**Figure 45**). Moreover, they were categorized into 1) specific anatomic octant and 2) cervical or trochanteric fracture, respectively. The cervical fracture was further classified into subcapital, transcervical, or basicervical region, similar to Schileo et al. (2014) [50].

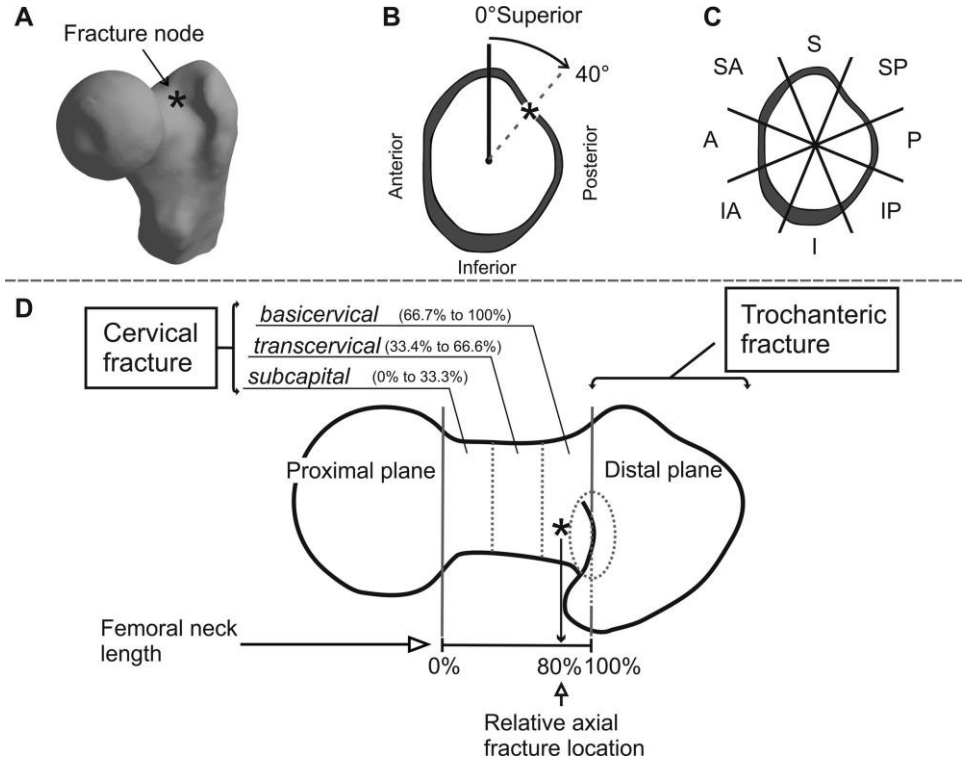

Figure 45. Estimation of hip fracture location. (A) An example of fracture node (*) on the surface. (B) The fracture location in the femoral neck cross-section was described as the polar angle (in °) in the clockwise direction. (C) The categorization of the measured polar angle into the specific equal 45° octant region. For example, the polar angle of 40° (* in B) belongs to the SP octant in C. (D) The relative axial fracture location (%) and its categorization into cervical (subcapital, transcervical, or basicervical) or trochanteric fracture. For example, the relative axial location of 80% (* in D) belongs to the basicervical region of cervical fracture. The detailed procedure determining the fracture location and its categorization can be found in the Publication II. (Reprinted from Publication II © 2018 Elsevier Ltd.)

4.5 Ricci-flow Conformal Mapping (RCM) (Publication IV)

To realize the 3D visual and spatial comparisons of the cortical thickness and fall-induced strain distribution within proximal femur between each exercise loading group and the control group, the Ricci-flow conformal mapping (RCM) (parametrization) and the subsequent template registration were implemented by one of the coauthors, Dr. Nathaniel Narra, PhD as a part of his doctoral research. The details of this method are found in his doctoral dissertation [600] and in the **Publication IV**. For the sake of clarity, the procedure is described briefly here.

4.5.1 Preparation

Nodal information (node ID and coordinates) of periosteal (outer) and endocortical (inner) surfaces was first extracted from each proximal femur FE model together with the corresponding periosteal nodal maximum and minimum principal strains. Based on the obtained nodal information, the outer and inner triangular surface meshes were subsequently reconstructed for each proximal femur cortical bone through down-sampling the nodes (from >80,000 to ~25,000 nodes) and cleaning errors in the surface topology using the medical image processing software MeshLab (Visual Computing Lab – ISTI – CNR, http:// meshlab.sourceforge.net/) and Avizo (FEI, Hillsboro, USA). Next, the cortical thickness was calculated as the shortest distance from each of the outer surface nodes to the inner surface. At last, the following information was attributed to each of the outer surface nodes: the cortical thickness, and the maximum and minimum principal strains.

4.5.2 RCM-based 3D-to-2D transformation – Parametrization

The reconstructed 3D outer surface mesh was transformed into a 2D planar domain (a disk-shaped mesh called M_{Disk}) by an angle preserving conformal Ricci-flow method, where locally preserved angles were stored as conformal factors [601]. Since this method enables to describe surface topological features on the 2D domain by parameters, such transformation is referred to as parametrization. This parametrized 2D M_{Disk} represents the conformal distribution map, where the distal end of proximal femur was considered as a single boundary ($\partial_1 M$) (**Figure 46**).

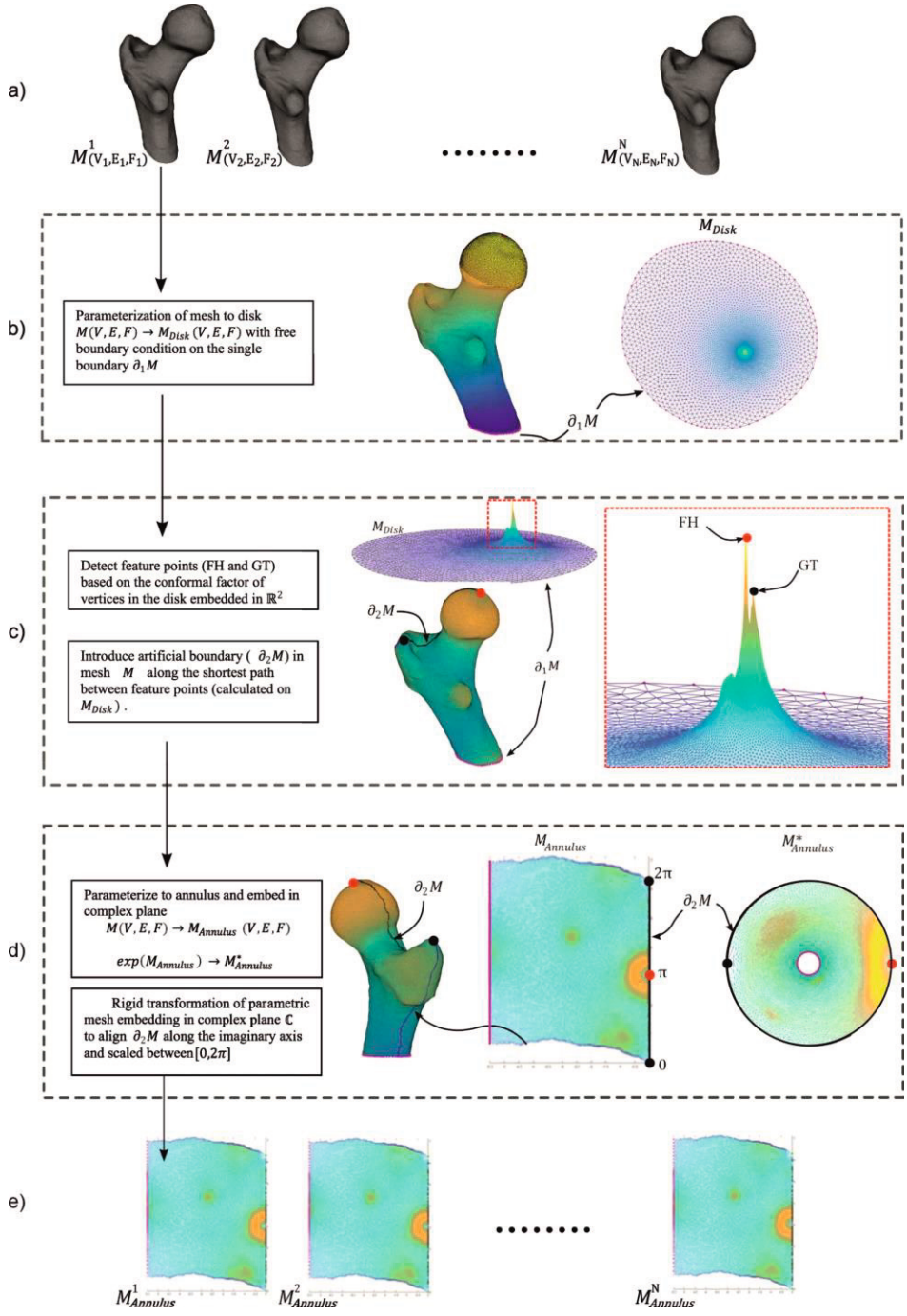

Figure 46. Ricci-flow conformal mapping (RCM) and the parametrization. Note: A process of femoral head and a tip of greater trochanter are abbreviated as FH and GT. Detail can be found in Publication IV. (Reprinted under CC BY 4.0 license from Publication IV © 2018 Authors).

This distal end lacks characteristic anatomical features (e.g., protrusion) and its location varied among the participants due to different image field of views. These would result in not only an unreliable reference for the subsequent template registration (described shortly) but also the difficulty to detect one of the key anatomical features such as the lessor trochanter that was necessary for the registration. Therefore, two additional parametrization steps were performed. First, by utilizing the preserved angles (conformal factors), two protruding anatomical features such as a process of femoral head and tip of the greater trochanter were identified on the M_{Disk}. A straight line connecting these two features was introduced as a new artificial boundary ($\partial_2 M$) (**Figure 46**). Two features were consistently found across all participants' proximal femora. Second, based on two boundaries ($\partial_1 M$ and $\partial_2 M$), the M_{Disk} was reshaped into an annulus ($M^*_{Annulus}$) mapped on the complex plane. This annulus ($M^*_{Annulus}$) was generated utilizing an exponential map of the complex coordinates and was subsequently reformed into another shaped mesh, called $M_{Annulus}$, mapped on the tailored coordinate system. In this coordinate system, the new boundary $(\partial_2 M)$ is placed on the imaginary axis while the distal end boundary ($\partial_1 M$) lays on the negative real axis, parallel to the $\partial_2 M$. The mesh ($M_{Annulus}$) was also resized so that the $\partial_2 M$ on the imaginary axis was scaled from 0 to 2π. Now, on the imaginary axis, the process of femoral head is placed on the midpoint (π) whereas the tip of greater trochanter is placed on the lower and upper ends (0 and 2π, respectively). Due to this symmetric arrangement, this $\partial_2 M$ boundary was considered a reliable reference for the subsequent registration. These multiple parametrization steps were performed to transform the 3D outer surface mesh of each proximal femur into the 2D common frame ($M_{Annulus}$) (**Figure 46**).

4.5.3 Standardized Template Registration

Despite the reliable reference established above, the parametrized annuluses ($M_{Annulus}$) cannot still be compared each other between different proximal femora. This was because each of anatomical positions/features (e.g., lessor trochanter) is not yet correctly corresponded each other between the femora. As described earlier, in computational anatomy, such correspondences are established by registering the bone geometry (or the medical image scans of individual bone) into a standardized space (a canonical template) by spatial normalization. This registration process is essential to realize the proper subsequent between-subject/group statistical analysis. A similar registration procedure was carried out in the present research (**Figure 47**).

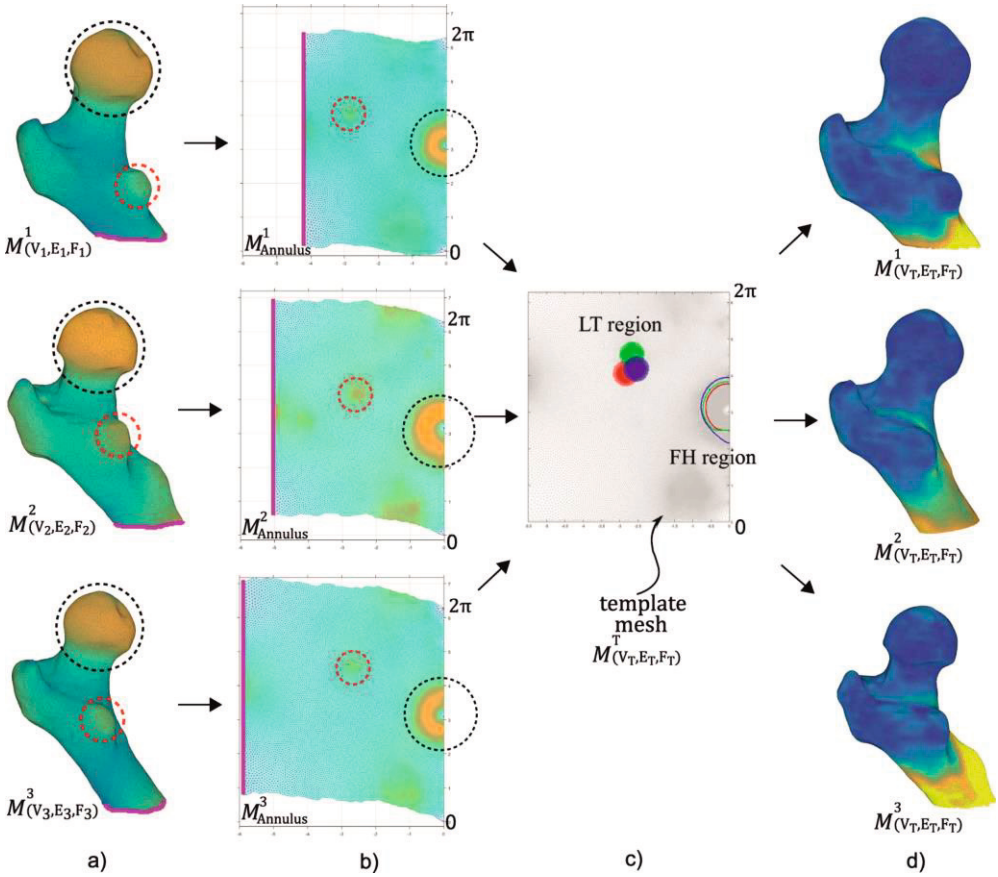

Figure 47. Standardized template registration. (a) Examples of outer surface mesh from three proximal femora. (b) The RCM-based parametrized 2D annulus meshes ($M_{Annulus}$) of each example femur. The locations of femoral head (FH, black-circle) and a tip of lessor trochanter (LT, red-circle) are shown. (c) Registration of the parametrized meshes into the template mesh (M^T) by the elastic registration technique. The deviations of the FH and LT locations on the template mesh (registration error) are clearly presented in color (red, green, and blue for each of three samples). (d) Nodal features such as the cortical thickness and principal strain (attributed to the specific node on the template mesh now) can be mapped back to the 3D surface of any proximal femur. The cortical thickness distribution is shown as the example. (Reprinted under CC BY 4.0 license from Publication IV © 2018 The Authors).

Each of 111 parametrized 2D meshes ($M_{Annulus}$) (for 111 study participants, 1 mesh per participant) was registered into the canonical template mesh (M^T) based on two established boundaries and three key anatomical features such as the process of femoral head, and tips of greater and lesser trochanters. In addition to the femoral head and greater trochanter which were already identified on the initial parametrized disk (M_{Disk}), the lesser trochanter was detected on the parametrized annulus

($M_{Annulus}$) (**Figure 47**). It should be noted that the earlier multiple parametrization steps did not only enable to establish the reliable reference, but also made the detection of the lesser trochanter easier on the parametrized annulus ($M_{Annulus}$) than on the initial disk (M_{Disk}). Using the boundaries and these three anatomical features identified, the registration was performed by elastic registration where the shape of every proximal femur surface mapped on the parametrized surface mesh was conformed to the template mesh. Once registered, some of anatomical features (e.g., lesser trochanter) do not necessarily coincide yet between other femora on the template mesh due to the anisotropic shape differences among sampled proximal femora (leading to the registration error). Correction of such deviation was performed based on two anatomical features such as the femoral head and lesser trochanter by radial basis functions [602], which deformed these features locally to match them on the template mesh. At last, each of anatomical positions and/or features are properly corresponded each other between different proximal femora through the canonical template mesh (standardized space) (**Figure 47**).

4.5.4 3D Feature Maps

One last step prior to the between-group statistical analyses was mapping the features of interest (cortical thickness and principal strains) on the common 3D surface shape. Once the parametrized mesh of each proximal femur was registered into the template mesh, the representative shape averaging all 111 proximal femoral shapes was created through generalized Procrustes analysis based on the 3D coordinates of the outer surface nodes of all femora stored in the template meshes. The features of interest registered in template nodes were mapped onto the surface of this representative shape, resulting in three 3D feature maps per participant: 1) the cortical thickness, 2) maximum principal strain, and 3) minimum principal strain distribution 3D feature maps.

4.6 Statistical Analyses

4.6.1 FE-derived Outcomes

For the **Publications I-III**, statistical analyses were performed with SPSS 22.0-25.0 (IBM Corp., Armonk NY, USA). Mean and SD were given as descriptive statistics. Prior to the following analyses, logarithmic transformation of the octant cortical stress, fall direction-wise fracture load, and MFS were performed to control the skewness of these data, followed by confirmation of the normality of the transformed data by the Shapiro-Wilk test. In the **Publication I**, the differences of the log-transformed octant cortical stresses in the three sites between each exercise loading group and the control group were estimated by a multivariable analysis of covariance (MANCOVA) with the individual impact force as a covariate where a Sidak correction was applied to control for the multiple comparisons. In the **Publications II and III**, a one-way analysis of variance (ANOVA) and analysis of covariance (ANCOVA) were performed to estimate the differences of the following log-transformed dependent variables between each exercise loading group and the control group: in the **Publication II**, the fracture loads in a single fall configuration (10°-15° direction) (BW as the covariate in ANCOVA); and, in the **Publication III**, the fracture loads in each of 12 fall directions and MFS (using BW or LM, separately, as a covariate in ANCOVA for both variables). Percentage differences in each variable above between each exercise loading group and the control group were computed by taking anti-log of the respective unadjusted and adjusted variables. Also, the between-group differences in the fracture locations (the polar angular and relative axial locations) were assessed by a non-parametric Mann-Whitney U test due to non-normal distributions of these sampled data (**Publication II**). Exercise loading groups were not compared each other in the above analyses.

In the **Publication III**, prior to the ANOVA and ANCOVA analyses, the effect of direction of fall (onto the greater trochanter) on the fracture load within and between groups were also investigated as follows. First, the association of fall angles a and β with fracture loads within each group was evaluated by a two-way repeated measures ANOVA where a Sidak correction was applied to control for the multiple comparisons. Next, it was determined whether the potential associations and interactions of a and β with the fracture loads varied between the groups by a split-plot ANOVA.

A $p < 0.05$ was considered statistically significant for all analyses above. It is noted that the BW and LM were chosen as the covariates (applied separately) over age and body height in the **Publication III** based on 1) the Pearson correlation analyses between these variables and the fracture loads and 2) checking a prerequisite for the independent variable(s) to be used as the covariate (the homogeneity of regression slope) (the details can be found in the **Publication III**).

4.6.2 RCM-derived Outcomes

The featured maps presenting the distributions of 1) the cortical thickness, 2) maximum principal strain, and 3) minimum principal strain were compared between each exercise loading group and the control group using the SPM (linear model) in the SurfStat package (http://www.math.mcgill.ca/keith/surfstat/) [603]. Based on the t-statistics, patches representing the significant difference in each feature was identified and displayed on the surface of the representative proximal femur shape. Compared to the **Publications I-III**, a stricter threshold $p < 0.005$ was considered statistically significant here. Since each individual map contained ~25,000 nodes, performing the between-group statistical analysis at every single node would lead to errors due to the enormous multiple comparisons. To correct this, a random field theory-based correction was applied.

The template registration was performed based on a few anatomical features as described earlier. Despite the correction attempted to decrease the registration error, this method still likely introduces such error to some extent systematically due to the anisotropic variations of the shapes between different femora. To mitigate this, the femoral shape and/or scale (size) were used as the additional confounding factors, as recommended by Gee and Treece [604], in the SPM linear model [582,587]. For the between-group analysis on the cortical thickness, BW, femoral shape, and scale were included as the confounding factors whereas the shape and subject-specific fall-induced peak impact force was used for the maximum and minimum principal strains. The femoral shape and scale for each participant were obtained through the SPM linear model and Procrustes analysis. Further details on the statistical analysis including the femoral shape and scale are found in the **Publication IV**.

5 RESULTS

This section presents key results from the **Publications I-IV**. The complete results can be found in these publications. Due to the similarity between unadjusted and BW-adjusted results, the % differences only in the BW-adjusted fracture load and MFS (**Publications II and III**) are presented here.

5.1 Descriptive Data of Participants

The descriptive data of age, height, body weight (BW), fat-%, lean body mass (LM), and the training histories characterized by the number of weekly training sessions, weekly sport-specific training hours, and the duration competing career (year) in each group are summarized in **Table 8**. In general, the athletes were leaner than the controls as expected. In addition to a > 8-year history of specific exercise loading, the weekly training volume (sessions and hours) were at least 2–3 times higher in the athletic groups than in the controls.

Table 8. Descriptive group characteristics

Group	N	Age (years)	Height (cm)	BW (kg)	Fat-%	LM (kg)	Weekly training sessions	Weekly sport-specific training hours	Competing career (years)
H-I	19	22.3 (4.1)	174 (6)	60.2 (5.4)	20.0 (3.9)	45.9 (3.1)	6.7 (1.4)	11.5 (2.3)	10.1 (3.4)
O-I	19	25.3 (6.7)	165 (8)	60.8 (8.3)	25.1 (5.9)	43.3 (4.2)	5.7 (1.4)	9.3 (2.7)	9.6 (4.8)
H-M	17	27.5 (6.3)	158 (3)	63.3 (13.2)	27.9 (7.4)	43.2 (5.9)	5.8 (2.0)	9.1 (2.7)	8.0 (4.7)
R-I	18	28.9 (5.6)	168 (5)	53.7 (3.4)	14.2 (3.6)	44.1 (3.1)	8.7 (2.1)	10.9 (3.4)	12.4 (6.7)
R-NI	18	19.7 (2.4)	173 (5)	65.1 (5.6)	25.1 (5.5)	46.7 (3.5)	11.4 (2.0)	19.9 (4.5)	9.1 (2.6)
Control	20	23.7 (3.8)	164 (5)	60.0 (7.4)	31.7 (5.8)	39.0 (4.2)	2.8 (1.0)	2.8 (0.9)	-

Mean (SD) is shown.

5.2 Octant Cortical Stresses (Publication I)

The group-wise mean octant cortical stresses at all three longitudinal sites are presented in **Figure 48**. In general, the relatively higher stresses are observed in the inferior and inferoposterior regions compared to other octants at the proximal site. These relatively higher stresses were shifted toward the superior, superoposterior, posterior and inferoanterior octants at the middle site whereas they were more concentrated in the superoposterior and posterior octants at the distal site.

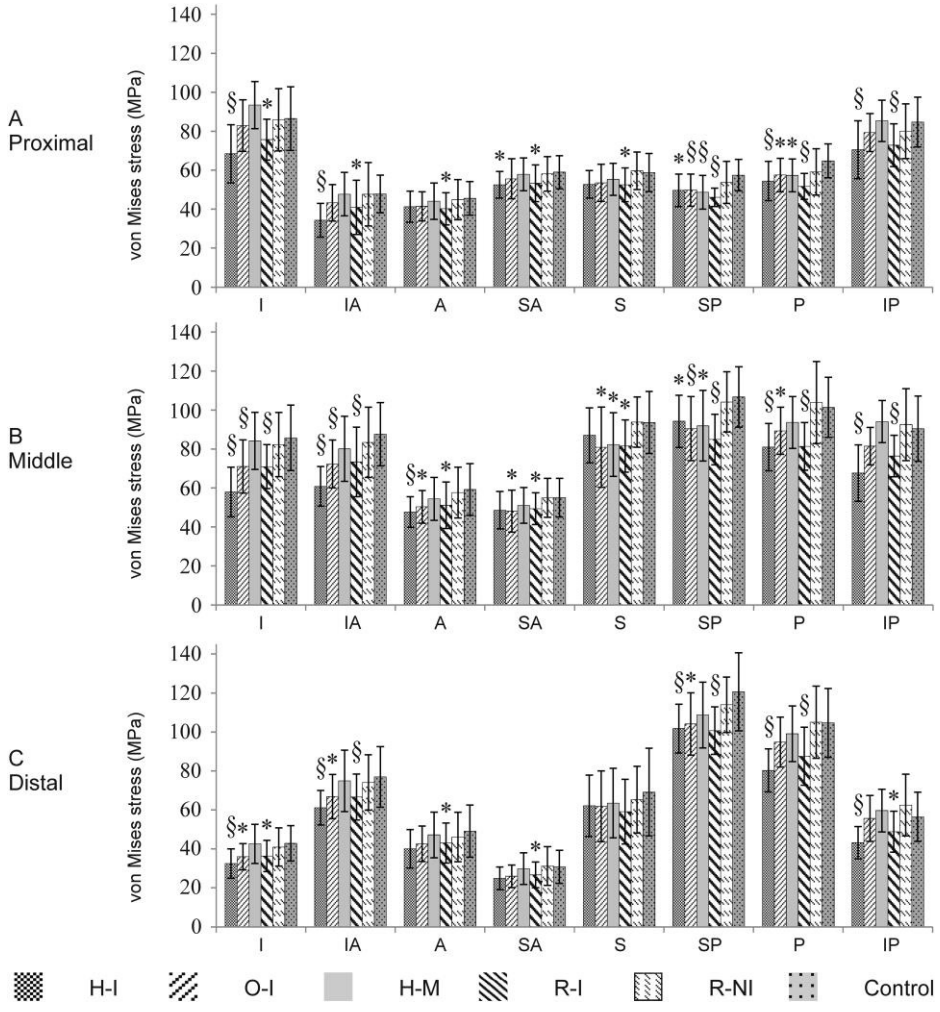

Figure 48. Result (Publication I) - Group-wise unadjusted mean (SD) octant cortical stress at the proximal, middle, and distal sites in the femoral neck. Based on the ANCOVA (the impact force as a covariate), * and § represent the statistical differences (vs. control) for $0.01 \leq p < 0.05$ and $p \leq 0.01$, respectively. (Reprinted from Publication I © 2016 Elsevier Inc.)

The highest mean octant cortical stresses of all groups across three sites were observed particularly in the superoposterior octant at the distal site. In addition, the typical stress distribution within the proximal femur in each group is presented in **Figure 49** where aforementioned high stresses in the superior, superoposterior, and posterior octants at the middle and distal sites can be clearly seen. The area of the very high stress (> 185 MPa) was notably larger in the R-NI and control groups than others (**Figure 49**).

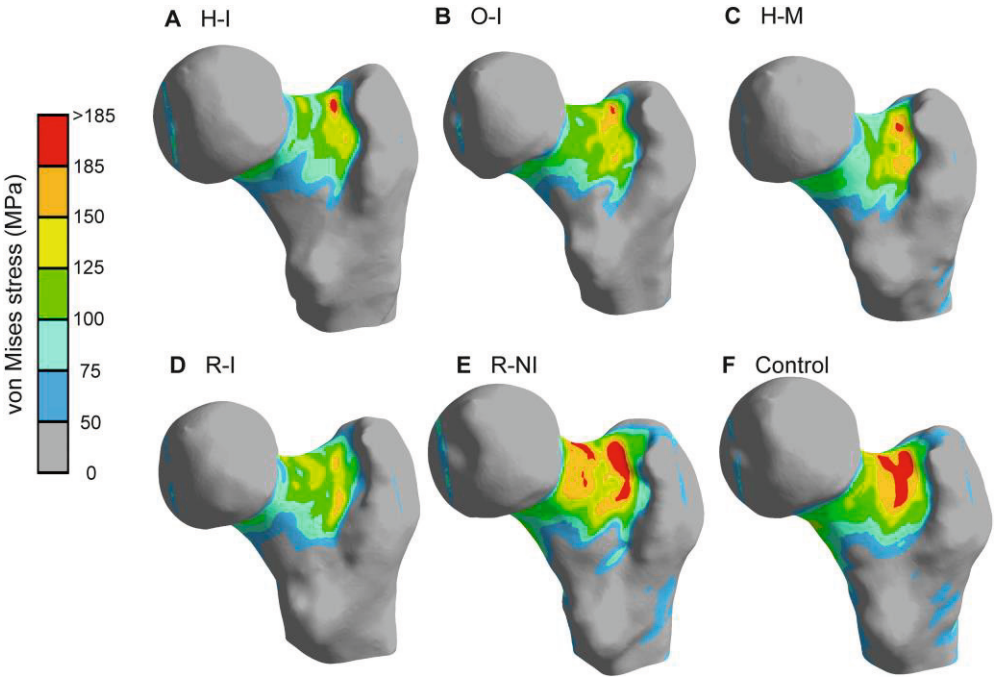

Figure 49. Result (Publication I) - Typical von Mises stress distribution within the proximal femur in each group. A, B, C, D, E, and F represent an example stress distribution in the respective exercise and control groups. (Reprinted from Publication I © 2016 Elsevier Inc.)

The impact exercise loading groups such as the H-I, O-I, and R-I groups had the significantly lower (impact force-adjusted) octant cortical stresses ($p < 0.05$) in the majority of octants compared to the control group. The H-I group had significantly ($p < 0.05$) ~10-32% lower stresses in 5 to 6 octants at every site whereas the R-I had significantly 12-23% lower stresses in nearly all (7 to 8) octants at each site. On the other hand, the O-I group had significantly 12-17% lower stresses in less octants (2, 7, and 3 octants at the proximal, middle, and distal sites, respectively). The H-M group had significantly 12-16% lower stresses in a few octants compared to the controls only at the proximal and middle sites (2 octants at each site). On the other

hand, the R-NI group did not have any lower octant stresses compared to the controls.

The superior, superoposterior, and posterior octants in the middle and distal sites where the relatively high stresses were observed (**Figure 48**) belong to the ROI such as the fracture-prone superolateral cortex of femoral neck, spanning the (upper half of) anterior, superoanterior, superior, superoposterior, and (upper half of) posterior octants. **Table 9** summarizes the statistically significant ($p < 0.05$) % differences in the (impact force-adjusted) mean octant cortical stress observed in this region. The impact exercise loading groups such as the H-I, O-I, and R-I groups had the significantly 10-22%, 12-16%, and 14-23% lower stresses compared to the controls in this region, respectively. Importantly, in the superoposterior octant at the distal site where the highest octant stresses were observed in all groups (**Figure 48**), they had 13%, 14%, and 19% lower stresses than the control, respectively. On the other hand, the H-M group had such lower stresses (13-15%, $p < 0.05$) only at the middle site although trends ($0.05 < p < 0.1$) for the lower stress (-9%) were seen at the distal site.

Table 9. Percentage differences in the impact force-adjusted mean octant cortical stresses between each exercise loading group and the control group in the fracture-prone superolateral femoral neck cortex

Group	Middle			Distal		
	S	SP	P	S	SP	P
H-I		**-10%**	**-19%**		**-13%**	**-22%**
O-I	**-16%**	**-16%**	**-12%**		**-14%**	-9%*
H-M	**-13%**	**-15%**			-9%*	
R-I	**-14%**	**-23%**	**-22%**	-17%*	**-19%**	**-20%**

The results of R-NI are not presented here since there was no difference compared to the control.

Statistically significant ($p < 0.05$) % differences based on ANCOVA (with the impact force as a covariate) are shown in bold.

* denotes trends for the lower stress compared to the control ($0.05 < p < 0.1$)

5.3 Fracture Load, Location, and Mode in a Single 10°-15° Fall Direction (Publication II)

Group-wise fracture loads and locations in the single fall configuration (10°-15° direction) are summarized in **Table 10**, including 1) the unadjusted mean fracture loads, 2) the % differences in the BW-adjusted mean fracture loads between each exercise loading group and the control group, and 3) the fracture locations (polar angular and relative axial locations). The fracture mode was due to the compression in all 111 proximal femora and the estimated individual fracture loads ranged from 2.1 kN to 4.4 kN. All three impact groups (H-I, O-I, and R-I) had significantly ($p < 0.05$) 14%, 11%, and 26% higher (BW-adjusted) mean fracture loads compared to the controls, respectively (**Table 10**). Neither of the H-M and R-NI groups had such higher fracture loads compared to the controls.

Table 10. Unadjusted mean fracture loads, the percentage differences in the BW-adjusted mean fracture load between each exercise loading group and the control group, and mean fracture locations (polar angle and relative axial locations) in a single 10°-15° fall direction

Group	Fracture load		Fracture location	
	Unadjusted load (N)	BW-adjusted % difference	*Polar angle* (°)	*Relative axial location* (%)
H-I	**3228 (408)***	**14.3%§**	30.1 (14.0)	**90.1 (16.9)***
O-I	**3164 (447)***	**11.4%***	30.7 (15.3)	**86.8 (9.9)§**
H-M	2960 (584)	0.2%	41.0 (24.0)	97.0 (5.5)
R-I	**3231 (538)***	**26.2%§**	36.5 (19.8)	98.0 (10.8)
R-NI	3068 (500)	2.1%	35.4 (13.0)	92.7 (14.2)
Control	2849 (551)	-	35.6 (13.7)	97.0 (8.3)

Mean (SD) are shown for unadjusted fracture load, *polar angle*, and *relative axial location* whereas only mean is shown for the BW-adjusted % difference for the fracture load.

Statistically significant results ($p < 0.05$) based on ANOVA and ANCOVA (for the fracture load comparisons), and Mann-Whitney U test (for the fracture location comparisons) are displayed in bold.

* and § represent the statistical significance of $0.01 \leq p < 0.05$ and $p \leq 0.01$, respectively.

In general, the mean polar angular and relative axial locations ranged from 30° to 41° and 87% to 98% (**Table 10**), corresponding to the superoposterior octant and basicervical femoral neck region (distal femoral neck site), respectively (**Figure 45** and **Figure 50**). The majority of simulated fractures were observed in these locations [68% (75 out of 111) in the SP octant and 81% (90 out of 111) in the basicervical region]. Over 50% of the fractures were located at the SP octant in the basicervical region (distal femoral neck site) (**Figure 50**). While the polar angular locations were

not statistically different between any of the exercise loading groups and the control group, the relative axial locations in the H-I and O-I groups were located significantly more proximal ($p < 0.05$; 7% and 10%, respectively) compared to the control group. The distribution of the fracture locations in each group is presented in **Figure 50**. It is noted that, although a total of 8 trochanteric fractures were observed, their locations were around the trochanteric fossa, very close to the basicervical region.

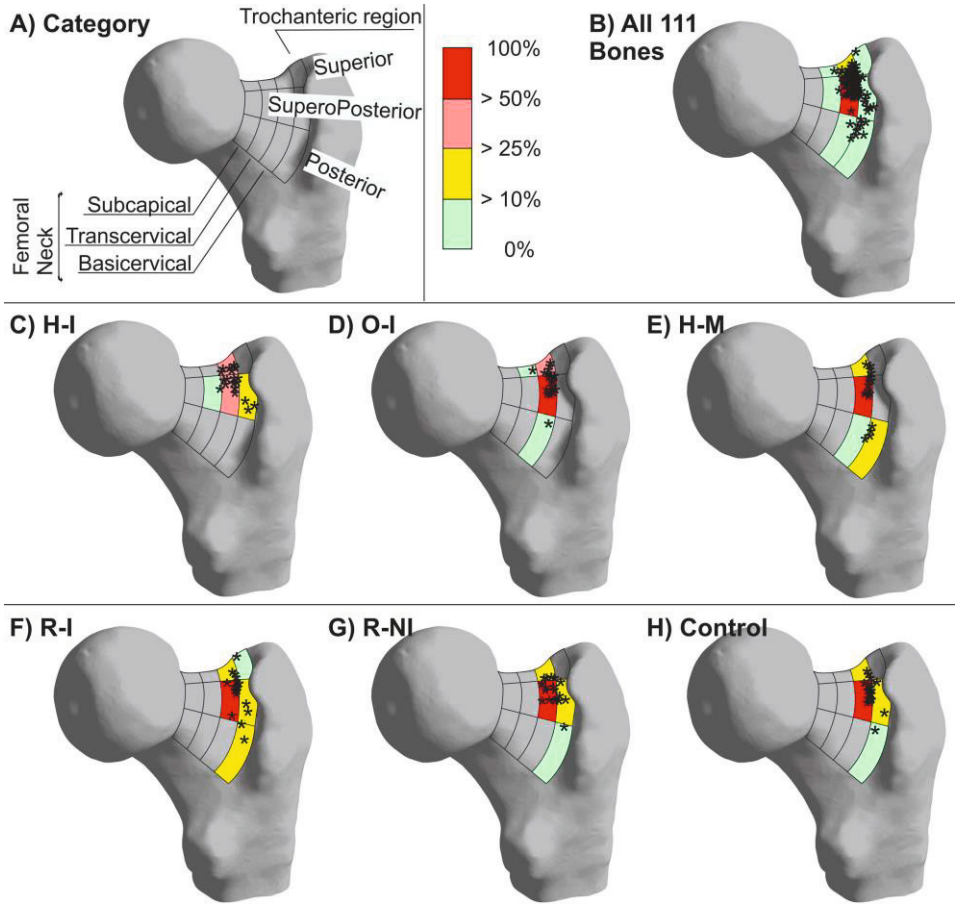

Figure 50. Result (Publication II) - Distribution of the fracture locations. (A) Regional categories – three octants (superior, superoposterior, and posterior), and femoral neck (subcapital, transcervical, and basicervical regions) or trochanteric regions. Note: only three octants are shown since all fractures were observed in these octants. Femoral neck (incl. three sub-regions) and trochanteric regions correspond to same respective regions described in Section 4.4.3 and **Figure 45**. Details can be found in Publication II. Proximal femora in this figure are also slightly rotated internally so that the posterior part of greater trochanter does not hide the defined trochanteric region (the rightmost region in A). (B) The distribution of the fracture locations (*) in all 111 proximal femora. (C-H) The distribution in each group. (Reprinted from Publication II © 2018 Elsevier Ltd.)

5.4 Effect of Fall Direction on Fracture Load (Publication III)

5.4.1 General Trend and Effect of Fall Direction

In general, the highest mean fracture loads were detected in the 0°-0° fall direction in all groups whereas the lowest means were observed in the 30°-30° except for the H-I and control groups (30°-15°). The group-wise mean fracture loads were decreased by up to 32-35% or 22-27% when the *a* or *β* angle increased from 0° to 30°, respectively. When both angles were changed from the 0°-0° to 30°-30° direction, the reduction reached up to 34-36%. Accordingly, the two-way repeated measures ANOVA showed significant interactions ($p < 0.001$) of the fall angles (*a* and *β*) with the fracture loads within each group. However, the effect(s) of *a* and/or *β* on the fracture loads were not significantly different between groups ($p > 0.05$ for terms *a**group, *β**group, and *a***β**group) based on the split-plot ANOVA.

5.4.2 Fall Direction-wise Analysis of Fracture Load

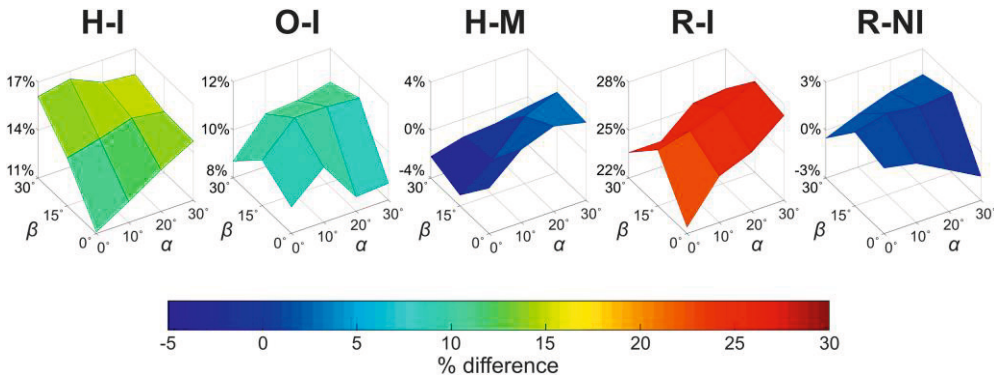

Figure 51. Result (Publication III) - The % differences in the BW-adjusted fracture loads between each exercise loading group and the control group in different directions of fall onto the greater trochanter. (Adapted under CC BY 4.0 license from Publication III © 2022 The Authors).

The % differences in the BW-adjusted fracture load between each exercise loading group and the control group in the 12 fall directions are displayed in **Figure 51** above. The fall direction-wise analyses of the fracture loads revealed that the H-I and R-I groups had the significantly ($p < 0.05$) 11-17% and 22-28% higher BW-adjusted

fracture loads compared to the controls in all 12 fall directions whereas the O-I group had the significantly 10-11% higher fracture loads in less, five fall directions [10°–0°, 10°–15°(near-significant, $p = 0.051$), 10°–30°, 20°–15°, and 30°–15°]. The O-I group also had trends ($0.05 \leq p < 0.1$) for the 9-11% higher fracture loads in the rest of the fall directions.

On the other hand, the fracture loads in the H-M and R-NI groups were not different ($p > 0.05$) from those in the control group in any directions of fall onto the greater trochanter. Furthermore, the LM-adjusted fracture loads were not different between any of the exercise loading groups and the control group in any directions.

5.4.3 Minimum Fall Strength (MFS)

Table 11 shows the unadjusted mean (SD) MFSs and the % differences in the BW- and LM-adjusted mean MFSs between each exercise loading group and the control group. The H-I, O-I, and R-I groups had the significantly higher BW-adjusted MFSs ($p < 0.05$; 15%, 11%, and 26%, respectively) compared to the control. The MFSs in the H-M and R-NI were not different compared to the controls. Once adjusted for LM, none of the exercise loading groups had the significantly different MFSs compared to the controls. Moreover, the occurrences of MFS were concentrated in the fall direction(s) where either or both fall angles α and β were the greatest: 1 in the 10°–30°, 13 in the 20°–30°, 23 in the 30°–0°, 34 in the 30°–15°, and 40 cases in the 30°–30°. Similar to the lowest fall direction-wise fracture loads, the 30°–30° fall direction had the most MFSs compared to any other directions.

Table 11. Unadjusted mean MFSs and the percentage differences in the BW- and LM-adjusted MFSs between each exercise loading group and the control group

Group	Unadjusted MFS Mean (SD) (N)	BW-adjusted % difference	LM-adjusted % difference
H-I	**2761 (366)***	**14.5%§**	3.1%
O-I	**2674 (346)***	**10.6%***	4.3%
H-M	2527 (465)	0.6%	-3.9%
R-I	**2752 (371)***	**25.9%§**	1.4%
R-NI	2576 (381)	0.7%	-7.3%
Control	2425 (452)	-	-

Statistically significant results ($p < 0.05$, compared to the control group) based on ANOVA and ANCOVA are presented in bold.

* and § denote the statistical significance of $0.01 \leq p < 0.05$ and $p \leq 0.01$, respectively

5.5 RCM-based 3D Analyses of Cortical Thickness and Principal Strain Distributions (Publication IV)

5.5.1 Cortical Thickness Distribution

Statistically significant ($p < 0.005$) differences in the cortical thickness between each exercise loading group and the control group are displayed visually on the representative average femur shape in **Figure 52**. The H-I group had the largest area of the colored patches, representing the significantly higher cortical thickness compared to the control, among all exercise loading groups. Except for the inferoanterior and superoposterior regions of femoral neck, the cortical thickness of femoral neck in the H-I group was >20% thicker than the control. Particularly, 40-70% and >110% thicker cortexes at the posterior and inferior femoral neck compared to the controls, respectively, are outstanding structural adaptations in the H-I exercise loading group. The mean difference ranged mostly from 20 to 50% (median: 40%) in the H-I group compared to the controls. Although the area and the degree are smaller than the H-I group, the O-I group also had the significantly thicker cortex at some regions of the femoral neck compared to the control group. Particularly, 10-50% and 40-60% thicker cortexes at the superior-to-superoanterior and inferior regions, respectively, were another noteworthy adaptation in the O-I group. The mean difference ranged mostly from 15-40% (median: 26%). Such widely distributed thicker cortical areas around the femoral neck were not present in the H-M and R-I groups. Despite this, the H-M group had a small thicker cortical area at the superior and superoanterior femoral neck with the mean difference ranging mostly from 25-40% (median: 32%). The R-I group had a small thicker cortical area at the lateral side of the greater trochanter with its difference ranging from 25-35% (median: 28%). The result of the R-NI group compared to the control is not shown in **Figure 52** since no difference in the cortical thickness was observed. It is noted, although the size of the patch is small, the O-I group had a trend ($p < 0.025$) for the thicker cortical bone in the superoposterior (octant) region of the distal femoral neck, where the highest octant cortical stress (**Publication I**) and the most of fracture locations (**Publication II**) were observed.

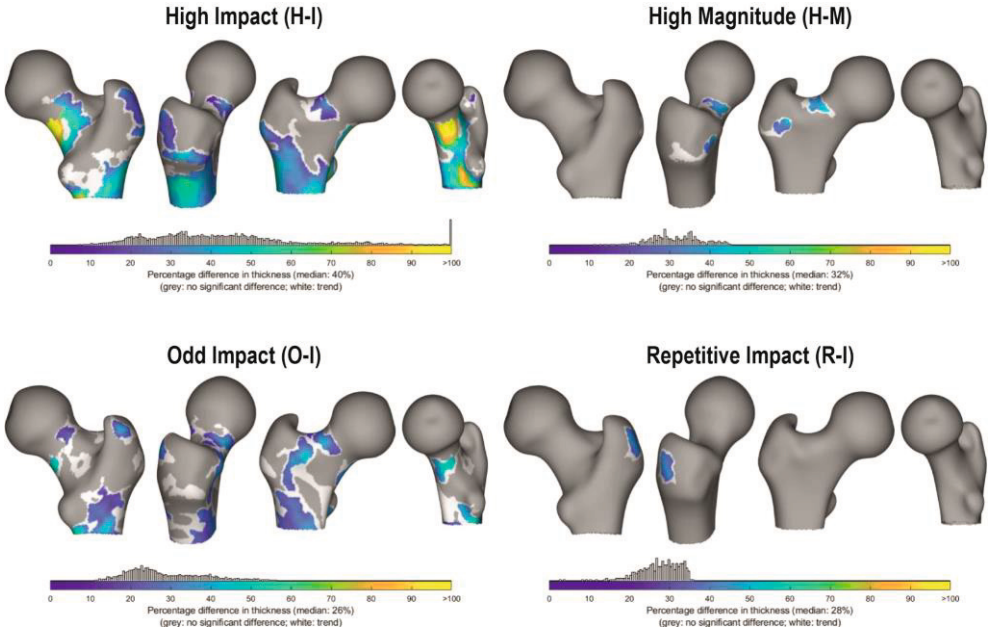

Figure 52. Result (Publication IV) – 3D distribution of the cortical thickness differences between each exercise loading group and the control group. The regions of the significantly ($p < 0.005$) higher cortical thickness in the exercise loading groups are presented as colored surface patches. Different colors correspond to the degree of the mean % difference in the thickness (% higher compared to the controls), which is depicted in the horizontal-colored bar. Vertical bars represent the distribution of the nodes, where the cortical thickness was significantly different. Trends for the higher cortical thickness ($p < 0.025$) were displayed as white patches whereas regions without the difference ($p \geq 0.025$) are shown in gray. (Reprinted under CC BY 4.0 license from Publication IV © 2018 The Authors).

5.5.2 Principal Strain Distribution

Statistically significant ($p < 0.005$) differences in the maximum and minimum principal strain distribution (with respect to their absolute magnitudes) at the proximal femur surface in a single fall configuration (10°-15°) between each exercise loading group and the control group are presented in **Figure 53**. It is noted again that the maximum and minimum principal strains describe the tensile and compressive strains, respectively.

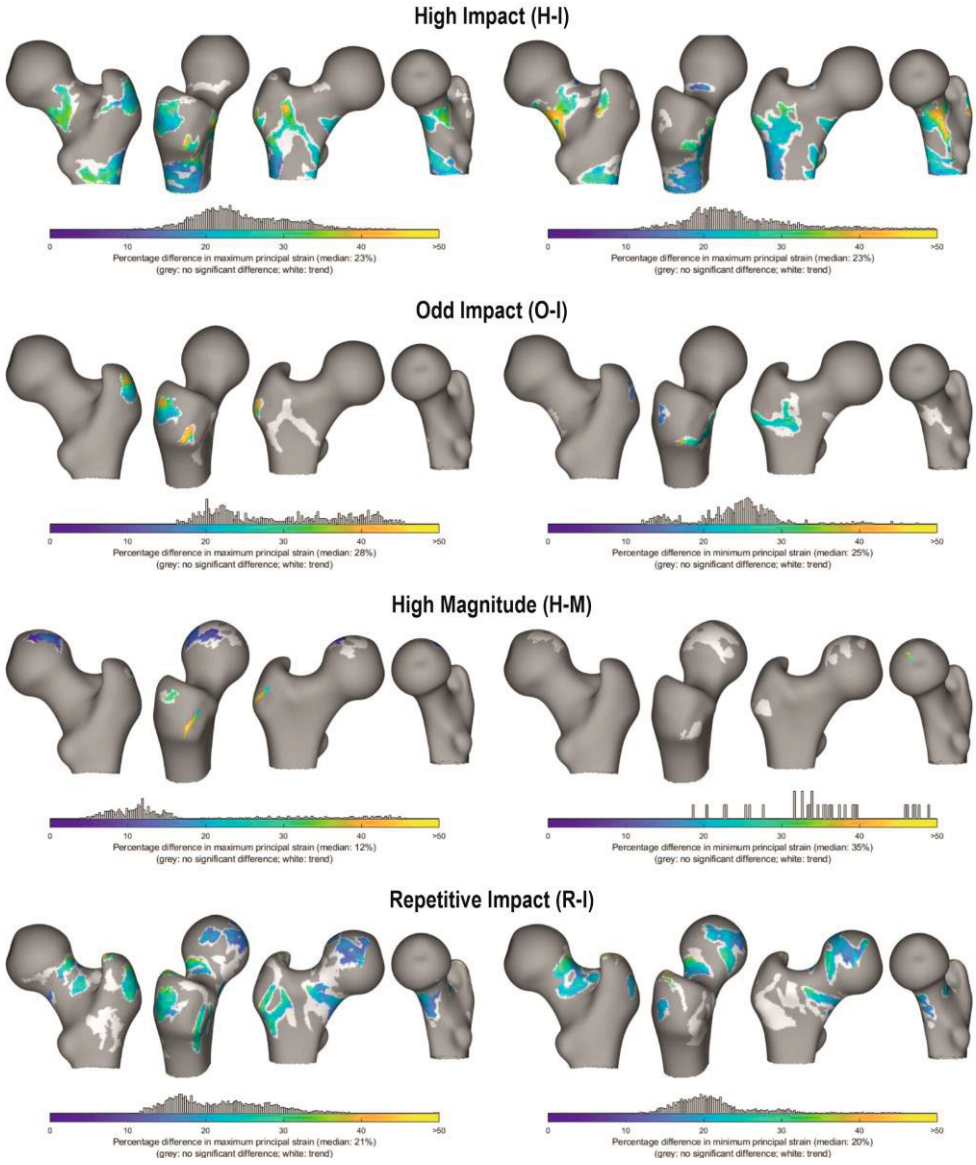

Figure 53. Result (Publication IV) – 3D distribution of the principal strain differences between each exercise loading group and the control group. The maximum and minimum principal strains are presented on left and right columns, respectively. The regions of the significantly ($p < 0.005$) lower magnitude of the strains (with respect to the absolute value) in the exercise loading groups are presented as colored surface patches. Different colors on the patches correspond to the degree of mean % difference (presented in the horizontal-colored bar). Vertical bars represent the distribution of the nodes, where the strains were significantly different. Trends for the lower principal strains ($p < 0.025$) were also displayed as white patches whereas regions without the differences ($p \geq 0.025$) are shown in gray. (Reprinted under CC BY 4.0 license from Publication IV © 2018 Authors).

Compared to the controls, the H-I had the large area of the significantly >20% lower magnitude of the maximum and minimum principal strains at the posterior and inferior femoral neck. Although there was no statistical significance and the size of patch is small, the distal superior and superoposterior femoral neck regions in the H-I group had trends ($p < 0.025$) for the lower magnitude of the minimum principal strains compared to the control group. In addition, the H-I group had the large areas of the significantly lower magnitudes of the maximum and minimum principal strains in the anterior and lateral trochanteric region. On the other hand, there were no such noteworthy differences in the femoral neck in either of the principal strains in the O-I and H-M groups compared to the controls. Another notable result was that the R-I group had the significantly 15-35% lower magnitude of the minimum principal strains at the superior, superoposterior, and posterior femoral neck compared to the controls. The R-I group also had some areas of the 10-30% lower maximum principal strains around the femoral neck. Similar to the cortical thickness, since the principal strains in the R-NI group were not different from the controls, its results are not included in **Figure 53**.

6 DISCUSSION

The primary objective of the present doctoral research was to scrutinize the effect of long-term specific exercise loading on the proximal femur bone strength in the fracture-causing fall situations. This was achieved by creating the proximal femur FE models of 91 young adult female competitive athletes with histories of five distinct exercise loadings and 20 nonathletic female controls in a single and multiple fall configuration(s). Based on the FE models, the fall-induced regional cortical stresses within the femoral neck, and fracture loads and locations were estimated, followed by their between-group statistical comparisons (**Publications I-III**). The secondary objective was to seek for the potential supporting evidence which could further explain the specific exercise-induced higher proximal femur bone strength based on the 3D morphological analyses of the proximal femur cortical bone adaptation to the specific exercise loadings. This was achieved by implementing a new computational anatomy method called Ricci-flow conformal mapping (RCM) which enabled to analyze the 3D distributions of the cortical thickness and fall-induced strain within the proximal femur and to perform the subsequent spatial between-group statistical comparisons (**Publication IV**). The results from this second objective were anticipated to help understand the findings of the primary objective.

6.1 Effect of Specific Exercise Loading History on Proximal Femur Bone Strength in Fall Situations

The H-I, O-I, and R-I groups had the significantly 10-22%, 12-16%, and 14-23% lower fall-induced octant cortical stresses at the fracture-prone superolateral femoral neck compared to the control group, respectively. Also, in the distal superoposterior octant where all the group-wise highest octant cortical stresses were observed, they had the significantly 13%, 14%, and 19% lower octant cortical stresses compared to the control group, respectively (**Publication I**). Since the stress alone is insufficient to infer the proximal femur bone strength in the fall situation, the fracture loads were estimated. Based on the proximal FE models simulated in the most examined single fall configuration (10°-15° direction), the fracture loads in aforementioned impact

exercise loading groups were significantly 14%, 11%, and 26% higher than the control group, respectively (**Publication II**). Athletes' bones are adapted to the long-term specific exercise loadings characterized by not only specific loading magnitude, rate, and frequency, but also direction. Thus, it stayed unclear whether these specific impact exercise-induced benefits in the fracture loads (proximal femur bone strength) were specific to only certain direction(s). Therefore, the study was extended to simulate each FE model in 12 different directions of fall onto the greater trochanter (**Publication III**). It was found that the H-I and R-I groups had the significantly 11-17% and 22-28% higher fracture loads compared to the control group, respectively, regardless of the directions. On the other hand, the benefits in the O-I group was more modest (10-11% higher than the controls) and specific to the fall direction. Furthermore, additional analyses of the MFSs also confirmed the higher proximal femur bone strengths in these impact exercise loading groups. The H-I, O-I, and R-I groups had the significantly 15%, 11%, and 26% higher MFSs compared to the control group, respectively (**Publication III**). Although the H-M group had the significantly 13-15% lower octant cortical stresses in the middle superior and superoposterior octants and a trend for the lower stress (-9%) in the distal superoposterior octant compared to the controls (**Publication I**), the fracture loads and MFSs in both H-M and R-NI groups were not different from those in the controls in any of fall directions (**Publications II and III**).

Despite a limited number of similar (FE) studies, the effects of other long-term impact and non-impact exercise loadings on the proximal femur bone strength (fracture load) in the fall situation have also been investigated by others [62,63]. Warden, Fuchs, and their colleagues (2020, 2021) reported that, compared to non-dominant leg, the long-term (> 6 years) impact exercise loading generated by the landing in the baseball or softball pitching led to the significantly 13% and 11% higher fall-induced fracture (onset) loads in the dominant leg of young adult male (aged 26.8 ± 2.1 years) and female pitchers (aged 20.4 ± 1.4 years), respectively. The baseball or softball pitching generates an asymmetric loading where the dominant leg (the contralateral side to the throwing arm) experiences more impact landings than the nondominant side. [62,63] The major difference between the present and their studies was that the within-subject dominant-to-nondominant leg difference in the proximal femur bone strength was evaluated in their study to account for selection bias whereas the between-group difference was examined in the present research. Despite this drawback, the present results are essentially in line with theirs, suggesting the association of the long-term impact exercise loading with the higher proximal femur bone strength to reduce fall-induced hip fracture risk. Altogether,

these findings suggest that the impact exercise loading is a key to improve or maintain the proximal femur bone strength in the fracture-causing fall situation.

The bone mass and size is influenced by the body size [605–608]. Therefore, to evaluate the anabolic effect of exercise training on the bone, these confounding effects need to be removed. In **Publication I**, the individual peak impact force was used as a covariate (confounder) since it takes into account both individual height and BW. For the later publications, the procedure to choose the covariate was refined by performing the additional analyses (checking for the homogeneity of regression slope and/or performing Pearson correlation analyses). In **Publication II**, only BW was used whereas BW and LM were applied separately in **Publication III**. Interestingly, the significant differences in the unadjusted and BW-adjusted fracture loads observed between the specific exercise loading groups and the control group disappeared once controlled for LM (**Publication III**). Based on bone's functional adaptation [2,3], the bone adapts to the prevalent mechanical environment which comprises mainly the gravitational (ground reaction) and internal muscle contraction forces. For the weight-bearing skeletons, the magnitude of the mechanical loading is primarily determined by the BW, which does not exclude the fat mass [606]. The LM can be used as a proxy for the muscle mass and force, and the physical activity level [609]. Importantly, the LM was found associated with femoral neck aBMD and size (CSA) [609,610]. The present exercise loading groups apparently had the higher physical activity level than the control group based on their larger training volume (**Table 8**). Therefore, controlling the fracture load (proximal femur bone strength) for the muscle mass and force, and the physical activity level (or their proxy, LM) likely remove the anabolic effect of exercise training on bone. The present research demonstrated this while highlighting the importance of choosing the appropriate confounder (covariate) to address the research question. In this regard, BW was deemed a more suitable choice since it considers both individual body size and the magnitude of loading in the daily mechanical environment [606].

6.2 Effect of Fall Direction onto the Greater Trochanter on the Fracture Load and the Weakest Fall Direction

The present results showed that the (group-wise) fracture loads decreased by up to 32-35% as the angle (α) between the ground and the femoral shaft increased from 0° to 30°, 22-27% as the hip internal rotation (β) angle increased from 0° to 30°, and

34-36% as both angles shifted from 0° to 30° (from 0°-0° to 30°-30° direction, **Publication III**). These are closely in concordance with previous experimental [48] and FE modeling studies of proximal femur in the multiple fall configurations [46,66,505,548]. Overall, these decreasing trends of the fracture loads suggest that proximal femur bone strength (to reduce fall-induced hip fracture risk) decreases if the fall-induced impact is applied to a more superior aspect (indicated by a greater α angle) and/or a more posterolateral aspect (indicated by a greater β angle) than the lateral aspect of the greater trochanter (e.g., 0°-0° direction). As a matter of fact, a recent cohort study of video-captured falls (> 2300 falls) of over 600 elderly persons (mean age: 83 years) reported that the most of hip fractures occurred when the impact was imposed on the posterolateral aspect of the pelvis (77%, 23 out of 30 cases) whereas only 13% (4 cases) of the fractures happened when the impact was imposed on the lateral aspect [69].

The fall is an unpredictable event, and thus predicting the fall direction or direction of fall onto the greater trochanter is unrealistic. Besides, the weakest fall direction is likely specific to each individual femur. Given these, Falcinelli, Qasim, and their colleagues (2014, 2016) proposed that the minimum fall strength (MFS) among the multiple fall directions is more appropriate to estimate the individual hip fracture risk instead of based on the direction-wise fracture load. In fact, they demonstrated that the MFS can discriminate the hip fracture cases from the non-cases slightly more accurately than a single direction-load (e.g., 10°-15°), aBMD (femoral neck, trochanteric, and total femur), and FRAX: respective AUCs were 0.79-0.88, 0.77, 0.73-0.79, and 0.69, respectively. [66,67] This highlights the importance of both the simulation of multiple fall directions and the estimation of MFS. To be in line with the above-mentioned decreasing trends, all MFS in the present study were also located where either or both angles were the greatest, confirming the decrease in the proximal femur bone strength as the fall impact is imposed to the more superior and/or posterolateral aspect of the greater trochanter.

6.3 Initiation of Compression-Induced Fracture at Superolateral Femoral Neck

In the fall configuration (10°-15° direction), the high octant cortical stresses were observed mainly in the superior and posterior aspects of superolateral femoral neck (the superior, superoposterior, and posterior octants at the middle and distal femoral neck). Besides, all groups had their highest stress values in the superoposterior octant

at the distal femoral neck site (**Publication I**). Similarly, the fracture location analyses from the **Publication II** showed that the majority of simulated fractures were observed in these regions, particularly in the superoposterior octant in the basicervical (=distal) femoral neck region (> 50% of 111 fractures, **Figure 50**). Besides, since the locations of all observed trochanteric fractures (8 out 111) were around the trochanteric fossa, all very close to the basicervical region, they could have been classified as the basicervical femoral neck fracture with a slightly more lenient definition of the fracture location. These results are, again, closely in line with both previous experimental [37,42,44,49] and FE modeling studies of proximal femora [36,41,43,45,47,50]. These studies consistently showed that the fractures initiated from this superolateral cortex, particularly in its posterior aspect (around the superoposterior octant), in the basicervical/distal femoral neck region due to the unusually high compressive loading caused by the fall onto the greater trochanter. In fact, all 111 proximal femora in the present study failed due to the compression (**Publication II**). This compression-induced fracture initiation in the superolateral cortex has also been confirmed in a recent clinical study where femoral neck cortical bone samples were extracted from the intracapsular hip fracture patients. Microscopic analyses of these samples demonstrated the higher density of the compressive microcracks in the superior than the inferior femoral neck cortex. [404]. Therefore, it was of great interest to find out, based on the 3D morphological rather than 2D planar analyses, if the present impact exercise loading groups had the thicker cortex at this fracture-prone superolateral femoral neck (particularly at its posterior aspect – superoposterior octant) or these higher fracture loads were attributed to the thicker cortical bone in other regions.

6.4 Supporting Evidence – Exercise-Induced Cortical Adaptation

6.4.1 For H-I and O-I Exercise Loading

The present higher proximal femur bone strengths in the fall observed in the H-I, O-I, and R-I groups can be mostly explained by the specific exercise-induced structural adaptation in femoral neck's cortical bone. According to the previous quadrant-based analyses on the same proximal femur data, Nikander et al. (2009) presented the H-I group had the ~20% thicker anterior and posterior cortices, and notably 60% thicker weight-bearing inferior cortex in the femoral neck compared to

the controls whereas the O-I group had consistently 15-20% thicker cortical bone around the femoral neck. It is noted, although the difference compared to the control did not reach the statistical significance ($p < 0.05$), the H-I and O-I groups had ~10% and ~15% thicker cortex at the vulnerable superior quadrant of femoral neck, respectively. Nevertheless, these observations were limited to the 2D analyses of femoral neck's cross-section. [60] Therefore, as the secondary objective of the present doctoral research, the RCM-based analyses were performed to evaluate the 3D morphological cortical bone adaptation to the specific exercise loadings within the proximal femur. These analyses may possibly elucidate further why aforementioned three impact groups had the higher proximal femur bone strengths (**Publication IV**). Compared to the controls, the H-I group had a large area of at least a 20% higher cortical thickness around the femoral neck except for the inferoanterior and superoposterior regions across the proximal, middle, and distal femoral neck. Especially, its posterior and inferior regions had substantially 40-70% and > 110% thicker cortical bone, respectively (**Figure 52**). Although the area and magnitude were smaller than the H-I group, the O-I group also had the significantly thicker cortex at some regions of the femoral neck compared to the controls. Notably, the O-I group had 10-50% and 40-60% thicker cortical walls at the superior-to-superoanterior and inferior femoral neck regions compared to the controls, respectively (**Figure 52**). Answering to the earlier question (raised in the end of the last paragraph), importantly, neither of these impact exercise groups had the apparently thicker cortical layer at the fracture-prone superoposterior aspect (octant) of the femoral neck (**Figure 52**). Therefore, their higher fracture loads compared to the controls are likely attributed to the thicker cortical bones at inferior, posterior, and/or superior-to-superoanterior femoral neck regions.

The presently observed medium-to-large areas of the beneficial cortical adaptation at the inferior femoral neck were also reported in the studies of the baseball and softball pitchers mentioned earlier based on the CBM method by Warden, Fuchs and their colleagues (2020, 2021). However, in contrast to the present study, such beneficial cortical adaptations were not observed in other femoral neck regions in their studies. [62,63] This discrepancy is likely attributed to the differences in the study design (between-group vs. within-subject) and in characteristics of the study participants between the present and their studies. Nonetheless, these three-dimensionally observed substantial regional cortical thickening are outstanding structural adaptations to these impact exercise loadings and likely led to the increase in the proximal femur bone strength. Altogether, both 2D and 3D analyses of the proximal femur cortical morphology strongly suggest the potential contribution of

these impact exercise-induced cortical structural adaptation to the higher proximal femur bone strength to reduce fall-induced hip fracture risk.

6.4.2 For R-I Exercise Loading

Another important observation from the present and previous research on the same proximal femur data was that, in opposition to the H-I and O-I groups, such potentially beneficial cortical thickening in the femoral neck was not observed in the R-I group through either of 2D [60] or present 3D analyses of proximal femur cortical bone (**Figure 52**) (**Publication IV**). This suggests that the observed apparent higher proximal femur bone strength in the fall configuration in the R-I group (**Publications I-III**) is attributed to other factors rather than the cortical thickness. Bryan et al. (2009) identified the femoral neck roundness (femoral neck diameter ratio), femoral neck-shaft angle, and anteversion angle as the important geometric factors among others, determining the proximal femur bone strength in the fall configuration [611]. In another previous analysis on the same proximal femur data as the present study, Narra et al. (2013) found the geometric shape of the femoral neck cross-section in the R-I group is more circular [612]. In principle, a more circular bone is mechanically more robust regardless of loading direction than an oval-shaped bone. Accordingly, it was demonstrated that the more circular femoral neck cross-section, typically observed in physically more active medieval people, experiences 1.3-1.5 times less fall-induced stress compared to the more oval-shaped cross-section common in present-day, habitually more sedentary people [613]. The present up to 30% benefits in the octant cortical stress (**Publication I**) and fracture loads regardless of the fall direction (**Publications II and III**) observed in the R-I group are closely in line with this estimation. Nevertheless, these considerations do not go beyond the speculation and call for further studies to investigate if the R-I proximal femora have any other characteristic geometric/structural features and their potential associations with the higher fracture loads to elucidate the sources of their higher proximal femur bone strength.

Next, it is noteworthy that the presence of regionally thicker cortical bones in the femoral neck in the H-I and O-I groups and its absence in the R-I group (**Publication IV**) may explain why the relative axial fracture locations only in the H-I and O-I groups were located significantly more (7-10%) proximal along the femoral neck axis compared to the controls. It can be speculated that the regionally thicker cortical bone in the femoral neck region induced by these H-I and O-I exercise

loadings (**Figure 52**) may have shifted the high bending loading towards more proximal side of femoral neck.

Moreover, the degree of the present benefits reflected in the fracture loads were slightly smaller in the O-I group compared to those observed in the H-I and R-I groups (**Publications I-III**). For example, the fracture loads in a single fall configuration (10°-15° direction) were 11%, 14%, and 26% higher in the O-I, H-I, and R-I groups than the controls, respectively (**Publication II**). The RCM-based 3D analyses of surface principal strain distribution in the same fall configuration largely explain this. The areas of the significantly smaller absolute minimum principal strains around the femoral neck compared to controls (which led to the higher fracture loads) were much larger in the H-I and R-I groups than in the O-I group (**Figure 53**).

Lastly, the apparently beneficial structural adaptation of the cortical bone around the femoral neck were either small in the H-M group or not observed in the R-NI group based on the previous 2D [60] and present 3D morphological analyses of the proximal femur cortical bone (**Figure 52**). This largely explains why no benefit in the proximal femur bone strength in the fall configuration was observed in these exercise loading groups.

6.5 Exploration of Characteristic Loading Properties in Specific Sports

Elaborating the loading characteristics of the five distinct exercise loading types examined in the present research may help understand essential loading properties that underlie specific exercise-induced beneficial adaptations in the proximal femur. Such information can be analyzed in terms of the ground impact or loads affecting the hip joint.

6.5.1 Loading Characteristics at Ground

The loading characteristics at the ground impact (except for R-NI – swimming) such as peak ground reaction forces (GRF, expressed in BW, measured by force platforms) and estimated maximum loading rates (BW/s) were obtained from the literature and summarized in **Table 12** for each exercise loading type. Based on this table, the common loading properties among the beneficial H-I, O-I, and R-I

exercise loading types are the moderate-to-high peak GRFs (12-20 BW, 2.5-3.5 BW, and 2-3 BW, respectively) and high loading rates (400-480 BW/s, 20-180 BW/s, and 60-150 BW/s, respectively). Although the O-I and R-I exercise loadings have the lower loading magnitudes (peak GRF) and rates compared to those in the H-I exercise loading, their loading frequencies are inherently higher.

Table 12. Loading characteristics of five distinct exercise loading types examined in the present research including the peak ground reaction force and loading rate.

Group	GRF (BW)	Loading rate (BW/s)	Study
H-I	12-20	400-480	[273,614]
O-I	2.5-3.5	20-180	[344,615–617]
H-M	2-3	5-6	[618]
R-I	2-3	60-150	[619–624]
R-NI	< 1.5	< 10	[625,626]

Note: [273] – Heinonen et al. (2001); [344] - Bailey & Brooke-Wavell (2010); [614] – Ramey & Williams (1985); [615] – Smith et al. (2004); [616] – Dayakidis & Boudolos (2006); [617] – Ball (2013); [618] – Swinton et al. (2012); [619] – Cavanagh & Lafortune (1980); [620] – Kluitenberg et al. (2012); [621] – Logan et al. (2010); [622] – Munro et al. (1987); [623] – Tominaga et al. (2016); [624] – Yu et al. (2021); [625] – Lyttle et al. (1999); and [626] – Blanksby et al. (1996).

In swimming, a high muscle activity and a large number of repetitive movements are involved. However, the magnitude of the mechanical loads is essentially smaller due to an aquatic hypo-gravitational environment generated by the buoyancy in water. Some impact loading still takes place at the push-off phase of turning in the swimming; however, its reaction force (< 1.5 BW) and loading rate (< 10 BW/s) are considerably smaller (**Table 12**). Next, although the extremely heavy weights are lifted in the H-M exercises such as squat and deadlift, their loading magnitudes (peak GRFs, 2-3 BW) are similar to those in the O-I and R-I exercise loadings (**Table 12**). Besides, the loading rate (5-6 BW/s) and frequency in the H-M exercise are essentially smaller compared to those in the impact exercise loadings because of the nature of the H-M exercises (inherently slow movement and the low number of repetition). Altogether, the moderate-to-high loading magnitude (GRF) alone appeared insufficient but needs to be generated at the high loading rate and/or frequency to induce the beneficial adaptations within the proximal femur cortical bone. These contemplations are essentially in concordance with the observations from the previous animal experimental studies [3,14–24,627]. It can be speculated that not only exercise types examined in the present doctoral research but also other exercise types which satisfy this condition likely induce the beneficial adaptation,

resulting in the increase or maintenance of the proximal femur bone strength in the fall situations.

Furthermore, it is worth mentioning that the loading characteristics of the weightlifting (snatch, clean, and jerk). Due to the similarities in the movements between powerlifting (such as squat and deadlift, H-M exercise in the present research) and weightlifting, they are often mistaken for each other. In contrast to the powerlifting, the weightlifting movements are typically more explosive and involve the higher impact: peak vertical GRFs and estimated loading rates are 2.5-4 times BW and 10-50 BW/s, respectively [628–631]. Thus, this warrants for the further investigation to examine the proximal femur strength of the weightlifters, in comparison with the controls and especially with the powerlifters.

6.5.2 Loading Characteristics at Hip Joint

The information on the loading properties at the ground discussed above may not be sufficient to characterize the effective exercise inducing the beneficial adaptation in the proximal femur. They do not necessarily convey how much loading is transmitted to the hip joint and proximal femur bone. Such information can be found in recent musculoskeletal FE modeling studies where the hip contact forces (in BW) and femoral neck strains were analyzed during numerous movements [632–635]. It was found that an unilateral vertical hopping and running at 6-12 km/h generate the considerably higher hip contact forces (7.5 BW and 6-10 BW, respectively) compared to the one (4-5 BW) in walking at 4 km/h [633,634]. On the other hand, the moderate H-M exercises such as hip resistance trainings (flexion, extension, adduction, and abduction exercises) at 40-80% of 1 repetition maximum (RM) produced comparable or even smaller hip contact forces compared to the walking [633].

On the basis of classic Frost's mechanostat theory [2] and bone remodeling theory by Huiskes et al. [636,637], the osteogenic adaptive bone response is induced when the loading-generated strain magnitude and/or strain energy exceeds the homeostatic thresholds around 1500 με or by 75%, respectively. Pellikaan et al. (2018) [633] demonstrated that the unilateral vertical hopping and running at 7-9 km/h generate the significantly higher compressive and tensile strains at both the inferior and superior femoral neck than the walking at 4km/h, exceeding the homeostatic threshold. Besides, the inferior femoral neck experiences up to 7 times higher strain in the unilateral vertical hopping than in the walking, which likely

account for the aforementioned > 60% thicker inferior femoral neck cortex observed in the H-I group based on the previous 2D [60] and the present 3D analyses (**Figure 52** and **Publication IV**). Furthermore, Martelli et al. (2014) [635] showed that the strain energies generated by the unilateral long and bilateral vertical jumps are also substantially high, exceeding the homeostatic threshold by ~500% and 200%, respectively. Overall, these observations on the high hip contact forces, and femoral neck strain magnitudes and energies during the jumping, hopping, and running exercises further underline the high potentials of these impact exercises in inducing the beneficial osteogenic adaptation within proximal femur. Regrettably, the analyses on the loading (strain) rate at the hip joint were not included in these musculoskeletal FE modeling studies [632–635]. Given its importance as identified through the present doctoral and previous animal experimental studies [19–21,218], comparisons of the strain rate at the hip joint or proximal femur among different exercises may elucidate the mechanism of exercise-induced osteogenic adaptation to a further extent.

Above-mentioned vertical hopping and jumping can be regarded as a moderate H-I exercise and/or a part of the O-I exercise excluding the multidirectional element. However, none of the musculoskeletal FE modeling studies discussed so far [632–635] have investigated the multidirectional O-I jumping/hopping exercises. The author of the present doctoral dissertation and his colleagues postulated that the strain could be more uniformly distributed over the femoral neck in such O-I exercises due to repeated impacts from varying unusual directions within a short period of time. Moreover, it was hypothesized that such uniform loading distribution may consequently facilitate a more symmetric osteogenic adaptation around the femoral neck's cortical bone including its vulnerable superolateral region. Nevertheless, the hip contact forces and femoral neck strains could be unexpectedly smaller in the O-I exercise than in H-I and R-I exercises. In order to maintain the kinematic posture, the loads generated by the ground impact from the unusual directions could be dispersed and absorbed by the muscular activities before reaching the hip joint. However, these do not go beyond the speculation and call for the future musculoskeletal FE modeling studies to evaluate the loading characteristics of the multidirectional impact exercises at the hip joint. Nonetheless, it should be noted that the beneficial effects of the daily multidirectional hopping exercise (a moderate H-I and O-I exercise) on the proximal femur have been reported for both males and females regardless of age through two 6–12-month RCTs by Allison et al. (2013, 2015) [345,346] and Bailey and Brooke-Wavell (2010) [344]. Compared to the control leg, such exercise intervention resulted in

considerable increases in femoral neck aBMD by 1.6-3.1%, BMC by 1.2-1.3%, CSA by 2.4%, and Z by 1.6% in the exercised leg. Particularly important findings were that these exercises led to the substantial regional bone gain at the vulnerable superolateral femoral neck: superior femoral neck aBMD and CBM-derived superoposterior cortical mass surface density were 3.1% and > 6% greater in the exercised leg than in the control leg, respectively. [344–346] Despite the lack of information on the loading properties of the multidirectional O-I exercises through the musculoskeletal FE modeling studies, these evidence from the RCTs support the effect of the multidirectional O-I exercise on inducing the beneficial osteogenic adaptation within the proximal femur.

6.6 Clinical Relevance

As to the clinical relevance, the present findings need to be interpreted with caution. Considering the present data were acquired from the young adult females, the findings cannot be extrapolated directly into the general or old populations. Since the exercise-induced beneficial adaption in bone is more evident in growth phase than later in life [343], the results from the young population help finding and designing the effective osteogenic exercise programs. However, their efficacy, safety, and feasibility need to be evaluated for the older generations prior to their implementation. Numerous RCTs and their meta-analyses confirmed the efficacy of the H-I, O-I, and R-I exercises in inducing the beneficial adaptations in the femoral neck (e.g., increases in aBMD, BMC, CSA, and Z) in both male and female regardless of age [298,299,305,344–346,348,351,352,356,363,364]. However, it should be noted that the efficacy of these exercises in male should remain inconclusive due to insufficient data available according to the meta-analyses [358,360,365]. Importantly, as mentioned above, two 6-12 month RCTs demonstrated that the daily multidirectional hopping exercise (a moderate H-I and O-I exercise) can induce the beneficial adaptations in the femoral neck including the fracture-prone superolateral regions [344,346]. In contrast, the H-M exercise alone were found ineffective at least in females in any ages [349,350,353,356].

Next, the safety and feasibility of the impact exercises should be carefully examined, especially for the frail old population. Despite the apparent benefits to the proximal femur bone strength, the H-I exercises accompanied with the extreme GRF (12-20 times BW, **Table 12**) is obviously too risky for the musculoskeletal injuries not only for the old population but also for sedentary people regardless of

age. On the other hand, due to more moderate impact magnitudes (2-3.5 times BW, **Table 12**), such risk is likely smaller in the O-I and R-I exercises. Therefore, these two impact exercises can provide a safer and more feasible alternative to the young sedentary and frail old population to minimize their fall-induced hip fracture risk. In fact, only a few injuries were reported in previous RCTs of exercise intervention including the multidirectional hopping in the old males and females as long as participants' exercises were supervised, and its intensity and volume were gradually increased [345,357].

Based on the musculoskeletal FE modeling studies [632,633,638], moderate R-I exercises such as fast walking (6km/h) and stair ambulation appeared also effective to induce potentially osteogenic higher strain at the fracture prone superior femoral neck than the normal walking (4km/h). These exercises can be easily incorporated into the habitual daily activities even in the elderly populations due to its higher safety and feasibility compared to running. Besides, a few meta-analyses of the RCTs in postmenopausal females confirmed that moderate R-I exercises (walking or jogging combined with walking and stair climbing) can increase femoral neck aBMD. However, the observed gains are likely too marginal to be of clinical significance regarding the hip fracture prevention. [351,639] The potency of these moderate R-I exercises likely remains preserving bone mass and alleviating age-dependent bone fragility and may not be extended to decrease the hip fracture risk. Nonetheless, this uncertainty calls for further studies to examine the minimum intensity (e.g., speed) and volume of such moderate R-I exercises to induce the beneficial bone adaptation and to reduce the hip fracture risk.

It is noted the above-mentioned studies reported the osteogenic effect of exercise on the bone trait (e.g., femoral neck aBMD) to infer the beneficial effect of some exercise types on the reduction of hip fracture risk. However, such causal relationship needs to be confirmed by RCTs of exercise-intervention, preferably with hip fracture as the end-point outcome. Despite its necessity, it has appeared difficult to conduct such RCT due to the following methodological reasons: compliance, drop-out, blinding, and long-term follow-up, and, in particular, the required large sample size [640,641]. According to Gregg et al. (2000), it was estimated that the sample size ranging from ~3500 to 7000 participants per group would be required to achieve sufficient statistical power with the following reasonable assumptions: a RCT has 5 years follow-up with type-I error of 5%, type-II error of 20%; hip fracture incidence of 3-6% in control group in 5 years; and a reduction in the hip fracture risk of 25% by exercise [642]. This makes it clear that conducting such study is costly and perhaps impractical [642–644]. Nevertheless, there has been a few exercise-

RCTs conducted, which reported the hip fractures as the outcome. However, they seem to face aforementioned sample size issues. Korpelainen et al. (2006, 2010) conducted a RCT of 3-years exercise-intervention including balance, leg strength, and multidirectional jumping (impact) training with 160 postmenopausal females (aged 70-73 years). Their results appeared to suggest that the exercise decreases the hip fracture risk: no hip fracture was observed in the exercise group while 5 participants had the hip fractures in the control group. However, the statistical analysis was not performed due to small sample size. [645,646] Accordingly, two recent meta-analyses of (R)CTs by Hoffmann et al. (2023) and de Souto Barreto et al. (2019) reported that the exercise intervention can result in a 16-23% reduction of fractures (including hip fractures) in people aged 54-87 years old. Although the hip fractures were reported in a few trials included in these meta-analyses, the statistical analyses solely on the hip fracture risk were not included because sufficient statistical power was not achieved due to a very small number of hip fractures per group and the small sample size. Besides, their analyses were not designed to identify the specific exercise types which are effective to reduce the (hip) fractures. [647,648] Therefore, it is reasonable to say that a higher level of evidence for the causal relationship between the (specific) exercise and reduced hip fracture risk has not yet been confirmed based on the RCTs and warrants further studies with the sufficiently large sample size.

Exercise helps preventing hip fracture not only by improving or maintaining the proximal femur bone strength but also by preventing people from falling. The fall can be prevented by improving mobility, physical functioning, muscle strength, balance, and coordination. [643,644] Based on the meta-analyses of numerous RCTs, the exercise intervention was found to significantly reduce the risks of fall and injurious fall resulting in fractures (at various anatomical sites including hip) by 10-15% [647,649,650] and ~65% [649,651], respectively, in the old people aged over 60 years. Although balance exercise was found particularly effective, other exercises types were also found effective: gait, strength, functional, endurance, and flexibility training [649–651]. However, again, the evidence for the effect of exercise intervention solely on the hip fracture is very limited, and thus further studies with the hip fracture as the end-point outcome are still needed in this respect as well.

6.7 Sustainability of Exercise-Induced Higher Proximal Femur Bone Strength to Reduce Fall-Induced Hip Fracture Risk

In the present doctoral research, the higher proximal femur bone strength to reduce fall-induced hip fracture risk were observed in the young adult females who had engaged in sport-specific (H-I, O-I, and/or R-I loading) training from childhood/adolescence to early adulthood. Therefore, an important question remains: can the exercise-induced higher proximal femur bone strength obtained during these early stages of life persist into the later stages, especially after age of 65 years when the hip fracture is more common? The mechanical loading through the exercise facilitates the new bone formation mainly on periosteal (outer) surface of bone during skeletal growth, resulting in the outer circumferential (periosteal) expansion. On the other hand, it triggers primarily the remodeling process on the endosteal (inner) surface after the growth to maintain bone mass or mitigating rate of bone resorption, leading to the maintenance of the endocortical width or slowing down the age-related endocortical expansion. [3] That being the case, theoretically speaking, the exercise-induced benefits in bone and consequent higher bone strength obtained during these early phases should be sustained into the older age. However, the cortical bone around the femoral neck also experience the age-related thinning (**Figure 20**) due to a gradual expansion of the femoral neck diameter caused by the combination of subperiosteal bone apposition and endosteal resorption [39,401,402]. This is a normal age-dependent physiological remodeling process and bone's smart regulatory system to maintain the bending resistance by gradually increasing the diameter to compensate for the age-related bone loss [38,39,401,403]. Whether the exercise-induced structural benefits and consequent higher proximal femur bone strength acquired from the early phases remains through this age-related femoral neck expansion is also unclear. Therefore, these aspects should be investigated by a retrospective and/or prospective observational studies.

According to the observational studies [652–656], exercise-induced benefits such as the higher proximal femur, femoral neck, and greater trochanter aBMD or BMC compared to nonathletic controls start diminishing rapidly during the twenties due to the cessation of sport-specific training or retirement from competing. However, such high rates of bone loss is lessened by the mid-50s and the rate of bone loss becomes similar to those in the nonathletic controls thereafter [655]. It is of interest to know if such exercise-induced higher aBMD sustained into the older ages despite its rapid loss. However, inconsistent results have been reported on whether such exercise-induced higher aBMD from pre-puberty, adolescence, and/or early

adulthood persist into the 40s, 50s, and over 60s, and it may depend on the exercise type and sex [654,655,657–665]. For example, based on the prospective studies, the significantly higher femoral neck and trochanteric aBMDs in the former male football players compared to their age-matched controls (2-11% and 13% higher, respectively) were maintained until the late 50s (retired for 19-29 years, started competing at age of ~14-17 years) but not in the late 60s [660,664]. However, such benefits were not observed already in their 40s [retired for a mean of ~10 years (5-20 years), starting age not reported] in the former female football players [654]. In contrast, the significantly higher proximal femur and femoral neck aBMDs compared to the age-matched controls (up to 9% and 13%, respectively) were maintained in the former female artistic gymnasts in their 40s (retired for a mean of ~24 years, started their gymnastics training at an average age of ~11 years) and the former female ballet dancers in their 50s (retirement period - unknown, started their ballet training at an average age of ~8 years) [658,665].

In contrast to aforementioned inconsistent results on the aBMD, importantly, the exercise-induced structural benefits appeared to persist into the older ages to some extent. Valdimarsson et al. (2005) reported that the significantly greater bone size (8% greater in femoral neck compared to the age-matched controls) observed in the former female football players (same as above) persisted into their 40s and 50s in opposition to their higher femoral neck aBMD not maintained into even their 40s [654]. This implies the loss of exercise-induced higher aBMD in the former football players is likely due to the loss of bone mass since the aBMD is calculated by dividing the bone mass (BMC) by area (= size). Similarly, Tveit et al. (2015) reported that the former male football players (same as above) had the significantly 4% and 2% greater femoral neck area in their late 50s and 60s compared to their age-matched controls, respectively [660].

This potential sustainability of aforementioned exercise-induced benefits from the early to later stages of life does not necessarily mean that these retired old athletes have the lower hip fracture risk compared to the nonathletic controls who did not participate in the sports during their early ages. Such risk still needs to be evaluated based on the actual hip fracture incidents between them in their older ages (e.g., > 50 years). Although the number of such studies are limited, to author's knowledge, a few studies approached this issue by comparing the hip and other fracture incidents between various former athletes and the controls [656,660,662,666]. Based on several large cohorts consisting of 400-2000 former old male athletes [aged > 50 years; incl. gymnastics, track and field (jumping, sprinting, and throwing), basketball, football, handball, boxing, ice hockey, wrestling, weightlifting, long-distance running,

canoeing, swimming, biathlon, race cycling, and more] and their nonathletic controls, any fractures (incl. proximal humerus, distal radius, vertebra, pelvis, hip, and tibial condyle fractures) over 50 years old are significantly ($p < 0.05$) 50-60% lower in the former athletes than controls [660,666]. Importantly, the hip fracture risk over 50 years old appears to be 20-40% lower in the former male athletes than the controls. However, its difference did not reach statistical significance ($p < 0.05$). [656,660,662,666] Besides, it should also be noted that these findings were unfortunately limited to only males and the analyses were performed by pooling different sport types except for one study by Tveit et al. (2015). Therefore, whether specific exercise-induced lower hip fracture risk can persist into the older age is still inconclusive, particularly in females calling for the further investigation.

Furthermore, the results from the previous studies discussed so far in this section were also based on the DXA-based 2D analyses. Therefore, the future studies should also be expanded to examine whether three-dimensionally detected exercise-induced benefits (e.g., regions with exercise-induced thicker cortical layer, **Figure 40** and **Figure 52**) can persist into the older ages using, for example, the computational anatomy methods. Whether the three-dimensionally observed regionally thicker femoral neck cortical layers in the present H-I and O-I athletes (**Figure 52**) can persist into their older ages is of great interest with respect to the prevention of hip fractures. Altogether, as to the implication for future studies, further prospective and/or retrospective observational studies should be conducted to investigate the sustainability of the exercise-induced benefits in proximal femur and lower hip fracture risk into the later stage of life including the 3D morphological analyses, particularly in females and specifically to each sport type.

Lastly, it is important to mention that long-term or lifelong continuation of exercise is likely a key to maintain the exercise-induced benefits in proximal femur and consequent lower hip fracture risk from the early to later stages of life [657,667–669]. Hagman et al. (2018, 2021) reported that lifelong trained 35 old female handball players (mean age: 64 years, ranging 60-80 years) and 35 male football players (mean age: 72 years, ranging 65-80 years) who continued playing for means of 43 and 61 years, respectively, had significantly 7-13% higher aBMD at femoral Ward's triangle and trochanteric sites compared to their age-matched nonathletic controls. Also, these old male football players had the significantly 8-9% higher proximal femur and femoral neck aBMD than the controls although such higher values were not observed in the female handball players. [668,669] Importantly, based on a large cohort of 1844 former male athletes and 1216 controls, Korhonen et al. (2022) reported that the former athletes who maintained vigorous exercise intensity of ≥ 6

METs for ≥ 75 mins/week also had the significantly ($p < 0.05$) up to 77% lower hip fracture risk than controls until age of ~75 years whereas such lower risk was not observed in these former athletes whose exercise intensity was lower. After age of ~85 years, the risk in these former athletes started increasing and became similar to that in the controls by age of ~90 years. [667] However, to author's knowledge, information on whether the continuation of exercise can lead to maintenance of the lower hip fracture risk in female is again missing in general, calling for the further investigation.

6.8 Potential Application – Space Travel – Can we or our bones come back to Earth?

An enactment of a bill, the Commercial Space Launch Competitiveness Act [also known as the Spurring Private Aerospace Competitiveness and Entrepreneurship (SPACE)], on 21.5.2015 (effective since 25.11.2015) opened the door for commercial space exploration and exploitation of space resources by private sector [670]. This has facilitated the rapid growth of aerospace industries for the last decade. For example, several milestone developments have been achieved by an American space transport company SpaceX. On 21.12.2015, SpaceX succeeded the first controlled landing of their orbital class reusable (reflightable) rocket (lift launch vehicle) called Falcon 9 [671,672]. According to SpaceX's website (https://www.spacex.com/vehicles/falcon-9/), the number of the reflights reached a total of 200 as of 3 November 2023. This reusable Falcon 9 has succeeded to reduce the launching costs substantially (~30%), realizing the more sustainable aerospace business model [673]. Subsequently, SpaceX realized the first private space missions by sending nonprofessional (non-NASA) astronauts to space on 15.9.2021 [674] and to the ISS on 9.4.2022 [675] by their spacecraft (space capsule) Crew Dragon lifted by Falcon 9. Given these, the day may come earlier than expected when human beings are able to go to the space travel. However, the author of the present doctoral research who investigated the effect of exercise on proximal femur bone strength would humbly like to raise the following concern on the potential risk of the space travel: Can we or our bones really come back to Earth and live normally after the long-term space travel?

The detrimental effect of micro- or nongravitational environment from the long-term spaceflights on the proximal femur bone strength and the effect of in-flight exercise program aiming to prevent the loss of the strength have been investigated

with the FE method as discussed earlier [577–579]. Importantly, Keyak et al. (2009) reported that 4.3-6.5 months spaceflight can result in up to ~12% reduction of the proximal femur bone strength in the fall configuration [a mean of 2% (0.6 % to 3.9%) reduction per month], equivalent to 27% of the lifetime loss. Some of the astronauts examined in this study even had their post-flight proximal femur bone strength similar to the strength in the elderly females who are typically at the greatest risk for the fracture. Thus, this indicates that these astronauts have the high hip fracture risk after their spaceflight unless their bone strengths are recovered quickly. [577] However, the reversibility of the bone loss after the spaceflight has not yet been confirmed. Although the analyses were limited to tibia and radius, Vico et al. (2017) reported that astronauts' tibiae failed to recover even after 1-year reambulation period since the return to Earth from the 4-6 months spaceflight. Their microstructural analyses showed that the tibial cortical porosity and trabecular bone (vBMD and volume fraction) did not recover unlike tibial cortical thickness and density. [676] This suggests either the full recovery takes longer, or the preflight bone strength may never be restored. Yet, further follow-ups (> 12 months) are needed to investigate this. Nonetheless, these findings turn the spotlight on the importance of the in-flight exercises aiming to maintain the proximal femur bone strength during the spaceflight.

Above-mentioned monthly 2% reduction of the proximal femur bone strength was observed despite the in-flight exercises the astronauts performed [2h/day, 4 days/week including treadmill running at 0.6G, cycling, squat, and some resistance exercises using the interim resistive exercise device (iRED with the maximum loading capability up to 1334 N)]. The exercises using the updated device called the Advanced Resistive Exercise device (ARED with the higher loading capacity up to 2669 N) resulted in the significantly less decline in the FE-predicted proximal femur bone strength in the fall (by ~4% decline after ~6 month flights compared to the pre-flight strength) than using the iRED (by ~10 % decline) [579]. Assuming astronaut's BW ranging from 60 kg to 80 kg, these iRED and ARED devices can generate the loading magnitude of 2-4 BW similar to those generated by the present H-M and three impact exercise loading groups (**Table 12**). However, importantly, both of iRED and ARED devices are designed mainly for the H-M exercises (e.g., squats, deadlifts, and bench press) [579,677,678]. In light of the present beneficial findings of the impact exercise loadings and the previous RCTs (hopping intervention) [344–346], it is of great interest to find out if the impact exercise loadings can 1) provide further preventive effects on the bone loss and the decline in the strength during the spaceflight, and 2) accelerate the recovery of the bone

strength in the postflight phase so that the space travelling would not be a one way ticket for our bones. For example, simple hopping exercises can be implemented using the ARED. Also, considering the present beneficial results of R-I exercise loading, the intensity of the treadmill running (0.6G) can also be increased somehow using e.g., an elastic band. The author of the present doctoral research wholeheartedly hopes that the present results will be found inspiring to the researchers in this field to help design the inflight exercises and spacecraft/station structure which withstands the impact exercise loadings.

6.9 Strengths and Contributions of the Present Research

The main strength of the present doctoral research is the large total sample size of 111, comprising 91 young adult female athletes and 20 nonathletic controls. Based on their proximal femur MRI data, the FE modeling and 3D RCM-based morphological analyses were performed. To author's knowledge, this large total sample size makes the present research one of the largest studies of proximal femur FE modeling and 3D computational anatomy. A particular importance was that these 91 athletic participants had the long-term (> 8 years) distinct exercise loadings. Together with the total sample size, this made it possible to classify these athletes into subgroups based on sport-specific loading patterns. Such classification enabled us to examine the effect of various exercise loading history not only on the proximal femur bone strength in fall situations, but also on 3D morphological adaptation of proximal femur cortical bone. Next, the analyses of the proximal femur bone strength in fall situations were performed thoroughly and in steps through 1) octant-wise cortical stress analyses on the femoral neck's cross-section along three longitudinal sub-sections of femoral neck (**Publication I**) and 2) evaluation of fracture load and location in a single fall configuration (**Publication II**). Furthermore, the research was extended by simulating each proximal femur FE model in 12 different directions of fall (onto the greater trochanter) to investigate whether the higher proximal femur bone strength in the specific exercise loading group depends on the direction of fall. Consequently, a total of 1332 FE models were created (111 individual proximal femora × 12 fall directions). Again, to author's knowledge, this makes the current research one of the largest proximal femur FE modeling studies, particularly among those which investigated the effect of exercises on proximal femur bone strength with the FE methods.

The major contribution of the present doctoral research is providing the stronger evidence that the long-term various impact exercise loading can lead to the higher proximal femur bone strength to reduce fall-induced hip fracture risk. Previously, the impact exercise-induced benefits reflected in bone traits (e.g., a/vBMD, BMC, femoral neck CSA, and Z) were well reported in literature [54–60,298,299,305,329–333,344–346,348,351,352,355,356,363,364]. However, the evidence on the higher proximal femur strength to reduce fall-induced hip fracture risk based on the fracture loads were very limited [62,63]. Furthermore, the information on the beneficial adaptations were mostly based on the 2D analyses of femoral neck cross-section. The present research addressed this issue and presented how the regional beneficial cortical adaptations to the specific exercise loading contributed to the higher proximal femur bone strength based on 3D rather than 2D analyses. Overall, the present research identified H-I, O-I, and R-I exercise types are potentially effective exercise types to increase or maintain the proximal femur bone strength in the fall situations. The present results can be used to facilitate devising these exercises into the habitual exercise routines, which would be of utility in practical preventive actions against the hip fractures. This could translate into not only reduced hip fracture incidence and associated financial burden to society due to the improved proximal femur bone strength, but also better quality of life and independent living of the old people because of improved neuromuscular performance and balance. Furthermore, the present research contributed to confirm the following previous findings well reported in literature: 1) the hip fracture risk increases if the fall-induced impact is applied on the posterolateral aspect of the greater trochanter or hip [46,48,66,69,505,548]; 2) the importance of simulating multiple fall directions and estimation of the MFS with respect to the prediction of hip fracture [66,67]; and 3) the hip fracture most likely initiates from the superolateral cortex of femoral neck due to fall-induced unusually high compressive loading [36,37,41–45,47,49,50]. Lastly, the present results could also be utilized to design in-spaceflight exercise programs to prevent the loss of the proximal femur bone strength due to micro- or nongravitational environment during the spaceflights.

6.10 Limitations of the Present Research

There are also some limitations involved in the present doctoral research. These limitations can be categorized into due to characteristics or specifications of 1) study

participants, 2) FE models, and 3) RCM method. The following sections discuss the limitations in each category.

6.10.1 Due to Characteristics of Study Participants

The present doctoral research mainly compared the between-group differences in the outcome variables (e.g., fracture loads, cortical thickness). The problem inherent to this type of study design is a selection bias that could result in under/overestimation of the true exposure-outcome relationship [318]. To minimize this type of the systematic error, a within-subject comparison can be implemented instead. Warden, Fuchs, and their colleagues (2020, 2021) realized this by comparing the dominant-to-nondominant leg difference in the proximal femur bone strength in the fall (onto the greater trochanter) configuration within each study participant. However, it is noted that there is a prerequisite to perform this type of analysis. A pair of proximal femora within a same person need to be exposed to the asymmetric loading where one side (e.g., dominant leg) experiences a greater and/or more unique mechanical loading compared to the other side (e.g., nondominant leg) during the sport-specific training. Such asymmetric loading can be observed, for example, during the baseball or softball pitching movement where the dominant leg (the contralateral side of a throwing arm) experiences more impact-generating landing than the other side. [62,63] However, it is reasonable to assume a more symmetric loading was applied to proximal femora at both sides in the most of exercise types examined in the present research although the high jumpers in the H-I group may have experienced the more asymmetric loading in their take-off legs. Therefore, the within-subject dominant-to-nondominant side comparison was deemed unapplicable in the present research.

Next, despite the large total sample size of 111, a sample size in each group ranged 17-20 in the present doctoral research. For a large effect size (δ = 0.8) of an independent variable (e.g., group), an appropriate group-wise sample size is ≥ 25 [the sample size, $n = 16/(\delta^2)$] [679]. Therefore, the present small group-wise sample sizes (n < 25) likely limited the statistical power, which can lead to increasing the probability of the Type II error [680].

Based on the mean ages and competing careers of athletic participants in the present doctoral research (**Table 8**), a mean starting age of the competitive career in each exercise loading group can be estimated as follows: H-I = 12.2 years; O-I = 15.7 years; H-M = 19.5 years; R-I = 16.5 years; and R-NI = 10.6 years. Hence, the

H-M does not only have the shortest competing career (a mean of 8 years) at the time of data collection, but also started the competitive career the latest compared to other exercise loading groups. This late starting age in the H-M group is ~7 years later than the H-I group. Furthermore, this indicates that the H-M athletes in the present research likely missed the window of opportunity (early adolescence) [337,341,342] to maximize the beneficial bone adaptation induced by the H-M exercise, even with a lenient assumption that the athletic participants naturally started their sport-specific training a few year prior to their first competition. Given this, the odds of detecting the beneficial results in the H-M group was likely lowered in the present research. However, of potential relevance, intensive powerlifting exercises such as squat, bench press, and deadlift with extremely heavy weights at an early age are generally not recommended due to the risk of musculoskeletal injuries, especially without supervision provided by qualified professionals [681]. Accordingly, a study of the elite powerlifters revealed that it is common to start the powerlifting training from age of 20-25 years [682]. These explain why the present H-M athletes started to compete later than other exercise loading groups.

Lastly, the present female control participants were rather physically active than sedentary and even participated in recreational exercises for a few times a week. This being case, if the between-group comparison was performed with truly sedentary controls, the specific exercise-induced benefits observed in the present study might have been greater.

6.10.2 Due to Specifications of FE Models

6.10.2.1 By the Use of MRI Data

The major source of the limitation in this category is the use of MRI data to create the proximal femur FE models. First, the resolution of the present MRI data (a pixel size of 0.9 mm × 0.9 mm) was almost twice larger than those from many of the recent QCT-based proximal femur FE modeling studies [43,45,46,50,65,67,112,151,395,502–504,507,509–511,521,526,683]. Although the MRI has been found adequately valid to evaluate the cortical structure [284–286], a more accurate segmentation of the cortical bone could have been realized with the higher in-plane resolution.

Next, the inhomogeneous material property assignment was not realized in the present doctoral research due to the inability to obtain the pertinent information

from the present MRI data. It is well known that the bone tissue, particularly internal trabecular bone, is a truly porous material, which results in heterogeneous distribution of the apparent bone density within the proximal femur. Accordingly, the material properties of bone such as the elastic modulus and strength depend on the density. [97,105] Therefore, this heterogeneous distribution of the density and resultant variation of the material properties within the proximal femur has been implemented through the density-based inhomogeneous material property mapping method in the most of the previous QCT-based FE modeling studies utilizing the CT scan data (voxel-based Hounsfield unit) [43,45,50,64,65,67,112,395,488,501–513]. Hence, the application of such material property assignment would likely have improved the model accuracy to a certain degree in the present doctoral research. Despite this, it should be noted that Taddei et al. (2006) reported that FE model accuracy of predicting the experimentally measured stress with the homogeneous material property assignment was only marginally less than the one with the inhomogeneous assignment (R^2 = 0.89 and 0.91, respectively). However, again, the accuracies of predicting the experimentally measured strains and fracture loads were not measured in this FE modeling study. Besides, the FE model was created from a single cadaveric femur and the simulation was limited to the physiological loading conditions (e.g., single leg stance). [112] This being a case, more studies with a large sample size are needed to scrutinize the validity of application of the homogeneous material property assignment in the proximal femur FE model for the evaluation of the fracture load based on the strain-based failure criterion, particularly in the fall configuration. Previously, Nikander et al. (2009) reported that the present athletic participants have the higher proximal femur aBMD than the controls [60]. Given this and considering the present controls are physically active, the beneficial results observed in the present exercise loading groups would likely be higher if the inhomogeneous material property assignment was implemented and the comparison counterpart was completely sedentary controls. It is also important to note that, as a consequence of adopting the homogeneous material properties, the present research resulted in exclusively evaluate the influence of cortical structure on the proximal femur bone strength in the fall configuration without considering the potential effect of inhomogeneous trabecular bone distribution. Furthermore, the low bone mineral density, particularly in trochanteric region, was found associated more with the trochanteric fracture than the femoral neck fracture where the structure plays more important role [372,405–409]. Given this, the present doctoral research may have focused more on the femoral neck fractures in the fall by adopting the homogeneous material property assignment. Therefore, the use of QCT would have not only

provided the higher in-plane/spatial resolution but also enabled the inhomogeneous material property assignment in the present study. However, it is very important to note that it would have been ethically unacceptable to expose fertile young adult females to ionizing X-ray radiation from the QCT for non-diagnostic purposes.

The presently observed between-group relative differences in the fracture load could be influenced by the adopted fixed elastic modulus values of 17 GPa and 1500 MPa for the cortical and trabecular bone compartments, respectively. To ensure this was not the case, the sensitivity analysis was performed in the **Publication II** to investigate the effect of the variation of cortical and trabecular elastic moduli on the relative between-group difference by changing the cortical and/or trabecular modulus values by 50%, 75%, 150%, and 200%. It was found that such variation causes only < 3% error in the difference that is essentially much smaller than the presently observed between-group differences in the fracture load compared to the controls in H-I, O-I, and R-I groups (11-14% in 10°-15°). Hence, it was considered that the presently adopted modulus values are appropriate to address the present research question adequately.

Furthermore, the present MRI-based proximal femur FE models were not validated by an experimental mechanical testing. Due to this, the boundary conditions were adopted from the previously validated QCT-based proximal femur FE models by others [43,50]. However, the MRI-based proximal femur FE model created by Rajapakse et al. (2020) was recently validated including the inhomogeneous material property assignment. In their study, a strong agreement was obtained between the experimental fracture loads and FE-derived ones: R^2 of 0.79 and 0.85 for yield and ultimate fracture loads, respectively. [684] Nonetheless, due to the differences between their and present research, the implementation of the inhomogeneous material properties may have anyway been unfeasible in the present research. Compared to the present research, not only the magnetic field strength was twice stronger in their research (1.5-T vs. 3.0-T MRI system, respectively), but also the spatial resolution was three times higher (0.9 mm × 0.9 mm × 1.0 mm vs. 0.3 mm × 0.3 mm × 0.3 mm, respectively). Owing to an improved signal-to-noise ratio, the 3.0-T MRI system can acquire the higher spatial resolution, leading to clearer and more detailed images, than the present 1.5-T MRI system. In fact, Phan et al. (2006) reported that the trabecular structure was more accurately captured by the 3.0-T MRI than the 1.5-T MRI system. [685] To realize the inhomogeneous material property assignment properly, Rajapakse, Chang, and their colleagues (2014) implied in their earlier MRI-based FE study [686] that the resolution of imaging should be smaller or at least similar to the trabecular thickness and spacing, ranging from 0.15 to 0.26

mm and 0.67 to 0.98 mm, respectively [687,688]. Apparently, the resolution of the present 1.5-T-based MRI data (0.9 mm × 0.9 mm × 1.0 mm) is too low to capture such microporous trabecular structure and consequent variation of the apparent density. Since the model validation and the inhomogeneous material property assignment were realized based on the high image resolution and 3.0-T MRI system in the study by Rajapakse et al. (2020), it was deemed that the inhomogeneous material property assignment was likely unapplicable to the present proximal femur MRI data.

Although the results from the present MRI-based FE models should be interpreted with a caution due to the lack of model validation, the present results such as the fracture loads from a total of 12 fall configurations, the MFSs, and the decreasing trends of fracture loads along with increasing fall angles appeared all quite comparable or slightly higher compared to those from the previous FE studies which either implemented the same failure criterion, or presented the fracture onset or yield loads [50,66,505,684]. For example, based on the present **Publications II and III**, the group-wise mean fracture loads in the single 10°-15° fall configuration, and from the 12 fall configurations ranged from 2849 N to 3231 N and 2474 N to 4311 N, respectively. In contrast, the respective values reported from the previous QCT-based FE studies were ~3100 N [50] and ~2000-3230 N [66,505], respectively. Moreover, aforementioned recent MRI-based FE study by Rajapakse et al. (2020) also reported a slightly lower mean of 2342 N. The author of this doctoral dissertation speculates that the present slightly higher fracture loads are most likely because the participants in the present research were younger and more athletic/physically active than those older participants (aged > ~60 years) recruited in the above-mentioned FE studies [50,66,505,684]. Yet, the presently observed fracture loads may still have been underestimated for the young adult athletic females due to the adoption of the trabecular modulus of 1500MPa. Based on a study by Nicks et al. (2013), femoral neck trabecular vBMD in the young females aged 20-28 years is an average of 0.268 g/cm^3 [689]. Using the density-modulus relationship [50,105,514], this density value yields the trabecular modulus of ~2600 MPa. Based on the sensitivity analysis performed in the **Publication II**, the estimated fracture loads would have been 10-15% higher if the trabecular modulus was increased from 1500 MPa to 2600 MPa. Hence, in absolute terms, the use of 1500MPa for the trabecular bone likely resulted in underestimation of the fracture loads for the present young adult females. (Further comparisons including the MFSs and the decreasing trends of the fracture load along with increasing fall angles between the

present research and previous studies by others can be found in the **Publication III**).

Similar to the present results, slightly higher fracture loads of 4519 N, 3190, N and 2931 N were reported in the fall direction of 10°-35° for young adult but male long and high jumpers, baseball pitchers, and their age-matched controls, respectively, in the recent QCT-based FE study by Warden et al. (2020) [62]. In the present research (**Publication III**), slightly lower group-wise mean values of 2487-2855N were reported in a similar fall direction (10°-30°). It was speculated that this was likely because all study participants were male in the study by Warden et al. (2020). It would be meaningful to compare the present fracture load results to those from the young adult female athletes reported from other studies. Although Fuchs, Warden, and their colleagues (2021) [63] recently conducted a similar proximal femur FE studies of the young adult female softball pitchers and cross-country runners, unfortunately, their fracture load values were not reported. Nevertheless, given that the present fracture loads and decreasing trends with the increases in the fall angles are quite comparable to those from previous QCT- and MRI-based FE modeling studies, it is reasonable to consider that the present MRI-based FE model was sufficiently valid, particularly for examining the relative strength of proximal femur between groups.

6.10.2.2 By the Choice of Isotropic over Anisotropic Mechanical Properties

The isotropic material properties were implemented in the present research. However, the mechanical properties of both cortical and trabecular bones are anisotropic [106]. Accordingly, the anisotropic mechanical properties have been implemented into the proximal femur FE models by several researchers [559–564]. Based on these studies, the high-resolution imaging (pixel size of ~80 μm) by HR-pQCT or μCT is typically required to realize the anisotropic FE model. Therefore, the implementation of the anisotropic mechanical properties appeared unfeasible in the present study due to the apparently too low image resolution. However, it should be noted that the accuracy of predicting the experimentally measured fracture load by the anisotropic FE models [562,563] has been reported not any higher than the isotropic model in the fall (onto the greater trochanter) configuration (**Table 7**). It has been speculated that this could be because the loading pattern in the fall configuration does not align with the orientation of trabecular alignment unlike in the stance or walking condition. Therefore, it is suspected that the fracture load may be less sensitive to the anisotropy of bone tissue (directionality) in the fall

configuration. [562] Besides, the anisotropic FE model is computationally more expensive than the isotropic model [560]. Given these, the author of the present research venture to claim the present use of the isotropic material properties in the FE model is a reasonable choice.

6.10.2.3 By the Choice of Quasi-Static over Dynamic Simulation

In the present research, the proximal femur FE models in the fall (onto the greater trochanter) configurations were simulated quasi-statically. For bone, the strain rate of < 0.1 s^{-1} is considered the quasi-static loading [137]. The quasi-static loading is likely still valid for the physiological loading conditions such as walking and running which induce strain rate ranging approximately 0.005 s^{-1} to 0.08 s^{-1} in human bone based on the experimental studies [131,552–554]. However, as mentioned earlier, the fall is a highly dynamic event and the impact velocity in a fall from the standing height is on average 3 m/s or higher [478,479]. Accordingly, it has been reported that the strain rate of 1 s^{-1} to 200 s^{-1} can be induced in the femoral head, neck, and greater trochanter in the fall configuration with the impact velocity of 3 m/s based on both dynamic impact experiment [555] and dynamic FE models of proximal femora [513]. Importantly, the bone is strain rate-dependent viscoelastic and viscoplastic material such that the mechanical properties such as the elastic modulus and strength vary depending on the strain rate [97,128,131,132]. Therefore, the use of the quasi-static loading in the present FE models results in disregarding not only these strain rate-dependent properties of bone but also other dynamic aspects such as potential hydraulic stiffening effect due to the bone fluid in the pores, inertial effect, and shock wave propagation [128,141,151,507,513]. Despite this, it is noted that at least the strain rate-dependent viscoelasticity can be implemented in the quasi-static FE models [50,151]. For example, utilizing the finding that the Young's modulus is approximately proportional to the strain rate to the power of 0.06 [97], Schileo et al. (2014) scaled the element-wise Young's modulus in their quasi-static FE models as follows:

$$E_{act} = E_{ref} \times \left(\frac{\dot{\varepsilon}_{act}}{\dot{\varepsilon}_{ref}}\right)^{0.06} \tag{28}$$

where E_{act} is an element-wise actual scaled Young's modulus, E_{ref} is an element-wise reference Young's modulus estimated from an empirical density-modulus relation [e.g., $E_{ref} = 6.85\rho_{app}^{1.49}$ [105]], $\dot{\varepsilon}_{act}$ is an actual strain rate obtained from the

validating mechanical testing for each FE model/method, and $\dot{\varepsilon}_{ref}$ was a reference strain rate (e.g., 0.005 s^{-1}) which was used to obtain aforementioned density-modulus relation [50]. Due to the lack of the validating mechanical testing in the present research, the actual strain rate was not available for scaling the element-wise E_{ref}, and thus the strain-rate viscoelasticity could not be incorporated in the present FE models.

Considering above, it is more appropriate to apply the dynamic loading in the proximal femur FE model in the fall configuration. However, the quasi-static loading was adopted in the most of previous proximal femur FE modeling studies. This was likely to avoid the aforementioned complexities associated with dynamic event. Nevertheless, a few investigators attempted to develop the dynamic FE models of proximal femur in the fall configuration [482,513,526]. However, the accuracy of predicting the (experimental) fracture loads were limited to $R^2 < 0.57$ [513,526], which is considerably smaller than the ones ($R^2 = 0.78$-0.9) by quasi-static FE models (**Table 7**) [45,50,64,65,503,524,525,529]. Besides, the dynamic FE simulation is clearly computationally more expensive. For example, 17-30 hours was required to simulate 40 milliseconds of the fall-induced impact event in the FE models created by Fleps et al. (2018, 2019) [482,506]. Therefore, the quasi-static FE modeling was deemed acceptable in the present doctoral research where a large number of FE models (= 1332 FE models) needed to be created.

6.10.2.4 By the Potential Overestimation of Fall-Induced Peak Impact Force

In the **Publication I**, the FE-derived octant cortical stresses in the fall (onto the greater trochanter) configuration were computed for each individual proximal femur by applying the subject-specific peak impact force. This subject-specific peak impact force was estimated using the **equation (21)** ($F_{peak} = \sqrt{2gh_{cg}KM}$) and the group-wise mean values ranged from 4738 N to 5285 N. These values may have been overestimated due to several reasons. First, in the **equation (21)**, the impact velocity was assumed to be $V = \sqrt{2gh_{cg}} \approx 4.43\sqrt{h_{cg}}$ (the **equation 20**). This velocity estimation was obtained from the simple point-mass model by van den Kroonenberg et al. (1995) while they also proposed the lower estimate: $V = 2.72\sqrt{h}$ (where *h* is a body height in m) based on their most accurate model (a two-link model with the trunk-flexion of 45°) [474]. If the latter velocity estimation was adopted in the **equation (21)** in the **Publication I**, the group-wise peak impact force would have been ~14% lower. Second, the effective pelvic stiffness *K* of 71 kN/m from

Robinovitch et al. (1991) [472] was adopted in the **equation (21)** in the **Publication I**. However, as shown in **Table 5**, more recent studies reported the stiffness values of ~20-60 kN/m [473,476,477]. For example, with *K* of 30 kN/m, the group-wise impact force in the **Publication I** would have been ~35% lower. However, it is noted that the recent inverted pendulum impact testing of cadaveric femur with hip soft tissue surrogate and corresponding dynamic FE models reported that the effective pelvic stiffness can be up to 490 kN/m in a more realistic dynamic fall (to the side) simulation [480–482]. This apparent discrepancy in the effective pelvic stiffness calls for a further investigation. Third, the impact force-attenuating effect of trochanteric soft tissue was not considered in the present research. Robinovitch et al. (1995) [483] and Fleps et al. (2018, 2019) [482,506] demonstrated in their respective experimental and dynamic FE modeling studies that every 1 mm of trochanteric soft tissue can absorb ~71 N and ~115 N of the impact force, respectively. Using the former, Bouxsein et al. (2007) reported that the impact force was reduced on average by 50-60% (from ~5700 N to 2500 N) with a 40-50 mm-thick trochanteric soft tissue in the postmenopausal females [475].

Despite the above-mentioned potential overestimation of the impact force, the presently estimated impact force values (4738N to 5285N) were quite comparable to those reported by others without considering the trochanteric soft tissue. The peak impact forces of 4260N and 5200N have been reported for the 95th percentile of females and for an average individual (males and females pooled) by van den Kroonenberg et al. (1995) [474] and Nasiri Sarvi & Luo (2017) [462], respectively. Therefore, the present impact forces may not be too far from the realistic estimates if the trochanteric soft tissue is not considered.

6.10.2.5 Remark

Lastly, in the present doctoral research, the fall-induced fracture onset load was estimated using the linear FE model. Regarding this, the author of the present doctoral dissertation would like to remark the followings. As described earlier, the crack initiation (or the onset of fracture) due to the local failure (yielding or buckling by compression) at the superolateral femoral cortex takes place before the ultimate fracture load is reached (where the macro-failure such as crush or collapse of the superolateral cortex occurs) [37,42–44,393]. Such initial damage could even be considered a partial fracture, which may already start restricting the patient's mobility and/or the patient may already feel pain from. Given this, predicting the ultimate fracture load can lead to an underestimation of the fall-induced hip fracture risk.

Besides, from the perspective of a potential future hip fracture patient, it is rather desirable that the onset of fracture is prevented, and the risk assessment is based on this fracture onset load. In this regard, the prediction of the fracture onset load is a more suitable and conservative approach than the other. Importantly, this fall-induced fracture onset load can be predicted quite accurately by the easily implementable linear FE model (R^2 of 0.81-0.9) [50,64], similar to the prediction of the fall-induced ultimate fracture load by the computationally more expensive nonlinear model (R^2 of 0.78-0.87) [45,65,524,525,529] (**Table 7**). Besides, the accuracy of predicting the experimental fracture loads in the fall configuration by the anisotropic ($R^2 < 0.87$) [562,563] or dynamic FE models ($R^2 < 0.57$) [513,526] were comparable to or even lower than the isotropic and quasi-static FE models (R^2 of 0.78-0.9, **Table 7**) [45,50,64,65,503,524,525,529]. Therefore, the author of the present doctoral research venture to claim that the prediction of the fall-induced fracture onset load by the computationally fast linear, inhomogeneous, isotropic, and quasi-static FE model is the attractive and optimal method today not only for clinical use, but also for research where a large number of proximal femur FE models need to be created like the present research. Nonetheless, the author also hopes that development of nonlinear, anisotropic FE model and/or its dynamic simulation continues, and they will eventually become a standard method with reasonable implementability and computational cost since these FE features represent bone's material properties and the dynamic fall event more realistically.

6.10.3 Due to Specification in RCM method

There are a few limitations due to the specification in the RCM-based 3D analyses and the subsequent between-group statistical comparisons. First, the correction of the registration error by the radial basis functions were performed based on only two anatomical features (femoral head and lesser trochanter). Therefore, it is not yet certain that other anatomical positions or features are correctly corresponded each other between proximal femora. An increase in the number of anatomical features for this correction is required for the improvement of the registration error. Next, a stricter threshold ($p < 0.005$) was used to detect the between-group statistically significant differences in the **Publication IV** compared to those ($p < 0.05$) used in the **Publications I-III**. In fact, the less strict threshold ($p < 0.05$) has been used in other previous computational anatomy studies where similar between-group statistical analyses were performed [346,587,690]. With a more lenient threshold (p

< 0.025), the thicker cortical bone was indeed observed at the fracture-prone superoposterior region of femoral neck in the O-I group (**Figure 52**). Therefore, the degree of beneficial results in the H-I, O-I, and/or R-I groups observed through the present RCM-based 3D analyses might have been greater if such threshold was adopted.

7 CONCLUSION

The present doctoral research explored the effect of long-term specific exercise loading on proximal femur bone strength in fracture-causing fall situations. Based on the proximal femur MRI data of 111 young adult females representing histories of distinct exercise loading, a total of 1332 pertinent proximal femur FE models were created in 12 multiple fall (onto the greater trochanter) configurations. The results of these models demonstrated that young adult females with the long-term exercise loading history of high ground impacts (H-I: e.g., triple/long and high jumps), ground impacts from unusual/odd directions (O-I: e.g., football/soccer, squash, and tennis), or a great number of repetitive ground impacts (R-I: e.g., endurance running) had the 10-22%, 12-16%, and 14-23% lower fall-induced cortical stress at the fracture-prone superolateral femoral neck and 11-17%, 10-11%, and 22-28% higher fracture loads (higher proximal femur bone strength) in the fall situations compared to non-athletic controls, respectively. These results indicate that the long-term H-I, O-I, and R-I exercise loadings may reduce the fall-induced hip fracture risk. Furthermore, the present results showed that the higher proximal femur bone strength to reduce fall-induced hip fracture risk in athletes engaged in the high-impact or repetitive-impact sports are robust and independent of the direction of fall onto the greater trochanter. In contrast, the higher strength attributed to the odd-impact exercise loading appears more modest and specific to the fall direction. The analysis of the minimum fall strength spanning the multiple fall directions also supported the higher proximal bone strength in the athletes engaged in these impact exercises. In concordance with the literature, the present results also confirmed in these young adult females that 1) the fall-induced fracture most likely initiates from the superolateral femoral neck's cortical bone, particularly at its posterior aspect (superoposterior cortex) in the distal femoral neck region and 2) the most dangerous fracture-causing fall direction is the one where the impact is imposed to the posterolateral aspect of the greater trochanter.

It would be ideal if impact exercise loading could induce beneficial cortical bone adaptation in the fracture-prone posterior aspect of superolateral femoral neck cortex. However, such apparently beneficial cortical adaptation was not observed in any of the impact or nonimpact exercise loading types examined in the present

research based on the supplementary RCM-based 3D morphological analyses of proximal femur cortical bone. This analysis importantly showed that the higher proximal femur bone strength to reduce fall-induced hip fracture risk in athletes engaged in the high- or odd-impact exercise types are likely due to thicker cortical layers in other femoral neck regions including the inferior, posterior, and/or superior-to-superoanterior regions. Interestingly, the higher proximal femur strength in the athletes with the repetitive-impact exercise loading was not supported by such cortical adaptation. This suggests that other structural/geometrical adaptation contributes to their higher strength. This calls for further studies to elucidate the source of the higher proximal femur bone strength in this type of athletes.

In contrast to the impact exercise loading histories, the exercise loading history of the high-magnitude (e.g., powerlifting) or repetitive, non-impact (e.g., swimming) was not associated with the higher proximal femur bone strength to reduce fall-induced hip fracture risk. This most likely reflects the lack of any beneficial structural adaptations of cortical bone around the femoral neck in the athletes with these exercise loading histories. Considering the loading characteristics of the exercise types examined in the present doctoral research, the moderate-to-high loading magnitude alone appears likely insufficient but needs to be generated at the high loading rate and/or frequency to induce the beneficial adaptation in the proximal femur cortical bone. Therefore, in addition to aforementioned three impact exercise loading types, other exercise or sport types satisfying this condition may also be effective to increase or maintain the proximal femur bone strength to reduce fall-induced hip fracture risk.

As a clinical prospect, the present findings highlight the importance of impact exercise in combating fall-induced hip fracture. Compared to the high-impact loading exercises (e.g., triple/long and high jumping exercises), the odd-impact [ball or invasion games (e.g., football/soccer, tennis)] and/or repetitive-impact loading exercises (e.g., endurance running, jogging, and perhaps vigorous walking) likely provide a safer and more feasible choice for the populations covering the sedentary adults to old people. This is due to the relatively more moderate ground impact involved in the odd- and repetitive-impact loading exercises than in the high-impact exercises. For young, physically active, and/or fit people, the above-mentioned or similar jumping exercises and any other exercise types consisting of the high ground impact (e.g., volleyball, basketball, gymnastics) can also be incorporated into their habitual exercise routines. Lastly, the present results were observed in the young adult females who had engaged in sport-specific training from their childhood/adolescence to early adulthood. Therefore, this calls for the prospective

and/or retrospective observational studies to investigate whether the higher proximal femur bone strength to reduce fall-induced hip fracture risk obtained from the long-term specific impact exercise loading during these early phases of life can sustain into the later stages, especially after age of 65 years when the hip fracture is generally more common.

8 REFERENCES

[1] N.H. Hart, S. Nimphius, T. Rantalainen, A. Ireland, A. Siafarikas, R.U. Newton, Mechanical basis of bone strength: influence of bone material, bone structure and muscle action, J. Musculoskelet. Neuronal Interact. 17 (2017) 114–139.

[2] H.M. Frost, Bone's mechanostat: A 2003 update, Anat. Rec. Discov. Mol. Cell Evol. Biol. 275 (2003) 1081–1101. https://doi.org/10.1002/ar.a.10119.

[3] C. Ruff, B. Holt, E. Trinkaus, Who's afraid of the big bad Wolff?: "Wolff's law" and bone functional adaptation, Am. J. Phys. Anthropol. 129 (2006) 484–498. https://doi.org/10.1002/ajpa.20371.

[4] M.K. Karlsson, Physical activity, skeletal health and fractures in a long term perspective, J. Musculoskelet. Neuronal Interact. 4 (2004) 12–21.

[5] R.P. Heaney, S. Abrams, B. Dawson-Hughes, A. Looker, R. Marcus, V. Matkovic, C. Weaver, Peak bone mass, Osteoporos. Int. 11 (2000) 985–1009. https://doi.org/10.1007/s001980070020.

[6] C.M. Weaver, C.M. Gordon, K.F. Janz, H.J. Kalkwarf, J.M. Lappe, R. Lewis, M. O'Karma, T.C. Wallace, B.S. Zemel, The National Osteoporosis Foundation's position statement on peak bone mass development and lifestyle factors: a systematic review and implementation recommendations, Osteoporos. Int. 27 (2016) 1281–1386. https://doi.org/10.1007/S00198-015-3440-3.

[7] B.A. Wallace, R.G. Cumming, Systematic review of randomized trials of the effect of exercise on bone mass in pre- and postmenopausal women, Calcif. Tissue Int. 67 (2000) 10–18. https://doi.org/10.1007/s00223001089.

[8] M. Nilsson, D. Sundh, D. Mellström, M. Lorentzon, Current Physical Activity Is Independently Associated With Cortical Bone Size and Bone Strength in Elderly Swedish Women, J. Bone Miner. Res. 32 (2017) 473–485. https://doi.org/10.1002/jbmr.3006.

[9] W. Kemmler, K. Engelke, S. von Stengel, Long-Term Exercise and Bone Mineral Density Changes in Postmenopausal Women-Are There Periods of Reduced Effectiveness?, J. Bone Miner. Res. 31 (2016) 215–222. https://doi.org/10.1002/jbmr.2608.

[10] D. Kerr, A. Morton, I. Dick, R. Prince, Exercise Effects on Bone Mass in Postmenopausal Women are Site-specific and Load-dependent, J. Bone Miner. Res. 11 (1996) 218–225. https://doi.org/10.1002/jbmr.5650110211.

[11] R. Nikander, H. Sievänen, K. Uusi-Rasi, A. Heinonen, P. Kannus, Loading modalities and bone structures at nonweight-bearing upper extremity and weight-bearing lower

extremity: A pQCT study of adult female athletes, Bone. 39 (2006) 886–894. https://doi.org/10.1016/j.bone.2006.04.005.

[12] R. Nikander, H. Sievänen, A. Heinonen, R.M. Daly, K. Uusi-Rasi, P. Kannus, Targeted exercise against osteoporosis: A systematic review and meta-analysis for optimising bone strength throughout life, BMC Med. 8 (2010) 47. https://doi.org/10.1186/1741-7015-8-47.

[13] M. Kistler-Fischbacher, B.K. Weeks, B.R. Beck, The effect of exercise intensity on bone in postmenopausal women (part 1): A systematic review, Bone. 143 (2021) 115696. https://doi.org/10.1016/J.BONE.2020.115696.

[14] T. Sugiyama, J.S. Price, L.E. Lanyon, Functional adaptation to mechanical loading in both cortical and cancellous bone is controlled locally and is confined to the loaded bones, Bone. 46 (2010) 314–321. https://doi.org/10.1016/j.bone.2009.08.054.

[15] L.E. Lanyon, C.T. Rubin, Static vs dynamic loads as an influence on bone remodelling, J. Biomech. 17 (1984) 897–905. https://doi.org/10.1016/0021-9290(84)90003-4.

[16] C.T. Rubin, L.E. Lanyon, Regulation of bone mass by mechanical strain magnitude, Calcif. Tissue Int. 37 (1985) 411–7. https://doi.org/10.1007/bf02553711.

[17] T. Sugiyama, L.B. Meakin, W.J. Browne, G.L. Galea, J.S. Price, L.E. Lanyon, Bones' Adaptive Response to Mechanical Loading Is Essentially Linear Between the Low Strains Associated With Disuse and the High Strains Associated With the Lamellar/Woven Bone Transition, J. Bone Miner. Res. 27 (2012) 1784–1793. https://doi.org/10.1002/jbmr.1599.

[18] D. Sun, M.D. Brodt, H.M. Zannit, N. Holguin, M.J. Silva, Evaluation of loading parameters for murine axial tibial loading: Stimulating cortical bone formation while reducing loading duration, J. Orthop. Res. 36 (2018) 682–691. https://doi.org/10.1002/JOR.23727.

[19] J.R. Mosley, L.E. Lanyon, Strain rate as a controlling influence on adaptive modeling in response to dynamic loading of the ulna in growing male rats, Bone. 23 (1998) 313–318. https://doi.org/10.1016/S8756-3282(98)00113-6.

[20] J.A. O'Connor, L.E. Lanyon, H. MacFie, The influence of strain rate on adaptive bone remodelling, J. Biomech. 15 (1982) 767–781. https://doi.org/10.1016/0021-9290(82)90092-6.

[21] C.H. Turner, I. Owan, Y. Takano, Mechanotransduction in bone: Role of strain rate, Am. J. Physiol. - Endocrinol. Metab. 269 (1995). https://doi.org/10.1152/ajpendo.1995.269.3.e438.

[22] C.T. Rubin, K.J. McLeod, Promotion of bony ingrowth by frequency-specific, low-amplitude mechanical strain, Clin. Orthop. (1994) 165–74.

[23] S.J. Warden, C.H. Turner, Mechanotransduction in the cortical bone is most efficient at loading frequencies of 5-10 Hz, Bone. 34 (2004) 261–270. https://doi.org/10.1016/j.bone.2003.11.011.

[24] Y.-F. Hsieh, C.H. Turner, Effects of Loading Frequency on Mechanically Induced Bone Formation, J. Bone Miner. Res. 16 (2001) 918–924. https://doi.org/10.1359/jbmr.2001.16.5.918.

[25] R. Marks, Hip fracture epidemiological trends, outcomes, and risk factors, 1970-2009, Int. J. Gen. Med. 3 (2010) 1–17. https://doi.org/10.2147/IJGM.S5906.

[26] N. Veronese, H. Kolk, S. Maggi, Epidemiology of Fragility Fractures and Social Impact, in: P. Falaschi, D. Marsh (Eds.), Orthogeriatrics Pract. Issues Geriatr., Springer, Cham, 2021. https://doi.org/10.1007/978-3-030-48126-1_2.

[27] O. Johnell, J.A. Kanis, An estimate of the worldwide prevalence, mortality and disability associated with hip fracture, Osteoporos. Int. 15 (2004) 897–902. https://doi.org/10.1007/s00198-004-1627-0.

[28] O. Johnell, J.A. Kanis, An estimate of the worldwide prevalence and disability associated with osteoporotic fractures, Osteoporos. Int. 17 (2006) 1726–1733. https://doi.org/10.1007/s00198-006-0172-4.

[29] S.R. Cummings, L.J. Melton, Epidemiology and outcomes of osteoporotic fractures, Lancet. 359 (2002) 1761–1767. https://doi.org/10.1016/S0140-6736(02)08657-9.

[30] J.A. Kanis, A. Oden, O. Johnell, C. De Laet, B. Jonsson, A.K. Oglesby, The components of excess mortality after hip fracture, Bone. 32 (2003) 468–473. https://doi.org/10.1016/S8756-3282(03)00061-9.

[31] O. Johnell, J.A. Kanis, A. Odén, I. Sernbo, I. Redlund-Johnell, C. Petterson, C. De Laet, B. Jönsson, Mortality after osteoporotic fractures, Osteoporos. Int. 15 (2004) 38–42. https://doi.org/10.1007/s00198-003-1490-4.

[32] C. Cooper, The crippling consequences of fractures and their impact on quality of life, Am. J. Med. 103 (1997) S12–S19. https://doi.org/10.1016/s0002-9343(97)90022-x.

[33] C. Cooper, G. Campion, L.J. Melton III, Hip fractures in the elderly: a world-wide projection, Osteoporos. Int. 2 (1992) 285–289. https://doi.org/10.1007/BF01623184.

[34] O. Johnell, The socioeconomic burden of fractures: today and in the 21st century, Am. J. Med. 103 (1997) 20S-25S. https://doi.org/10.1016/S0002-9343(97)90023-1.

[35] P. Husu, J. Suni, H. Vähä-Ypyä, H. Sievänen, K. Tokola, H. Valkeinen, T. Mäki-Opas, T. Vasankari, Objectively measured sedentary behavior and physical activity in a sample of Finnish adults: a cross-sectional study, BMC Public Health. 16 (2016) 920. https://doi.org/10.1186/s12889-016-3591-y.

[36] J.C. Lotz, E.J. Cheal, W.C. Hayes, Stress distributions within the proximal femur during gait and falls: Implications for osteoporotic fracture, Osteoporos. Int. 5 (1995) 252–261. https://doi.org/10.1007/BF01774015.

[37] P.M. de Bakker, S.L. Manske, V. Ebacher, T.R. Oxland, P.A. Cripton, P. Guy, During sideways falls proximal femur fractures initiate in the superolateral cortex: Evidence from high-speed video of simulated fractures, J. Biomech. 42 (2009) 1917–1925. https://doi.org/10.1016/j.jbiomech.2009.05.001.

[38] P.M. Mayhew, C.D. Thomas, J.G. Clement, N. Loveridge, T.J. Beck, W. Bonfield, C.J. Burgoyne, J. Reeve, Relation between age, femoral neck cortical stability, and hip fracture risk, Lancet. 366 (2005) 129–135. https://doi.org/10.1016/S0140-6736(05)66870-5.

[39] B.C.C. Khoo, K. Brown, J.R. Lewis, E. Perilli, R.L. Prince, Ageing Effects on 3-Dimensional Femoral Neck Cross-Sectional Asymmetry: Implications for Age-Related Bone Fragility in Falling, J. Clin. Densitom. 22 (2019) 153–161. https://doi.org/10.1016/J.JOCD.2018.08.001.

[40] K.E. Poole, P.M. Mayhew, C.M. Rose, J.K. Brown, P.J. Bearcroft, N. Loveridge, J. Reeve, Changing structure of the femoral neck across the adult female lifespan, J. Bone Miner. Res. 25 (2010) 482–491. https://doi.org/10.1359/jbmr.090734.

[41] E. Verhulp, B. van Rietbergen, R. Huiskes, Load distribution in the healthy and osteoporotic human proximal femur during a fall to the side, Bone. 42 (2008) 30–35. https://doi.org/10.1016/j.bone.2007.08.039.

[42] L. Zani, P. Erani, L. Grassi, F. Taddei, L. Cristofolini, Strain distribution in the proximal Human femur during in vitro simulated sideways fall, J. Biomech. 48 (2015) 2130–2143. https://doi.org/10.1016/J.JBIOMECH.2015.02.022.

[43] B. Helgason, S. Gilchrist, O. Ariza, J.D. Chak, G. Zheng, R.P. Widmer, S.J. Ferguson, P. Guy, P.A. Cripton, Development of a balanced experimental-computational approach to understanding the mechanics of proximal femur fractures, Med. Eng. Phys. 36 (2014) 793–799. https://doi.org/10.1016/j.medengphy.2014.02.019.

[44] L. Grassi, J. Kok, A. Gustafsson, Y. Zheng, S.P. Väänänen, J.S. Jurvelin, H. Isaksson, Elucidating failure mechanisms in human femurs during a fall to the side using bilateral digital image correlation, J. Biomech. 106 (2020) 109826. https://doi.org/10.1016/J.JBIOMECH.2020.109826.

[45] D. Dragomir-Daescu, J. Op Den Buijs, S. McEligot, Y. Dai, R.C. Entwistle, C. Salas, L.J. Melton, K.E. Bennet, S. Khosla, S. Amin, Robust QCT/FEA models of proximal femur stiffness and fracture load during a sideways fall on the hip, Ann. Biomed. Eng. 39 (2011) 742–755. https://doi.org/10.1007/s10439-010-0196-y.

[46] M. Bessho, I. Ohnishi, T. Matsumoto, S. Ohashi, J. Matsuyama, K. Tobita, M. Kaneko, K. Nakamura, Prediction of proximal femur strength using a CT-based nonlinear finite element method: Differences in predicted fracture load and site with changing load and boundary conditions, Bone. 45 (2009) 226–231. https://doi.org/10.1016/j.bone.2009.04.241.

[47] C.M. Ford, T.M. Keaveny, W.C. Hayes, The Effect of Impact Direction on the Structural Capacity of the Proximal Femur During Falls, J. Bone Miner. Res. 11 (1996) 377–383. https://doi.org/10.1002/jbmr.5650110311.

[48] T.P. Pinilla, K.C. Boardman, M.L. Bouxsein, E.R. Myers, W.C. Hayes, Impact direction from a fall influences the failure load of the proximal femur as much as age-related bone loss, Calcif. Tissue Int. 58 (1996) 231–235. https://doi.org/10.1007/BF02508641.

[49] S. Nawathe, B.P. Nguyen, N. Barzanian, H. Akhlaghpour, M.L. Bouxsein, T.M. Keaveny, Cortical and trabecular load sharing in the human femoral neck, J. Biomech. 48 (2015) 816–822. https://doi.org/10.1016/j.jbiomech.2014.12.022.

[50] E. Schileo, L. Balistreri, L. Grassi, L. Cristofolini, F. Taddei, To what extent can linear finite element models of human femora predict failure under stance and fall loading configurations?, J. Biomech. 47 (2014) 3531–3538. https://doi.org/10.1016/j.jbiomech.2014.08.024.

[51] J.A. Grisso, J.L. Kelsey, B.L. Strom, G.Y. Chiu, G. Maislin, L.A. O'Brien, S. Hoffman, F. Kaplan, Risk factors for falls as a cause of hip fracture in women, N. Engl. J. Med. 324 (1991) 1326–1331. https://doi.org/10.1056/NEJM199105093241905.

[52] J. Parkkari, P. Kannus, M. Palvanen, A. Natri, J. Vainio, H. Aho, I. Vuori, M. Järvinen, Majority of hip fractures occur as a result of a fall and impact on the greater trochanter of the femur: a prospective controlled hip fracture study with 206 consecutive patients, Calcif. Tissue Int. 65 (1999) 183–187. https://doi.org/10.1007/s002239900679.

[53] C.M. Court-Brown, N.D. Clement, A.D. Duckworth, L.C. Biant, M.M. McQueen, The changing epidemiology of fall-related fractures in adults, Injury. 48 (2017) 819–824. https://doi.org/10.1016/J.INJURY.2017.02.021.

[54] M. Bellver, L. Del Rio, E. Jovell, F. Drobnic, A. Trilla, Bone mineral density and bone mineral content among female elite athletes, Bone. 127 (2019) 393–400. https://doi.org/10.1016/J.BONE.2019.06.030.

[55] A. Heinonen, P. Oja, P. Kannus, H. Sievänen, A. Mänttäri, I. Vuori, Bone mineral density of female athletes in different sports, Bone Miner. 23 (1993) 1–14. https://doi.org/10.1016/S0169-6009(08)80086-4.

[56] A. Heinonen, P. Oja, P. Kannus, H. Sieväinen, H. Haapasalo, A. Mänttäri, I. Vuori, Bone mineral density in female athletes representing sports with different loading characteristics of the skeleton, Bone. 17 (1995) 197–203. https://doi.org/10.1016/8756-3282(95)00151-3.

[57] R. Nikander, H. Sievänen, A. Heinonen, P. Kannus, Femoral Neck Structure in Adult Female Athletes Subjected to Different Loading Modalities, J Bone Min. Res. 20 (2005) 520–528. https://doi.org/10.1359/JBMR.041119.

[58] T.A. Scerpella, B. Bernardoni, S. Wang, P.J. Rathouz, Q. Li, J.N. Dowthwaite, Site-specific, adult bone benefits attributed to loading during youth: A preliminary longitudinal analysis, Bone. 85 (2016) 148–159. https://doi.org/10.1016/J.BONE.2016.01.020.

[59] A.S. Tenforde, M. Fredericson, Influence of Sports Participation on Bone Health in the Young Athlete: A Review of the Literature, PM R. 3 (2011) 861–867. https://doi.org/10.1016/j.pmrj.2011.05.019.

[60] R. Nikander, P. Kannus, P. Dastidar, M. Hannula, L. Harrison, T. Cervinka, N.G. Narra, R. Aktour, T. Arola, H. Eskola, S. Soimakallio, A. Heinonen, J. Hyttinen, H. Sievänen, Targeted exercises against hip fragility, Osteoporos. Int. 20 (2009) 1321–1328. https://doi.org/10.1007/s00198-008-0785-x.

[61] T.F. Lang, I.H. Saeed, T. Streeper, J. Carballido-Gamio, R.J. Harnish, L.A. Frassetto, S.M.C. Lee, J.D. Sibonga, J.H. Keyak, B.A. Spiering, C.M. Grodsinsky, J.J. Bloomberg, P.R. Cavanagh, Spatial heterogeneity in the response of the proximal femur to two lower-body resistance exercise regimens, J. Bone Miner. Res. 29 (2014) 1337–1345. https://doi.org/10.1002/jbmr.2155.

[62] S.J. Warden, J. Carballido-Gamio, A.M. Weatherholt, J.H. Keyak, C. Yan, M.E. Kersh, T.F. Lang, R.K. Fuchs, Heterogeneous Spatial and Strength Adaptation of the Proximal Femur to Physical Activity: A Within-Subject Controlled Cross-Sectional Study, J. Bone Miner. Res. 35 (2020) 681–690. https://doi.org/10.1002/jbmr.3939.

[63] R.K. Fuchs, J. Carballido-Gamio, J.H. Keyak, M.E. Kersh, S.J. Warden, Physical activity induced adaptation can increase proximal femur strength under loading from a fall onto the greater trochanter, Bone. 152 (2021) 116090. https://doi.org/10.1016/j.bone.2021.116090.

[64] J.H. Keyak, S.A. Rossi, K.A. Jones, H.B. Skinner, Prediction of femoral fracture load using automated finite element modeling, J. Biomech. 31 (1998) 125–133. https://doi.org/10.1016/S0021-9290(97)00123-1.

[65] J.E.M. Koivumäki, J. Thevenot, P. Pulkkinen, V. Kuhn, T.M. Link, F. Eckstein, T. Jämsä, Ct-based finite element models can be used to estimate experimentally measured failure loads in the proximal femur, Bone. 50 (2012) 824–829. https://doi.org/10.1016/j.bone.2012.01.012.

[66] C. Falcinelli, E. Schileo, L. Balistreri, F. Baruffaldi, B. Bordini, M. Viceconti, U. Albisinni, F. Ceccarelli, L. Milandri, A. Toni, F. Taddei, Multiple loading conditions analysis can improve the association between finite element bone strength estimates and proximal femur fractures: A preliminary study in elderly women, Bone. 67 (2014) 71–80. https://doi.org/10.1016/j.bone.2014.06.038.

[67] M. Qasim, G. Farinella, J. Zhang, X. Li, L. Yang, R. Eastell, M. Viceconti, Patient-specific finite element estimated femur strength as a predictor of the risk of hip fracture: the effect of methodological determinants, Osteoporos. Int. 27 (2016) 2815–2822. https://doi.org/10.1007/s00198-016-3597-4.

[68] S.N. Robinovitch, L. Inkster, J. Maurer, B. Warnick, Strategies for avoiding hip impact during sideways falls., J. Bone Miner. Res. 18 (2003) 1267–1273. https://doi.org/10.1359/jbmr.2003.18.7.1267.

[69] Y. Yang, V. Komisar, N. Shishov, B. Lo, A.M.B. Korall, F. Feldman, S.N. Robinovitch, The Effect of Fall Biomechanics on Risk for Hip Fracture in Older Adults: A Cohort Study of Video-Captured Falls in Long-Term Care, J. Bone Miner. Res. 35 (2020) 1914–1922. https://doi.org/10.1002/JBMR.4048.

[70] Y. Yang, D.C. Mackey, T. Liu-Ambrose, F. Feldman, S.N. Robinovitch, Risk factors for hip impact during real-life falls captured on video in long-term care, Osteoporos. Int. 27 (2016) 537–547. https://doi.org/10.1007/s00198-015-3268-x.

[71] G.J. Tortora, B. Derrickson, Principles of Anatomy & Physiology, 13th Editi, John Wiley & Sons, Inc., 2011.

[72] Benno.M. Nigg, Walter. Herzog, Biomechanics of the Musculo-skeletal System Second Edition, John Wiley & Sons, Inc., 1999.

[73] B. Clarke, Normal bone anatomy and physiology, Clin. J. Am. Soc. Nephrol. CJASN. 3 Suppl 3 (2008) S131–S139. https://doi.org/10.2215/CJN.04151206.

[74] N. Su, J. Yang, Y. Xie, X. Du, H. Chen, H. Zhou, L. Chen, Bone function, dysfunction and its role in diseases including critical illness, Int. J. Biol. Sci. 15 (2019) 776–787. https://doi.org/10.7150/ijbs.27063.

[75] A. Mizokami, T. Kawakubo-Yasukochi, M. Hirata, Osteocalcin and its endocrine functions, Biochem. Pharmacol. 132 (2017) 1–8. https://doi.org/10.1016/j.bcp.2017.02.001.

[76] A.L. Boskey, R. Coleman, Aging and bone, J. Dent. Res. 89 (2010) 1333–1348. https://doi.org/10.1177/0022034510377791.

[77] C.A. Goodman, T.A. Hornberger, A.G. Robling, Bone and skeletal muscle: Key players in mechanotransduction and potential overlapping mechanisms, Bone. 80 (2015) 24–36. https://doi.org/10.1016/j.bone.2015.04.014.

[78] D.J. DiGirolamo, T.L. Clemens, S. Kousteni, The skeleton as an endocrine organ, Nat. Rev. Rheumatol. 8 (2012) 674–683. https://doi.org/10.1038/nrrheum.2012.157.

[79] R. Florencio-Silva, G.R.D.S. Sasso, E. Sasso-Cerri, M.J. Simões, P.S. Cerri, Biology of Bone Tissue: Structure, Function, and Factors That Influence Bone Cells, BioMed Res. Int. 2015 (2015). https://doi.org/10.1155/2015/421746.

[80] F.J. Frassica, N. Inoue, P. Virolainen, E.Y.S. Chao, Skeletal system: Biomechanical concepts and relationships to normal and abnormal conditions, Semin. Nucl. Med. 27 (1997) 321–327. https://doi.org/10.1016/S0001-2998(97)80004-9.

[81] E.F. Morgan, G.L. Barnes, T.A. Einhorn, The Bone Organ System. Form and Function, in: R. Marcus, F. David, D.W. Dempster, L. Marjorie, J.A. Cauley (Eds.), Osteoporos. Fourth Ed., Elsevier Inc., 2013: pp. 3–20. https://doi.org/10.1016/B978-0-12-415853-5.00001-7.

[82] M. Raissaki, S. Demetriou, K. Spanakis, C. Skiadas, N. Katzilakis, E.G. Velivassakis, E. Stiakaki, A.H. Karantanas, Multifocal bone and bone marrow lesions in children — MRI findings, Pediatr. Radiol. 47 (2017) 342–360. https://doi.org/10.1007/s00247-016-3737-1.

[83] J.G. Betts, K.A. Young, J.A. Wise, E. Johnson, B. Poe, D.H. Kruse, O. Korol, J.E. Johnson, M. Womble, P. Desaix, Anatomy and Physiology, OpenStax, Houston, Texas, 2013.

[84] D.A. Neumann, Kinesiology of the musculoskeletal system : foundations for rehabilitation, 1st ed., Mosby, Inc., St. Louis, Missouri, 2002.

[85] F. Eyüboğlu, Ç. Sayaca, M. Çalik, D. Korkem, L.N. Tascilar, D. Kaya, Kinesiology of the hip, in: Comp. Kinesiol. Hum. Body, Elsevier, 2020: pp. 375–392. https://doi.org/10.1016/b978-0-12-812162-7.00021-7.

[86] L. Voo, M. Armand, M. Kleinberger, Stress fracture risk analysis of the human femur based on computational biomechanics, Johns Hopkins APL Tech. Dig. Appl. Phys. Lab. 25 (2004) 223–230.

[87] Richard.L. Drake, W. Vogl, Adam.W.M. Mitchell, Gray's anatomy for student, Fourth Edi, Elsevier, 2020.

[88] S.E. Sheehan, J.Y. Shyu, M.J. Weaver, A.D. Sodickson, B. Khurana, Proximal femoral fractures: What the orthopedic surgeon wants to know, Radiographics. 35 (2015) 1563–1584. https://doi.org/10.1148/rg.2015140301.

[89] J.Y. Rho, L. Kuhn-Spearing, P. Zioupos, Mechanical properties and the hierarchical structure of bone, Med. Eng. Phys. 20 (1998) 92–102. https://doi.org/10.1016/S1350-4533(98)00007-1.

[90] M. Sadat-Shojai, M.T. Khorasani, E. Dinpanah-Khoshdargi, A. Jamshidi, Synthesis methods for nanosized hydroxyapatite with diverse structures, Acta Biomater. 9 (2013) 7591–7621. https://doi.org/10.1016/j.actbio.2013.04.012.

[91] A.L. Boskey, Bone composition: relationship to bone fragility and antiosteoporotic drug effects, BoneKEy Rep. 2 (2013) 1–11. https://doi.org/10.1038/bonekey.2013.181.

[92] J.D. Currey, Bones: Structure and Mechanics, Princeton University Press, 2013.

[93] E.A. Zimmermann, B. Busse, R.O. Ritchie, The fracture mechanics of human bone: influence of disease and treatment, BoneKEy Rep. 4 (2015) 743. https://doi.org/10.1038/bonekey.2015.112.

[94] F.A. Shah, P. Thomsen, A. Palmquist, Osseointegration and current interpretations of the bone-implant interface, Acta Biomater. 84 (2019) 1–15. https://doi.org/10.1016/j.actbio.2018.11.018.

[95] D. Sommerfeldt, C. Rubin, Biology of bone and how it orchestrates the form and function of the skeleton, Eur. Spine J. 10 (2001) S86–S95. https://doi.org/10.1007/s005860100283.

[96] M. Brotto, L. Bonewald, Bone and muscle: Interactions beyond mechanical, Bone. 80 (2015) 109–114. https://doi.org/10.1016/j.bone.2015.02.010.

[97] D.R. Carter, W.C. Hayes, The compressive behavior of bone as a two-phase porous structure, J. Bone Joint Surg. Am. 59 (1977) 954–62.

[98] Stephen.C. Cowin, Bone Mechanics Handbook, 2nd ed., Boca Raton: Taylor & Francis Group, 2001.

[99] F.P. Beer, E.R. Johnston, J.T. DeWofl, Mechanics of Materials, 3rd ed., McGraw-Hill, 2002.

[100] A. Bedford, K.M. Liechti, Mechanics of materials, Prentice Hall, 2000.

[101] U. Wolfram, J. Schwiedrzik, Post-yield and failure properties of cortical bone, BoneKEy Rep. 5 (2016) 829. https://doi.org/10.1038/bonekey.2016.60.

[102] W.C. Hayes, D.R. Carter, Postyield behavior of subchondral trabecular bone, J. Biomed. Mater. Res. 10 (1976) 537–544. https://doi.org/10.1002/JBM.820100409.

[103] M. Charlebois, M. Pretterklieber, P.K. Zysset, The role of fabric in the large strain compressive behavior of human trabecular bone, J. Biomech. Eng. 132 (2010) 121006. https://doi.org/10.1115/1.4001361.

[104] C.D. Thomas, P.M. Mayhew, J. Power, K.E. Poole, N. Loveridge, J.G. Clement, C.J. Burgoyne, J. Reeve, Femoral neck trabecular bone: loss with ageing and role in preventing fracture, J. Bone Miner. Res. 24 (2009) 1808–1818. https://doi.org/10.1359/jbmr.090504.

[105] E.F. Morgan, H.H. Bayraktar, T.M. Keaveny, Trabecular bone modulus-density relationships depend on anatomic site, J. Biomech. 36 (2003) 897–904. https://doi.org/10.1016/S0021-9290(03)00071-X.

[106] E.F. Morgan, G.U. Unnikrisnan, A.I. Hussein, Bone Mechanical Properties in Healthy and Diseased States, Annu. Rev. Biomed. Eng. 20 (2018) 119–143. https://doi.org/10.1146/ANNUREV-BIOENG-062117-121139.

[107] S.A. Goldstein, The mechanical properties of trabecular bone: dependence on anatomic location and function, J. Biomech. 20 (1987) 1055–1061. https://doi.org/10.1016/0021-9290(87)90023-6.

[108] D.C. Wirtz, N. Schiffers, T. Pandorf, K. Radermacher, D. Weichert, R. Forst, Critical evaluation of known bone material properties to realize anisotropic FE-simulation of the proximal femur, J. Biomech. 33 (2000) 1325–1330. https://doi.org/10.1016/S0021-9290(00)00069-5.

[109] E.F. Morgan, T.M. Keaveny, Dependence of yield strain of human trabecular bone on anatomic site, J. Biomech. 34 (2001) 569–577. https://doi.org/10.1016/S0021-9290(01)00011-2.

[110] M.J. Ciarelli, S.A. Goldstein, J.L. Kuhn, D.D. Cody, M.B. Brown, Evaluation of orthogonal mechanical properties and density of human trabecular bone from the major metaphyseal regions with materials testing and computed tomography, J. Orthop. Res. 9 (1991) 674–682. https://doi.org/10.1002/JOR.1100090507.

[111] S.A. Goldstein, D.L. Wilson, D.A. Sonstegard, L.S. Matthews, The mechanical properties of human tibial trabecular bone as a function of metaphyseal location, J. Biomech. 16 (1983) 965–969. https://doi.org/10.1016/0021-9290(83)90097-0.

[112] F. Taddei, L. Cristofolini, S. Martelli, H.S. Gill, M. Viceconti, Subject-specific finite element models of long bones: An in vitro evaluation of the overall accuracy, J. Biomech. 39 (2006) 2457–2467. https://doi.org/10.1016/j.jbiomech.2005.07.018.

[113] B. Helgason, E. Perilli, E. Schileo, F. Taddei, S. Brynjólfsson, M. Viceconti, Mathematical relationships between bone density and mechanical properties: A literature review, Clin. Biomech. 23 (2008) 135–146. https://doi.org/10.1016/j.clinbiomech.2007.08.024.

[114] B. Helgason, S. Gilchrist, O. Ariza, P. Vogt, W. Enns-Bray, R.P. Widmer, T. Fitze, H. Pálsson, Y. Pauchard, P. Guy, S.J. Ferguson, P.A. Cripton, The influence of the

modulus-density relationship and the material mapping method on the simulated mechanical response of the proximal femur in side-ways fall loading configuration, Med. Eng. Phys. 38 (2016) 679–689. https://doi.org/10.1016/J.MEDENGPHY.2016.03.006.

[115] I. Fleps, H. Bahaloo, P.K. Zysset, S.J. Ferguson, H. Pálsson, B. Helgason, Empirical relationships between bone density and ultimate strength: A literature review, J. Mech. Behav. Biomed. Mater. 110 (2020) 103866. https://doi.org/10.1016/J.JMBBM.2020.103866.

[116] J.Y. Rho, T.Y. Tsui, G.M. Pharr, Elastic properties of human cortical and trabecular lamellar bone measured by nanoindentation, Biomaterials. 18 (1997) 1325–1330. https://doi.org/10.1016/S0142-9612(97)00073-2.

[117] C.H. Turner, J. Rho, Y. Takano, T.Y. Tsui, G.M. Pharr, The elastic properties of trabecular and cortical bone tissues are similar: Results from two microscopic measurement techniques, J. Biomech. 32 (1999) 437–441. https://doi.org/10.1016/S0021-9290(98)00177-8.

[118] P.K. Zysset, X. Edward Guo, C. Edward Hoffler, K.E. Moore, S.A. Goldstein, Elastic modulus and hardness of cortical and trabecular bone lamellae measured by nanoindentation in the human femur, J. Biomech. 32 (1999) 1005–1012. https://doi.org/10.1016/S0021-9290(99)00111-6.

[119] J.C. Lotz, T.N. Gerhart, W.C. Hayes, Mechanical properties of metaphyseal bone in the proximal femur, J. Biomech. 24 (1991) 317–329. https://doi.org/10.1016/0021-9290(91)90350-V.

[120] C. Öhman, M. Baleani, C. Pani, F. Taddei, M. Alberghini, M. Viceconti, M. Manfrini, Compressive behaviour of child and adult cortical bone, Bone. 49 (2011) 769–776. https://doi.org/10.1016/j.bone.2011.06.035.

[121] T.S. Kaneko, J.S. Bell, M.R. Pejcic, J. Tehranzadeh, J.H. Keyak, Mechanical properties, density and quantitative CT scan data of trabecular bone with and without metastases, J. Biomech. 37 (2004) 523–530. https://doi.org/10.1016/J.JBIOMECH.2003.08.010.

[122] T.S. Keller, Predicting the compressive mechanical behavior of bone, J. Biomech. 27 (1994) 1159–1168. https://doi.org/10.1016/0021-9290(94)90056-6.

[123] H. Zilch, A. Rohlmann, G. Bergmann, R. Kölbel, Material properties of femoral cancellous bone in axial loading. Part II: Time dependent properties, Arch. Orthop. Trauma Surg. 97 (1980) 257–262. https://doi.org/10.1007/BF00380706.

[124] S.M. Haddock, O.C. Yeh, P.V. Mummaneni, W.S. Rosenberg, T.M. Keaveny, Similarity in the fatigue behavior of trabecular bone across site and species, J. Biomech. 37 (2004) 181–187. https://doi.org/10.1016/S0021-9290(03)00245-8.

[125] H. Leng, X.N. Dong, X. Wang, Progressive post-yield behavior of human cortical bone in compression for middle-aged and elderly groups, J. Biomech. 42 (2009) 491–497. https://doi.org/10.1016/J.JBIOMECH.2008.11.016.

[126] J.S. Nyman, H. Leng, X. Neil Dong, X. Wang, Differences in the mechanical behavior of cortical bone between compression and tension when subjected to progressive loading, J. Mech. Behav. Biomed. Mater. 2 (2009) 613–619. https://doi.org/10.1016/J.JMBBM.2008.11.008.

[127] Y.N. Yeni, R.R. Shaffer, K.C. Baker, X.N. Dong, M.J. Grimm, C.M. Les, D.P. Fyhrie, The effect of yield damage on the viscoelastic properties of cortical bone tissue as measured by dynamic mechanical analysis, J. Biomed. Mater. Res. A. 82 (2007) 530–537. https://doi.org/10.1002/JBM.A.31169.

[128] T.P.M. Johnson, S. Socrate, M.C. Boyce, A viscoelastic, viscoplastic model of cortical bone valid at low and high strain rates, Acta Biomater. 6 (2010) 4073–4080. https://doi.org/10.1016/J.ACTBIO.2010.04.017.

[129] S.C. Cowin, Bone poroelasticity, J. Biomech. 32 (1999) 217–238. https://doi.org/10.1016/S0021-9290(98)00161-4.

[130] S.C. Cowin, L. Cardoso, Blood and interstitial flow in the hierarchical pore space architecture of bone tissue, J. Biomech. 48 (2015) 842–854. https://doi.org/10.1016/J.JBIOMECH.2014.12.013.

[131] U. Hansen, P. Zioupos, R. Simpson, J.D. Currey, D. Hynd, The effect of strain rate on the mechanical properties of human cortical bone, J. Biomech. Eng. 130 (2008) 011011. https://doi.org/10.1115/1.2838032.

[132] T.M. Keaveny, W.C. Hayes, A 20-Year Perspective on the Mechanical Properties of Trabecular Bone, J. Biomech. Eng. 115 (1993) 534–542. https://doi.org/10.1115/1.2895536.

[133] J.H. McElhaney, Dynamic response of bone and muscle tissue, J. Appl. Physiol. 21 (1966) 1231–1236. https://doi.org/10.1152/JAPPL.1966.21.4.1231.

[134] R.D. Crowninshield, M.H. Pope, The response of compact bone in tension at various strain rates, Ann. Biomed. Eng. 2 (1974) 217–225. https://doi.org/10.1007/BF02368492.

[135] T.M. Wright, W.C. Hayes, Tensile testing of bone over a wide range of strain rates: effects of strain rate, microstructure and density, Med. Biol. Eng. 14 (1976) 671–680. https://doi.org/10.1007/BF02477046.

[136] W.S. Enns-Bray, S.J. Ferguson, B. Helgason, Strain rate dependency of bovine trabecular bone under impact loading at sideways fall velocity, J. Biomech. 75 (2018) 46–52. https://doi.org/10.1016/J.JBIOMECH.2018.04.042.

[137] M. Prot, T.J. Cloete, D. Saletti, S. Laporte, The behavior of cancellous bone from quasi-static to dynamic strain rates with emphasis on the intermediate regime, J. Biomech. 49 (2016) 1050–1057. https://doi.org/10.1016/J.JBIOMECH.2016.02.021.

[138] V.P.W. Shim, L.M. Yang, J.F. Liu, V.S. Lee, Characterisation of the dynamic compressive mechanical properties of cancellous bone from the human cervical spine, Int. J. Impact Eng. 32 (2005) 525–540. https://doi.org/10.1016/J.IJIMPENG.2005.03.006.

[139] A. Pilcher, X. Wang, Z. Kaltz, J.G. Garrison, G.L. Niebur, J. Mason, B. Song, M. Cheng, W. Chen, High strain rate testing of bovine trabecular bone, J. Biomech. Eng. 132 (2010) 081012. https://doi.org/10.1115/1.4000086.

[140] J.H. Hong, S.H. Song, Poroelastic behavior of trabecular bone: The effect of strain rate, KSME Int. J. 12 (1998) 421–428. https://doi.org/10.1007/BF02946357.

[141] S. Le Pense, Y. Chen, Contribution of fluid in bone extravascular matrix to strain-rate dependent stiffening of bone tissue - A poroelastic study, J. Mech. Behav. Biomed. Mater. 65 (2017) 90–101. https://doi.org/10.1016/J.JMBBM.2016.08.016.

[142] M.A.K. Liebschner, T.S. Keller, Hydraulic strengthening affects the stiffness and strength of cortical bone, Ann. Biomed. Eng. 33 (2005) 26–38. https://doi.org/10.1007/S10439-005-8960-0.

[143] T.H. Lim, J.H. Hong, Poroelastic properties of bovine vertebral trabecular bone, J. Orthop. Res. 18 (2000) 671–677. https://doi.org/10.1002/JOR.1100180421.

[144] T.H. Lim, J.H. Hong, Poroelastic Model of Trabecular Bone in Uniaxial Strain Conditions, J. Musculoskelet. Res. 2 (1998) 167–180. https://doi.org/10.1142/S0218957798000172.

[145] J.D. Bryant, Letter to the Editor: On hydraulic strengthening of bones: Kafka, V. (1993) J. Biomechanics 26, 761–762, J. Biomech. 28 (1995) 353–354. https://doi.org/10.1016/0021-9290(95)90563-L.

[146] V. Kafka, On hydraulic strengthening of bones, J. Biomech. 26 (1993) 761–762. https://doi.org/10.1016/0021-9290(93)90038-G.

[147] J.D. Bryant, The effect of impact on the marrow pressure of long bones in vitro, J. Biomech. 16 (1983) 659–665. https://doi.org/10.1016/0021-9290(83)90117-3.

[148] J.D. Bryant, On the mechanical function of marrow in long bones, Eng. Med. 17 (1988) 55–58. https://doi.org/10.1243/EMED_JOUR_1988_017_017_02.

[149] J.A. Ochoa, A.P. Sanders, D.A. Heck, B.M. Hillberry, Stiffening of the femoral head due to inter-trabecular fluid and intraosseous pressure, J. Biomech. Eng. 113 (1991) 259–262. https://doi.org/10.1115/1.2894882.

[150] J.A. Ochoa, A.P. Sanders, T.W. Kiesler, D.A. Heck, J.P. Toombs, K.D. Brandt, B.M. Hillberry, In vivo observations of hydraulic stiffening in the canine femoral head, J. Biomech. Eng. 119 (1997) 103–108. https://doi.org/10.1115/1.2796051.

[151] I.T. Haider, A.D. Speirs, H. Frei, Effect of boundary conditions, impact loading and hydraulic stiffening on femoral fracture strength, J. Biomech. 46 (2013) 2115–2121. https://doi.org/10.1016/j.jbiomech.2013.07.004.

[152] D. Roylance, Mechanics of materials, John Wiley & Sons, Inc., 1996.

[153] E. Novitskaya, P.Y. Chen, S. Lee, A. Castro-Ceseña, G. Hirata, V.A. Lubarda, J. McKittrick, Anisotropy in the compressive mechanical properties of bovine cortical bone and the mineral and protein constituents, Acta Biomater. 7 (2011) 3170–3177. https://doi.org/10.1016/J.ACTBIO.2011.04.025.

[154] B. Brunet-Imbault, G. Lemineur, C. Chappard, R. Harba, C.L. Benhamou, A new anisotropy index on trabecular bone radiographic images using the fast Fourier transform, BMC Med. Imaging. 5 (2005) 4. https://doi.org/10.1186/1471-2342-5-4.

[155] H. Sugita, M. Oka, J. Toguchida, T. Nakamura, T. Ueo, T. Hayami, Anisotropy of osteoporotic cancellous bone, Bone. 24 (1999) 513–516. https://doi.org/10.1016/S8756-3282(99)00021-6.

[156] R. Oftadeh, M. Perez-Viloria, J.C. Villa-Camacho, A. Vaziri, A. Nazarian, Biomechanics and Mechanobiology of Trabecular Bone: A Review, J. Biomech. Eng. 137 (2015) 0108021. https://doi.org/10.1115/1.4029176.

[157] D. Liu, S. Weiner, H.D. Wagner, Anisotropic mechanical properties of lamellar bone using miniature cantilever bending specimens, J. Biomech. 32 (1999) 647–654. https://doi.org/10.1016/S0021-9290(99)00051-2.

[158] J.D. Currey, The structure and mechanics of bone, J. Mater. Sci. 47 (2012) 41–54. https://doi.org/10.1007/S10853-011-5914-9.

[159] T.M. Keaveny, E.F. Morgan, G.L. Niebur, O.C. Yeh, Biomechanics of Trabecular Bone, Annu. Rev. Biomed. Eng. 3 (2001) 307–333. https://doi.org/10.1146/ANNUREV.BIOENG.3.1.307.

[160] R. Shahar, P. Zaslansky, M. Barak, A.A. Friesem, J.D. Currey, S. Weiner, Anisotropic Poisson's ratio and compression modulus of cortical bone determined by speckle interferometry, J. Biomech. 40 (2007) 252–264. https://doi.org/10.1016/j.jbiomech.2006.01.021.

[161] K. Hasegawa, C.H. Turner, D.B. Burr, Contribution of collagen and mineral to the elastic anisotropy of bone, Calcif. Tissue Int. 55 (1994) 381–386. https://doi.org/10.1007/BF00299319.

[162] C.H. Turner, A. Chandran, R.M.V. Pidaparti, The anisotropy of osteonal bone and its ultrastructural implications, Bone. 17 (1995) 85–89. https://doi.org/10.1016/8756-3282(95)00148-7.

[163] N. Sasaki, T. Ikawa, A. Fukuda, Orientation of mineral in bovine bone and the anisotropic mechanical properties of plexiform bone, J. Biomech. 24 (1991) 57–61. https://doi.org/10.1016/0021-9290(91)90326-I.

[164] Y. Takano, C.H. Turner, I. Owan, R.B. Martin, S.T. Lau, M.R. Forwood, D.B. Burr, Elastic anisotropy and collagen orientation of osteonal bone are dependent on the mechanical strain distribution, J. Orthop. Res. 17 (1999) 59–66. https://doi.org/10.1002/JOR.1100170110.

[165] S. Li, E. Demirci, V.V. Silberschmidt, Variability and anisotropy of mechanical behavior of cortical bone in tension and compression, J. Mech. Behav. Biomed. Mater. 21 (2013) 109–120. https://doi.org/10.1016/J.JMBBM.2013.02.021.

[166] B. Van Rietbergen, A. Odgaard, J. Kabel, R. Huiskes, Direct mechanics assessment of elastic symmetries and properties of trabecular bone architecture, J. Biomech. 29 (1996) 1653–1657. https://doi.org/10.1016/S0021-9290(96)80021-2.

[167] M. Matsuura, F. Eckstein, E.-M. Lochmüller, P.K. Zysset, M. Matsuura, F. Eckstein, E.-M. Lochmüller, P.K. Zysset, The role of fabric in the quasi-static compressive mechanical properties of human trabecular bone from various anatomical locations, Biomech. Model. Mechanobiol. 7 (2008) 27–42. https://doi.org/10.1007/S10237-006-0073-7.

[168] V. Giurgiutiu, Chapter 2 - Fundamentals of Aerospace Composite Materials, in: V. Giurgiutiu (Ed.), Struct. Health Monit. Aerosp. Compos., Academic Press, Oxford, 2016: pp. 25–65. https://doi.org/10.1016/B978-0-12-409605-9.00002-7.

[169] J. Kang, E. Dong, D. Li, S. Dong, C. Zhang, L. Wang, Anisotropy characteristics of microstructures for bone substitutes and porous implants with application of additive manufacturing in orthopaedic, Mater. Des. 191 (2020) 108608. https://doi.org/10.1016/J.MATDES.2020.108608.

[170] G. Yang, J. Kabel, B. Van Rietbergen, A. Odgaard, R. Huiskes, S.C. Cowin, The Anisotropic Hooke's Law for Cancellous Bone and Wood, J. Elast. 53 (1998) 125–146. https://doi.org/10.1023/A:1007575322693

[171] D.T. Reilly, A.H. Burstein, V.H. Frankel, The elastic modulus for bone, J. Biomech. 7 (1974) 273–275. https://doi.org/10.1016/0021-9290(74)90018-9.

[172] M.J. Mirzaali, J.J. Schwiedrzik, S. Thaiwichai, J.P. Best, J. Michler, P.K. Zysset, U. Wolfram, Mechanical properties of cortical bone and their relationships with age, gender, composition and microindentation properties in the elderly, Bone. 93 (2016) 196–211. https://doi.org/10.1016/J.BONE.2015.11.018.

[173] X.N. Dong, R.L. Acuna, Q. Luo, X. Wang, Orientation dependence of progressive post-yield behavior of human cortical bone in compression, J. Biomech. 45 (2012) 2829–2834. https://doi.org/10.1016/J.JBIOMECH.2012.08.034.

[174] X.N. Dong, X.E. Guo, The dependence of transversely isotropic elasticity of human femoral cortical bone on porosity, J. Biomech. 37 (2004) 1281–1287. https://doi.org/10.1016/J.JBIOMECH.2003.12.011.

[175] K.J. Jepsen, D.T. Davy, Comparison of damage accumulation measures in human cortical bone, J. Biomech. 30 (1997) 891–894. https://doi.org/10.1016/S0021-9290(97)00036-5.

[176] D.T. Reilly, A.H. Burstein, The elastic and ultimate properties of compact bone tissue, J. Biomech. 8 (1975) 393–405. https://doi.org/10.1016/0021-9290(75)90075-5.

[177] A.H. Burstein, D.T. Reilly, M. Martens, Aging of bone tissue: mechanical properties, J. Bone Joint Surg. Am. 58 (1976) 82–86.

[178] H.H. Bayraktar, E.F. Morgan, G.L. Niebur, G.E. Morris, E.K. Wong, T.M. Keaveny, Comparison of the elastic and yield properties of human femoral trabecular and cortical bone tissue, J. Biomech. 37 (2004) 27–35. https://doi.org/10.1016/S0021-9290(03)00257-4.

[179] Y.E. Yu, Y.J. Hu, B. Zhou, J. Wang, X.E. Guo, Microstructure Determines Apparent-Level Mechanics Despite Tissue-Level Anisotropy and Heterogeneity of Individual

Plates and Rods in Normal Human Trabecular Bone, J. Bone Miner. Res. 36 (2021) 1796–1807. https://doi.org/10.1002/JBMR.4338.

[180] D.T. Reilly, A.H. Burstein, Review Article. The mechanical properties of cortical bone, J. Bone Jt. Surg. 56 (1974) 1001–1022.

[181] G.L. Niebur, M.J. Feldstein, J.C. Yuen, T.J. Chen, T.M. Keaveny, High-resolution finite element models with tissue strength asymmetry accurately predict failure of trabecular bone, J. Biomech. 33 (2000) 1575–1583. https://doi.org/10.1016/S0021-9290(00)00149-4.

[182] R.L. Duncan, C.H. Turner, Mechanotransduction and the functional response of bone to mechanical strain, Calcif. Tissue Int. 57 (1995) 344–358. https://doi.org/10.1007/BF00302070.

[183] R. Huiskes, If bone is the answer, then what is the question?, J. Anat. 197 (2000) 145–156. https://doi.org/10.1046/j.1469-7580.2000.19720145.x.

[184] L.E. Lanyon, Functional strain in bone tissue as an objective, and controlling stimulus for adaptive bone remodelling, J. Biomech. 20 (1987) 1083–1093. https://doi.org/10.1016/0021-9290(87)90026-1.

[185] L.E. Lanyon, Using functional loading to influence bone mass and architecture: objectives, mechanisms, and relationship with estrogen of the mechanically adaptive process in bone, Bone. 18 (1996) S37–S43. https://doi.org/10.1016/8756-3282(95)00378-9.

[186] J.R. Mosley, B.M. March, J. Lynch, L.E. Lanyon, Strain magnitude related changes in whole bone architecture in growing rats, Bone. 20 (1997) 191–198. https://doi.org/10.1016/S8756-3282(96)00385-7.

[187] C.T. Rubin, L.E. Lanyon, Regulation of bone formation by applied dynamic loads, J Bone Jt. Surg Am. 66 (1984) 397–402.

[188] G.H. Meyer, Die Architektur der Spongiosa, Arch. Für Den Anat. Physiol. Wiss. Im Med. 34 (1867) 615–628.

[189] W. Roux, Der Kampf der Theile im Organismus. Ein Beitrag zur vervollständigung der mechanischen Zweckmässigkeitslehre, W. Engelmann, Leipzig, 1881.

[190] J. Wolff, Das Gesetz der Transformation der Knochen., A. Hirchwild, Berlin, 1892.

[191] C.H. Turner, Skeletal adaptation to mechanical loading, Clin. Rev. Bone Miner. Metab. 5 (2007) 181–194. https://doi.org/10.1007/s12018-008-9010-x.

[192] A. Robling, A. Castillo, C.H. Turner, Biomechanical and Molecular Regulation of Bone Remodeling, Annu. Rev. Biomed. Eng. 8 (2006) 455–498. https://doi.org/10.1146/annurev.bioeng.8.061505.095721.

[193] I. Matic, B.G. Matthews, X. Wang, N.A. Dyment, D.L. Worthley, D.W. Rowe, D. Grcevic, I. Kalajzic, Quiescent Bone Lining Cells Are a Major Source of Osteoblasts During Adulthood, Stem Cells. 34 (2016) 2930–2942. https://doi.org/10.1002/stem.2474.

[194] A.F. Van Tol, V. Schemenz, W. Wagermaier, A. Roschger, H. Razi, I. Vitienes, P. Fratzl, B.M. Willie, R. Weinkamer, The mechanoresponse of bone is closely related to the osteocyte lacunocanalicular network architecture, Proc. Natl. Acad. Sci. U. S. A. 117 (2020) 32251–32259. https://doi.org/10.1073/pnas.2011504117.

[195] J.A. Gasser, M. Kneissel, Bone physiology and biology, in: S. Smith, A. Varela, R. Samadfam (Eds.), Bone Toxicol. Mol. Integr. Toxicol., Springer, Cham, 2017: pp. 27–94. https://doi.org/10.1007/978-3-319-56192-9_2.

[196] R. Baron, M. Kneissel, WNT signaling in bone homeostasis and disease: from human mutations to treatments, Nat. Med. 19 (2013) 179–192. https://doi.org/10.1038/nm.3074.

[197] M.R. Allen, D.B. Burr, Chapter 4 - Bone Modeling and Remodeling, in: D.B. Burr, M.R. Allen (Eds.), Basic Appl. Bone Biol., Academic Press, San Diego, 2014: pp. 75–90. https://doi.org/10.1016/B978-0-12-416015-6.00004-6.

[198] H.M. Frost, Bone "mass" and the "mechanostat": A proposal, Anat. Rec. 219 (1987) 1–9. https://doi.org/10.1002/ar.1092190104.

[199] C.J. Hernandez, G.S. Beaupré, D.R. Carter, A model of mechanobiologic and metabolic influences on bone adaptation, J. Rehabil. Res. Dev. 37 (2000) 235–244.

[200] A.M. Parfitt, Osteonal and hemi-osteonal remodeling: The spatial and temporal framework for signal traffic in adult human bone, J. Cell. Biochem. 55 (1994) 273–286. https://doi.org/10.1002/jcb.240550303.

[201] E.F. Eriksen, L. Mosekilde, F. Melsen, Effect of sodium fluoride, calcium, phosphate, and vitamin D2 on trabecular bone balance and remodeling in osteoporotics, Bone. 6 (1985) 381–389. https://doi.org/10.1016/8756-3282(85)90337-0.

[202] M.F. Faienza, G. Lassandro, M. Chiarito, F. Valente, L. Ciaccia, P. Giordano, How physical activity across the lifespan can reduce the impact of bone ageing: A literature review, Int. J. Environ. Res. Public. Health. 17 (2020) 1862. https://doi.org/10.3390/ijerph17061862.

[203] H. Sievänen, Hormonal influences on the muscle-bone feedback system: A perspective, J. Musculoskelet. Neuronal Interact. 5 (2005) 255–261.

[204] M.R. Forwood, C.H. Turner, Skeletal adaptations to mechanical usage: results from tibial loading studies in rats, Bone. 17 (1995) S197–S205. https://doi.org/10.1016/8756-3282(95)00292-L.

[205] D.B. Burr, Orthopedic principles of skeletal growth, modeling and remodeling, in: D.S. Carlson, S.A. Goldstein (Eds.), Bone Biodyn. Orthod. Orthop. Treeatment, Center for Human Growth and Development, The University of Michigan, Ann Arbor, Michigan, U.S.A., 1992.

[206] R.B. Martin, D.B. Burr, N.A. Sharkey, D.P. Fyhrie, Mechanical Adaptability of the Skeleton, in: Skelet. Tissue Mech., Springer New York, 2015: pp. 275–354. https://doi.org/10.1007/978-1-4939-3002-9_6.

[207] P. Pivonka, A. Park, M.R. Forwood, Functional adaptation of bone: The mechanostat and beyond, in: P. Pivonka (Ed.), Multiscale Mechanobiol. Bone Remodel. Adapt.

CISM Int. Cent. Mech. Sci., Springer, Cham, 2018: pp. 1–60. https://doi.org/10.1007/978-3-319-58845-2_1.

[208] C.H. Turner, M.R. Forwood, J. -Y Rho, T. Yoshikawa, Mechanical loading thresholds for lamellar and woven bone formation, J. Bone Miner. Res. 9 (1994) 87–97. https://doi.org/10.1002/jbmr.5650090113.

[209] C.H. Turner, Three rules for bone adaptation to mechanical stimuli, Bone. 23 (1998) 399–407. https://doi.org/10.1016/S8756-3282(98)00118-5.

[210] C.H. Turner, F.M. Pavalko, Mechanotransduction and functional response of the skeleton to physical stress: The mechanisms and mechanics of bone adaptation, J. Orthop. Sci. 3 (1998) 346–355. https://doi.org/10.1007/s007760050064.

[211] D.B. Burr, A.G. Robling, C.H. Turner, Effects of biomechanical stress on bones in animals, Bone. 30 (2002) 781–786. https://doi.org/10.1016/S8756-3282(02)00707-X.

[212] J. Hert, M. Lisková, B. Landrgot, Influence of the long-term, continuous bending on the bone. An experimental study on the tibia of the rabbit, Folia Morphol Praha. 17 (1969) 389–399.

[213] J. Hert, M. Lisková, J. Landa, Reaction of bone to mechanical stimuli. 1. Continuous and intermittent loading of tibia in rabbit, Folia Morphol Praha. 19 (1971) 290–300.

[214] M. Lisková, J. Hert, Reaction of bone to mechanical stimuli. 2. Periosteal and endosteal reaction of tibial diaphysis in rabbit to intermittent loading, Folia Morphol Praha. 19 (1971) 301–317.

[215] J. Hert, E. Pribylová, M. Lisková, Reaction of bone to mechanical stimuli. 3. Microstructure of compact bone of rabbit tibia after intermittent loading, Acta Anat Basel. 82 (1972) 218–230.

[216] A.G. Robling, K.M. Duijvelaar, J.V. Geevers, N. Ohashi, C.H. Turner, Modulation of appositional and longitudinal bone growth in the rat ulna by applied static and dynamic force, Bone. 29 (2001) 105–113. https://doi.org/10.1016/S8756-3282(01)00488-4.

[217] Y. Umemura, T. Ishiko, T. Yamauchi, M. Kurono, S. Mashiko, Five jumps per day increase bone mass and breaking force in rats, J. Bone Miner. Res. 12 (1997) 1480–1485. https://doi.org/10.1359/jbmr.1997.12.9.1480.

[218] J.M. LaMothe, N.H. Hamilton, R.F. Zernicke, Strain rate influences periosteal adaptation in mature bone, Med. Eng. Phys. 27 (2005) 277–284. https://doi.org/10.1016/j.medengphy.2004.04.012.

[219] C.H. Turner, M.R. Forwood, M.W. Otter, Mechanotransduction in bone: do bone cells act as sensors of fluid flow?, FASEB J. 8 (1994) 875–878. https://doi.org/10.1096/fasebj.8.11.8070637.

[220] A.G. Robling, D.B. Burr, C.H. Turner, Recovery periods restore mechanosensitivity to dynamically loaded bone, J. Exp. Biol. 204 (2001) 3389–3399. https://doi.org/10.1242/jeb.204.19.3389.

[221] S. Srinivasan, D.A. Weimer, S.C. Agans, S.D. Bain, T.S. Gross, Low-magnitude mechanical loading becomes osteogenic when rest is inserted between each load cycle, J. Bone Miner. Res. 17 (2002) 1613–1620. https://doi.org/10.1359/jbmr.2002.17.9.1613.

[222] A.G. Robling, F.M. Hinant, D.B. Burr, C.H. Turner, Improved bone structure and strength after long-term mechanical loading is greatest if loading is separated into short bouts, J. Bone Miner. Res. 17 (2002) 1545–1554. https://doi.org/10.1359/jbmr.2002.17.8.1545.

[223] A.G. Robling, F.M. Hinant, D.B. Burr, C.H. Turner, Shorter, more frequent mechanical loading sessions enhance bone mass, Med. Sci. Sports Exerc. 34 (2002) 196–202. https://doi.org/10.1097/00005768-200202000-00003.

[224] A.G. Robling, D.B. Burr, C.H. Turner, Partitioning a daily mechanical stimulus into discrete loading bouts improves the osteogenic response to loading, J. Bone Miner. Res. 15 (2000) 1596–1602. https://doi.org/10.1359/jbmr.2000.15.8.1596.

[225] J.L. Schriefer, S.J. Warden, L.K. Saxon, A.G. Robling, C.H. Turner, Cellular accommodation and the response of bone to mechanical loading, J. Biomech. 38 (2005) 1838–1845. https://doi.org/10.1016/j.jbiomech.2004.08.017.

[226] L.K. Saxon, A.G. Robling, I. Alam, C.H. Turner, Mechanosensitivity of the rat skeleton decreases after a long period of loading, but is improved with time off, Bone. 36 (2005) 454–464. https://doi.org/10.1016/j.bone.2004.12.001.

[227] H.K. Uhthoff, Z.F.G. Jaworski, Bone loss in response to long-term immobilisation, J. Bone Joint Surg. Br. 60 B (1978) 420–429. https://doi.org/10.1302/0301-620x.60b3.681422.

[228] Z.F.G. Jaworski, M. Liskova-Kiar, H.K. Uhthoff, Effect of long-term immobilization on the pattern of bone loss in older dogs, J. Bone Joint Surg. Br. 62 B (1980) 104–110. https://doi.org/10.1302/0301-620x.62b1.6985912.

[229] G.O. Matheson, D.B. Clement, D.C. Mckenzie, J.E. Taunton, D.R. Lloyd-Smith, J.G. Macintyre, Stress fractures in athletes: A study of 320 cases, Am. J. Sports Med. 15 (1987) 46–58. https://doi.org/10.1177/036354658701500107.

[230] K. Khan, J. Brown, S. Way, N. Vass, K. Crichton, R. Alexander, A. Baxter, M. Butler, J. Wark, Overuse Injuries in Classical Ballet, Sports Med. 19 (1995) 341–357. https://doi.org/10.2165/00007256-199519050-00004.

[231] M.R. Forwood, D.B. Burr, Physical activity and bone mass: exercises in futility?, Bone Miner. 21 (1993) 89–112. https://doi.org/10.1016/S0169-6009(08)80012-8.

[232] C.H. Turner, A.G. Robling, Exercise as an anabolic stimulus for bone, Curr. Pharm. Des. 10 (2004) 2629–2641. https://doi.org/10.2174/1381612043383755.

[233] L. Lanyon, T. Skerry, Postmenopausal osteoporosis as a failure of bone's adaptation to functional loading: a hypothesis, J. Bone Miner. Res. 16 (2001) 1937–1947. https://doi.org/10.1359/jbmr.2001.16.11.1937.

[234] K. Lee, H. Jessop, R. Suswillo, G. Zaman, L. Lanyon, Bone adaptation requires oestrogen receptor-α, Nature. 424 (2003) 389. https://doi.org/10.1038/424389a.

[235] I. Pajamäki, Mechanosensitivity of Bone, Tampere University Press, 2007. https://trepo.tuni.fi/handle/10024/67682 (accessed January 31, 2023).

[236] S.J. Warden, J.A. Hurst, M.S. Sanders, C.H. Turner, D.B. Burr, J. Li, Bone adaptation to a mechanical loading program significantly increases skeletal fatigue resistance, J. Bone Miner. Res. 20 (2005) 809–816. https://doi.org/10.1359/JBMR.041222.

[237] S. Bass, L. Saxon, R. Daly, C.H. Turner, a G. Robling, E. Seeman, S. Stuckey, The effect of mechanical loading on the size and shape of bone in pre-, peri-, and postpubertal girls: a study in tennis players, J. Bone Miner. Res. 17 (2002) 2274–2280. https://doi.org/10.1359/jbmr.2002.17.12.2274.

[238] G. Ducher, R.M. Daly, S.L. Bass, Effects of repetitive loading on bone mass and geometry in young male tennis players: A quantitative study using MRI, J. Bone Miner. Res. 24 (2009) 1686–1692. https://doi.org/10.1359/jbmr.090415.

[239] S.B. Going, J.N. Farr, Exercise and Bone Macro-architecture: Is Childhood a Window of Opportunity for Osteoporosis Prevention?, Int. J. Body Compos. Res. 8 (2010) 1–9.

[240] R. Daly, The effect of exercise on bone mass and structural geometry during growth, Med. Sport Sci. 51 (2007) 33–49. https://doi.org/10.1159/000103003.

[241] S.D. Bain, M.C. Bailey, M.W. Edwards, The anabolic effect of estrogen on endosteal bone formation in the mouse is attenuated by ovariohysterectomy: A role for the uterus in the skeletal response to estrogen?, Calcif. Tissue Int. 51 (1992) 223–228. https://doi.org/10.1007/BF00334551.

[242] M.W. Edwards, S.D. Bain, M.C. Bailey, M.M. Lantry, G.A. Howard, 17β Estradiol stimulation of endosteal bone formation in the ovariectomized mouse: An animal model for the evaluation of bone-targeted estrogens, Bone. 13 (1992) 29–34. https://doi.org/10.1016/8756-3282(92)90358-4.

[243] R.T. Turner, D.S. Colvard, T.C. Spelsberg, Estrogen inhibition of periosteal bone formation in rat long bones: Down-regulation of gene expression for bone matrix proteins, Endocrinology. 127 (1990) 1346–1651. https://doi.org/10.1210/endo-127-3-1346.

[244] H. Haapasalo, S. Kontulainen, H. Sievänen, P. Kannus, M. Järvinen, I. Vuori, Exercise-induced bone gain is due to enlargement in bone size without a change in volumetric bone density: A peripheral quantitative computed tomography study of the upper arms of male tennis players, Bone. 27 (2000) 351–357. https://doi.org/10.1016/S8756-3282(00)00331-8.

[245] H. Jones, J. Priest, W. Hayes, C. Tichenor, D. Nagel, Humeral hypertrophy in response to exercise, J Bone Jt. Surg Am. 59 (1977) 204–208.

[246] M.P. Yavropoulou, J.G. Yovos, The molecular basis of bone mechanotransduction, J Musculoskelet Neuronal Interact. 16 (2016) 221–236.

[247] Y. Uda, E. Azab, N. Sun, C. Shi, P.D. Pajevic, Osteocyte Mechanobiology, Curr. Osteoporos. Rep. 15 (2017) 318–325. https://doi.org/10.1007/s11914-017-0373-0.

[248] A.G. Robling, The interaction of biological factors with mechanical signals in bone adaptation: Recent developments, Curr. Osteoporos. Rep. 10 (2012) 126–131. https://doi.org/10.1007/s11914-012-0099-y.

[249] A.G. Robling, C.H. Turner, Mechanical signaling for bone modeling and remodeling, Crit. Rev. Eukaryot. Gene Expr. 19 (2009) 319–338. https://doi.org/10.1615/CritRevEukarGeneExpr.v19.i4.50.

[250] R. Alfieri, M. Vassalli, F. Viti, Flow-induced mechanotransduction in skeletal cells, Biophys. Rev. 11 (2019) 729–743. https://doi.org/10.1007/s12551-019-00596-1.

[251] L.F. Bonewald, Mechanosensation and transduction in osteocytes, BoneKEy-Osteovision. 3 (2006) 7–15. https://doi.org/10.1138/20060233.

[252] J. Klein-Nulend, R.G. Bacabac, A.D. Bakker, Mechanical loading and how it affects bone cells: The role of the osteocyte cytoskeleton in maintaining our skeleton, Eur. Cell. Mater. 24 (2012) 278–291. https://doi.org/10.22203/eCM.v024a20.

[253] P.V. Hinton, S.M. Rackard, O.D. Kennedy, In Vivo Osteocyte Mechanotransduction: Recent Developments and Future Directions, Curr. Osteoporos. Rep. 16 (2018) 746–753. https://doi.org/10.1007/s11914-018-0485-1.

[254] Y. Han, S.C. Cowin, M.B. Schaffler, S. Weinbaum, Mechanotransduction and strain amplification in osteocyte cell processes, Proc. Natl. Acad. Sci. U. S. A. 101 (2004) 16689–16694. https://doi.org/10.1073/pnas.0407429101.

[255] Y. Wang, L.M. McNamara, M.B. Schaffler, S. Weinbaum, A model for the role of integrins in flow induced mechanotransduction in osteocytes, Proc. Natl. Acad. Sci. U. S. A. 104 (2007) 15941–15946. https://doi.org/10.1073/pnas.0707246104.

[256] P. Cabahug-Zuckerman, D. Frikha-Benayed, R.J. Majeska, A. Tuthill, S. Yakar, S. Judex, M.B. Schaffler, Osteocyte Apoptosis Caused by Hindlimb Unloading is Required to Trigger Osteocyte RANKL Production and Subsequent Resorption of Cortical and Trabecular Bone in Mice Femurs, J. Bone Miner. Res. 31 (2016) 1356–1365. https://doi.org/10.1002/jbmr.2807.

[257] G.M. Blake, I. Fogelman, Technical principles of dual energy X-ray absorptiometry, Semin. Nucl. Med. 27 (1997) 210–228. https://doi.org/10.1016/S0001-2998(97)80025-6.

[258] A. El Maghraoui, C. Roux, DXA scanning in clinical practice, QJM Int. J. Med. 101 (2008) 605–617. https://doi.org/10.1093/qjmed/hcn022.

[259] H.H. Bolotin, H. Sievänen, Inaccuracies inherent in dual-energy x-ray absorptiometry in vivo bone mineral density can seriously mislead diagnostic/prognostic interpretations of patient-specific bone fragility, J. Bone Miner. Res. 16 (2001) 799–805. https://doi.org/10.1359/jbmr.2001.16.5.799.

[260] O.L. Svendsen, C. Hassager, V. Skødt, C. Christiansen, Impact of soft tissue on in vivo accuracy of bone mineral measurements in the spine, hip, and forearm: a human cadaver study, J. Bone Miner. Res. 10 (1995) 868–873. https://doi.org/10.1002/jbmr.5650100607.

[261] T.J. Beck, Extending DXA beyond bone mineral density: understanding hip structure analysis, Curr. Osteoporos. Rep. 5 (2007) 49–55. https://doi.org/10.1007/s11914-007-0002-4.

[262] T.J. Beck, C.B. Ruff, K.E. Warden, W.W.J. Scott, G.U. Rao, Predicting Femoral Neck Strength From Bone Mineral Data: A Structural Approach, Invest. Radiol. 25 (1990) 6–18.

[263] T. Yoshikawa, C.H. Turner, M. Peacock, C.W. Slemenda, C.M. Weaver, D. Teegarden, P. Markwardt, D.B. Burr, Geometric structure of the femoral neck measured using dual-energy X-ray absorptiometry, J. Bone Miner. Res. 9 (1994) 1053–1064. https://doi.org/10.1002/jbmr.5650090713.

[264] K.E. Ackerman, L. Pierce, G. Guereca, M. Slattery, H. Lee, M. Goldstein, M. Misra, Hip Structural Analysis in Adolescent and Young Adult Oligoamenorrheic and Eumenorrheic Athletes and Nonathletes, J. Clin. Endocrinol. Metab. 98 (2013) 1742–1749. https://doi.org/10.1210/jc.2013-1006.

[265] K.G. Faulkner, W.K. Wacker, H.S. Barden, C. Simonelli, P.K. Burke, S. Ragi, L. Del Rio, Femur strength index predicts hip fracture independent of bone density and hip axis length, Osteoporos. Int. 17 (2006) 593–599. https://doi.org/10.1007/s00198-005-0019-4.

[266] A.Z. LaCroix, T.J. Beck, J.A. Cauley, C.E. Lewis, T. Bassford, R. Jackson, G. Wu, Z. Chen, Hip Structural Geometry and Incidence of Hip Fracture in Postmenopausal Women: What does it add to conventional bone mineral density?, Osteoporos. Int. 21 (2010) 919–929. https://doi.org/10.1007/s00198-009-1056-1.

[267] I.C. Levine, S.P. Pretty, P.K. Nouri, M. Mourtzakis, A.C. Laing, Pelvis and femur geometry: Relationships with impact characteristics during sideways falls on the hip, J. Biomech. 80 (2018) 72–78. https://doi.org/10.1016/j.jbiomech.2018.08.029.

[268] D.A. Nelson, D.A. Barondess, S.L. Hendrix, T.J. Beck, Cross-Sectional Geometry, Bone Strength, and Bone Mass in the Proximal Femur in Black and White Postmenopausal Women, J. Bone Miner. Res. 15 (2000) 1992–1997. https://doi.org/10.1359/JBMR.2000.15.10.1992.

[269] L.W. Goldman, Principles of CT and CT Technology, J. Nucl. Med. Technol. 35 (2007) 115–128. https://doi.org/10.2967/jnmt.107.042978.

[270] J.E. Adams, Quantitative computed tomography, Eur. J. Radiol. 71 (2009) 415–424. https://doi.org/10.1016/j.ejrad.2009.04.074.

[271] D.M. Black, M.L. Bouxsein, L.M. Marshall, S.R. Cummings, T.F. Lang, J.A. Cauley, K.E. Ensrud, C.M. Nielson, E.S. Orwoll, Proximal femoral structure and the prediction of hip fracture in men: a large prospective study using QCT, J. Bone Miner. Res. 23 (2008) 1326–1333. https://doi.org/10.1359/jbmr.080316.

[272] J. Clotet, Y. Martelli, S. Di Gregorio, L.M. del Río Barquero, L. Humbert, Structural Parameters of the Proximal Femur by 3-Dimensional Dual-Energy X-ray Absorptiometry Software: Comparison With Quantitative Computed Tomography, J. Clin. Densitom. 21 (2018) 550–562. https://doi.org/10.1016/j.jocd.2017.05.002.

[273] A. Heinonen, H. Sievänen, H. Kyröläinen, J. Perttunen, P. Kannus, Mineral mass, size, and estimated mechanical strength of triple jumpers' lower limb, Bone. 29 (2001) 279–285. https://doi.org/10.1016/S8756-3282(01)00574-9.

[274] A. Ireland, M. Korhonen, A. Heinonen, H. Suominen, C. Baur, S. Stevens, H. Degens, J. Rittweger, Side-to-side differences in bone strength in master jumpers and sprinters, J. Musculoskelet. Neuronal Interact. 11 (2011) 298–305.

[275] R. Nikander, H. Sievänen, A. Heinonen, T. Karstila, P. Kannus, Load-specific differences in the structure of femoral neck and tibia between world-class moguls skiers and slalom skiers, Scand. J. Med. Sci. Sports. 18 (2008) 145–153. https://doi.org/10.1111/j.1600-0838.2007.00643.x.

[276] K. Ramamurthi, O. Ahmad, K. Engelke, R.H. Taylor, K. Zhu, S. Gustafsson, R.L. Prince, K.E. Wilson, An in vivo comparison of hip structure analysis (HSA) with measurements obtained by QCT, Osteoporos. Int. 23 (2012) 543–551. https://doi.org/10.1007/s00198-011-1578-1.

[277] T. Rantalainen, R. Nikander, R.M. Daly, A. Heinonen, H. Sievänen, Exercise loading and cortical bone distribution at the tibial shaft, Bone. 48 (2011) 786–791. https://doi.org/10.1016/j.bone.2010.11.013.

[278] E.J. Samelson, B.A. Christiansen, S. Demissie, K.E. Broe, Q. Louie-Gao, L.A. Cupples, B.J. Roberts, R. Manoharam, J. D'Agostino, T. Lang, D.P. Kiel, M.L. Bouxsein, QCT Measures of Bone Strength at the Thoracic and Lumbar Spine: The Framingham Study, J. Bone Miner. Res. 27 (2012) 654–663. https://doi.org/10.1002/jbmr.1482.

[279] J. Damilakis, J.E. Adams, G. Guglielmi, T.M. Link, Radiation exposure in X-ray-based imaging techniques used in osteoporosis, Eur. Radiol. 20 (2010) 2707–2714. https://doi.org/10.1007/s00330-010-1845-0.

[280] J.A. MacNeil, S.K. Boyd, Improved reproducibility of high-resolution peripheral quantitative computed tomography for measurement of bone quality, Med. Eng. Phys. 30 (2008) 792–799. https://doi.org/10.1016/j.medengphy.2007.11.003.

[281] S. Stagi, L. Cavalli, T. Cavalli, M. de Martino, M.L. Brandi, Peripheral quantitative computed tomography (pQCT) for the assessment of bone strength in most of bone affecting conditions in developmental age: a review, Ital. J. Pediatr. 42 (2016) 88. https://doi.org/10.1186/s13052-016-0297-9.

[282] S. Azhar, L.R. Chong, Clinician's guide to the basic principles of MRI, Postgrad. Med. J. 99 (2022) 894–903. https://doi.org/10.1136/pmj-2022-141998.

[283] V.P.B. Grover, J.M. Tognarelli, M.M.E. Crossey, I.J. Cox, S.D. Taylor-Robinson, M.J.W. McPhail, Magnetic Resonance Imaging: Principles and Techniques: Lessons for Clinicians, J. Clin. Exp. Hepatol. 5 (2015) 246–255. https://doi.org/10.1016/j.jceh.2015.08.001.

[284] H. Sievänen, T. Karstila, P. Apuli, P. Kannus, Magnetic resonance imaging of the femoral neck cortex, Acta Radiol. 48 (2007) 308–314. https://doi.org/10.1080/02841850601182147.

[285] B.R. Gomberg, P.K. Saha, F.W. Wehrli, Method for cortical bone structural analysis from magnetic resonance images, Acad. Radiol. 12 (2005) 1320–1332. https://doi.org/10.1016/j.acra.2005.06.012.

[286] S.L. Manske, T. Liu-Ambrose, P.M. De Bakker, D. Liu, S. Kontulainen, P. Guy, T.R. Oxland, H.A. McKay, Femoral neck cortical geometry measured with magnetic resonance imaging is associated with proximal femur strength, Osteoporos. Int. 17 (2006) 1539–1545. https://doi.org/10.1007/s00198-006-0162-6.

[287] H.A. McKay, H. Sievänen, M.A. Petit, K.J. MacKelvie, K.M. Forkheim, K.P. Whittall, B.B. Forster, H. Macdonald, Application of Magnetic Resonance Imaging to Evaluation of Femoral Neck Structure in Growing Girls, J. Clin. Densitom. 7 (2004) 161–168. https://doi.org/10.1385/JCD:7:2:161.

[288] F.W. Wehrli, Structural and functional assessment of trabecular and cortical bone by micro magnetic resonance imaging, J. Magn. Reson. Imaging. 25 (2007) 390–409. https://doi.org/10.1002/jmri.20807.

[289] A. Heinonen, H. Sievänen, P. Kannus, P. Oja, I. Vuori, Site-specific skeletal response to long-term weight training seems to be attributable to principal loading modality: A pQCT study of female weightlifters, Calcif. Tissue Int. 70 (2002) 469–474. https://doi.org/10.1007/s00223-001-1019-9.

[290] L. Liu, R. Maruno, T. Mashimo, K. Sanka, T. Higuchi, K. Hayashi, Y. Shirasaki, N. Mukai, S. Saitoh, K. Tokuyama, Effects of physical training on cortical bone at midtibia assessed by peripheral QCT, J. Appl. Physiol. 95 (2003) 219–24. https://doi.org/10.1152/japplphysiol.01055.2002.

[291] R. Nikander, P. Kannus, T. Rantalainen, K. Uusi-Rasi, A. Heinonen, H. Sievänen, Cross-sectional geometry of weight-bearing tibia in female athletes subjected to different exercise loadings, Osteoporos. Int. 21 (2010) 1687–1694. https://doi.org/10.1007/s00198-009-1101-0.

[292] T. Rantalainen, R. Nikander, A. Heinonen, H. Suominen, H. Sievänen, Direction-specific diaphyseal geometry and mineral mass distribution of tibia and fibula: A pQCT study of female athletes representing different exercise loading types, Calcif. Tissue Int. 86 (2010) 447–454. https://doi.org/10.1007/s00223-010-9358-z.

[293] T. Rantalainen, R. Nikander, A. Heinonen, T. Cervinka, H. Sievänen, R.M. Daly, Differential effects of exercise on tibial shaft marrow density in young female athletes, J. Clin. Endocrinol. Metab. 98 (2013) 2037–2044. https://doi.org/10.1210/jc.2012-3748.

[294] A.M. Weatherholt, S.J. Warden, Tibial Bone Strength is Enhanced in the Jump Leg of Collegiate-Level Jumping Athletes: A Within-Subject Controlled Cross-Sectional Study, Calcif. Tissue Int. 98 (2016) 129–139. https://doi.org/10.1007/s00223-015-0078-2.

[295] D.C. Wilks, K. Winwood, S.F. Gilliver, A. Kwiet, M. Chatfield, I. Michaelis, L.W. Sun, J.L. Ferretti, A.J. Sargeant, D. Felsenberg, J. Rittweger, Bone mass and geometry of the tibia and the radius of master sprinters, middle and long distance runners, race-

walkers and sedentary control participants: A pQCT study, Bone. 45 (2009) 91–97. https://doi.org/10.1016/j.bone.2009.03.660.

[296] D.C. Wilks, K. Winwood, S.F. Gilliver, A. Kwiet, L.W. Sun, C. Gutwasser, J.L. Ferretti, A.J. Sargeant, D. Felsenberg, J. Rittweger, Age-dependency in bone mass and geometry: a pQCT study on male and female master sprinters, middle and long distance runners, race-walkers and sedentary people, J. Musculoskelet. Neuronal Interact. 9 (2009) 236–246.

[297] S. Adami, D. Gatti, V. Braga, D. Bianchini, M. Rossini, Site-specific effects of strength training on bone structure and geometry of ultradistal radius in postmenopausal women, J. Bone Miner. Res. 14 (1999) 120–124. https://doi.org/10.1359/jbmr.1999.14.1.120.

[298] A. Heinonen, P. Oja, H. Sievänen, M. Pasanen, I. Vuori, Effect of Two Training Regimens on Bone Mineral Density in Healthy Perimenopausal Women: A Randomized Controlled Trial, J. Bone Miner. Res. 13 (1998) 483–490. https://doi.org/10.1359/jbmr.1998.13.3.483.

[299] A. Heinonen, P. Kannus, H. Sievänen, P. Oja, M. Pasanen, M. Rinne, K. Uusi-Rasi, I. Vuori, Randomised controlled trial of effect of high-impact exercise on selected risk factors for osteoporotic fractures, Lancet. 348 (1996) 1343–1347. https://doi.org/10.1016/S0140-6736(96)04214-6.

[300] A. Heinonen, H. Sievänen, P. Kannus, P. Oja, I. Vuori, Effects of unilateral strength training and detraining on bone mineral mass and estimated mechanical characteristics of the upper limb bones in young women, J. Bone Miner. Res. 11 (1996) 490–501. https://doi.org/10.1002/jbmr.5650110410.

[301] T.Y.L. Liu-Ambrose, K.M. Khan, J.J. Eng, A. Heinonen, H.A. McKay, Both resistance and agility training increase cortical bone density in 75- to 85-year-old women with low bone mass: A 6-month randomized controlled trial, J. Clin. Densitom. 7 (2004) 390–398. https://doi.org/10.1385/JCD:7:4:390.

[302] H.M. Macdonald, S.A. Kontulainen, K.M. Khan, H.A. McKay, Is a school-based physical activity intervention effective for increasing tibial bone strength in boys and girls?, J. Bone Miner. Res. 22 (2007) 434–446. https://doi.org/10.1359/jbmr.061205.

[303] H.M. Macdonald, D.M.L. Cooper, H.A. McKay, Anterior-posterior bending strength at the tibial shaft increases with physical activity in boys: Evidence for non-uniform geometric adaptation, Osteoporos. Int. 20 (2009) 61–70. https://doi.org/10.1007/s00198-008-0636-9.

[304] T.H. Suominen, M.T. Korhonen, M. Alén, A. Heinonen, A. Mero, T. Törmäkangas, H. Suominen, Effects of a 20-week high-intensity strength and sprint training program on tibial bone structure and strength in middle-aged and older male sprint athletes: a randomized controlled trial, Osteoporos. Int. 28 (2017) 2663–2673. https://doi.org/10.1007/s00198-017-4107-z.

[305] A. Vainionpää, R. Korpelainen, J. Leppäluoto, T. Jämsä, Effects of high-impact exercise on bone mineral density: A randomized controlled trial in premenopausal

women, Osteoporos. Int. 16 (2005) 191–197. https://doi.org/10.1007/s00198-004-1659-5.

[306] A. Vainionpää, R. Korpelainen, H. Sievänen, E. Vihriälä, J. Leppäluoto, T. Jämsä, Effect of impact exercise and its intensity on bone geometry at weight-bearing tibia and femur, Bone. 40 (2007) 604–611. https://doi.org/10.1016/j.bone.2006.10.005.

[307] I. Vuori, A. Heinonen, H. Sievänen, P. Kannus, M. Pasanen, P. Oja, Effects of unilateral strength training and detraining on bone mineral density and content in young women: a study of mechanical loading and deloading on human bones, Calcif. Tissue Int. 55 (1994) 59–67. https://doi.org/10.1007/BF00310170.

[308] D.L. Nichols, C.F. Sanborn, A.M. Love, Resistance training and bone mineral density in adolescent females, J. Pediatr. 139 (2001) 494–500. https://doi.org/10.1067/mpd.2001.116698.

[309] P. Balasundaram, I.D. Avulakunta, Human Growth and Development, in: StatPearls, StatPearls Publishing, Treasure Island (FL), 2022. http://www.ncbi.nlm.nih.gov/books/NBK567767/ (accessed January 30, 2023).

[310] World Health Organization, Adolescent friendly health services : an agenda for change, World Health Organization, 2003. https://apps.who.int/iris/handle/10665/67923 (accessed January 31, 2023).

[311] R.J. Bonnie, C. Stroud, H. Breiner, S. Committee on Improving the Health, Y. Board on Children, I. of Medicine, N.R. Council, Investigating in the Health and Well-Being of Young Adults, National Academies Press (US), 2015. https://www.ncbi.nlm.nih.gov/books/NBK284791/ (accessed January 30, 2023).

[312] R.A. Faulkner, M.R. Forwood, T.J. Beck, J.C. Mafukidze, K. Russell, W. Wallace, Strength indices of the proximal femur and shaft in prepubertal female gymnasts, Med. Sci. Sports Exerc. 35 (2003) 513–518. https://doi.org/10.1249/01.MSS.0000053724.33480.8B.

[313] U. Pettersson, P. Nordström, H. Alfredson, K. Henriksson-Larsén, R. Lorentzon, Effect of high impact activity on bone mass and size in adolescent females: A comparative study between two different types of sports, Calcif. Tissue Int. 67 (2000) 207–214. https://doi.org/10.1007/s002230001131.

[314] A. Gustavsson, K. Thorsen, P. Nordström, A 3-year longitudinal study of the effect of physical activity on the accrual of bone mineral density in healthy adolescent males, Calcif. Tissue Int. 73 (2003) 108–114. https://doi.org/10.1007/s00223-002-2026-1.

[315] H. Sievänen, P. Zagorski, B. Drozdzowska, H. Vähä-Ypyä, D. Boron, P. Adamczyk, W. Pluskiewicz, Alpine skiing is associated with higher femoral neck bone mineral density, J. Musculoskelet. Neuronal Interact. 15 (2015) 264–269.

[316] D.A. Greene, G.A. Naughton, J.N. Briody, A. Kemp, H. Woodhead, Assessment of bone strength at differentially-loaded skeletal regions in adolescent middle-distance runners, J. Sci. Med. Sport. 9 (2006) 221–230. https://doi.org/10.1016/j.jsams.2006.03.030.

[317] B. Ferry, M. Duclos, L. Burt, P. Therre, F. Le Gall, C. Jaffré, D. Courteix, Bone geometry and strength adaptations to physical constraints inherent in different sports: Comparison between elite female soccer players and swimmers, J. Bone Miner. Metab. 29 (2011) 342–351. https://doi.org/10.1007/s00774-010-0226-8.

[318] G. Tripepi, K.J. Jager, F.W. Dekker, C. Zoccali, Selection Bias and Information Bias in Clinical Research, Nephron Clin. Pract. 115 (2010) c94–c99. https://doi.org/10.1159/000312871.

[319] P. Kannus, H. Haapasalo, M. Sankelo, H. Sievänen, M. Pasanen, A. Heinonen, P. Oja, I. Vuori, Effect of starting age of physical activity on bone mass in the dominant arm of tennis and squash players, Ann. Intern. Med. 123 (1995) 27–31. https://doi.org/10.7326/0003-4819-123-1-199507010-00003.

[320] N. Ashizawa, K. Nonaka, S. Michikami, T. Mizuki, H. Amagai, K. Tokuyama, M. Suzuki, Tomographical description of tennis-loaded radius: Reciprocal relation between bone size and volumetric BMD, J. Appl. Physiol. 86 (1999) 1347–1351. https://doi.org/10.1152/jappl.1999.86.4.1347.

[321] H. Haapasalo, H. Sievänen, P. Kannus, A. Heinonen, P. Oja, I. Vuori, Dimensions and estimated mechanical characteristics of the humerus after long-term tennis loading, J. Bone Miner. Res. 11 (1996) 864–872. https://doi.org/10.1002/jbmr.5650110619.

[322] S. Kontulainen, H. Sievänen, P. Kannus, M. Pasanen, I. Vuori, Effect of long-term impact-loading on mass, size, and estimated strength of humerus and radius of female racquet-sports players: a peripheral quantitative computed tomography study between young and old starters and controls, J. Bone Miner. Res. 18 (2002) 352–359. https://doi.org/10.1359/jbmr.2003.18.2.352.

[323] S.J. Warden, S.M. Mantila Roosa, M.E. Kersh, A.L. Hurd, G.S. Fleisig, M.G. Pandy, R.K. Fuchs, Physical activity when young provides lifelong benefits to cortical bone size and strength in men, Proc. Natl. Acad. Sci. U. S. A. 111 (2014) 5337–5342. https://doi.org/10.1073/pnas.1321605111.

[324] S.J. Warden, E.D. Bogenschutz, H.D. Smith, A.R. Gutierrez, Throwing induces substantial torsional adaptation within the midshaft humerus of male baseball players, Bone. 45 (2009) 931–941. https://doi.org/10.1016/J.BONE.2009.07.075.

[325] R.K. Fuchs, W.R. Thompson, A.M. Weatherholt, S.J. Warden, Baseball and Softball Pitchers are Distinct Within-Subject Controlled Models for Exploring Proximal Femur Adaptation to Physical Activity, Calcif. Tissue Int. 104 (2019) 373–381. https://doi.org/10.1007/s00223-019-00519-y.

[326] J. Wu, S. Ishizaki, Y. Kato, Y. Kuroda, S. Fukashiro, The side-to-side differences of bone mass at proximal femur in female rhythmic sports gymnasts, J. Bone Miner. Res. 13 (1998) 900–906. https://doi.org/10.1359/JBMR.1998.13.5.900.

[327] H. Sievänen, V. Koskue, A. Rauhio, P. Kannus, A. Heinonen, I. Vuori, Peripheral quantitative computed tomography in human long bones: evaluation of in vitro and in vivo precision, J. Bone Miner. Res. 13 (1998) 871–882. https://doi.org/10.1359/jbmr.1998.13.5.871.

[328] A.K.O. Wong, A Comparison of Peripheral Imaging Technologies for Bone and Muscle Quantification: a Mixed Methods Clinical Review, Curr. Osteoporos. Rep. 14 (2016) 359–373. https://doi.org/10.1007/S11914-016-0334-Z.

[329] L.A. Burt, D.A. Greene, G. Ducher, G.A. Naughton, Skeletal adaptations associated with pre-pubertal gymnastics participation as determined by DXA and pQCT: A systematic review and meta-analysis, J. Sci. Med. Sport. 16 (2013) 231–239. https://doi.org/10.1016/j.jsams.2012.07.006.

[330] L.A. Burt, D.A. Greene, G.A. Naughton, Bone health of young male gymnasts: A systematic review, Pediatr. Exerc. Sci. 29 (2017) 456–464. https://doi.org/10.1123/pes.2017-0046.

[331] G. Lozano-Berges, Á. Matute-Llorente, A. González-Agüero, A. Gómez-Bruton, A. Gómez-Cabello, G. Vicente-Rodríguez, J.A. Casajús, Soccer helps build strong bones during growth: a systematic review and meta-analysis, Eur. J. Pediatr. 177 (2018) 295–310. https://doi.org/10.1007/s00431-017-3060-3.

[332] E. Stojanović, D. Radovanović, V.J. Dalbo, V. Jakovljević, N. Ponorac, R.R. Agostinete, Z. Svoboda, A.T. Scanlan, Basketball players possess a higher bone mineral density than matched non-athletes, swimming, soccer, and volleyball athletes: a systematic review and meta-analysis, Arch. Osteoporos. 15 (2020) 123. https://doi.org/10.1007/s11657-020-00803-7.

[333] M.A. Wewege, R.E. Ward, Bone mineral density in pre-professional female ballet dancers: A systematic review and meta-analysis, J. Sci. Med. Sport. 21 (2018) 783–788. https://doi.org/10.1016/j.jsams.2018.02.006.

[334] A. Gomez-Bruton, J. Montero-Marín, A. González-Agüero, J. García-Campayo, L.A. Moreno, J.A. Casajús, G. Vicente-Rodríguez, The Effect of Swimming During Childhood and Adolescence on Bone Mineral Density: A Systematic Review and Meta-Analysis, Sports Med. 46 (2016) 365–379. https://doi.org/10.1007/s40279-015-0427-3.

[335] A. Gomez-Bruton, J. Montero-Marín, A. González-Agüero, A. Gómez-Cabello, J. García-Campayo, L.A. Moreno, J.A. Casajús, G. Vicente-Rodríguez, Swimming and peak bone mineral density: A systematic review and meta-analysis, J. Sports Sci. 36 (2018) 365–377. https://doi.org/10.1080/02640414.2017.1307440.

[336] A. Gómez-Bruton, A. Gónzalez-Agüero, A. Gómez-Cabello, J.A. Casajús, G. Vicente-Rodríguez, Is Bone Tissue Really Affected by Swimming? A Systematic Review, PLoS One. 8 (2013) e70119. https://doi.org/10.1371/journal.pone.0070119.

[337] K. Hind, M. Burrows, Weight-bearing exercise and bone mineral accrual in children and adolescents: A review of controlled trials, Bone. 40 (2007) 14–27. https://doi.org/10.1016/j.bone.2006.07.006.

[338] C. Lindén, G. Alwis, H. Ahlborg, P. Gardsell, O. Valdimarsson, S. Stenevi-Lundgren, J. Besjakov, M.K. Karlsson, Exercise, bone mass and bone size in prepubertal boys: One-year data from the pediatric osteoporosis prevention study, Scand. J. Med. Sci. Sports. 17 (2007) 340–347. https://doi.org/10.1111/j.1600-0838.2006.00568.x.

[339] B. Löfgren, F. Detter, M. Dencker, S. Stenevi-Lundgren, J.Å. Nilsson, M.K. Karlsson, Influence of a 3-year exercise intervention program on fracture risk, bone mass, and bone size in prepubertal children, J. Bone Miner. Res. 26 (2011) 1740–1747. https://doi.org/10.1002/jbmr.381.

[340] Ö. Valdimarsson, C. Linden, O. Johnell, P. Gardsell, M.K. Karlsson, Daily physical education in the school curriculum in prepubertal girls during 1 year is followed by an increase in bone mineral accrual and bone width--data from the prospective controlled Malmö pediatric osteoporosis prevention study, Calcif. Tissue Int. 78 (2006) 65–71. https://doi.org/10.1007/s00223-005-0096-6.

[341] B. Specker, N.W. Thiex, R.G. Sudhagoni, Does Exercise Influence Pediatric Bone? A Systematic Review, Clin. Orthop. 473 (2015) 3658–3672. https://doi.org/10.1007/s11999-015-4467-7.

[342] S. Ishikawa, Y. Kim, M. Kang, D.W. Morgan, Effects of weight-bearing exercise on bone health in girls: A meta-analysis, Sports Med. 43 (2013) 875–892. https://doi.org/10.1007/s40279-013-0060-y.

[343] L. Santos, K.J. Elliott-Sale, C. Sale, Exercise and bone health across the lifespan., Biogerontology. 18 (2017) 931–946. https://doi.org/10.1007/s10522-017-9732-6.

[344] C.A. Bailey, K. Brooke-Wavell, Optimum frequency of exercise for bone health: Randomised controlled trial of a high-impact unilateral intervention, Bone. 46 (2010) 1043–1049. https://doi.org/10.1016/j.bone.2009.12.001.

[345] S.J. Allison, J.P. Folland, W.J. Rennie, G.D. Summers, K. Brooke-Wavell, High impact exercise increased femoral neck bone mineral density in older men: A randomised unilateral intervention, Bone. 53 (2013) 321–328. https://doi.org/10.1016/j.bone.2012.12.045.

[346] S.J. Allison, K.E.S. Poole, G.M. Treece, A.H. Gee, C. Tonkin, W.J. Rennie, J.P. Folland, G.D. Summers, K. Brooke-Wavell, The Influence of High-Impact Exercise on Cortical and Trabecular Bone Mineral Content and 3D Distribution Across the Proximal Femur in Older Men: A Randomized Controlled Unilateral Intervention, J. Bone Miner. Res. 30 (2015) 1709–1716. https://doi.org/10.1002/jbmr.2499.

[347] O.O. Babatunde, J.J. Forsyth, C.J. Gidlow, A meta-analysis of brief high-impact exercises for enhancing bone health in premenopausal women, Osteoporos. Int. 23 (2012) 109–119. https://doi.org/10.1007/s00198-011-1801-0.

[348] M. Kistler-Fischbacher, B.K. Weeks, B.R. Beck, The effect of exercise intensity on bone in postmenopausal women (part 2): A meta-analysis, Bone. 143 (2021) 115697. https://doi.org/10.1016/j.bone.2020.115697.

[349] M. Martyn-St James, S. Carroll, Progressive High-Intensity Resistance Training and Bone Mineral Density Changes Among Premenopausal Women, Sports Med. 36 (2006) 683–704. https://doi.org/10.2165/00007256-200636080-00005.

[350] M. Martyn-St James, S. Carroll, High-intensity resistance training and postmenopausal bone loss: a meta-analysis, Osteoporos. Int. 17 (2006) 1225–1240. https://doi.org/10.1007/s00198-006-0083-4.

[351] M. Martyn-St James, S. Carroll, A meta-analysis of impact exercise on postmenopausal bone loss: the case for mixed loading exercise programmes, Br. J. Sports Med. 43 (2009) 898–908. https://doi.org/10.1136/BJSM.2008.052704.

[352] M. Martyn-St James, S. Carroll, Effects of different impact exercise modalities on bone mineral density in premenopausal women: A meta-analysis, J. Bone Miner. Metab. 28 (2010) 251–267. https://doi.org/10.1007/s00774-009-0139-6.

[353] M. Shojaa, S. von Stengel, M. Kohl, D. Schoene, W. Kemmler, Effects of dynamic resistance exercise on bone mineral density in postmenopausal women: a systematic review and meta-analysis with special emphasis on exercise parameters, Osteoporos. Int. 31 (2020) 1427–1444. https://doi.org/10.1007/s00198-020-05441-w.

[354] R. Zhao, M. Zhao, L. Zhang, Efficiency of Jumping Exercise in Improving Bone Mineral Density Among Premenopausal Women: A Meta-Analysis, Sports Med. 44 (2014) 1393–1402. https://doi.org/10.1007/s40279-014-0220-8.

[355] R. Zhao, M. Zhang, Q. Zhang, The effectiveness of combined exercise interventions for preventing postmenopausal bone loss: A systematic review and meta-analysis, J. Orthop. Sports Phys. Ther. 47 (2017) 241–251. https://doi.org/10.2519/jospt.2017.6969.

[356] Renqing. Zhao, Meihua. Zhao, Z. Xu, The effects of differing resistance training modes on the preservation of bone mineral density in postmenopausal women: a meta-analysis, Osteoporos. Int. 26 (2015) 1605–1618. https://doi.org/10.1007/s00198-015-3034-0.

[357] S.L. Watson, B.K. Weeks, L.J. Weis, A.T. Harding, S.A. Horan, B.R. Beck, High-Intensity Resistance and Impact Training Improves Bone Mineral Density and Physical Function in Postmenopausal Women With Osteopenia and Osteoporosis: The LIFTMOR Randomized Controlled Trial, J. Bone Miner. Res. 33 (2018) 211–220. https://doi.org/10.1002/jbmr.3284.

[358] M.C. Ashe, I.K.D. Santos, N.Y. Edward, L.A. Burnett, R. Barnes, L. Fleig, J.H. Puyat, J.E.M. Sale, H.A. McKay, L.M. Giangregorio, Physical Activity and Bone Health in Men: A Systematic Review and Meta-Analysis, J. Bone Metab. 28 (2021) 27–39. https://doi.org/10.11005/jbm.2021.28.1.27.

[359] S. Kast, M. Shojaa, M. Kohl, S. von Stengel, M. Gosch, F. Jakob, K. Kerschan-Schindl, B. Kladny, N. Klöckner, U. Lange, S. Middeldorf, S. Peters, D. Schoene, C. Sieber, F. Thomasius, M. Uder, W. Kemmler, Effects of different exercise intensity on bone mineral density in adults: a comparative systematic review and meta-analysis, Osteoporos. Int. 33 (2022) 1643–1657. https://doi.org/10.1007/s00198-022-06329-7.

[360] W. Kemmler, M. Shojaa, M. Kohl, S. von Stengel, Exercise effects on bone mineral density in older men: a systematic review with special emphasis on study interventions, Osteoporos. Int. 29 (2018) 1493–1504. https://doi.org/10.1007/s00198-018-4482-0.

[361] E.A. Marques, J. Mota, J. Carvalho, Exercise effects on bone mineral density in older adults: A meta-analysis of randomized controlled trials, Age. 34 (2012) 1493–1515. https://doi.org/10.1007/s11357-011-9311-8.

[362] I.B. Rodrigues, M. Ponzano, Z. Hosseini, L. Thabane, P.D. Chilibeck, D.A. Butt, M.C. Ashe, J. Stapleton, J. Wark, L.M. Giangregorio, The Effect of Impact Exercise (Alone or Multicomponent Intervention) on Health-Related Outcomes in Individuals at Risk of Fractures: A Systematic Review and Meta-Analysis of Randomized Controlled Trials, Sports Med. 51 (2021) 1273–1292. https://doi.org/10.1007/s40279-021-01432-x.

[363] B.R. Hamilton, K.A. Staines, G.A. Kelley, K.S. Kelley, W.M. Kohrt, Y. Pitsiladis, F.M. Guppy, The Effects of Exercise on Bone Mineral Density in Men: A Systematic Review and Meta-Analysis of Randomised Controlled Trials, Calcif. Tissue Int. 110 (2022) 41–56. https://doi.org/10.1007/s00223-021-00893-6.

[364] G.A. Kelley, K.S. Kelley, W.M. Kohrt, Exercise and bone mineral density in men: A meta-analysis of randomized controlled trials, Bone. 53 (2013) 103–111. https://doi.org/10.1016/j.bone.2012.11.031.

[365] M. Mages, M. Shojaa, M. Kohl, S. von Stengel, C. Becker, M. Gosch, F. Jakob, K. Kerschan-Schindl, B. Kladny, N. Klöckner, U. Lange, S. Middeldorf, S. Peters, D. Schoene, C.C. Sieber, R. Tholen, F.E. Thomasius, M. Uder, W. Kemmler, Exercise Effects on Bone Mineral Density in Men, Nutrients. 13 (2021) 4244. https://doi.org/10.3390/nu13124244.

[366] M. Bhandari, M. Swiontkowski, Management of Acute Hip Fracture, N. Engl. J. Med. 377 (2017) 2053–2062. https://doi.org/10.1056/NEJMcp1611090.

[367] M. Parker, A. Johansen, Hip fracture, BMJ. 333 (2006) 27–30. https://doi.org/10.1136/bmj.333.7557.27.

[368] K.E. Leblanc, H.L. Muncie, L.L. Leblanc, Hip Fracture: Diagnosis, Treatment, and Secondary Prevention, Am. Fam. Physician. 89 (2014) 945–951.

[369] M.R. Karagas, G.L. Lu-Yao, J.A. Barrett, M.L. Beach, J.A. Baron, Heterogeneity of hip fracture: age, race, sex, and geographic patterns of femoral neck and trochanteric fractures among the US elderly, Am. J. Epidemiol. 143 (1996) 677–682. https://doi.org/10.1093/oxfordjournals.aje.a008800.

[370] A.T. Hantouly, A. AlBarazanji, M. Al-Juboori, M. Alebbini, A.A. Toubasi, A. Mohammed, O. Alzobi, G. Ahmed, Epidemiology of proximal femur fractures in the young population of Qatar, Eur. J. Orthop. Surg. Traumatol. (2023). https://doi.org/10.1007/s00590-023-03664-1.

[371] H.C. Bäcker, C.H. Wu, M. Maniglio, S. Wittekindt, S. Hardt, C. Perka, Epidemiology of proximal femoral fractures, J. Clin. Orthop. Trauma. 12 (2021) 161–165. https://doi.org/10.1016/j.jcot.2020.07.001.

[372] K.M. Fox, S.R. Cummings, E. Williams, K. Stone, Femoral Neck and Intertrochanteric Fractures Have Different Risk Factors : A Prospective Study, Osteoporos Int. 11 (2000) 1018–1023. https://doi.org/10.1007/s001980070022.

[373] N.M. Romeo, R. Firoozabadi, Classifications in Brief: The Pipkin Classification of Femoral Head Fractures, Clin. Orthop. 476 (2018) 1114–1119. https://doi.org/10.1007/s11999.0000000000000045.

[374] P.V. Giannoudis, G. Kontakis, Z. Christoforakis, M. Akula, T. Tosounidis, C. Koutras, Management, complications and clinical results of femoral head fractures, Injury. 40 (2009) 1245–1251. https://doi.org/10.1016/j.injury.2009.10.024.

[375] M.F. Swiontkowski, Current concepts review: Intracapsular fractures of the hip, J. Bone Jt. Surg. 76 (1994) 129–138. https://doi.org/10.2106/00004623-199401000-00019.

[376] K. Wendt, D. Heim, C. Josten, R. Kdolsky, H.J. Oestern, H. Palm, J.B. Sintenie, R. Komadina, C. Copuroglu, Recommendations on hip fractures, Eur. J. Trauma Emerg. Surg. 42 (2016) 425–431. https://doi.org/10.1007/s00068-016-0684-3.

[377] J. Panula, H. Pihlajamäki, V.M. Mattila, P. Jaatinen, T. Vahlberg, P. Aarnio, S.-L. Kivelä, Mortality and cause of death in hip fracture patients aged 65 or older: a population-based study, BMC Musculoskelet. Disord. 12 (2011) 105. https://doi.org/10.1186/1471-2474-12-105.

[378] O. Johnell, J.A. Kanis, Epidemiology of osteoporotic fractures, Osteoporos. Int. 16 (2005) 6–10. https://doi.org/10.1007/s00198-004-1702-6.

[379] L.E. Wehren, J. Magaziner, Hip fracture: risk factors and outcomes, Curr. Osteoporos. Rep. 1 (2003) 78–85. https://doi.org/10.1007/s11914-003-0013-8.

[380] J.C. Davies, D.P. Manning, G.J. Kemp, S.P. Frostick, The rising number of underfoot accidents after the menopause causes both fractures and non-fracture injuries, QJM Int. J. Med. 94 (2001) 699–707. https://doi.org/10.1093/qjmed/94.12.699.

[381] T.L.N. Järvinen, K. Michaëlsson, P. Aspenberg, H. Sievänen, Osteoporosis: the emperor has no clothes, J. Intern. Med. 277 (2015) 662–73. https://doi.org/10.1111/joim.12366.

[382] P. Nordström, F. Eklund, U. Björnstig, A. Nordström, R. Lorentzon, H. Sievänen, Y. Gustafson, Do both areal BMD and injurious falls explain the higher incidence of fractures in women than in men?, Calcif. Tissue Int. 89 (2011) 203–210. https://doi.org/10.1007/s00223-011-9507-z.

[383] E. Banks, G.K. Reeves, V. Beral, A. Balkwill, B. Liu, A. Roddam, Hip Fracture Incidence in Relation to Age, Menopausal Status, and Age at Menopause: Prospective Analysis, PLoS Med. 6 (2009) e1000181. https://doi.org/10.1371/JOURNAL.PMED.1000181.

[384] N. Veronese, S. Maggi, Epidemiology and social costs of hip fracture, Injury. 49 (2018) 1458–1460. https://doi.org/10.1016/j.injury.2018.04.015.

[385] P. Vestergaard, L. Rejnmark, L. Mosekilde, Increased mortality in patients with a hip fracture-effect of pre-morbid conditions and post-fracture complications, Osteoporos. Int. 18 (2007) 1583–1593. https://doi.org/10.1007/S00198-007-0403-3.

[386] J.D. Rupp, C.A.C. Flannagan, S.M. Kuppa, An injury risk curve for the hip for use in frontal impact crash testing, J. Biomech. 43 (2010) 527–531. https://doi.org/10.1016/J.JBIOMECH.2009.09.038.

[387] L. Cristofolini, M. Juszczyk, S. Martelli, F. Taddei, M. Viceconti, In vitro replication of spontaneous fractures of the proximal human femur, J. Biomech. 40 (2007) 2837–2845. https://doi.org/10.1016/j.jbiomech.2007.03.015.

[388] M. Viceconti, F. Taddei, L. Cristofolini, S. Martelli, C. Falcinelli, E. Schileo, Are spontaneous fractures possible? An example of clinical application for personalised, multiscale neuro-musculo-skeletal modelling, J. Biomech. 45 (2012) 421–426. https://doi.org/10.1016/j.jbiomech.2011.11.048.

[389] M.J. Parker, T.R. Twemlow, Spontaneous hip fractures, 44/872 in a prospective study, Acta Orthop. Scand. 68 (1997) 325–326. https://doi.org/10.3109/17453679708996170.

[390] T. Horiuchi, M. Igarashi, S. Karube, H. Oda, H. Tokuyama, T.J. Huang, S. Inoue, Spontaneous fractures of the hip in the elderly, Orthopedics. 11 (1988) 1277–1280. https://doi.org/10.3928/0147-7447-19880901-09.

[391] J.D. Michelson, A. Myers, R. Jinnah, Q. Cox, M. van Natta, Epidemiology of hip fractures among the elderly. Risk factors for fracture type, Clin. Orthop. 311 (1995) 129–135.

[392] F. Johannesdottir, K.E.S. Poole, J. Reeve, K. Siggeirsdottir, T. Aspelund, B. Mogensen, B.Y. Jonsson, S. Sigurdsson, T.B. Harris, V.G. Gudnason, G. Sigurdsson, Distribution of cortical bone in the femoral neck and hip fracture: A prospective case-control analysis of 143 incident hip fractures; the AGES-REYKJAVIK Study, Bone. 48 (2011) 1268–1276. https://doi.org/10.1016/j.bone.2011.03.776.

[393] S. Gilchrist, K.K. Nishiyama, P. de Bakker, P. Guy, S.K. Boyd, T. Oxland, P.A. Cripton, Proximal femur elastic behaviour is the same in impact and constant displacement rate fall simulation, J. Biomech. 47 (2014) 3744–3749. https://doi.org/10.1016/j.jbiomech.2014.06.040.

[394] M.M. Juszczyk, L. Cristofolini, M. Viceconti, The human proximal femur behaves linearly elastic up to failure under physiological loading conditions, J. Biomech. 44 (2011) 2259–2266. https://doi.org/10.1016/j.jbiomech.2011.05.038.

[395] E. Schileo, F. Taddei, L. Cristofolini, M. Viceconti, Subject-specific finite element models implementing a maximum principal strain criterion are able to estimate failure risk and fracture location on human femurs tested in vitro, J. Biomech. 41 (2008) 356–367. https://doi.org/10.1016/j.jbiomech.2007.09.009.

[396] J. Borggrefe, T. de Buhr, S. Shrestha, L.M. Marshall, E. Orwoll, K. Peters, D.M. Black, C.C. Glüer, Association of 3D Geometric Measures Derived From Quantitative Computed Tomography With Hip Fracture Risk in Older Men, J. Bone Miner. Res. 31 (2016) 1550–1558. https://doi.org/10.1002/jbmr.2821.

[397] J. Carballido-Gamio, R. Harnish, I. Saeed, T. Streeper, S. Sigurdsson, S. Amin, E.J. Atkinson, T.M. Therneau, K. Siggeirsdottir, X. Cheng, L.J. Melton III, J.H. Keyak, V. Gudnason, S. Khosla, T.B. Harris, T.F. Lang, Proximal femoral density distribution

and structure in relation to age and hip fracture risk in women, J. Bone Miner. Res. 28 (2013) 537–546. https://doi.org/10.1002/jbmr.1802.

[398] J. Carballido-Gamio, R. Harnish, I. Saeed, T. Streeper, S. Sigurdsson, S. Amin, E.J. Atkinson, T.M. Therneau, K. Siggeirsdottir, X. Cheng, L.J. Melton, J.H. Keyak, V. Gudnason, S. Khosla, T.B. Harris, T.F. Lang, Structural patterns of the proximal femur in relation to age and hip fracture risk in women, Bone. 57 (2013) 290–299. https://doi.org/10.1016/j.bone.2013.08.017.

[399] P. Milovanovic, D. Djonic, R.P. Marshall, M. Hahn, S. Nikolic, V. Zivkovic, M. Amling, M. Djuric, Micro-structural basis for particular vulnerability of the superolateral neck trabecular bone in the postmenopausal women with hip fractures, Bone. 50 (2012) 63–68. https://doi.org/10.1016/J.BONE.2011.09.044.

[400] T.J. Beck, a C. Looker, C.B. Ruff, H. Sievänen, H.W. Wahner, Structural trends in the aging femoral neck and proximal shaft: analysis of the Third National Health and Nutrition Examination Survey dual-energy X-ray absorptiometry data, J. Bone Miner. Res. 15 (2000) 2297–2304. https://doi.org/10.1359/jbmr.2000.15.12.2297.

[401] S. Kaptoge, N. Dalzell, R.W. Jakes, N. Wareham, N.E. Day, K.T. Khaw, T.J. Beck, N. Loveridge, J. Reeve, Hip section modulus, a measure of bending resistance, is more strongly related to reported physical activity than BMD, Osteoporos. Int. 14 (2003) 941–949. https://doi.org/10.1007/S00198-003-1484-2.

[402] J. Power, N. Loveridge, A. Lyon, N. Rushton, M. Parker, J. Reeve, Osteoclastic cortical erosion as a determinant of subperiosteal osteoblastic bone formation in the femoral neck's response to BMU imbalance. Effects of stance-related loading and hip fracture, Osteoporos. Int. 16 (2005) 1049–1056. https://doi.org/10.1007/S00198-004-1803-2.

[403] O. Demontiero, C. Vidal, G. Duque, Aging and bone loss: new insights for the clinician, Ther. Adv. Musculoskelet. Dis. 4 (2012) 61–76. https://doi.org/10.1177/1759720X11430858.

[404] T. Tang, P.A. Cripton, P. Guy, H.A. McKay, R. Wang, Clinical hip fracture is accompanied by compression induced failure in the superior cortex of the femoral neck, Bone. 108 (2018) 121–131. https://doi.org/10.1016/J.BONE.2017.12.020.

[405] P. Pulkkinen, J. Partanen, P. Jalovaara, T. Jämsä, BMD T-score discriminates trochanteric fractures from unfractured controls, whereas geometry discriminates cervical fracture cases from unfractured controls of similar BMD, Osteoporos. Int. 21 (2010) 1269–1276. https://doi.org/10.1007/s00198-009-1070-3.

[406] S.L. Greenspan, E.R. Myers, L.A. Maitland, T.H. Kido, M.B. Krasnow, W.C. Hayes, Trochanteric bone mineral density is associated with type of hip fracture in the elderly, J. Bone Miner. Res. 9 (1994) 1889–1894. https://doi.org/10.1002/jbmr.5650091208.

[407] A.M. Schott, D. Hans, F. Duboeuf, P. Dargent-Molina, T. Hajri, G. Bréart, P.J. Meunier, Quantitative ultrasound parameters as well as bone mineral density are better predictors of trochanteric than cervical hip fractures in elderly women. Results from the EPIDOS study, Bone. 37 (2005) 858–863. https://doi.org/10.1016/j.bone.2005.06.024.

[408] E. Vega, C. Mautalen, H. Gómez, A. Garrido, L. Melo, A.O. Sahores, Bone mineral density in patients with cervical and trochanteric fractures of the proximal femur, Osteoporos. Int. 1 (1991) 81–86. https://doi.org/10.1007/BF01880448.

[409] A. Stewart, R.W. Porter, W.R. Primrose, L.G. Walker, D.M. Reid, Cervical and trochanteric hip fractures: Bone mass and other parameters, Clin. Rheumatol. 18 (1999) 201–206. https://doi.org/10.1007/s100670050085.

[410] K.M. Fox, J. Magaziner, J.R. Hebel, J.E. Kenzora, T.M. Kashner, Intertrochanteric versus femoral neck hip fractures: differential characteristics, treatment, and sequelae, J. Gerontol. Ser. A. 54 (1999) M635–M640. https://doi.org/10.1093/gerona/54.12.m635.

[411] J.A. Kanis, F. Borgstrom, C. De Laet, H. Johansson, O. Johnell, B. Jonsson, A. Oden, N. Zethraeus, B. Pfleger, N. Khaltaev, Assessment of fracture risk, Osteoporos Int. 16 (2005) 581–589. https://doi.org/10.1007/s00198-004-1780-5.

[412] S.R. Cummings, M.C. Nevitt, W.S. Browner, K. Stone, K.M. Fox, K.E. Ensrud, J. Cauley, D. Black, T.M. Vogt, Risk Factors for Hip Fracture in White Women, N. Engl. J. Med. 332 (1995) 767–773. https://doi.org/10.1056/NEJM199503233321202.

[413] J.A. Kanis, A. Oden, O. Johnell, H. Johansson, C. De Laet, J. Brown, P. Burckhardt, C. Cooper, C. Christiansen, S. Cummings, J.A. Eisman, S. Fujiwara, C. Glüer, D. Goltzman, D. Hans, M.A. Krieg, A. La Croix, E. McCloskey, D. Mellstrom, L.J. Melton, H. Pols, J. Reeve, K. Sanders, A.M. Schott, A. Silman, D. Torgerson, T. Van Staa, N.B. Watts, N. Yoshimura, The use of clinical risk factors enhances the performance of BMD in the prediction of hip and osteoporotic fractures in men and women, Osteoporos. Int. 18 (2007) 1033–1046. https://doi.org/10.1007/s00198-007-0343-y.

[414] J.A. Kanis, E. V McCloskey, Evaluation of the risk of hip fracture, Bone. 18 (1996) S127-S132. https://doi.org/10.1016/8756-3282(95)00493-9.

[415] S. Karinkanta, M. Piirtola, H. Sievänen, K. Uusi-Rasi, P. Kannus, Physical therapy approaches to reduce fall and fracture risk among older adults, Nat. Rev. Endocrinol. 6 (2010) 396–407. https://doi.org/10.1038/nrendo.2010.70.

[416] M.R. McClung, Pathogenesis of osteoporotic hip fractures, Clin. Cornerstone. 5 (2003) S22–S29. https://doi.org/10.1016/s1098-3597(03)90044-5.

[417] D. Metcalfe, The pathophysiology of osteoporotic hip fracture, McGill J. Med. 11 (2008) 51–57.

[418] R. Wiklund, A. Toots, M. Conradsson, B. Olofsson, H. Holmberg, E. Rosendahl, Y. Gustafson, H. Littbrand, Risk factors for hip fracture in very old people: a population-based study, Osteoporos. Int. 27 (2016) 923–931. https://doi.org/10.1007/s00198-015-3390-9.

[419] O. Johnell, J.A. Kanis, A. Oden, H. Johansson, C. De Laet, P. Delmas, J.A. Eisman, S. Fujiwara, H. Kroger, D. Mellstrom, P.J. Meunier, L.J. Melton, T. O'Neill, H. Pols, J. Reeve, A. Silman, A. Tenenhouse, Predictive value of BMD for hip and other

fractures, J. Bone Miner. Res. 20 (2005) 1185–1194. https://doi.org/10.1359/JBMR.050304.

[420] D. Marshall, O. Johnell, H. Wedel, Meta-analysis of how well measures of bone mineral density predict occurrence of osteoporotic fractures, BMJ. 312 (1996) 1254. https://doi.org/10.1136/bmj.312.7041.1254.

[421] S. Baim, W.D. Leslie, Assessment of fracture risk, Curr. Osteoporos. Rep. 10 (2012) 28–41. https://doi.org/10.1007/s11914-011-0093-9.

[422] C.A. Mautalen, E.M. Vega, T.A. Einhorn, Are the etiologies of cervical and trochanteric hip fractures different?, Bone. 18 (1996) S133–S137. https://doi.org/10.1016/8756-3282(95)00490-4.

[423] K.G. Faulkner, S.R. Cummings, D. Black, L. Palermo, C.-C. Glüer, H.K. Genant, Simple measurement of femoral geometry predicts hip fracture: The study of osteoporotic fractures, J. Bone Miner. Res. 8 (1993) 1211–1217. https://doi.org/10.1002/jbmr.5650081008.

[424] T.L.N. Järvinen, H. Sievänen, K.M. Khan, A. Heinonen, P. Kannus, Shifting the focus in fracture prevention from osteoporosis to falls, BMJ. 336 (2008) 124–126. https://doi.org/10.1136/bmj.39428.470752.AD.

[425] P. Kannus, H. Sievänen, M. Palvanen, T. Järvinen, J. Parkkari, Prevention of falls and consequent injuries in elderly people, Lancet. 366 (2005) 1885–1893. https://doi.org/10.1016/S0140-6736(05)67604-0.

[426] A.Z. Moore, G. Caturegli, E.J. Metter, S. Makrogiannis, S.M. Resnick, T.B. Harris, L. Ferrucci, Difference in muscle quality over the adult life span and biological correlates in the baltimore longitudinal study of aging, J. Am. Geriatr. Soc. 62 (2014) 230–236. https://doi.org/10.1111/jgs.12653.

[427] M.E. Tinetti, Preventing Falls in Elderly Persons, N. Engl. J. Med. 348 (2003) 42–49. https://doi.org/10.1056/NEJMcp020719.

[428] P. Kannus, K. Uusi-Rasi, M. Palvanen, J. Parkkari, Non-pharmacological means to prevent fractures among older adults, Ann. Med. 37 (2005) 303–310. https://doi.org/10.1080/07853890510007197.

[429] S.L. Hui, C.W. Slemenda, C.C. Johnston, Age and bone mass as predictors of fracture in a prospective study, J. Clin. Invest. 81 (1988) 1804–1809. https://doi.org/10.1172/JCI113523.

[430] H. Johansson, J.A. Kanis, A. Oden, O. Johnell, E. McCloskey, BMD, clinical risk factors and their combination for hip fracture prevention, Osteoporos. Int. 20 (2009) 1675–1682. https://doi.org/10.1007/s00198-009-0845-x.

[431] J.A. Kanis, O. Johnell, A. Oden, B. Jonsson, C. De Laet, A. Dawson, Risk of hip fracture according to the World Health Organization criteria for osteopenia and osteoporosis, Bone. 27 (2000) 585–590. https://doi.org/10.1016/S8756-3282(00)00381-1.

[432] C.E.D.H. De Laet, B.A. Van Hout, H. Burger, A. Hofman, H.A.P. Pols, Bone density and risk of hip fracture in men and women: Cross sectional analysis, BMJ. 315 (1997) 221–225. https://doi.org/10.1136/bmj.315.7102.221.

[433] M.R. Law, A.K. Hackshaw, A meta-analysis of cigarette smoking, bone mineral density and risk of hip fracture: Recognition of a major effect, BMJ. 315 (1997) 841–846. https://doi.org/10.1136/bmj.315.7112.841.

[434] D.G. Ampelas, Current and former smokers and hip fractures, J. Frailty Sarcopenia Falls. 3 (2018) 148–154. https://doi.org/10.22540/jfsf-03-148.

[435] X. Zhang, Z. Yu, M. Yu, X. Qu, Alcohol consumption and hip fracture risk, Osteoporos. Int. 26 (2015) 531–542. https://doi.org/10.1007/s00198-014-2879-y.

[436] D.B. Maurel, N. Boisseau, C.L. Benhamou, C. Jaffre, Alcohol and bone: Review of dose effects and mechanisms, Osteoporos. Int. 23 (2012) 1–16. https://doi.org/10.1007/s00198-011-1787-7.

[437] J.A. Marrone, G.F. Maddalozzo, A.J. Branscum, K. Hardin, L. Cialdella-Kam, K.A. Philbrick, A.C. Breggia, C.J. Rosen, R.T. Turner, U.T. Iwaniec, Moderate alcohol intake lowers biochemical markers of bone turnover in postmenopausal women, Menopause. 19 (2012) 974–979. https://doi.org/10.1097/gme.0b013e31824ac071.

[438] J.A. Kanis, H. Johansson, A. Oden, O. Johnell, C. De Laet, L. Joseph Melton, A. Tenenhouse, J. Reeve, A.J. Silman, H.A.P. Pols, J.A. Eisman, E.V. McCloskey, D. Mellstrom, A meta-analysis of prior corticosteroid use and fracture risk, J. Bone Miner. Res. 19 (2004) 893–899. https://doi.org/10.1359/JBMR.040134.

[439] F. De Vries, M. Bracke, H.G.M. Leufkens, J.W.J. Lammers, C. Cooper, T.P. Van Staa, Fracture risk with intermittent high-dose oral glucocorticoid therapy, Arthritis Rheum. 56 (2007) 208–214. https://doi.org/10.1002/art.22294.

[440] E. Canalis, G. Mazziotti, A. Giustina, J.P. Bilezikian, Glucocorticoid-induced osteoporosis: Pathophysiology and therapy, Osteoporos. Int. 18 (2007) 1319–1328. https://doi.org/10.1007/s00198-007-0394-0.

[441] R.C.Y. Cheung, C. Gray, A. Boyde, S.J. Jones, Effects of ethanol on bone cells in vitro resulting in increased resorption, Bone. 16 (1995) 143–147. https://doi.org/10.1016/8756-3282(95)80025-L.

[442] H.W. Sampson, Alcohol's harmful effects on bone, Alcohol Health Res. World. 22 (1998) 190–194.

[443] P. Torricelli, M. Fini, G. Giavaresi, V. Borsari, L. Rimondini, R. Rimondini, A. Carrassi, R. Giardino, Intermittent exposure to ethanol vapor affects osteoblast behaviour more severely than estrogen deficiency does. In vitro study on rat osteoblasts, Toxicology. 237 (2007) 168–176. https://doi.org/10.1016/j.tox.2007.05.010.

[444] P. Vestergaard, L. Mosekilde, Fracture risk associated with smoking: A meta-analysis, J. Intern. Med. 254 (2003) 572–583. https://doi.org/10.1111/j.1365-2796.2003.01232.x.

[445] B.E. Christopher Nordin, A.G. Need, T. Steurer, H.A. Morris, B.E. Chatterton, M. Horowitz, Nutrition, osteoporosis, and aging, Ann. N. Y. Acad. Sci. 854 (1998) 336–351. https://doi.org/10.1111/j.1749-6632.1998.tb09914.x.

[446] Y. Luo, A biomechanical sorting of clinical risk factors affecting osteoporotic hip fracture, Osteoporos. Int. 27 (2016) 423–439. https://doi.org/10.1007/s00198-015-3316-6.

[447] J.C. Lotz, W.C. Hayes, The use of quantitative computed tomography to estimate risk of fracture of the hip from falls, J. Bone Jt. Surg. Am. 72 (1990) 689–700.

[448] C. De Laet, J.A. Kanis, A. Odén, H. Johanson, O. Johnell, P. Delmas, J.A. Eisman, H. Kroger, S. Fujiwara, P. Garnero, E.V. McCloskey, D. Mellstrom, L.J. Melton, P.J. Meunier, H.A.P. Pols, J. Reeve, A. Silman, A. Tenenhouse, Body mass index as a predictor of fracture risk: A meta-analysis, Osteoporos. Int. 16 (2005) 1330–1338. https://doi.org/10.1007/s00198-005-1863-y.

[449] S. Morin, J.F. Tsang, W.D. Leslie, Weight and body mass index predict bone mineral density and fractures in women aged 40 to 59 years, Osteoporos. Int. 20 (2009) 363–370. https://doi.org/10.1007/s00198-008-0688-x.

[450] J.A. Kanis, N.C. Harvey, H. Johansson, E. Liu, L. Vandenput, M. Lorentzon, W.D. Leslie, E.V. McCloskey, A decade of FRAX: how has it changed the management of osteoporosis?, Aging Clin. Exp. Res. 32 (2020) 187–196. https://doi.org/10.1007/s40520-019-01432-y.

[451] J.A. Kanis, E.V. McCloskey, H. Johansson, A. Oden, L.J. Melton, N. Khaltaev, A reference standard for the description of osteoporosis, Bone. 42 (2008) 467–475. https://doi.org/10.1016/j.bone.2007.11.001.

[452] J.A. Kanis, H. Johansson, N.C. Harvey, E.V. McCloskey, A brief history of FRAX, Arch. Osteoporos. 13 (2018) 118. https://doi.org/10.1007/s11657-018-0510-0.

[453] S.L. Greenspan, E.R. Myers, L.A. Maitland, N.M. Resnick, W.C. Hayes, Fall Severity and Bone Mineral Density as Risk Factors for Hip Fracture in Ambulatory Elderly, JAMA. 271 (1994) 128–133. https://doi.org/10.1001/jama.1994.03510260060029.

[454] J.A. Kanis, O. Johnell, A. Oden, H. Johansson, E. McCloskey, FRAX™ and the assessment of fracture probability in men and women from the UK, Osteoporos. Int. 19 (2008) 385–397. https://doi.org/10.1007/s00198-007-0543-5.

[455] K.L. Stone, D.G. Seeley, L.Y. Lui, J.A. Cauley, K. Ensrud, W.S. Browner, M.C. Nevitt, S.R. Cummings, BMD at Multiple Sites and Risk of Fracture of Multiple Types: Long-Term Results From the Study of Osteoporotic Fractures, J. Bone Miner. Res. 18 (2003) 1947–1954. https://doi.org/10.1359/jbmr.2003.18.11.1947.

[456] W.D. Leslie, L.M. Lix, H. Johansson, A. Oden, E. McCloskey, J.A. Kanis, Independent clinical validation of a Canadian FRAX tool: Fracture prediction and model calibration, J. Bone Miner. Res. 25 (2010) 2350–2358. https://doi.org/10.1002/jbmr.123.

[457] E.S. Siris, S. Baim, A. Nattiv, Primary care use of FRAX®: Absolute fracture risk assessment in postmenopausal women and older men, Postgrad. Med. 122 (2010) 82–90. https://doi.org/10.3810/pgm.2010.01.2102.

[458] N.D. Nguyen, S.A. Frost, J.R. Center, J.A. Eisman, T.V. Nguyen, Development of prognostic nomograms for individualizing 5-year and 10-year fracture risks, Osteoporos. Int. 19 (2008) 1431–1444. https://doi.org/10.1007/s00198-008-0588-0.

[459] J. Hippisley-Cox, C. Coupland, Predicting risk of osteoporotic fracture in men and women in England and Wales: Prospective derivation and validation of QFractureScores, BMJ. 339 (2009) 1291–1295. https://doi.org/10.1136/bmj.b4229.

[460] M.J. Bolland, A.T. Siu, B.H. Mason, A.M. Horne, R.W. Ames, A.B. Grey, G.D. Gamble, I.R. Reid, Evaluation of the FRAX and Garvan fracture risk calculators in older women, J. Bone Miner. Res. 26 (2011) 420–427. https://doi.org/10.1002/jbmr.215.

[461] K.L. Holloway-Kew, Y. Zhang, A.G. Betson, K.B. Anderson, D. Hans, N.K. Hyde, G.C. Nicholson, N.A. Pocock, M.A. Kotowicz, J.A. Pasco, How well do the FRAX (Australia) and Garvan calculators predict incident fractures? Data from the Geelong Osteoporosis Study, Osteoporos. Int. 30 (2019) 2129–2139. https://doi.org/10.1007/s00198-019-05088-2.

[462] M. Nasiri Sarvi, Y. Luo, Sideways fall-induced impact force and its effect on hip fracture risk: a review, Osteoporos. Int. 28 (2017) 2759–2780. https://doi.org/10.1007/s00198-017-4138-5.

[463] M.L. Bouxsein, Determinants of skeletal fragility, Best Pract. Res. Clin. Rheumatol. 19 (2005) 897–911. https://doi.org/10.1016/J.BERH.2005.07.004.

[464] J.F. Griffith, H.K. Genant, Bone mass and architecture determination: state of the art, Best Pract. Res. Clin. Endocrinol. Metab. 22 (2008) 737–764. https://doi.org/10.1016/J.BEEM.2008.07.003.

[465] N.J. Crabtree, H. Kroger, A. Martin, H.A.P. Pols, R. Lorenc, J. Nijs, J.J. Stepan, J.A. Falch, T. Miazgowski, S. Grazio, P. Raptou, J. Adams, A. Collings, K.T. Khaw, N. Rushton, M. Lunt, A.K. Dixon, J. Reeve, Improving risk assessment: Hip geometry, bone mineral distribution and bone strength in hip fracture cases and controls. The EPOS study, Osteoporos. Int. 13 (2002) 48–54. https://doi.org/10.1007/s198-002-8337-y.

[466] M.B. Sabick, J.G. Hay, V.K. Goel, S.A. Banks, Active responses decrease impact forces at the hip and shoulder in falls to the side, J. Biomech. 32 (1999) 993–998. https://doi.org/10.1016/S0021-9290(99)00079-2.

[467] M. Nankaku, H. Kanzaki, T. Tsuboyama, T. Nakamura, Evaluation of hip fracture risk in relation to fall direction, Osteoporos. Int. 16 (2005) 1315–1320. https://doi.org/10.1007/s00198-005-1843-2.

[468] B.E. Groen, V. Weerdesteyn, J. Duysens, The relation between hip impact velocity and hip impact force differs between sideways fall techniques, J. Electromyogr. Kinesiol. 18 (2008) 228–234. https://doi.org/10.1016/J.JELEKIN.2007.06.002.

[469] B.E. Groen, V. Weerdesteyn, J. Duysens, Martial arts fall techniques decrease the impact forces at the hip during sideways falling, J. Biomech. 40 (2007) 458–462. https://doi.org/10.1016/J.JBIOMECH.2005.12.014.

[470] A.M. van der Zijden, B.E. Groen, E. Tanck, B. Nienhuis, N. Verdonschot, V. Weerdesteyn, Can martial arts techniques reduce fall severity? An in vivo study of femoral loading configurations in sideways falls, J. Biomech. 45 (2012) 1650–1655. https://doi.org/10.1016/J.JBIOMECH.2012.03.024.

[471] A.J. van den Kroonenberg, W.C. Hayes, T.A. McMahon, Hip impact velocities and body configurations for voluntary falls from standing height, J. Biomech. 29 (1996) 807–811. https://doi.org/10.1016/0021-9290(95)00134-4.

[472] S.N. Robinovitch, W.C. Hayes, T.A. McMahon, Prediction of femoral impact forces in falls on the hip, J. Biomech. Eng. 113 (1991) 366–374. https://doi.org/10.1115/1.2895414.

[473] S.N. Robinovitch, W.C. Hayes, T.A. Mcmahon, Distribution of contact force during impact to the hip, Ann. Biomed. Eng. 25 (1997) 499–508. https://doi.org/10.1007/BF02684190.

[474] A.J. van den Kroonenberg, W.C. Hayes, T.A. McMahon, Dynamic models for sideways falls from standing height, J. Biomech. Eng. 117 (1995) 309–318. https://doi.org/10.1115/1.2794186.

[475] M.L. Bouxsein, P. Szulc, F. Munoz, E. Thrall, E. Sornay-Rendu, P.D. Delmas, Contribution of trochanteric soft tissues to fall force estimates, the factor of risk, and prediction of hip fracture risk, J. Bone Miner. Res. 22 (2007) 825–831. https://doi.org/10.1359/jbmr.070309.

[476] A.C. Laing, S.N. Robinovitch, Characterizing the effective stiffness of the pelvis during sideways falls on the hip, J. Biomech. 43 (2010) 1898–1904. https://doi.org/10.1016/J.JBIOMECH.2010.03.025.

[477] D.R. Martel, I.C. Levine, S.P. Pretty, A.C. Laing, The influence of muscle activation on impact dynamics during lateral falls on the hip, J. Biomech. 66 (2018) 111–118. https://doi.org/10.1016/J.JBIOMECH.2017.11.002.

[478] F. Feldman, S.N. Robinovitch, Reducing hip fracture risk during sideways falls: Evidence in young adults of the protective effects of impact to the hands and stepping, J. Biomech. 40 (2007) 2612–2618. https://doi.org/10.1016/J.JBIOMECH.2007.01.019.

[479] S.N. Robinovitch, R. Brumer, J. Maurer, Effect of the "squat protective response" on impact velocity during backward falls, J. Biomech. 37 (2004) 1329–1337. https://doi.org/10.1016/J.JBIOMECH.2003.12.015.

[480] I. Fleps, A. Fung, P. Guy, S.J. Ferguson, B. Helgason, P.A. Cripton, Subject-specific ex vivo simulations for hip fracture risk assessment in sideways falls, Bone. 125 (2019) 36–45. https://doi.org/10.1016/J.BONE.2019.05.004.

[481] I. Fleps, M. Vuille, A. Melnyk, S.J. Ferguson, P. Guy, B. Helgason, P.A. Cripton, A novel sideways fall simulator to study hip fractures ex vivo, PLoS One. 13 (2018) e0201096. https://doi.org/10.1371/journal.pone.0201096.

[482] I. Fleps, P. Guy, S.J. Ferguson, P.A. Cripton, B. Helgason, Explicit Finite Element Models Accurately Predict Subject-Specific and Velocity-Dependent Kinetics of Sideways Fall Impact, J. Bone Miner. Res. 34 (2019) 1837–1850. https://doi.org/10.1002/JBMR.3804.

[483] S.N. Robinovitch, T.A. McMahon, W.C. Hayes, Force attenuation in trochanteric soft tissues during impact from a fall, J. Orthop. Res. 13 (1995) 956–962. https://doi.org/10.1002/JOR.1100130621.

[484] D.D. Cody, G.J. Gross, F. J. Hou, H.J. Spencer, S.A. Goldstein, D. P. Fyhrie, Femoral strength is better predicted by finite element models than QCT and DXA, J. Biomech. 32 (1999) 1013–1020. https://doi.org/10.1016/S0021-9290(99)00099-8.

[485] F. Johannesdottir, E. Thrall, J. Muller, T.M. Keaveny, D.L. Kopperdahl, M.L. Bouxsein, Comparison of non-invasive assessments of strength of the proximal femur, Bone. 105 (2017) 93–102. https://doi.org/10.1016/J.BONE.2017.07.023.

[486] J.N. Reddy, Introduction to the Finite Element Method, 4th ed., McGraw Hill Education, New York, 2019. https://www.accessengineeringlibrary.com/content/book/9781259861901.

[487] A. Bobet, A. Fakhimi, S. Johnson, J. Morris, F. Tonon, M.R. Yeung, Numerical Models in Discontinuous Media: Review of Advances for Rock Mechanics Applications, J. Geotech. Geoenvironmental Eng. 135 (2009) 1547–1561. https://doi.org/10.1061/(ASCE)GT.1943-5606.0000133.

[488] J.H. Keyak, J.M. Meagher, H.B. Skinner, C.D. Mote, Automated three-dimensional finite element modelling of bone: a new method, J. Biomed. Eng. 12 (1990) 389–397. https://doi.org/10.1016/0141-5425(90)90022-F.

[489] J.H. Keyak, H.B. Skinner, Three-dimensional finite element modelling of bone: effects of element size, J. Biomed. Eng. 14 (1992) 483–489. https://doi.org/10.1016/0141-5425(92)90100-Y.

[490] J.H. Keyak, M.G. Fourkas, J.H. Meagher, H.B. Skinner, Validation of an automated method of three-dimensional finite element modelling of bone, J. Biomed. Eng. 15 (1993) 505–509. https://doi.org/10.1016/0141-5425(93)90066-8.

[491] J.C. Lotz, E.J. Cheal, W.C. Hayes, Fracture prediction for the proximal femur using finite element models: Part II-Nonlinear analysis, J. Biomech. Eng. 113 (1991) 361–365. https://doi.org/10.1115/1.2895413.

[492] J.C. Lotz, E.J. Cheal, W.C. Hayes, Fracture prediction for the proximal femur using finite element models: Part I-Linear analysis, J. Biomech. Eng. 113 (1991) 353–360. https://doi.org/10.1115/1.2895412.

[493] J.H. Keyak, S.A. Rossi, K.A. Jones, C.M. Les, H.B. Skinner, Prediction of fracture location in the proximal femur using finite element models, Med. Eng. Phys. 23 (2001) 657–664. https://doi.org/10.1016/S1350-4533(01)00094-7.

[494] J.H. Keyak, I.Y. Lee, H.B. Skinner, Correlations between orthogonal mechanical properties and density of trabecular bone: Use of different densitometric measures, J. Biomed. Mater. Res. 28 (1994) 1329–1336. https://doi.org/10.1002/JBM.820281111.

[495] M. Lengsfeld, J. Schmitt, P. Alter, J. Kaminsky, R. Leppek, Comparison of geometry-based and CT voxel-based finite element modelling and experimental validation, Med. Eng. Phys. 20 (1998) 515–522. https://doi.org/10.1016/S1350-4533(98)00054-X.

[496] B. Helgason, F. Taddei, H. Pálsson, E. Schileo, L. Cristofolini, M. Viceconti, S. Brynjólfsson, A modified method for assigning material properties to FE models of bones, Med. Eng. Phys. 30 (2008) 444–453. https://doi.org/10.1016/j.medengphy.2007.05.006.

[497] G.N. Duda, M. Heller, J. Albinger, O. Schulz, E. Schneider, L. Claes, Influence of muscle forces on femoral strain distribution, J. Biomech. 31 (1998) 841–846. https://doi.org/10.1016/S0021-9290(98)00080-3.

[498] K. Polgár, H.S. Gill, M. Viceconti, D.W. Murray, J.J. O'Connor, Strain distribution within the human femur due to physiological and simplified loading: finite element analysis using the muscle standardized femur model, Proc. Inst. Mech. Eng. H. 217 (2003) 173–189. https://doi.org/10.1243/095441103765212677.

[499] K. Polgár, H.S. Gill, M. Viceconti, D.W. Murray, J.J. O'Connor, Development and Numerical Validation of a Finite Element Model of the Muscle Standardized Femur, Proc. Inst. Mech. Eng. H. 217 (2003) 165–172. https://doi.org/10.1243/095441103765212668.

[500] M. Lengsfeld, J. Kaminsky, B. Merz, R.P. Franke, Sensitivity of femoral strain pattern analyses to resultant and muscle forces at the hip joint, Med. Eng. Phys. 18 (1996) 70–78. https://doi.org/10.1016/1350-4533(95)00033-X.

[501] E.S. Orwoll, L.M. Marshall, C.M. Nielson, S.R. Cummings, J. Lapidus, J.A. Cauley, K. Ensrud, N. Lane, P.R. Hoffmann, D.L. Kopperdahl, T.M. Keaveny, Finite Element Analysis of the Proximal Femur and Hip Fracture Risk in Older Men, J. Bone Miner. Res. 24 (2009) 475–483. https://doi.org/10.1359/JBMR.081201.

[502] M. Bessho, I. Ohnishi, J. Matsuyama, T. Matsumoto, K. Imai, K. Nakamura, Prediction of strength and strain of the proximal femur by a CT-based finite element method, J. Biomech. 40 (2007) 1745–1753. https://doi.org/10.1016/j.jbiomech.2006.08.003.

[503] K.K. Nishiyama, S. Gilchrist, P. Guy, P. Cripton, S.K. Boyd, Proximal femur bone strength estimated by a computationally fast finite element analysis in a sideways fall configuration, J. Biomech. 46 (2013) 1231–1236. https://doi.org/10.1016/j.jbiomech.2013.02.025.

[504] L. Grassi, E. Schileo, F. Taddei, L. Zani, M. Juszczyk, L. Cristofolini, M. Viceconti, Accuracy of finite element predictions in sideways load configurations for the proximal human femur, J. Biomech. 45 (2012) 394–399. https://doi.org/10.1016/j.jbiomech.2011.10.019.

[505] Z. Altai, M. Qasim, X. Li, M. Viceconti, The effect of boundary and loading conditions on patient classification using finite element predicted risk of fracture, Clin. Biomech. 68 (2019) 137–143. https://doi.org/10.1016/J.CLINBIOMECH.2019.06.004.

[506] I. Fleps, W.S. Enns-Bray, P. Guy, S.J. Ferguson, P.A. Cripton, B. Helgason, On the internal reaction forces, energy absorption, and fracture in the hip during simulated sideways fall impact, PLoS One. 13 (2018) e0200952. https://doi.org/10.1371/journal.pone.0200952.

[507] P. Varga, J. Schwiedrzik, P.K. Zysset, L. Fliri-Hofmann, D. Widmer, B. Gueorguiev, M. Blauth, M. Windolf, Nonlinear quasi-static finite element simulations predict in vitro strength of human proximal femora assessed in a dynamic sideways fall setup, J. Mech. Behav. Biomed. Mater. 57 (2016) 116–127. https://doi.org/10.1016/j.jmbbm.2015.11.026.

[508] Z. Yosibash, R. Padan, L. Joskowicz, C. Milgrom, A CT-based high-order finite element analysis of the human proximal femur compared to in-vitro experiments, J. Biomech. Eng. 129 (2007) 297–309. https://doi.org/10.1115/1.2720906.

[509] L. Duchemin, D. Mitton, E. Jolivet, V. Bousson, J.D. Laredo, W. Skalli, An anatomical subject-specific FE-model for hip fracture load prediction, Comput. Methods Biomech. Biomed. Engin. 11 (2008) 105–111. https://doi.org/10.1080/10255840701535965.

[510] M. Mirzaei, M. Keshavarzian, V. Naeini, Analysis of strength and failure pattern of human proximal femur using quantitative computed tomography (QCT)-based finite element method, Bone. 64 (2014) 108–114. https://doi.org/10.1016/j.bone.2014.04.007.

[511] H. Liebl, E.G. Garcia, F. Holzner, P.B. Noel, R. Burgkart, E.J. Rummeny, T. Baum, J.S. Bauer, In-vivo assessment of femoral bone strength using finite element analysis (FEA) based on routine MDCT imaging: A preliminary study on patients with vertebral fractures, PLoS One. 10 (2015) e0116907. https://doi.org/10.1371/journal.pone.0116907.

[512] D.D. Cody, F.J. Hou, G.W. Divine, D.P. Fyhrie, Femoral structure and stiffness in patients with femoral neck fracture, J. Orthop. Res. 18 (2000) 443–448. https://doi.org/10.1002/jor.1100180317.

[513] W.S. Enns-Bray, H. Bahaloo, I. Fleps, O. Ariza, S. Gilchrist, R. Widmer, P. Guy, H. Pálsson, S.J. Ferguson, P.A. Cripton, B. Helgason, Material mapping strategy to improve the predicted response of the proximal femur to a sideways fall impact, J. Mech. Behav. Biomed. Mater. 78 (2018) 196–205. https://doi.org/10.1016/J.JMBBM.2017.10.033.

[514] E. Schileo, E. Dall'Ara, F. Taddei, A. Malandrino, T. Schotkamp, M. Baleani, M. Viceconti, An accurate estimation of bone density improves the accuracy of subject-specific finite element models, J. Biomech. 41 (2008) 2483–2491. https://doi.org/10.1016/j.jbiomech.2008.05.017.

[515] F. Taddei, A. Pancanti, M. Viceconti, An improved method for the automatic mapping of computed tomography numbers onto finite element models, Med. Eng. Phys. 26 (2004) 61–69. https://doi.org/10.1016/S1350-4533(03)00138-3.

[516] E. Schileo, F. Taddei, A. Malandrino, L. Cristofolini, M. Viceconti, Subject-specific finite element models can accurately predict strain levels in long bones, J. Biomech. 40 (2007) 2982–2989. https://doi.org/10.1016/j.jbiomech.2007.02.010.

[517] F. Taddei, E. Schileo, B. Helgason, L. Cristofolini, M. Viceconti, The material mapping strategy influences the accuracy of CT-based finite element models of bones: An evaluation against experimental measurements, Med. Eng. Phys. 29 (2007) 973–979. https://doi.org/10.1016/j.medengphy.2006.10.014.

[518] W.A. Kalender, A phantom for standardization and quality control in spinal bone mineral measurements by QCT and DXA: design considerations and specifications, Med. Phys. 19 (1992) 583–586. https://doi.org/10.1118/1.596899.

[519] F. Taddei, C. Falcinelli, L. Balistreri, P. Henys, F. Baruffaldi, S. Sigurdsson, V. Gudnason, T.B. Harris, R. Dietzel, G. Armbrecht, S. Boutroy, E. Schileo, Left-right differences in the proximal femur's strength of post-menopausal women: a multicentric finite element study, Osteoporos. Int. 27 (2016) 1519–1528. https://doi.org/10.1007/s00198-015-3404-7.

[520] C. Zannoni, R. Mantovani, M. Viceconti, Material properties assignment to finite element models of bone structures: a new method, Med. Eng. Phys. 20 (1999) 735–740. https://doi.org/10.1016/S1350-4533(98)00081-2.

[521] E. Schileo, J. Pitocchi, C. Falcinelli, F. Taddei, Cortical bone mapping improves finite element strain prediction accuracy at the proximal femur, Bone. 136 (2020) 115348. https://doi.org/10.1016/J.BONE.2020.115348.

[522] F. Taddei, I. Palmadori, W.R. Taylor, M.O. Heller, B. Bordini, A. Toni, E. Schileo, European Society of Biomechanics S.M. Perren Award 2014: Safety factor of the proximal femur during gait: A population-based finite element study, J. Biomech. 47 (2014) 3433–3440. https://doi.org/10.1016/j.jbiomech.2014.08.030.

[523] J.H. Keyak, Improved prediction of proximal femoral fracture load using nonlinear finite element models, Med. Eng. Phys. 23 (2001) 165–173. https://doi.org/10.1016/S1350-4533(01)00045-5.

[524] J.H. Keyak, T.F. Lang, Finite element modeling of proximal femoral load capacity under fall loading, Trans Orthop Res Soc. 37 (2012) 189.

[525] E. Dall'Ara, B. Luisier, R. Schmidt, F. Kainberger, P. Zysset, D. Pahr, A nonlinear QCT-based finite element model validation study for the human femur tested in two configurations in vitro, Bone. 52 (2013) 27–38. https://doi.org/10.1016/j.bone.2012.09.006.

[526] O. Ariza, S. Gilchrist, R.P. Widmer, P. Guy, S.J. Ferguson, P.A. Cripton, B. Helgason, Comparison of explicit finite element and mechanical simulation of the proximal femur during dynamic drop-tower testing, J. Biomech. 48 (2015) 224–232. https://doi.org/10.1016/j.jbiomech.2014.11.042.

[527] J.H. Keyak, S.A. Rossi, Prediction of femoral fracture load using finite element models: An examination of stress- and strain-based failure theories, J. Biomech. 33 (2000) 209–214. https://doi.org/10.1016/S0021-9290(99)00152-9.

[528] J.H. Keyak, S. Sigurdsson, G.S. Karlsdottir, D. Oskarsdottir, A. Sigmarsdottir, J. Kornak, T.B. Harris, G. Sigurdsson, B.Y. Jonsson, K. Siggeirsdottir, G. Eiriksdottir, V. Gudnason, T.F. Lang, Effect of finite element model loading condition on fracture risk assessment in men and women: The AGES-Reykjavik study, Bone. 57 (2013) 18–29. https://doi.org/10.1016/j.bone.2013.07.028.

[529] B.J. Roberts, D. Kopperdahl, E. Thrall, J.A. Muller, T.M. Keaveny, M.L. Bouxsein, Prediction of femoral strength in a sideways fall configuration using QCT-based finite element analysis, Bone. 44 (2009) S72. https://doi.org/10.1016/j.bone.2009.01.158.

[530] D.C. Drucker, W. Prager, SOIL MECHANICS AND PLASTIC ANALYSIS OR LIMIT DESIGN, Q Appl Math. 10 (1952) 157–165.

[531] G.C. Reilly, J.D. Currey, The development of microcracking and failure in bone depends on the loading mode to which it is adapted, J. Exp. Biol. 202 (1999) 543–552. https://doi.org/10.1242/JEB.202.5.543.

[532] R.K. Nalla, J.H. Kinney, R.O. Ritchie, Mechanistic fracture criteria for the failure of human cortical bone, Nat. Mater. 2 (2003) 164–168. https://doi.org/10.1038/NMAT832.

[533] D. Taylor, How does bone break?, Nat. Mater. 2 (2003) 133–134. https://doi.org/10.1038/nmat843.

[534] W.C.W. Chang, T.M. Christensen, T.P. Pinilla, T.M. Keaveny, Uniaxial yield strains for bovine trabecular bone are isotropic and asymmetric, J. Orthop. Res. 17 (1999) 582–585. https://doi.org/10.1002/JOR.1100170418.

[535] S.C. Cowin, Q.C. He, Tensile and compressive stress yield criteria for cancellous bone, J. Biomech. 38 (2005) 141–144. https://doi.org/10.1016/J.JBIOMECH.2004.03.003.

[536] J.D. Currey, Tensile yield in compact bone is determined by strain, post-yield behaviour by mineral content, J. Biomech. 37 (2004) 549–556. https://doi.org/10.1016/J.JBIOMECH.2003.08.008.

[537] D.L. Kopperdahl, T.M. Keaveny, Yield strain behavior of trabecular bone, J. Biomech. 31 (1998) 601–608. https://doi.org/10.1016/S0021-9290(98)00057-8.

[538] C.M. Ford, T.M. Keaveny, The dependence of shear failure properties of trabecular bone on apparent density and trabecular orientation, J. Biomech. 29 (1996) 1309–1317. https://doi.org/10.1016/0021-9290(96)00062-0.

[539] G. Bevill, F. Farhamand, T.M. Keaveny, Heterogeneity of yield strain in low-density versus high-density human trabecular bone, J. Biomech. 42 (2009) 2165–2170. https://doi.org/10.1016/J.JBIOMECH.2009.05.023.

[540] H.H. Bayraktar, A. Gupta, R.Y. Kwon, P. Papadopoulos, T.M. Keaveny, The modified super-ellipsoid yield criterion for human trabecular bone, J. Biomech. Eng. 126 (2004) 677–684. https://doi.org/10.1115/1.1763177.

[541] J.E.M. Koivumäki, J. Thevenot, P. Pulkkinen, V. Kuhn, T.M. Link, F. Eckstein, T. Jämsä, Cortical bone finite element models in the estimation of experimentally measured failure loads in the proximal femur, Bone. 51 (2012) 737–740. https://doi.org/10.1016/j.bone.2012.06.026.

[542] T. Rossman, V. Kushvaha, D. Dragomir-Daescu, QCT/FEA predictions of femoral stiffness are strongly affected by boundary condition modeling, Comput. Methods Biomech. Biomed. Engin. 19 (2016) 208–216. https://doi.org/10.1080/10255842.2015.1006209.

[543] A.C. Courtney, E.F. Wachtel, E.R. Myers, W.C. Hayes, Effects of loading rate on strength of the proximal femur, Calcif. Tissue Int. 55 (1994) 53–58. https://doi.org/10.1007/BF00310169.

[544] A.C. Courtney, E.F. Wachtel, E.R. Myers, W.C. Hayes, Age-related reductions in the strength of the femur tested in a fall-loading configuration, J. Bone Joint Surg. Am. 77 (1995) 387–395. https://doi.org/10.2106/00004623-199503000-00008.

[545] P. Bhattacharya, Z. Altai, M. Qasim, M. Viceconti, A multiscale model to predict current absolute risk of femoral fracture in a postmenopausal population, Biomech. Model. Mechanobiol. 18 (2019) 301–318. https://doi.org/10.1007/S10237-018-1081-0.

[546] N. Wakao, A. Harada, Y. Matsui, M. Takemura, H. Shimokata, M. Mizuno, M. Ito, Y. Matsuyama, N. Ishiguro, The effect of impact direction on the fracture load of osteoporotic proximal femurs, Med. Eng. Phys. 31 (2009) 1134–1139. https://doi.org/10.1016/j.medengphy.2009.07.010.

[547] K.K. Nishiyama, M. Ito, A. Harada, S.K. Boyd, Classification of women with and without hip fracture based on quantitative computed tomography and finite element analysis, Osteoporos. Int. 25 (2014) 619–626. https://doi.org/10.1007/s00198-013-2459-6.

[548] J.H. Keyak, H.B. Skinner, J.A. Fleming, Effect of force direction on femoral fracture load for two types of loading conditions, J. Orthop. Res. 19 (2001) 539–544. https://doi.org/10.1016/S0736-0266(00)00046-2.

[549] S. Backman, The proximal end of the femur: investigations with special reference to the etiology of femoral neck fractures; anatomical studies; roentgen projections; theoretical stress calculations; experimental production of fractures, Acta Radiol Suppl. 146 (1957) 1–166.

[550] R.C. Hibbeler, Engineering mechanics. Statics, Fourteenth edition in SI units / SI conversion by Kai Beng Yap., Global edition., Pearson, Hoboken, 2017.

[551] R.C. Hibbeler, Engineering Mechanics: Dynamics, 13th ed. edition, Prentice Hall, Upper Saddle River, NJ, 2012.

[552] D.B. Burr, C. Milgrom, D. Fyhrie, M. Forwood, M. Nyska, A. Finestone, S. Hoshaw, E. Saiag, A. Simkin, In vivo measurement of human tibial strains during vigorous activity, Bone. 18 (1996) 405–410. https://doi.org/10.1016/8756-3282(96)00028-2.

[553] L.E. Lanyon, W.G. Hampson, A.E. Goodship, J.S. Shah, Bone deformation recorded in vivo from strain gauges attached to the human tibial shaft, Acta Orthop. Scand. 46 (1975) 256–268. https://doi.org/10.3109/17453677508989216.

[554] C.T. Rubin, L.E. Lanyon, Limb Mechanics as A Function of Speed and Gait: A Study of Functional Strains in the Radius and Tibia of Horse and Dog, J. Exp. Biol. 101 (1982) 187–211. https://doi.org/10.1242/jeb.101.1.187.

[555] F. Jazinizadeh, H. Mohammadi, C.E. Quenneville, Comparing the fracture limits of the proximal femur under impact and quasi-static conditions in simulation of a sideways fall, J. Mech. Behav. Biomed. Mater. 103 (2020) 103593. https://doi.org/10.1016/J.JMBBM.2019.103593.

[556] H. Bahaloo, W.S. Enns-Bray, I. Fleps, O. Ariza, S. Gilchrist, R.W. Soyka, P. Guy, H. Palsson, S.J. Ferguson, P.A. Cripton, B. Helgason, On the Failure Initiation in the Proximal Human Femur Under Simulated Sideways Fall, Ann. Biomed. Eng. 46 (2018) 270–283. https://doi.org/10.1007/s10439-017-1952-z.

[557] W.S. Enns-Bray, H. Bahaloo, I. Fleps, Y. Pauchard, E. Taghizadeh, S. Sigurdsson, T. Aspelund, P. Büchler, T. Harris, V. Gudnason, S.J. Ferguson, H. Pálsson, B. Helgason, Biofidelic finite element models for accurately classifying hip fracture in a retrospective clinical study of elderly women from the AGES Reykjavik cohort, Bone. 120 (2019) 25–37. https://doi.org/10.1016/J.BONE.2018.09.014.

[558] S. Askarinejad, J.E. Johnson, N. Rahbar, K.L. Troy, Effects of loading rate on the of mechanical behavior of the femur in falling condition, J. Mech. Behav. Biomed. Mater. 96 (2019) 269–278. https://doi.org/10.1016/j.jmbbm.2019.04.038.

[559] D.C. Wirtz, T. Pandorf, F. Portheine, K. Radermacher, N. Schiffers, A. Prescher, D. Weichert, F.U. Niethard, Concept and development of an orthotropic FE model of the proximal femur, J. Biomech. 36 (2003) 289–293. https://doi.org/10.1016/S0021-9290(02)00309-3.

[560] W.S. Enns-Bray, J.S. Owoc, K.K. Nishiyama, S.K. Boyd, Mapping anisotropy of the proximal femur for enhanced image based finite element analysis, J. Biomech. 47 (2014) 3272–3278. https://doi.org/10.1016/J.JBIOMECH.2014.08.020.

[561] W.S. Enns-Bray, O. Ariza, S. Gilchrist, R.P. Widmer Soyka, P.J. Vogt, H. Palsson, S.K. Boyd, P. Guy, P.A. Cripton, S.J. Ferguson, B. Helgason, Morphology based anisotropic finite element models of the proximal femur validated with experimental data, Med. Eng. Phys. 38 (2016) 1339–1347. https://doi.org/10.1016/J.MEDENGPHY.2016.08.010.

[562] J. Panyasantisuk, E. Dall'Ara, M. Pretterklieber, D.H. Pahr, P. Zysset, Mapping anisotropy improves QCT-based finite element estimation of hip strength in pooled stance and side-fall load configurations, Med. Eng. Phys. 59 (2018) 36–42. https://doi.org/10.1016/J.MEDENGPHY.2018.06.004.

[563] B. Luisier, E. Dall'Ara, D.H. Pahr, Orthotropic HR-pQCT-based FE models improve strength predictions for stance but not for side-way fall loading compared to isotropic QCT-based FE models of human femurs, J. Mech. Behav. Biomed. Mater. 32 (2014) 287–299. https://doi.org/10.1016/J.JMBBM.2014.01.006.

[564] J. Hazrati Marangalou, K. Ito, B. van Rietbergen, A new approach to determine the accuracy of morphology-elasticity relationships in continuum FE analyses of human proximal femur, J. Biomech. 45 (2012) 2884–2892. https://doi.org/10.1016/j.jbiomech.2012.08.022.

[565] S.C. Cowin, The relationship between the elasticity tensor and the fabric tensor, Mech. Mater. 4 (1985) 137–147. https://doi.org/10.1016/0167-6636(85)90012-2.

[566] T.F. Lang, S. Sigurdsson, G. Karlsdottir, D. Oskarsdottir, A. Sigmarsdottir, J. Chengshi, J. Kornak, T.B. Harris, G. Sigurdsson, B.Y. Jonsson, K. Siggeirsdottir, G. Eiriksdottir, V. Gudnason, J.H. Keyak, Age-related loss of proximal femoral strength in elderly men and women: The Age Gene/Environment Susceptibility Study - Reykjavik, Bone. 50 (2012) 743–748. https://doi.org/10.1016/j.bone.2011.12.001.

[567] T.M. Keaveny, D. Kopperdahl, L. Melton, P. Hoffmann, S. Amin, B. Riggs, S. Khosla, Age-Dependence of Femoral Strength in White Women and Men, J. Bone Miner. Res. 25 (2010) 994–1001. https://doi.org/10.1359/jbmr.091033.

[568] J.H. Keyak, T.S. Kaneko, S. Khosla, S. Amin, E.J. Atkinson, T.F. Lang, J.D. Sibonga, Hip load capacity and yield load in men and women of all ages, Bone. 137 (2020) 115321. https://doi.org/10.1016/j.bone.2020.115321.

[569] J.H. Keyak, S. Sigurdsson, G. Karlsdottir, D. Oskarsdottir, A. Sigmarsdottir, S. Zhao, J. Kornak, T.B. Harris, G. Sigurdsson, B.Y. Jonsson, K. Siggeirsdottir, G. Eiriksdottir, V. Gudnason, T.F. Lang, Male-female differences in the association between incident hip fracture and proximal femoral strength: A finite element analysis study, Bone. 48 (2011) 1239–1245. https://doi.org/10.1016/j.bone.2011.03.682.

[570] M. Viceconti, M. Qasim, P. Bhattacharya, X. Li, Are CT-Based Finite Element Model Predictions of Femoral Bone Strength Clinically Useful?, Curr. Osteoporos. Rep. 16 (2018) 216–223. https://doi.org/10.1007/S11914-018-0438-8.

[571] C.M. Langton, S. Pisharody, J.H. Keyak, Comparison of 3D finite element analysis derived stiffness and BMD to determine the failure load of the excised proximal femur, Med. Eng. Phys. 31 (2009) 668–672. https://doi.org/10.1016/J.MEDENGPHY.2008.12.007.

[572] J. Kok, L. Grassi, A. Gustafsson, H. Isaksson, Femoral strength and strains in sideways fall: Validation of finite element models against bilateral strain measurements, J. Biomech. 122 (2021) 110445. https://doi.org/10.1016/J.JBIOMECH.2021.110445.

[573] K.C. Lian, T.F. Lang, J.H. Keyak, G.W. Modin, Q. Rehman, L. Do, N.E. Lane, Differences in hip quantitative computed tomography (QCT) measurements of bone mineral density and bone strength between glucocorticoid-treated and glucocorticoid-naïve postmenopausal women, Osteoporos. Int. 16 (2005) 642–650. https://doi.org/10.1007/s00198-004-1736-9.

[574] T.M. Keaveny, M.R. McClung, H.K. Genant, J.R. Zanchetta, D. Kendler, J.P. Brown, S. Goemaere, C. Recknor, M.L. Brandi, R. Eastell, D.L. Kopperdahl, K. Engelke, T. Fuerst, H.-S. Radcliffe, C. Libanati, Femoral and Vertebral Strength Improvements

in Postmenopausal Women With Osteoporosis Treated With Denosumab, J. Bone Miner. Res. 29 (2014) 158–165. https://doi.org/10.1002/jbmr.2024.

[575] R. Zebaze, C. Libanati, M.R. McClung, J.R. Zanchetta, D.L. Kendler, A. Høiseth, A. Wang, A. Ghasem-Zadeh, E. Seeman, Denosumab Reduces Cortical Porosity of the Proximal Femoral Shaft in Postmenopausal Women With Osteoporosis, J. Bone Miner. Res. 31 (2016) 1827–1834. https://doi.org/10.1002/jbmr.2855.

[576] T.M. Keaveny, P.F. Hoffmann, M. Singh, L. Palermo, J.P. Bilezikian, S.L. Greenspan, D.M. Black, Femoral bone strength and its relation to cortical and trabecular changes after treatment with PTH, alendronate, and their combination as assessed by finite element analysis of quantitative CT scans., J. Bone Miner. Res. 23 (2008) 1974–1982. https://doi.org/10.1359/jbmr.080805.

[577] J.H. Keyak, A.K. Koyama, A. LeBlanc, Y. Lu, T.F. Lang, Reduction in proximal femoral strength due to long-duration spaceflight, Bone. 44 (2009) 449–453. https://doi.org/10.1016/j.bone.2008.11.014.

[578] A.S. Michalski, S. Amin, A.M. Cheung, D.D. Cody, J.H. Keyak, T.F. Lang, D.P. Nicolella, E.S. Orwoll, S.K. Boyd, J.D. Sibonga, Hip load capacity cut-points for Astronaut Skeletal Health NASA Finite Element Strength Task Group Recommendations, NPJ Microgravity. 5 (2019) 6. https://doi.org/10.1038/S41526-019-0066-3.

[579] J. Sibonga, T. Matsumoto, J. Jones, J. Shapiro, T. Lang, L. Shackelford, S.M. Smith, M. Young, J.H. Keyak, K. Kohri, H. Ohshima, E. Spector, A. LeBlanc, Resistive exercise in astronauts on prolonged spaceflights provides partial protection against spaceflight-induced bone loss, Bone. 128 (2019) 112037. https://doi.org/10.1016/J.BONE.2019.07.013.

[580] F. Johannesdottir, B. Allaire, M.L. Bouxsein, Fracture Prediction by Computed Tomography and Finite Element Analysis: Current and Future Perspectives, Curr. Osteoporos. Rep. 16 (2018) 411–422. https://doi.org/10.1007/s11914-018-0450-z.

[581] J. Carballido-Gamio, D.P. Nicolella, Computational anatomy in the study of bone structure, Curr. Osteoporos. Rep. 11 (2013) 237–245. https://doi.org/10.1007/S11914-013-0148-1.

[582] G.M. Treece, A.H. Gee, C. Tonkin, S.K. Ewing, P.M. Cawthon, D.M. Black, K.E. Poole, Predicting Hip Fracture Type With Cortical Bone Mapping (CBM) in the Osteoporotic Fractures in Men (MrOS) Study, J. Bone Miner. Res. 30 (2015) 2067–2077. https://doi.org/10.1002/jbmr.2552.

[583] G.M. Treece, A.H. Gee, P.M. Mayhew, K.E.S. Poole, High resolution cortical bone thickness measurement from clinical CT data, Med. Image Anal. 14 (2010) 276–290. https://doi.org/10.1016/J.MEDIA.2010.01.003.

[584] G.M. Treece, K.E.S. Poole, A.H. Gee, Imaging the femoral cortex: Thickness, density and mass from clinical CT, Med. Image Anal. 16 (2012) 952–965. https://doi.org/10.1016/J.MEDIA.2012.02.008.

[585] G.M. Treece, A.H. Gee, Independent measurement of femoral cortical thickness and cortical bone density using clinical CT, Med. Image Anal. 20 (2015) 249–264. https://doi.org/10.1016/J.MEDIA.2014.11.012.

[586] K.E.S. Poole, G.M. Treece, P.M. Mayhew, J. Vaculík, P. Dungl, M. Horák, J.J. Štěpán, A.H. Gee, Cortical Thickness Mapping to Identify Focal Osteoporosis in Patients with Hip Fracture, PLoS One. 7 (2012) e38466. https://doi.org/10.1371/JOURNAL.PONE.0038466.

[587] K.E.S. Poole, L. Skingle, A.H. Gee, T.D. Turmezei, F. Johannesdottir, K. Blesic, C. Rose, M. Vindlacheruvu, S. Donell, J. Vaculik, P. Dungl, M. Horak, J.J. Stepan, J. Reeve, G.M. Treece, Focal osteoporosis defects play a key role in hip fracture, Bone. 94 (2017) 124–134. https://doi.org/10.1016/j.bone.2016.10.020.

[588] J. Ashburner, K.J. Friston, Voxel-based morphometry - the methods, NeuroImage. 11 (2000) 805–821. https://doi.org/10.1006/NIMG.2000.0582.

[589] J. Carballido-Gamio, S. Bonaretti, I. Saeed, R. Harnish, R. Recker, A.J. Burghardt, J.H. Keyak, T. Harris, S. Khosla, T.F. Lang, Automatic multi-parametric quantification of the proximal femur with quantitative computed tomography, Quant. Imaging Med. Surg. 5 (2015) 552–568. https://doi.org/10.3978/J.ISSN.2223-4292.2015.08.02.

[590] A. Yu, J. Carballido-Gamio, L. Wang, T.F. Lang, Y. Su, X. Wu, M. Wang, J. Wei, C. Yi, X. Cheng, Spatial Differences in the Distribution of Bone Between Femoral Neck and Trochanteric Fractures, J. Bone Miner. Res. 32 (2017) 1672–1680. https://doi.org/10.1002/jbmr.3150.

[591] C. Davatzikos, M. Vaillant, S.M. Resnick, J.L. Prince, S. Letovsky, R.N. Bryan, A computerized approach for morphological analysis of the corpus callosum, J. Comput. Assist. Tomogr. 20 (1996) 88–97. https://doi.org/10.1097/00004728-199601000-00017.

[592] E.A. Marques, J. Carballido-Gamio, V. Gudnason, G. Sigurdsson, S. Sigurdsson, T. Aspelund, K. Siggeirsdottir, L. Launer, G. Eiriksdottir, T. Lang, T.B. Harris, Sex differences in the spatial distribution of bone in relation to incident hip fracture: Findings from the AGES-Reykjavik study, Bone. 114 (2018) 72–80. https://doi.org/10.1016/J.BONE.2018.05.016.

[593] P.A. Yushkevich, J. Piven, H.C. Hazlett, R.G. Smith, S. Ho, J.C. Gee, G. Gerig, User-guided 3D active contour segmentation of anatomical structures: Significantly improved efficiency and reliability, NeuroImage. 31 (2006) 1116–1128. https://doi.org/10.1016/j.neuroimage.2006.01.015.

[594] D.D. Cody, F.J. Hou, G.W. Divine, D.P. Fyhrie, Short Term In Vivo Precision of Proximal Femoral Finite Element Modeling, Ann. Biomed. Eng. 28 (2000) 408–14. https://doi.org/10.1114/1.278.

[595] C.S. Rajapakse, A. Hotca, B.T. Newman, A. Ramme, S. Vira, E.A. Kobe, R. Miller, S. Honig, G. Chang, Patient-specific Hip Fracture Strength Assessment with Microstructural MR Imaging-based Finite Element Modeling, Radiology. 283 (2017) 854–861. https://doi.org/10.1148/RADIOL.2016160874.

[596] G. Taubin, Curve and surface smoothing without shrinkage, in: Proc. IEEE Int. Conf. Comput. Vis., IEEE Computer Society, Cambridge, MA, USA, 1995: pp. 852–857. https://doi.org/10.1109/ICCV.1995.466848.

[597] A.D. Sylvester, P.A. Kramer, Young's Modulus and Load Complexity: Modeling Their Effects on Proximal Femur Strain, Anat. Rec. 301 (2018) 1189–1202. https://doi.org/10.1002/AR.23796.

[598] L. Cristofolini, G. Conti, M. Juszczyk, S. Cremonini, S. Van Sint Jan, M. Viceconti, Structural behaviour and strain distribution of the long bones of the human lower limbs, J. Biomech. 43 (2010) 826–835. https://doi.org/10.1016/J.JBIOMECH.2009.11.022.

[599] S.L. Manske, T. Liu-Ambrose, D.M. Cooper, S. Kontulainen, P. Guy, B.B. Forster, H.A. McKay, Cortical and trabecular bone in the femoral neck both contribute to proximal femur failure load prediction, Osteoporos. Int. 20 (2009) 445–453. https://doi.org/10.1007/s00198-008-0675-2.

[600] N. Narra, Multiscale Geometric Methods for Isolating Exercise Induced Morphological Adaptations in the Proximal Femur, Tampere University of Technology, 2018. https://trepo.tuni.fi/handle/10024/114757 (accessed July 4, 2022).

[601] W. Zeng, D. Samaras, D. Gu, Ricci flow for 3D shape analysis, IEEE Trans. Pattern Anal. Mach. Intell. 32 (2010) 662–677. https://doi.org/10.1109/TPAMI.2009.201.

[602] M. Fornefett, K. Rohr, H.S. Stiehl, Radial basis functions with compact support for elastic registration of medical images, Image Vis. Comput. 19 (2001) 87–96. https://doi.org/10.1016/S0262-8856(00)00057-3.

[603] K.J. Worsley, J.E. Taylor, F. Tomaiuolo, J. Lerch, Unified univariate and multivariate random field theory, NeuroImage. 23 (2004) S189–S195. https://doi.org/10.1016/J.NEUROIMAGE.2004.07.026.

[604] A.H. Gee, G.M. Treece, Systematic misregistration and the statistical analysis of surface data, Med. Image Anal. 18 (2014) 385–393. https://doi.org/10.1016/J.MEDIA.2013.12.007.

[605] S.B. Heymsfield, P. Hwaung, F. Ferreyro-Bravo, M. Heo, D.M. Thomas, J.M. Schuna Jr, Scaling of adult human bone and skeletal muscle mass to height in the US population, Am. J. Hum. Biol. 31 (2019) e23252. https://doi.org/10.1002/ajhb.23252.

[606] U.T. Iwaniec, R.T. Turner, Influence of body weight on bone mass, architecture and turnover, J. Endocrinol. 230 (2016) R115–R130. https://doi.org/10.1530/JOE-16-0089.

[607] A.M. Nevill, R.L. Holder, N. Maffulli, J.C.Y. Cheng, S.S.S.F. Leung, W.T.K. Lee, J.T.F. Lau, Adjusting Bone Mass for Differences in Projected Bone Area and Other Confounding Variables: An Allometric Perspective, J. Bone Miner. Res. 17 (2002) 703–708. https://doi.org/10.1359/jbmr.2002.17.4.703.

[608] C.B. Ruff, Body size, body shape, and long bone strength in modern humans, J. Hum. Evol. 38 (2000) 269–290. https://doi.org/10.1006/jhev.1999.0322.

[609] L.T. Ho-Pham, U.D.T. Nguyen, T.V. Nguyen, Association between lean mass, fat mass, and bone mineral density: a meta-analysis, J. Clin. Endocrinol. Metab. 99 (2014) 30–38. https://doi.org/10.1210/jc.2014-v99i12-30A.

[610] W.D. Leslie, E.S. Orwoll, C.M. Nielson, S.N. Morin, S.R. Majumdar, H. Johansson, A. Odén, E.V. McCloskey, J.A. Kanis, Estimated Lean Mass and Fat Mass Differentially Affect Femoral Bone Density and Strength Index but Are Not FRAX Independent Risk Factors for Fracture, J. Bone Miner. Res. 29 (2014) 2511–2519. https://doi.org/10.1002/jbmr.2280.

[611] R. Bryan, P.B. Nair, M. Taylor, Use of a statistical model of the whole femur in a large scale, multi-model study of femoral neck fracture risk, J. Biomech. 42 (2009) 2171–2176. https://doi.org/10.1016/j.jbiomech.2009.05.038.

[612] N. Narra, R. Nikander, J. Viik, J. Hyttinen, H. Sievänen, Femoral neck cross-sectional geometry and exercise loading, Clin. Physiol. Funct. Imaging. 33 (2013) 258–266. https://doi.org/10.1111/cpf.12022.

[613] H. Sievänen, L. Józsa, I. Pap, M. Järvinen, T.A. Järvinen, P. Kannus, T.L. Järvinen, Fragile External Phenotype of Modern Human Proximal Femur in Comparison With Medieval Bone, J. Bone Miner. Res. 22 (2007) 537–543. https://doi.org/10.1359/jbmr.070102.

[614] M.R. Ramey, K.R. Williams, Ground Reaction Forces in the Triple Jump, Int. J. Sports Biomech. 1 (1985) 233–239. https://doi.org/10.1123/ijsb.1.3.233.

[615] N. Smith, R. Dyson, L. Janaway, Ground reaction force measures when running in soccer boots and soccer training shoes on a natural turf surface, Sports Eng. 7 (2004) 159–167. https://doi.org/10.1007/BF02844054.

[616] M.K. Dayakidis, K. Boudolos, Ground reaction force data in functional ankle instability during two cutting movements, Clin. Biomech. 21 (2006) 405–411. https://doi.org/10.1016/j.clinbiomech.2005.11.010.

[617] K. Ball, Loading and performance of the support leg in kicking, J. Sci. Med. Sport. 16 (2013) 455–459. https://doi.org/10.1016/j.jsams.2012.10.008.

[618] P.A. Swinton, R. Lloyd, J.W. Keogh, I. Agouris, A.D. Stewart, A biomechanical comparison of the traditional squat, powerlifting squat, and box squat, J. Strength Cond. Res. 26 (2012) 1805–1816. https://doi.org/10.1519/JSC.0b013e3182577067.

[619] P.R. Cavanagh, M.A. Lafortune, Ground reaction forces in distance running, J. Biomech. 13 (1980) 397–406. https://doi.org/10.1016/0021-9290(80)90033-0.

[620] B. Kluitenberg, S.W. Bredeweg, S. Zijlstra, W. Zijlstra, I. Buist, Comparison of vertical ground reaction forces during overground and treadmill running. A validation study, BMC Musculoskelet. Disord. 13 (2012) 235. https://doi.org/10.1186/1471-2474-13-235.

[621] S. Logan, I. Hunter, J.T. Hopkins, J.B. Feland, A.C. Parcell, Ground reaction force differences between running shoes, racing flats, and distance spikes in runners, J. Sports Sci. Med. 9 (2010) 147–153.

[622] C.F. Munro, D.I. Miller, A.J. Fuglevand, Ground reaction forces in running: A reexamination, J. Biomech. 20 (1987) 147–155. https://doi.org/10.1016/0021-9290(87)90306-X.

[623] R. Tominaga, Y. Ishii, T. Ueda, T. Kurokawa, The Effects of Running Speed on Ground Reaction Forces and Lower Limb Kinematics During Single-Leg Stop Movement, J. Strength Cond. Res. 30 (2016) 1224–1230. https://doi.org/10.1519/JSC.0000000000000286.

[624] L. Yu, Q. Mei, L. Xiang, W. Liu, N.I. Mohamad, B. István, J. Fernandez, Y. Gu, Principal Component Analysis of the Running Ground Reaction Forces With Different Speeds, Front. Bioeng. Biotechnol. 9 (2021) 629809. https://doi.org/10.3389/fbioe.2021.629809.

[625] A.D. Lyttle, B.A. Blanksby, B.C. Elliott, D.G. Lloyd, Investigating Kinetics in the Freestyle Flip Turn Push-Off, J. Appl. Biomech. 15 (1999) 242–252. https://doi.org/10.1123/jab.15.3.242.

[626] B.A. Blanksby, D.G. Gathercole, R.N. Marshall, Force plate and video analysis of the tumble turn by age-group swimmers, J. Swim. Res. 11 (1996) 40–45.

[627] T.M. Skerry, One mechanostat or many? Modifications of the site-specific response of bone to mechanical loading by nature and nurture, J Musculoskelet Neuronal Interact. 6 (2006) 122–127.

[628] P. Comfort, M. Allen, P. Graham-Smith, Comparisons of peak ground reaction force and rate of force development during variations of the power clean, J. Strength Cond. Res. 25 (2011) 1235–1239. https://doi.org/10.1519/JSC.0b013e3181d6dc0d.

[629] P. Comfort, M. Allen, P. Graham-Smith, Kinetic comparisons during variations of the power clean, J Strength Cond Res. 25 (2011) 3269–3273. https://doi.org/10.1519/JSC.0b013e3182184dea.

[630] W. Baumann, V. Gross, K. Quade, P. Galbierz, A. Schvvirtz, The Snatch Technique of World Class Weightlifiers at the 1985 World Championships, Int. J. Sport Biomech. 4 (1988) 68–89. https://doi.org/10.1123/IJSB.4.1.68

[631] M.A. Lauder, J.P. Lake, Biomechanical comparison of unilateral and bilateral power snatch lifts, J. Strength Cond. Res. 22 (2008) 653–660. https://doi.org/10.1519/JSC.0b013e3181660c89.

[632] M.E. Kersh, S. Martelli, R. Zebaze, E. Seeman, M.G. Pandy, Mechanical Loading of the Femoral Neck in Human Locomotion, J. Bone Miner. Res. 33 (2018) 1999–2006. https://doi.org/10.1002/jbmr.3529.

[633] P. Pellikaan, G. Giarmatzis, J. Vander Sloten, S. Verschueren, I. Jonkers, Ranking of osteogenic potential of physical exercises in postmenopausal women based on femoral neck strains, PLoS One. 13 (2018) e0195463. https://doi.org/10.1371/journal.pone.0195463.

[634] G. Giarmatzis, I. Jonkers, M. Wesseling, S. Van Rossom, S. Verschueren, Loading of Hip Measured by Hip Contact Forces at Different Speeds of Walking and Running, J. Bone Miner. Res. 30 (2015) 1431–1440. https://doi.org/10.1002/jbmr.2483.

[635] S. Martelli, M.E. Kersh, A.G. Schache, M.G. Pandy, Strain energy in the femoral neck during exercise, J. Biomech. 47 (2014) 1784–1791. https://doi.org/10.1016/j.jbiomech.2014.03.036.

[636] R. Huiskes, H. Weinans, H.J. Grootenboer, M. Dalstra, B. Fudala, T.J. Slooff, Adaptive bone-remodeling theory applied to prosthetic-design analysis, J. Biomech. 20 (1987) 1135–1150. https://doi.org/10.1016/0021-9290(87)90030-3.

[637] J. Kerner, R. Huiskes, G.H. van Lenthe, H. Weinans, B. van Rietbergen, C.A. Engh, A.A. Amis, Correlation between pre-operative periprosthetic bone density and post-operative bone loss in THA can be explained by strain-adaptive remodelling, J. Biomech. 32 (1999) 695–703. https://doi.org/10.1016/S0021-9290(99)00041-X.

[638] S. Martelli, B. Beck, D. Saxby, D. Lloyd, P. Pivonka, M. Taylor, Modelling Human Locomotion to Inform Exercise Prescription for Osteoporosis, Curr. Osteoporos. Rep. 18 (2020) 301–311. https://doi.org/10.1007/S11914-020-00592-5.

[639] M. Martyn-St James, S. Carroll, Meta-analysis of walking for preservation of bone mineral density in postmenopausal women, Bone. 43 (2008) 521–531. https://doi.org/10.1016/j.bone.2008.05.012.

[640] H. Sievänen, P. Kannus, Physical activity reduces the risk of fragility fracture, PLoS Med. 4 (2007) e222. https://doi.org/10.1371/journal.pmed.0040222.

[641] K. Michaëlsson, H. Olofsson, K. Jensevik, S. Larsson, H. Mallmin, L. Berglund, B. Vessby, H. Melhus, Leisure physical activity and the risk of fracture in men, PLoS Med. 4 (2007) e199. https://doi.org/10.1371/journal.pmed.0040199.

[642] E.W. Gregg, M.A. Pereira, C.J. Caspersen, Physical activity, falls, and fractures among older adults: A review of the epidemiologic evidence, J. Am. Geriatr. Soc. 48 (2000) 883–893. https://doi.org/10.1111/j.1532-5415.2000.tb06884.x.

[643] A. Moayyeri, The Association Between Physical Activity and Osteoporotic Fractures: A Review of the Evidence and Implications for Future Research, Ann. Epidemiol. 18 (2008) 827–835. https://doi.org/10.1016/j.annepidem.2008.08.007.

[644] M. Karlsson, Has exercise an antifracture efficacy in women?, Scand. J. Med. Sci. Sports. 14 (2004) 2–15. https://doi.org/10.1111/j.1600-0838.2003.00322.x.

[645] R. Korpelainen, S. Keinänen-Kiukaanniemi, J. Heikkinen, K. Väänänen, J. Korpelainen, Effect of exercise on extraskeletal risk factors for hip fractures in elderly women with low BMD: A population-based randomized controlled trial, J. Bone Miner. Res. 21 (2006) 772–779. https://doi.org/10.1359/jbmr.060116.

[646] R. Korpelainen, S. Keinänen-Kiukaanniemi, P. Nieminen, J. Heikkinen, K. Väänänen, J. Korpelainen, Long-term outcomes of exercise: Follow-up of a randomized trial in older women with osteopenia, Arch. Intern. Med. 170 (2010) 1548–1556. https://doi.org/10.1001/archinternmed.2010.311.

[647] P. de Souto Barreto, Y. Rolland, B. Vellas, M. Maltais, Association of Long-term Exercise Training with Risk of Falls, Fractures, Hospitalizations, and Mortality in Older Adults: A Systematic Review and Meta-analysis, JAMA Intern. Med. 179 (2019) 394–405. https://doi.org/10.1001/jamainternmed.2018.5406.

[648] I. Hoffmann, M. Kohl, S. von Stengel, F. Jakob, K. Kerschan-Schindl, U. Lange, S. Peters, D. Schoene, C. Sieber, F. Thomasius, H.A. Bischoff-Ferrari, M. Uder, W. Kemmler, Exercise and the prevention of major osteoporotic fractures in adults: a systematic review and meta-analysis with special emphasis on intensity progression and study duration, Osteoporos. Int. 34 (2023) 15–28. https://doi.org/10.1007/s00198-022-06592-8.

[649] L.D. Gillespie, M.C. Robertson, W.J. Gillespie, C. Sherrington, S. Gates, L.M. Clemson, S.E. Lamb, Interventions for preventing falls in older people living in the community, Cochrane Database Syst. Rev. 2012 (2012) CD007146. https://doi.org/10.1002/14651858.CD007146.pub3.

[650] J.M. Guirguis-Blake, Y.L. Michael, L.A. Perdue, E.L. Coppola, T.L. Beil, Interventions to prevent falls in older adults: Updated evidence report and systematic review for the US Preventive Services Task Force, JAMA. 319 (2018) 1705–1716. https://doi.org/10.1001/jama.2017.21962.

[651] F. El-Khoury, B. Cassou, M.A. Charles, P. Dargent-Molina, The effect of fall prevention exercise programmes on fall induced injuries in community dwelling older adults: Systematic review and meta-analysis of randomised controlled trials, BMJ. 347 (2013) f6234. https://doi.org/10.1136/bmj.f6234.

[652] T. Tervo, P. Nordström, A. Nordström, Effects of badminton and ice hockey on bone mass in young males: a 12-year follow-up, Bone. 47 (2010) 666–672. https://doi.org/10.1016/J.BONE.2010.06.022.

[653] J. Kudlac, D.L. Nichols, C.F. Sanborn, N.M. DiMarco, Impact of detraining on bone loss in former collegiate female gymnasts, Calcif. Tissue Int. 75 (2004) 482–487. https://doi.org/10.1007/S00223-004-0228-4.

[654] Ö. Valdimarsson, H.G. Alborg, H. Düppe, F. Nyquist, M. Karlsson, Reduced training is associated with increased loss of BMD, J. Bone Miner. Res. 20 (2005) 906–912. https://doi.org/10.1359/JBMR.050107.

[655] M.M. Minett, L. Weidauer, H.E. Wey, T.L. Binkley, T.M. Beare, B.L. Specker, Sports Participation in High School and College Leads to High Bone Density and Greater Rates of Bone Loss in Young Men: Results from a Population-Based Study, Calcif. Tissue Int. 103 (2018) 5–15. https://doi.org/10.1007/S00223-017-0383-Z.

[656] A. Nordström, C. Karlsson, F. Nyquist, T. Olsson, P. Nordström, M. Karlsson, Bone loss and fracture risk after reduced physical activity, J. Bone Miner. Res. 20 (2005) 202–207. https://doi.org/10.1359/JBMR.041012.

[657] M.A. Strope, P. Nigh, M.I. Carter, N. Lin, J. Jiang, P.S. Hinton, Physical Activity–Associated Bone Loading During Adolescence and Young Adulthood Is Positively Associated With Adult Bone Mineral Density in Men, Am. J. Mens Health. 9 (2015) 442–450. https://doi.org/10.1177/1557988314549749.

[658] N.K. Pollock, E.M. Laing, C.M. Modlesky, P.J. O'Connor, R.D. Lewis, Former college artistic gymnasts maintain higher BMD: a nine-year follow-up, Osteoporos. Int. 17 (2006) 1691–1697. https://doi.org/10.1007/S00198-006-0181-3.

[659] M.K. Karlsson, C. Linden, C. Karlsson, O. Johnell, K. Obrant, E. Seeman, Exercise during growth and bone mineral density and fractures in old age, Lancet Lond. Engl. 355 (2000) 469–470. https://doi.org/10.1016/S0140-6736(00)82020-6.

[660] M. Tveit, B.E. Rosengren, J.A. Nilsson, M.K. Karlsson, Exercise in youth: High bone mass, large bone size, and low fracture risk in old age, Scand. J. Med. Sci. Sports. 25 (2015) 453–461. https://doi.org/10.1111/sms.12305.

[661] M. Tveit, B.E. Rosengren, J.Å. Nilsson, H.G. Ahlborg, M.K. Karlsson, Bone mass following physical activity in young years: a mean 39-year prospective controlled study in men, Osteoporos. Int. 24 (2013) 1389–1397. https://doi.org/10.1007/S00198-012-2081-Z.

[662] J.A. Kettunen, O. Impivaara, U.M. Kujala, M. Linna, J. Mäki, H. Räty, E. Alanen, J. Kaprio, T. Videman, S. Sarna, Hip fractures and femoral bone mineral density in male former elite athletes, Bone. 46 (2010) 330–335. https://doi.org/10.1016/J.BONE.2009.10.008.

[663] M. Nilsson, C. Ohlsson, A.L. Eriksson, K. Frändin, M. Karlsson, Ö. Ljunggren, D. Mellström, M. Lorentzon, Competitive physical activity early in life is associated with bone mineral density in elderly Swedish men, Osteoporos. Int. 19 (2008) 1557–1566. https://doi.org/10.1007/S00198-008-0600-8.

[664] K. Uzunca, M. Birtane, G. Durmus-Altun, F. Ustun, High bone mineral density in loaded skeletal regions of former professional football (soccer) players: what is the effect of time after active career?, Br. J. Sports Med. 39 (2005) 154–157. https://doi.org/10.1136/BJSM.2003.011494.

[665] K.M. Khan, K.L. Bennell, J.L. Hopper, L. Flicker, C.A. Nowson, A.J. Sherwin, K.J. Crichton, P.R. Harcourt, J.D. Wark, Self-reported ballet classes undertaken at age 10-12 years and hip bone mineral density in later life, Osteoporos. Int. 8 (1998) 165–173. https://doi.org/10.1007/BF02672514.

[666] M. Tveit, B.E. Rosengren, F. Nyquist, J.Å. Nilsson, M.K. Karlsson, Former male elite athletes have lower incidence of fragility fractures than expected, Med. Sci. Sports Exerc. 45 (2013) 405–410. https://doi.org/10.1249/MSS.0B013E318274FDF3.

[667] M.T. Korhonen, U.M. Kujala, J. Kettunen, O.V. Korhonen, J. Kaprio, S. Sarna, T. Törmäkangas, Longitudinal Associations of High-Volume and Vigorous-Intensity Exercise With Hip Fracture Risk in Men, J. Bone Miner. Res. 37 (2022) 1562–1570. https://doi.org/10.1002/JBMR.4624.

[668] M. Hagman, E.W. Helge, B. Fristrup, N.R. Jørgensen, J.W. Helge, P. Krustrup, High bone mineral density in lifelong trained female team handball players and young elite football players, Eur. J. Appl. Physiol. 121 (2021) 2825–2836. https://doi.org/10.1007/S00421-021-04755-9.

[669] M. Hagman, E.W. Helge, T. Hornstrup, B. Fristrup, J.J. Nielsen, N.R. Jørgensen, J.L. Andersen, J.W. Helge, P. Krustrup, Bone mineral density in lifelong trained male

football players compared with young and elderly untrained men, J. Sport Health Sci. 7 (2018) 159–168. https://doi.org/10.1016/j.jshs.2017.09.009.

[670] H.R.2262 - 114th Congress (2015-2016): U.S. Commercial Space Launch Competitiveness Act | Congress.gov | Library of Congress, n.d. https://www.congress.gov/bill/114th-congress/house-bill/2262 (accessed November 28, 2022).

[671] E. Howell, See the evolution of SpaceX rockets in pictures, Space.Com. (2022). https://www.space.com/40547-spacex-rocket-evolution.html (accessed November 28, 2022).

[672] SpaceX - Falcon 9, (n.d.). https://www.spacex.com/vehicles/falcon-9/ (accessed November 28, 2022).

[673] Peter.B. de Selding, SpaceX's reusable Falcon 9: What are the real cost savings for customers?, Spacenews.Com. (2015). https://spacenews.com/spacexs-reusable-falcon-9-what-are-the-real-cost-savings-for-customers/ (accessed November 28, 2022).

[674] J. Foust, SpaceX launches Crew Dragon on first private mission - SpaceNews, Spacenews.Com. (2021). https://spacenews.com/spacex-launches-crew-dragon-on-first-private-mission/ (accessed November 28, 2022).

[675] M. Wall, SpaceX Dragon arrives at space station with all-private Ax-1 astronaut crew, Space.Com. (2022). https://www.space.com/spacex-ax-1-private-astroanuts-space-station-docking (accessed November 28, 2022).

[676] L. Vico, B. van Rietbergen, N. Vilayphiou, M.-T. Linossier, H. Locrelle, M. Normand, M. Zouch, M. Gerbaix, N. Bonnet, V. Novikov, T. Thomas, G. Vassilieva, Cortical and Trabecular Bone Microstructure Did Not Recover at Weight-Bearing Skeletal Sites and Progressively Deteriorated at Non-Weight-Bearing Sites During the Year Following International Space Station Missions, J. Bone Miner. Res. 32 (2017) 2010–2021. https://doi.org/10.1002/jbmr.3188.

[677] S.M. Schneider, W.E. Amonette, K. Blazine, J. Bentley, S.M.C. Lee, J.A. Loehr, A.D. Moore, M. Rapley, E.R. Mulder, S.M. Smith, Training with the International Space Station Interim Resistive Exercise Device, Med. Sci. Sports Exerc. 35 (2003) 1935–1945. https://doi.org/10.1249/01.MSS.0000093611.88198.08.

[678] H. Lavelle, Human Research Program – Space Station. Crew's Wednesday Schedule Focuses on Exercise, Science, and Maintenance, NASA Space Stn. (2022). https://blogs.nasa.gov/spacestation/tag/human-research-program/ (accessed November 29, 2022).

[679] J.C. Allen, Sample Size Calculation for Two Independent Groups: A Useful Rule of Thumb, Proc. Singap. Healthc. 20 (2011) 138–140. https://doi.org/10.1177/201010581102000213.

[680] C.C. Serdar, M. Cihan, D. Yücel, M.A. Serdar, Sample size, power and effect size revisited: simplified and practical approaches in pre-clinical, clinical and laboratory studies, Biochem. Medica. 31 (2021) 010502. https://doi.org/10.11613/BM.2021.010502.

[681] A.D. Faigenbaum, G.D. Myer, Resistance training among young athletes: safety, efficacy and injury prevention effects, Br. J. Sports Med. 44 (2010) 56–63. https://doi.org/10.1136/BJSM.2009.068098.

[682] M. Lovera, J. Keogh, Anthropometric profile of powerlifters: differences as a function of bodyweight class and competitive success, J Sports Med Phys Fit. 55 (2015) 478–487.

[683] Z. Yosibash, N. Trabelsi, C. Milgrom, Reliable simulations of the human proximal femur by high-order finite element analysis validated by experimental observations, J. Biomech. 40 (2007) 3688–3699. https://doi.org/10.1016/j.jbiomech.2007.06.017.

[684] C.S. Rajapakse, A.R. Farid, D.C. Kargilis, B.C. Jones, J.S. Lee, A.J. Johncola, A.S. Batzdorf, S.S. Shetye, M.W. Hast, G. Chang, MRI-based assessment of proximal femur strength compared to mechanical testing, Bone. 133 (2020) 115227. https://doi.org/10.1016/J.BONE.2020.115227.

[685] C.M. Phan, M. Matsuura, J.S. Bauer, T.C. Dunn, D. Newitt, E.M. Lochmueller, F. Eckstein, S. Majumdar, T.M. Link, Trabecular Bone Structure of the Calcaneus: Comparison of MR Imaging at 3.0 and 1.5 T with Micro-CT as the Standard of Reference, Radiology. 239 (2006) 488–496. https://doi.org/10.1148/RADIOL.2392050574.

[686] G. Chang, S. Honig, R. Brown, C.M. Deniz, K.A. Egol, J.S. Babb, R.R. Regatte, C.S. Rajapakse, Finite Element Analysis Applied to 3-T MR Imaging of Proximal Femur Microarchitecture: Lower Bone Strength in Patients with Fragility Fractures Compared with Control Subjects, Radiology. 272 (2014) 464–474. https://doi.org/10.1148/radiol.14131926.

[687] K. Chiba, A.J. Burghardt, M. Osaki, S. Majumdar, Heterogeneity of bone microstructure in the femoral head in patients with osteoporosis: an ex vivo HR-pQCT study, Bone. 56 (2013) 139–146. https://doi.org/10.1016/J.BONE.2013.05.019.

[688] S. Mori, R. Harruff, W. Ambrosius, D.B. Burr, Trabecular bone volume and microdamage accumulation in the femoral heads of women with and without femoral neck fractures, Bone. 21 (1997) 521–526. https://doi.org/10.1016/S8756-3282(97)00200-7.

[689] K.M. Nicks, S. Amin, L.J. Melton III, E.J. Atkinson, L.K. McCready, B.L. Riggs, K. Engelke, S. Khosla, Three-dimensional structural analysis of the proximal femur in an age-stratified sample of women, Bone. 55 (2013) 179–188. https://doi.org/10.1016/J.BONE.2013.02.009.

[690] K.E. Poole, G.M. Treece, A.H. Gee, J.P. Brown, M.R. McClung, A. Wang, C. Libanati, Denosumab Rapidly Increases Cortical Bone in Key Locations of the Femur: A 3D Bone Mapping Study in Women With Osteoporosis, J. Bone Miner. Res. 30 (2015) 46–54. https://doi.org/10.1002/jbmr.2325.

PUBLICATION I

Exercise loading history and femoral neck strength in a sideways fall: A three-dimensional finite element modeling study

Shinya Abe, Nathaniel Narra, Riku Nikander, Jari Hyttinen, Reijo Kouhia, and Harri Sievänen

Bone. 2016 Nov;92:9-17
doi: 10.1016/j.bone.2016.07.021

Bone 92 (2016) 9–17

Contents lists available at ScienceDirect

Bone

journal homepage: www.elsevier.com/locate/bone

Full Length Article

Exercise loading history and femoral neck strength in a sideways fall: A three-dimensional finite element modeling study

Shinya Abe [a,*], Nathaniel Narra [b], Riku Nikander [c,d,e], Jari Hyttinen [b], Reijo Kouhia [a], Harri Sievänen [f,**]

[a] Department of Mechanical Engineering and Industrial Systems, Tampere University of Technology, Tampere, Finland
[b] Department of Electronics and Communications Engineering, BioMediTech, Tampere University of Technology, Tampere, Finland
[c] Gerontology Research Center, Department of Health Sciences, University of Jyväskylä, Jyväskylä, Finland
[d] Central Hospital of Central Finland, Jyväskylä, Finland
[e] GeroCenter Foundation for Aging Research and Development, Jyväskylä, Finland
[f] The UKK Institute for Health Promotion Research, Tampere, Finland

ARTICLE INFO

Article history:
Received 7 February 2016
Revised 27 July 2016
Accepted 27 July 2016
Available online 28 July 2016

Keywords:
Bone strength
Finite element modeling
Exercise
Falling
Osteoporosis
Hip fracture

ABSTRACT

Over 90% of hip fractures are caused by falls. Due to a fall-induced impact on the greater trochanter, the posterior part of the thin superolateral cortex of the femoral neck is known to experience the highest stress, making it a fracture-prone region. Cortical geometry of the proximal femur, in turn, reflects a mechanically appropriate form with respect to habitual exercise loading. In this finite element (FE) modeling study, we investigated whether specific exercise loading history is associated with femoral neck structural strength and estimated fall-induced stresses along the femoral neck. One hundred and eleven three-dimensional (3D) proximal femur FE models for a sideways falling situation were constructed from magnetic resonance (MR) images of 91 female athletes (aged 24.7 ± 6.1 years, >8 years competitive career) and 20 non-competitive habitually active women (aged 23.7 ± 3.8 years) that served as a control group. The athletes were divided into five distinct groups based on the typical loading pattern of their sports: high-impact (H-I: triple-jumpers and high-jumpers), odd-impact (O-I: soccer and squash players), high-magnitude (H-M: power-lifters), repetitive-impact (R-I: endurance runners), and repetitive non-impact (R-NI: swimmers). The von Mises stresses obtained from the FE models were used to estimate mean fall-induced stresses in eight anatomical octants of the cortical bone cross-sections at the proximal, middle, and distal sites along the femoral neck axis. Significantly ($p < 0.05$) lower stresses compared to the control group were observed: the H-I group — in the superoposterior (10%) and posterior (19%) octants at the middle site, and in the superoposterior (13%) and posterior (22%) octants at the distal site; the O-I group — in the superior (16%), superoposterior (16%), and posterior (12%) octants at the middle site, and in the superoposterior (14%) octant at the distal site; the H-M group — in the superior (13%) and superoposterior (15%) octants at the middle site, and a trend ($p = 0.07$, 9%) in the superoposterior octant at the distal site; the R-I group — in the superior (14%), superoposterior (23%) and posterior (22%) octants at the middle site, and in the superoposterior (19%) and posterior (20%) octants at the distal site. The R-NI group did not differ significantly from the control group. These results suggest that exercise loading history comprising various impacts in particular is associated with a stronger femoral neck in a falling situation and may have potential to reduce hip fragility.

1. Introduction

Bone structure adapts to habitual mechanical loading [1,2]. Walking, as the predominant form of human locomotion, causes higher compressive stress at the inferior cortex and smaller tensile stress at the superior cortex of the femoral neck. This asymmetric loading results in a thicker inferior and thinner superior cortical bone [3,4]. With aging, cortical thinning becomes evident; the thickness of the posterior part of the superolateral cortex, called the superoposterior cortex, declines from a mean 1.6 mm at the age of 25 to 0.3 mm at the age of 85 years in females [4,5]. Mayhew and colleagues [4] suggested that the thinning of the superoposterior cortex contributes significantly to hip fragility. Cortical thinning increases the elastic instability of the cortical shell and can lead to a fracture because of local buckling under compressive load [4]. When one falls sideways, the superolateral cortex experiences unusually high compressive stress due to a high impact force imposed on the greater trochanter [6,7]. The peak magnitude of such a fall-induced stress can

* Correspondence to: S. Abe, Department of Mechanical Engineering and Industrial Systems, Tampere University of Technology, Korkeakoulunkatu 10, FI-33720, Tampere, Finland.
** Correspondence to: H. Sievänen, The UKK Institute for Health Promotion Research, Kaupinpuistonkatu 1, FI-33500, Tampere, Finland.
E-mail addresses: shinya.abe@tut.fi (S. Abe), harri.sievanen@uta.fi (H. Sievänen).

http://dx.doi.org/10.1016/j.bone.2016.07.021
8756-3282/

be 4 times greater than the stress induced by normal gait [3]. Accordingly, it has been speculated that the fracture initiates from this thin cortical layer of the superolateral region [4,7,8]. Several finite element (FE) modeling and cadaveric experimental studies have consistently shown that a sideways fall exposes the femoral neck to the greatest risk of a fracture [7,9–13]. Indeed, over 90% of hip fractures are directly caused by falls [14,15]. Therefore, if the superolateral cortical thickness could be maintained or even increased with appropriate exercise training, bone strength may be maintained and hip fracture risk reduced in old age.

In our previous studies [16,17], we found that female athletes with a history of high impact and/or impact exercises from unusual directions have higher areal bone mineral density (aBMD), section modulus, and thicker cortical bone of the femoral neck including the superolateral cortex. However, the influence of this exercise-induced structural benefit on femoral neck strength in the sideways fall was not examined. Several FE modeling studies have been conducted to obtain a better understanding of the hip fracture mechanism [3,6,9,11–13,18–22]. To the best of our knowledge, however, no FE modeling study has so far been conducted to investigate the influence of specific exercise loading history on the structural strength of the femoral neck in a falling situation. In particular, it is not known whether specific exercise loading history is associated with lower stresses during a fall.

The purpose of the present study is to investigate whether the femoral necks adapted to distinct exercise loading patterns show different stress profiles in a sideways fall. For this purpose, proximal femur FE models were created from three-dimensional (3D) image data of 111 female participants with distinct exercise loading histories. These results are expected to provide further insight into the potential of specific exercise types in strengthening the proximal femur and alleviating hip fracture risk.

2. Materials and methods

2.1. Participants

Magnetic resonance (MR) image data of proximal femurs from 91 adult female athletes (aged 24.7 ± 6.1 years) competing actively at national or international level and 20 habitually active, but non-competitive female control participants (aged 23.7 ± 3.8 years) were obtained from our previous study [17]. The study protocol was approved by the Ethics Committee of the Pirkanmaa Hospital District, and written informed consent was obtained from each participant before the study.

The athletes were recruited from national sports associations and local athletic clubs, and the control participants were mostly students from local medical and nursing schools. The control participants did recreational exercise 2–3 times a week, but had previously never taken part in any competitive sports. The athletes comprised nine triple-jumpers, ten high-jumpers, nine soccer players, ten squash players, 17 power-lifters, 18 endurance runners, and 18 swimmers. According to our previous exercise classification scheme [16,23], the athletes were divided into five different groups based on the typical loading patterns of their sports: high-impact (H-I) (triple- and high-jumpers); odd-impact (O-I) (soccer and squash players); high-magnitude (H-M) (power-lifters); repetitive-impact (R-I) (endurance runners); and the repetitive, non-impact group (R-NI) (swimmers).

Wearing only light indoor clothing without shoes, the body height and weight of the participants were measured using standard methods. Questionnaires were completed by all participants in order to obtain their training history including weekly sport-specific training hours and the number of training sessions during at least the five preceding years. Other information such as medications, diseases, menstrual status, use of hormonal contraceptives, calcium intake, alcohol, smoking, coffee consumption, and previous injuries and fractures was also collected [17].

2.2. MR image scanning procedure

The hip regions of all participants were scanned using a 1.5-T MR imaging system (Avanto Syngo MR B15, Siemens, Erlangen, Germany). The scanned region covered the proximal femur from the top of the femoral head to the subtrochanteric level of the femoral diaphysis. Using two half-Fourier acquisition single-shot turbo spin-echo localization series, sagittal, axial, and coronal images of the hip region of the dominant side were scanned. The reconstructed imaging plane was adjusted so that the cross-sectional plane of the femoral neck was perpendicular to the femoral neck axis. The MR imaging sequence used was a standardized axial T1-weighted gradient echo volumetric interpolated breath-hold (VIBE)-examination with the following parameters: FOV 35 × 26 cm, TR 15.3 ms, TE 3.32 ms, slice thickness 1 mm without gaps, echo train length = 1, flip angle = 10°, matrix 384 × 288, the in-plane resolution (pixel size) 0.9 mm × 0.9 mm [17].

2.3. FE model construction

The MR images of all participants were first manually segmented by delineating the periosteal and endocortical boundaries of the cortical bone using a touch panel (Wacom Tablet Cintiq 12WX, Wacom Technology Corp., Vancouver, WA, USA) with ITK-SNAP (www.itksnap.org) image processing software [24]. The in vivo precision of periosteal and endocortical delineations of the femoral neck cortex is about 1% [17, 25]. The segmented bone geometries were then converted into a volume mesh using the free mesh generation MATLAB (MathWorks, Inc., Natick, MA, USA) tool called iso2mesh [26]. The surface was then smoothed in MeshLab (Visual Computing Lab – ISTI – CNR, http://meshlab.sourceforge.net/) using a method described by Taubin [27]. This method was chosen for its known performance in minimizing the shrinkage of the geometry during the smoothing process. The smoothed proximal femur geometries were subsequently imported into SolidWorks (SolidWorks Corp., Waltham, MA, USA) for the generation

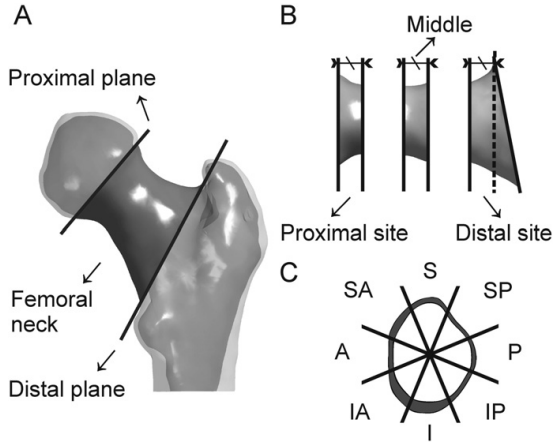

Fig. 1. Division of the femoral neck volume into anatomical sites and octants for the estimation of octant cortical stresses. (A) Posterior view of proximal femur. Dark grey-colored geometry defines the femoral neck geometry of interest. The proximal cross-sectional plane of the defined neck geometry was located at the femoral head-neck junction dividing the femoral head and the femoral neck. The distal plane was adjusted so that the distal plane met following conditions: its superior side is close to trochanteric fossa-greater trochanter junction, its anterior side is close to intertrochanteric line, and its inferior side is close to the lesser trochanter. This distal plane divides the trochanteric region and the femoral neck. (B) The division of the defined femoral neck regions into proximal, middle, and distal sites. The length of the superior surface was kept same for all sites. (C) The equal 45° anatomical octant division in the cross-section of the femoral neck. The femoral neck axis was used as the center of octant division.

of 3D solid bodies. The resulting proximal femur geometry comprised individually segmented cortical bone and trabecular bone volumes, the latter denoting the volume within the endocortical bone boundary. Although trabecular bone is truly a porous structure, in the present study it was modeled as a non-porous homogeneous material.

The individual 3D solid body geometries of the proximal femur were finally imported into ANSYS 16.1 (ANSYS Inc., Houston, PA, USA) for the FE meshing and model analysis. The ANSYS Academic Research license was obtained from CSC – IT Center for Science Ltd. (Espoo, Finland). First, the femoral neck geometry was defined (Fig. 1), and then similar boundary conditions (BCs) from the previous studies [22,28] were used in the present study. Force and restraining BCs were applied through the femoral head and trochanter-protecting polymethyl methacrylate (PMMA) caps, and aluminum distal pot (Fig. 2). A 10-noded tetrahedral finite element was used to mesh all materials. The element size was set to 1 mm for the entire proximal femur bone geometry, the caps, and the boundary between the distal end of the bone and the distal pot. The body of the distal pot, away from the boundary, was meshed with a 4 mm element size. The maximum error in octant stress (described in Section 2.4) was estimated based on the converged solution that was obtained by extrapolating the results from the 3 mm, 2 mm, 1.5 mm, 1 mm, and 0.75 mm FE mesh models. The estimated errors were 6.7%, 4.2%, 3.4%, 2.4%, and 2.1% for the 3 mm, 2 mm, 1.5 mm, 1 mm, 0.75 mm meshes, respectively. Based on these findings, a 1 mm mesh element size for the models in this study was deemed satisfactory. On average, each bone model comprised approximately 1,600,000 elements and 2,300,000 nodes. The cortical and trabecular bones of the proximal femur were modeled as homogeneous isotropic, linear elastic materials. Young's moduli of 17 GPa [29–31], 1500 MPa [30,31], 70 GPa [22], and 2 GPa [22] were set for the cortical, trabecular bone, the aluminum distal pot, and the protecting PMMA caps, respectively. Poisson's ratio was assumed as 0.33 [29–31] for all materials.

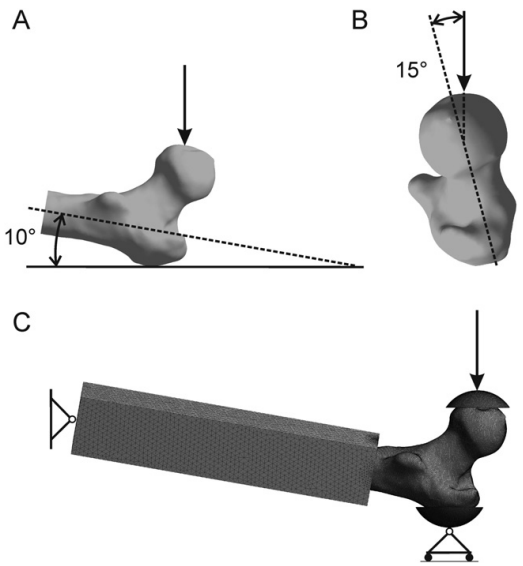

Fig. 2. Loading/falling angles (A & B) and boundary conditions of the FE model. The femoral shaft was tilted at 10° with respect to the ground (A) and the femoral neck was internally rotated by 15° (B). Force was applied to the whole upper face of the head-protecting cap, at a described angle. A 200 mm long aluminum pot was placed at 15–20 mm below the most projected part of the lesser trochanter of each proximal femur. A hinge-type constraining boundary condition was applied to nodes of the distal face of the aluminum pot. This allowed nodes at the hinge-axis to freely rotate in the quasi-frontal plane, while all other degrees of freedom were constrained. Greater trochanter cap's surface nodes were restrained in the direction of the force (C).

To simulate sideways falling, the most commonly used force direction from previous experimental studies [10,32,33] was chosen. The femoral shaft was tilted at 10° with respect to the ground and the femoral neck was internally rotated by 15° (Fig. 2) [10,32,33]. The individual impact force was estimated using the equation proposed by Bouxsein et al. [34]:

$$F_{peak} = \sqrt{2gh_{cg}KM},$$

where g is the gravitational constant (9.81 m/s^2), h_{cg} is the height of the center of gravity of the body assumed as 0.51 × height (m), K is the stiffness constant (71 kN/m), and M is the effective mass calculated by $(^7/_{20}$ × total body mass).

The force described above was then applied to the entire upper face of the femoral head cap at a defined angle while the trochanter cap was restrained in the direction of the force (Fig. 2) [22]. The femoral head and trochanter caps covered a depth of 5 mm of the femoral head and the lateral side of the trochanter [6]. The distal pot was placed at 15–20 mm below the most projected part of the lesser trochanter of each proximal femur. The distance between the most proximal part of the proximal femur to the distal part of the aluminum pot was in the range of 280–306 mm and was similar to the previous study [35]. A hinge-type restraining BC was applied to the distal side of the aluminum pot. This allowed nodes at the hinge-axis to freely rotate in the quasi-frontal plane, while all other degrees of freedom were constrained [22, 28].

2.4. FE derived stress within the femoral neck cortical bone

From each FE model, the nodal cortical von Mises stresses were calculated for the entire femoral neck region. These von Mises stresses were imported into MATLAB for further post-FE analysis. The entire femoral neck region was first divided into three sub-volumes along the femoral neck axis: proximal, middle, and distal volumes. For clarity, these sub-volumes are henceforth referred to as proximal, middle, and distal sites (Fig. 1). This division was performed so that the length of the most superior surface was equal for each site. Next, these three sites were divided into equal 45° octant regions each representing different anatomic directions of the respective cross-section of the femoral neck. This octant division was performed similar to previous studies [4, 17,36,37] except that the femoral neck axis was used as a reference for the center of the octant instead of the geometric centroid. In the present study, the femoral neck axis was defined similar to a previous study [38] so that it goes through the center of the femoral head and the geometric center of the thinnest femoral neck cross-section. The center of the femoral head was identified as the center of the sphere that best fitted the periosteal surface. The octants were anatomically defined as inferior (I), inferoanterior (IA), anterior (A), superoanterior (SA), superior (S), superoposterior (SP), posterior (P), and inferoposterior region (IP) (Fig. 1). For each individual proximal femur FE model, the mean cortical von Mises stresses in each octant (*octant cortical stress*) were calculated for all three sites.

2.5. Statistical analysis

Statistical analyses were performed with SPSS 22.0 (IBM Corp., Armonk, NY, USA). Mean and SD were given as descriptive statistics. Differences in octant cortical stresses in the three sites between each exercise group and the control group were estimated by multivariable analysis of covariance (MANCOVA) using the individual impact force as a covariate. Exercise groups were not compared to each other. Sidak correction was used to control for multiple comparisons in the post-hoc tests. Logarithmic transformations of the octant cortical stresses were performed prior to MANCOVA to control skewness of the data. Percentage differences of the octant cortical stress between each

exercise loading group and control group were calculated by taking anti-log of the impact force-adjusted mean octant cortical stress. A p value of <0.05 was considered statistically significant.

3. Results

3.1. Descriptive data of participants

Table 1 shows the descriptive data of age, sport-specific training hours/week, training sessions/week, duration of competitive career, height, body weight (BW), and estimated impact force in each exercise loading and control group. Further details of body composition and muscular performance have been reported previously [17]. In addition to a competitive career of >8 years, athletic participants clearly had much longer training hours and more training sessions per week compared with the non-competitive habitually active control participants.

3.2. Octant cortical stresses in general

Fig. 3 shows the unadjusted mean octant cortical stresses for proximal, middle, and distal femoral neck sites for each group. At the proximal site, higher stress levels were generally observed in the inferior and inferoposterior regions, while at the middle site higher stress levels were generally evident in the superior, superoposterior, and posterior regions. At the distal site, higher stresses were generally observed in the posterior region and became prominent in the superoposterior region. Fig. 4 presents example subjects from each group of the study population to illustrate typical stress distributions in each group. Stresses higher than 185 MPa were observed in the region spanning the superoposterior and posterior part of the femoral neck. Notably, a large contiguous area of >185 MPa stresses can be seen in the stress distributions of the repetitive non-impact group (R-NI) and the control proximal femora. Table 2 shows the impact force-adjusted mean percentage differences in octant cortical stresses for the proximal, middle, and distal femoral neck sites between each exercise loading group and the control group.

3.2.1. Proximal octant stress

The high-impact (H-I) group had significantly lower octant stresses ($p < 0.05$) than in the control group in the inferior (21%), inferoanterior (29%), superoanterior (9%), superoposterior (12%), posterior (15%), and inferoposterior (17%) octants. The odd-impact (O-I) group had significantly lower stresses in the superoposterior (14%) and posterior (12%) octants. The high-magnitude (H-M) group had significantly lower stresses in the superoposterior (16%) and posterior (12%) octants. The repetitive-impact (R-I) group had significantly lower stresses in the inferior (14%), inferoanterior (19%), anterior (16%), superoanterior (13%), superior (12%), superoposterior (21%), posterior (22%), and inferoposterior (15%) octants.

3.2.2. Middle octant stress

The H-I group had significantly lower octant stresses ($p < 0.05$) than in the control group in the inferior (32%), inferoanterior (29%), anterior (16%), superoposterior (10%), posterior (19%), and inferoposterior (25%) octants. The O-I group had significantly lower stresses in the inferior (17%), inferoanterior (17%), anterior (14%), superoanterior (14%), superior (16%), superoposterior (16%), and posterior (12%) octants. The H-M group had significantly lower stresses in the superior (13%) and superoposterior (15%) octants. The R-I group had significantly lower stresses in the inferior (20%), inferoanterior (21%), anterior (18%), superoanterior (13%), superior (14%), superoposterior (23%), posterior (22%), and inferoposterior (17%) octants. Also, a trend for lower stresses when compared to controls was observed in the H-I group in the superoanterior ($p = 0.07$, 11%) octant.

3.2.3. Distal octant stress

The H-I group had significantly lower octant stresses ($p < 0.05$) than in the control group in the inferior (24%), inferoanterior (18%), superoposterior (13%), posterior (22%), and inferoposterior (22%) octants. The O-I group had significantly lower stresses in the inferior (16%), inferoanterior (13%), and superoposterior (14%) octants. The R-I group had significant lower stresses in the inferior (17%), inferoanterior (17%), anterior (18%), superoanterior (18%), superoposterior (19%), posterior (20%), and inferoposterior (16%) octants. Also, trends for lower stresses when compared to controls were observed in the H-I group in the anterior ($p = 0.06$, 15%) and superoanterior ($p = 0.06$, 16%) octants. In the O-I group, trends for lower stresses were observed in the superoanterior ($p = 0.08$, 14%) and posterior ($p = 0.07$, 9%) octants. In the H-M group, similar trends were observed in the superoposterior ($p = 0.07$, 9%) octant and in the superior ($p = 0.08$, 17%) octant in the R-I group.

4. Discussion

In this large FE modeling study of female athletes, the association of specific exercise loading history with femoral neck structural strength in a sideways falling situation was elaborated. As expected from the findings of previous studies [6,7], high stresses were primarily distributed over the superolateral cortex region of the femoral neck: specifically, in the superior, superoposterior, and posterior octants at the middle site, and in the superoposterior and posterior octants at the distal sites. Present results suggest that exercise loading history during adolescences and early adulthood that involves either high impacts (H-I), impacts from unusual directions (O-I), a large number of repetitive impacts (R-I), or extreme muscle forces (H-M) is associated with significantly lower (10–23%) fall-induced stresses at these vulnerable femoral neck regions (the five octants listed above) when compared to the control group. Importantly, the highest octant stresses were observed in the fracture-prone posterior part of the superolateral cortex region (superoposterior octant in the distal site in Fig. 1 and Fig. 3), which is in agreement with the findings of a study by Mayhew et al. [4]. We found that the femoral neck in the H-I, the O-I, and the R-I groups experienced significantly lower (13–19%) stress in this octant compared to the control group. Although a significant difference was not observed, the H-M group exhibited a trend for lower stress ($p = 0.07$, 9%) in the same octant. These results may translate into a reduced risk of hip fractures caused by falling.

The present findings are largely explained by the specific structural adaptation of the cortical bone to impact loading. Previously, Nikander

Table 1
Group characteristics.

Group	n	Age (years)	Sport-specific training hours/week	Training sessions/week	Competing career (years)	Height (cm)	Weight (kg)	Impact force (N)
H-I	19	22.3 (4.1)	11.5 (2.3)	6.7 (1.4)	10.1 (3.4)	174 (6)	60.2 (5.4)	5102.1 (268.3)
O-I	19	25.3 (6.7)	9.3 (2.7)	5.7 (1.4)	9.6(4.8)	165 (8)	60.8 (8.3)	4991.0 (450.5)
H-M	17	27.5 (6.3)	9.1 (2.7)	5.8 (2.0)	8.0 (4.7)	158 (3)	63.3 (13.2)	4974.0 (531.9)
R-I	18	28.9 (5.6)	10.9 (3.4)	8.7 (2.1)	12.4 (6.7)	168 (5)	53.7 (3.4)	4737.8 (198.2)
R-NI	18	19.7 (2.4)	19.9 (4.5)	11.4 (2.0)	9.1 (2.6)	173 (5)	65.1 (5.6)	5284.7 (251.1)
Control	20	23.7 (3.8)	2.8 (0.9)	2.8 (1.0)	–	164 (5)	60.0 (7.4)	4943.5 (363.6)

Mean and (SD).

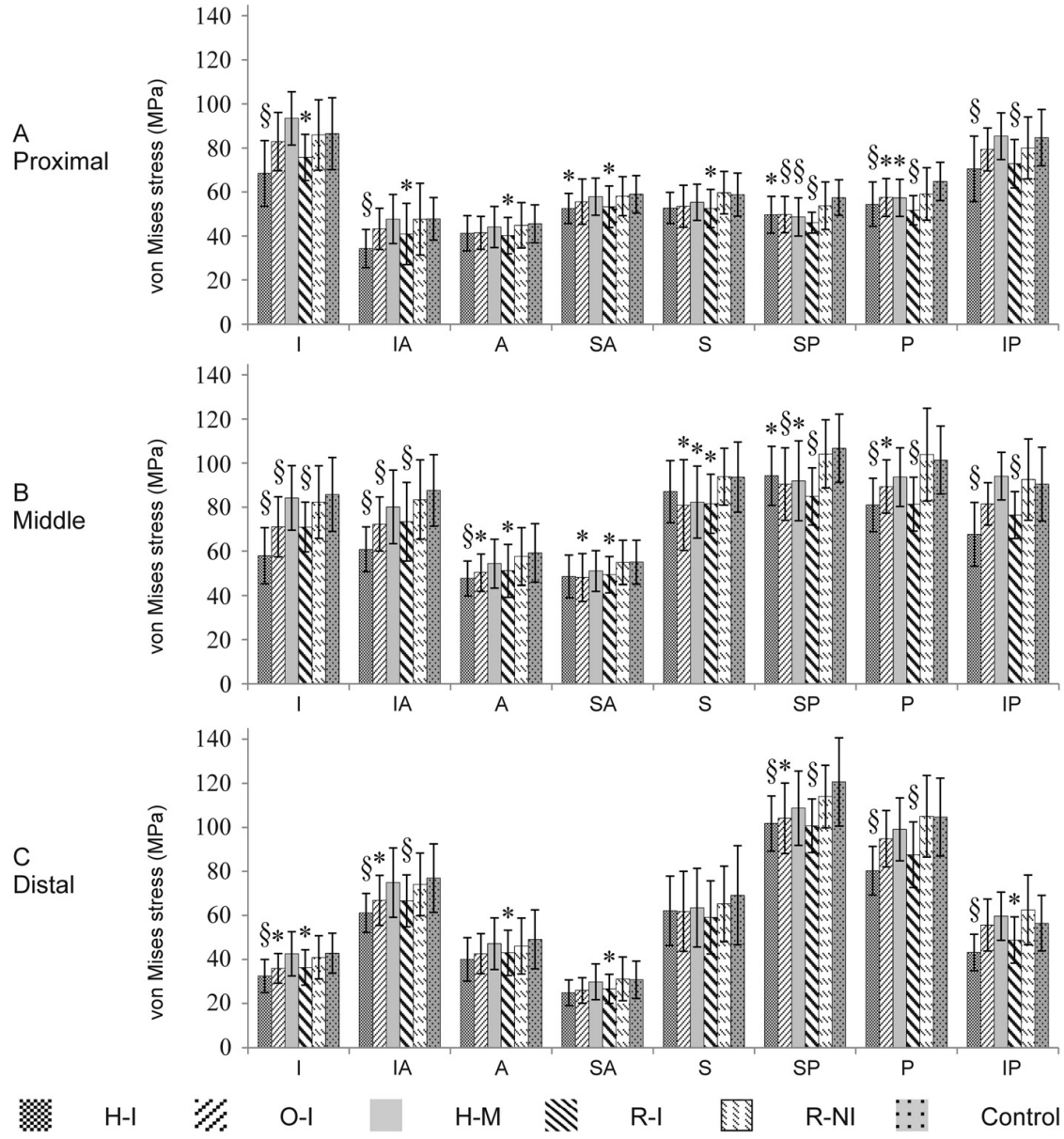

Fig. 3. Group unadjusted mean (SD) octant cortical stress at the proximal, middle, and distal sites of the femoral neck (see Fig. 1). Each bar represents each group's unadjusted mean octant stress with SD. According to the MANCOVA, * and § show the statistical significance of $0.01 \leq p < 0.05$ and $p < 0.01$ respectively.

et al. [17] found that the femoral neck of athletes in the H-I group had a thicker cortex in the inferior, anterior, and posterior quadrants, while the O-I group had a consistently thicker cortex in the anterior, posterior, and superior quadrants of the femoral neck. Notably, the lower stresses in the inferior, inferoanterior, and inferoposterior octant regions in the H-I group can be attributed to a very thick inferior cortex: approximately 60% thicker than in the habitually active control group [17].

A particularly interesting finding in the present study was that the femoral neck in the R-I (endurance runners) group also showed significant and similar low stresses to those observed in the H-I group. Previously, Nikander et al. [17] reported that the cortical bone of the femoral neck in the R-I group was not thicker than in the control group. This indicates that the lower stresses in the R-I may be attributed to other geometrical factors, that is, the more circular shape of the femoral neck cross-section shown by Narra et al. [39]. Basically, a more circular bone is mechanically more robust in all directions than an oval shaped bone. Sievänen et al. [40] observed that physically more active medieval people had a more circular femoral neck cross-section in contrast to present-day people who have a more oval-shaped cross-section. It was estimated that the oval-shaped femoral neck of present-day people may experience 1.3–

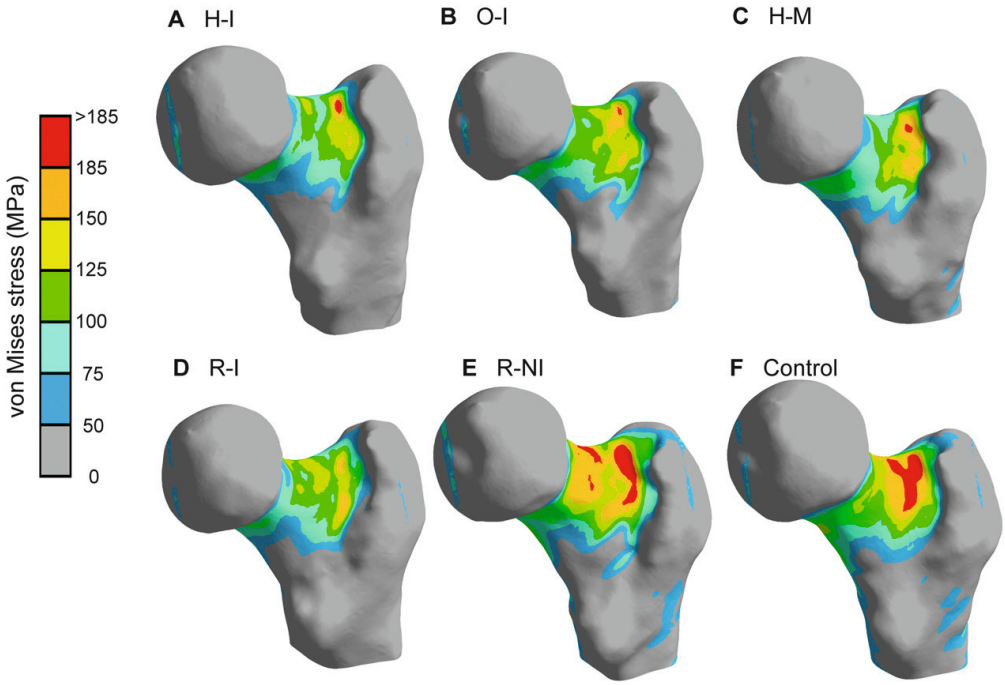

Fig. 4. Examples of typical von Mises stress distribution from each group. A, B, C, D, E, and F show an example stress distribution from the H-I, O-I, H-M, R-I, R-NI, and control groups, respectively.

1.5 times higher fall-induced stress in a sideways fall than the circular femoral neck of the medieval people [40]. This estimation is consistent with the results of the present study that show almost 20% lower stress in the R-I group than in the control group. Running (or walking) is a natural form of locomotion and a common type of exercise. In particular, the human skeleton is particularly fitted for endurance running [41], but as alluring as the present finding is from the evolutionary point of view, the beneficial results in the endurance running group remain at best speculative and warrant further elaboration.

The R-NI group showed no apparent reduction in stress at any femoral neck octant. This agrees with the findings by Nikander et al. [17] that showed no exercise-related benefit to the cortical geometry among swimmers. The typical movements in swimming require a lot of repetitive muscle contractions and can be intensive, but they are also smooth and without impacts. The H-M group, in turn, showed less reduced octant stresses compared to the control group than the H-I, O-I, and R-I groups did in spite of extreme muscle forces involved in power-lifting (e.g., a squat). Again, this is likely attributable to the inherent nature of movement. During H-M exercises, the movement is slow by nature, and therefore its rate of loading is low.

Moderate to high ground reaction forces and a high rate of force development due to the ground impact are common factors in exercise loading that seem to be beneficial for femoral neck strength. Peak vertical ground reaction forces are 12–20 times BW [42,43] for H-I exercise, 2.5–3.5 times BW [44–46] for O-I exercise, 2–3 times BW [47] for H-M exercise (squat), and 2–2.5 times BW [48,49] for R-I exercise while the estimated impact loading rates (BW s^{-1}) are about 400–480 BW s^{-1} [42], 20–180 BW s^{-1} [44,45], 5–6 BW s^{-1} [47], and 60–150 BW s^{-1} [48–50], respectively. In swimming, peak reaction force and loading rate at the push-off phase of turning are estimated to be <1.5 times BW [51,52] and <10 BW s^{-1} [51], respectively. Such a combination of reaction force and loading rate in the R-NI exercise seems to be insufficient to improve femoral neck strength. While ground reaction force in the H-M exercise may be similar in magnitude to those in the O-I and R-I exercises, the rate of force development is significantly lower. In light of the results for the H-M group, this indicates that in spite of the moderate-to-high ground reaction force, the stimulus for beneficial geometric adaptation seems to be diminished by the lower rate of loading. Differing from power-lifting (squat, bench press, and deadlift), weightlifting movements such as the snatch, clean, and jerk are explosive and involve more impact: peak vertical ground reaction forces are 2.5–4 times BW and estimated impact loading rates vary from about 10–50 BW s^{-1} [53–56]. This warrants further investigation of femoral neck strength among weightlifters.

The mean starting ages of the competitive careers of the athletic participants were the following: H-I = 12.2 years; O-I = 15.7 years; H-M 19.5 years; R-I = 16.5 years; R-NI = 10.6 yrs. Accordingly, the H-M group started their sport-specific career the latest of any groups and their careers were also the shortest (mean 8 years) at the time of the study. The H-I group started their career at the age of 12.2 years, which is 7 years earlier than that of the H-M group. Indeed, the starting age of 19.5 years of the H-M group is almost close to skeletal maturity [57]. It is well established that starting the exercise training in early adolescence is the most beneficial for bone strength compared with a later start of training [58]. Lorentzon et al. [59] reported that higher aBMD, cortical bone size, and trabecular density were observed among those who started their training career before the age of 13 than those who started their training later. Further, the duration of the training in adolescence is associated with improved bone traits as well [59,60]. This being the case, the odds of finding a clear exercise-related reduction in fall-induced stress in the H-M group may have been attenuated. However, it is worth noting that starting intensive power-lifting exercises (squat, bench press, and deadlift) at an early age is not recommended, which may explain the later starting age in the H-M group. On the

Table 2
Impact force-adjusted mean percentage differences (95% CI) in octant cortical stresses for proximal, middle, and distal sites between each exercise group and control group.

	Proximal	*Middle*	*Distal*	*Proximal*	*Middle*	*Distal*
Inferior (I)				*Superior (S)*		
H-I	**−20.6**	**−32.2**	**−23.6**	H-I	−8.2	−5.8	−6.2
	(−28.6 to −11.8)	**(−39.1 to −24.6)**	**(−31.5 to −15.0)**		(−14.5 to −1.2)	(−12.9 to 1.8)	(−18.6 to 7.8)
O-I	−3.4	**−16.6**	**−15.7**	O-I	−8.8	**−15.5**	−9.6
	(−11.5 to 5.7)	**(−24.2 to −8.3)**	**(−23.4 to −7.3)**		(−16.0 to −1.1)	**(−23.5 to −6.7)**	(−22.1 to 4.6)
H-M	9.4	−1.1	−1.1	H-M	−5.8	**−12.5**	−6.9
	(0.2 to 19.5)	(−10.6 to 9.4)	(−12.1 to 11.1)		(−13.2 to 2.2)	**(−20.1 to −4.0)**	(−20.2 to 8.7)
R-I	**−13.5**	**−20.0**	**−17.0**	R-I	**−12.3**	**−13.9**	−17.0
	(−20.8 to −5.5)	**(−27.1 to −12.4)**	**(−25.3 to −7.8)**		**(−19.5 to −4.6)**	**(−20.8 to −6.5)**	(−28.4 to −3.7)
R-NI	−0.2	−3.2	−4.3	R-NI	0.5	0.5	2.6
	(−10.3 to 10.8)	(−13.6 to 8.7)	(−14.9 to 7.7)		(−8.0 to 9.5)	(−7.5 to 9.1)	(−12.2 to 19.8)
InferoAnterior (IA)				*SuperoPosterior (SP)*		
H-I	**−28.6**	**−29.4**	**−18.0**	H-I	**−11.9**	**−9.8**	**−12.9**
	(−36.1 to −19.9)	**(−35.1 to −23.0)**	**(−24.2 to −11.1)**		**(−17.9 to −5.3)**	**(−15.5 to −3.6)**	**(−18.6 to −6.9)**
O-I	−9.2	**−17.2**	**−12.9**	O-I	**−13.5**	**−16.1**	**−13.5**
	(−18.1 to 0.5)	**(−24.1 to −9.8)**	**(−20.3 to −4.7)**		**(−19.6 to −7.1)**	**(−22.6 to −8.8)**	**(−20.0 to −6.4)**
H-M	−0.9	−8.8	−2.7	H-M	**−15.7**	**−14.5**	−9.4
	(−11.5 to 10.8)	(−17.3 to 0.6)	(−12.1 to 7.9)		**(−22.2 to −8.6)**	**(−21.5 to −6.9)**	(−16.3 to −2.1)
R-I	**−18.5**	**−20.6**	**−16.8**	R-I	**−20.7**	**−22.6**	**−19.3**
	(−29.3 to −6.4)	**(−28.1 to −12.1)**	**(−23.9 to −9.0)**		**(−25.5 to −15.5)**	**(−27.9 to −16.7)**	**(−24.6 to −13.8)**
R-NI	−7.5	−4.3	−0.9	R-NI	−6.2	−0.5	−0.5
	(−20.7 to 7.8)	(−14.2 to 6.8)	(−10.4 to 9.8)		(−14.1 to 2.2)	(−7.7 to 7.3)	(−7.5 to 7.3)
Anterior (A)				*Posterior (P)*		
H-I	−6.0	**−16.2**	−14.7	H-I	**−14.7**	**−19.3**	**−21.5**
	(−13.9 to 2.8)	**(−23.5 to −8.4)**	(−24.2 to −4.0)		**(−20.9 to −8.1)**	**(−25.0 to −13.2)**	**(−26.8 to −15.6)**
O-I	−8.6	**−14.3**	−12.5	O-I	**−11.5**	**−11.7**	−9.0
	(−16.5 to 0.1)	**(−21.9 to −5.7)**	(−22.2 to −1.5)		**(−17.0 to −5.4)**	**(−17.8 to −5.3)**	(−15.3 to −2.0)
H-M	−2.9	−7.3	−3.2	H-M	**−11.7**	−7.5	−4.7
	(−12.2 to 7.2)	(−16.4 to 2.7)	(−14.6 to 9.9)		**(−17.4 to −5.5)**	(−14.0 to −0.3)	(−12.0 to 3.2)
R-I	**−15.5**	**−18.0**	**−18.2**	R-I	**−21.8**	**−21.5**	**−20.0**
	(−23.5 to −6.6)	**(−26.3 to −8.7)**	**(−27.0 to −8.1)**		**(−26.8 to −16.6)**	**(−27.1 to −15.5)**	**(−25.9 to −13.5)**
R-NI	1.2	1.6	−0.9	R-NI	−8.0	1.4	3.3
	(−9.4 to 12.9)	(−9.8 to 14.3)	(−14.2 to 14.2)		(−15.2 to 0.1)	(−7.5 to 11.0)	(−-5.6 to 12.8)
SuperoAnterior (SA)				*InferoPosterior (IP)*		
H-I	**−9.0**	−11.3	−15.7	H-I	**−16.6**	**−25.4**	**−22.2**
	(−15.0 to −2.8)	(−19.2 to −2.6)	(−25.6 to −4.5)		**(−24.0 to −8.6)**	**(−32.6 to −17.3)**	**(−29.9 to −13.4)**
O-I	−6.2	**−13.5**	−14.1	O-I	−6.0	−8.6	−0.2
	(−13.6 to 1.5)	**(−21.6 to −4.7)**	(−23.7 to −3.0)		(−12.1 to 0.6)	(−15.7 to −1.1)	(−10.4 to 10.9)
H-M	−1.8	−6.9	−2.1	H-M	1.2	5.4	6.7
	(−8.8 to 5.9)	(−15.2 to 2.1)	(−14.6 to 12.2)		(−5.8 to 8.6)	(−3.3 to 14.8)	(−4.7 to 19.5)
R-I	**−13.3**	**−12.7**	**−17.6**	R-I	**−15.3**	**−17.0**	**−15.9**
	(−20.0 to −6.0)	**(−20.2 to −4.7)**	**(−27.5 to −6.5)**		**(−21.5 to −8.6)**	**(−24.0 to −9.5)**	**(−24.7 to −5.8)**
R-NI	−0.5	0.9	4.2	R-NI	−5.8	0.7	9.4
	(−7.9 to 7.7)	(−9.0 to 11.7)	(−11.7 to 22.9)		(−13.7 to 2.7)	(−9.5 to 12.3)	(−3.9 to 24.5)

Statistically significant p values ($p < 0.05$) based on MANCOVA are shown in bold.

other hand, it is likely that the H-M group was involved in various, less specific exercise training during adolescence.

Observed reductions in the octant stress (10–30%) along the femoral neck in the sideways falling situation, attributable to exercise-induced structural adaptations, may be clinically important. It is noteworthy that the control group was comprised of young healthy women who did recreational exercises 2–3 times a week. Thus, our control participants were physically active, but not athletes. This being the case, it is possible that actual exercise-induced benefit in the femoral neck strength in sideways falling could be even higher when compared with the average, less physically active population.

As to the clinical relevance of the present results, caution is needed. Since the data were obtained from young female athletes, the results cannot be extrapolated to the general population. Despite the clear benefits, H-I exercise does not provide a panacea against hip fragility and fractures. Extreme impact forces (12–20 times BW) [42,43] in the H-I exercises are obviously too risky not only for older people but also for sedentary people regardless of age. Since the O-I and R-I exercises produce moderate impacts, the risk of musculoskeletal injuries remains lower. Thus, exercise involving impacts from unusual directions and a large number of repeated impacts may offer a more feasible and equally effective option to increase femoral neck strength. For the young, physically active, and/or fit people, not only O-I and R-I exercises but also appropriate H-I exercises are feasible in order to maintain and/or increase femoral neck strength. It is worth mentioning that along with O-I and R-I exercises (e.g. jogging), H-M exercises (squat, deadlift, etc.) may also be beneficial for the overall health of the proximal femur for people with a sedentary background or the elderly. This is, of course, contingent on the people having no preexisting musculoskeletal maladies, having sufficient mobility, and weights being chosen according to their physical conditioning.

Another important question is whether the exercise-induced skeletal benefits from early adulthood can be sustained into old age. It is known that the exercise-induced bone thickening during growth occurs through new bone formation on the periosteal bone surface, while the age-related bone loss takes place at the endocortical bone surface [2]. Should the femoral neck cortical bone be thicker during young adulthood, it may be more resistant against fractures in old age. It is noteworthy that retired ice hockey and soccer players > 60 years old have lower fracture risk compared to matched controls despite some loss in exercise-induced high aBMD due to retirement from sports [61]. This finding indicates that the exercise-induced structural benefits to the femoral neck during young adulthood may be sustained into old age and highlights the importance of exercise in adolescence and young adulthood in terms of preventing future hip fractures. Further, the effect of exercise on bone may vary

depending on the period of life. During adolescence, exercise can increase bone strength, and continued exercise may help maintain exercise-induced bone strength in adulthood. Moreover, exercise may attenuate a decrease in bone strength due to age-related bone loss [60].

The major strength of the present study is the large total sample size of 111 individual FE models that represent a variety of distinct exercise loading histories. This makes the present study one of the largest proximal femur FE modeling studies. Further, the large total sample size made it possible to divide the athletes into smaller subgroups, which enabled us to investigate the association of the distinct exercise loading pattern with femoral neck strength in a sideways falling situation. However, the marginal differences in the H-M group, despite group-differences of a similar magnitude, indicate limited statistical power in some subgroup analyses.

In addition to somewhat limited statistical power, there are other limitations as well. The main limitation was the use of the MR images for the construction of the proximal femur geometry which was not validated against actual mechanical testing. While QCT would have provided high-resolution image data on femoral neck geometry and bone apparent density, MR imaging has been found to be adequately valid for the assessment of cortical geometry [25,62]. The pixel size in the previous QCT-based proximal femur studies [13,19,20] has been around 0.5 mm in contrast to the 0.9 mm pixel size in the present study. Obviously, a higher in-plane resolution would have provided a more accurate segmentation of the cortical bone. Therefore, to comply with valid QCT-based proximal femur FE modeling studies, we adopted similar BCs and loading conditions [22,28]. In the present study, however, trabecular bone was modeled as a non-porous homogeneous structure in contrast to its actual non-uniform structure [63], which could cause <10% error in the maximum stress reported in the literature [19]. However, according to Koivumäki et al., inclusion of the trabecular bone in the sideways falling FE models may not play a crucial role, and the proximal femoral strength can be evaluated with reasonable accuracy using a cortical bone FE model only [64]. Further, Holzer et al. [65] reported that the complete removal of the trabecular bone led to a relatively small reduction in bone strength while the cortical bone is primarily responsible for load bearing and transmitting forces. Indeed, the present study mainly focused on evaluating the influence of cortical geometry on the stress distribution in the simulated sideways fall while modeling the trabecular bone as non-porous homogeneous material in every individual model. While the use of QCT-based FE models would have also allowed the estimation of inhomogeneous elastic properties using the voxel-based Hounsfield unit data (density) [11–13,18–22], the assumption of homogeneous material properties is acceptable. Taddei et al. [19] compared the homogeneous proximal femur bone model with the inhomogeneous model and found only a marginal improvement in accuracy of prediction; R^2 between FE predicted stress and experimental stress was 0.91 for the inhomogeneous model and 0.89 for the homogeneous model. Finally, exposing fertile young adult women to ionizing radiation from QCT for non-diagnostic purposes would have been ethically unacceptable.

5. Conclusion

The present FE study is the first study that employed a large number of individual 3D proximal femur FE models obtained from young adult female athletes representing distinct exercise loading patterns. The results showed that the athletes with a history of impact exercises from endurance running induced repetitive impacts, soccer and squash induced odd direction impact, to extreme vertical jumping sports showed clinically relevant lower stresses at the fracture prone regions of the femoral neck in a sideways falling simulation. In addition to impacts, high magnitude strength training may also be beneficial for maintaining the robustness of the femoral neck. This requires further study, however. The results of this study also give new insights into the prevention of hip fragility with targeted exercises.

Funding

This work was supported by Tampere University of Technology's (TUT) Graduate School; the Doctoral Education Council of Computing and Electrical Engineering of TUT; and Human Spare Parts project (40345/11) funded by the Finnish Funding Agency for Innovation (TEKES).

Disclosures

All authors state that they have no conflicts of interest.

Authorship

All authors contributed to the study design. NN, RN, JH, and HS were responsible for the data collection. Modeling and simulation were performed by SA and supervised by JH and RK. Data analysis was performed by SA, NN, RN, RK, and HS. The manuscript was drafted by SA and HS. All authors are responsible for revising and approving the final version of manuscript. SA takes responsibility for the integrity of the data analysis.

Acknowledgements

The authors thank all study participants. We also thank Antti Ylinen, DSc, and Ossi Heinonen, MSc, for assisting in the construction of the FE models and Peter Heath, MA, for the language editing.

References

[1] H.M. Frost, Bone's mechanostat: a 2003 update, Anat. Rec. A. Discov. Mol. Cell Evol. Biol. 275 (2003) 1081–1101.
[2] C. Ruff, B. Holt, E. Trinkaus, Who's afraid of the big bad Wolff?: "Wolff's law" and bone functional adaptation, Am. J. Phys. Anthropol. 129 (2006) 484–498.
[3] J.C. Lotz, E.J. Cheal, W.C. Hayes, Stress distributions within the proximal femur during gait and falls: implications for osteoporotic fracture, Osteoporos. Int. 5 (1995) 252–261.
[4] P.M. Mayhew, C.D. Thomas, J.G. Clement, N. Loveridge, T.J. Beck, W. Bonfield, C.J. Burgoyne, J. Reeve, Relation between age, femoral neck cortical stability, and hip fracture risk, Lancet 366 (2005) 129–135.
[5] K.E. Poole, P.M. Mayhew, C.M. Rose, J.K. Brown, P.J. Bearcroft, N. Loveridge, J. Reeve, Changing structure of the femoral neck across the adult female lifespan, J. Bone Miner. Res. 25 (2010) 482–491.
[6] E. Verhulp, B. van Rietbergen, R. Huiskes, Load distribution in the healthy and osteoporotic human proximal femur during a fall to the side, Bone 42 (2008) 30–35.
[7] P.M. de Bakker, S.L. Manske, V. Ebacher, T.R. Oxland, P.A. Cripton, P. Guy, During sideways falls proximal femur fractures initiate in the superolateral cortex: evidence from high-speed video of simulated fractures, J. Biomech. 42 (2009) 1917–1925.
[8] R.D. Carpenter, G.S. Beaupré, T.F. Lang, E.S. Orwoll, D.R. Carter, New QCT analysis approach shows the importance of fall orientation on femoral neck strength, J. Bone Miner. Res. 20 (2005) 1533–1542.
[9] C.M. Ford, T.M. Keaveny, W.C. Hayes, The effect of impact direction on the structural capacity of the proximal femur during falls, J. Bone Miner. Res. 11 (1996) 377–383.
[10] T.P. Pinilla, K.C. Boardman, M.L. Bouxsein, E.R. Myers, W.C. Hayes, Impact direction from a fall influences the failure load of the proximal femur as much as age-related bone loss, Calcif. Tissue Int. 58 (1996) 231–235.
[11] J.H. Keyak, S.A. Rossi, K.A. Jones, H.B. Skinner, Prediction of femoral fracture load using automated finite element modeling, J. Biomech. 31 (1997) 125–133.
[12] J.H. Keyak, H.B. Skinner, J.A. Fleming, Effect of force direction on femoral fracture load for two types of loading conditions, J. Orthop. Res. 19 (2001) 539–544.
[13] M. Bessho, I. Ohnishi, T. Matsumoto, S. Ohashi, J. Matsuyama, K. Tobita, M. Kaneko, K. Nakamura, Prediction of proximal femur strength using a CT-based nonlinear finite element method: differences in predicted fracture load and site with changing load and boundary conditions, Bone 45 (2009) 226–231.
[14] J.A. Grisso, J.L. Kelsey, B.L. Strom, G.Y. Chiu, G. Maislin, L.A. O'Brien, S. Hoffman, F. Kaplan, Risk factors for falls as a cause of hip fracture in women. The Northeast Hip Fracture Study Group, N. Engl. J. Med. 324 (1991) 1326–1331.
[15] J. Parkkari, P. Kannus, M. Palvanen, A. Natri, J. Vainio, H. Aho, I. Vuori, M. Järvinen, Majority of hip fractures occur as a result of a fall and impact on the greater trochanter of the femur: a prospective controlled hip fracture study with 206 consecutive patients, Calcif. Tissue Int. 65 (1999) 183–187.
[16] R. Nikander, H. Sievänen, A. Heinonen, P. Kannus, Femoral neck structure in adult female athletes subjected to different loading modalities, J. Bone Miner. Res. 20 (2005) 520–528.
[17] R. Nikander, P. Kannus, P. Dastidar, M. Hannula, L. Harrison, T. Cervinka, N.G. Narra, R. Aktour, T. Arola, H. Eskola, S. Soimakallio, A. Heinonen, J. Hyttinen, H. Sievänen, Targeted exercises against hip fragility, Osteoporos. Int. 20 (2009) 1321–1328.

[18] J.H. Keyak, S.A. Rossi, K.A. Jones, C.M. Les, H.B. Skinner, Prediction of fracture location in the proximal femur using finite element models, Med. Eng. Phys. 23 (2001) 657–664.
[19] F. Taddei, L. Cristofolini, S. Martelli, H.S. Gill, M. Viceconti, Subject-specific finite element models of long bones: an in vitro evaluation of the overall accuracy, J. Biomech. 39 (2006) 2457–2467.
[20] M. Bessho, I. Ohnishi, J. Matsuyama, T. Matsumoto, K. Imai, K. Nakamura, Prediction of strength and strain of the proximal femur by a CT-based finite element method, J. Biomech. 40 (2007) 1745–1753.
[21] Z. Yosibash, N. Trabelsi, C. Milgrom, Reliable simulations of the human proximal femur by high-order finite element analysis validated by experimental observations, J. Biomech. 40 (2007) 3688–3699.
[22] E. Schileo, L. Balistreri, L. Grassi, L. Cristofolini, F. Taddei, To what extent can linear finite element models of human femora predict failure under stance and fall loading configurations? J. Biomech. 47 (2014) 3531–3538.
[23] R. Nikander, H. Sievänen, K. Uusi-Rasi, A. Heinonen, P. Kannus, Loading modalities and bone structures at nonweight-bearing upper extremity and weight-bearing lower extremity: a pQCT study of adult female athletes, Bone 39 (2006) 886–894.
[24] P.A. Yushkevich, J. Piven, H.C. Hazlett, R.G. Smith, S. Ho, J.C. Gee, G. Gerig, User-guided 3D active contour segmentation of anatomical structures: significantly improved efficiency and reliability, NeuroImage 31 (2006) 1116–1128.
[25] H. Sievänen, T. Karstila, P. Apuli, P. Kannus, Magnetic resonance imaging of the femoral neck cortex, Acta Radiol. 48 (2007) 308–314.
[26] Q. Fang, D.A. Boas, Tetrahedral mesh generation from volumetric binary and grayscale images, Proc. - 2009 IEEE Int. Symp. Biomed. Imaging From Nano to Macro, ISBI 2009IEEE 2009, pp. 1142–1145.
[27] G. Taubin, Curve and surface smoothing without shrinkageProc. - 1999 IEEE Int. Conf. Comput. Vis. 1995, pp. 852–857.
[28] B. Helgason, S. Gilchrist, O. Ariza, J.D. Chak, G. Zheng, R.P. Widmer, S.J. Ferguson, P. Guy, P.A. Cripton, Development of a balanced experimental-computational approach to understanding the mechanics of proximal femur fractures, Med. Eng. Phys. 36 (2014) 793–799.
[29] M. Lengsfeld, J. Kaminsky, B. Merz, R.P. Franke, Sensitivity of femoral strain pattern analyses to resultant and muscle forces at the hip joint, Med. Eng. Phys. 18 (1996) 70–78.
[30] G.N. Duda, M. Heller, J. Albinger, O. Schulz, E. Schneider, L. Claes, Influence of muscle forces on femoral strain distribution, J. Biomech. 31 (1998) 841–846.
[31] K. Polgár, H.S. Gill, M. Viceconti, D.W. Murray, J.J. O'Connor, Strain distribution within the human femur due to physiological and simplified loading: finite element analysis using the muscle standardized femur model, Proc. Inst. Mech. Eng. H. 217 (2003) 173–189.
[32] A.C. Courtney, E.F. Wachtel, E.R. Myers, W.C. Hayes, Effects of loading rate on strength of the proximal femur, Calcif. Tissue Int. 55 (1994) 53–58.
[33] A.C. Courtney, E.F. Wachtel, E.R. Myers, W.C. Hayes, Age-related reductions in the strength of the femur tested in a fall-loading configuration, J. Bone Joint Surg. Am. 77 (1995) 387–395.
[34] M.L. Bouxsein, P. Szulc, F. Munoz, E. Thrall, E. Sornay-Rendu, P.D. Delmas, Contribution of trochanteric soft tissues to fall force estimates, the factor of risk, and prediction of hip fracture risk, J. Bone Miner. Res. 22 (2007) 825–831.
[35] O. Ariza, S. Gilchrist, R.P. Widmer, P. Guy, S.J. Ferguson, P.A. Cripton, B. Helgason, Comparison of explicit finite element and mechanical simulation of the proximal femur during dynamic drop-tower testing, J. Biomech. 48 (2015) 224–232.
[36] S.L. Manske, T. Liu-Ambrose, D.M. Cooper, S. Kontulainen, P. Guy, B.B. Forster, H.A. McKay, Cortical and trabecular bone in the femoral neck both contribute to proximal femur failure load prediction, Osteoporos. Int. 20 (2009) 445–453.
[37] C.D. Thomas, P.M. Mayhew, J. Power, K.E. Poole, N. Loveridge, J.G. Clement, C.J. Burgoyne, J. Reeve, Femoral neck trabecular bone: loss with ageing and role in preventing fracture, J. Bone Miner. Res. 24 (2009) 1808–1818.
[38] J.D. Wilson, W. Eardley, S. Odak, A. Jennings, To what degree is digital imaging reliable? Validation of femoral neck shaft angle measurement in the era of picture archiving and communication systems, Br. J. Radiol. 84 (2011) 375–379.
[39] N. Narra, R. Nikander, J. Viik, J. Hyttinen, H. Sievänen, Femoral neck cross-sectional geometry and exercise loading, Clin. Physiol. Funct. Imaging 33 (2013) 258–266.
[40] H. Sievänen, L. Józsa, I. Pap, M. Järvinen, T.A. Järvinen, P. Kannus, T.L. Järvinen, Fragile external phenotype of modern human proximal femur in comparison with medieval bone, J. Bone Miner. Res. 22 (2007) 537–543.
[41] D.M. Bramble, D.E. Lieberman, Endurance running and the evolution of *Homo*, Nature 432 (2004) 345–352.
[42] M.R. Ramey, K.R. Williams, Ground reaction forces in the triple jump, Int. J. Sport. Biomech. 1 (1985) 233–239.
[43] A. Heinonen, H. Sievänen, H. Kyröläinen, J. Perttunen, P. Kannus, Mineral mass, size, and estimated mechanical strength of triple jumpers' lower limb, Bone 29 (2001) 279–285.
[44] N. Smith, R. Dyson, L. Janaway, Ground reaction force measures when running in soccer boots and soccer training shoes on a natural turf surface, Sport. Eng. 7 (2004) 159–167.
[45] M.K. Dayakidis, K. Boudolos, Ground reaction force data in functional ankle instability during two cutting movements, Clin. Biomech. 21 (2006) 405–411.
[46] K. Ball, Loading and performance of the support leg in kicking, J. Sci. Med. Sport 16 (2013) 455–459.
[47] P.A. Swinton, R. Lloyd, J.W. Keogh, I. Agouris, A.D. Stewart, A biomechanical comparison of the traditional squat, powerlifting squat, and box squat, J. Strength Cond. Res. 26 (2012) 1805–1816.
[48] C.F. Munro, D.I. Miller, A.J. Fuglevand, Ground reaction forces in running: a reexamination, J. Biomech. 20 (1987) 147–155.
[49] S. Logan, I. Hunter, J.T. Hopkins, J.B. Feland, A.C. Parcell, Ground reaction force differences between running shoes, racing flats, and distance spikes in runners, J. Sport. Sci. Med. 9 (2010) 147–153.
[50] B. Kluitenberg, S.W. Bredeweg, S. Zijlstra, W. Zijlstra, I. Buist, Comparison of vertical ground reaction forces during overground and treadmill running. A validation study, BMC Musculoskelet. Disord. 13 (2012) 235.
[51] A.D. Lyttle, B.A. Blanksby, B.C. Elliott, D.G. Lloyd, Investigating kinetics in the freestyle flip turn push-off, J. Appl. Biomech. 15 (1999) 242–252.
[52] B.A. Blanksby, D.G. Gathercole, R.N. Marshall, Force plate and video analysis of the tumble turn by age-group swimmers, J. Swim. Res. 11 (1996) 40–45.
[53] P. Comfort, M. Allen, P. Graham-Smith, Comparisons of peak ground reaction force and rate of force development during variations of the power clean, J. Strength Cond. Res. 25 (2011) 1235–1239.
[54] P. Comfort, M. Allen, P. Graham-Smith, Kinetic comparisons during variations of the power clean, J. Strength Cond. Res. 25 (2011) 3269–3273.
[55] W. Baumann, V. Gross, K. Quade, P. Galbierz, A. Schvvirtz, The snatch technique of world class weightlifiers at the 1985 World Championships, Int. J. Sport Biomech. 4 (1988) 68–89.
[56] M.A. Lauder, J.P. Lake, Biomechanical comparison of unilateral and bilateral power snatch lifts, J. Strength Cond. Res. 22 (2008) 653–660.
[57] H. Haapasalo, P. Kannus, H. Sievänen, M. Pasanen, K. Uusi-Rasi, A. Heinonen, P. Oja, I. Vuori, Development of mass, density, and estimated mechanical characteristics of bones in Caucasian females, J. Bone Miner. Res. 11 (1996) 1751–1760.
[58] P. Kannus, H. Haapasalo, M. Sankelo, H. Sievänen, M. Pasanen, A. Heinonen, P. Oja, I. Vuori, Effect of starting age of physical activity on bone mass in the dominant arm of tennis and squash players, Ann. Intern. Med. 123 (1995) 27–31, http://dx.doi.org/10.7326/0003-4819-123-1-199507010-00003.
[59] M. Lorentzon, D. Mellström, C. Ohlsson, Association of amount of physical activity with cortical bone size and trabecular volumetric BMD in young adult men: the GOOD study, J. Bone Miner. Res. 20 (2005) 1936–1943.
[60] C.A. Boreham, H.A. McKay, Physical activity in childhood and bone health, Br. J. Sports Med. 45 (2011) 877–879.
[61] A. Nordström, C. Karlsson, F. Nyquist, T. Olsson, P. Nordström, M. Karlsson, Bone loss and fracture risk after reduced physical activity, J. Bone Miner. Res. 20 (2005) 202–207.
[62] B.R. Gomberg, P.K. Saha, F.W. Wehrli, Method for cortical bone structural analysis from magnetic resonance images, Acad. Radiol. 12 (2005) 1320–1332.
[63] A.G. Robling, A.B. Castillo, C.H. Turner, Biomechanical and molecular regulation of bone remodeling, Annu. Rev. Biomed. Eng. 8 (2006) 455–498.
[64] J.E. Koivumäki, J. Thevenot, P. Pulkkinen, V. Kuhn, T.M. Link, F. Eckstein, T. Jämsä, Cortical bone finite element models in the estimation of experimentally measured failure loads in the proximal femur, Bone 51 (2012) 737–740.
[65] G. Holzer, G. von Skrbensky, L.A. Holzer, W. Pichl, Hip fractures and the contribution of cortical versus trabecular bone to femoral neck strength, J. Bone Miner. Res. 24 (2009) 468–474.

PUBLICATION II

Impact loading history modulates hip fracture load and location: A finite element simulation study of the proximal femur in female athletes

Shinya Abe, Nathaniel Narra, Riku Nikander, Jari Hyttinen, Reijo Kouhia, and Harri Sievänen

Journal of Biomechanics. 2018 Jul;76:136-143
doi: 10.1016/j.jbiomech.2018.05.037

Journal of Biomechanics 76 (2018) 136–143

Contents lists available at ScienceDirect

Journal of Biomechanics

journal homepage: www.elsevier.com/locate/jbiomech
www.JBiomech.com

Impact loading history modulates hip fracture load and location: A finite element simulation study of the proximal femur in female athletes

Shinya Abe [a,*], Nathaniel Narra [b], Riku Nikander [c,d,e], Jari Hyttinen [b], Reijo Kouhia [a], Harri Sievänen [f,**]

[a] Laboratory of Civil Engineering, Tampere University of Technology, Tampere, Finland
[b] BioMediTech Institute and Faculty of Biomedical Sciences and Engineering, Tampere University of Technology, Tampere, Finland
[c] Gerontology Research Center, Faculty of Sports Sciences, University of Jyväskylä, Jyväskylä, Finland
[d] Central Hospital of Central Finland, Jyväskylä, Finland
[e] GeroCenter Foundation for Aging Research and Development, Jyväskylä, Finland
[f] The UKK Institute for Health Promotion Research, Tampere, Finland

ARTICLE INFO

Article history:
Accepted 30 May 2018

Keywords:
Bone strength
Finite element modeling
Exercise
Falling
Femoral neck

ABSTRACT

Sideways falls impose high stress on the thin superolateral cortical bone of the femoral neck, the region regarded as a fracture-prone region of the hip. Exercise training is a natural mode of mechanical loading to make bone more robust. Exercise-induced adaptation of cortical bone along the femoral neck has been previously demonstrated. However, it is unknown whether this adaption modulates hip fracture behavior. The purpose of this study was to investigate the influence of specific exercise loading history on fall-induced hip fracture behavior by estimating fracture load and location with proximal femur finite element (FE) models created from magnetic resonance images (MRI) of 111 women with distinct exercise histories: 91 athletes (aged 24.7 ± 6.1 years, >8 years competitive career) and 20 women as controls (aged 23.7 ± 3.8 years). The athletes were divided into five groups based on typical loading patterns of their sports: high-impact (H-I: 9 triple-jumpers and 10 high jumpers), odd-impact (O-I: 9 soccer and 10 squash players), high-magnitude (H-M: 17 power-lifters), repetitive-impact (R-I: 18 endurance runners), and repetitive non-impact (R-NI: 18 swimmers). Compared to the controls, the H-I, O-I, and R-I groups had significantly higher (11–26%, $p < 0.05$) fracture loads. Also, the fracture location in the H-I and O-I groups was significantly more proximal (7–10%) compared to the controls. These results suggest that an exercise loading history of high impacts, impacts from unusual directions, or repetitive impacts increases the fracture load and may lower the risk of fall-induced hip fracture.

1. Introduction

Cortical bone at the inferomedial side of the human femoral neck is thicker than at the superolateral side because of asymmetric loading in bipedal locomotion, which imposes higher compressive and smaller tensile stress at the inferomedial and superolateral cortices, respectively (Lotz et al., 1995; Mayhew et al., 2005). With aging, the amount of vigorous physical activity (PA) decreases, and PA mainly consists of less intensive walking (Husu et al., 2016). Decreased skeletal loading may accentuate thinning of the femoral neck cortex, and it has been observed that the cortical thickness at the posterior side of the superolateral region decreases fivefold from the age of 25 years to the age of 85 years (Poole et al., 2010). This site-specific cortical thinning is likely to contribute to hip fragility (Mayhew et al., 2005).

More than 90% of the hip fractures are caused by falls (Grisso et al., 1991; Parkkari et al., 1999; Yang et al., 2016). The superolateral cortex of the femoral neck is considered particularly vulnerable during a sideways fall, which imposes high impact force on the greater trochanter and unusually high compressive stress at the superolateral region (de Bakker et al., 2009; Verhulp et al., 2008). Peak magnitude of this fall-induced stress can be four times greater than during normal gait (Lotz et al., 1995). Consistent evidence indicates that hip fractures mostly initiate in this region (Carpenter et al., 2005; de Bakker et al., 2009).

General PA and specific exercise training are natural modes of mechanical loading of bones. Since bone structure adapts to habitual mechanical loading (Frost, 2003; Ruff et al., 2006), effective

* Corresponding author at: Laboratory of Civil Engineering, Tampere University of Technology, Tekniikankatu 12, FI-33720 Tampere, Finland.
** Corresponding author at: The UKK Institute for Health Promotion Research, Kaupinpuistonkatu 1, FI-33500 Tampere, Finland.
E-mail addresses: shinya.abe@tut.fi (S. Abe), harri.sievanen@uta.fi (H. Sievänen).

https://doi.org/10.1016/j.jbiomech.2018.05.037
0021-9290/

loading modes can make bone stronger. Previously, we showed that the femoral neck cortical bone in female athletes with a history of high impact loading and/or impact loading from unusual directions was thicker also in the superolateral region (Nikander et al., 2009). Moreover, finite element (FE) models created from the same proximal femur data (Abe et al., 2016) indicated that the history of not only aforementioned impact exercises but also repetitive impacts generated by endurance running were associated with lower fall-induced stress at the superolateral cortex. However, whether this apparent structural adaptation translates into a reduced hip fracture risk is not yet known, as stress alone is not sufficient to infer the risk. Evaluating fracture loads, as suggested by numerous studies, is essential for evaluating fracture risk (Bessho et al., 2009; Dragomir-Daescu et al., 2011; Keyak et al., 1998; Koivumäki et al., 2012; Schileo et al., 2014). Therefore, the objective of the present study was to elaborate whether specific long-term exercise loading history can modulate fracture load and location that may eventually lower hip fracture risk.

2. Materials and methods

2.1. Participants

Proximal femur magnetic resonance images (MRI) of 91 adult female athletes (aged 24.7 ± 6.1 years), competing actively at national or international level, and 20 habitually active female control participants (aged 23.7 ± 3.8 years) were obtained from our previous study (Nikander et al., 2009). According to our standard exercise classification scheme (Nikander et al., 2006, 2005), the athletes were divided into five different groups based on the typical loading patterns of their sports: high-impact (H-I) (9 triple- and 10 high-jumpers); odd-impact (O-I) (9 soccer and 10 squash players); high-magnitude (H-M) (17 power-lifters); repetitive-impact (R-I) (18 endurance runners); and the repetitive, non-impact group (R-NI) (18 swimmers). The control participants did recreational exercise 2–3 times a week, but had never taken part in any sports at the competitive level. The study protocol was approved by the Ethics Committee of the Pirkanmaa Hospital District, and written informed consent was obtained from each participant.

Body height and weight (BW) of the participants were measured in light indoor clothing without shoes with standard methods. Questionnaires were completed by all participants in order to obtain their training history including weekly sport-specific training hours and the number of training sessions during at least the five preceding years (Nikander et al., 2009).

2.2. MRI scanning procedure

Participants' hip regions were scanned using a 1.5-T MRI system (Avanto Syngo MR B15, Siemens, Erlangen, Germany). The imaging sequence was a standardized axial T1-weighted gradient echo volumetric interpolated breath-hold (VIBE)-examination with the following parameters: FOV 35 × 26 cm, TR 15.3 ms, TE 3.32 ms, slice thickness 1 mm without gaps, echo train length = 1, flip angle = 1 0°, matrix 384 × 288, the in-plane resolution (pixel size) 0.9 mm × 0.9 mm. Sagittal, axial, and coronal images of the hip region of the dominant side were scanned with two half-Fourier acquisition single-shot turbo spin-echo localization series. The scanned body volume covered the proximal femur from the top of the femoral head to the subtrochanteric level of the femoral diaphysis. The reconstructed imaging plane was adjusted so that the cross-sectional plane of the femoral neck was perpendicular to the femoral neck axis (Nikander et al., 2009).

2.3. FE model construction

The proximal femur FE models from the MRI data of all 111 participants were created previously (Abe et al., 2016). In short, the MRI data were first manually segmented by delineating the periosteal and endocortical boundaries of cortical bone along the proximal femur with in vivo precision of about 1% (Sievänen et al., 2007b). Then, the obtained femur geometries were converted into a volume mesh and its surface was smoothed using a method by Taubin (1995) prior to the generation of 3D solid bodies in SolidWorks (SolidWorks Corp., Waltham, MA, USA). The resulting proximal femur geometry consisted of individually segmented cortical and trabecular bone volumes, the latter denoting the volume within the endocortical bone boundary. Trabecular bone is a non-homogeneous porous structure, but in this study, it was modeled as a non-porous homogeneous material. This was because pertinent information could not be obtained from the present MRI data. Therefore, the present study exclusively assessed the influence of the cortical geometry on the hip fracture behavior, whereas the potential influence of inhomogeneous trabecular bone distribution was not addressed. The individual 3D solid body geometries of the proximal femur were then imported into ANSYS (ANSYS Inc., Houston, PA, USA) for the FE meshing and analysis.

To simulate a sideways fall, the femoral shaft was tilted at 10° with respect to the ground and the femoral neck was internally rotated by 15° (Fig. 1) (Courtney et al., 1994). Similar boundary conditions (BC) used in previous studies (Helgason et al., 2014; Schileo et al., 2014) were adopted in the present models (Fig. 1). The loading force and restraining BCs were applied through the femoral head- and trochanter-protecting PMMA caps, and an alu-

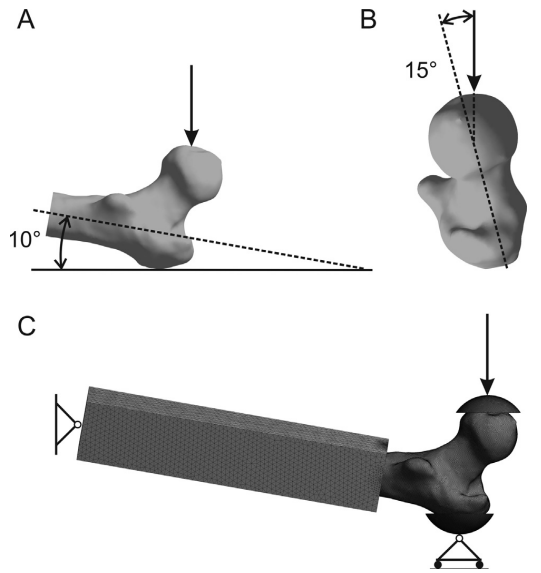

Fig. 1. Loading/falling angles (A & B) and boundary conditions of the FE model (C). The femoral shaft was tilted at 10° with respect to the ground (A) and the femoral neck was internally rotated by 15° (B). Force was applied to the whole upper face of the head-protecting PMMA cap, at a described angle, while the trochanter PMMA cap was restrained in the direction of the force (Schileo et al., 2014). A 200 mm long aluminum pot was placed at 15–20 mm below the most projected part of the lesser trochanter of each proximal femur. A hinge-type restraining BC was applied to the distal side of the aluminum pot. This allowed nodes at the hinge-axis to freely rotate in the quasi-frontal plane, while all other degrees of freedom were constrained (C). This figure was adopted from Abe et al. (2016).

minum distal pot. The force was applied to the femoral head through the cap at a defined angle. The trochanter PMMA cap was restrained in the direction of the force while a hinge-type restraining BC was applied to the distal side of the aluminum pot. A 10-noded tetrahedral finite element was used to mesh all components. For the entire proximal femur, the PMMA caps, and the boundary between the distal end of the modeled proximal femur bone and the distal pot, 1 mm element size was used while 4 mm element size was set for the rest of the distal pot. On average, each bone model comprised approximately 1,600,000 elements and 2,300,000 nodes. The bone tissue was modeled as a homogeneous isotropic, linear elastic material; cortical and trabecular bones were modeled separately. Young's moduli (E) of 17 GPa (Duda et al., 1998; Lengsfeld et al., 1996; Polgár et al., 2003), 1500 MPa (Duda et al., 1998; Polgár et al., 2003), 70 GPa (Schileo et al., 2014), and 2 GPa (Schileo et al., 2014) were applied to the cortical bone, trabecular bone, the aluminum distal pot, and the protecting PMMA caps, respectively. Poisson's ratio was assumed as 0.33 for all materials (Duda et al., 1998; Lengsfeld et al., 1996; Polgár et al., 2003).

2.4. Fracture load

For estimating the fracture load of each proximal femur, a simple maximum principal strain criterion (Schileo et al., 2014, 2008b) was adopted. First, surface nodal strains of the whole proximal femur and their nodal coordinates were obtained from the FE models. Each nodal strain was averaged with its neighboring nodal strains within a circle of 3 mm radius to remove local effects and to ensure the hypothesis of continuum media (Schileo et al., 2014; Verhulp et al., 2008). Then, principal strains were calculated for each node from the average nodal strain tensor. The fracture load was defined as the load when either one nodal maximum principal strain was greater than tensile yield limit (0.73%) or the absolute value of the minimum principal strain was greater than compressive yield limit (1.04%) (Bayraktar et al., 2004). Using the linearity of the model, the magnitude of load was increased until one nodal principal strain value exceeded the elastic limit. In addition, the fracture mode (by tension or compression) was also determined for each femur. Due to the use of linear FE models, the predicted fracture load in this study denotes the load at the onset of fracture similar to the previous studies (Nishiyama et al., 2013; Schileo et al., 2014; Verhulp et al., 2008).

2.5. Fracture location

Surface nodal coordinates obtained from the fracture load estimation were utilized to determine the fracture location. The fracture location was determined in two ways: (1) as a *polar angle* (in °) and (2) as a *relative axial location* (in %) (Fig. 2). The polar angle was defined as how far the fracture node was, in clockwise direction, from the most superior point (0°) of the femoral neck cross-section (Fig. 2B). Furthermore, this *polar angular location* was presented as octant-wise categories within 45° octant regions each representing the following anatomic segments of the given femoral neck cross-section: superior (S), superoposterior (SP), posterior (P), inferoposterior (IP), inferior (I), inferoanterior (IA), anterior (A), and superoanterior (SA) octants (Fig. 2C).

The *relative axial location* was defined as the relative location (in %) from the most proximal cross-section of the femoral neck along its axis to the distal cross-section where femoral neck meets the greater trochanter (Fig. 2D). The *relative axial location* was also categorized into either (1) cervical fracture if the fracture location was between the proximal (0%) and the distal (100%) cross-sections otherwise it was categorized as (2) trochanteric fracture (>100%). Furthermore, the cervical fracture was divided into three equally long macro-regions: subcapital (between 0% and 33.3%), transcervical (between 33.4% and 66.6%) and basicervical (between 66.7% and 100%) regions similarly to the previous study (Schileo et al., 2014) (Fig. 2D). MATLAB (MathWorks, Inc., Natick, MA, USA) was used to estimate the fracture load and location.

2.6. Statistical analysis

Statistical analyses were performed with SPSS 24.0 (IBM Corp., Armonk, NY, USA). Mean and SD of fracture load and locations were given as descriptive statistics. Differences in fracture load between each exercise group and the control group was estimated by analysis of variance (ANOVA) and analysis of covariance (ANCOVA) using body weight as a covariate. Logarithmic transformations of the fracture load was performed prior to both ANOVA and ANCOVA to control for the skewness of the data. Percentage differences of the fracture load between each exercise loading group and control group were calculated by taking anti-log of unadjusted and BW-adjusted mean fracture loads. Since fracture locations (the *polar angular* and *relative axial locations*) were not normally distributed, between-group differences were estimated by non-parametric Mann-Whitney *U* test. Exercise groups were not compared to each other. A p value of less than 0.05 was considered statistically significant.

3. Results

3.1. Descriptive data of participants

Age, body height, BW, sport-specific training hours/week, training sessions/week, and duration of competitive career of loading groups are shown in Table 1. Compared with control participants, athletes had more training hours and training sessions per week, besides their long history of competing career. Also, majority of athletes in the present study started their sport-specific training in adolescence or early adulthood (Table 1).

3.2. Fracture load

Table 2 shows unadjusted mean (SD) of the fracture load, and unadjusted and BW-adjusted mean percentage differences (95% CI) in the fracture loads between each exercise group and the control group. Fracture loads ranged from 2.1 kN to 4.4 kN. Fracture loads in the H-I, O-I, and R-I groups were significantly ($p < 0.05$) higher compared to the control group. Unadjusted mean differences of H-I, O-I, and R-I compared with the control group were 15%, 12%, and 14% respectively. Similarly, BW-adjusted mean differences of H-I, O-I, and R-I were 14%, 11%, and 26% respectively. Compression was the failure mode in all 111 cases.

3.3. Fracture location

Table 3 shows means (SD), and ranges of the *polar angular* and the *relative axial fracture locations*. Table 4 shows their anatomical regional locations. Fracture locations were also mapped in each group (Fig. 3). In general, the mean *polar angular location* among the loading groups ranged from 30 to 41° (Table 3). This angular span was in the superoposterior octant where the majority of simulated fractures (75 out of 111, 68%) were located (Table 4). There was no significant difference in the *polar angular location* observed between any of exercise and the control group. The mean *relative axial location* ranged from 87 to 98% (Table 3) corresponding to basicervical region (Table 4). Majority of simulated fractures (90 out of 111, 81%) were located in this region (Table 4). The *relative axial locations* in the H-I and O-I were significantly ($p < 0.05$) different (7% and 10% more proximal respectively) compared to the control group.

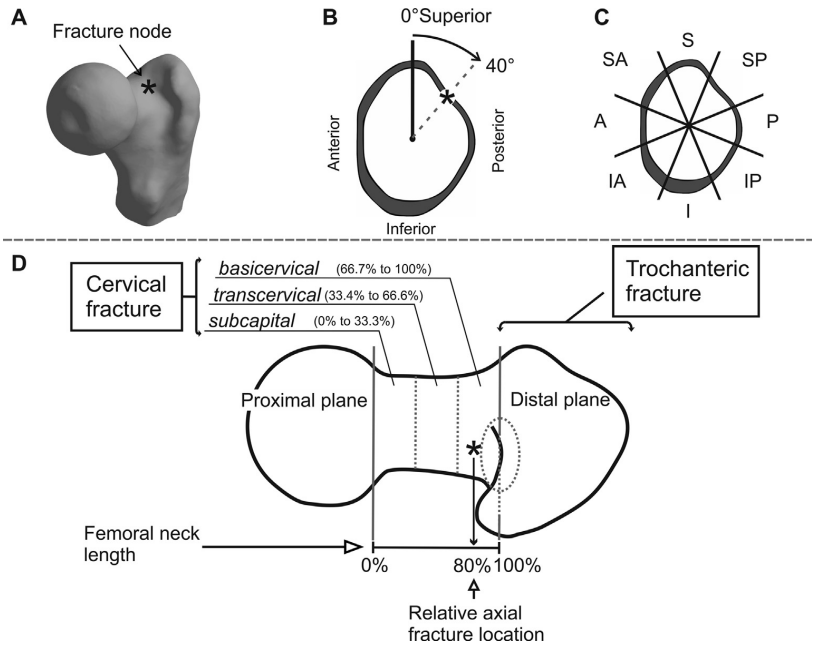

Fig. 2. Fracture location in the *polar angle* and in the *relative axial location*, and their categorizations. (A) An example of the fracture node (*) which principal strain value exceeds the elastic yield limit. (B) This describes the fracture location in the *polar angle* on the cross-section of the femoral neck. (C) This shows the division of the femoral neck cross-section into equal 45° octant regions. The example (40° in B) corresponds to SP octant in C. (D) This shows the *relative axial fracture location* and their categorization. The *relative axial location* was defined as the relative location (in %) to the femoral neck region defined by the proximal and distal planes perpendicular to the femoral neck axis. The proximal plane was defined as the plane at which the rate of change in cross-sectional area at junction from femoral head to femoral neck was the greatest while the distal plane was defined at which superior side of the femoral neck merges with the greater trochanter above the trochanteric fossa shown as a dashed-line ellipse in (D).

Table 1
Descriptive group characteristics (mean (SD)).

Group	N	Age (years)	Height (cm)	Weight (kg)	Sport-specific training hours/week	Training sessions/week	Competing career (years)
H-I	19	22.3 (4.1)	174 (6)	60.2 (5.4)	11.5 (2.3)	6.7 (1.4)	10.1 (3.4)
O-I	19	25.3 (6.7)	165 (8)	60.8 (8.3)	9.3 (2.7)	5.7 (1.4)	9.6 (4.8)
H-M	17	27.5 (6.3)	158 (3)	63.3 (13.2)	9.1 (2.7)	5.8 (2.0)	8.0 (4.7)
R-I	18	28.9 (5.6)	168 (5)	53.7 (3.4)	10.9 (3.4)	8.7 (2.1)	12.4 (6.7)
R-NI	18	19.7 (2.4)	173 (5)	65.1 (5.6)	19.9 (4.5)	11.4 (2.0)	9.1 (2.6)
Control	20	23.7 (3.8)	164 (5)	60.0 (7.4)	2.8 (0.9)	2.8 (1.0)	–

Table 2
Mean (SD) estimated fracture load, and unadjusted and BW-adjusted mean percentage differences (95% CI) in the fracture load between the exercise loading group and the control group.

Group	Mean (SD) in N	Unadjusted		Weight-adjusted	
		% diff	*p*	% diff	*p*
H-I	3228 (408)	14.6 (6.2 to 23.6)	**0.014**	14.3 (6.7 to 22.5)	**0.008**
O-I	3164 (447)	12.0 (3.5 to 21.3)	**0.045**	11.4 (3.2 to 20.3)	**0.049**
H-M	2960 (584)	3.9 (−5.6 to 14.4)	0.553	0.2 (−7.5 to 8.8)	0.948
R-I	3231 (538)	14.0 (4.4 to 24.4)	**0.034**	26.2 (16.2 to 36.9)	**<0.001**
R-NI	3068 (500)	8.3 (−0.5 to 18.0)	0.177	2.1 (−6.0 to 10.6)	0.741
Control	2849 (551)	–	–	–	–

Statistically significant *p* values ($p < 0.05$) based on ANOVA and ANCOVA are shown in bold.

4. Discussion

Fracture loads and locations at the proximal femur were estimated in this study using proximal femur FE models of 111 young adult women to evaluate whether the specific long-term exercise history modulated the fall-induced fracture behavior. In general, the magnitudes of observed fracture loads (2.1–4.4 kN) were within the range reported by Schileo et al. (2014). The present results also showed that the fracture initiated mostly at the superolateral region of the femoral neck, especially at the superoposte-

Table 3
Mean (SD) and ranges of the fracture location in the *polar angle* and the *relative axial location*, and *p*-values for the difference between the exercise loading group and the control group.

	Polar angle (°)			Relative axial location (%)		
Group	Mean (SD)	Range	*p*	Mean (SD)	Range	*p*
H-I	30.1 (14.0)	13.3–59.5°	0.214	90.1 (16.9)	65.6–130.0%	**0.038**
O-I	30.7 (15.3)	10.9–74.8°	0.224	86.8 (9.9)	50–96.2%	**<0.001**
H-M	41.0 (24.0)	14.8–86.4°	0.821	97.0 (5.5)	85.7–104.5%	0.798
R-I	36.5 (19.8)	7.0–81.4°	0.828	98.0 (10.8)	77.8–119.0%	0.919
R-NI	35.4 (13.0)	17.7–68.5°	0.965	92.7 (14.2)	69.2–116.7%	0.317
Control	35.6 (13.7)	15.6–72.3°	–	97.0 (8.3)	84.0–122.7%	–

Statistically significant *p* values ($p < 0.05$) based on Mann-Whitney U tests are shown in bold.

Table 4
Anatomical regional fracture location in different groups.

		Polar angular location			*Relative axial location*			
Group	N	Superior	Superoposterior	Posterior	Cervical			Trochanteric
					Subcapital	Transcervical	Basicervical	
H-I	19	6	13	0	0	1	15	3
O-I	19	6	12	1	0	1	18	0
H-M	17	4	9	4	0	0	14	3
R-I	18	4	12	2	0	0	13	5
R-NI	18	4	13	1	0	0	13	5
Control	20	3	16	1	0	0	17	3

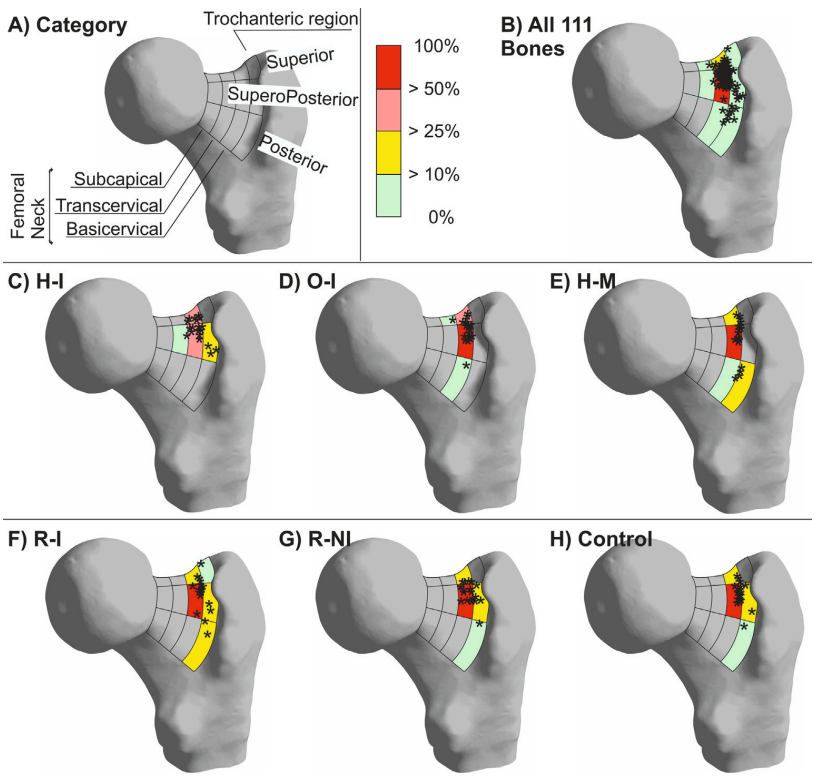

Fig. 3. Fracture location map. (A) This describes corresponding regions in the octants and in the axial location either cervical (subcapital, transcervical, and basicervical) and trochanteric region. (B) All 111 proximal femurs' fracture locations were mapped with *s. Different colors indicate proportion of the number of fracture in a region to the total number of fractures. C, D, E, F, G, and H are mapped fracture locations in H-I, O-I, H-M, R-I, R-NI, and control groups, respectively.

rior octant of the basicervical region (Table 4 and Fig. 3). This was in close agreement with previous experimental and modeling studies (Carpenter et al., 2005; de Bakker et al., 2009; Dragomir-Daescu et al., 2011; Lotz et al., 1995; Nawathe et al., 2015; Schileo et al., 2014; Verhulp et al., 2008). A particularly important finding in the present study was that the mean fracture loads in the H-I, O-I, and R-I groups were significantly higher (11–26%) compared to the control group. This indicates that exercise loading history comprising high vertical impacts, impacts from unusual directions, or a great number of repetitive impacts during adolescence and early adulthood may contribute to the reduced hip fracture risk.

The present observations in the H-I, O-I, and R-I groups are most likely attributed to the exercise-induced adaptation of the femoral neck cortical bone: through regional cortical thickening in the H-I and O-I groups, and different femoral neck geometry in the R-I group. Regional cortical thickening was evident at the inferior, anterior, and posterior quadrants of the femoral neck in the H-I group; and at the anterior, posterior, and superior quadrants in the O-I group (Nikander et al., 2009). In contrast, such a regional cortical thickening was not found in the R-I group (Nikander et al, 2009) whereas the geometric shape of the femoral neck cross-section was more circular in this group (Narra et al., 2013). A round shape of the femoral neck cross-section is an important geometric factor contributing to its strength (Bryan et al., 2009). Compared to an oval-shaped bone, a circular bone is mechanically more robust regardless of the loading direction. Moreover, a circular femoral neck cross-section, typically observed among physically more active medieval people, were estimated to experience 1.3–1.5 times less fall-induced stress compared to a more oval-shaped cross-section typical in present-day, habitually more sedentary people (Sievänen et al., 2007a). The BW-adjusted 26% benefit in fracture load observed in the present R-I group is fully consistent with this estimation.

Another notable finding was that the *relative axial fracture locations* in the H-I and O-I groups were slightly but significantly more proximal (along the neck axis) compared to the control group while the R-I group did not differ from the controls. This shift may be due to the regionally thicker cortical bone in the typical fracture-prone region which may transfer the peak bending stresses towards the narrower femoral neck (mid neck). This further indicates that higher fracture load results in the H-I and O-I groups might be due to the regional cortical thickening while the finding in the R-I group was due to the more circular femoral neck cross-section.

Based on the bone remodeling theory (Huiskes et al., 1987), new bone formation occurs when the loading induced strain energy exceeds certain homeostatic values by 75% (Kerner et al., 1999). The distribution of strain energy on the femoral neck during 15 different exercise types (long jump, vertical jump, walking, stair walking, squat with and without weight, and more) have been evaluated using both FE and musculoskeletal modeling (Kłodowski et al., 2011; Martelli et al., 2014). Martelli et al. (2014) reported that the H-I exercise (one-legged long jump) caused substantially high strain energy at femoral neck exceeding homeostatic value by about 500%. Elaborating the loading characteristics of the five distinct exercise types assessed in this study may explain why no beneficial results were observed in the H-M and R-NI groups despite high loading magnitudes or volume of training. Combination of moderate-to-high peak reaction forces and high rate of loading rate due to the ground impacts seems essential for the beneficial structural adaptation of the femoral neck cortical bone. The peak reaction forces and the estimated impact rates (BW s^{-1}) are 12–20 times BW and 400–480 BW s^{-1} in the H-I loading (Heinonen et al., 2001; Ramey and Williams, 1985), and 2–3.5 times BW and 20–180 BW s^{-1} in the O-I and R-I loading (Ball, 2013; Dayakidis and Boudolos, 2006; Kluitenberg et al., 2012; Logan et al., 2010; Munro et al., 1987; Smith et al., 2004). In swimming, some impact loading may occur at the push-off phase of turning, but the peak reaction force and loading rate are considerably smaller (<1.5 times BW, and <10 BW s^{-1} respectively) (Blanksby et al., 1996; Lyttle et al., 1999). While the peak reaction forces in the H-M are comparable (2–3 times BW) to the O-I and R-I exercises, the loading rate remains essentially smaller (5–6 BW s^{-1}) (Swinton et al., 2012). Altogether, moderate-to-high reaction force alone seems inadequate but it needs to be delivered at high loading rate to attain beneficial structural adaption within the femoral neck cortical bone.

There are limitations in the present study. First, the pixel size (0.9 mm) of the original MRI data was almost twice larger compared to previous QCT-based FE modeling studies (Bessho et al., 2009; Dragomir-Daescu et al., 2011; Koivumäki et al., 2012; Nishiyama et al., 2013; Schileo et al., 2014). However, while the QCT provides higher resolution and data on bone apparent density (proxy of material property), MRI has been found adequately valid for cortical geometry (Gomberg et al., 2005; Sievänen et al., 2007b). Besides, exposing fertile young adult women to ionizing radiation from QCT for non-diagnostic purposes would have been ethically unacceptable.

Second, due to inability to measure bone apparent density data with MRI, it was not possible to assign inhomogeneous material properties in the present study. It is known that the proximal femur is almost completely filled with porous structure of the trabecular bone, which is usually modeled as an inhomogeneous density-based material in the FE model. Obviously, the use of inhomogeneous material properties for the trabecular bone may have enhanced the model accuracy to some extent. However, it has been found previously that a homogeneous FE-model resulted in only marginally less accurate stress predictions compared to the actual experimental stress than the inhomogeneous model (R^2 = 0.89 and 0.91 respectively) (Taddei et al., 2006). Also, Koivumäki et al. (2010) reported 85% agreement between the homogeneous models with the experimental fracture location. On the other hand, the comparison by Taddei et al. (2006) was based only on a single femur model and in the physiological conditions including walking and single leg stance, but not in the sideways falling situation. Thus, this calls for further investigation on the validity of applying homogeneous material properties in the sideways falling situation with a larger sample size. Because we employed fixed Young's moduli for cortical (17 GPa) and trabecular (1500 MPa) bone compartments and treated them as the homogeneous material, the present study was limited to evaluate only the influence of the cortical geometry on the fracture load during a fall. The sensitivity of our models to the variation of cortical and trabecular E values were also evaluated in the present study (Details of this sensitivity analysis and results are available in the Supplementary material). According to this sensitivity analysis, the error in between-group differences of unadjusted mean fracture load induced by the substantial variation of cortical and trabecular moduli was within 3%, which was clearly smaller than observed in the H-I, O-I and R-I groups (11–14%, Table 2). Therefore, our choice to employ homogeneous material properties can be considered adequate in terms of evaluating the influence of the cortical geometry on fracture load.

Third, the present FE models created from proximal femur MRI were not validated against mechanical testing unlike previous QCT-based FE modeling studies of cadaver bones (Bessho et al., 2009; Koivumäki et al., 2012; Schileo et al., 2014). Due to these aforementioned limitations, and to comply with validated QCT-based proximal femur FE modeling studies, we adopted similar BCs and loading conditions (Helgason et al., 2014; Schileo et al., 2014). Importantly, despite the MRI-related limitations, the range of fracture loads in the present study was completely in line with

the previously reported values of QCT-based FEM study (Schileo et al., 2014). However, proximal femora in their study were obtained from older people aged from 62 to 84 years, which casts some doubt on the fracture load range found in the present young physically active population where higher fracture loads could have been expected. Nicks et al. (2013) reported the femoral neck trabecular volumetric bone mineral density (vBMD) from 20 to 29 years old female was 0.268 g/cm^3. By converting this vBMD value to the Young's modulus using equations found in literature (Morgan et al., 2003; Schileo et al., 2014, 2008a), a Young's modulus of about 2600 MPa is yielded, which is much higher than 1500 MPa used in the present study. Thus, the present fracture load values in the young athletic population was likely underestimated. It was shown that the mean fracture load was increased by approximately 15% by changing the trabecular E value from 1500 MPa to 3000 MPa (Fig. A1 in Supplementary material). The effect of the variation of cortical and trabecular E values on the magnitude of fracture load was also evaluated in the sensitivity analysis (Details are available in Supplementary material). However, it is noted that the main focus of the present study was to evaluate the relative fracture load of the proximal femur between each exercise group and the control group. Considering the apparent fact that the athletic groups have higher bone density at the proximal femur than their nonathletic peers (Nikander et al, 2009), it is likely that between-group difference in fracture load could have been higher.

In conclusion, the present simulation study based on a large sample study of the proximal femora indicates that long-term exercise loading history of high vertical impacts, impacts from unusual directions, or a great number of repetitive impacts led to higher fracture load and altered fracture location, which may translate into lower risk to sustain a hip fracture as a result of a fall. As a clinical prospect, it can be speculated that the impact exercises provide natural mechanical loading to femoral neck for increasing or maintaining its strength against fall-induced impacts.

Conflict of interest

All authors state that they have no conflicts of interest.

Acknowledgements

The authors thank all study participants. This work was funded by Tampere University of Technology's (TUT) Graduate School; the Doctoral Education Council of Computing and Electrical Engineering of TUT; and Human Spare Parts project from the Finnish Funding Agency for Technology and Innovation (TEKES).

Appendix A. Supplementary material

Supplementary data associated with this article can be found, in the online version, at https://doi.org/10.1016/j.jbiomech.2018.05.037.

References

Abe, S., Narra, N., Nikander, R., Hyttinen, J., Kouhia, R., Sievänen, H., 2016. Exercise loading history and femoral neck strength in a sideways fall: a three-dimensional finite element modeling study. Bone 92, 9–17.

Ball, K., 2013. Loading and performance of the support leg in kicking. J. Sci. Med. Sport 16, 455–459.

Bayraktar, H.H., Morgan, E.F., Niebur, G.L., Morris, G.E., Wong, E.K., Keaveny, T.M., 2004. Comparison of the elastic and yield properties of human femoral trabecular and cortical bone tissue. J. Biomech. 37, 27–35.

Bessho, M., Ohnishi, I., Matsumoto, T., Ohashi, S., Matsuyama, J., Tobita, K., Kaneko, M., Nakamura, K., 2009. Prediction of proximal femur strength using a CT-based nonlinear finite element method: differences in predicted fracture load and site with changing load and boundary conditions. Bone 45, 226–231.

Blanksby, B.A., Gathercole, D.G., Marshall, R.N., 1996. Force plate and video analysis of the tumble turn by age-group swimmers. J. Swim. Res. 11, 40–45.

Bryan, R., Nair, P.B., Taylor, M., 2009. Use of a statistical model of the whole femur in a large scale, multi-model study of femoral neck fracture risk. J. Biomech. 42, 2171–2176.

Carpenter, R.D., Beaupré, G.S., Lang, T.F., Orwoll, E.S., Carter, D.R., 2005. New QCT analysis approach shows the importance of fall orientation on femoral neck strength. J. Bone Miner. Res. 20, 1533–1542.

Courtney, A.C., Wachtel, E.F., Myers, E.R., Hayes, W.C., 1994. Effects of loading rate on strength of the proximal femur. Calcif. Tissue Int. 55, 53–58.

Dayakidis, M.K., Boudolos, K., 2006. Ground reaction force data in functional ankle instability during two cutting movements. Clin. Biomech. 21, 405–411.

de Bakker, P.M., Manske, S.L., Ebacher, V., Oxland, T.R., Cripton, P.A., Guy, P., 2009. During sideways falls proximal femur fractures initiate in the superolateral cortex: evidence from high-speed video of simulated fractures. J. Biomech. 42, 1917–1925.

Dragomir-Daescu, D., Op Den Buijs, J., McEligot, S., Dai, Y., Entwistle, R.C., Salas, C., Melton, L.J., Bennet, K.E., Khosla, S., Amin, S., 2011. Robust QCT/FEA models of proximal femur stiffness and fracture load during a sideways fall on the hip. Ann. Biomed. Eng. 39, 742–755.

Duda, G.N., Heller, M., Albinger, J., Schulz, O., Schneider, E., Claes, L., 1998. Influence of muscle forces on femoral strain distribution. J. Biomech. 31, 841–846.

Frost, H.M., 2003. Bone's mechanostat: a 2003 update. Anat Rec. A. Discov. Mol. Cell Evol. Biol. 275, 1081–1101.

Gomberg, B.R., Saha, P.K., Wehrli, F.W., 2005. Method for cortical bone structural analysis from magnetic resonance images. Acad. Radiol. 12, 1320–1332.

Grisso, J.A., Kelsey, J.L., Strom, B.L., Chiu, G.Y., Maislin, G., O'Brien, L.A., Hoffman, S., Kaplan, F., 1991. Risk factors for falls as a cause of hip fracture in women. The northeast hip fracture study group. N. Engl. J. Med. 324, 1326–1331.

Heinonen, A., Sievänen, H., Kyröläinen, H., Perttunen, J., Kannus, P., 2001. Mineral mass, size, and estimated mechanical strength of triple jumpers' lower limb. Bone 29, 279–285.

Helgason, B., Gilchrist, S., Ariza, O., Chak, J.D., Zheng, G., Widmer, R.P., Ferguson, S.J., Guy, P., Cripton, P.A., 2014. Development of a balanced experimental-computational approach to understanding the mechanics of proximal femur fractures. Med. Eng. Phys. 36, 793–799.

Huiskes, R., Weinans, H., Grootenboer, H.J., Dalstra, M., Fudala, B., Slooff, T.J., 1987. Adaptive bone-remodeling theory applied to prosthetic-design analysis. J. Biomech. 20, 1135–1150.

Husu, P., Suni, J., Vähä-Ypyä, H., Sievänen, H., Tokola, K., Valkeinen, H., Mäki-Opas, T., Vasankari, T., 2016. Objectively measured sedentary behavior and physical activity in a sample of Finnish adults: a cross-sectional study. BMC Public Health 16, 920.

Kerner, J., Huiskes, R., van Lenthe, G.H., Weinans, H., van Rietbergen, B., Engh, C.A., Amis, A.A., 1999. Correlation between pre-operative periprosthetic bone density and post-operative bone loss in THA can be explained by strain-adaptive remodelling. J. Biomech. 32, 695–703.

Keyak, J.H., Rossi, S.A., Jones, K.A., Skinner, H.B., 1998. Prediction of femoral fracture load using automated finite element modeling. J. Biomech. 31, 125–133.

Kłodowski, A., Rantalainen, T., Mikkola, A., Heinonen, A., Sievänen, H., 2011. Flexible multibody approach in forward dynamic simulation of locomotive strains in human skeleton with flexible lower body bones. Multibody Syst. Dyn. 25, 395–409.

Kluitenberg, B., Bredeweg, S.W., Zijlstra, S., Zijlstra, W., Buist, I., 2012. Comparison of vertical ground reaction forces during overground and treadmill running. A validation study. BMC Musculoskelet. Disord. 13, 235.

Koivumäki, J.E.M., Thevenot, J., Pulkkinen, P., Kuhn, V., Link, T.M., Eckstein, F., Jämsä, T., 2012. Ct-based finite element models can be used to estimate experimentally measured failure loads in the proximal femur. Bone 50, 824–829.

Koivumäki, J.E.M., Thevenot, J., Pulkkinen, P., Salmi, J.A., Kuhn, V., Lochmüller, E.M., Link, T.M., Eckstein, F., Jämsä, T., 2010. Does femoral strain distribution coincide with the occurrence of cervical versus trochanteric hip fractures? An experimental finite element study. Med. Biol. Eng. Comput. 48, 711–717.

Lengsfeld, M., Kaminsky, J., Merz, B., Franke, R.P., 1996. Sensitivity of femoral strain pattern analyses to resultant and muscle forces at the hip joint. Med. Eng. Phys. 18, 70–78.

Logan, S., Hunter, I., Hopkins, J.T., Feland, J.B., Parcell, A.C., 2010. Ground reaction force differences between running shoes, racing flats, and distance spikes in runners. J. Sport. Sci. Med. 9, 147–153.

Lotz, J.C., Cheal, E.J., Hayes, W.C., 1995. Stress distributions within the proximal femur during gait and falls: implications for osteoporotic fracture. Osteoporos. Int. 5, 252–261.

Lyttle, A.D., Blanksby, B.A., Elliott, B.C., Lloyd, D.G., 1999. Investigating kinetics in the freestyle flip turn push-off. J. Appl. Biomech. 15, 242–252.

Martelli, S., Kersh, M.E., Schache, A.G., Pandy, M.G., 2014. Strain energy in the femoral neck during exercise. J. Biomech. 47, 1784–1791.

Mayhew, P.M., Thomas, C.D., Clement, J.G., Loveridge, N., Beck, T.J., Bonfield, W., Burgoyne, C.J., Reeve, J., 2005. Relation between age, femoral neck cortical stability, and hip fracture risk. Lancet 366, 129–135.

Morgan, E.F., Bayraktar, H.H., Keaveny, T.M., 2003. Trabecular bone modulus-density relationships depend on anatomic site. J. Biomech. 36, 897–904.

Munro, C.F., Miller, D.I., Fuglevand, A.J., 1987. Ground reaction forces in running: a reexamination. J. Biomech. 20, 147–155.

Narra, N., Nikander, R., Viik, J., Hyttinen, J., Sievänen, H., 2013. Femoral neck cross-sectional geometry and exercise loading. Clin. Physiol. Funct. Imaging 33, 258–266.

Nawathe, S., Nguyen, B.P., Barzanian, N., Akhlaghpour, H., Bouxsein, M.L., Keaveny, T.M., 2015. Cortical and trabecular load sharing in the human femoral neck. J. Biomech. 48, 816–822.
Nicks, K.M., Amin, S., Melton, L.J., Atkinson, E.J., McCready, L.K., Riggs, B.L., Engelke, K., Khosla, S., 2013. Three-dimensional structural analysis of the proximal femur in an age-stratified sample of women. Bone 55, 179–188.
Nikander, R., Kannus, P., Dastidar, P., Hannula, M., Harrison, L., Cervinka, T., Narra, N. G., Aktour, R., Arola, T., Eskola, H., Soimakallio, S., Heinonen, A., Hyttinen, J., Sievänen, H., 2009. Targeted exercises against hip fragility. Osteoporos. Int. 20, 1321–1328.
Nikander, R., Sievänen, H., Heinonen, A., Kannus, P., 2005. Femoral neck structure in adult female athletes subjected to different loading modalities. J. Bone Miner. Res. 20, 520–528.
Nikander, R., Sievänen, H., Uusi-Rasi, K., Heinonen, A., Kannus, P., 2006. Loading modalities and bone structures at nonweight-bearing upper extremity and weight-bearing lower extremity: a pQCT study of adult female athletes. Bone 39, 886–894.
Nishiyama, K.K., Gilchrist, S., Guy, P., Cripton, P., Boyd, S.K., 2013. Proximal femur bone strength estimated by a computationally fast finite element analysis in a sideways fall configuration. J. Biomech. 46, 1231–1236.
Parkkari, J., Kannus, P., Palvanen, M., Natri, A., Vainio, J., Aho, H., Vuori, I., Järvinen, M., 1999. Majority of hip fractures occur as a result of a fall and impact on the greater trochanter of the femur: a prospective controlled hip fracture study with 206 consecutive patients. Calcif. Tissue Int. 65, 183–187.
Polgár, K., Gill, H.S., Viceconti, M., Murray, D.W., O'Connor, J.J., 2003. Strain distribution within the human femur due to physiological and simplified loading: finite element analysis using the muscle standardized femur model. Proc. Inst. Mech. Eng. H. 217, 173–189.
Poole, K.E., Mayhew, P.M., Rose, C.M., Brown, J.K., Bearcroft, P.J., Loveridge, N., Reeve, J., 2010. Changing structure of the femoral neck across the adult female lifespan. J. Bone Miner. Res. 25, 482–491.
Ramey, M.R., Williams, K.R., 1985. Ground Reaction Forces in the Triple Jump. Int. J. Sport. Biomech. 1, 233–239.
Ruff, C., Holt, B., Trinkaus, E., 2006. Who's afraid of the big bad Wolff?: "Wolff's law" and bone functional adaptation. Am. J. Phys. Anthropol. 129, 484–498.
Schileo, E., Balistreri, L., Grassi, L., Cristofolini, L., Taddei, F., 2014. To what extent can linear finite element models of human femora predict failure under stance and fall loading configurations? J. Biomech. 47, 3531–3538.
Schileo, E., Dall'Ara, E., Taddei, F., Malandrino, A., Schotkamp, T., Baleani, M., Viceconti, M., 2008a. An accurate estimation of bone density improves the accuracy of subject-specific finite element models. J. Biomech. 41, 2483–2491.
Schileo, E., Taddei, F., Cristofolini, L., Viceconti, M., 2008b. Subject-specific finite element models implementing a maximum principal strain criterion are able to estimate failure risk and fracture location on human femurs tested in vitro. J. Biomech. 41, 356–367.
Sievänen, H., Józsa, L., Pap, I., Järvinen, M., Järvinen, T.A., Kannus, P., Järvinen, T.L., 2007a. Fragile external phenotype of modern human proximal femur in comparison with medieval bone. J. Bone Miner. Res. 22, 537–543.
Sievänen, H., Karstila, T., Apuli, P., Kannus, P., 2007b. Magnetic resonance imaging of the femoral neck cortex. Acta Radiol. 48, 308–314.
Smith, N., Dyson, R., Janaway, L., 2004. Ground reaction force measures when running in soccer boots and soccer training shoes on a natural turf surface. Sport. Eng. 7, 159–167.
Swinton, P.A., Lloyd, R., Keogh, J.W., Agouris, I., Stewart, A.D., 2012. A biomechanical comparison of the traditional squat, powerlifting squat, and box squat. J. Strength Cond. Res. 26, 1805–1816.
Taddei, F., Cristofolini, L., Martelli, S., Gill, H.S., Viceconti, M., 2006. Subject-specific finite element models of long bones: an in vitro evaluation of the overall accuracy. J. Biomech. 39, 2457–2467.
Taubin, G., 1995. Curve and surface smoothing without shrinkage. Proc. IEEE Int. Conf. Comput. Vis. 852–857.
Verhulp, E., van Rietbergen, B., Huiskes, R., 2008. Load distribution in the healthy and osteoporotic human proximal femur during a fall to the side. Bone 42, 30–35.
Yang, Y., Mackey, D.C., Liu-Ambrose, T., Feldman, F., Robinovitch, S.N., 2016. Risk factors for hip impact during real-life falls captured on video in long-term care. Osteoporos. Int. 27, 537–547.

PUBLICATION III

Effect of fall direction on the lower hip fracture risk in athletes with different loading histories: A finite element modeling study in multiple sideways fall configurations

Shinya Abe, Reijo Kouhia, Riku Nikander, Nathaniel Narra, Jari Hyttinen, and Harri Sievänen

Bone. 2022 May;158:116351
doi: 10.1016/j.bone.2022.116351

Bone 158 (2022) 116351

Contents lists available at ScienceDirect

Bone

journal homepage: www.elsevier.com/locate/bone

Full Length Article

Effect of fall direction on the lower hip fracture risk in athletes with different loading histories: A finite element modeling study in multiple sideways fall configurations

Shinya Abe [a,*], Reijo Kouhia [a], Riku Nikander [b,c], Nathaniel Narra [d,1], Jari Hyttinen [d], Harri Sievänen [e]

[a] Structural Mechanics, Faculty of Built Environment, Tampere University, Tampere, Finland
[b] Gerontology Research Center, Faculty of Sports Sciences, University of Jyväskylä, Jyväskylä, Finland
[c] Central Hospital of Central Finland, Jyväskylä, Finland
[d] BioMediTech Unit, Faculty of Medicine and Health Technology, Tampere University, Tampere, Finland
[e] The UKK Institute for Health Promotion Research, Tampere, Finland

ARTICLE INFO

Keywords:
Hip fracture
Bone strength
Fracture prevention
Exercise
Finite element modeling
Fall

ABSTRACT

Physical loading makes bones stronger through structural adaptation. Finding effective modes of exercise to improve proximal femur strength has the potential to decrease hip fracture risk. Previous proximal femur finite element (FE) modeling studies have indicated that the loading history comprising impact exercises is associated with substantially higher fracture load. However, those results were limited only to one specified fall direction. It remains thus unclear whether exercise-induced higher fracture load depends on the fall direction. To address this, using magnetic resonance images of proximal femora from 91 female athletes (mean age 24.7 years with >8 years competitive career) and their 20 non-athletic but physically active controls (mean age 23.7 years), proximal femur FE models were created in 12 different sideways fall configurations. The athletes were divided into five groups by typical loading patterns of their sports: high-impact (H-I: 9 triple- and 10 high-jumpers), odd-impact (O-I: 9 soccer and 10 squash players), high-magnitude (H-M: 17 powerlifters), repetitive-impact (R-I: 18 endurance runners), and repetitive non-impact (R-NI: 18 swimmers). Compared to the controls, the FE models showed that the H-I and R-I groups had significantly ($p < 0.05$) higher fracture loads, 11–17% and 22–28% respectively, in all fall directions while the O-I group had significantly 10–11% higher fracture loads in four fall directions. The H-M and R-NI groups did not show significant benefit in any direction. Also, the analyses of the minimum fall strength (MFS) among these multiple fall configurations confirmed significantly 15%, 11%, and 14% higher MFSs in these impact groups, respectively, compared to the controls. These results suggest that the lower hip fracture risk indicated by higher fracture loads in athletes engaged in high impact or repetitive impact sports is independent of fall direction whereas the lower fracture risk attributed to odd-impact exercise is more modest and specific to the fall direction. Moreover, in concordance with the literature, the present study also confirmed that the fracture risk increases if the impact is imposed on the more posterolateral aspect of the hip. The present results highlight the importance of engaging in the impact exercises to prevent hip fractures and call for retrospective studies to investigate whether specific impact exercise history in adolescence and young adulthood is also associated with lower incidence of hip fractures in later life.

1. Introduction

Bone structure and density, constituting its strength [1], adapt to prevalent mechanical loading [2,3]. Physical activity and exercise provide natural ways to apply mechanical loading to the bone. These activities largely contribute to bone strength by promoting bone formation in growth [4] and help maintain skeletal strength or slow down age-related bone loss with aging [5,6]. However, not all exercises are

* Corresponding author at: Structural Mechanics, Faculty of Built Environment, Tampere University, P.O.Box 600, FI-33014 Tampere, Finland.
E-mail address: shinya.abe@tuni.fi (S. Abe).
[1] Present address: Computing Sciences Unit, Faculty of Information Technology and Communication Sciences, Tampere University, Pori, Finland.

https://doi.org/10.1016/j.bone.2022.116351
Received 11 June 2021; Received in revised form 1 February 2022; Accepted 1 February 2022
Available online 4 February 2022

equally osteogenic and the effectiveness may vary between anatomical sites [7,8]. Animal experimental studies suggest that the effective loading types are dynamic and include sufficiently high-magnitude strains produced at high strain rate or frequencies [3,9]. For the proximal femur, finding effective exercises is highly important because of increasing social and economic burden caused by hip fractures.

Hip fracture is a major public health problem leading to high rates of disability, morbidity, and mortality in the elderly population and huge financial burden to societies [10]. Over 90% of hip fractures are caused by falls [11,12]. A typical sideways fall imposes a high impact force on the greater trochanter resulting in unusually high compressive loading on the superolateral cortex of the femoral neck [13–16], where the bone structure is inherently fragile due to substantial age-related cortical thinning [17–20]. Hence, if a specific type of exercise can increase or maintain bone strength, hip fracture risk may be decreased through this exercise. There is convincing epidemiological evidence that physical activity is associated with lower hip fracture risk in a dose-response manner [21,22]. Lower fracture risk is also confirmed in a meta-analysis of exercise randomized controlled trials (RCT) [23].

Comparing the bones between athletes and non-athletic people provides a unique opportunity to explore long-term adaptation of bones to specific exercise loading. Such studies based on dual-energy X-ray absorptiometry (DXA) have found that young female athletes with a history of high-impact (e.g., jumps generating high ground reaction forces) and/or odd-impact exercise (e.g., generating ground impact from unusual directions common in ball games like football, tennis, and squash) had greater areal bone mineral density (aBMD), bone mineral content, cross-sectional area, and section modulus at the femoral neck compared to non-athletic female controls [24–28]. Our previous study based on magnetic resonance imaging (MRI) [29] has shown that the cortical bone around the femoral neck cross-section was distributed differently in athletes representing different sports: long-term high-impact and odd-impact exercises were associated with ~20% thicker cortical bone around the femoral neck including the vulnerable superolateral region. Subsequently, we have created proximal femur finite element (FE) models utilizing the same MRI data in a sideways fall configuration to examine whether the exercise-induced benefits at the athletes' femoral neck could translate into reduced fracture risk [30,31]. It was found that the proximal femur subjected to not only high-impact and odd-impact exercises, but also repetitive impact loading (e.g., endurance running) had significantly higher fracture loads suggesting the lower fall-induced fracture risk compared to the controls [30,31]. However, in these previous studies, our FE analyses were limited only to a single sideways fall direction. Since the athletes' bones are adapted to long-term exercise loading characterized by specific magnitude, rate, frequency, and direction, it remains unclear whether the exercise-induced higher fracture load is specific to only certain fall directions.

Previous experimental or FE modeling studies of multiple fall configurations have confirmed the following points: 1) fracture loads vary depending on the fall directions [32–36]; 2) fall-induced strain distributions within the loaded bone structure differ depending on the fall directions [14,37]; and 3) the simulation of multiple fall configurations is essential for evaluating the ability of FE-derived hip strength to predict the actual hip fracture occurrence in clinical applications [34–36,38–40]. However, to the present authors' knowledge, no study so far has addressed whether the exercise-induced gains in the proximal femur strength persist regardless of the fall direction or whether they are fall-direction specific. Furthermore, since falling is an unpredictable event, it is difficult to predict its direction and the weakest fall orientation is likely femur-specific. Therefore, a concept of a minimum fall strength (MFS) among the multiple fall conditions, indicating the lowest fracture load, has been recently proposed as a more advantageous variable to predict the hip fracture risk [35,40]. In fact, Falcinelli et al. [35] and Qasim et al. [40] reported that MFS can identify the actual hip fracture cases more accurately than the fracture load in a single specific fall direction or proximal femur aBMD.

The present study was therefore undertaken to expand our previous FE studies of the proximal femur in young adult female athletes and their controls [30,31] by simulating multiple sideways fall configurations. The primary objective was to evaluate whether and how the high femoral strength attributed to the specific exercise loading history depended on the fall direction. The secondary objective of the present study was to investigate whether the minimum fall strength among the multiple fall configurations differed between the exercise loading groups and their controls.

2. Materials and methods

2.1. Study participants

Proximal femur MRI data of 91 adult female athletes (aged 24.7 ± 6.1 years), competing actively at national or international level, and 20 habitually active female controls (aged 23.7 ± 3.8 years) were obtained from our previous study [29]. According to our standard exercise classification scheme [24,41], the athletes were divided into five different groups based on the typical loading patterns of their sports: high-impact (H-I) (9 triple- and 10 high-jumpers); odd-impact (O-I) (9 soccer and 10 squash players); high-magnitude (H-M) (17 powerlifters); repetitive-impact (R-I) (18 endurance runners); and the repetitive, non-impact group (R-NI) (18 swimmers). The controls indulged in recreational exercise 2–3 times a week but had never taken part in any sport at a competitive level. The study protocol was approved by the Ethics Committee of the Pirkanmaa Hospital District, and written informed consent was obtained from each participant.

Body height and weight (BW) were measured in light indoor clothing without shoes with standard methods. The body fat-% and lean body mass (LM) were measured with DXA (GE Lunar Prodigy Advance, Madison, WI, USA). Questionnaires were completed by all participants to obtain their training history including weekly sport-specific training hours and the number of training sessions during at least five preceding years [29].

2.2. MRI scanning procedure

Participants' hip regions were scanned using 1.5-T MRI system (Avanto Syngo MR B15, Siemens, Erlangen, Germany). The scanned hip region volume covered the proximal femur from the top of the femoral head to the subtrochanteric level of the femoral diaphysis. The imaging sequence was a standardized axial T1-weighted gradient echo volumetric interpolated breath-hold (VIBE)-examination with the following parameters: FOV 35 × 26 cm, TR 15.3 ms, TE 3.32 ms, in-plane resolution (pixel size) 0.9 mm × 0.9 mm, slice thickness 1 mm without gaps, echo train length = 1, flip angle = 10°, matrix 384 × 288. With two half-Fourier acquisition single-shot turbo spin-echo localization series, sagittal, axial, and coronal images of the hip region of the dominant side were scanned. The reconstructed imaging plane was adjusted so that the cross-sectional plane of the femoral neck was perpendicular to the femoral neck axis [29].

2.3. FE modeling and multiple sideways fall simulation

The procedure for creating the proximal femur FE models from the MRI data is described in detail elsewhere [30,31]. In short, the proximal femur MRI data were first manually segmented by delineating the periosteal and endocortical boundaries of cortical bone [42]. For the present study, the effect of segmentation error on the estimated fracture load was evaluated by re-segmenting MRI data from 12 randomly selected proximal femora, two from each group. Root-mean-square coefficient of variation (RMS-CV) and mean CV were calculated as indices of intra-operator reproducibility. The present 2.3% RMS-CV was comparable to RMS-CV of 1.9–3.6% for duplicate scans reported elsewhere [43,44]. In these two studies, the in-plane image resolution was similar

to the present study. The present 0.9% mean CV was higher than the 0.23% CV for the yield strength in a recent MRI based study [45]. This difference was likely due to ~4 times higher in-plane image resolution (0.234 mm × 0.234 mm) compared to ours (0.9 mm × 0.9 mm). Nonetheless, the present re-segmentation error was considered marginal to evaluate the expectedly much higher between-group differences in the fracture load.

After the segmention, the proximal femur geometries were converted into a volume mesh, which surface was smoothed using a method by Taubin [46]. Then, the 3D solid bodies of the proximal femur were created in SolidWorks (SolidWorks Corp., Waltham, MA, USA) before importing them into ANSYS (ANSYS Inc., Houston, PA, USA) for FE meshing and analysis.

The cortical and trabecular bone tissues in the proximal femur were modeled as homogeneous isotropic, linear elastic materials with Young's moduli of 17 GPa [47–49] and 1500 MPa [47,49], respectively. Poisson's ratio was assumed as 0.33 for all materials [47–49]. Similar cortical modulus (~15–20 GPa) was also reported for the adult population aged 22–61 years [50] and thus the choice of 17GPa was considered appropriate for the present study. As regards the trabecular modulus, Sylvester and Kramer [51] compared recently their homogeneous proximal femur FE models to the experimental data of Cristofolini et al. [52] and concluded that the modulus of the entire trabecular compartment of the proximal femur likely varies between 500 MPa and 1500 MPa.

A total of 12 different sideways fall configurations were created for each of the 111 proximal femur FE models by increasing the hip adduction angle α (an angle between the femoral shaft and the ground) in steps of 10° (0°, 10°, 20°, and 30°) and the internal rotation angle β of the femoral neck in steps of 15° (0°, 15°, and 30°) (Fig. 1), similar to previous studies [14,35,37,40]. Note that each fall direction is represented by a α–β pair henceforth (e.g., 10°–15°: $\alpha = 10°$ and $\beta = 15°$).

Boundary conditions simulating the complex loading and constraining conditions in the experimental sideways fall setting [53] were used in the present study (Fig. 2). The loading force and restraining conditions were applied through polymethyl methacrylate (PMMA) caps and an aluminum distal pot. All materials were modeled with 10-noded tetrahedral finite elements and a 2 mm element size was used for the entire proximal femur, the PMMA caps, and the boundary between the distal end of the proximal femur bone and the distal pot. The convergence analysis was conducted with four different element sizes (4 mm, 3 mm, 2 mm, and 1 mm) in the FE model (in 10°–15°) using 30 randomly selected proximal femora, five from each group. The converged solution was obtained by extrapolating the fracture loads from these element-sized FE models. Compared to the converged solution, the mean absolute percentage error in the fracture load for 4 mm, 3 mm, 2 mm, and 1 mm element-sized FE models were 5.5%, 4.7%, 2.9%, and 2.2%, respectively. Furthermore, the absolute errors in the relative difference in bone strength (Section 2.4) were 3.6%, 4.1%, 1.5%, and 1.6%, respectively. The 2 mm element size was considered acceptable, as the estimated errors remained consistently below 3%. Fracture load was estimated using a simple maximum principal strain criterion [53,54], described in detail elsewhere [31,53]. MATLAB (MathWorks, Inc., Natick, MA, USA) was used to estimate the fracture load. MFS (minimum fall strength) was defined as the lowest fracture load among the 12 different fall configurations in each proximal femur [35,36,40].

2.4. Statistical analysis

Statistical analyses were performed using SPSS 25.0 (IBM Corp., Armonk NY, USA). Mean and standard deviation (SD) of participants' background characteristics, fall direction-wise fracture loads, and MFSs were given as descriptive statistics. Prior to following statistical analyses, logarithmic transformation of the fall direction-wise fracture load and MFS were performed to control for the skewness of the data, and the normality of the transformed data was confirmed by the Shapiro-Wilk test.

The primary objective of the present study was addressed in three different statistical analyses. First, a two-way repeated measures analysis of variance (ANOVA) was performed to evaluate the association of fall angles α and β with fracture loads within each group. A Sidak correction was used to control for multiple comparisons in this analysis. Second, a split-plot ANOVA was performed to evaluate whether the potential associations and interactions of α and β with the fracture loads differed between the groups. Third, both one-way ANOVA and analysis of covariance (ANCOVA) using BW or LM as a covariate were performed to estimate the differences in the fracture loads between each exercise loading group and the control group in each fall direction. Covariates were selected through the following process. Pearson correlation analyses showed that the height, BW, and LM had significant ($p < 0.05$) low-to-moderate correlations ($r = 0.29$, 0.33 and 0.50, respectively) with

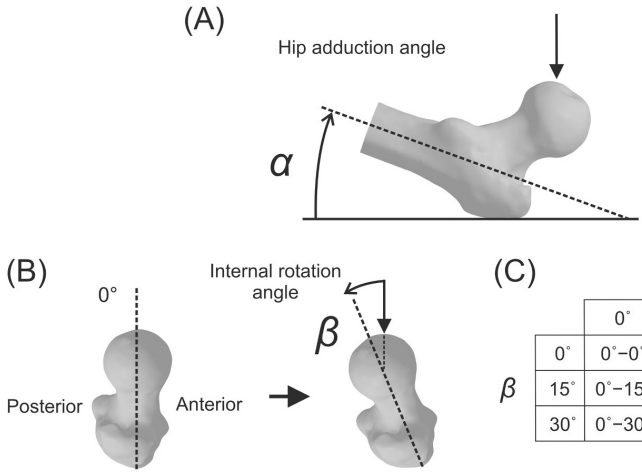

β \ α	0°	10°	20°	30°
0°	0°–0°	10°–0°	20°–0°	30°–0°
15°	0°–15°	10°–15°	20°–15°	30°–15°
30°	0°–30°	10°–30°	20°–30°	30°–30°

Fig. 1. Multiple sideways fall configuration. An angle α denotes the hip adduction angle or the angle between the femoral shaft and the ground (A) while the angle β denotes the internal rotation angle of femoral neck (B). This angle α was rotated in steps from 0°, 10°, 20°, to 30° while the angle β was increased in steps from 0°, 15°, and 30°. A total of 12 different fall directions were simulated by combining four α angles and three β angles, and each direction is represented by a $\alpha - \beta$ pair (C).

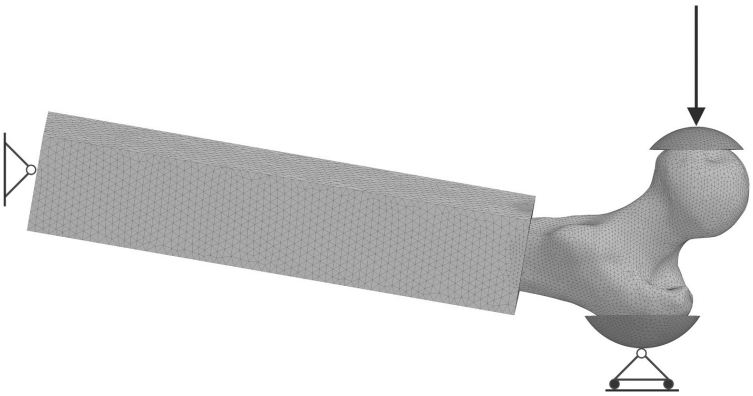

Fig. 2. Boundary conditions of the FE model. The loading force was applied to the whole upper face of the head-protecting PMMA cap at defined angles while the restraining boundary condition was applied to the trochanter PMMA cap, prohibiting the movement in the direction of the force [53]. A 200 mm long aluminum pot was installed at 15–20 mm below the most projected part of the lesser trochanter of each proximal femur. A hinge-type restraining boundary condition was assigned to the distal face of the aluminum pot, allowing nodes at the hinge-axis to freely rotate in the quasi-frontal plane whereas all other degrees of freedom were constrained. Young's modulus of 70 GPa and 2 GPa were applied to aluminum pot and PMMA cup respectively [53]. All materials were modeled with a 10-noded tetrahedral finite element and 2 mm element size was used for the entire proximal femur, the PMMA caps, and the boundary between the distal end of the proximal femur bone and the distal pot. The rest of the distal pot was modeled with 4 mm-sized element. Each proximal femur model, on average, had 194,000 elements and 292,000 nodes.

fracture loads, but the age did not ($r = 0.02$, $p = 0.76$). Also, the assumption of homogeneity of regression slopes was violated for age and height. Given these, BW and LM were used separately as the covariate in ANCOVA. Percentage differences in the fracture load between each exercise loading group and the control group (relative differences in bone strength) were calculated for each fall configuration by taking anti-log of unadjusted, BW-adjusted, and LM-adjusted mean fracture loads.

For the secondary objective, the differences in the MFS between each exercise loading group and the control group were also estimated by the ANOVA and ANCOVA using BW or LM as the covariate. The percentage difference was calculated similarly. A p-value of less than 0.05 was considered statistically significant.

3. Results

3.1. Descriptive data of participants

Group-wise descriptive data of age, height, weight, fat-%, lean body mass, and training histories characterized by the duration of competing career, the number of weekly training sessions, and weekly sport-specific training hours are presented in Table 1. The weekly mean training volume was at least three times higher among the athletic groups compared to the control group.

3.2. Fracture load

3.2.1. General trend and effect of fall angles

Group-wise unadjusted mean (SD) fracture loads in each fall direction are presented in Table 2. In every group, the highest mean fracture loads were observed in the 0°–0° direction. The lowest mean values were observed in the 30°–30° direction in all groups except for the H-I and control groups where the lowest values were in the 30°–15° direction. In general, when the angle α between the femoral shaft and the ground increased from 0° to 30°, the mean fracture loads decreased by 32–35%, 22–26%, and 12–15% at $\beta = 0°$, 15°, and 30°, respectively among the six groups investigated. Similarly, when the hip internal rotation angle β increased from 0° to 30°, the mean fracture loads decreased by 22–27%, 12–18%, 6–11%, and 1–7% at $\alpha = 0°$, 10°, 20°, and 30°, respectively. When both angles shifted from 0°–0° to 30°–30° fall direction, the mean fracture loads decreased by 34–36%.

The above consistent reductions in the mean fracture load were indicated by the two-way repeated-measures ANOVA which showed significant interactions of α and β ($p < 0.001$) with fracture loads within each group. However, according to the split-plot ANOVA, the interaction of α and/or β with the fracture loads did not differ statistically between the groups ($p = 0.601$, 0.507, and 0.151 for terms α*group*, β*group*, and α*β*group*, respectively). However, the total mean fracture loads calculated by averaging the fracture loads from all 12 fall configurations indicated a significant between-group difference ($p = 0.033$). Compared to the control group (mean ± SD: 2867 ± 500 N), the total mean fracture loads of H-I (3259 ± 388 N, $p = 0.007$), O-I (3146 ± 389 N, $p = 0.046$), and R-I (3257 ± 485 N, $p = 0.018$) were significantly different while those of H-M (2971 ± 542 N, $p = 0.541$) and R-NI (3054 ± 471 N, $p = 0.220$) were not.

3.2.2. Fall direction-wise fracture load

The percentage differences in unadjusted and BW-adjusted mean fracture loads between each exercise loading group and the control group in each fall direction are shown in Fig. 3. Both unadjusted and BW-adjusted fracture loads in the H-I and R-I groups were significantly ($p < 0.05$) higher in all 12 fall directions compared to the control group, except for the near-significant difference for the unadjusted fracture

Table 1
Descriptive group characteristics.

Group	N	Age (years)	Height (cm)	Weight (kg)	Fat-%	Lean body mass (kg)	Competing career (years)	Training sessions/week	Sport-specific training hours/week
H-I	19	22.3 (4.1)	174 (6)	60.2 (5.4)	20.0 (3.9)	45.9 (3.1)	10.1 (3.4)	6.7 (1.4)	11.5 (2.3)
O-I	19	25.3 (6.7)	165 (8)	60.8 (8.3)	25.1 (5.9)	43.3 (4.2)	9.6 (4.8)	5.7 (1.4)	9.3 (2.7)
H-M	17	27.5 (6.3)	158 (3)	63.3 (13.2)	27.9 (7.4)	43.2 (5.9)	8.0 (4.7)	5.8 (2.0)	9.1 (2.7)
R-I	18	28.9 (5.6)	168 (5)	53.7 (3.4)	14.2 (3.6)	44.1 (3.1)	12.4 (6.7)	8.7 (2.1)	10.9 (3.4)
R-NI	18	19.7 (2.4)	173 (5)	65.1 (5.6)	25.1 (5.5)	46.7 (3.5)	9.1 (2.6)	11.4 (2.0)	19.9 (4.5)
Control	20	23.7 (3.8)	164 (5)	60.0 (7.4)	31.7 (5.8)	39.0 (4.2)	–	2.8 (1.0)	2.8 (0.9)

Mean and (SD).

Table 2
Unadjusted mean (SD) estimated fracture load (in N) and p values from ANOVA and ANCOVA (only BW-adjusted). A p value in each cell is the one from ANOVA (unadjusted) while a p^* is the one from ANCOVA (BW-adjusted). The p values from ANCOVA with LM as the covariate are not included in this table since they are all nonsignificant ($p > 0.15$).

H-I	$\alpha = 0°$	$\alpha = 10°$	$\alpha = 20°$	$\alpha = 30°$
$\beta = 0°$	**4311 (565)**	**3551 (423)**	**3141 (352)**	**2951 (332)**
	$p = 0.044$, $p^* = 0.031$	**$p = 0.018$, $p^* = 0.009$**	**$p = 0.008$, $p^* = 0.003$**	**$p = 0.004$, $p^* = 0.001$**
$\beta = 15°$	**3803 (512)**	**3268 (410)**	**2995 (374)**	**2826 (357)**
	$p = 0.018$, $p^* = 0.010$	**$p = 0.013$, $p^* = 0.007$**	**$p = 0.009$, $p^* = 0.005$**	**$p = 0.007$, $p^* = 0.004$**
$\beta = 30°$	**3356 (415)**	**3112 (424)**	**2944 (425)**	**2855 (420)**
	$p = 0.003$, $p^* = 0.002$	**$p = 0.004$, $p^* = 0.002$**	**$p = 0.009$, $p^* = 0.006$**	**$p = 0.012$, $p^* = 0.009$**
O-I	$\alpha = 0°$	$\alpha = 10°$	$\alpha = 20°$	$\alpha = 30°$
$\beta = 0°$	4253 (612)	**3507 (481)**	3017 (389)	2816 (388)
	$p = 0.09$, $p^* = 0.10$	**$p = 0.045$, $p^* = 0.047$**	$p = 0.074$, $p^* = 0.076$	$p = 0.07$, $p^* = 0.071$
$\beta = 15°$	3673 (437)	**3189 (440)**	**2907 (401)**	**2747 (382)**
	$p = 0.065$, $p^* = 0.068$	**$p = 0.048$, $p^* = 0.046$**	**$p = 0.043$, $p^* = 0.046$**	**$p = 0.036$, $p^* = 0.039$**
$\beta = 30°$	3156 (396)	**2947 (335)**	2809 (338)	2734 (330)
	$p = 0.079$, $p^* = 0.083$	**$p = 0.042$, $p^* = 0.044$**	$p = 0.051$, $p^* = 0.055$	$p = 0.0504$, $p^* = 0.054$
H-M	$\alpha = 0°$	$\alpha = 10°$	$\alpha = 20°$	$\alpha = 30°$
$\beta = 0°$	4029 (838)	3351 (633)	2950 (508)	2724 (439)
	$p = 0.663$, $p^* = 0.973$	$p = 0.401$, $p^* = 0.701$	$p = 0.297$, $p^* = 0.540$	$p = 0.326$, $p^* = 0.599$
$\beta = 15°$	3379 (660)	2952 (584)	2760 (534)	2628 (475)
	$p = 0.907$, $p^* = 0.551$	$p = 0.684$, $p^* = 0.838$	$p = 0.414$, $p^* = 0.765$	$p = 0.308$, $p^* = 0.590$
$\beta = 30°$	2937 (518)	2743 (520)	2631 (542)	2568 (522)
	$p = 0.839$, $p^* = 0.637$	$p = 0.711$, $p^* = 0.752$	$p = 0.671$, $p^* = 0.791$	$p = 0.614$, $p^* = 0.877$
R-I	$\alpha = 0°$	$\alpha = 10°$	$\alpha = 20°$	$\alpha = 30°$
$\beta = 0°$	**4387 (783)**	**3624 (643)**	**3190 (548)**	**3004 (482)**
	$p = 0.053$, **$p^* = 0.002$**	**$p = 0.025$, $p^* < 0.001$**	**$p = 0.015$, $p^* < 0.001$**	**$p = 0.006$, $p^* < 0.001$**
$\beta = 15°$	**3780 (607)**	**3258 (524)**	**2986 (471)**	**2860 (451)**
	$p = 0.048$, $p^* = 0.001$	**$p = 0.034$, $p^* < 0.001$**	**$p = 0.023$, $p^* < 0.001$**	**$p = 0.01$, $p^* < 0.001$**
$\beta = 30°$	**3277 (425)**	**3014 (392)**	**2894 (395)**	**2807 (388)**
	$p = 0.021$, $p^* < 0.001$	**$p = 0.024$, $p^* < 0.001$**	**$p = 0.022$, $p^* < 0.001$**	**$p = 0.026$, $p^* < 0.001$**
R-NI	$\alpha = 0°$	$\alpha = 10°$	$\alpha = 20°$	$\alpha = 30°$
$\beta = 0°$	4133 (630)	3390 (511)	2936 (451)	2699 (393)
	$p = 0.267$, $p^* = 0.844$	$p = 0.205$, $p^* = 0.896$	$p = 0.270$, $p^* = 0.931$	$p = 0.356$, $p^* = 0.743$
$\beta = 15°$	3610 (634)	3111 (519)	2826 (443)	2682 (417)
	$p = 0.217$, $p^* = 0.795$	$p = 0.165$, $p^* = 0.716$	$p = 0.160$, $p^* = 0.749$	$p = 0.125$, $p^* = 0.699$
$\beta = 30°$	3033 (500)	2835 (474)	2728 (464)	2669 (463)
	$p = 0.422$, $p^* = 0.935$	$p = 0.316$, $p^* = 0.955$	$p = 0.254$, $p^* = 0.871$	$p = 0.218$, $p^* = 0.813$
Control	$\alpha = 0°$	$\alpha = 10°$	$\alpha = 20°$	$\alpha = 30°$
$\beta = 0°$	3902 (709)	3176 (544)	2776 (470)	2583 (427)
$\beta = 15°$	3360 (644)	2877 (564)	2622 (502)	2474 (444)
$\beta = 30°$	2905 (494)	2683 (465)	2558 (477)	2487 (485)

Statistically significant p values ($p < 0.05$) based on ANOVA and ANCOVA are shown in bold.

load in the R-I group in the 0°–0° direction ($p = 0.053$) (Table 2). The unadjusted and BW-adjusted percentage differences in the H-I group ranged from 11% to 17% compared to the control group (Fig. 3). Similarly, the unadjusted and BW-adjusted differences in the R-I group ranged from 13% to 16% and 22 to 28%, respectively (Fig. 3).

The unadjusted and BW-adjusted fracture loads in the O-I group were significantly higher in five fall directions (10°–0°, 10°–15°, 10°–30°, 20°–15°, and 30°–15°), except there was a near-significant ($p = 0.051$) difference for the BW-adjusted fracture load in the 10°–15° direction, compared to the controls (Table 2). In these directions, the unadjusted and BW-adjusted percentage differences in the O-I group ranged from 11% to 12% and 10% to 11%, respectively (Fig. 3). In the rest of the fall directions in the O-I group, there were trends ($p \leq 0.1$) for 9% to 11% higher unadjusted and BW-adjusted fracture load (Table 2 and Fig. 3).

The mean fracture loads in the H-M and R-NI groups did not differ significantly from the controls in any fall direction (Table 2). Compared to the control group, the unadjusted and BW-adjusted percentage differences in the H-M group ranged from 1% to 6% and − 3% to 3% throughout the 12 fall directions, respectively (Fig. 3). Those in the R-NI group ranged from 5% to 9% and − 2 to 2%, respectively (Fig. 3).

In contrast, once adjusted for LM, none of the exercise loading groups had significantly higher fracture loads in any fall direction compared to the control group ($p > 0.05$). Respective LM-adjusted percentage differences in each exercise loading group ranged in the 12 fall configuration as follows: H-I, from 0% to 5%, $p > 0.42$; O-I, from 2% to 6%, $p > 0.35$; H-M, from −8% to −1%, $p > 0.16$; R-I, from 0% to 4%, $p > 0.53$; and R-NI, from −10% to −6%, $p > 0.15$. Exact values of the unadjusted, BW-adjusted, and LM-adjusted percentage differences with 95% CI in all exercise loading groups compared to controls are given in the Supplementary data (Table A-1).

3.2.3. Minimum fall strength (MFS)

The occurrence of MFS in each fall configuration is shown in Table 3. The MFSs occurred only when either or both of the fall angles α and β were the greatest: 1 in the 10°–30°, 13 in the 20°–30°, 23 in the 30°–0°, 34 in the 30°–15°, 40 cases in the 30°–30°.

Group-wise unadjusted mean (SD) MFSs and the percentage differences in the unadjusted, BW-adjusted, and LM-adjusted mean MFSs between each exercise loading group and the control group are presented in Table 4. Compared to the control group, the unadjusted MFSs in the H-I, O-I, and R-I groups were significantly ($p < 0.05$) 15%, 11%, and 14% higher while their BW-adjusted MFSs were significantly 15%, 11%, and 26% higher, respectively (Table 4). The unadjusted and BW-adjusted MFSs in the H-M and R-NI groups did not significantly differ

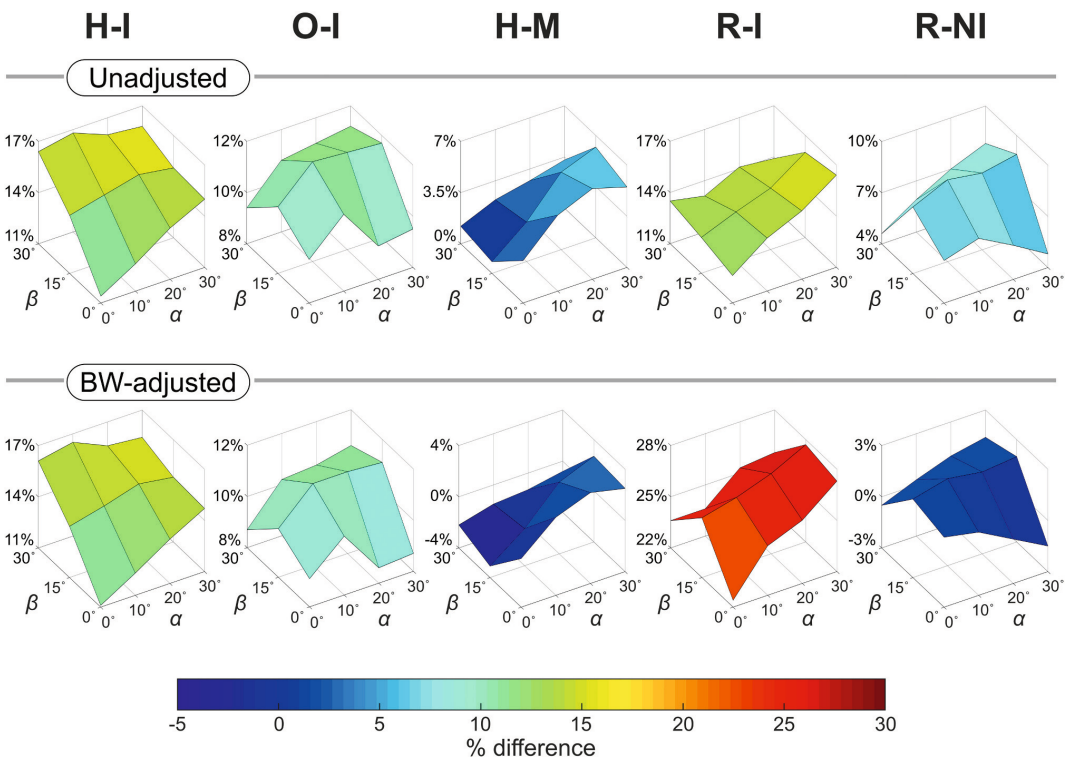

Fig. 3. Unadjusted and BW-adjusted mean percentage (%) differences in the fracture loads of exercise loading groups compared to the control group. Vertical axis in each surface plot shows % difference.

Table 3
The number of MFS observed in each falling configuration. The column for α = 0° is omitted since there was no MFSs observed in that direction.

	$\alpha = 10°$		$\alpha = 20°$		$\alpha = 30°$	
$\beta = 0°$					H-I	5
					O-I	6
					H-M	2
					R-I	1
					R-NI	6
					Control	3
					Total	**23**
$\beta = 15°$					H-I	5
					O-I	5
					H-M	4
					R-I	8
					R-NI	3
					Control	9
					Total	**34**
$\beta = 30°$			H-I	2	H-I	7
			O-I	2	O-I	6
			H-M	4	H-M	7
	R-I	1	R-I	2	R-I	6
			R-NI	2	R-NI	7
			Control	1	Control	7
	Total	**1**	**Total**	**13**	**Total**	**40**

from the control group. Lastly, none of the exercise loading groups had significantly different LM-adjusted MFS compared to the controls (Table 4).

4. Discussion

In the present study, we elaborated whether the higher bone strength in athletes attributed to specific exercise loading history persisted regardless of the fall direction. This analysis was performed by simulating proximal femur FE models of 91 female athletes, representing several distinct exercise loading types, and their 20 controls in multiple fall directions and estimated the corresponding fracture loads. The fall directions were associated with the fracture loads in all groups. Overall, the fracture loads decreased by 12–35% as the tilt angle (α) of the femoral shaft increased from 0° to 30°, 1–27% as the hip internal rotation angle (β) increased from 0° to 30°, and 34–36% as both angles increased from 0° to 30°. These trends are in line with previous experimental [32] and FE modeling studies of the multiple fall configurations [33–36]. However, it is noted that the two FE studies [35,36] reported slightly different decreases in the fracture load due to changes in α or β alone and both of them; respective decreases were 4–12%, 14–20%, and 24% [35], and 33–36%, 7–15%, and 38% [36]. The exact reasons behind these discrepancies remain unknown. However, we speculate that they were likely due to young and athletic participants of the present study and methodological differences in the FE models (e.g., the use of homogeneous material property assignment and different distal

Table 4
Minimum fall strength (MFS) – unadjusted mean (SD) MFS (in N) and percentage differences in unadjusted, BW-, or LM-adjusted mean MFSs between each exercise group and the control group with 95CI.

Group	MFS mean (SD)	Unadjusted	*p*	BW-adjusted	*p*	LM-adjusted	*p*
		% diff		% diff		%diff	
H-I	**2761 (366)**	**14.9 (3.4 to 27.6)**	**0.011**	**14.5 (3.9 to 26.2)**	**0.007**	3.1 (−10.0 to 18.2)	0.652
O-I	**2674 (346)**	**11.3 (0.2 to 23.5)**	**0.046**	**10.6 (0.1 to 22.1)**	**0.048**	4.3 (−6.5 to 16.4)	0.440
H-M	2527 (465)	4.4 (−7.7 to 18.1)	0.484	0.6 (−8.9 to 11.1)	0.900	−3.9 (−14.2 to 7.7)	0.486
R-I	**2752 (371)**	**14.4 (2.5 to 27.6)**	**0.018**	**25.9 (13.2 to 40.1)**	**<0.001**	1.4 (−9.6 to 13.8)	0.804
R-NI	2576 (381)	7.0 (−4.3 to 19.6)	0.229	0.7 (−9.6 to 12.3)	0.891	−7.3 (−19.8 to 7.2)	0.298
Control	2425 (452)	–	–	–	–	–	–

Statistically significant *p* values ($p < 0.05$) based on ANOVA and ANCOVA are shown in bold.

constraining conditions). Altogether, these findings suggest that hip fracture risk increases if the fall impact is imposed on a more superior aspect (reflected by a greater α angle) and/or more posterolateral aspect (reflected by a greater β angle) than the lateral aspect (e.g., 0°–0° condition) of the greater trochanter. In fact, a recent cohort study of video-captured falls of over 600 elderly persons demonstrated that 77% (23 out of 30 cases) of the fall-induced hip fractures were sustained when the impact was imposed on the posterolateral aspect while 13% of hip fractures occurred when the impact was imposed on the lateral aspect [55].

A particularly important finding in the present study, based on the fall direction-wise fracture loads, was that the mean fracture loads in the H-I and R-I groups were significantly higher (11–17% and 22–28%, respectively) compared to the control group regardless of the fall direction. In contrast, the mean fracture loads in the O-I group were significantly higher (10–11%) in fewer fall directions. These results suggest that the higher bone strength against the hip fracture risk associated with H-I and the R-I exercise loading types seems robust regardless of fall direction whereas the benefit attributed to O-I exercise loading appears more modest and specific to the fall direction.

The aforementioned benefits in the H-I, O-I, and R-I groups were further confirmed by the significantly higher MFSs (15%, 11%, and 26%, respectively) compared to the control group. Importantly, Falcinelli et al. [35] and Qasim et al. [40] found that MFS from the multiple fall conditions can predict the hip fracture risk slightly more accurately than a single direction-load (e.g., 10°–15°), aBMD (femoral neck, trochanteric, and total femur), and FRAX: areas under the curve (AUC) in the receiver operating characteristics for these variables were 0.79–0.88, 0.77, 0.73–0.79, and 0.69, respectively. This highlights the importance of not only simulating multiple fall directions but also analyzing the minimum fall strength among them. It is important to note that the group-wise mean MFSs ranged from 2425 N to 2761 N in the present study (Table 4) which were quite comparable to those (2060–2729 N) observed in another multiple fall FE study by Altai et al. [36] and the two above-mentioned FE studies [35,40].

The analysis of the fall direction-wise fracture loads suggest that the weakest fall orientation of the proximal femur takes place when both of the α and β angles reach their maximum (30°–30°). The highest 36% occurrence of MFSs (40 out 111 cases, Table 3) corresponded to this orientation similar to previous studies employing the multiple fall conditions [35,40]. However, it is noted that the occurrence of MFS in the other studies was more widespread among the fall directions including even the lateral fall direction (0°–0°) [35,40], whereas the present occurrence of MFSs was more concentrated on the greatest values of either or both α and β. We hypothesize again that this discrepancy can be attributed to the differences in characteristics of participants and methodologies between studies.

One interesting observation in the present study is that the benefits observed in unadjusted and BW-adjusted higher fracture loads among the specific exercise loading groups disappeared once controlled for LM. According to bone's functional adaptation [2,3], the bone adapts to the prevalent mechanical environment, which does not exclude the contribution from the fat mass. It is the body weight that largely determines the magnitude of mechanical loading. The mechanical environment of bone comprises the gravitational ground reaction forces both in static (e.g., lying, sitting, and standing) and dynamic situations (e.g., daily physical activities such as walking, stair ambulation and sport-specific exercises such as running and jumping) as well as the internal muscle contraction forces [56]. LM can be used as a proxy for muscle mass and also muscle forces. However, the muscle mass does not necessarily equate with the actual maximal muscle forces employed in specific dynamic performances. High muscle force largely results from vigorous, long-term physical training that improves specific muscle performance via increased muscle mass and cross-sectional area, and/or enhanced neuromuscular networks [57]. Nonetheless, controlling the bone strength for muscle force (or its proxy LM) may eliminate the anabolic effect of exercise training on the bone that was the focus of the present study. The present study demonstrated this while pinpointing the importance of selecting the reasonable covariate for the research questions. In this respect, BW is a reasonable covariate as it takes into account both the person's body size and the loading caused by habitual weight-bearing physical activities and related ground reaction forces [56].

The present beneficial observations in the H-I, O-I, and R-I groups are likely attributed to exercise-induced structural adaptation in the cortical bone. Based on our previous study of the same proximal femur data [29], the femoral neck in the H-I group has ~10% thicker superior cortex, ~20% thicker anterior and posterior cortex, and notably 60% thicker weight-bearing inferior cortex compared to the controls while the O-I group has consistently 15–20% thicker cortical bone around the femoral neck. Compared to O-I exercise loading, a remarkable adaptation inherent to H-I exercise loading is ~60% thicker cortex in the weight-bearing inferior femoral neck compared to the controls [29]. Finding an effective exercise to load and strengthen the fracture-prone superolateral femoral neck has been the primary focus in previous studies [29,58–63]. However, should this be difficult, the importance of thickening the inferior cortex ought not to be underestimated. From an engineering perspective, thickening the inferior cortex would lead to an inferior shift of the neutral axis of the femoral neck in bending. Such a shift increases the bone cross-sectional area above the axis where compressive force is applied in the sideways fall situation, and thus decreases the magnitude of load (stress or strain) at the superior femoral neck. This was also suggested in a recent proximal femur FE modeling study of young adult male athletes by Warden et al. [58]. However, it is also noted that the neutral axis is also a function of the loading direction. Besides, the contribution of even a small amount of bone to fracture

prevention is greater if the bone accrual occurs at the structurally weakest location in terms of a typical fall direction. Elderly people typically display modest osteogenic responses to exercise training, and then adding even a small amount of bone at the critical location of the proximal femur may reduce the risk of hip fracture. In fact, in a 12-month exercise RCT of older males aged 70 years, Allison et al. [60] reported that daily multidirectional moderate impact hopping exercise, generating impact magnitudes of about 3 BW, resulted in regional bone accrual also at the fracture-prone superolateral cortex. Nonetheless, whether such a regional adaptation at the femoral neck would contribute to the fracture prevention remains speculative and calls for a further study examining, e.g., whether thickening inferior cortex can compensate for superior cortex thinning and its effect on the fracture load.

The higher femoral strength attributed to H-I or moderate impact exercise loadings has also been reported in recent studies of young male and female athletes by Warden et al. and Fuchs et al. [58,63]. Warden et al. [58] reported that the FE-estimated bone strength in the male jumpers, representing H-I exercise loading, was significantly higher in the sideways fall situation compared to the matched controls, similar to the present results of female athletes. Fuchs et al. [63] also demonstrated that female softball pitchers exhibited 11% dominant-to-nondominant leg side differences in the FE-estimated yield strength in the sideways fall. The softball pitching imposes an asymmetric loading such that the dominant leg, the contralateral side to their throwing arm, experiences more impact-generating landing than the non-dominant leg. This finding further confirms the benefit of impact loading on the proximal femur strength.

In contrast to the H-I and O-I groups, the R-I group did not show such regional cortical thickening of the femoral neck [29]. This indicates that the observed substantial benefit in the bone strength attributed to R-I exercise loading reflects other mechanical factors than the cortical thickness. The femoral neck cross-section in the R-I group appeared more circular [64], which provides a mechanically more robust structure in all directions compared to an oval-shaped bone. A recent study identified the femoral neck roundness as an important geometric factor among other geometrical parameters that determines its strength against fall-induced fracture [65]. Similarly, 1.3–1.5 times lower fall-induced stress was estimated in a more circular femoral neck cross-section of medieval people compared to the oval-shaped femoral neck of present-day, habitually more sedentary people [66]. The present BW-adjusted 22–28% higher fracture load in the R-I group complies closely with this estimation. However, these considerations are speculative and the apparent benefits in the proximal femur strength in the R-I group warrant further investigation.

No benefit in bone strength was observed in the H-M and R-NI groups in any fall direction. Likewise, their MFSs were not any higher than the controls. These findings most likely reflect the lack of beneficial structural adaptations in the proximal femora of these groups [24,29].

Exploring the loading characteristics of the five distinct exercise loading types in the present study may help identify essential components that underlie loading-specific beneficial adaptations in the proximal femur. Peak ground reaction forces (GRF expressed in BW) and estimated maximum loading rates (BW s^{-1}) are 12–20 BW and 400–480 BW s^{-1} for H-I [67,68]; 2.5–3.5 BW and 20–180 BW s^{-1} for O-I [59,69–71]; and 2–2.5 BW and 60–150 BW s^{-1} for R-I loadings [72–74]. Despite slightly lower GRFs and loading rates in O-I and R-I exercise loading compared to H-I exercise loading, the O-I and R-I exercises naturally have higher loading frequencies. A large number of repetitive movements and high muscle activity are also involved in swimming. However, the magnitude of mechanical loads is substantially lower in water due to its buoyancy, making it an aquatic hypo-gravitational environment. Some impact in swimming may occur during the push-off phase of turning against the pool wall, but its reaction force and loading rate are essentially smaller ($<$1.5 BW, and $<$10 BW s^{-1} respectively) [75,76]. Despite the extreme weights lifted, the peak GRF in the H-M exercise (e.g. a squat and deadlift) is comparable (2–3 times BW) [77] to those in the O-I and R-I exercises. Besides, due to the nature of H-M exercises (inherent slow movement and the low number of repetitions), the loading rate (5–6 BW s^{-1}) as well as the loading frequency remain marginal compared to the impact exercises [77]. Overall, the moderate-to-high GRF alone may not be sufficient but it needs to be applied at a high loading rate or frequency to trigger the beneficial structural adaptations within the cortical bone of the proximal femur. These considerations are essentially in line with observations from previous animal experimental studies [3,9].

Information on exercise-specific GRFs and loading rates may not be sufficient to characterize effective exercises since they convey information about loading only at the ground level, but do not necessarily tell how much loading is actually transferred to the hip joint and proximal femur. Recent musculoskeletal modeling studies with the FE analyses have evaluated hip contact force (HCF) and femoral neck strain during various movements [61,62,78,79]. Compared to the HCF (4–5 BW) in walking at 4 km/h, unilateral vertical hopping and running at 6–12 km/h induced substantially higher HCFs: 7.5 BW and 6–10 BW, respectively [62,78]. In contrast, hip resistance training (abduction, adduction, flexion, and extension exercises) at 40–80% of 1 repetition maximum (RM) induced similar or even smaller HCFs than that in walking [62]. These musculoskeletal modeling studies provide estimates of joint reaction and muscle forces. However, caution is needed when interpreting these results mainly because of two reasons. First, calculations in the (inverse) kinematic analysis may amplify the noise present in the measured data and result in substantial errors in the estimated joint forces, especially in highly dynamic vigorous movements and sports performances involving maximum efforts and rapid accelerations or decelerations. Second, the estimation of muscle forces is mostly based on the optimization using energy minimization norms which most likely does not reflect the extreme performances inherent in sports. In fact, estimated muscle forces have not been validated [62].

According to classic Frost's mechanostat theory [2] and bone remodeling theory by Huiskes et al. [80,81], the osteogenic adaptive bone response is triggered if the strain magnitude and/or strain energy exceeds the homeostatic threshold around 1500 με or by 75% respectively. Pellikaan et al. [62] showed that, compared to walking at 4 km/h, unilateral vertical hopping and running at 7–9 km/h induced significantly higher compressive and tensile strains at both the inferior and superior femoral neck, exceeding the homeostatic threshold. It is noteworthy that the unilateral vertical hopping induced up to 7 times higher strain at the inferior femoral neck than walking. This may further explain the aforementioned ~60% thicker inferior femoral neck cortical bone in the H-I group [29]. Martelli et al. [79] demonstrated that unilateral long jump and bilateral vertical jump can induce considerably high strain energy at the femoral neck exceeding homeostatic value by about 500% and 200%, respectively. However, it is noted that in these studies [62,79] dynamic loading activities were discretized into several time-instances, at each of which these estimates were obtained by static FE models. Therefore, future studies should consider dynamic FE models to include the relevant dynamic bone behavior such as strain-rate dependent viscoelasticity and a potential contribution of pore pressure [82,83]. The unilateral vertical hopping can be considered a moderate H-I exercise and/or a part of the O-I exercise excluding the multidirectional components. Thus, these high HCFs, and femoral neck strain and energy induced by the jumping, hopping, and running exercises further support the effectiveness of impact exercises in triggering osteogenic adaptation within the proximal femur.

Multidirectional O-I exercise has not been specifically analyzed in the previous musculoskeletal FE modeling studies [61,62,78,79]. We hypothesized that the O-I exercise can cause more uniform strain distribution across the femoral neck due to repeated impacts from varying directions within a short period of time. Thus, it may promote a more symmetric osteogenic adaptation around the femoral neck cortical bone, including the vulnerable superolateral femoral neck. However, the hip

contact forces and femoral neck strains during O-I exercise may be smaller than those in H-I and R-I exercises. Loads generated by ground impacts from unusual directions may be largely dissipated by the activity of muscles that maintain the kinematic posture before reaching the hip joint. It is important to note that a recent review by Martelli et al. [84] analyzed the hip strains during different exercises assessed in musculoskeletal and FE modeling studies. They did not only confirm the anabolic osteogenic effect of moderate H-I exercises (e.g., vertical hopping) on the proximal femur including the fracture-prone superolateral region of the femoral neck but also suggested that the multidirectional O-I exercises may also confer such a beneficial effect owing to its non-habitual strain patterns within the femoral neck, supporting thus our speculation. Therefore, this calls for future musculoskeletal FE modeling studies to include the multidirectional O-I exercise. Besides, considering the importance of the loading rate, an additional analysis on such information at the hip joint from these musculoskeletal FE modeling studies [61,62,78,79] may further elucidate the mechanism of exercise-induced osteogenic adaptation.

The clinical relevance of present results should be interpreted with caution. Since our study was conducted in young adult females, the findings cannot be translated directly into the general or older population. However, the efficacy of the H-I, O-I, and R-I impact exercises in inducing beneficial adaptation in the femoral neck has been confirmed in several meta-analyses of RCTs regardless of age, including pre- and postmenopausal females [85–87]. Nonetheless, the feasibility of impact exercises for the older population should be carefully considered. Despite clear benefits on bone, the H-I exercise generating extreme ground reaction forces (12–20 times BW) is too risky not only for older people but also for sedentary persons regardless of age. In contrast, the risk of musculoskeletal injuries is likely lower for the O-I and R-I exercises due to more moderate impact magnitudes. Thus, these exercises can offer a safe and feasible option to increase or maintain the proximal femur strength. Moderate R-I exercises such as fast walking (6 km/h) and stair ambulation have been found to induce potentially osteogenic higher strain at the fracture-prone superior femoral neck compared to normal walking (4 km/h) [61,62,84]. Since these exercises are safe and require less effort than running, they can be easily implemented into habitual daily activities even in the elderly population. However, it should be noted that although a few meta-analyses of (R)CTs in postmenopausal females have reported that walking or combined jogging with walking and stair ambulation can increase the femoral neck aBMD, the observed increases have remained too small to be of clinical significance concerning the reduction of hip fractures [87,88]. The potential of these moderate R-I exercises is likely limited in preserving bone mass and mitigating age-related bone fragility. Whether these moderate R-I exercises can decrease the hip fracture risk is yet unclear and calls further investigation including the effective intensity (walking speed) and volume of these exercises to prevent hip fractures.

There are several limitations in the present study. First, the homogeneous material property assignment was used instead of density-based inhomogeneous material property assignment. The trabecular bone is a two-phased material comprising a mineralized bone tissue (solid phase), forming a highly porous three-dimensional lattice structure, and a fluid phase such as interstitial fluid and bone marrow, filling the interconnected pores. The apparent density due to the porosity is strongly related to mechanical properties of bone, including strength and modulus [89,90]. Ununiform distribution of apparent density and subsequent variation in the modulus within the proximal femur are typically implemented by inhomogeneous material property mapping technique in the previous QCT-based FE models [16,33–38,40,53,54,91,92]. However, this inhomogeneous material property assignment could not be realized in the present study due to the inherent limitation to the present MRI data. Nonetheless, the use of inhomogeneous material properties may have enhanced the model accuracy to some extent. However, considering that the present athletic groups have a higher proximal femur aBMD than their nonathlete peers [29], if the inhomogeneous material properties were applied in the present study, the between-group differences in the fracture load could have been higher. Moreover, the present controls were physically active and engaged in recreational exercise 2–3 times a week. Given this, the benefits observed in the exercise loading groups could have been higher if the comparisons were made against truly sedentary people. Although the use of QCT would have enabled us to include the inhomogeneous material property assignment through utilizing data on bone apparent density derived from the voxel-based Hounsfield unit, exposing fertile young adult females to ionizing X-ray radiation from QCT for non-diagnostic purposes would have been ethically unacceptable.

Moreover, the trabecular elastic modulus of 1500 MPa employed in the present study may have been too low for young and athletic females. Nicks et al. [93] reported that the mean femoral neck trabecular volumetric BMD among 20–29 years old females was 0.268 g/cm^3, which yields trabecular modulus of ~2600 MPa through the density-modulus relationship [53,90,94]. We have previously shown that the use of this high modulus would increase the estimated fracture loads by 10–15% [31], and thus in absolute terms, the present fracture loads were underestimated. However, the present study primarily aimed to evaluate the relative differences in the fracture load between groups. In our previous study [31], we also investigated the influence of varying cortical and trabecular moduli on relative between-group strengths and found only a negligible less than 3% effect by this variation. Therefore, the moduli adopted in the present study are conceivable to address the present research questions properly.

Another major limitation of the present study pertains to MRI-based FE models not being validated by an experimental mechanical testing. However, Rajapakse et al. [95] recently validated their proximal femur MRI-based FE models including inhomogeneous material property assignment. They achieved a strong agreement between experimental fracture loads and FE-derived ones ($r = 0.89$ for yield load; $r = 0.92$ for failure load). The main differences between our and their studies pertain to the field strength (1.5 T vs. 3.0 T) and the spatial resolution (0.9 mm $\times$ 0.9 mm $\times$ 1 mm vs. 0.3 mm $\times$ 0.3 mm $\times$ 0.3 mm) of the MRI system used. Because of a better signal-to-noise ratio, 3.0 T MRI achieves a higher spatial resolution than 1.5 T MRI, resulting in clearer and more detailed images. Phan et al. [96] have reported better performance for 3.0 T MRI in capturing the trabecular structure than the 1.5 T MRI. Based on the high-resolution pQCT data obtained from proximal femur ex vivo specimens from osteoporotic females aged from 67 to 94 years [97], Chang et al. [98] implied that it would be ideal if the resolution of imaging is comparable to the mean trabecular thickness varying site-specifically from 0.19 to 0.26 mm and the mean trabecular spacing varying from 0.67 mm to 0.98 mm. Among younger females aged from 16 to 66 years, the trabecular thickness and separation are comparable being 0.15 mm and 0.75 mm on average, respectively [99]. Obviously, the resolution of our MRI data is larger than these numbers and not able to capture the actual porous trabecular structure. Accordingly, we considered the inhomogeneous material property assignment unreasonable to our MRI-based FE-model.

Due to the lack of validation of our MRI-based FE model, caution is needed when interpreting the results. However, our results were quite similar to those studies which employed either the same failure criterion or presented the yield strength. The group-wise mean fracture loads from the 12 fall directions ranged from 2474 N to 4311 N in the present study of young adult females. These values were slightly higher than the mean values in QCT-based FE studies of old persons aged over 60 years where either only single fall direction (10°–15°) or multiple fall directions were simulated: 3099 N [53] in the 10°–15° direction; 2284–2995 N [35] and 1999–3227 N [36] in similar multiple fall configurations to the present study. A slightly lower mean fracture load (2342 N) was also reported in a recent MRI-based FE study of old persons with a mean age of 76 years [95]. As discussed earlier, the present fracture load values were underestimated for the young athletic females because of the low elastic modulus (1500 MPa) for trabecular bone. A recent QCT-based FE study of young adult male long and high jumpers,

baseball pitchers, and their age-matched controls showed mean fracture loads of 4519 N, 3190 N, and 2931 N in the fall direction of 10°–35°, respectively [58]. However, the fact that the participants were all male likely explains the higher values compared to the present study, where the respective group-wise mean values (10°–30°) were 2487–2855 N. Their recent FE study [63] similarly analyzed the proximal femur of young adult female softball pitchers and cross-country runners but the fracture loads were not reported. Furthermore, as discussed earlier, both the MFSs and the decreasing trends of fracture loads along with increasing fall angles were also comparable to those reported in QCT-based FE studies of the multiple fall configurations [35,36,40]. Considering the present fracture loads and their trends being comparable to those from previous QCT/MRI-based FE studies, we venture to claim that our MRI-based FE model is adequately valid, especially for evaluating the relative strength of proximal femur between exercise loading groups.

Besides the application of the homogeneous material property assignment, the proximal femur was modeled as the quasi-static linear isotropic FE models in the present study. It is known that the mechanical properties of the cortical and trabecular bones depend on the strain rate such that the elastic modulus and strength values rise as the strain rate is increased [89,100,101]. Thus, this strain-rate dependent mechanical behavior has been taken into account in recent FE studies [16,53,91]. Fall is a highly dynamic event and the impact velocity to the hip reaches approximately 3.0 m/s or higher [102]. A drawback of quasi-static modeling of the proximal femur in a fall situation is that it disregards important dynamic mechanical properties of bone such as viscoelasticity, viscoplasticity, inertia, and shock-propagation. Recent studies [91,92] have developed dynamic proximal femur FE models and observed strain rates from 1/s to 200/s [91] at elements in the femoral head, neck, and greater trochanter. These findings underline the importance of including the strain-rate dependency in future FE modeling studies. Furthermore, the complex microarchitecture of the trabecular bone results in anisotropic mechanical properties, which have also been implemented in proximal femur FE models utilizing high-resolution pQCT (spatial resolution <100 μm) [103,104]. These aspects were not considered in the present study and their inclusion would likely result in improved model accuracy.

Estimation of the fracture load in the fall is only one aspect of assessing the hip fracture risk. The risk is also largely influenced by the likelihood of the fall and fall dynamics [105,106]. Participant's body height and weight, as well as the fall-specific impact velocity, determine largely the impact force while the trochanteric soft tissue may attenuate the impact force and absorb energy during the impact [106]. Recent biofidelic dynamic FE models by Fleps et al. [92,107] demonstrated that, depending on the thickness of soft tissue, ~30–50% of the peak impact force and ~30% of impact energy can be absorbed by the soft tissue. Importantly, these findings highlight the beneficial results observed in the impact loading exercise groups since the exercise can decrease the hip fracture risk not only by increasing bone strength but also by improving neuromuscular performance, coordination, and balance. The latter improvements decrease the fall risk, and in case of a fall, more muscle tissue around the hip increases the absorption of the impact energy.

In conclusion, the present MRI-based FE study of 111 young adult females representing histories of distinct exercise loading patterns, based on 1332 pertinent FE models covering 12 multiple fall directions, demonstrated that the lower risk of hip fracture judged from higher estimated fracture loads in athletes engaged in high impact or repetitive impact sports is independent of the fall direction. In contrast, the lower fracture risk attributed to the odd-impact exercise remains more modest and specific to the fall direction. The analysis of the minimum fall strength spanning the multiple fall directions also indicated lower hip fracture risk in these athletes. In concordance with the literature, the present results confirmed that the most critical fall direction is the posterolateral direction. As a clinical prospect, the present results highlight the importance of impact exercises in combat against hip fracture, and therefore, even the elderly should be provided feasible and moderate impact exercises as strategies for falls and fracture prevention. Because the present participants were young adult females, for ethical reasons, it was necessary to use MRI in bone imaging instead of QCT, which led to employing homogeneous material property assignment and non-validated FE-models. However, a thorough comparison to the literature provided sufficient evidence for the validity of the present models and gave credibility to the findings. Lastly, the present results call for retrospective studies to investigate whether a specific impact exercise history in adolescence and young adulthood is specifically associated with a lower incidence of hip fractures in later life.

CRediT authorship contribution statement

Shinya Abe: Conceptualization, Methodology, Software, Validation, Formal analysis, Data Curation, Writing – original draft and review & editing, Visualization, Funding acquisition. **Reijo Kouhia:** Conceptualization, Writing – review & editing, Supervision, Funding acquisition. **Riku Nikander:** Conceptualization, Formal analysis, Investigation, Resources, Writing – review & editing, Supervision. **Nathaniel Narra:** Conceptualization, Investigation, Resources, Writing – review & editing, Funding acquisition. **Jari Hyttinen:** Conceptualization, Investigation, Writing – review & editing, Supervision, Funding acquisition. **Harri Sievänen:** Conceptualization, Validation, Formal analysis, Investigation, Resources, Writing – original draft and review & editing, Supervision, Funding acquisition.

Declaration of competing interest

All authors declare no conflict of interest.

Acknowledgements

This work was funded by Tampere University's (former Tampere University of Technology's: TUT) Graduate School and Industrial Research Fund; Pirkanmaa Regional Fund from Finnish Cultural Foundation; Päivikki and Sakari Sohlberg Foundation; the Doctoral Education Council of Computing and Electrical Engineering of TUT; and Human Spare Parts project from the Finnish Funding Agency for Technology and Innovation (TEKES).

Appendix A. Supplementary data

Supplementary data to this article can be found online at https://doi.org/10.1016/j.bone.2022.116351.

References

[1] N.H. Hart, S. Nimphius, T. Rantalainen, A. Ireland, A. Siafarikas, R.U. Newton, Mechanical basis of bone strength: influence of bone material, bone structure and muscle action, J. Musculoskelet. Neuronal Interact. 17 (2017) 114–139.
[2] H.M. Frost, Bone's mechanostat: A 2003 update, Anat Rec A Discov Mol Cell Evol Biol. 275 (2003) 1081–1101.
[3] C. Ruff, B. Holt, E. Trinkaus, Who's afraid of the big bad Wolff?: "Wolff's law" and bone functional adaptation, Am. J. Phys. Anthropol. 129 (2006) 484–498.
[4] C.M. Weaver, C.M. Gordon, K.F. Janz, H.J. Kalkwarf, J.M. Lappe, R. Lewis, M. O'Karma, T.C. Wallace, B.S. Zemel, The National Osteoporosis Foundation's position statement on peak bone mass development and lifestyle factors: a systematic review and implementation recommendations, Osteoporos. Int. 27 (2016) 1281–1386.
[5] B.A. Wallace, R.G. Cumming, Systematic review of randomized trials of the effect of exercise on bone mass in pre- and postmenopausal women, Calcif. Tissue Int. 67 (2000) 10–18.
[6] W. Kemmler, K. Engelke, S. von Stengel, Long-term exercise and bone mineral density changes in postmenopausal women-are there periods of reduced effectiveness? J. Bone Miner. Res. 31 (2016) 215–222.
[7] M. Kistler-Fischbacher, B.K. Weeks, B.R. Beck, The effect of exercise intensity on bone in postmenopausal women (part 1): a systematic review, Bone 143 (2021), 115696.

[8] R. Nikander, H. Sievänen, A. Heinonen, R.M. Daly, K. Uusi-Rasi, P. Kannus, Targeted exercise against osteoporosis: a systematic review and meta-analysis for optimising bone strength throughout life, BMC Med. 8 (2010) 47.

[9] T.M. Skerry, One mechanostat or many? Modifications of the site-specific response of bone to mechanical loading by nature and nurture, J Musculoskelet Neuronal Interact. 6 (2006) 122–127.

[10] N. Veronese, H. Kolk, S. Maggi, Epidemiology of fragility fractures and social impact, in: P. Falaschi, D. Marsh (Eds.), Orthogeriatrics Manag Older Patients with Fragility Fract, Springer, Cham, 2020, pp. 19–34.

[11] J. Parkkari, P. Kannus, M. Palvanen, A. Natri, J. Vainio, H. Aho, I. Vuori, M. Järvinen, Majority of hip fractures occur as a result of a fall and impact on the greater trochanter of the femur: a prospective controlled hip fracture study with 206 consecutive patients, Calcif. Tissue Int. 65 (1999) 183–187.

[12] C.M. Court-Brown, N.D. Clement, A.D. Duckworth, L.C. Biant, M.M. McQueen, The changing epidemiology of fall-related fractures in adults, Injury 48 (2017) 819–824.

[13] P.M. de Bakker, S.L. Manske, V. Ebacher, T.R. Oxland, P.A. Cripton, P. Guy, During sideways falls proximal femur fractures initiate in the superolateral cortex: evidence from high-speed video of simulated fractures, J. Biomech. 42 (2009) 1917–1925.

[14] L. Zani, P. Erani, L. Grassi, F. Taddei, L. Cristofolini, Strain distribution in the proximal human femur during in vitro simulated sideways fall, J. Biomech. 48 (2015) 2130–2143.

[15] L. Grassi, J. Kok, A. Gustafsson, Y. Zheng, S.P. Väänänen, J.S. Jurvelin, H. Isaksson, Elucidating failure mechanisms in human femurs during a fall to the side using bilateral digital image correlation, J. Biomech. 106 (2020), 109826.

[16] B. Helgason, S. Gilchrist, O. Ariza, J.D. Chak, G. Zheng, R.P. Widmer, S. J. Ferguson, P. Guy, P.A. Cripton, Development of a balanced experimental-computational approach to understanding the mechanics of proximal femur fractures, Med. Eng. Phys. 36 (2014) 793–799.

[17] B.C.C. Khoo, K. Brown, J.R. Lewis, E. Perilli, R.L. Prince, Ageing effects on 3-dimensional femoral neck cross-sectional asymmetry: implications for age-related bone fragility in falling, J. Clin. Densitom. 22 (2019) 153–161.

[18] K.E. Poole, P.M. Mayhew, C.M. Rose, J.K. Brown, P.J. Bearcroft, N. Loveridge, J. Reeve, Changing structure of the femoral neck across the adult female lifespan, J. Bone Miner. Res. 25 (2010) 482–491.

[19] J. Carballido-Gamio, R. Harnish, I. Saeed, T. Streeper, S. Sigurdsson, S. Amin, E. J. Atkinson, T.M. Therneau, K. Siggeirsdottir, X. Cheng, L.J. Melton III, J. H. Keyak, V. Gudnason, S. Khosla, T.B. Harris, T.F. Lang, Proximal femoral density distribution and structure in relation to age and hip fracture risk in women, J. Bone Miner. Res. 28 (2013) 537–546.

[20] F. Johannesdottir, B. Allaire, M.L. Bouxsein, Fracture prediction by computed tomography and finite element analysis: current and future perspectives, Curr. Osteoporos. Rep. 16 (2018) 411–422.

[21] Y.T. Lagerros, E. Hantikainen, K. Michaëlsson, W. Ye, H.O. Adami, R. Bellocco, Physical activity and the risk of hip fracture in the elderly: a prospective cohort study, Eur. J. Epidemiol. 32 (2017) 983–991.

[22] M.J. LaMonte, J. Wactawski-Wende, J.C. Larson, X. Mai, J.A. Robbins, M. S. LeBoff, Z. Chen, R.D. Jackson, A.Z. LaCroix, J.K. Ockene, K.M. Hovey, J. A. Cauley, WHI, Association of physical activity and fracture risk among postmenopausal women, JAMA Netw Open. 2 (2019), e1914084.

[23] P. de Souto Barreto, Y. Rolland, B. Vellas, M. Maltais, Association of Long-term Exercise Training with risk of falls, fractures, hospitalizations, and mortality in older adults: a systematic review and meta-analysis, JAMAIntern. Med. 179 (2019) 394–405.

[24] R. Nikander, H. Sievänen, A. Heinonen, P. Kannus, Femoral neck structure in adult female athletes subjected to different loading modalities, J. Bone Miner. Res. 20 (2005) 520–528.

[25] A. Heinonen, P. Oja, P. Kannus, H. Sieväinen, H. Haapasalo, A. Mänttäri, I. Vuori, Bone mineral density in female athletes representing sports with different loading characteristics of the skeleton, Bone 17 (1995) 197–203.

[26] M. Bellver, L. Del Rio, E. Jovell, F. Drobnic, A. Trilla, Bone mineral density and bone mineral content among female elite athletes, Bone 127 (2019) 393–400.

[27] T.A. Scerpella, B. Bernardoni, S. Wang, P.J. Rathouz, Q. Li, J.N. Dowthwaite, Site-specific, adult bone benefits attributed to loading during youth: a preliminary longitudinal analysis, Bone 85 (2016) 148–159.

[28] A.S. Tenforde, M. Fredericson, Influence of sports participation on bone health in the young athlete: a review of the literature, PM R 3 (2011) 861–867.

[29] R. Nikander, P. Kannus, P. Dastidar, M. Hannula, L. Harrison, T. Cervinka, N. G. Narra, R. Aktour, T. Arola, H. Eskola, S. Soimakallio, A. Heinonen, J. Hyttinen, H. Sievänen, Targeted exercises against hip fragility, Osteoporos. Int. 20 (2009) 1321–1328.

[30] S. Abe, N. Narra, R. Nikander, J. Hyttinen, R. Kouhia, H. Sievänen, Exercise loading history and femoral neck strength in a sideways fall: a three-dimensional finite element modeling study, Bone 92 (2016) 9–17.

[31] S. Abe, N. Narra, R. Nikander, J. Hyttinen, R. Kouhia, H. Sievänen, Impact loading history modulates hip fracture load and location: a finite element simulation study of the proximal femur in female athletes, J. Biomech. 76 (2018) 136–143.

[32] T.P. Pinilla, K.C. Boardman, M.L. Bouxsein, E.R. Myers, W.C. Hayes, Impact direction from a fall influences the failure load of the proximal femur as much as age-related bone loss, Calcif. Tissue Int. 58 (1996) 231–235.

[33] J.H. Keyak, H.B. Skinner, J.A. Fleming, Effect of force direction on femoral fracture load for two types of loading conditions, J. Orthop. Res. 19 (2001) 539–544.

[34] M. Bessho, I. Ohnishi, T. Matsumoto, S. Ohashi, J. Matsuyama, K. Tobita, M. Kaneko, K. Nakamura, Prediction of proximal femur strength using a CT-based nonlinear finite element method: differences in predicted fracture load and site with changing load and boundary conditions, Bone 45 (2009) 226–231.

[35] C. Falcinelli, E. Schileo, L. Balistreri, F. Baruffaldi, B. Bordini, M. Viceconti, U. Albisinni, F. Ceccarelli, L. Milandri, A. Toni, F. Taddei, Multiple loading conditions analysis can improve the association between finite element bone strength estimates and proximal femur fractures: a preliminary study in elderly women, Bone 67 (2014) 71–80.

[36] Z. Altai, M. Qasim, X. Li, M. Viceconti, The effect of boundary and loading conditions on patient classification using finite element predicted risk of fracture, Clin. Biomech. 68 (2019) 137–143.

[37] L. Grassi, E. Schileo, F. Taddei, L. Zani, M. Juszczyk, L. Cristofolini, M. Viceconti, Accuracy of finite element predictions in sideways load configurations for the proximal human femur, J. Biomech. 45 (2012) 394–399.

[38] K.K. Nishiyama, M. Ito, A. Harada, S.K. Boyd, Classification of women with and without hip fracture based on quantitative computed tomography and finite element analysis, Osteoporos. Int. 25 (2014) 619–626.

[39] P. Bhattacharya, Z. Altai, M. Qasim, M. Viceconti, A multiscale model to predict current absolute risk of femoral fracture in a postmenopausal population, Biomech. Model. Mechanobiol. 18 (2019) 301–318.

[40] M. Qasim, G. Farinella, J. Zhang, X. Li, L. Yang, R. Eastell, M. Viceconti, Patient-specific finite element estimated femur strength as a predictor of the risk of hip fracture: the effect of methodological determinants, Osteoporos. Int. 27 (2016) 2815–2822.

[41] R. Nikander, H. Sievänen, K. Uusi-Rasi, A. Heinonen, P. Kannus, Loading modalities and bone structures at nonweight-bearing upper extremity and weight-bearing lower extremity: a pQCT study of adult female athletes, Bone 39 (2006) 886–894.

[42] H. Sievänen, T. Karstila, P. Apuli, P. Kannus, Magnetic resonance imaging of the femoral neck cortex, Acta Radiol. 48 (2007) 308–314.

[43] J. Carballido-Gamio, S. Bonaretti, I. Saeed, R. Harnish, R. Recker, A.J. Burghardt, J.H. Keyak, T. Harris, S. Khosla, T.F. Lang, Automatic multi-parametric quantification of the proximal femur with quantitative computed tomography, Quant Imaging Med Surg. 5 (2015) 552–568.

[44] D.D. Cody, F.J. Hou, G.W. Divine, D.P. Fyhrie, Short term in vivo precision of proximal femoral finite element modeling, Ann. Biomed. Eng. 28 (2000) 408–414.

[45] C.S. Rajapakse, A. Hotca, B.T. Newman, A. Ramme, S. Vira, E.A. Kobe, R. Miller, S. Honig, G. Chang, Patient-specific hip fracture strength assessment with microstructural MR imaging-based finite element modeling, Radiology 283 (2017) 854–861.

[46] G. Taubin, Curve and surface smoothing without shrinkage, in: Proc IEEE Int Conf Comput Vis, IEEE Computer Society, Cambridge, MA, USA, 1995, pp. 852–857.

[47] G.N. Duda, M. Heller, J. Albinger, O. Schulz, E. Schneider, L. Claes, Influence of muscle forces on femoral strain distribution, J. Biomech. 31 (1998) 841–846.

[48] M. Lengsfeld, J. Kaminsky, B. Merz, R.P. Franke, Sensitivity of femoral strain pattern analyses to resultant and muscle forces at the hip joint, Med. Eng. Phys. 18 (1996) 70–78.

[49] K. Polgár, H.S. Gill, M. Viceconti, D.W. Murray, J.J. O'Connor, Strain distribution within the human femur due to physiological and simplified loading: finite element analysis using the muscle standardized femur model, Proc. Inst. Mech. Eng. H J. Eng. Med. 217 (2003) 173–189.

[50] C. Öhman, M. Baleani, C. Pani, F. Taddei, M. Alberghini, M. Viceconti, M. Manfrini, Compressive behaviour of child and adult cortical bone, Bone 49 (2011) 769–776.

[51] A.D. Sylvester, P.A. Kramer, Young's modulus and load complexity: modeling their effects on proximal femur strain, Anat Rec (Hoboken). 301 (2018) 1189–1202.

[52] L. Cristofolini, G. Conti, M. Juszczyk, S. Cremonini, S. Van Sint Jan, M. Viceconti, Structural behaviour and strain distribution of the long bones of the human lower limbs, J. Biomech. 43 (2010) 826–835.

[53] E. Schileo, L. Balistreri, L. Grassi, L. Cristofolini, F. Taddei, To what extent can linear finite element models of human femora predict failure under stance and fall loading configurations? J. Biomech. 47 (2014) 3531–3538.

[54] E. Schileo, F. Taddei, L. Cristofolini, M. Viceconti, Subject-specific finite element models implementing a maximum principal strain criterion are able to estimate failure risk and fracture location on human femurs tested in vitro, J. Biomech. 41 (2008) 356–367.

[55] Y. Yang, V. Komisar, N. Shishov, B. Lo, A.M.B. Korall, F. Feldman, S. N. Robinovitch, The effect of fall biomechanics on risk for hip fracture in older adults: a cohort study of video-captured falls in long-term care, J. Bone Miner. Res. 35 (2020) 1914–1922.

[56] U.T. Iwaniec, R.T. Turner, Influence of body weight on bone mass, architecture and turnover, J. Endocrinol. 230 (2016) R115–R130.

[57] E.J. Jones, P.A. Bishop, A.K. Woods, J.M. Green, Cross-sectional area and muscular strength: a brief review, Sport Med. 38 (2008) 987–994.

[58] S.J. Warden, J. Carballido-Gamio, A.M. Weatherholt, J.H. Keyak, C. Yan, M. E. Kersh, T.F. Lang, R.K. Fuchs, Heterogeneous spatial and strength adaptation of the proximal femur to physical activity: a within-subject controlled cross-sectional study, J. Bone Miner. Res. 35 (2020) 681–690.

[59] C.A. Bailey, K. Brooke-Wavell, Optimum frequency of exercise for bone health: randomised controlled trial of a high-impact unilateral intervention, Bone 46 (2010) 1043–1049.

[60] S.J. Allison, K.E.S. Poole, G.M. Treece, A.H. Gee, C. Tonkin, W.J. Rennie, J. P. Folland, G.D. Summers, K. Brooke-Wavell, The influence of high-impact exercise on cortical and trabecular bone mineral content and 3D distribution

across the proximal femur in older men: a randomized controlled unilateral intervention, J. Bone Miner. Res. 30 (2015) 1709–1716.
[61] M.E. Kersh, S. Martelli, R. Zebaze, E. Seeman, M.G. Pandy, Mechanical loading of the femoral neck in human locomotion, J. Bone Miner. Res. 33 (2018) 1999–2006.
[62] P. Pellikaan, G. Giarmatzis, J. Vander Sloten, S. Verschueren, I. Jonkers, Ranking of osteogenic potential of physical exercises in postmenopausal women based on femoral neck strains, PLoS One. 13 (2018), e0195463.
[63] R.K. Fuchs, J. Carballido-Gamio, J.H. Keyak, M.E. Kersh, S.J. Warden, Physical activity induced adaptation can increase proximal femur strength under loading from a fall onto the greater trochanter, Bone 152 (2021), 116090.
[64] N. Narra, R. Nikander, J. Viik, J. Hyttinen, H. Sievänen, Femoral neck cross-sectional geometry and exercise loading, Clin. Physiol. Funct. Imaging 33 (2013) 258–266.
[65] R. Bryan, P.B. Nair, M. Taylor, Use of a statistical model of the whole femur in a large scale, multi-model study of femoral neck fracture risk, J. Biomech. 42 (2009) 2171–2176.
[66] H. Sievänen, L. Józsa, I. Pap, M. Järvinen, T.A. Järvinen, P. Kannus, T.L. Järvinen, Fragile external phenotype of modern human proximal femur in comparison with medieval bone, J. Bone Miner. Res. 22 (2007) 537–543.
[67] A. Heinonen, H. Sievänen, H. Kyröläinen, J. Perttunen, P. Kannus, Mineral mass, size, and estimated mechanical strength of triple jumpers' lower limb, Bone 29 (2001) 279–285.
[68] M.R. Ramey, K.R. Williams, Ground reaction forces in the triple jump, Int. J. Sport Biomech. 1 (1985) 233–239.
[69] N. Smith, R. Dyson, L. Janaway, Ground reaction force measures when running in soccer boots and soccer training shoes on a natural turf surface, Sport Eng. 7 (2004) 159–167.
[70] M.K. Dayakidis, K. Boudolos, Ground reaction force data in functional ankle instability during two cutting movements, Clin. Biomech. 21 (2006) 405–411.
[71] K. Ball, Loading and performance of the support leg in kicking, J. Sci. Med. Sport 16 (2013) 455–459.
[72] C.F. Munro, D.I. Miller, A.J. Fuglevand, Ground reaction forces in running: a reexamination, J. Biomech. 20 (1987) 147–155.
[73] S. Logan, I. Hunter, J.T. Hopkins, J.B. Feland, A.C. Parcell, Ground reaction force differences between running shoes, racing flats, and distance spikes in runners, J Sport Sci Med. 9 (2010) 147–153.
[74] B. Kluitenberg, S.W. Bredeweg, S. Zijlstra, W. Zijlstra, I. Buist, Comparison of vertical ground reaction forces during overground and treadmill running. A validation study, BMC Musculoskelet Disord. 13 (2012) 235.
[75] B.A. Blanksby, D.G. Gathercole, R.N. Marshall, Force plate and video analysis of the tumble turn by age-group swimmers, J. Swim. Res. 11 (1996) 40–45.
[76] A.D. Lyttle, B.A. Blanksby, B.C. Elliott, D.G. Lloyd, Investigating kinetics in the freestyle Flip turn push-off, J. Appl. Biomech. 15 (1999) 242–252.
[77] P.A. Swinton, R. Lloyd, J.W. Keogh, I. Agouris, A.D. Stewart, A biomechanical comparison of the traditional squat, powerlifting squat, and box squat, J. Strength Cond. Res. 26 (2012) 1805–1816.
[78] G. Giarmatzis, I. Jonkers, M. Wesseling, S. Van Rossom, S. Verschueren, Loading of hip measured by hip contact forces at different speeds of walking and running, J. Bone Miner. Res. 30 (2015) 1431–1440.
[79] S. Martelli, M.E. Kersh, A.G. Schache, M.G. Pandy, Strain energy in the femoral neck during exercise, J. Biomech. 47 (2014) 1784–1791.
[80] R. Huiskes, H. Weinans, H.J. Grootenboer, M. Dalstra, B. Fudala, T.J. Slooff, Adaptive bone-remodeling theory applied to prosthetic-design analysis, J. Biomech. 20 (1987) 1135–1150.
[81] J. Kerner, R. Huiskes, G.H. van Lenthe, H. Weinans, B. van Rietbergen, C.A. Engh, A.A. Amis, Correlation between pre-operative periprosthetic bone density and post-operative bone loss in THA can be explained by strain-adaptive remodelling, J. Biomech. 32 (1999) 695–703.
[82] T.P.M. Johnson, S. Socrate, M.C. Boyce, A viscoelastic, viscoplastic model of cortical bone valid at low and high strain rates, Acta Biomater. 6 (2010) 4073–4080.
[83] S. Le Pense, Y. Chen, Contribution of fluid in bone extravascular matrix to strain-rate dependent stiffening of bone tissue - a poroelastic study, J. Mech. Behav. Biomed. Mater. 65 (2017) 90–101.
[84] S. Martelli, B. Beck, D. Saxby, D. Lloyd, P. Pivonka, M. Taylor, Modelling human locomotion to inform exercise prescription for osteoporosis, Curr Osteoporos Rep. 18 (2020) 301–311.
[85] R. Zhao, M. Zhao, Z. Xu, The effects of differing resistance training modes on the preservation of bone mineral density in postmenopausal women: a meta-analysis, Osteoporos. Int. 26 (2015) 1605–1618.
[86] M. Martyn-St James, S. Carroll, Effects of different impact exercise modalities on bone mineral density in premenopausal women: a meta-analysis, J. Bone Miner. Metab. 28 (2010) 251–267.
[87] M. Martyn-St James, S. Carroll, A meta-analysis of impact exercise on postmenopausal bone loss: the case for mixed loading exercise programmes, Br. J. Sports Med. 43 (2009) 898–908.
[88] M. Martyn-St James, S. Carroll, Meta-analysis of walking for preservation of bone mineral density in postmenopausal women, Bone 43 (2008) 521–531.
[89] D.R. Carter, W.C. Hayes, The compressive behavior of bone as a two-phase porous structure, J. Bone Joint Surg. Am. 59 (1977) 954–962.
[90] E.F. Morgan, H.H. Bayraktar, T.M. Keaveny, Trabecular bone modulus-density relationships depend on anatomic site, J. Biomech. 36 (2003) 897–904.
[91] W.S. Enns-Bray, H. Bahaloo, I. Fleps, O. Ariza, S. Gilchrist, R. Widmer, P. Guy, H. Pálsson, S.J. Ferguson, P.A. Cripton, B. Helgason, Material mapping strategy to improve the predicted response of the proximal femur to a sideways fall impact, J. Mech. Behav. Biomed. Mater. 78 (2018) 196–205.
[92] I. Fleps, P. Guy, S.J. Ferguson, P.A. Cripton, B. Helgason, Explicit finite element models accurately predict subject-specific and velocity-dependent kinetics of sideways fall impact, J. Bone Miner. Res. 34 (2019) 1837–1850.
[93] K.M. Nicks, S. Amin, L.J. Melton III, E.J. Atkinson, L.K. McCready, B.L. Riggs, K. Engelke, S. Khosla, Three-dimensional structural analysis of the proximal femur in an age-stratified sample of women, Bone 55 (2013) 179–188.
[94] E. Schileo, E. Dall'Ara, F. Taddei, A. Malandrino, T. Schotkamp, M. Baleani, M. Viceconti, An accurate estimation of bone density improves the accuracy of subject-specific finite element models, J. Biomech. 41 (2008) 2483–2491.
[95] C.S. Rajapakse, A.R. Farid, D.C. Kargilis, B.C. Jones, J.S. Lee, A.J. Johncola, A. S. Batzdorf, S.S. Shetye, M.W. Hast, G. Chang, MRI-based assessment of proximal femur strength compared to mechanical testing, Bone 133 (2020), 115227.
[96] C.M. Phan, M. Matsuura, J.S. Bauer, T.C. Dunn, D. Newitt, E.M. Lochmueller, F. Eckstein, S. Majumdar, T.M. Link, Trabecular bone structure of the calcaneus: comparison of MR imaging at 3.0 and 1.5 T with micro-CT as the standard of reference, Radiology 239 (2006) 488–496.
[97] K. Chiba, A.J. Burghardt, M. Osaki, S. Majumdar, Heterogeneity of bone microstructure in the femoral head in patients with osteoporosis: an ex vivo HR-pQCT study, Bone 56 (2013) 139–146.
[98] G. Chang, S. Honig, R. Brown, C.M. Deniz, K.A. Egol, J.S. Babb, R.R. Regatte, C. S. Rajapakse, Finite element analysis applied to 3-T MR imaging of proximal femur microarchitecture: lower bone strength in patients with fragility fractures compared with control subjects, Radiology 272 (2014) 464–474.
[99] S. Mori, R. Harruff, W. Ambrosius, D.B. Burr, Trabecular bone volume and microdamage accumulation in the femoral heads of women with and without femoral neck fractures, Bone 21 (1997) 521–526.
[100] U. Hansen, P. Zioupos, R. Simpson, J.D. Currey, D. Hynd, The effect of strain rate on the mechanical properties of human cortical bone, J. Biomech. Eng. 130 (2008), 011011.
[101] W.S. Enns-Bray, S.J. Ferguson, B. Helgason, Strain rate dependency of bovine trabecular bone under impact loading at sideways fall velocity, J. Biomech. 75 (2018) 46–52.
[102] F. Feldman, S.N. Robinovitch, Reducing hip fracture risk during sideways falls: evidence in young adults of the protective effects of impact to the hands and stepping, J. Biomech. 40 (2007) 2612–2618.
[103] W.S. Enns-Bray, J.S. Owoc, K.K. Nishiyama, S.K. Boyd, Mapping anisotropy of the proximal femur for enhanced image based finite element analysis, J. Biomech. 47 (2014) 3272–3278.
[104] W.S. Enns-Bray, O. Ariza, S. Gilchrist, R.P. Widmer Soyka, P.J. Vogt, H. Palsson, S. K. Boyd, P. Guy, P.A. Cripton, S.J. Ferguson, B. Helgason, Morphology based anisotropic finite element models of the proximal femur validated with experimental data, Med. Eng. Phys. 38 (2016) 1339–1347.
[105] V. Komisar, S.N. Robinovitch, The role of fall biomechanics in the cause and prevention of bone fractures in older adults, Curr Osteoporos Rep. 19 (2021) 381–390.
[106] M. Nasiri Sarvi, Y. Luo, Sideways fall-induced impact force and its effect on hip fracture risk: a review, Osteoporos. Int. 28 (2017) 2759–2780.
[107] I. Fleps, W.S. Enns-Bray, P. Guy, S.J. Ferguson, P.A. Cripton, B. Helgason, On the internal reaction forces, energy absorption, and fracture in the hip during simulated sideways fall impact, PLoS One. 13 (2018), e0200952.

PUBLICATION IV

Ricci-flow based conformal mapping of the proximal femur to identify exercise loading effects

Nathaniel Narra, Shinya Abe, Vassil Dimitrov, Riku Nikander, Reijo Kouhia, Harri Sievänen, and Jari Hyttinen

Scientific Reports. 2018 Mar;8:4823
doi: 10.1038/s41598-018-23248-y

SCIENTIFIC REPORTS

OPEN

Ricci-flow based conformal mapping of the proximal femur to identify exercise loading effects

Received: 7 September 2017
Accepted: 7 March 2018
Published online: 19 March 2018

Nathaniel Narra[1], Shinya Abe[2], Vassil Dimitrov[3,8], Riku Nikander[4,5,6], Reijo Kouhia[2], Harri Sievänen[7] & Jari Hyttinen[1]

The causal relationship between habitual loading and adaptive response in bone morphology is commonly explored by analysing the spatial distribution of mechanically relevant features. In this study, 3D distribution of features in the proximal femur of 91 female athletes (5 exercise loading groups representing habitual loading) is contrasted with 20 controls. A femur specific Ricci-flow based conformal mapping procedure was developed for establishing correspondence among the periosteal surfaces. The procedure leverages the invariance of the conformal mapping method to isometric shape differences to align surfaces in the 2D parametric domain, to produce dense correspondences across an isotopological set of surfaces. This is implemented through a multi-parametrisation approach to detect surface features and to overcome the issue of inconsistency in the anatomical extent present in the data. Subsequently, the group-wise distribution of two mechanically relevant features was studied – cortical thickness and surface principal strains (simulation results of a sideways fall). Statistical inferences over the surfaces were made by contrasting the athlete groups with the controls through statistical parametric mapping. With the aid of group-wise and composite-group maps, proximal femur regions affected by specific loading groups were identified with a high degree of spatial localisation.

Bone is an adaptive hard tissue which, among its other characteristics, is designed to be robust against physiological loads. The position of the bone and its function within the skeletal frame limits its range of motion through linkages between bones, joints and muscle attachments. This results in a constrained envelope of loading directions that a particular load bearing bone can experience during common habitual movements. In humans, the femur is indispensable for locomotion and load-bearing functions within a large range of motion under potentially high load magnitudes and impacts. The ability of the femur to withstand these loads is achieved through adaptive processes that modulate its morphology and composition. The cortical geometry at the proximal femur consequently reflects the most robust construction adapted for the specific loading it habitually experiences (e.g., locomotion and physical activity). Thus, consistent loading in specific directions, such as physical training of athletes over a long period of time, can induce corresponding local adaptations in the cortical geometry[1,2]. While loading stimuli have the most pronounced effect in adolescence[3], their effectiveness in stimulating an adaptation decreases after bone reaches maturity[4]. However, it is known that the exercise-induced bone thickening during growth occurs through new bone formation on the periosteal bone surface, while age-related bone loss takes place at the endocortical bone surface[5]. Thus, beneficial geometric adaptations accrued during adolescence and young adulthood may have lasting benefits in senescence despite associated bone loss[6]. This was observed in retired (>60 years) ice-hockey and soccer players as reduced fracture risk, in comparison to age matched controls, despite some loss of exercise-induced gain in bone[7]. Moreover, studies have shown that beneficial bone adaptation can be observed through exercise even in older people[8] and can help in arresting the attenuation of bone strength due to age-related bone loss[9]. Studying this cause-effect relationship between physical loading and regional adaptation is an area of active pursuit. Understanding the mechanisms that modulate specific adaptations at bone

[1]BioMediTech Institute and Faculty of Biomedical Sciences and Engineering, Tampere University of Technology, Tampere, Finland. [2]Laboratory of Civil Engineering, Tampere University of Technology, Tampere, Finland. [3]Department of Electrical and Computer Engineering, University of Calgary, Calgary, Canada. [4]Department of Health Sciences, University of Jyväskylä, Jyväskylä, Finland. [5]GeroCenter Foundation for Aging Research and Development, Jyväskylä, Finland. [6]Jyväskylä Central Hospital, Jyväskylä, Finland. [7]The UKK Institute for Health Promotion Research, Tampere, Finland. [8]Geometric Energy Corporation, Calgary, Canada. Correspondence and requests for materials should be addressed to N.N. (email: nathaniel.narragirish@tut.fi)

regions susceptible to fractures can be used as paradigms for preventing age-related degradation of bone robusticity, or alternatively, increased bone fragility. Also, establishing morphological features that result from specific loading patterns may help in recreating activity of past populations in the field of archaeological anthropology[10].

Studies exploring the spatial heterogeneity in the adaptive response to physical loading have traditionally analysed bone cross-sections with respect to mechanically relevant (morphometric) features. To increase the detectability of this heterogeneity it is necessary to increase the spatial resolution of analyses. Within femoral neck cross-sections this has been achieved by partitioning into quadrants[1], octants or higher angular divisions[2,11,12] defined with respect to anatomical directions (e.g. superior, posterior, anterior). Access to 3D tomographic data has extended the potential for such detailed analyses. Concepts of computational anatomy[13] and statistical parametric mapping[14] make it possible to investigate the distribution of relevant parameters over 3D regions[15–17] and assess their statistical significance. In large sample studies, establishing anatomical correspondence across samples is a prerequisite. Often noise and varying, or even incomplete, anatomical extents in the data can compromise the consistency in the shape registration process. Thus, methods that can provide computationally reliable registration across multiple surface instances can expand the tool-set beyond the commonly used iterative closest point (ICP) based methods[18].

This study introduces a novel application of the conformal mapping method for establishing correspondence between proximal femur instances. The method treats the surface as a differentiable manifold and converts the 3D registration problem into 2D. This dimension reduction is achieved by a parametrisation procedure where the surface is conformally mapped to the planar domain using discrete surface Ricci-flow[19,20] implemented in MATLAB (Release 2016b, The MathWorks, Inc., Natick, Massachusetts, United States). The advantages of this method in shape registration and indexing[21] have been exhibited for anatomical objects such as brain[22] and colon[23]. As a supporting case study, this registration approach was developed into a procedural chain to analyse the spatial distribution of geometric adaptation in the proximal femur in response to long-term habitual physical activity. The present dataset consists of young adult female athletes whose consistent and vigorous training regimen represented habitual activity. Geometric morphology was quantified in terms of the spatial distribution of cortical thickness. Adaptation was consequently defined spatially as regions exhibiting statistically significant differences from the controls. Adaptation can also be studied in terms of behaviour under specific mechanical loading. The recent finite element (FE) study conducted by Abe and colleagues simulated a 'supra-physiological' loading caused by sideways falling, to assess fracture risk of proximal femur[24]. Utilizing the results of this simulation, we illustrated the influence of adapted geometry in lowering fall-induced stresses in the femoral neck region. A geometric adaptation that can improve 'bone mechanical performance' at critical fracture sites can help identify beneficial exercises and mobility patterns.

Methods

Data preparation. The data consisted of tomographic Magnetic Resonance (MR) images of the proximal femur of 111 participants - 91 female athletes (age: 24.7 ± 6.1 years) and 20 physically active women serving as a control group (age: 23.7 ± 3.8 years). The MR imaging protocol was based on axial T1-weighted gradient echo VIBE examination with ($0.9\,mm \times 0.9\,mm$) in-plane pixel size and $1\,mm$ slice thickness[1]. The study protocol was approved by the Ethics Committee of the Pirkanmaa Hospital District and each participant gave a written informed consent before the study. All methods implemented and used on the data for analysis in this study were in accordance with relevant guidelines and regulations. The athletes were categorised into mutually exclusive exercise loading groups by their characteristic loading patterns in their respective sports according to our standard procedure[1,25]: high impact (HI) group associated with maximal vertical jumps and high impacts (High jumpers and long jumpers, $N = 19$); odd impact (OI) group associated with rapid acceleration and deceleration as well as moderate to high impacts and bending forces from varying directions (Squash and soccer players, $N = 19$); high magnitude (HM) group associated with movements with coordinated high muscle force production at low rate (Powerlifters, $N = 17$), repetitive impact (RI) group associated with highly repetitive weight bearing impacts and bending forces (Endurance runners, $N = 18$) and repetitive non-impact (RNI) group associated with highly repetitive movements lacking ground impacts (Swimmers, $N = 18$). The anatomy of interest – proximal femur cortical geometry – was manually segmented from the MR image data of each participant. Apparently, the limited in-plane resolution of the native MR images compromises reliable inferences at locations with very thin cortices such as the femoral head and some regions of the femoral neck and the trochanters. However, it has been shown that MR-imaged cross-sections of the femoral neck are sufficiently precise and accurate for study purposes[26]. To extract the proximal femur cortical geometry, the image data of each participant was manually segmented by delineating periosteal and endosteal cortical surfaces. Thereafter the segmented geometry was converted into a volume mesh (10-node tetrahedral elements) for constructing a finite element (FE) model[24]. The nodes from the periosteal and endosteal surfaces of the volume mesh were extracted, along with the maximum and minimum principal strain values from the above-noted simulation results. The selected nodes were used to reconstruct the inner and outer triangular surface meshes of the cortical bone in MeshLab (Visual Computing Lab-ISTI-CNR, http://meshlab.sourceforge.net/). The nodes in the point cloud ($n > 80{,}000$) were first down-sampled to ($n \approx 25{,}000$) using the Poisson disk sampling module[27] and a surface reconstructed using the ball-pivoting module[28]. After checking for and cleaning any major errors (e.g. intersections, face flips, duplicates, holes) in the surfaces, they were remeshed to improve the quality (aspect ratio < 20) of the mesh in Avizo (FEI, Hillsboro, USA). The module implemented in this software attempts isotropic vertex placement based on Lloyd relaxation[29]. The final result of these preparation steps were the inner and outer surface meshes of the cortical bone. The image data included femoral anatomy from the femoral head to the proximal diaphysis of the femur below lesser trochanter. Thus, the open surfaces contained a single boundary at the lower extent of the data representing the distal extent of the femoral diaphysis. The feature vector at every node of the outer surface consisted of the cortical thickness

and the maximum and minimum principal strains. Cortical thickness was calculated at the nodes of the outer surface and defined as the shortest distance to the inner surface.

Planar parametrisation: Discrete Ricci-flow. To analyse and contrast the group-wise morphology of the proximal femurs, it was essential to establish correspondence between all individual surface meshes. The approach used in this work transforms the 3D surfaces into 2D (planar domain) using an angle preserving conformal method based on Ricci-flow. This approach leverages the methodological advantages of invariance towards rigid motion, scale and isometric deformations[21]. The residual deformations such as large non-isotropic deformations can then subsequently be accounted for in the 2D domain – which is a relatively simpler task. We present here a very brief description of the geometric basis for the implemented approach. For details, we refer readers to the textbook by Zeng & Gu where relevant references for the proofs can be found[30]. The discrete representation of the femur surfaces embedded in the Euclidean space $\mathbb{R}^3$ allows them to be treated as differentiable manifolds (2-manifold). Any surface in Euclidean space is a Riemannian surface with an inherent metric called Riemannian metric and a conformal structure. The Uniformisation theorem states that the Riemannian metric can be deformed to admit uniform curvature over the surface: $+1$, 0 or -1. Thus any closed Riemannian surface can be conformally mapped to one of these fundamental surface domains: unit sphere ($+1$), Euclidean plane (0) or hyperbolic plane (-1). The embedding in the relevant domain, referred to as parametrisation, reflects an angle preserving (conformal) transformation. Ricci-flow is a robust curvature flow method introduced by Hamilton[31] that evolves the metric towards uniformisation as a heat diffusion process. It is a powerful method that provides the flexibility to design the final metric based on user-defined distribution of target Gaussian curvature. However, the total curvature is determined by the topology of the surface (S) according to the Gauss-Bonnet theorem: $2\pi\chi(S)$. For an open orientable surface of genus (g) and number of boundaries (b), the Euler number is given by $\chi(S) = 2 - 2g - b$. The genus of a closed surface can be intuitively thought of as the number of handles contained. The proximal femur data presented challenges that were addressed by tailoring specific solutions. The foremost challenge was the lack of anatomical correspondence at the distal boundary (femur diaphysis) of the surfaces across subjects because of different image field of views. This inconsistency of the boundary made it an unreliable reference for the subsequent correspondence detection. Thus appropriate references were derived from surface features through a two-step parametrisation procedure. The first step was devised to detect shape features to introduce a consistently defined reference feature for each mesh. The second step was devised to produce a mapping in a common coordinate space using the reference points for alignment (Fig. 1). The topology of the outer cortical surface ($\chi = 1; g = 0; b = 1$) is conformally equivalent to a disk $\mathbb{R}^2$ (Fig. 1b). Ricci-flow mapping was performed by assigning zero target curvature to all interior points and leaving the boundary node metric unchanged (i.e. a free boundary condition). The resulting conformal factor distribution was used to investigate detectable surface features. Two prominent feature processes were identified from the disk parametrisation – the femoral head (FH) and the greater trochanter (GT). The two features can be seen as peaks whose representative centres were designated as feature points (Fig. 1c). These feature points were used consistently across all participants to introduce a stable reference in the form of an inter-feature geodesic. This was achieved by inserting a boundary (mesh slit) along the inter-feature geodesic path in the parametrised disk (i.e. straight line) and reflected in the native 3D surface. This modified surface ($\chi = 0; g = 0; b = 2$) is conformally equivalent to a Euclidean annulus. The mapping was performed by assigning a target curvature of 0 to all nodes. A cut graph between the GT point and the distal boundary was calculated and the mesh slit along the edges. This enabled the fundamental domain of mapping to be embedded in the complex plane. Subsequently the embedded mesh was oriented so that the inter-feature boundary lay on the imaginary axis with the distal boundary parallel to it and incident on the negative real axis. Finally the mesh was resized such that the inter-feature boundary (on the imaginary axis) was scaled to $[0, 2\pi]$ (Fig. 1d). The annulus was produced through an exponential map of the complex coordinates. The implemented MATLAB script accepts the 3D proximal femur surfaces as input and outputs the parametrised annulus with no user input required in between.

Femur correspondence: planar domains. The result of the above-described parametrisation process produced 111 parametrised meshes embedded in a 2D complex coordinate frame. The embedded nodes benefit from the invariance accorded by the conformal method. That is, any node on the surface would retain its position in the parametric plane even if subjected to rigid, affine or isometric deformations in the native 3D domain. Consequently, the approach for establishing correspondence relied on matching a canonical template mesh (2D) to each of the individual 111 parametrized meshes. For each participant, the nodes of the template were designated with a natural representation[32] which described their position with respect to the target mesh in barycentric coordinates. The 3D coordinates of the template nodes were calculated from the target nodes. This resulted in an elastic registration, where the template mesh conformed to the shape of every proximal femur surface in the dataset. The nodes of the template mesh were used as a dense set of corresponding feature locations across the 111 femur instances. If the variations in the proximal femoral anatomy only exhibited pure isometries then the template nodes would be aligned so that they represented correspondence. However, the shapes did exhibit differences that reflected anisotropic deformations. Thus, in the parametric plane, algorithmically detected features were mapped to clustered locations but were not precisely coincident. Figure 2 illustrates this for five distinct anatomic features[33] that were independently annotated by three researchers experienced in femur anatomy, from 30 different proximal femora meshes randomly chosen from the dataset. Within each annotation cluster, their relative deviation from each other indicates the extent of anisotropy present in the sampled shapes. This deviation, and its contribution towards registration error, was reduced by locally deforming the parametrised template mesh to match the target mesh. In the present work, deformations of the template to correct anisotropic variations (Fig. 3) were based on two feature regions: femoral head and lesser trochanter (LT). Each region consisted of the feature point and the surrounding nodes, which acted as the feature support. The support nodes were defined

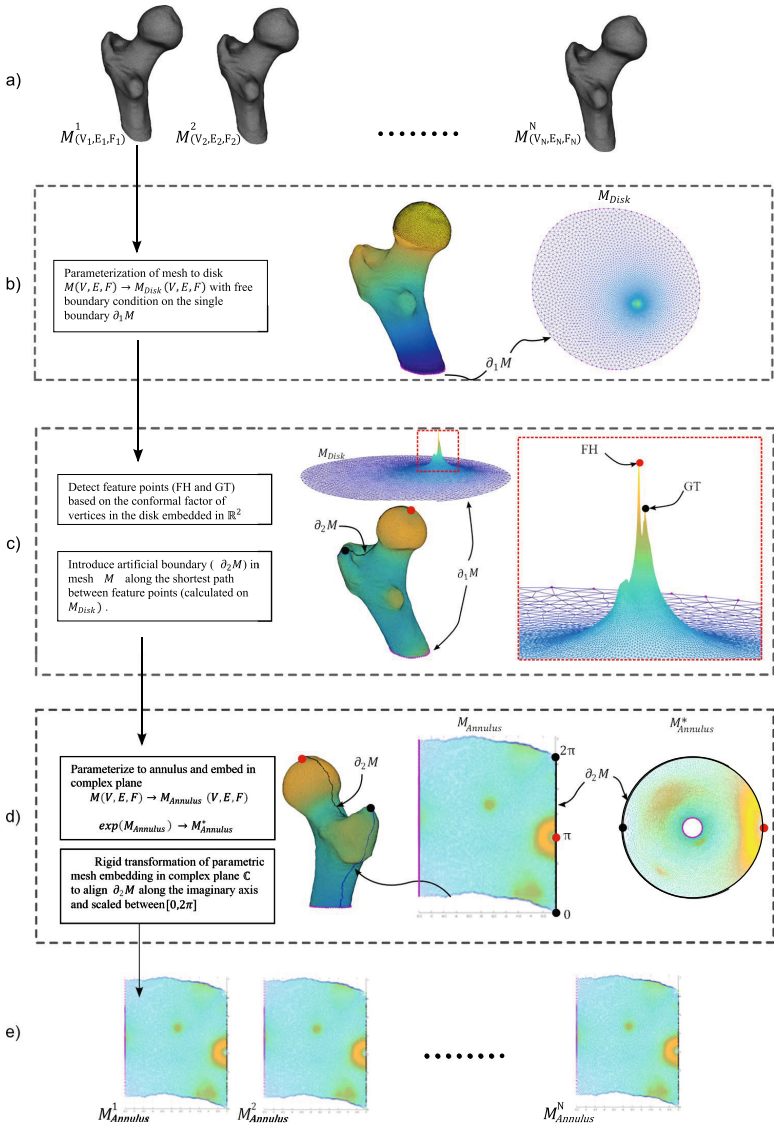

Figure 1. An illustrated description of the parametrising procedure developed for (**a**) proximal femur triangular surface meshes $M_N(V, E, F)$; where V = set of nodes; E = set of edges; F = set of faces ($N = 111$, in this study). (**b**) In the first parametrisation step, the surface is conformally mapped to its topological equivalent: disk. The single boundary ($\partial_1 M$) at the distal end of the proximal femur (shaft) is mapped to the edge of the disk under a free boundary condition, where the metric on the boundary nodes is left unchanged (colour map: conformal factor). (**c**) The parametrised disk along with the conformal factor at the nodes as a height map. The femoral head (FH) and greater trochanter (GT) features are detected as the peaks (inset). The straight line between these features is used to introduce a second boundary ($\partial_2 M$) by slitting the mesh along the line. (**d**) In the first parametrisation step, the surface is conformally mapped to its topological equivalent: annulus. The map is embedded in the complex plane by introducing a cut graph between the GT node and $\partial_1 M$. The embedded meshes are then transformed such that the $\partial_2 M$ boundary lies on the imaginary axis scaled within $[0, 2\pi]$. An exponential map consequently results in the annulus. (**e**) Parametrised meshes in the a common coordinate frame. The boundary edges and feature points are colour coded consistently across all images.

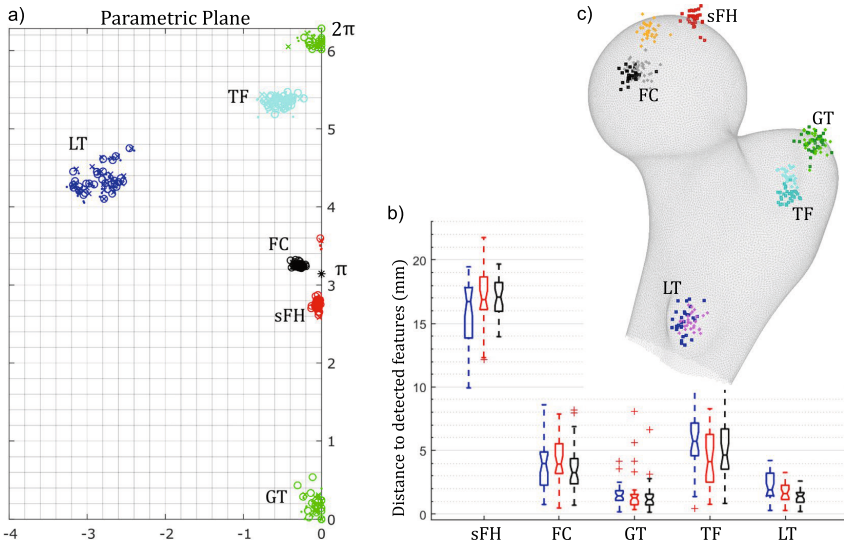

Figure 2. Assessment of the ability of the procedure to establish correspondence through expert annotations. 5 features were annotated by 3 experts on the surfaces of 30 subjects. The subjects were chosen randomly from the dataset of 111. The sites annotated were: superiormost point of femoral head (sFH), fovea capitis centre (FC), tip of greater trochanter (GT), trochanteric fossa centre (TF) and tip of lesser trochanter process(LT). (**a**) Clustering of features in the parametric plane: each surface was parametrised and the position of the annotated node plotted in the parametric plane. The sites are plotted in colour (sFH - red; FC - balck; GT - green; TF - cyan; LT - blue) and each annotator is indicated by a different marker ('x', 'o' and '.'). It should be noted that the boundary introduced along the geodesic between the two algorithmically detected features lies along imaginary axis (femoral head feature at π & greater trochanter feature at $[0, 2\pi]$). Thus, the GT and sFH annotations are reflected about this symmetry. (**b**) Box-plots of the distance between annotations and the associated feature, detected algorithmically, for each annotator (3 experts: each in blue, red and black). (**c**) A visual illustration of the distributions of the annotations (of one expert) and the detected features for 30 samples. Expert annotations are coloured in darker shades and detected features are coloured in lighter shades. The rendered surface of the femur is only for representation to convey a sense of location over the surface.

as those within one standard deviation of the Gaussian surface centred on the feature point, that best fits the particular feature process. The feature processes were observed by mapping the conformal factor distribution over the planar parametrised mesh. The support nodes for each feature in the template were matched by deforming the nodes to occupy corresponding support region in the target parametrised mesh. The FH region was identified from the parametrised disk and the LT region was identified from the parametrised annulus. Smooth deformation of the template mesh was solved through Wendland based radial basis functions[34], driven by the explicit deformations calculated within the two feature regions (FH and LT). To gauge the ability of the procedure in establishing correspondence, the mean distance between the annotations and their associated feature points (detected geometrically) were calculated for each annotator and illustrated as box plots (Fig. 2b). In order to visualize the 3D distribution of the features with respect to the annotations, the annotations of one expert for all 30 samples were mutually aligned using generalised Procrustes analysis. Subsequently, the corresponding transformations were applied to the associated feature points. This was used as a visual confirmation of the relative consistency in the distances between the features and the annotations (Fig. 2c). it should be noted that while the definitions of 4 landmark sites (FC, GT, TF and LT) coincide with their associated geometric feature points, FH and sFH are defined differently. FH represents the femoral head process as a geometric feature, while sFH is defined as the superiormost point on the head. This explains the large average distance between Fh and sFH. However, the plots indicate a consistency in their relative locations, displayed in the restricted spread in the box plots and the 3D distribution render.

The implemented script accepts the user defined template mesh and the stack of 111 parametrised target meshes. The output is a stack of morphed template meshes registered to each of the targets. The nodes of the morphed template meshes were attached with the natural representation with respect to their respective target meshes. The 3D coordinates at the nodes of the 111 morphed templates formed a set of 111 isotopological surfaces (i.e. same number of nodes and connectivity). The nodes were used as a dense set of correspondences established over the surface topologies across all individuals.

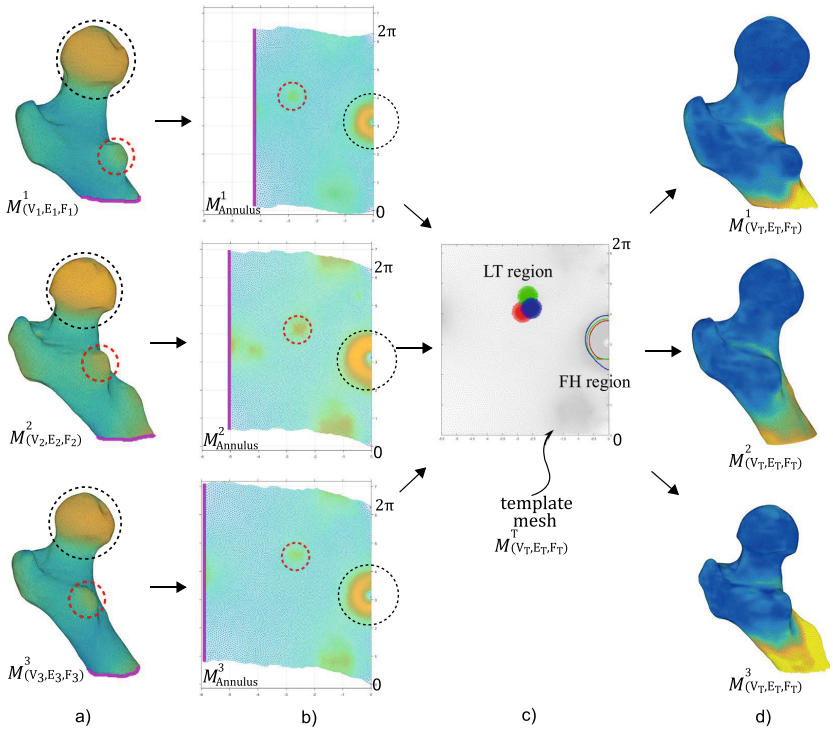

Figure 3. The correspondence procedure illustrated on 3 sample femur shapes from the dataset. (**a**) The three shapes chosen, were selected as they show clearly the differences in femoral neck lengths, shaft lengths and relative positions between the main feature processes - femoral head (FH), greater trochanter (GT) & lesser trochanter (LT). (**b**) The parametric meshes embedded in complex domain illustrate the positions of the FH (black circle) and LT (red circle). The consistent boundary of the mesh is aligned along the imaginary axis. (**c**) The canonical template mesh is matched to each of the parametrisations. The relative positions of the main features (LT and FH regions) in the common coordinate frame are illustrated in colour (red, blue and green for each of the 3 samples femurs). This misalignment is corrected locally on the template mesh through radial basis functions. (**d**) the resulting elastic registration of template mesh to each femoral instance produces an isotopological set of surfaces. The distribution of the cortical thickness values at the nodes are displayed as colour maps for illustrative purposes.

Feature mapping and statistical analysis. After defining correspondence between the individual shapes, the average shape was calculated by generalised Procrustes analysis of the 3D coordinates attached to the nodes. The features of interest (thickness and principal strains) were calculated at the template node locations with respect to the target nodes of the individual mesh based on the natural representation. This resulted in feature maps for every participant, which were subsequently used for making statistical inferences. However making group-wise statistical tests at every node would introduce errors due to the large number of comparisons ($n \approx 25{,}000$). Statistical parametric mapping (SPM) as implemented in the SurfStat package[35] was used to correct for multiple comparisons (http://www.math.mcgill.ca/keith/surfstat/). The significance of the group term was tested by calculating the t-statistics, and subsequently random field theory based multiple comparison correction was performed. Patches were identified on the surface where the features of the loading group differed significantly from the controls. The identified patches represented a cluster of contiguous surface nodes that showed significance. In this study, a threshold of $p < 0.005$ was used for defining supra-threshold clusters and subsequently $p < 0.05$ as random field theory-correlated cluster threshold. Additionally, in order to account for the resolution limitation of the MRI dataset, regions with cortical thickness < 1 *mm* were masked out in SurfStat. The spatial distribution of these clusters is visualised over the surface of the canonical femur to intuitively illustrate their extent. In this work, true anatomical correspondence was implicitly approximated through the parametrisation of representative geometric features. In the presence of anisotropic variations, the algorithm would likely systematically misregister the surfaces. To alleviate the effects of such registration errors the method recommended by Gee and Treece[36] was implemented here by including shape modes as confounding factors. The first 5 shape modes which contain most (≈80%) of the variation were included in the SPM linear model[37,38]. The shape modes were

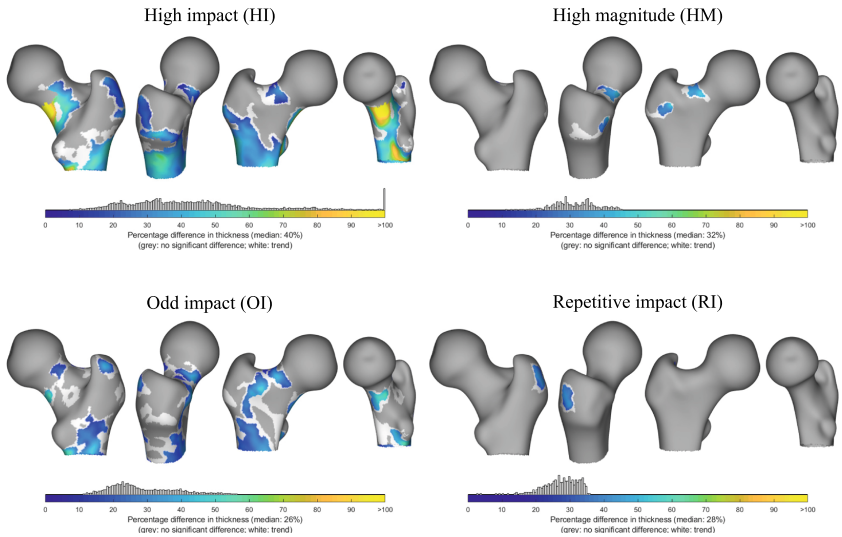

Figure 4. Regions of significant difference in cortical thickness (adjusted for weight, femur size and shape) illustrated on the surface of an average femur as colour patches. Colour maps in these patches represent mean percentage difference in cortical thickness between each exercise loading group and the control group (% higher than control). Their distribution within the patches is plotted as node counts above the colour bar. A relaxed multiple-comparison correction threshold ($p < 0.025$) for defining supra-threshold clusters (in white) was used purely to illustrate the trend in the distribution of these clusters; no formal inferences were made or discussed. The RNI group did not show any significant difference from controls, due to which it was omitted from this illustration.

calculated from vertex deformations, from their mean positions, following a generalised Procrustes alignment. As the scale was normalised in the procrustes analysis, the first shape mode did not reflect the scale and was thus included as a confounding factor. The linear model used for analysing the cortical thickness distribution involved the following variables – exercise loading group, body weight, shape and femur scale (size). Scale factor of each participant was defined relative to the average (canonical) shape which was transformed (Procrustes) to each shape in the isotopological dataset. The linear model variables for the principal strains (maximum and minimum) distribution were group, shape and individually estimated impact force. This impact force was obtained from the previous study[24] and represented the applied force under which the respective FE models were simulated. The weight and height of each subject was used in calculating this force and thus, were excluded from the linear model.

Data availability. The MATLAB code for the procedure developed in this study are available in the GitHub repository, Repository-link https://github.com/NathanielNarra/Femur-RicciFlow. The datasets generated during the current study and a select sample of 20 femur shapes from the dataset (for testing purposes) are also made available.

Results

All parametrisation and registration processes were implemented in MATLAB. When the triangular surface meshes were treated for mesh quality, the parametrisation of a single femur mesh (≈25,000 nodes) took approximately 2 minutes on a desktop computer (Intel Xeon 2.4 GHz, RAM 54 GB). Bad triangle quality in the input mesh increased the convergence time of the evolving metric (≈4–5 mins).

The cortical thickness distribution in each loading group was contrasted with the control group, and statistical significances inferred by controlling for body weight, femur scale and shape (Fig. 4). The average femur shape of the entire dataset was used to illustrate the node clusters that differed statistically significantly from the control group. The percentage differences in cortical thickness at the nodes within these significant clusters were mapped in colour. In the HI group, the area covered by the clusters was the largest among all groups, indicating a greater extent of response in this group. Clusters were observed in the inferior and posterior regions of the femoral neck, with up to 90–110% thicker cortices. Significant response was also observed below the inter-trochanteric line in the metaphysis/proximal diaphysis regions, with mean differences in the identified clusters mostly in the range of 20–50% (median: 40%). In the OI group, large clusters were seen in the medial and posterior regions around lesser trochanter. Interestingly, a large cluster spanned the anterior aspect of the proximal femur; extending into the important superior region of the femoral neck. The mean percentage differences in the clusters were mostly in the range of 15–40% (median: 26%). The HM group showed a relatively minor cluster extent in the superior and

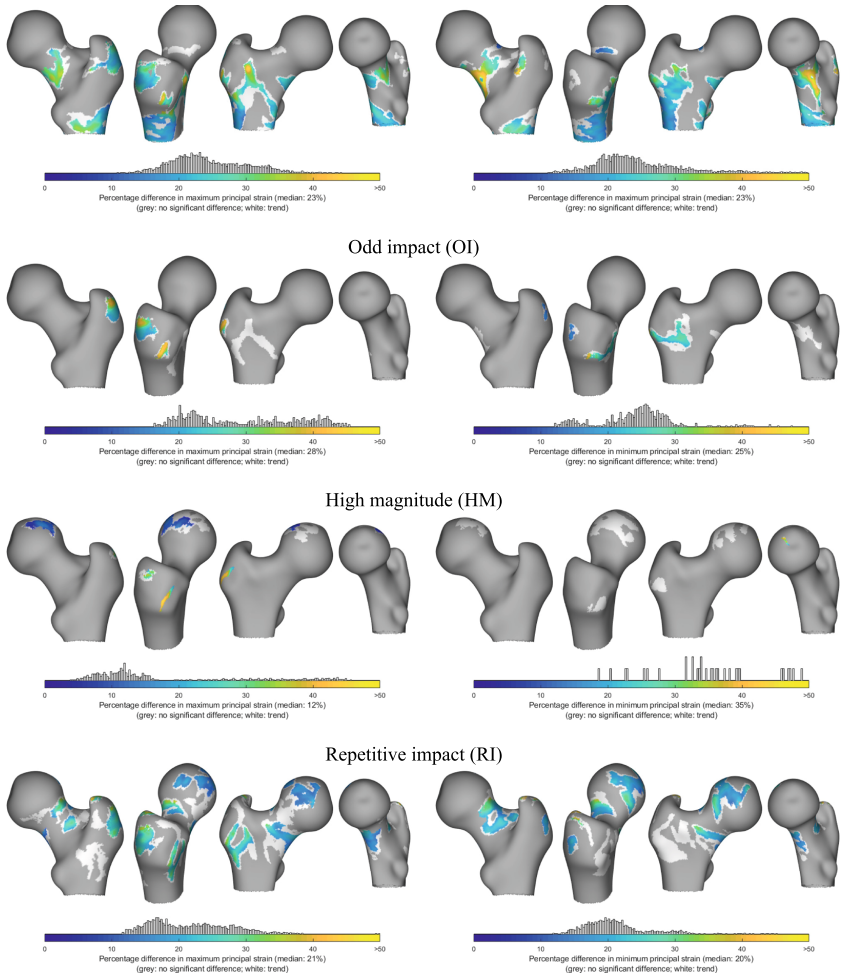

Figure 5. Regions of significant difference in maximum and minimum principal strains at the surface nodes (adjusted for individual impact force and shape) illustrated on the surface of an average femur as colour patches. Colour maps in these patches represent mean percentage difference in the principal strains between each exercise loading group and the control group (% lower than control). Their distribution within the patches is plotted as node counts above the colour bar. A relaxed multi-comparison correction threshold ($p < 0.025$) for defining supra-threshold clusters (in white) was used purely to illustrate the trend in the distribution of these clusters; no formal inferences were made or discussed. The RNI group did not show any significant difference from controls, due to which it was omitted from this illustration.

supero-anterior regions of the femoral neck; with the mean percentage difference in the cluster within 25–40% (median: 32%). The RI group showed a small region of significant clusters with a median 28% difference in cortical thickness on the lateral side of the greater trochanteric process. The RNI group did not show significant differences in the cortical distribution from the control group.

Surface maximum and minimum principal strain distribution revealed differences in response regions when exercise loading groups were contrasted with the controls (Fig. 5). Statistical significances were inferred by controlling for estimated individual impact force during a sideways fall. The HI group showed large cluster extents in the inferior and posterior regions of the femoral neck. Clusters were also observed in the anterior region roughly extending distally from the inter-trochanteric line. In the OI group a large cluster was found spanning the anterior aspect of the inter-trochanteric line. The RI group showed large clusters nearly all around the femoral neck region except a small span at the supero-anterior region. Other clusters in the RI group were also found in the lateral

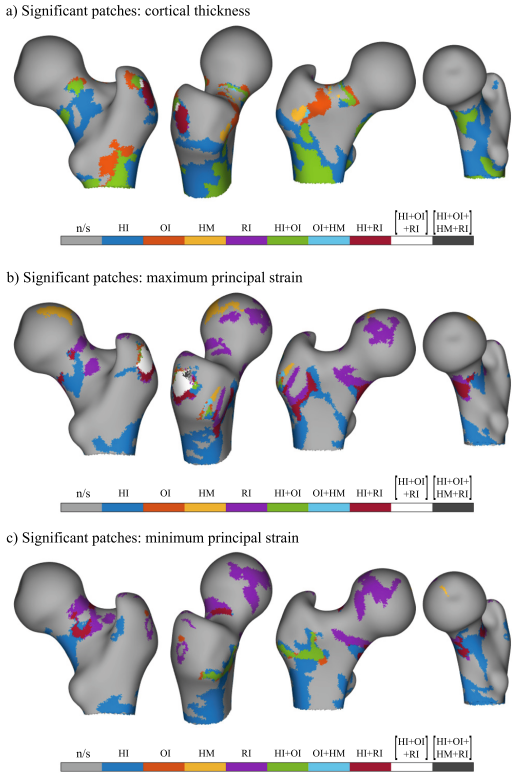

Figure 6. The significant clusters from the loading groups are combined into a single map. The regions are colour coded according to the specific or combination of loading groups responsible (n/s: no significance). The combination regions are where multiple loading groups (as indicated) show significant differences from controls. Compiled from the results for (**a**) cortical thickness (**b**) maximum principal strain (**c**) minimum principal strain.

region of the greater trochanter and superior region of the femoral head. In the HM group, only a tiny cluster was found while the RNI group showed no significantly differing clusters from the control group.

The group-wise clusters were used to construct a single composite surface visualisation for cortical thickness (Fig. 6a), maximum principal strain (Fig. 6b) and minimum principal strain (Fig. 6c). Here, unique regions were identified that showed significant response to specific loading regimes. Moreover, regions that might respond to combinations of different loading types were also identified.

Discussion

In large sample analyses of the proximal femur geometry, the co-registration of multiple femur instances is an essential pre-processing step. The task of establishing correspondence is commonly done by first removing rigid motion to normalise the global pose of the femur shapes. Subsequently non-rigid registration is performed, relying typically on iterative closest point and b-splines to perform non-rigid registration. The external phenotype of the femur is relatively simple (as a geometric topology) and largely similar within population. However, distinct anatomical features that can be reliably detected are sparse in number. Some studies have supplemented the count with derived landmarks and have created procedures that perform the identifications autonomously[39]. A majority of these features are located in the proximal and distal epiphysis of the femur. The femur dataset studied in this work is not only incomplete representing the proximal part only but also inconsistent in its anatomical extent, which made the registration process challenging. Thus, an elegant solution was sought to manage these challenges and in turn to develop a tool for proximal femur registration.

This study presents an application of Ricci-flow based conformal surface parametrisation for analysing the proximal femur morphology. The implemented procedural chain defines correspondence between the surface meshes by using only three consistently detectable anatomic features (automated landmarks). In its current form, the algorithm relies on the presence of the complete epiphysis to enable the detection of the femoral head and greater trochanter processes. Inconsistencies in the femur anatomy distal to the inter-trochanteric line are accommodated. Thus the method was designed to establish correspondence between surfaces with varying femur shaft

lengths. The robustness of Ricci-flow based conformal mapping method was leveraged to establish isometry invariant global correspondence through a dimension reduction approach (3D↦2D). This could be observed in Fig. 3 where the three sample femurs illustrate differences in femoral neck length, shaft length and lesser trochanter position. It can be seen that the protrusion near the lesser trochanter (Fig. 3a, mesh: $M^2_{(V_2,E_2,F_2)}$) and the varying shaft lengths in all three did not skew the registration process. The residual variations in the shape that are not isometric in nature can manifest as differences in the relative distances between the features. This can be observed by the plotted lesser trochanter regions and the head-neck contour (Fig. 3c). Residual variations were locally handled in the 2D planar domain using simple 2D deformation methods, specifically using radial basis functions.

While the procedure developed in this work is entirely tuned towards the analysis of the proximal femur, the Ricci flow method provides flexibility to handle any topology. By perceiving the surface data as a geometric manifold, their topological invariance can be used to compute conformal maps. Working within the constraints of the Gauss-Bonnet theorem, consequently any number of parametrisations can be computed to facilitate feature detection. Different parametrisations result in different conformal factors distributions that can be used as additional parameters in detecting surface features. In this work, the femur was parametrised in two different ways to detect three anatomic features, represented in terms of their geometric shape. Disk parametrisation was used to detect the greater trochanter and femoral head, while the annulus parametrisation was used to detect the lesser trochanter. Though not used in this work, multiple such parametrisations can be used to further decrease area distortion related registration errors[32]. Further avenues for improvements that will be explored in the future include using features like the trochanteric fossa, fovea capitis and the greater trochanteric process. Geodesics between features (e.g. inter-trochanteric line) can be used to improve co-registration between shapes in the inter-feature regions to estimate the closest anatomical correspondence.

The developed method was applied to investigate morphological adaptations in the proximal femur in response to long-term exercise loading. The 3D distribution of the cortical thickness was contrasted between five exclusive exercise loading groups and controls. Analysing its distribution over the surface helped localise the regions, in terms of coloured patches of surface node clusters, where the response was significant in comparison to controls. Thus, the present study complements the inferences drawn from previous studies with this data[1,2,24,40]. The HI and OI groups showed large clusters, while the HM and RI groups showed small clusters. The RNI group showed no significant response. In the HI group the clusters were broadly in the inferior, anterior and posterior regions of the femoral neck; at and below the lateral aspect of the greater trochanter and in the proximal diaphysis below the inter trochanteric line. In the OI group, smaller patches were observed in the femoral neck region and the proximal diaphysis, the regions mostly coincident with those of HI group. The HM group showed much smaller clusters but they were located in the superior and supero-anterior sector of the femoral neck. The RI group had a single cluster located at the lateral side of the greater trochanter process. In terms of cortical thickness, the results clearly indicate that the HI and OI groups demonstrate spatially diverse response. The composite map in Fig. 6a, maps identified clusters to the specific exercise loading group or their combinations.

Similar analysis of the maximum and minimum principal strains at the surface nodes extracted from a simulation study revealed large response regions in the HI and RI groups. Smaller regions were observed in the OI and HM groups, while the RNI group did not differ from the controls. The composite images in Fig. 6b,c shows that the response in the RI group is spatially distributed around most of the femoral neck. In the HI group, the response in the femoral neck is predominantly in the inferior and posterior regions. Interestingly, the OI and HM group showed very little response. When comparing with the results of octant analysis of von Mises stresses performed by Abe *et al.*[24], the present results suggest that the OI group do not differ from controls in terms of principal strain. The discrepancy in the OI group between the present and earlier study may be due to the fact that only the surface strains were studied here while the previous study analyses stresses through volume aggregates within octant sectors. Thus in the future a more comprehensive study will be conducted for volume averaged stress and strain maps. Nevertheless, the surface stain maps illustrate an apparent increase in robustness due to repetitive loading activity (RI group), seemingly achieved without an associated increase in cortical thickness. This is in line with the results reported in the study by Abe *et al.*[24], and based on the cross-sectional shape differences for this group reported by Narra *et al.*[2], it likely points to the role of curvature of the cortical shell in the improved performance. Thus, the procedure of mapping FE simulation results, enhances the ability to explore and localise significant patterns in the distribution of mechanically relevant features.

The method developed and the case study have limitations that ultimately temper the derived statistical inferences. The relatively low in-plane resolution of the MR images, while shown to be sufficient for the analysis of the entire femoral neck cross-section[26], precludes drawing conclusions in regions with very thin cortices locally (e.g. femoral head and some femoral neck regions). In addition, the highly adaptive trabecular bone which plays a significant role in buttressing the thin cortical shells in the proximal femur were not included in this analysis. Thus, the results should not be interpreted as an exhaustive study of the total adaptive response due to each of the loading types. The analyses should be read within the context of purely geometric changes in the cortical shell due to long-term habitual exercise. In the registration task, manual annotations on a sample subset illustrated the insufficiency of the conformal method in accommodating anisotropic shape differences. While the isometric invariance of the method mapped all annotations into clusters, the spread of these clusters indicates the anisometric deformations between shapes (Fig. 2a). These deformations were only explicitly handled at the three algorithmically detected features (LT, GT and FH), which may be insufficient to establish precise correspondence in the inter-feature regions. Moreover, these three features do not necessarily represent anatomical features, as their detection was performed in terms of the surface geometry. Residual errors in terms of true anatomical homology probably persist (Fig. 2b). Sliding semilandmarks-based[41] procedures can be used to improve correspondence in the vicinity of identifiable features. They typically require manual annotations of specific sites, which can

potentially be extended to work with features detected on the parametrised surface. Alternatively, best-fit based local searches can be implemented to account for anisometries in the inter-feature regions to increase the accuracy in correspondence. Similarity metrics such as mean curvature and conformal factor (i.e. area distortion) can be used[32]. It should be noted that there are faster tools based on ICP that can be used to establish acceptably imprecise correspondence. However, they introduce limited arbitrariness due to the reliance on the initial pose estimation and are susceptible to noise in the surface. The conformal map approach to the issue of shape matching has many appealing qualities, foremost among which are: (1) consistency in the treatment of surfaces regardless of initialization, surface noise and isometric deformations; (2) utility in registering incomplete anatomies without a need for either fine tuning initial pose or enforcing constraints. We demonstrated an unexplored application of conformal mapping to the proximal femur where distinct features are few. Its potential can be realised by employing more sophisticated 2D matching processes of the parametrised meshes (2D registration) to improve correspondence in the inter-feature regions. Thus, the present method can be used to address specific challenges posed by data collection such as incomplete surface data and anatomies with sparse features.

References

1. Nikander, R. *et al*. Targeted exercises against hip fragility. *Osteoporosis International* **20**, 1321–1328, https://doi.org/10.1007/s00198-008-0785-x (2009).
2. Narra, N., Nikander, R., Viik, J., Hyttinen, J. & Sievänen, H. Femoral neck cross-sectional geometry and exercise loading. *Clinical Physiology and Functional Imaging* **33**, 258–266, https://doi.org/10.1111/cpf.12022 (2013).
3. Kannus, P. *et al*. Effect of starting age of physical activity on bone mass in the dominant arm of tennis and squash players. *Annals of Internal Medicine* **123**, 27–31, https://doi.org/10.7326/0003-4819-123-1-199507010-00003 (1995).
4. Boskey, A. L. & Coleman, R. Aging and bone. *Journal of Dental Research* **89**, 1333–1348 (2010).
5. Ruff, C., Holt, B. & Trinkaus, E. Who's afraid of the big bad wolff?: "wolff's law" and bone functional adaptation. *American Journal of Physical Anthropology* **129**, 484–498, https://doi.org/10.1002/ajpa.20371 (2006).
6. Warden, S. J. & Mantila Roosa, S. M. Physical activity completed when young has residual bone benefits at 94 years of age: a within-subject controlled case study. *Journal of Musculoskeletal and Neuronal Interactions* **14**, 239–243 (2014).
7. Nordström, A. *et al*. Bone loss and fracture risk after reduced physical activity. *Journal of Bone and Mineral Research* **20**, 202–207, https://doi.org/10.1359/jbmr.041012 (2004).
8. Allison, S. J. *et al*. The influence of high-impact exercise on cortical and trabecular bone mineral content and 3D distribution across the proximal femur in older men: A randomized controlled unilateral intervention. *Journal of Bone and Mineral Research* **30**, 1709–1716, https://doi.org/10.1002/jbmr.2499 (2015).
9. Boreham, C. A. G. & McKay, H. A. Physical activity in childhood and bone health. *British Journal of Sports Medicine* **45**, 877–879, https://doi.org/10.1136/bjsports-2011-090188 (2011).
10. Ruff, C. & Larsen, C. *Long Bone Structural Analyses And The Reconstruction Of Past Mobility: A Historical Review*. (Springer, US, 2014; 13–29.
11. Ito, K., Minka-II, M.-A., Leunig, M., Werlen, S. & Ganz, R. Femoroacetabular impingement and the cam-effect. *Bone & Joint Journal* **83-B**, 171–176, https://doi.org/10.1302/0301-620X.83B2.11092 (2001).
12. Mayhew, P. M. *et al*. Relation between age, femoral neck cortical stability, and hip fracture risk. *Lancet* **366**, 129–135 (2005).
13. Carballido-Gamio, J. & Nicolella, D. P. Computational anatomy in the study of bone structure. *Current Osteoporosis Reports* **11**, 237–245, https://doi.org/10.1007/s11914-013-0148-1 (2013).
14. Friston, K. J. *et al*. Statistical parametric maps in functional imaging: A general linear approach. *Human Brain Mapping* **2**, 189–210, https://doi.org/10.1002/hbm.460020402 (1994).
15. Treece, G. M., Gee, A. H., Mayhew, P. M. & Poole, K. E. High resolution cortical bone thickness measurement from clinical CT data. *Medical Image Analysis* **14**, 276–290 (2010).
16. Poole, K. E. *et al*. Cortical thickness mapping to identify focal osteoporosis in patients with hip fracture. *PLoS One* **7**, e38466, https://doi.org/10.1371/journal.pone.0038466 (2012).
17. Johannesdottir, F., Turmezei, T. & Poole, K. E. Cortical bone assessed with clinical computed tomography at the proximal femur. *Journal of Bone and Mineral Research* **29**, 771–783 (2014).
18. Rusinkiewicz, S. & Levoy, M. Efficient variants of the ICP algorithm. In *Proceedings Third International Conference on 3-D Digital Imaging and Modeling*, 145–152, https://doi.org/10.1109/IM.2001.924423 (2001).
19. Chow, B. & Luo, F. Combinatorial Ricci flows on surfaces. *Journal of Differential Geometry* **63**, 97–129, https://doi.org/10.4310/jdg/1080835659 (2003).
20. Jin, M., Kim, J., Luo, F. & Gu, X. Discrete surface Ricci flow. *IEEE Transactions on Visualization and Computer Graphics* **14**, 1030–1043 (2008).
21. Zeng, W., Samaras, D. & Gu, D. Ricci flow for 3D shape analysis. *IEEE Transactions on Pattern Analysis and Machine Intelligence* **32**, 662–677, https://doi.org/10.1109/TPAMI.2009.201 (2010).
22. Wang, Y. *et al*. Brain surface conformal parameterization with the Ricci flow. *IEEE Transactions on Medical Imaging* **31**, 251–264 (2012).
23. Zeng, W., Shi, R., Su, Z. & Gu, D. X. *Colon Surface Registration Using Ricci Flow*. (Springer, US, Boston, MA, 2014; 389–419.
24. Abe, S. *et al*. Exercise loading history and femoral neck strength in a sideways fall: A three-dimensional finite element modeling study. *Bone* **92**, 9–17, https://doi.org/10.1016/j.bone.2016.07.021 (2016).
25. Nikander, R., Sievänen, H., Heinonen, A. & Kannus, P. Femoral neck structure in adult female athletes subjected to different loading modalities. *Journal of Bone and Mineral Research* **20**, 520–528, https://doi.org/10.1359/JBMR.041119 (2005).
26. Sievänen, H., Karstila, T., Apuli, P. & Kannus, P. Magnetic resonance imaging of the femoral neck cortex. *Acta Radiologica* **48**, 308–314, https://doi.org/10.1080/02841850601182147 (2007).
27. Corsini, M., Cignoni, P. & Scopigno, R. Efficient and flexible sampling with blue noise properties of triangular meshes. *IEEE Transactions on Visualization and Computer Graphics* **18**, 914–924, https://doi.org/10.1109/TVCG.2012.34 (2012).
28. Bernardini, F., Mittleman, J., Rushmeier, H., Silva, C. & Taubin, G. The ball-pivoting algorithm for surface reconstruction. *IEEE Transactions on Visualization and Computer Graphics* **5**, 349–359, https://doi.org/10.1109/2945.817351 (1999).
29. Zilske, M., Lamecker, H. & Zachow, S. Adaptive remeshing of non-manifold surfaces. In Mania, K. & Reinhard, E. (eds) *Eurographics 2008 - Short Papers* (The Eurographics Association, 2008). https://doi.org/10.2312/egs.20081013.
30. Zeng, W. & Gu, X. D. *Ricci Flow for Shape Analysis and Surface Registration: Theories, Algorithms and Applications* (Springer Publishing Company, Incorporated, 2013).
31. Hamilton, R. S. The Ricci flow on surfaces. *Contemporary Mathematics* **71**, 237–262, https://doi.org/10.1090/conm/071 (1988).
32. Zeng, W. *et al*. 3D non-rigid surface matching and registration based on holomorphic differentials. In *The 10th European Conference on Computer Vision* (Pittsburgh, PA, 2008).
33. Harmon, E. H. The shape of the hominoid proximal femur: a geometric morphometric analysis. *Journal of Anatomy* **210**, 170–185, https://doi.org/10.1111/j.1469-7580.2006.00688.x (2007).

34. Fornefett, M., Rohr, K. & Stiehl, H. Radial basis functions with compact support for elastic registration of medical images. *Image and Vision Computing* **19**, 87–96, https://doi.org/10.1016/S0262-8856(00)00057-3 (2001).
35. Worsley, K. J., Taylor, J. E., Tomaiuolo, F. & Lerch, J. Unified univariate and multivariate random field theory. *NeuroImage* **23**, S189–S195, https://doi.org/10.1016/j.neuroimage.2004.07.026, Mathematics in Brain Imaging (2004).
36. Gee, A. H. & Treece, G. M. Systematic misregistration and the statistical analysis of surface data. *Medical Image Analysis* **18**, 385–393, https://doi.org/10.1016/j.media.2013.12.007 (2014).
37. Treece, G. M. *et al*. Predicting hip fracture type with cortical bone mapping (CBM) in the osteoporotic fractures in men (MrOS) study. *Journal of Bone and Mineral Research* **30**, 2067–2077, https://doi.org/10.1002/jbmr.2552 (2015).
38. Poole, K. E. *et al*. Focal osteoporosis defects play a key role in hip fracture. *Bone* **94**, 124–134, https://doi.org/10.1016/j.bone.2016.10.020 (2017).
39. Väänänen, S. P. *et al*. Assessment of the 3-D shape and mechanics of the proximal femur using a shape template and a bone mineral density image. *Biomechanics and Modeling in Mechanobiology* **10**, 529–538 (2011).
40. Niinimäki, S. *et al*. The relationship between loading history and proximal femoral diaphysis cross-sectional geometry. *American Journal of Human Biology* **29**, e22965–n/a, https://doi.org/10.1002/ajhb.22965.E22965 (2017).
41. Adams, D., Collyer, M., Kaliontzopoulou, A. & Sherratt, E. Geomorph: Software for geometric morphometric analyses. r package version 3.0.5, https://cran.r-project.org/package=geomorph (2017).

Acknowledgements

The authors would like to thank Prof. X. Gu for guidance in understanding the implementation aspects of the Ricci-flow algorithm. The authors would like to acknowledge the following sources of funds that made this work feasible: Tampere University of Technology - Graduate School (Shinya Abe); NSERC, Canada (Vassil Dimitrov).

Author Contributions

N.N., V.D. and J.H. designed the study; N.N., V.D. and S.A. collected data and developed the procedure; R.N., R.K., H.S. and J.H. analysed the results. N.N., H.S. and J.H. wrote the manuscript text. All authors reviewed the manuscript.

Additional Information

Competing Interests: The authors declare no competing interests.

Publisher's note: Springer Nature remains neutral with regard to jurisdictional claims in published maps and institutional affiliations.